# THE CHARACTERISATION OF ANTENNAS AND TEST SITES FOR THE MEASUREMENT OF RADIATED EMISSIONS

Simon Michael Mann

Submitted for the degree of Doctor of Philosophy

University of York
Department of Electronics

February 1993

# Contents

# List of Figures

# List of Tables

# Acknowledgements

First of all I would like to thank my supervisor, Dr. Andy Marvin, for his help and guidance with the experimental and practical work contained herein. Thanks also are due for his constructive criticism during the preparation of this thesis. I would like to point out that, since paper is made from trees, this thesis has actually been written on wood.

I am very grateful to my partner, Dr. Naomi Jarvis, for her help proof reading and translating my dreadful grammar into reasonably well flowing prose. I would also like to thank her for her encouragement and support during the sometimes painful preparation of this thesis.

Finally I would like to thank my colleagues: Dr. Stuart Porter, for his help with the NEC computer code, and Dr. Theo Carr-Brion for writing the data acquisition software used for the experimental work in this thesis.

# Declaration

Portions of the work reported in this thesis have been published previously in the papers below.

1. S. M. Mann and A. C. Marvin. "The measurement and use of ground plane reflection coefficients for improving the accuracy of radiation measurements using open-field test sites." *1991 British Electromagnetics Conference.* National Physical Laboratory, Teddington, Middlesex.

2. S. M. Mann and A. C. Marvin. "A computer study of the calibration of the skeletal biconical antenna and the resonant dipole antenna." *IEE colloquium on "Radiated Emission Test Facilities."* 2nd June 1992.

The following two papers were written on related works by the author during the preparation of this thesis:

3. L. Dawson, S. M. Mann and A. C. Marvin. "A statistical description of field uniformity and its effect on the measured immunity of an equipment under test." *IEE colloquium on "The Role of Statistics in EMC Specification, Design and Clearance."* 13th May 1992.

4. L. Dawson, S. M. Mann and A. C. Marvin. "Some measurements of field uniformity within commonly used environments for radiated susceptibility testing." *8th IEE Int. conf. EMC*, Herriot Watt University, Edinburgh, U.K., 21–24 September 1992.

The author was also involved in the preparation of the following paper:

5. A. C. Marvin, J. M. Tealby, T. J. F. Carr-Brion, S. J. Porter and S. M. Mann. "Computer aided design for radio-frequency interference reduction." *7th IEE Int. conf. EMC*, University of York, York, U.K., 28–31 August 1990.

These papers are appended to the thesis.

# Abstract

This thesis describes theoretical and experimental work carried out to investigate the use of antennas for the characterisation of open-area test sites. Particular emphasis is placed upon the use of classical site attenuation and a novel technique is presented for the measurement of ground plane reflection coefficients.

The work was performed using resonant dipole and skeletal biconical antennas and these were characterised by modelling with the Numerical Electromagnetics Code (NEC). An optimised model is developed for the skeletal biconical antenna by comparing its predicted drive-point impedance with the measured drive-point impedance. A novel calibration technique is used to measure the scattering parameters of the balun of this antenna and they are combined with the NEC simulation to give a model of the complete real antenna.

NEC is used to predict classical site attenuations between resonant dipoles in various geometries and these are compared with the less rigorous predictions calculated using the applied EMF method and a simple optical propagation model similar to those used by EMC standards. It is found that a simple optical propagation model may be in error by up to 4 dB below 60 MHz, 2 dB between 60 MHz and 200 MHz and by 1 dB above 200 MHz. The applied EMF method is found to give predictions always within 0.6 dB of NEC.

Normalised site attenuation has been introduced by EMC standards to allow the use of broadband antennas. This is shown to cause site attenuation measurement procedures to give misleading results that depend more upon antenna calibration and the accuracy of the propagation models used than upon the characteristics of the test site under investigation. This thesis presents a method that allows a broadband measurement of classical site attenuation with skeletal biconical antennas to be compared with predictions that are accurate to within 1 dB. This permits rigorous test site characterisation.

# Introduction

## Electromagnetic Compatibility

Electromagnetic compatibility is that condition in which separate items of electronic equipment are able to carry out their normal functions without interfering with one another. In order to achieve electromagnetic compatibility, any item of equipment must neither produce excessive electromagnetic emissions nor be overly susceptible to any electromagnetic disturbance that it is exposed to. Design for electromagnetic compatibility aims to ensure that an item of equipment satisfies these requirements and standards specify the test procedures that are used for verification.

The work in this thesis is only concerned with radio frequency emissions, of which there are two types that may be generated within an item of electronic equipment. They are conducted emissions, which leave the equipment via its connecting cables, and radiated emissions, which leave as electromagnetic waves in the space around the equipment. This thesis is only concerned with the latter, and with a particular test environment that is used for the measurement of radiated field strengths.

There are three main types of test environment in which radiated emissions are measured. Screened rooms are inexpensive and high field strengths can be used for immunity testing within them because they are self-contained. Unfortunately measurements performed within them may have uncertainty levels as high as 40 dB due to reflections and highly tuned cavity resonances. Anechoic chambers are essentially screened rooms lined with radio frequency absorber material to absorb reflections and damp out resonances. They can give measurement uncertainties as low as 6 dB, but are comparably expensive, and there is usually a frequency around 100 MHz below which their performance becomes degraded due to the absorber materials not being a sufficient proportion of a wavelength thick. The third and final measurement environment is the open-area test site, and forms the subject of this thesis.

Open-area test sites are flat reflecting surfaces above which the equipment un-

der test (EUT) is mounted at a defined height and horizontal separation from a measuring antenna. They are the most accurate test environments and, with good design, should be able to give measurement uncertainties of ±1 dB. The disadvantages of open-area test sites are that they are not self-contained and that their measurement antennas are exposed to radiation from sources other than the EUT. Broadcast radio signals and other interfering signals can saturate receivers and obscure radiation from the EUT.

Open-area test sites are usually used for measurements over the frequency range of 30 MHz to 1 GHz. Linearly polarised electric field antennas of either a biconical or log-periodic type are normally used, with the former usually being used up to 300 MHz and the latter above 300 MHz. Occasionally resonant dipole antennas are used for certain types of measurements, but these are not broadband and have to be mechanically tuned at every frequency. The calibration of these antennas is such that a simple scaling factor, known as the antenna factor, is used to convert their terminal voltages into field strengths.

# Background

Whilst working as a member of the Electromagnetic Compatibility Research Group at the University of York, the author was involved with a project that required measurements to be made using an open-area test site. For the purposes of those measurements, it was necessary to consider the test site to behave in an ideal way. No information was known about the reflectivity of the ground plane or the effect of buildings surrounding the test site upon its propagation characteristics. Test site validation procedures such as the measurement of site attenuation aim to quantify such effects.

Site attenuation is defined as the attenuation between the terminals of two antennas coupled together over the ground plane of an open-area test site. Standards specify that the site attenuation of a given test site must be shown to be within ±4 dB of predictions for the same antennas over an ideal test site. This figure allows 1 dB of error for the calibration of each antenna, 1 dB of propagation error over the site and 1 dB of error in the calculation of the predicted site attenuation with an ideal site. Clearly it is difficult to quantify propagation problems from this procedure since any measurement could have up to 3 dB of error introduced from other sources.

Apart from the problem mentioned above, the author became concerned about whether the theoretical models used for the derivation of predicted site attenuations

were capable of giving accuracy of 1 dB, or if antenna calibrations were sufficiently accurate to give only 1 dB of uncertainty. This thesis investigates such concepts and proposes improved validation procedures for open-area test sites.

## Aims and Objectives

The first aim of this thesis was to analyse current procedures used for test site validation and determine the factors affecting their accuracy. It was then intended to develop practical alternative procedures that could give more insight into the characteristics of a given real open-area test site.

Before test site validation procedures could be developed it was intended to characterise the antennas that were to be used accurately so that attenuation could be calculated between them on an ideal open-area test site. Once this had been done, the accuracy of current procedures for calculating predicted attenuations was to be deduced by comparing their results with the more rigorous models.

Finally, it was intended to apply the newly developed rigorous validation procedures to the open-area test site at the University of York to find how close its performance was to that of an ideal open-area test site. This was to include deducing the effects of the buildings surrounding it and also the non-ideal nature of its ground plane.

## Literature

This thesis grew out of a project to develop computer aided design tools for the prediction of radiated emissions from data processing equipment. These emissions were required to be predicted on an open-area test site and therefore a literature search on the subject of open-area test sites was conducted using the IEE's INSPEC data base. The citations from these papers were used to obtain other papers of interest and many useful papers were also found from a scan of recent IEEE transactions.

The resonant dipole antenna is well-understood and is discussed by most good antenna textbooks, as is the infinite biconical antenna. Very little literature has been found upon the skeletal biconical antenna and its development appears to have been largely empirical. Antenna calibration procedures are described in EMC standards and a variety of papers have been located that describe improvements and corrections that can be applied to them.

Several papers have also been located upon the subject of site attenuation

but they have all been either only for resonant dipole antennas or for the use of a normalised site attenuation formulation with broadband antennas. This thesis presents a classical site attenuation formulation that may be used with broadband antennas.

## Structure of the Thesis

The main body of this thesis has been divided into six chapters, with a seventh chapter summarising the overall conclusions. The contents of each individual chapter have been organised in the following way:

**Chapter 1** describes propagation of electromagnetic waves over an ideal open-area test site and presents theory to describe the fields set up by infinitesimal dipoles above a perfect ground plane. Design considerations necessary to produce a perfect ground plane are contrasted with the design of the open-area test site at the University of York in order to predict its performance. The theoretical predictions are used to deduce the dipole moment of an electrically small noise source from its measured fields.

**Chapter 2** presents theory to describe the resonant dipole and skeletal biconical antennas in terms of their drive-point impedances. The resonant dipole is a well-understood antenna and is analysed using the applied EMF method and Numerical Electromagnetics Code (NEC). Predictions from both models are compared with measurements in order to gain confidence in the modelling tools. The skeletal biconical antenna has not been rigorously characterised by previous authors and NEC is used to develop a suitable model that is used for the investigation of its electrical characteristics. The predicted performance of this antenna is contrasted with that of the resonant dipole in order to deduce their relative merits and shortcomings. Finally, the NEC model is optimised to give predicted drive-point impedances as close to measurement as possible over the 30–300 MHz frequency range.

**Chapter 3** introduces the concept of site attenuation as a validation tool for open-area test sites. The attenuation between two antennas over an open-area test site is first calculated from a geometrical optics approach, similar to the one used by current EMC standards, then a more rigorous model is presented using the applied EMF method for resonant dipole antennas to formulate the loss in terms of self and mutual impedances. An analogous formulation is then developed in terms of scattering parameters that are obtained from a NEC

simulation of the two antennas over a test site. A new method is then used to combine the measured scattering parameters of the baluns of both antennas with the NEC simulation to give accurately calculated values of classical site attenuation. This allows a more rigorous comparison of measured and predicted site attenuations than has been possible to date.

**Chapter 4** extends upon the modelling work of chapter 2 in order to calculate the antenna factors of the resonant dipole and skeletal biconical antennas. These are known to vary as a function of antenna height above a ground plane and the limits of these variations have been calculated by previous authors for the resonant dipole but not for the skeletal biconical antenna. The chapter also describes the techniques used for the measurement of the drive-point impedances of both antennas and a novel calibration procedure that was used to measure the scattering parameters of the balun of the skeletal biconical antenna. These scattering parameters were incorporated with the optimised NEC model of the biconical antenna in order to develop a numerical model of the complete real antenna.

**Chapter 5** contrasts the results from the three different models that were used in chapter 3 to calculate the site attenuation between resonant dipoles. Previous authors have used these three models; however, their results have not been rigorously compared before under all test site conditions. This chapter compares results obtained using the geometrical optical and the applied EMF methods with those from NEC in order to deduce their respective limitations. Measurements of site attenuation with resonant dipoles over the York test site are compared with predictions in order to characterise the site at the frequencies specified by EMC standards, then a novel broadband measurement is performed using skeletal biconical antennas to give continuous site attenuation data over the 30–300 MHz frequency range.

**Chapter 6** presents a novel technique that can be used to measure the reflection coefficient of the ground plane of an open-area test site. The method combines image theory with measurements of the drive-point impedance of a resonant dipole in order to deduce the quality of a given ground plane. The technique is applied to the test site at the University of York and is shown to be able to deduce the effect of a truncated ground plane at the lower frequencies of test site operation.

**Chapter 7** gives the overall conclusions of the thesis. These are that current test site validation procedures advocated by EMC standards give misleading results. This is because inappropriate antenna calibration procedures and poor theoretical models are likely to give larger errors than the propagation non-idealities of the test sites under investigation. This necessitates a return to classical site attenuation based procedures but need not rule out the use of broadband antennas. This thesis has shown that accurate predicted values of classical site attenuation may be calculated between broadband antennas using the NEC computer code and the measured scattering parameters of their baluns.

# Chapter 1

# The Open-Area Test Site

Open-area test sites (OATS) represent potentially accurate and repeatable measurement environments in which radiated emissions from electronic equipment may be observed and measured. Ideally an OATS is simply the volume of space above a flat ground plane in which a radiating source and instrumentation for the measurement of fields from it are contained. The environment has apparently simple theoretical behaviour with point sources and sinks of radiation, but real electromagnetic sources and measurement antennas behave in a much more complicated way as this thesis will show.

At first, open-area test sites were constructed with a variety of ground plane designs, of which some were poor conductors such as tarmac or concrete. It was soon realised that measurements that were repeatable on other test sites could not be made over these types of ground plane [1]. A more detailed examination of the size of flat ground plane required and how flat it should be was carried out by Dvorak and Meyer [2]; and they and several other authors [3], [4] also considered propagation over ground planes of finite conductivity by using image theory. Polarisation rotation effects due to different direct and reflected wave path lengths were investigated by Dvorak [5], and shown to cause measured radiation in a specific polarisation to not be representative of radiation from an equipment under test (EUT) in that polarisation. Bennett [6] investigated the conditions required for radiation measurements to be made in the far field of a finite sized EUT and explained how measurement distances must increase for larger EUTs.

In this chapter, §1.1 introduces theory to describe the fields that are set up above the ground plane of an OATS by infinitesimal dipoles. The resulting plots of field strength are used to investigate the way that direct and reflected waves propagate over an OATS. After propagation has been discussed over an ideal test site, the design considerations affecting a real test site are discussed with particular reference to the one at the University of York. Aspects such as ground plane design

with a truncated metal mesh are discussed and some brief performance predictions are made so that confidence can be had in measurements made in this thesis using the test site. Finally, in §1.3 the radiation from a small source of broadband noise is measured using the test site and conclusions are drawn about site performance and the dipole moment of the source.

## 1.1 The Ideal Open-Area Test Site

An ideal open-area test site is the infinite half-space above a flat, perfectly conducting surface. Within the half-space are a source and a sink of electromagnetic radiation at a defined horizontal separation and each at a defined height above the conducting surface. These three dimensions define a given test site and figure 1.1 shows the symbols that are used in this thesis to define it.

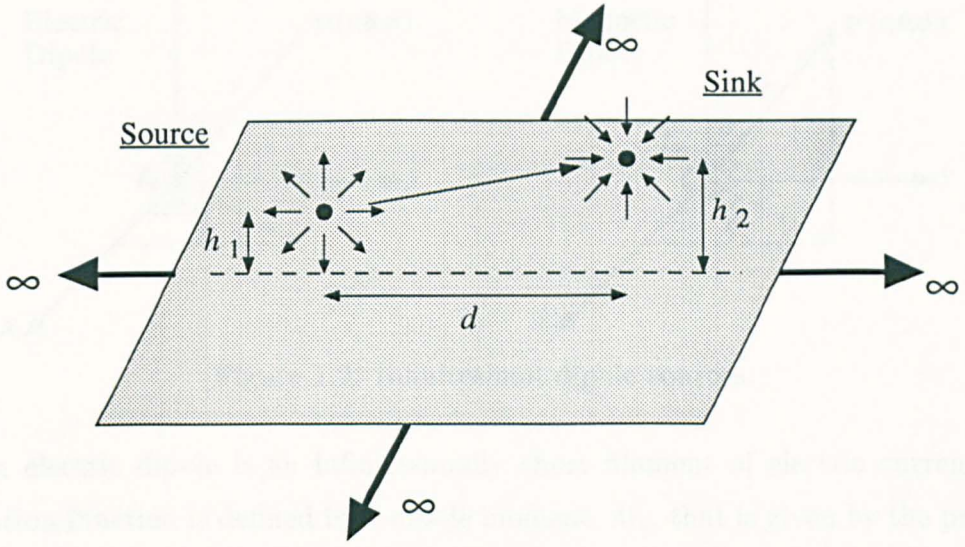


Figure 1.1: An ideal open-area test site

| | |
|---|---|
| $d$ | Horizontal separation of the EUT and antenna. |
| $h_1$ | Height of the EUT above the conducting surface. |
| $h_2$ | Height of the measuring antenna. |

When an OATS is used as a radiation measurement environment, the source of electromagnetic radiation is an equipment under test (EUT) and the sink is an antenna that is used to measure the field.

The conducting surface beneath the open-area test site is known as the ground plane, and acts as a reflector so that there are two paths by which radiation travels from the EUT to the measurement antenna; one wave propagates directly, whilst the other is reflected off the ground plane. The field strength at the receiving antenna is therefore the sum of these two waves, i.e.

$$E_t = E_d + E_r \tag{1.1}$$

where $E_t$ is the total wave at the receiving antenna, $E_d$ is the direct wave and $E_r$ is the reflected wave. In order to appreciate the significance of (1.1) it is necessary to consider the behaviour of real sources of electromagnetic radiation over an open-area test site.

### 1.1.1 Infinitesimal Dipole Antennas

The simplest types of real sources of electromagnetic radiation are known as infinitesimal dipoles. These are vanishingly small current carrying elements and exist in two different forms: electric dipoles and magnetic dipoles. Figure 1.2 shows the physical characteristics of these sources.

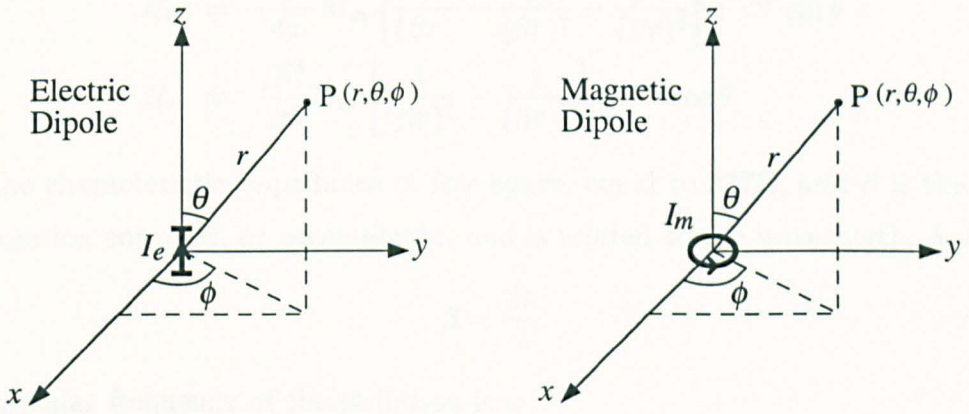


Figure 1.2: Infinitesimal dipole sources.

An electric dipole is an infinitesimally short filament of electric current. Its excitation function is defined by a dipole moment, $M_e$, that is given by the product of its current and length. A magnetic dipole is an infinitesimally small loop of current and has a dipole moment, $M_m$, given by the product of its current and the loop area.

$$M_e = I_e \cdot \delta l \quad \text{Am} \tag{1.2}$$

$$M_m = I_m \cdot \delta A \quad \text{Am}^2 \tag{1.3}$$

The field components from both of these sources can be found in a spherical polar coordinate system by a consideration of their vector potential [7], [8] hence their field components can be found on an open-area test site.

#### The Electric Dipole

The field components due to an infinitesimal electric dipole, at an observation point P, having the spherical polar coordinates $(r, \theta, \phi)$ in free space are:

$$E_\theta = \frac{j\eta\beta^2}{4\pi} M_e \left[ \frac{1}{(\beta r)} - \frac{j}{(\beta r)^2} - \frac{1}{(\beta r)^3} \right] e^{-j\beta r} \sin\theta \tag{1.4}$$

$$E_r = \frac{\eta\beta^2}{2\pi} M_e \left[ \frac{1}{(\beta r)^2} - \frac{j}{(\beta r)^3} \right] e^{-j\beta r} \cos\theta \tag{1.5}$$

$$H_\phi = \frac{j\beta^2}{4\pi} M_e \left[ \frac{1}{(\beta r)} - \frac{j}{(\beta r)^2} \right] e^{-j\beta r} \sin\theta \tag{1.6}$$

### The Magnetic Dipole

The field components due to an infinitesimal magnetic dipole, at an observation point P, having the spherical polar coordinates $(r, \theta, \phi)$ in free space are:

$$E_\phi = \frac{\eta\beta^3}{4\pi} M_m \left[\frac{1}{(\beta r)} - \frac{j}{(\beta r)^2}\right] e^{-j\beta r} \sin\theta \tag{1.7}$$

$$H_\theta = \frac{-\beta^3}{4\pi} M_m \left[\frac{1}{(\beta r)} - \frac{j}{(\beta r)^2} - \frac{1}{(\beta r)^3}\right] e^{-j\beta r} \sin\theta \tag{1.8}$$

$$H_r = \frac{j\beta^3}{2\pi} M_m \left[\frac{1}{(\beta r)^2} - \frac{j}{(\beta r)^3}\right] e^{-j\beta r} \cos\theta \tag{1.9}$$

$\eta$ is the characteristic impedance of free space, equal to $377\Omega$, and $\beta$ is the phase propagation constant, or wavenumber, and is related to the wavelength, $\lambda$, by

$$\beta = \frac{2\pi}{\lambda} \tag{1.10}$$

The angular frequency of the radiation is $\omega$.

## 1.1.2 Analysis of the Field Components

Equations (1.4) to (1.9) give the magnitude of the field components from infinitesimal dipole sources but there is also an implicit $e^{j\omega t}$ factor that has been omitted and expresses the time dependence of the fields.

Equations (1.4) to (1.9) can be seen to contain several different types of terms within their square brackets; these describe separate elements that sum together to make up the total field component. In general, all of these terms contribute to the field, but at certain distances from the source some of the terms dominate and others become negligible according to whether the value of $\beta r$ is greater than or less than unity.

The Poynting vector, S, describes the flow of power in the field and is given by

$$\mathbf{S} = \mathbf{E} \times \mathbf{H}$$

From this it can be seen that the Poynting vector is at right angles to the plane containing **E** and **H** and so its magnitude and direction are also affected by changes in the value of $\beta r$. The following three regions in which the fields have different characteristics can be identified:

**Near Field.** This region is usually taken to extend away from the source up to a distance of $\lambda/10$, i.e. to where $\beta r = \pi/5$. Here the terms in $1/\beta r$ to the higher powers tend to dominate so that the electric field becomes mostly radially directed and the Poynting vector tends to circulate around the current

element. This corresponds to stored energy rather than radiated energy and is termed the near field of the source.

**Transition Field.** This extends from $\lambda/10$ away from the source up to $3\lambda$ from it. In this region all the terms in equations (1.4) to (1.9) are significant and so both near and far field properties are present.

**Far Field.** This is taken to extend from $3\lambda$ away from the source to infinity and therefore the terms in $1/\beta r$ dominate. The electric and magnetic field components then become purely $\theta$ and $\phi$-directed so that the Poynting vector is directed away from the source. Power flow is therefore away from the source and this is the radiation field.

### 1.1.3 Ground Plane Analysis by the Method of Images

The method of images [9] offers a convenient way for analysing structures above ground planes because it enables the ground plane to be replaced by an image of the structures above it. The image structure is the same distance below the ground plane as the object is above it and so the object and image structures may be modelled together as a single combined structure.

A consideration of the boundary conditions at a plane conducting surface shows that the currents on the image structure are equal to those on the object structure multiplied by the reflection coefficient of the ground plane. Figures 1.3 and 1.4 show the equivalent source configurations corresponding to horizontally polarised and vertically polarised infinitesimal electric dipoles above the perfectly conducting ground plane of an ideal open-area test site.

The method of images is strictly only valid for the analysis of structures above perfectly conducting ground planes because of skin depth considerations. A ground plane having a significant skin depth will not have a clearly defined image position due to the current in the ground plane not flowing entirely at the surface. Bannister [10] has suggested adding a complex distance to the image depth as a way of accounting for significant skin depths, but this is only accurate for determining field strengths at distances from the source where grazing angles on the ground plane are small.

The method of images can be used to analyse the characteristics of sources of electromagnetic radiation above the ground planes of open-area test sites because they are designed to be perfectly reflecting. The following two sections show how it can be used to analyse an infinitesimal electric dipole source above a conducting ground plane.

### Horizontal Polarisation

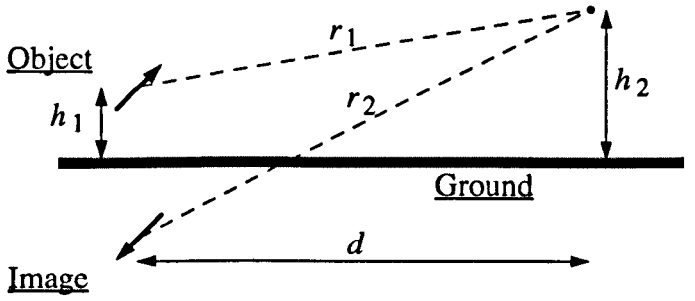


Figure 1.3: Horizontally polarised infinitesimal electric dipole above a conducting ground plane.

In this case the image has a dipole moment in antiphase to that of the object because of the boundary condition that electric field parallel to the ground must become zero at its surface. This implies a ground plane reflection coefficient for horizontally flowing currents of $-1$. The horizontally polarised electric field strength at the observation point can be seen to depend only on the $\theta$-directed components given by (1.4), so that it is given by

$$E_H = E_{\theta 1} - E_{\theta 2} \tag{1.11}$$

where

$$E_{\theta 1} = \frac{j\eta\beta^2}{4\pi} M_e \left[ \frac{1}{(\beta r_1)} - \frac{j}{(\beta r_1)^2} - \frac{1}{(\beta r_1)^3} \right] e^{-j\beta r_1} \tag{1.12}$$

$$E_{\theta 2} = \frac{j\eta\beta^2}{4\pi} M_e \left[ \frac{1}{(\beta r_2)} - \frac{j}{(\beta r_2)^2} - \frac{1}{(\beta r_2)^3} \right] e^{-j\beta r_2} \tag{1.13}$$

and

$$r_1 = \sqrt{d^2 + (h_2 - h_1)^2} \tag{1.14}$$

$$r_2 = \sqrt{d^2 + (h_2 + h_1)^2} \tag{1.15}$$

### Vertical polarisation

The reflection coefficient is $+1$ in this case and so the image current is in phase with the object current. Figure 1.4 shows that the $\theta$ and radially directed components of electric field from both sources contribute to the vertical component at the observation point and so they must be resolved in that direction. Hence

$$E_V = E_{r1}\cos\theta_1 - E_{\theta 1}\sin\theta_1 + E_{r2}\cos\theta_2 - E_{\theta 2}\sin\theta_2 \tag{1.16}$$

The sines and cosines of the angles $\theta_1$ and $\theta_2$ are given by

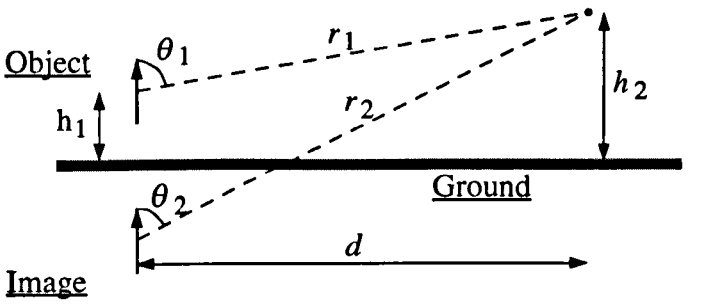


Figure 1.4: Vertically polarised infinitesimal electric dipole above a conducting ground plane.

$$\sin\theta_1 = \frac{d}{r_1} \qquad \cos\theta_1 = \frac{h_2 - h_1}{r_1}$$

$$\sin\theta_2 = \frac{d}{r_2} \qquad \cos\theta_2 = \frac{h_2 + h_1}{r_2}$$

so that

$$E_{r1}\cos\theta_1 = \frac{\eta\beta^2}{2\pi} I_e l \left[\frac{1}{(\beta r_1)^2} - \frac{j}{(\beta r_1)^3}\right]\left(\frac{h_2 - h_1}{r_1}\right)^2 e^{-j\beta r_1} \tag{1.17}$$

$$E_{\theta 1}\sin\theta_1 = \frac{j\eta\beta^2}{4\pi} M_e \left[\frac{1}{(\beta r_1)} - \frac{j}{(\beta r_1)^2} - \frac{1}{(\beta r_1)^3}\right]\left(\frac{d}{r_1}\right)^2 e^{-j\beta r_1} \tag{1.18}$$

$$E_{r2}\cos\theta_2 = \frac{\eta\beta^2}{2\pi} M_e \left[\frac{1}{(\beta r_2)^2} - \frac{j}{(\beta r_2)^3}\right]\left(\frac{h_2 + h_1}{r_2}\right)^2 e^{-j\beta r_2} \tag{1.19}$$

$$E_{\theta 2}\sin\theta_2 = \frac{j\eta\beta^2}{4\pi} M_e \left[\frac{1}{(\beta r_2)} - \frac{j}{(\beta r_2)^2} - \frac{1}{(\beta r_2)^3}\right]\left(\frac{d}{r_2}\right)^2 e^{-j\beta r_2} \tag{1.20}$$

### 1.1.4 Theoretical Results

Computer programs were written incorporating equations (1.11) to (1.20) so that the variation in field strength at an observation point could be examined as a function of position and frequency of excitation of an electric dipole source. Figure 1.5 shows typical results for horizontally and vertically polarised sources, having dipole moments of 1 Am, and at a height of 1 m above the ground plane. The observation point is at a height of 1 m and a horizontal distance of 3 m from the source and the excitation frequencies are from 1 MHz to 1 GHz.

Figure 1.5 shows that there are essentially three frequency ranges of operation in which the ideal test site behaves differently. At low frequencies the field at the observation point falls with increasing frequency, it then passes through a minimum and rises in strength until, above a certain frequency, closely spaced maxima and minima occur alternately. These three regions arise because of the field components

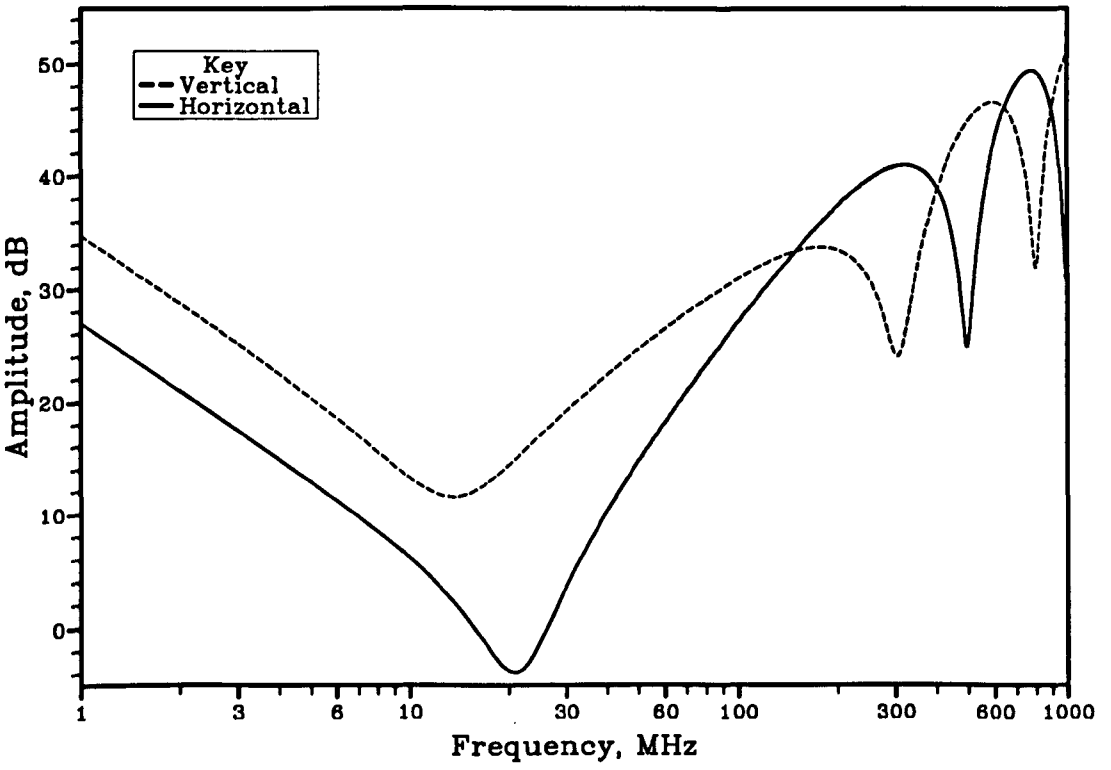


Figure 1.5: Field strength at an observation point due to an electric dipole source having a dipole moment of 1 Am.

described in §1.1.2 and are characterised as described below.

### Quasi-Near Field

The field strength falls at first with increasing frequency for both polarisations because the field components from both the direct and reflected waves are dominated by the $1/(\beta r)^3$ terms of equations (1.4) to (1.6). These terms give a field that is inversely proportional to frequency when multiplied by the $\beta^2$ term in the coefficient of the equations.

At low frequencies, the direct and reflected path lengths are considerably less than a wavelength long, therefore the only significant phase change that occurs during propagation from the source to the observation point is the phase inversion suffered by the reflected wave from a horizontally polarised source on reflection. This causes the direct and reflected waves to sum together in phase with a horizontally polarised source and out of phase with a vertically polarised one. It therefore accounts for the fact that the field at the observation point is some 10 dB higher for vertical polarisation in figure 1.5 below 10 MHz.

This region exists for frequencies where the direct and reflected path lengths

are much shorter than a wavelength, and if a criterion that

$$r_1, r_2 < \frac{\lambda}{2\pi}$$

is selected, the region will extend up to 16 MHz for a 3 m site and 5 MHz for a 10 m site. Most test sites are only used down to 30 MHz and so the influence of this region will be small and only significant for short test sites.

### Quasi-Far Field

For frequencies where the direct and reflected paths are longer than $\lambda/2\pi$, the phase shifts along the paths are no longer negligible. As frequency increases, these phase shifts increase so that the vertically polarised waves begin to cancel out and the horizontally polarised ones cancel out less. Eventually the phase shifts increase to a point where the sum of the direct and reflected waves is equal for both polarisations and this occurs at a frequency where the difference between the direct and reflected path lengths is exactly $\lambda/4$. This occurs where

$$\sqrt{d^2 + (h_1 + h_2)^2} - \sqrt{d^2 + (h_1 - h_2)^2} = \frac{\lambda}{4}$$

and for the test site geometry of figure 1.5, this occurs at a frequency of 124 MHz.

In this region all of the terms of equations (1.4) to (1.6) are significant at lower frequencies, but the terms in $1/(\beta r)$ begin to dominate at higher frequencies so that the field rises and becomes proportional to frequency. The phase change effects of the above paragraph cause the vertically polarised field to increase more slowly than this, whilst the horizontally polarised field increases more rapidly.

### Interference Zone

Where the difference between the direct and reflected path lengths becomes more than a wavelength, the waves alternately reinforce and subtract from each other as frequency increases. This region occurs above approximately 100 MHz on a 3 m site and above 200 MHz on a 10 m site, only the $1/(\beta r)$ terms are significant in equations (1.4) to (1.6).

## 1.1.5 The Interference Pattern

The interference pattern produced between the direct and reflected waves from an infinitesimal electric dipole source was examined as a function of frequency of excitation and observation point height. The dipole was allowed to radiate in both horizontal and vertical polarisations at a height of 68 cm, chosen to coincide with

later measurements in §1.3. The observation point was set at a horizontal distance of 3 m and 10 m and was allowed to vary from 1 cm to 4 m in height. The resulting fields are shown as contour plots in figures 1.6 to 1.9 over the frequency range from 1 MHz to 1 GHz.

The maxima in the interference patterns are broad whereas the minima are much narrower so any field strength measurements made near the minima will be very sensitive to changes in height and hence subject to large measurement errors. It is for this reason that the receiving antenna is scanned through a height range to obtain the maximum field strength when performing radiated emission measurements using open-area test sites. In this way the measurement will always be made away from minima.

The patterns with the shorter, 3 m site length have more maxima and minima than the 10 m patterns. This is because the path lengths of the direct and reflected waves become more similar as site length increases, and so a higher frequency is necessary to obtain the same phase difference between them.

As the height of the observation point tends towards zero, the field tends towards zero with a horizontally polarised source, or to a maximum with a vertically polarised source. This is because the direct and reflected path lengths become equal at zero observation point height, and the phase change on reflection with the horizontally polarised source then gives total cancellation.

At low frequencies, the fields at the observation point are greater with a vertically polarised source than with a horizontally polarised one. This is again due to the phase change on reflection that occurs with horizontal polarisation and explains why vertically polarised measurements are preferred for low frequency measurements with open-area test sites.

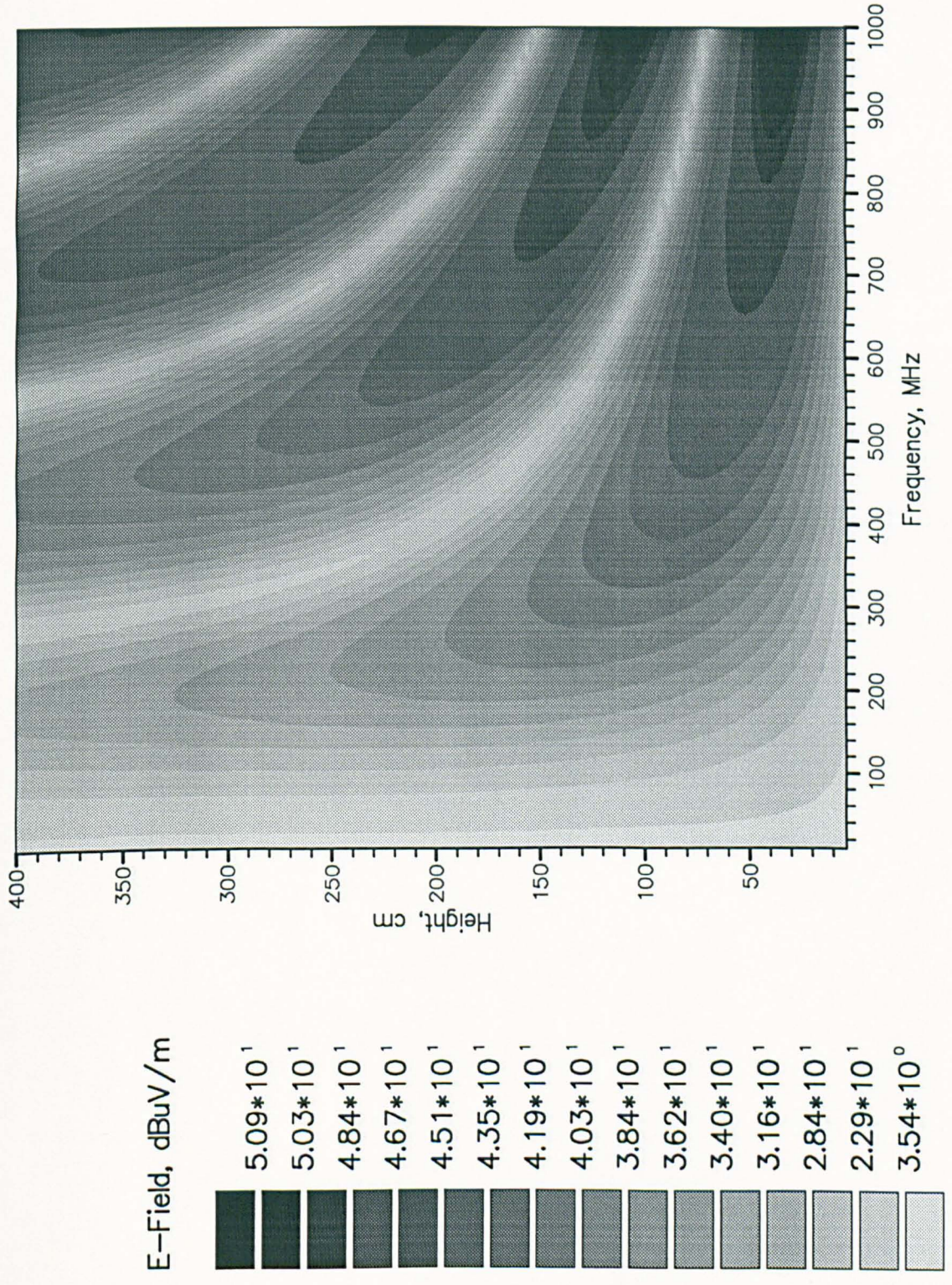


Figure 1.6: Variation of field strength with observation point height and excitation frequency for a horizontally polarised infinitesimal electric dipole source. The source has a dipole moment of 1 Am and is set at a height of 68 cm above the ground plane of a 3 m test site.

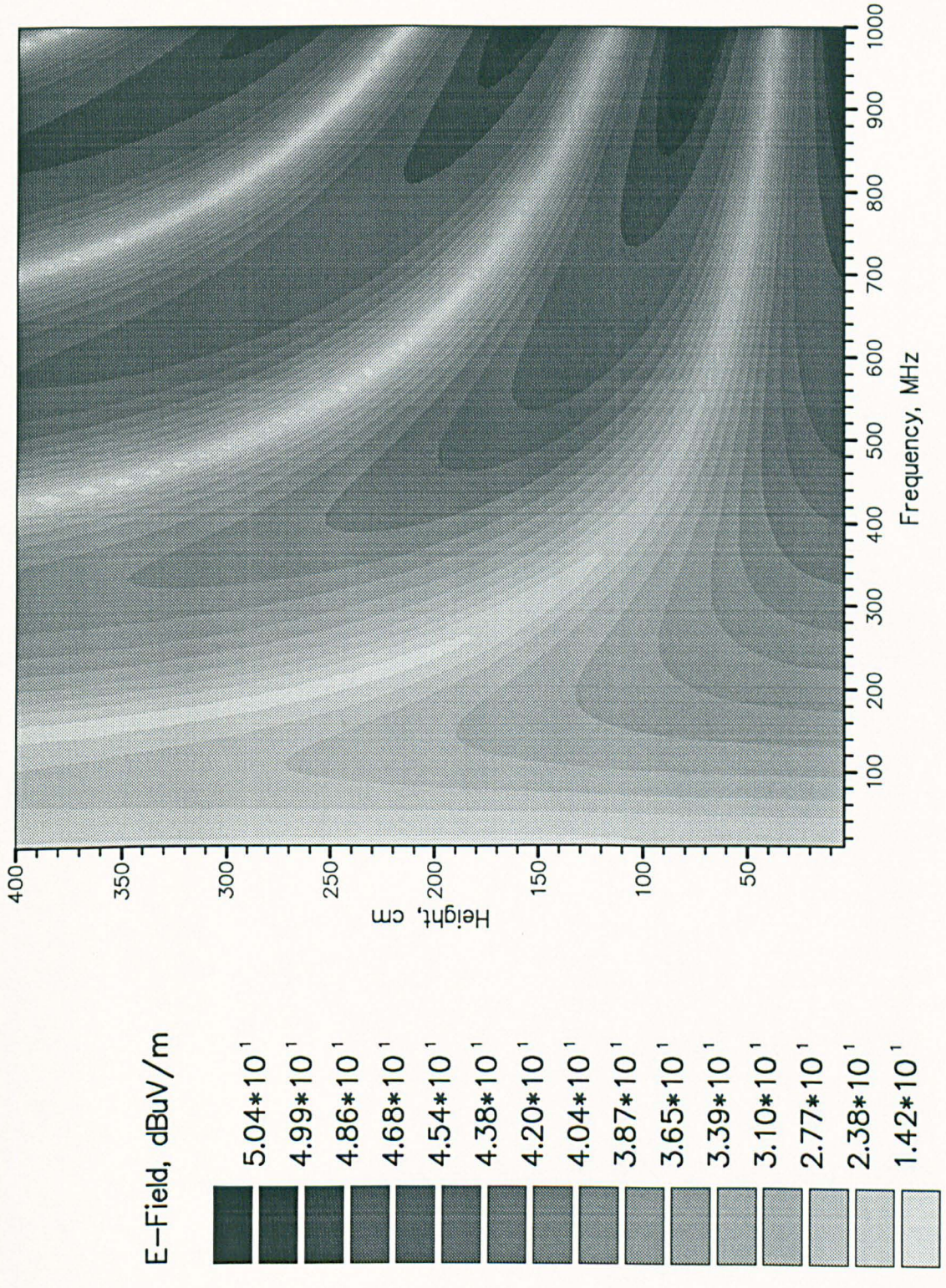


Figure 1.7: Variation of field strength with observation point height and excitation frequency for a vertically polarised infinitesimal electric dipole source. The source has a dipole moment of 1 Am and is set at a height of 68 cm above the ground plane of a 3 m test site.

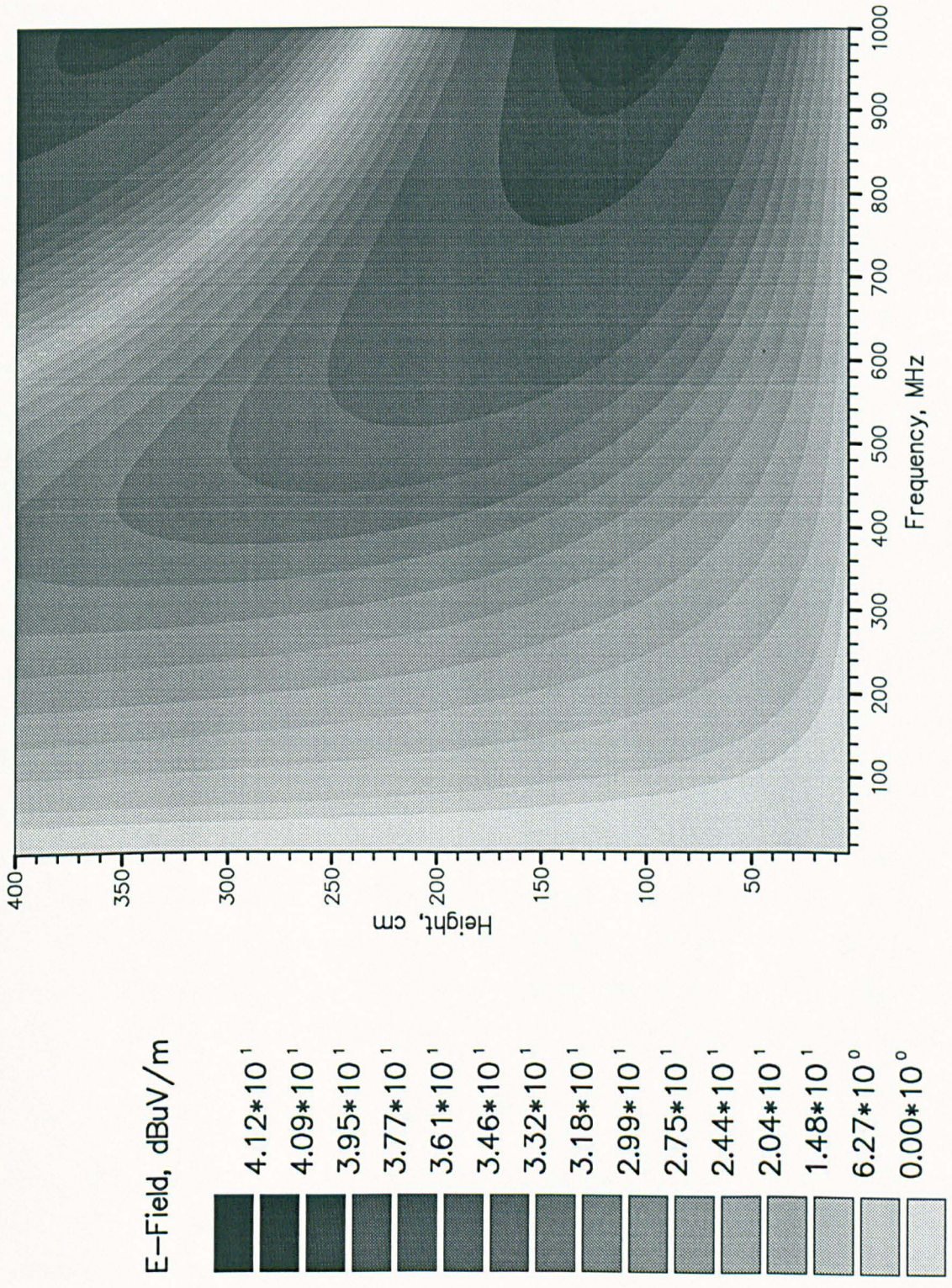


Figure 1.8: Variation of field strength with observation point height and excitation frequency for a horizontally polarised infinitesimal electric dipole source. The source has a dipole moment of 1 Am and is set at a height of 68 cm above the ground plane of a 10 m test site.

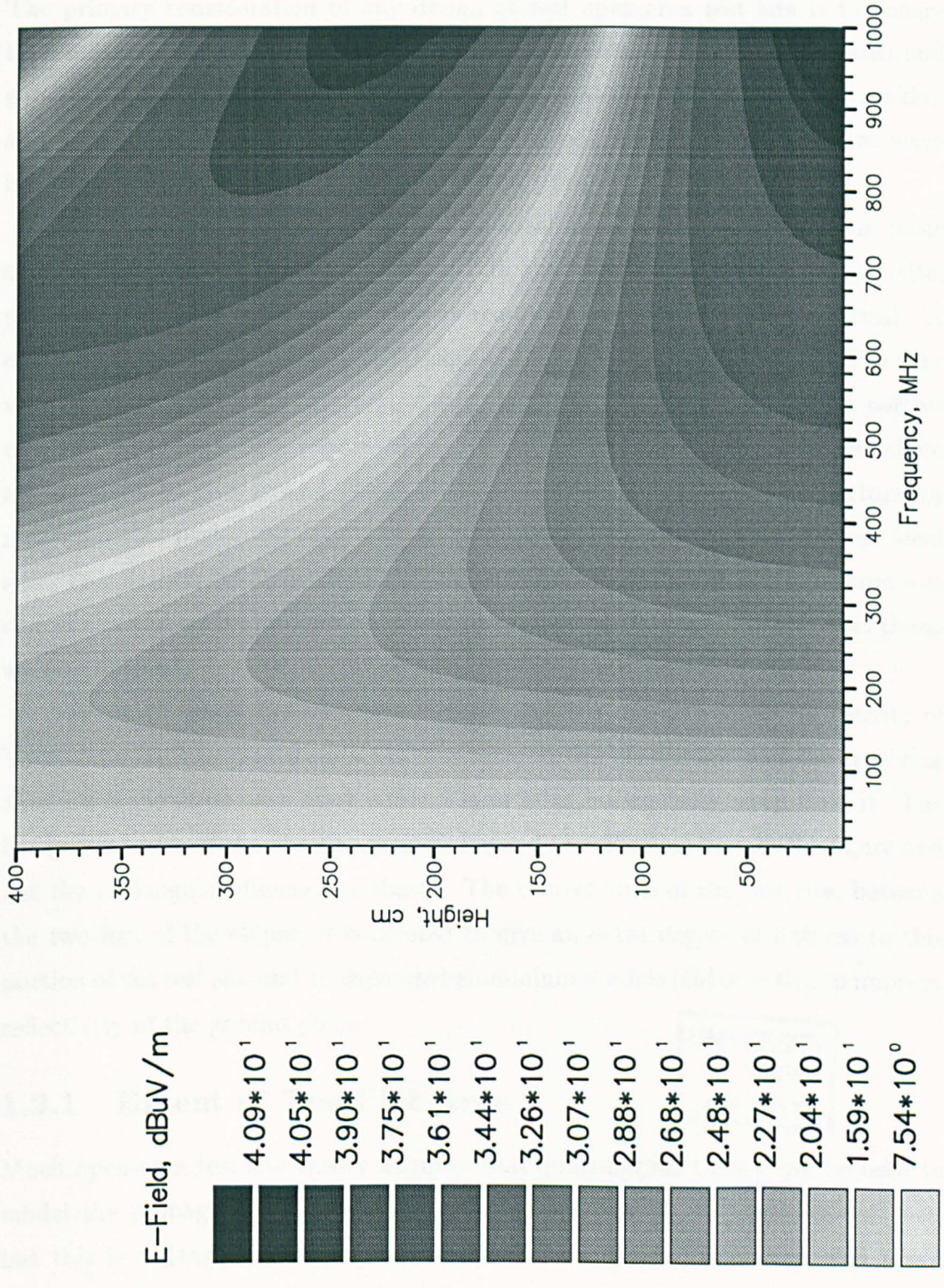


Figure 1.9: Variation of field strength with observation point height and excitation frequency for a vertically polarised infinitesimal electric dipole source. The source has a dipole moment of 1 Am and is set at a height of 68 cm above the ground plane of a 10 m test site.

## 1.2 A Real Open-Area Test Site

The primary consideration of any design of real open-area test site is to ensure that measurements performed using it are repeatable on all other test sites and good ground plane design is critical to this. Repeatability is achieved by making all ground planes as close to perfect reflectors as possible so that the reflected wave has the same amplitude and phase on all test sites.

The previous section has described an ideal OATS and presented some basic theory to describe propagation over it. It has been explained that an infinite, perfectly reflecting flat ground plane is required, but this is hardly practical. A compromise has to be made in the design of the ground planes of real OATSs that will give a ground plane of practical size, but that will approximate to a perfect reflector. Standards have evolved that give design rules for real test sites and these are intended to give ground planes that are near enough to perfect reflectors for measurements performed over them to be equivalent to ones performed on an ideal site. This section briefly reviews the design rules and describes the open-area test site at the University of York on which the measurements presented in this thesis were performed.

Figure 1.10 shows the structure of the open-area test site at the University of York. The EUT is placed on a wooden table in the plastic hut and the receiving antenna is mounted on a mast either 3 m or 10 m horizontally away from it. The flat grassed area of the test site extends beyond the elliptical area in the figure and has the rectangular dimensions shown. The central strip of the test site, between the two foci of the ellipse, is concreted to give an extra degree of flatness to this portion of the test site and an expanded aluminium mesh is laid over this to improve reflectivity of the ground plane.



### 1.2.1 Extent of The Flat Area

Much open-area test site theory assumes that quasi-optical theory can be used to model the propagation of direct and reflected waves over an open-area test site, but this is a dangerous assumption because of the lower frequencies, and hence longer wavelengths, involved. Optical theory considers coupling between point sources and small apertures above reflecting ground planes, but typical antennas and sources used over open-area test site ground planes are not small, and have typical dimensions of up to a metre (or more, if resonant dipole antennas are used).

The minimum flat, obstruction-free area of ground plane that is recommended by standards is the CISPR ellipse [11] and is shown in figure 1.10. This has a minor

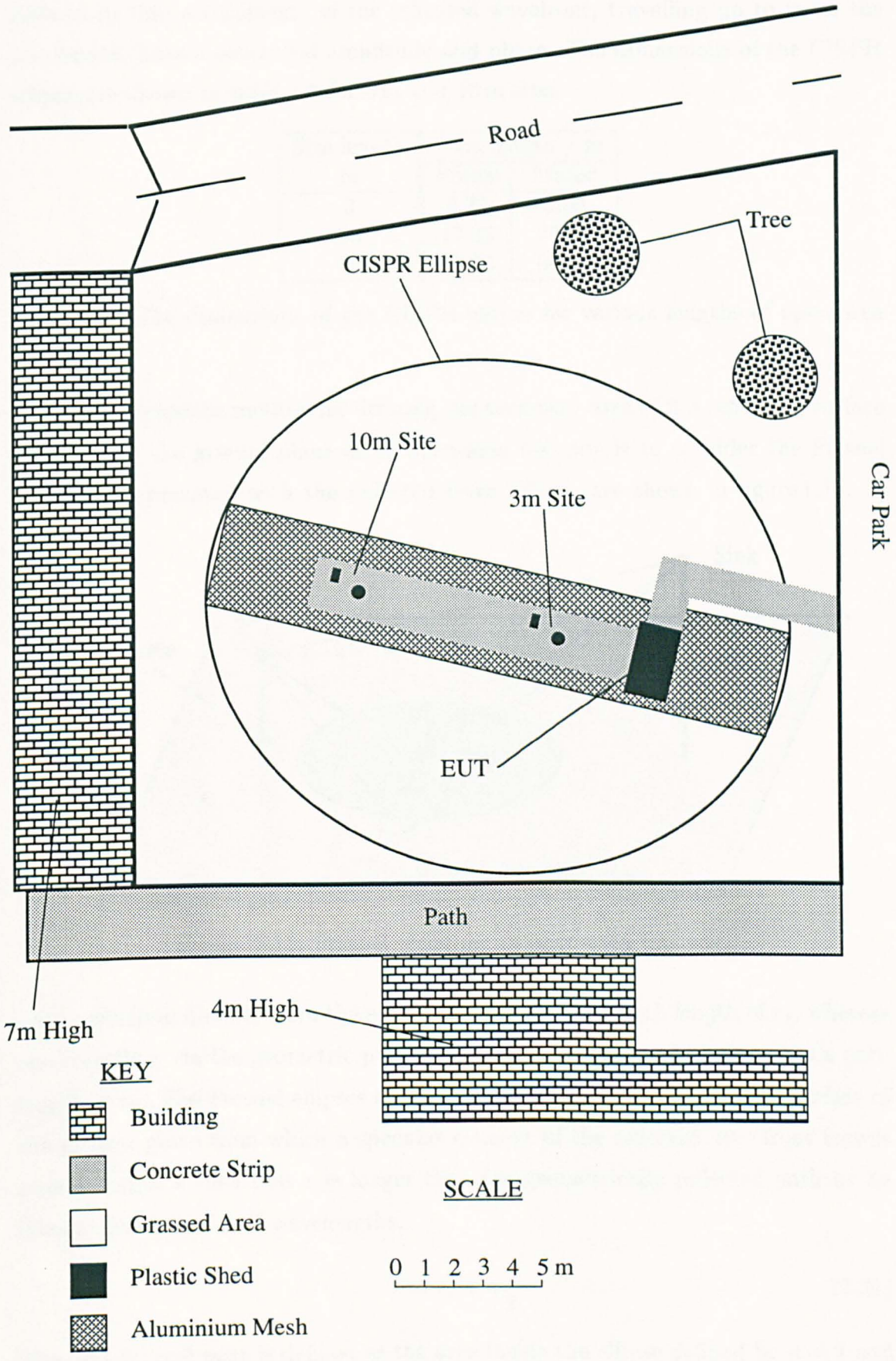


Figure 1.10: The open-area test site at the University of York.

axis of $\sqrt{3}$ times the site length and a major axis of twice the site length. It is defined so that all elements of the reflected wavefront, travelling up to twice the site length, have a controlled amplitude and phase. The dimensions of the CISPR ellipse are shown in table 1.1 for 3 m and 10 m sites.

| Site length | Axis length / m | |
|---|---|---|
| m | Minor | Major |
| 3 | 5.20 | 6.00 |
| 10 | 17.32 | 20.00 |
| 30 | 51.96 | 60.00 |

Table 1.1: The dimensions of the CISPR ellipse for various lengths of open-area test site.

A more scientific method for defining the necessary area of flat reflecting surface required for the ground plane of an open-area test site is to consider the Fresnel zones [12] associated with the reflected wave. These are shown in figure 1.11. A

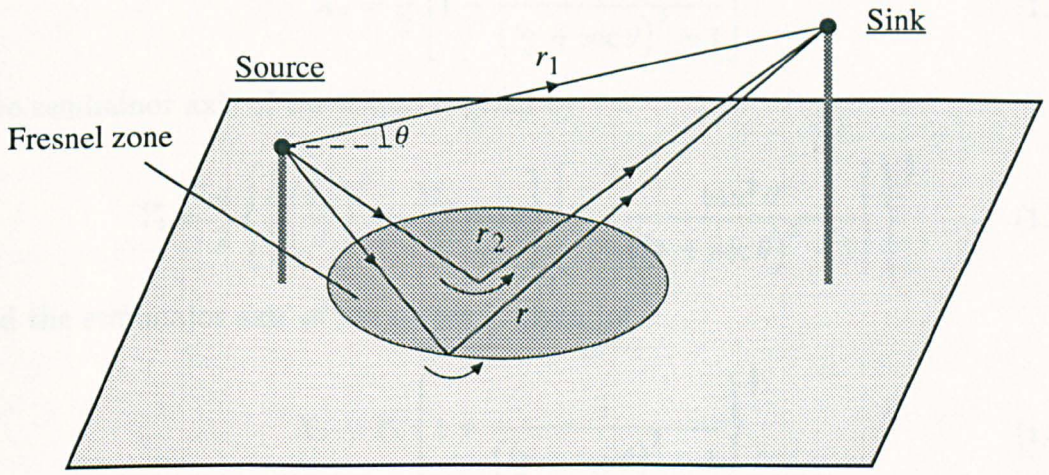


Figure 1.11: Fresnel zones on an open-area test site.

wave travelling directly from the source to the sink has a path length of $r_1$, whereas one travelling via the geometric point of reflection on the ground plane has a path length of $r_2$. The Fresnel ellipses are defined as the loci of points on the surface of the ground plane from which a specular element of the reflected wavefront travels a path length $r$ such that $r$ is longer than the geometrically reflected path by an integer multiple of half wavelengths.

$$r = r_2 + n\frac{\lambda}{2} \tag{1.21}$$

The first Fresnel zone is defined as the area inside the ellipse defined by $n = 1$ and reflections from this region contribute the majority of the power to the reflected wave front. For this reason the flat area required for the ground plane of a test

site is that occupied by the first Fresnel zone at a given operating frequency and geometry.

It can be seen from equation (1.21) that the largest Fresnel zones occur for the longest wavelength of radiation that is measured on a given test site. This is 30 MHz and corresponds to a wavelength of 10 m. The effect of varying source and sink heights on the position and size of the Fresnel zones is not as clear, but reference [13] gives expressions for these dimensions in terms of the test site geometry. The difference in path length between the direct wave and an element of the wavefront that is reflected specularly from the edge of the $n$th Fresnel zone is

$$\delta_n = r_2 - r_1 + n\frac{\lambda}{2} \tag{1.22}$$

The centre of the $n$th Fresnel ellipse is displaced from the source by a distance $X_0$ along the surface of the ground plane in the direction of the sink where

$$X_0 = \frac{d}{2}\left[1 - \frac{\tan^2\theta}{\left(\frac{\delta_n}{d} + \sec\theta\right)^2 - 1}\right] \tag{1.23}$$

The semiminor axis of the ellipse is given by

$$Y_1 = \frac{d}{2}\left\{\left[\left(\frac{\delta_n}{d}\right)^2 + \frac{2\delta_n}{d}\sec\theta\right]\left[1 - \frac{\tan^2\theta}{\left(\frac{\delta_n}{d} + \sec\theta\right)^2 - 1}\right]\right\}^{\frac{1}{2}} \tag{1.24}$$

and the semimajor axis of the ellipse is given by

$$X_1 = Y_1\left\{1 + \frac{1}{\left(\frac{\delta_n}{d} + \sec\theta\right)^2 - 1}\right\}^{\frac{1}{2}} \tag{1.25}$$

The angle $\theta$ is shown in figure 1.11 and is defined as the elevation angle above horizontal of the direct wave from the source to the sink.

It can be seen from equations (1.24) and (1.25) that the first Fresnel zone is largest for the greatest source and sink heights, and it has also been shown to be largest at 30 MHz, hence it is possible to determine the maximum extent of the first Fresnel zone on an open-area test site. This has been calculated in reference [13] to have the dimensions shown in table 1.2.

Tables 1.1 and 1.2 show that the CISPR ellipse covers the entire first Fresnel zone of 10 m and 30 m open-area test sites at all frequencies and should therefore be of sufficient extent to act as a good reflecting surface. The CISPR ellipse of the 3 m site does not extend up to the first Fresnel zone and so is not an adequate flat area to ensure a well behaved ground plane. The open-area test site at the University of York has a flat area extending beyond that required by the CISPR

| Dimensions in metres | | | | | | |
|---|---|---|---|---|---|---|
| Site length $d$ | Frequency MHz | Antenna heights | | Ellipse axes | | Ellipse centre $X_0$ |
| | | Source $h_1$ | Sink $h_2$ | Minor $Y_1$ | Major $X_1$ | |
| 3 | 30 | 1 | 4 | 9.54 | 9.93 | 1.38 |
| | 50 | | | 7.22 | 7.68 | 1.30 |
| | 100 | | | 5.34 | 5.86 | 1.20 |
| | 200 | | | 4.32 | 4.85 | 1.11 |
| | 500 | | | 3.66 | 4.20 | 1.03 |
| | 1000 | | | 3.43 | 3.97 | 0.96 |
| 10 | 30 | 2 | 4 | 13.02 | 16.28 | 4.89 |
| | 50 | | | 10.35 | 14.15 | 4.83 |
| | 100 | | | 8.09 | 12.44 | 4.73 |
| | 200 | | | 6.81 | 11.49 | 4.63 |
| | 500 | | | 5.95 | 10.85 | 4.54 |
| | 1000 | | | 5.65 | 10.62 | 4.49 |
| 30 | 30 | 2 | 6 | 19.18 | 34.60 | 14.40 |
| | 50 | | | 15.10 | 31.94 | 14.07 |
| | 100 | | | 11.36 | 29.28 | 13.49 |
| | 200 | | | 9.02 | 27.22 | 12.84 |
| | 500 | | | 7.33 | 25.28 | 12.10 |
| | 1000 | | | 6.70 | 24.39 | 11.73 |

Table 1.2: Maximum extent of the first Fresnel ellipse for various lengths of open-area test site.

ellipse for the 10 m site and so it does actually cover the first Fresnel zone of the 3 m site.

The above theoretical arguments as to the correct size of the flat reflecting surface beneath an open-area test site have been developed for point sources and sinks over a flat ground plane. Practical antennas and EUTs have significant dimensions and therefore require larger flat areas to accommodate them. It is therefore sensible to have a flat area several metres larger than the CISPR ellipse if at all possible.

### 1.2.2 Rayleigh Optical Flatness Criterion

The Rayleigh criterion for optical flatness [14] is suitable for determining the flatness tolerance required for open-area test site ground planes. This is defined so that any spurious phase changes undergone by elements of the reflected wavefront, due to the roughness of the ground plane, are less than $\lambda/2$.

Figure 1.12 shows two rays, $b_1$ and $b_2$, reflected from a surface of roughness $h$. $b_1$ is reflected from a crest on the surface whilst $b_2$ is reflected from a trough so the path length difference between the rays, $\Delta b$, can be calculated as a function of the grazing angle, $\psi$. The

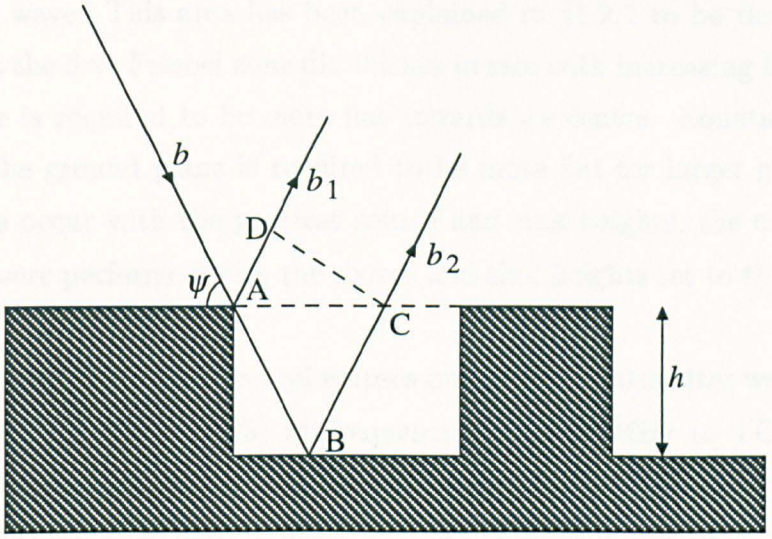


Figure 1.12: Scattering of two elements of a reflected wavefront from an uneven surface.

difference between the two paths is given by

$$\begin{aligned}
\Delta b &= \mathrm{AB} + \mathrm{BC} - \mathrm{AD} \\
&= \frac{h}{\sin\psi} + \frac{h}{\sin\psi} - \mathrm{AC}\cos\psi \\
&= \frac{2h}{\sin\psi} - \frac{2h\cos\psi}{\tan\psi} \\
&= \frac{2h(1-\cos^2\psi)}{\sin\psi} \\
&= 2h\sin\psi
\end{aligned} \tag{1.26}$$

and this corresponds to a phase shift $\Delta\phi$ given by

$$\Delta\phi = \frac{4\pi h}{\lambda}\sin\psi \tag{1.27}$$

The Rayleigh criterion states that $\Delta\phi < \frac{\pi}{2}$, therefore

$$h < \frac{\lambda}{8\sin\psi} \tag{1.28}$$

In the above analysis the plane of incidence is normal to the reflecting surface but this only occurs for elements of the reflected wavefront that are reflected directly along the axis of the site. If the plane of incidence is at an angle other than normal, the grazing angle will become reduced so that the ground plane does not have to be as flat.

### 1.2.3 Flatness Profile of the Ground Plane

Equation (1.28) gives the flatness tolerance that must be obeyed by the ground plane of a test site over the portion of it that is chiefly responsible for scattering

the reflected wave. This area has been explained in §1.2.1 to be the first Fresnel zone, and, as the first Fresnel zone diminishes in size with increasing frequency, the ground plane is required to be more flat towards its centre. Equation (1.28) also shows that the ground plane is required to be more flat for larger grazing angles and, as these occur with the greatest source and sink heights, the calculations in this section were performed with the source and sink heights set to their maximum usual values.

The positions of the first Fresnel ellipses on 3, 10 and 30 m sites were calculated from equations (1.23) to (1.25) at frequencies from 30 MHz to 1 GHz with the source and sink heights set to their maximum usual values, as shown in table 1.2. Equation (1.28) was then used to calculate the tolerance profile required for ground plane flatness over the various site lengths under the conditions shown in table 1.2. The results are shown in figures 1.13 to 1.18.

The flat portion at the centre of the curves shown in figures 1.13 to 1.18 corresponds to the first Fresnel zone at 1 GHz. It can be seen that the ground plane is required to be most flat in this region with the ground plane of a 3 m site required to be within 4.37 cm of flat. The ground planes of longer sites do not have to be as flat because of the smaller grazing angles that occur, so the ground plane of a 10 m site must be within 7.28 cm of flat and that of a 30 m site within 14.54 cm. The size of the first Fresnel zone increases with frequency, but not very quickly, so the flatness tolerance becomes rapidly less critical as one moves away from the 1 GHz first Fresnel zone.

It is important to note that the flatness tolerances shown in figures 1.13 to 1.18 have been derived from the Rayleigh optical flatness criterion (equation (1.28)) that ensures that no elements of the reflected wavefront have a phase change corresponding to greater than half a wavelength due to the uneveness of the ground plane. Practically, a tighter criterion would be better for open-area test sites and a spurious phase change of less than $\lambda/4$ may be more appropriate. This would halve the flatness tolerances and present a difficult challenge to level the required area, particularly for the 3 m site.

The open-area test site at the University of York (see figure 1.10) has a 1.8 m wide concreted strip along its central axis to ensure a greater degree of flatness than could be guaranteed with a purely grassed area.

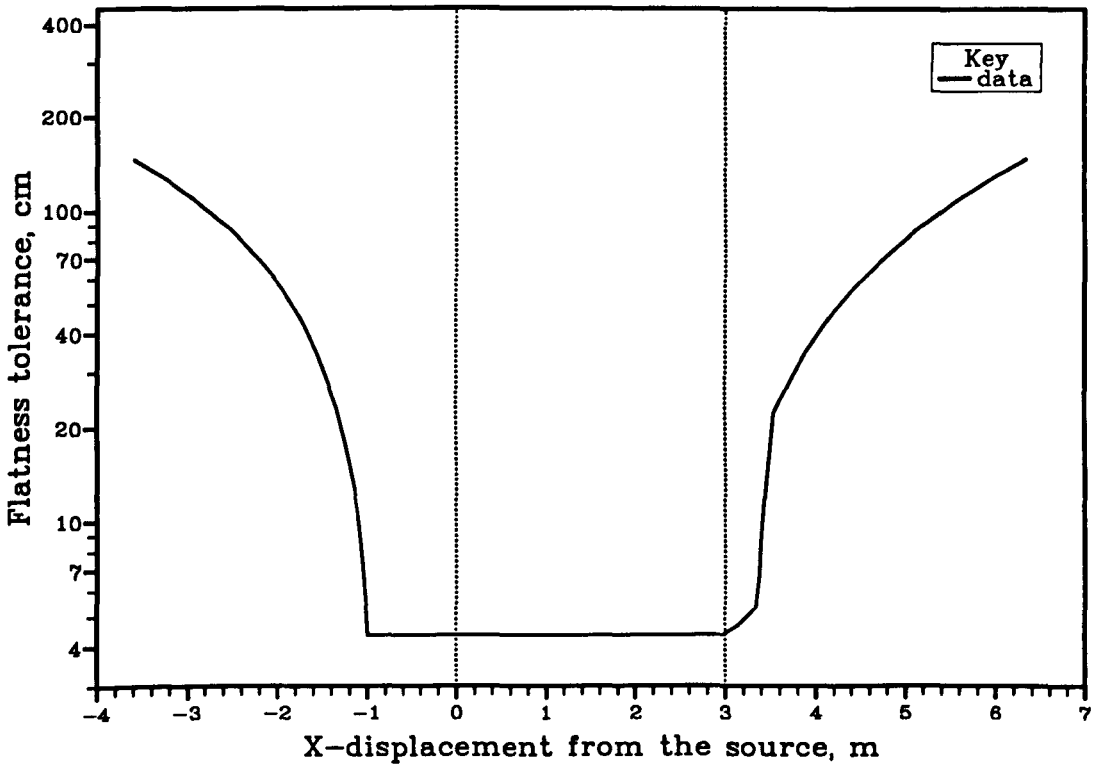


Figure 1.13: 3 m site – axial flatness tolerance of the ground plane.

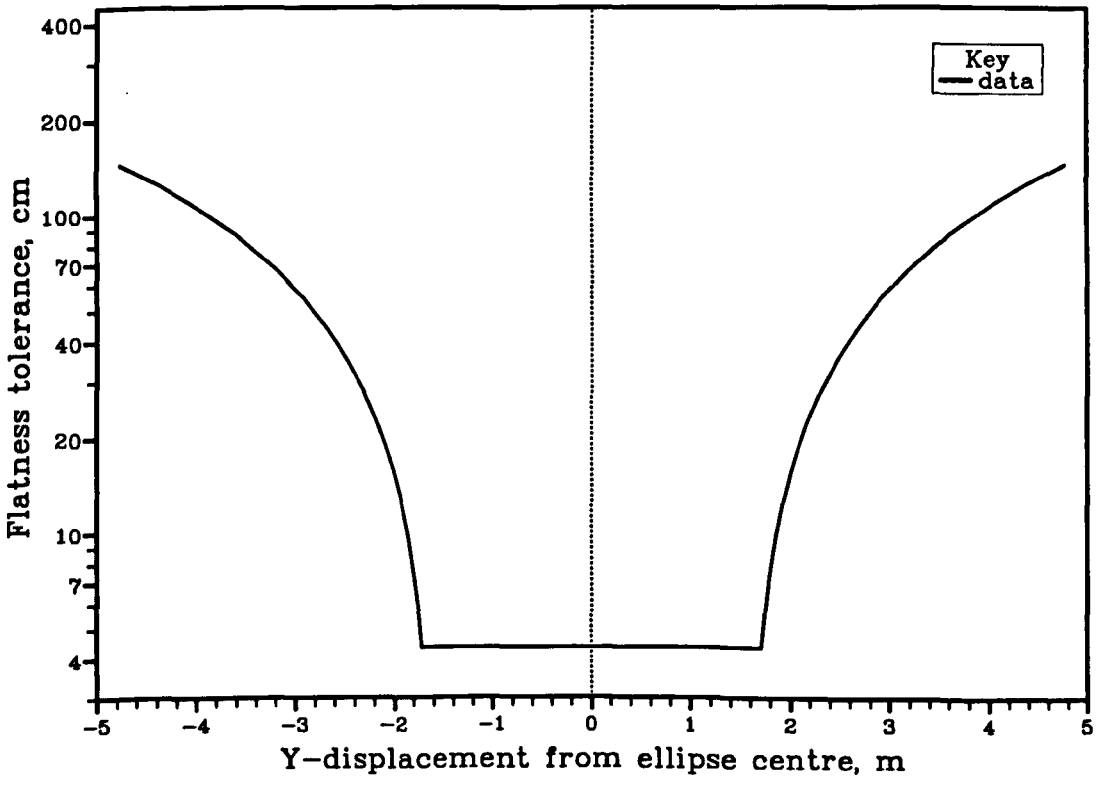


Figure 1.14: 3 m site – transverse flatness tolerance of the ground plane.

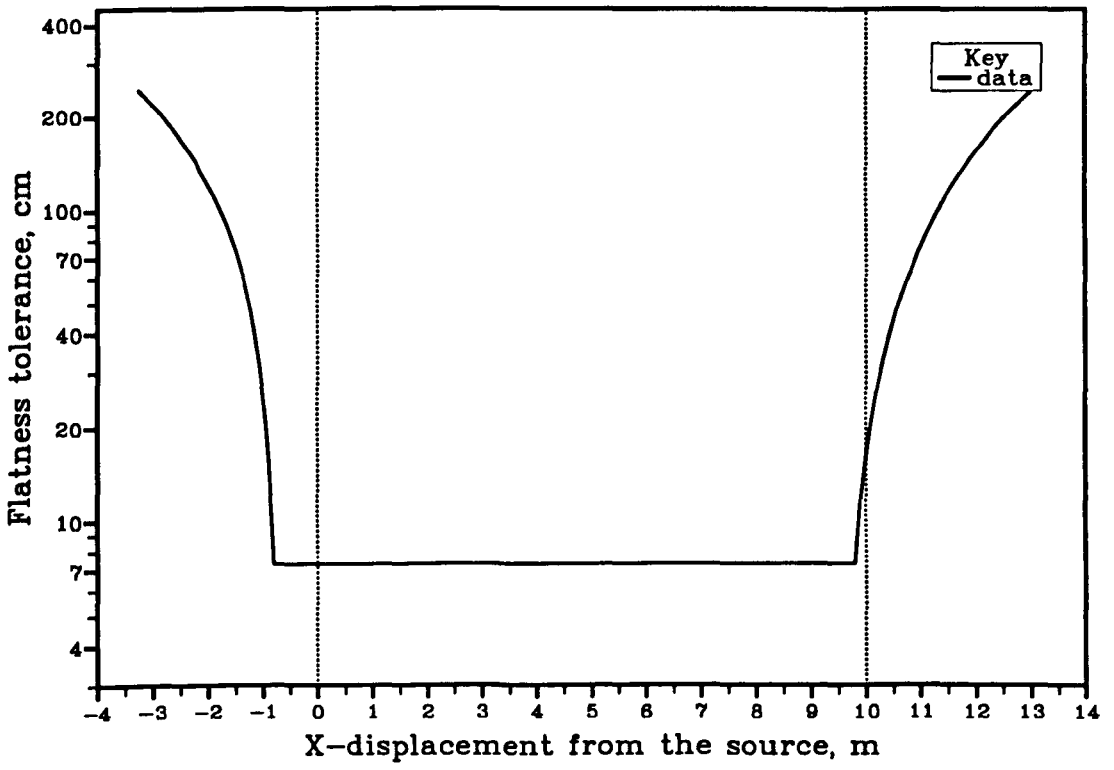


Figure 1.15: 10 m site – axial flatness tolerance of the ground plane.

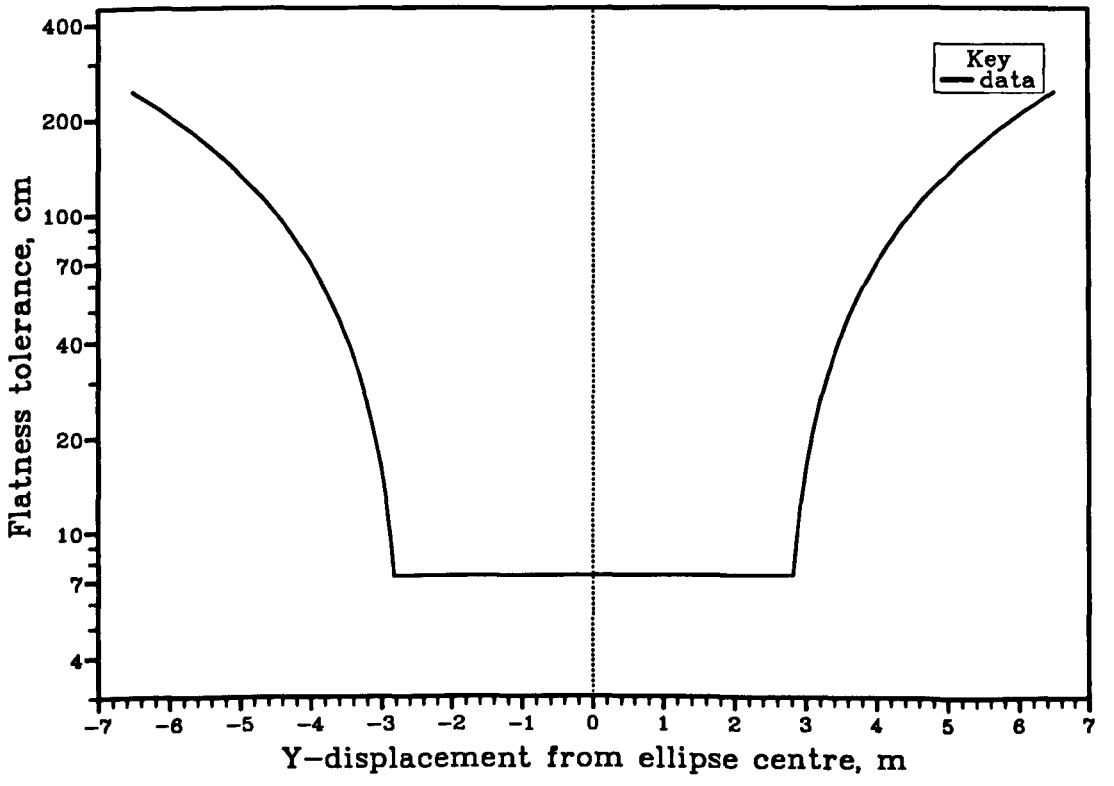


Figure 1.16: 10 m site – transverse flatness tolerance of the ground plane.

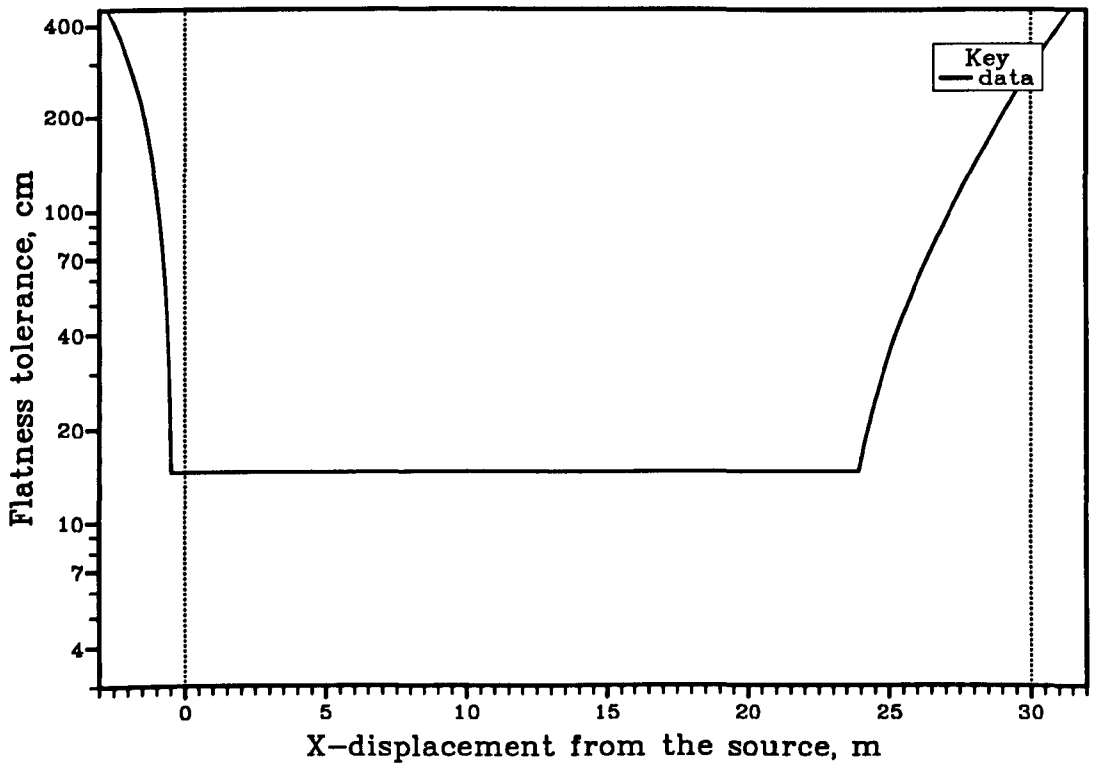


Figure 1.17: 30 m site – axial flatness tolerance of the ground plane.

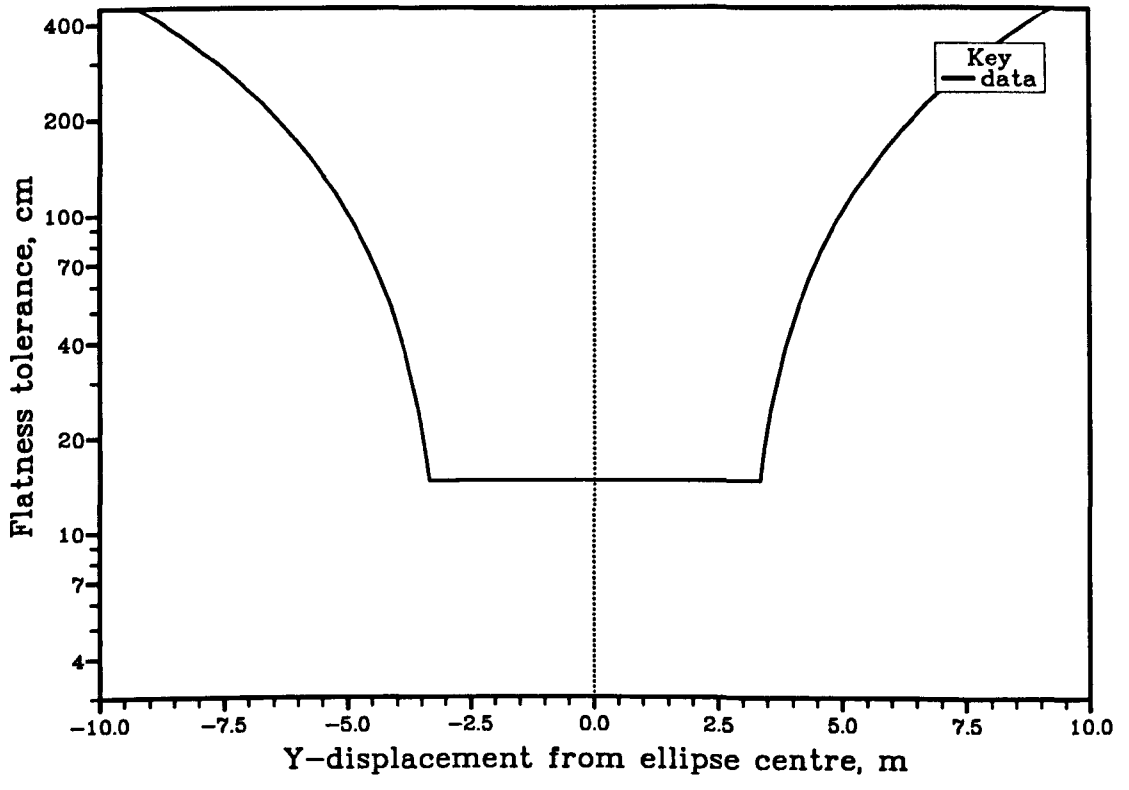


Figure 1.18: 30 m site – transverse flatness tolerance of the ground plane.

### 1.2.4 Metallised Area of the Ground Plane

The ground plane of an open-area test site is required to behave as a perfect reflector, i.e. it must be a good conductor, but the surface that is beneath most test sites does not necessarily have this property. Typical surfaces are a poorly conductive area of grassed earth or even worse conductors such as asphalt or concrete. It is usual to improve the conductivity, and hence the reflectivity, of a ground plane by covering at least part of the area up to the CISPR ellipse with either a solid sheet of metal or a mesh, but this has to be done carefully or it can introduce as many problems as it solves.

The most important property of the metallised area is that it should be of a sufficient size to act as a reflector. From the arguments of the previous sections, it should cover at least the first Fresnel ellipse and hence suitable dimensions for a rectangular sheet to be laid at the centre of test sites are shown in table 1.3. The metal sheet employed on the 3 m and 10 m site at the University of York is

| Dimensions in metres | | |
|---|---|---|
| Site length | Metal sheet | |
| | Length | Width |
| 3 | 10.2 | 9.6 |
| 10 | 16.6 | 13.1 |
| 30 | 35.8 | 19.2 |

Table 1.3: Minimum dimensions of the rectangular metal sheet that should be placed at the centre of various lengths of open-area test sites.

19.6×3.8 m and so is not wide enough to cover the entire first Fresnel zone and is a potential problem. Fortunately the area around the sheet is of particularly damp grassed earth that is a reasonable conductor itself and measurements have shown the premature truncation of this metal sheet does not cause significant errors.

Standards [15] specify the required size of the metal ground plane in terms of the dimensions of the measurement antenna and EUT rather than in terms of Fresnel zones. The metal portion of the ground plane is required to be 1 m wider than the measurement antenna over the entire length of the site and 2 m wider than the maximum dimension of the EUT in the region beneath it. Under this specification the ground plane of the test site at the University of York is suitable for EUTs having dimensions of up to 1.8 m and a maximum antenna length of 2.8 m. This permits the use of any broadband EMC antenna or a resonant dipole antenna at frequencies down to 50 MHz. The theoretical basis behind this approach to ground plane specification is not clear and the Fresnel zones based approach would be of more use.

### 1.2.5 Mesh Ground Planes

It is very important that the metal area of a ground plane is connected by a low impedance path to the surrounding earth, so that currents can flow between it and earth. Failure to ensure this can result in resonant currents in the metal that will cause large measurement errors. The metal ground plane of the test site at the University of York is connected to earth by metal spikes, bonded to it and driven into the ground at 1 m intervals along its edges. It can be seen from figure 1.10 that the metal is of a mesh construction and is laid over grass along the sides of the central concrete strip. This has allowed the grass to grow through the mesh and therefore helped to ensure an even better connection to earth.

Solid metal ground planes tend to suffer from warping due to expansion on hot days and are also more expensive than mesh ground planes. For this reason it is better to employ a ground plane having a mesh type of construction such as a chicken-wire type material or an expanded plate.

The holes in a mesh ground plane must be electrically small for the surface to act as a good reflector and this is usually taken to mean that they must be no more than a tenth of a wavelength across at the maximum frequency of illumination. For an open-area test site used at frequencies up to 1 GHz, this corresponds to a maximum hole diameter of 3 cm.

For a more rigorous understanding of the behaviour of a mesh of electrically small holes, it is necessary to determine its effective surface impedance. Casey [16] has performed this analysis for a mesh having square holes as a means to determining its shielding effectiveness but, as this is the reciprocal magnitude of the transmission coefficient through a mesh, the method is equally valid for calculation of the reflection coefficient from a mesh of electrically small holes. The model will not be reproduced here, but it is summarised in appendix A.

The mesh ground plane of the test site at the University of York is of an expanded plate construction, having holes shaped as shown in figure 1.19. Casey's model is derived to calculate the effective surface impedance of a mesh of square holes and so is not able to model the ground plane as shown. In order to model the actual mesh, an equivalent square mesh was developed with holes of the same area and cylindrical wires having the same cross sectional area. This gave a pitch for the mesh of 34.28 mm and a radius of 1.5 mm for the wires.

The square mesh was illuminated under the conditions that would give rise to the most degraded reflection coefficient, and these were for a plane wave, polarised with its electric field parallel to the plane of incidence, at the largest grazing angle.

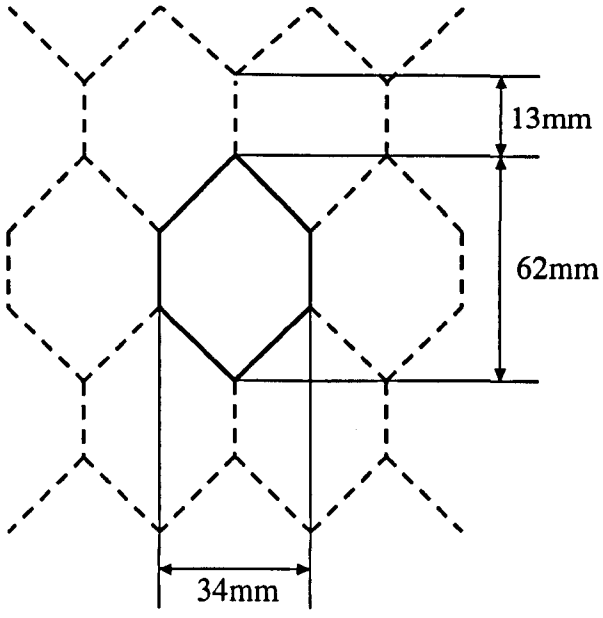


Figure 1.19: Mesh ground plane of the open-area test site at the University of York.

| Frequency MHz | Reflection Coefficient | |
|---|---|---|
| | Magnitude | Phase |
| 100 | 0.9994 | −1.88 |
| 200 | 0.9977 | −3.77 |
| 500 | 0.9865 | −9.35 |
| 1000 | 0.9495 | −18.24 |

Table 1.4: The reflection coefficient of the mesh ground plane of the OATS at the University of York for a plane wave polarised parallel to its plane of incidence.

The largest grazing angle that can usually occur on an OATS is 59° and this occurs for a 3 m site with 1 m source and 4 m sink heights. The calculated reflection coefficients under these conditions are shown in table 1.4.

Table 1.4 shows that there is little degradation of the magnitude of the reflection coefficient of this mesh for frequencies of up to 1 GHz but the phase shift will however be significant. This will shift the positions of the maxima as the receiving antenna is scanned in height so that they do not occur in the positions predicted by the theory of §1.1. Fortunately this will not affect the measurement because scanning the receiving antenna will ensure that the field strength is still measured where the direct and reflected waves add together in phase.

It should be noted that the above analysis was performed for a worst case scenario and, as such, the medium below the mesh was assumed to be free space. On a real test site, the mesh is laid over a medium that may well be conductive and so there would be even less degradation of reflection.

### 1.2.6 The Environment around the OATS

Due to the unbounded nature of the fields on an open-area test site, there are several aspects of the environment around it that can influence its behaviour. The boundary of an open-area test site is usually taken to be the perimeter of the CISPR ellipse and the environment outside this is not generally under the control of test site users.

The ambient r.f. noise in industrialised areas tends to be considerably higher than in other areas, but electronics companies tend to be located in industrialised areas. This often means that it may be difficult to measure, or even detect, the emissions from an EUT on an open-area test site unless their exact frequencies are known beforehand. The only possible solution to this problem is to use a narrower measurement bandwidth, if the ambient noise is broadband, but this can greatly increase measurement times and will not give any advantage over narrow band noise signals such as broadcast radio stations.

At a certain distance from the CISPR ellipse there will inevitably be buildings. The effect on radiation measurements of stray reflections from these is difficult to assess since they are usually non-metallic and only partial reflectors. It is possible to calculate their worst potential effects by assuming they are perfect reflectors, but even this requires powerful computer codes that are not widely available.

The real open-area test site shown in figure 1.10 has two buildings close to its CISPR ellipse. The biggest problem is caused by the building behind the receiving antenna of the 10 m site. In chapter 5 this is shown to introduce a ripple of $\pm 2$ dB and periodicity of 25 MHz onto measurements made using the 10 m site. The periodicity results from the path length from the receiving antenna to the face of the building and back again becoming equal to integer multiples of a wavelength, and hence a specularly reflected wave via this path adds constructively or destructively at the receiving antenna depending upon the precise excitation frequency.

### 1.2.7 Other Structures of the OATS

It has been explained that an ideal open-area test site consists of a source and a sink of electromagnetic radiation above a flat, perfectly reflecting surface. On a real test site the source of radiation is the equipment under test (EUT) and the sink is the receiving antenna. Both of these items of equipment need supporting at controlled heights above the ground plane and so a typical real OATS has a structure similar to that shown in figure 1.20.

The table upon which the EUT is mounted, the weatherproof enclosure around

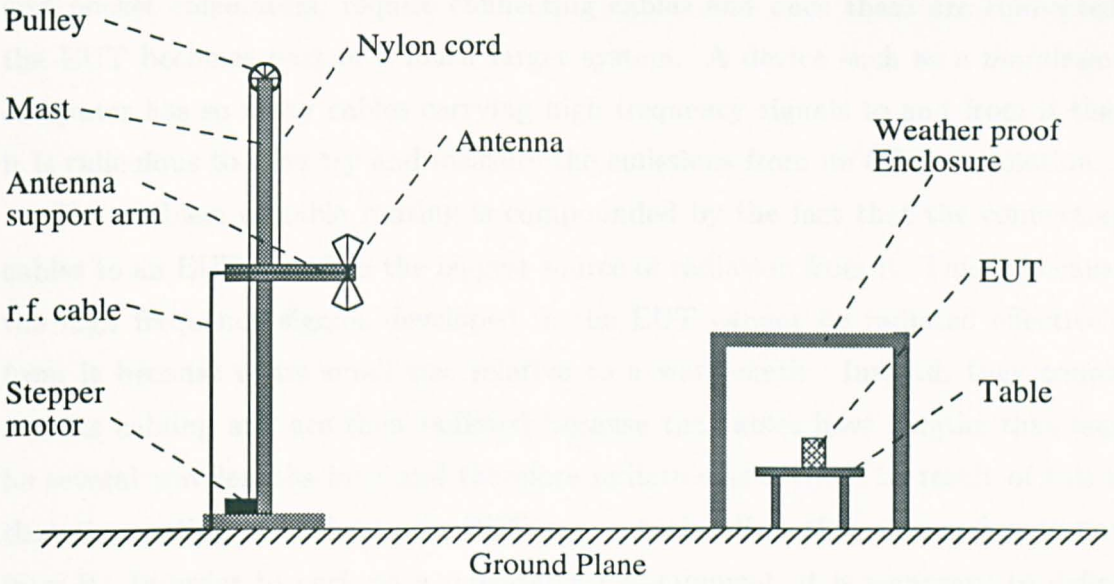


Figure 1.20: Structures of a practical OATS.

it and the receiving antenna positioning mast must all be made from non-conducting materials such as plastic or dry wood so that they are as transparent to electromagnetic waves as possible.

### The Receiving Antenna Positioning Mast

The receiving antenna positioning mast is the most elaborate structure of the OATS and a diagram of it is shown in figure 1.20. It scans the receiving antenna through the required height range above the ground plane, so measurements of radiated emissions can be made where they are at their maximum. The major problem with masts is associated with the mechanics of raising the antenna, since this is difficult to achieve without using metal components.

The EMCO mast that is used on the test site at the University of York has a metal enclosure containing a stepper motor at its base and a system of pulleys connecting this, via a static Nylon rope, to the antenna support arm. The dimensions of the stepper motor enclosure are $36 \times 24 \times 16$ cm, and so it is not electrically small at the higher frequencies of test site operation. The effect of its presence on measurements is not known, but it would clearly be better to have a motor mounted beneath the metal ground plane.

### Routing of Cables

The best way of routing cabling to an EUT is a question that arises because of a much wider philosophical problem: that of the definition of an EUT. Virtually all EUTs, with the exception of certain hand held devices such as cellular phones

and pocket calculators, require connecting cables and once these are connected, the EUT becomes part of a much larger system. A device such as a mainframe computer has so many cables carrying high frequency signals to and from it that it is ridiculous to even try and measure the emissions from its CPU in isolation.

The problem of cable routing is compounded by the fact that the connecting cables to an EUT are often the biggest source of radiation from it. This is because the high frequency signals developed in the EUT cannot be radiated effectively from it because of its small size relative to a wavelength. Instead, they couple into its cabling and are then radiated because the cables have lengths that may be several wavelengths long and therefore radiate efficiently. The result of this is that the routing of cables to an EUT may greatly affect the measured radiation from it. In order to perform a repeatable measurement, it is necessary to define the position of every cable carefully. Standards do not state clearly how cables are to be routed but it is normal to take them down to ground plane level behind the EUT and back along the site axis.

The coaxial cable connecting to the receiving antenna does not present a great problem for measurements made with the antenna horizontally polarised because it leaves the antenna in the the plane that is normal to the measured electric field and so does not interact heavily with the antenna. With vertical polarisation, the cable is parallel to the radiators of the antenna and so is capable of interacting with them and causing increased measurement uncertainties. Bennett [17] has performed measurements that confirm the presence of this problem but Smith [18] has made similar measurements of site attenuation that conflict and show the coupling to be negligible.

## 1.3 Radiation Measurement using an Open-Area Test Site

The most important aspect of any electromagnetic compatibility measurement is that it must be repeatable. This aim is central to the radiation measurement procedure using open-area test sites. The radiated field strength that would be measured from a standard EUT using one test site must be the same as that that would be measured with the same EUT on all other test sites to within known error bounds. This section briefly describes the basic measurement procedure, without becoming involved in the subtle details of precise standards, and describes a typical measurement that was made of the dipole moment of an electrically small source of broadband noise.

### 1.3.1 The Measurement Procedure

The field that would be measured from an EUT on an OATS is not the same as the field that would be measured in free space because there are two radiation paths from the EUT to the measurement point on the test site. This is not a problem because the measurement can still be repeatable, so long as the waves via these two paths do not sum together out of phase at the measurement point. To achieve this the measurement antenna is scanned in height, as shown in figure 1.21, and the maximum field strength within the height range is taken to be the radiated field from the EUT at each frequency of interest. Table 1.5 shows the usual receiving

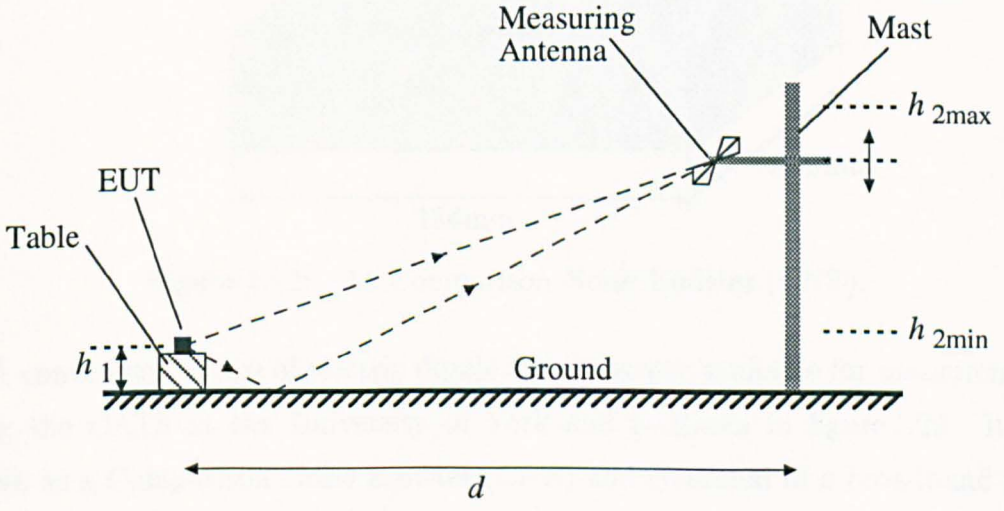


Figure 1.21: Radiation measurement using an open-area test site.

antenna height scan ranges for various lengths of open-area test site.

The EUT is mounted on a table that is made from a non-conducting material such as wood or perspex, and the mast that supports the receiving antenna is

| Site Length m | Mast Height Range m |
|---|---|
| 3 | 1–4 |
| 10 | 1–4 |
| 30 | 2–6 |

Table 1.5: Typical receiving antenna height scan ranges.

also made from similar materials. This is to minimise interactions between the structures of the test site and the measurement apparatus that might lead to a degradation in repeatability from one test site to another.

### 1.3.2 Measurement of the Interference Pattern

It has been shown that the fields from any electrically small source can be fully defined by a set of three orthogonal electric dipoles superimposed on top of three orthogonal magnetic dipoles, each having the correct excitation current magnitudes and phases [19]. Electrical smallness is typically taken to mean that the largest physical dimension of the source is less than a tenth of a wavelength across.

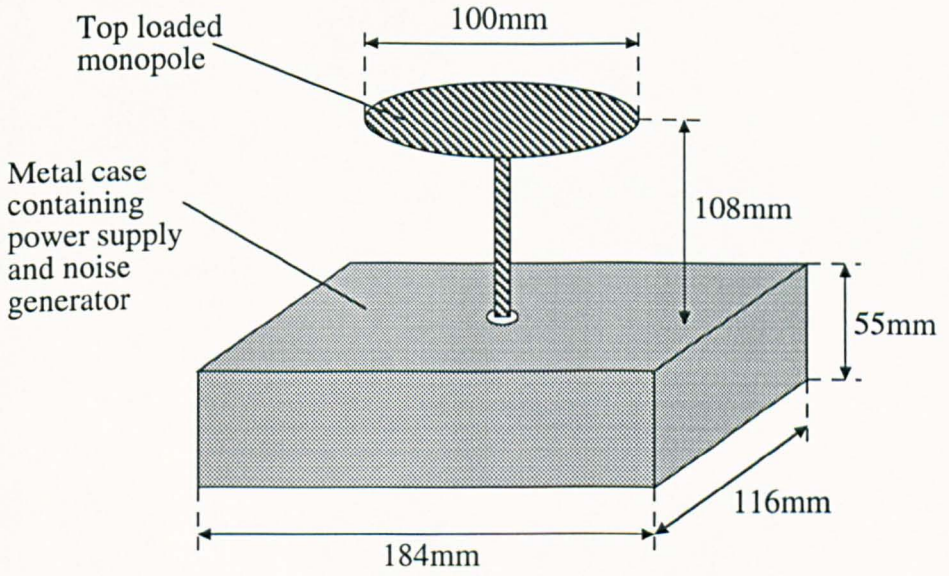


Figure 1.22: The Comparison Noise Emitter (CNE).

A convenient source of electric dipole radiation was available for measurements using the OATS at the University of York and is shown in figure 1.22. It was known as a Comparison Noise Emitter (CNE) and consisted of a broadband noise generator, having a nominal bandwidth of 1 GHz, encapsulated in a rectangular aluminium box with its own battery power supply. This excited a short monopole antenna above one face of the box so that the combined structure behaved as a source of electric dipole radiation. The largest dimension of the CNE was 30 cm and so it was not electrically small, but the monopole antenna was sub-resonant

at frequencies up to 1 GHz and so it was a suitable tool for investigation of the interference pattern produced at the receiving antenna by the direct and reflected waves over an OATS.

The CNE was placed on a wooden table on 3 m and 10 m test sites in both horizontal and vertical polarisations. The field strength from it was then measured with a biconical antenna in the frequency range of 30–200 MHz and a log-periodic antenna above 200 MHz and up to 1 GHz. The manufacturers' quoted antenna factors were used to convert the measured voltages with these antennas into field strengths. The resulting fields, measured in a 1 MHz bandwidth, are plotted in in figures 1.23 to 1.26 as functions of receiving antenna height and frequency. The axes of the graphs are the same as the theoretical plots, calculated in §1.1, and shown in figures 1.6 to 1.9, so that they may easily be compared. The height of the centre of the CNE body was 68 cm above the ground plane and the theoretical plots were derived with this source height.

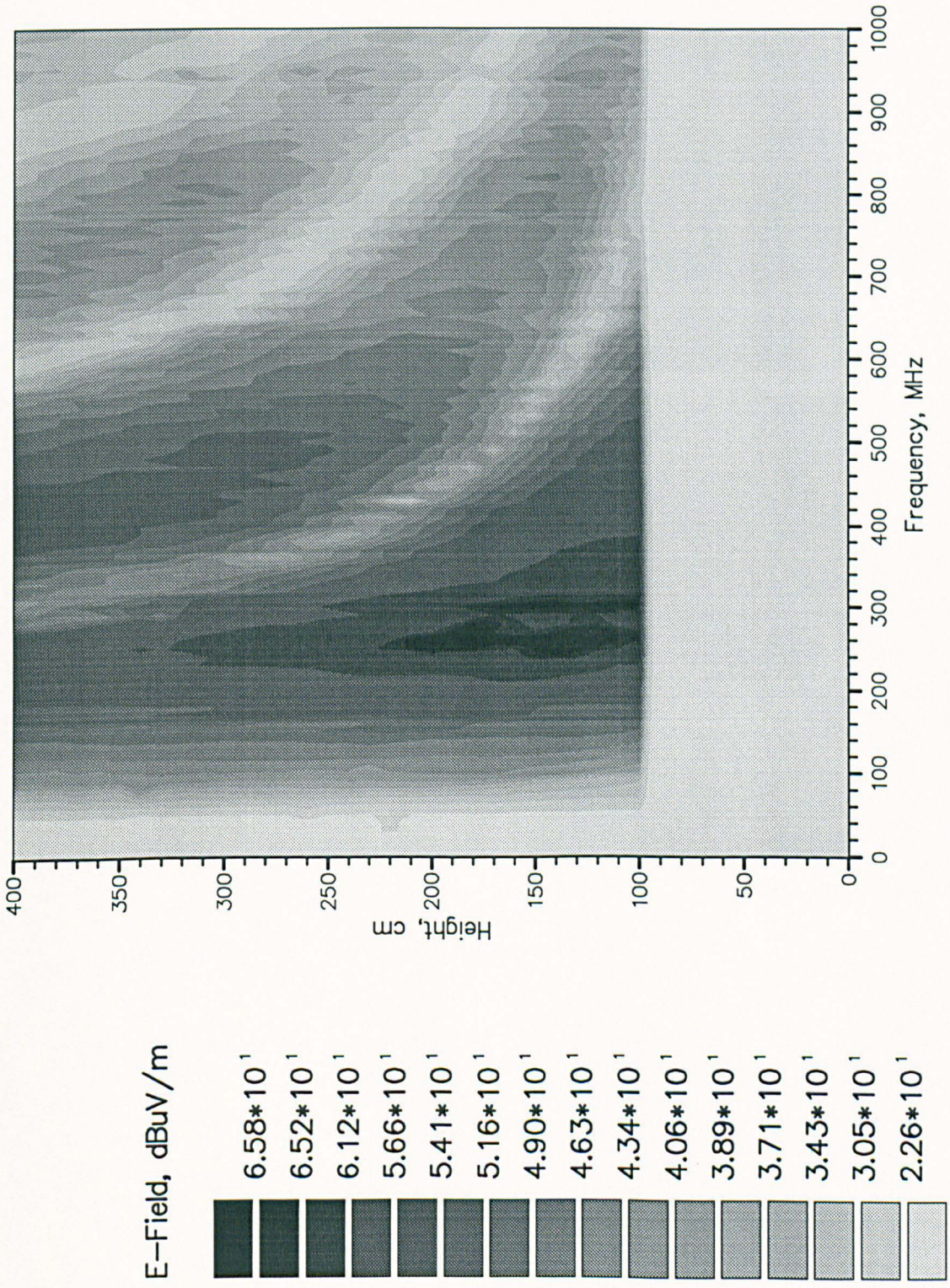


Figure 1.23: Measured electric field strength from the CNE in a 1 MHz bandwidth against receiving antenna height and measurement frequency. Horizontal polarisation on a 3 m site with an EUT height of 68 cm.

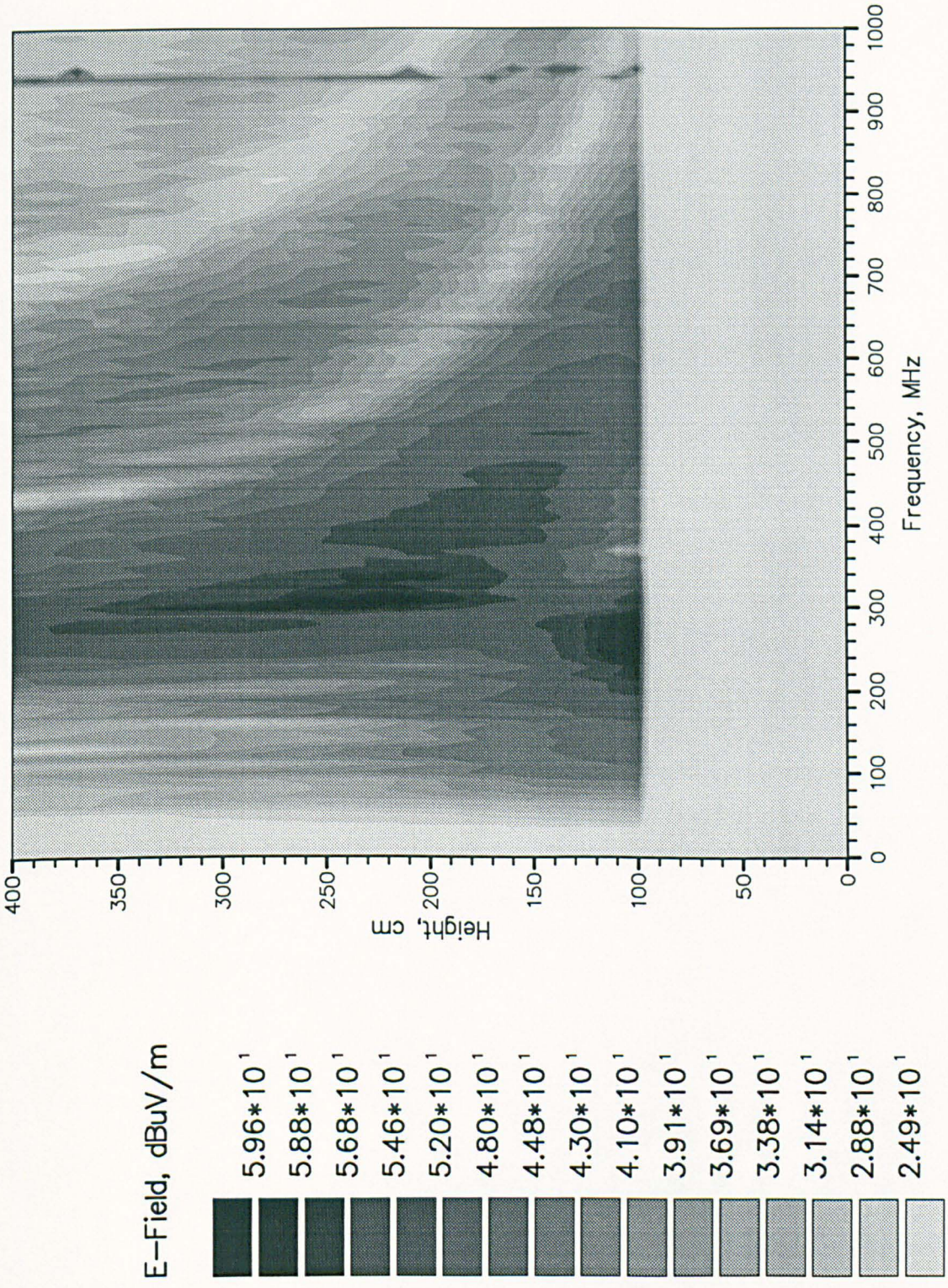


Figure 1.24: Measured electric field strength from the CNE in a 1 MHz bandwidth against receiving antenna height and measurement frequency. Vertical polarisation on a 3 m site with an EUT height of 68 cm.

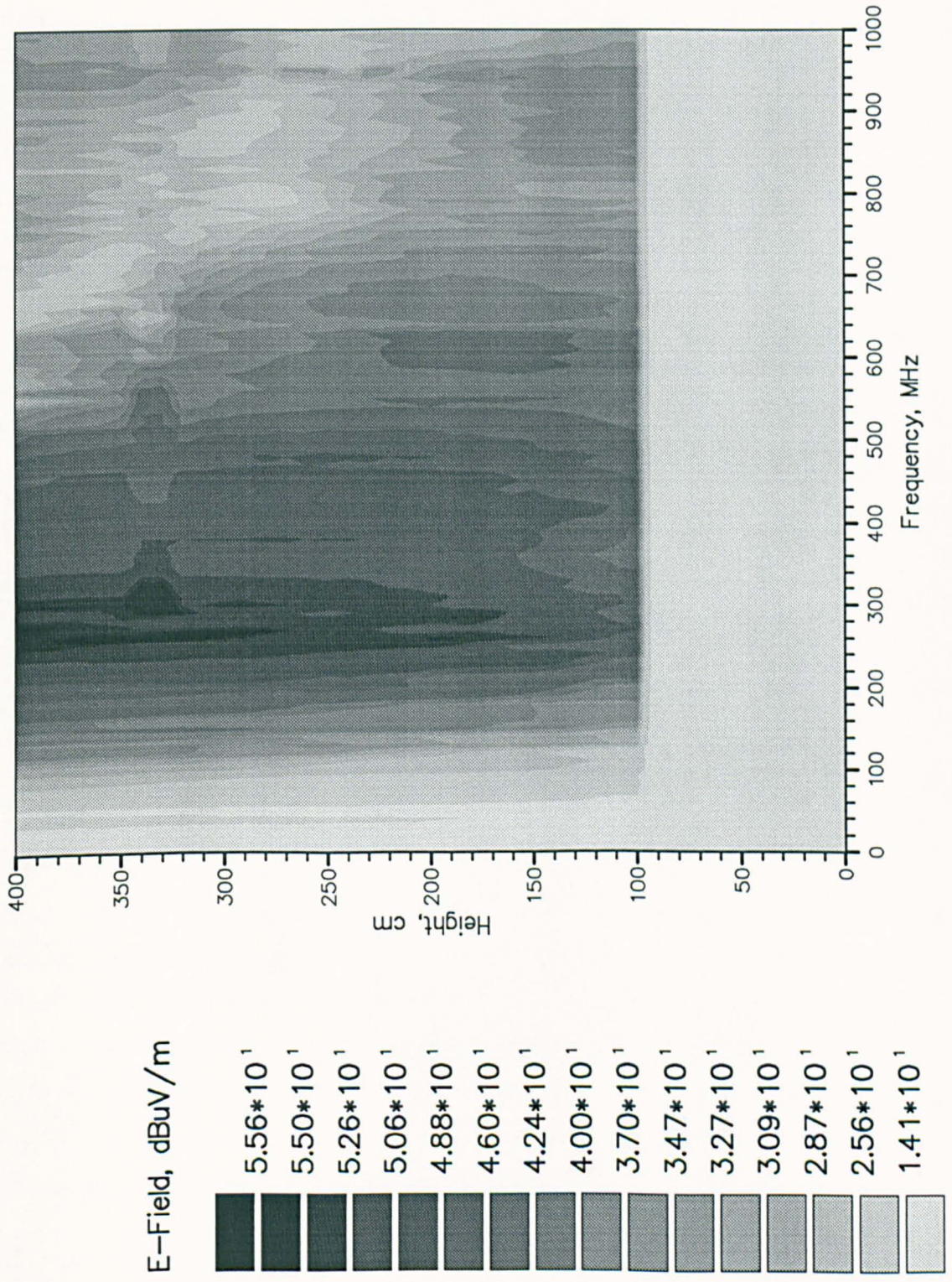


Figure 1.25: Measured electric field strength from the CNE in a 1 MHz bandwidth against receiving antenna height and measurement frequency. Horizontal polarisation on a 10 m site with an EUT height of 68 cm.

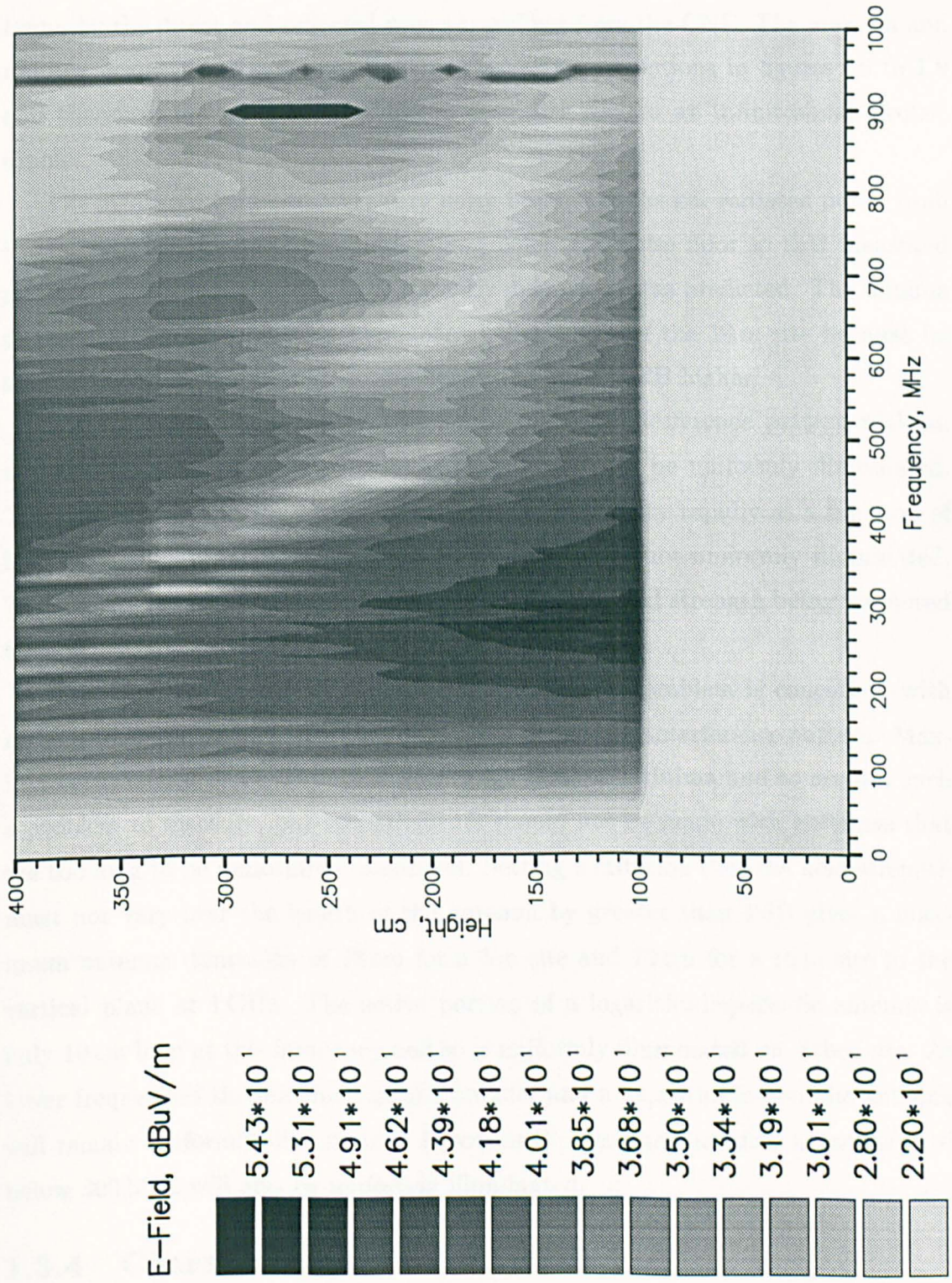


Figure 1.26: Measured electric field strength from the CNE in a 1 MHz bandwidth against receiving antenna height and measurement frequency. Vertical polarisation on a 10 m site with an EUT height of 68 cm.

### 1.3.3 Interpretation of Results

Figures 1.23 to 1.26 show the interference pattern produced at the receiving antenna by the direct and reflected waves travelling from the CNE. The maxima and minima occur in the same positions as the earlier predictions in figures 1.6 to 1.9 and therefore the CNE is behaving in a similar way to an infinitesimal electric dipole.

The measured field data were very noisy because of the low radiated power from the CNE. This resulted in minima falling below the noise floor so that measured minima that were not as deep, or as clearly defined, as was predicted. The minima of the 3 m site were rather better defined than those of the 10 m site because its shorter path lengths gave measured fields that were 10 dB higher.

Another problem associated with measuring the interference pattern with an antenna that has finite dimensions is that it may not be uniformly illuminated. The field strength in the region of the minima varies very rapidly as a function of height, so any antenna used to measure the minima is not uniformly illuminated. This results in smoothing of the minima and a higher field strength being measured than is actually present.

The other implication of the uniform illumination problem is concerned with radiation measurements that are made at maxima in the interference pattern. Maxima occur over a much broader height range than the minima and so are not such a problem to measure, but measurements should not be made with antennas that are too long to be uniformly illuminated. Setting a criterion that the field strength must not vary over the length of the antenna by greater than 1 dB gives a maximum antenna dimension of 28 cm for a 3 m site and 72 cm for a 10 m site in the vertical plane at 1 GHz. The active portion of a logarithmic-periodic antenna is only 10 cm long at this frequency and so is uniformly illuminated on either site. At lower frequencies the maxima become broader and a logarithmic-periodic antenna will remain uniformly illuminated. Resonant dipoles and biconical antennas used below 300 MHz will also be uniformly illuminated.

### 1.3.4 Characterisation of the CNE

The measured field patterns from the CNE on the OATS were compared with the theory of §1.1 in order to calculate its dipole moment and total radiated power. The horizontally polarised data measured on the 3 m site were used for the analysis because this was the clearest and least noisy of all the data sets shown in figures 1.23 to 1.26.

The maximum field that occurred in the receiving antenna height scan range was found and compared with the maximum predicted field from a 1 Am electric dipole at each frequency. It can be seen from equations (1.4) to (1.6) that radiated field strength is proportional to dipole moment; therefore, by assuming that the CNE behaved as an infinitesimal electric dipole and that the test site behaved in an ideal way, it was possible to calculate the dipole moment of the CNE in the 1 MHz measurement bandwidth. This dipole moment was then converted to a dipole moment per root Hz because the radiation from the CNE was broadband. The results are shown in figure 1.27.

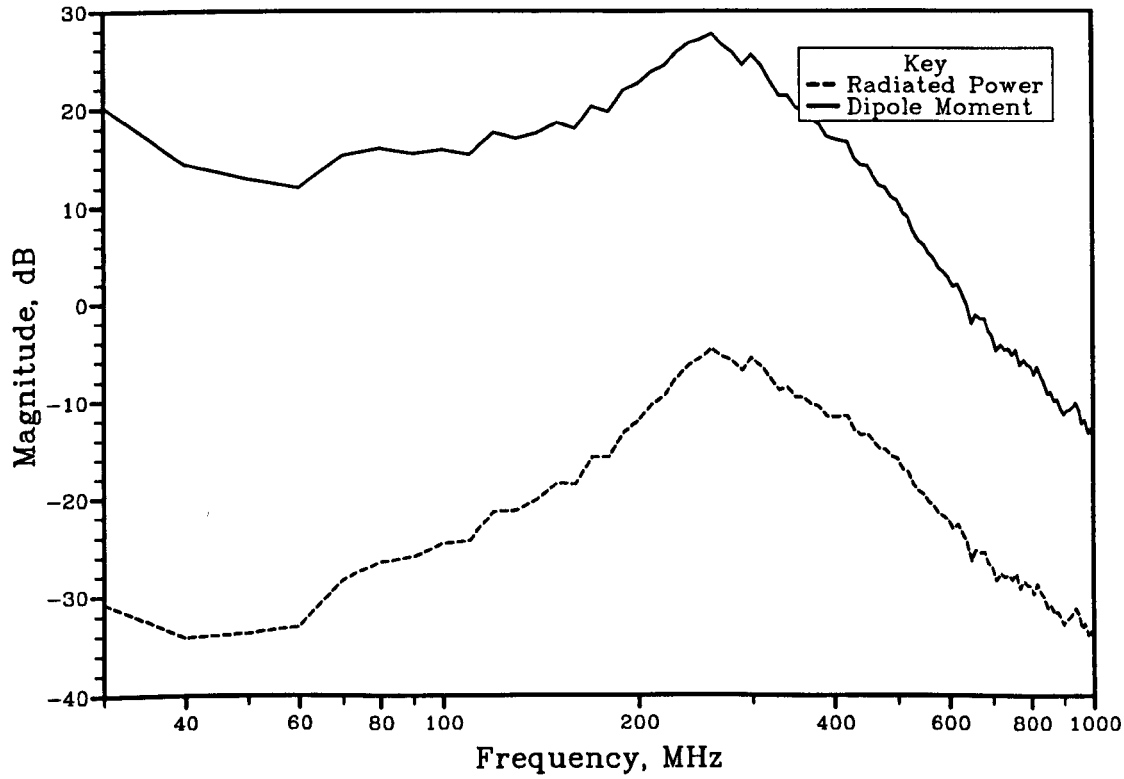


Figure 1.27: Dipole moment of the CNE in dBnAmHz$^{-\frac{1}{2}}$ and its Effective Isotropic Radiated Power in dBpWHz$^{-1}$.

The radiation resistance $R_{rad}$ of a short electric dipole is given in reference [20] as,

$$R_{rad} = \frac{2\pi\eta}{3}\left(\frac{l}{\lambda}\right)^2 \tag{1.29}$$

where $l$ is the length of the dipole. The total radiated power from the dipole is given by $P_{rad} = I^2 R_{rad}$, where $I$ is the excitation current, therefore the radiated power from the dipole is related to its dipole moment, $M_e$, by

$$P_{rad} = \frac{2\pi\eta}{3}\left(\frac{M_e}{\lambda}\right)^2 \tag{1.30}$$

Equation (1.30) was used to obtain the effective isotropic radiated power (EIRP) from the CNE and this is also plotted over the frequency range in figure 1.27.

It can be seen from figure 1.27 that the CNE does not radiate a constant spectral power density. It radiates most strongly at 260 MHz and the radiation level then tails off at 40 dB per decade above this frequency and then at 80 dB per decade above 480 MHz. Dipole moment falls with a slope greater than that of radiated power by a further 20 dB per decade. Below 260 MHz power spectral density also falls, although not as rapidly, and without a clearly defined slope rate.

The origin of the radiating characteristics of the CNE was not within the scope of this thesis, but the measurements in this section serve to show how the OATS may be used to characterise an electrically small radiating source.

## 1.4 Summary and Conclusions

Radiation measurements performed on an open-area test site differ from those performed in free space because, in addition to a direct path, there is a second path by which radiation travels from the source to the measurement antenna. This is a reflected path from the ground plane whose amplitude and phase is therefore affected by the reflection coefficient of the ground plane.

The direct and reflected waves sum together at the receiving antenna with phases that differ according to the excitation frequency and antenna polarisation. Below 100 MHz on a 3 m site and 200 MHz on a 10 m site the phase shifts along the paths are dominated by the phase shift associated with reflection at the ground plane surface. With a perfectly conducting ground plane this is 180° for a wave from a horizontally polarised antenna and 0° for a wave from a vertically polarised antenna. Consequently, the two waves tend to cancel out at low frequencies with horizontal polarisation and reinforce with vertical polarisation. This causes the repeatability of horizontally polarised measurements on longer test sites to be poor at low frequencies as their direct and reflected path lengths are most similar.

Above 100 MHz on a 3 m site and 200 MHz on a 10 m site the direct and reflected waves will sum together in phase at at least one point within a 1–4 m height range above the ground plane. Scanning the receiving antenna through this height range and recording the maximum field strength ensures that the measurement will be repeatable on any test site that has a good conducting ground plane.

Great care is required in the design of the ground planes of open-area test sites. For 3 m and 10 m test sites they are required to be flat to within better than 4.37 cm and 7.28 cm respectively over the entire area of the first Fresnel zone. This area must also act as a perfect reflector and so should be covered with either a solid metal plate or a mesh of electrically small holes. The edges of the plate must be connected by a low impedance plate to the bulk earth beneath and surrounding it or resonant currents may flow within it.

Buildings around the test site should be sufficiently far from it that any stray reflections travelling via them have significantly longer path lengths than the direct and ground plane reflected waves between the source and sink. The CISPR ellipse is a general guide but large faced buildings just outside it can still cause several dBs of perturbation.

# Chapter 2

# Analysis of Wire Antenna Structures

This chapter describes various computer models that were used to simulate resonant dipole antennas and a skeletal form of the biconical antenna that is often used for EMC measurements. The objective of the simulations was to model each antenna accurately, so that the coupled power between pairs of such antennas could be calculated above the ground plane of an ideal open-area test site. This chapter describes the development of the models of the antennas, but it is left until chapter 3 to calculate coupled powers.

Both the resonant dipole antenna and the skeletal biconical antenna are formed from thin wire radiators and have been analysed by a variety of different approaches, of which some are more accurate than others. A brief summary of the modelling approaches that have been used to calculate the scattered fields from wire antennas is given in §2.1, and the remainder of this chapter describes the models that were used in this thesis.

The simplest method that may be used for the simulation of resonant dipole antennas is the applied EMF method, and it is discussed in §2.2. It assumes that the current on the resonant dipole is distributed sinusoidally along the length of the antenna, with a null at either end and maximum at the central feed point. The method therefore cannot be used for antenna structures having more complicated current distributions, including the skeletal biconical antenna.

In order to model the resonant dipole antenna more accurately, it is necessary to determine its actual current distribution. This is accomplished by deducing and solving integral equations; §2.3 describes an integral equation, known as Hallèn's integral equation, which may be used to model the current distribution on the resonant dipole antenna. A modification to the method also allows the current distribution on coupled resonant dipole antennas to be modelled. An approximate solution to the coupled antenna integral equation was used for the analysis of a

resonant dipole over a ground plane, and this is also described in §2.3.

The most accurate method used for the simulation of wire antennas in this thesis was a numerical technique known as the method of moments. More general integral equations than Hallèn's can be developed to model the current distributions on wire structures more complicated than the resonant dipole antenna. The method of moments can be used to solve these integral equations and thereby calculate the current distributions on complicated wire antennas, including the skeletal biconical antenna. The software implementation of the method of moments that was used in this thesis is known as Numerical Electromagnetics Code (NEC) [21] and the use of it for modelling the resonant dipole antenna is described in §2.4.

The drive point impedance of an antenna is the impedance presented at the exact point where its feeding transmission line flares out into the radiating structures. This quantity will be referred to frequently in this chapter and it is important to realise that it is not necessarily the impedance that will be measured at the coaxial connector of a real antenna. This is because there is usually an intervening two-port network between the coaxial connector of a real antenna and its drive point. Chapter 4 considers the implications of this for antenna calibration in more detail.

§2.5 compares measured drive point impedances of the resonant dipole antenna with predictions obtained from simulations using NEC and the applied EMF method in order to deduce the accuracy of each model.

There is no simple theory to describe the behaviour of the skeletal biconical antenna and so it could only be analysed by simulation with the NEC computer code. §2.6 describes how this was done and gives predictions of the antenna's characteristics and drive point impedance. The drive point impedance predicted by NEC is compared with measurement in §2.7, and the model is optimised to give the closest possible agreement between prediction and measurement. Finally, §2.8 summarises the chapter and presents some brief conclusions.

## 2.1 Review of Analysis of Wire Antennas

In order to calculate parameters such as the gain, impedance or radiation pattern of an antenna, it is necessary to have a precise knowledge of the magnitude and phase of the current distribution that flows on its conducting surfaces. This short section gives a brief historical review of the techniques that have been used for the simulation of antenna structures made up of thin wires. The simplest wire antenna structure, and for many years the only one that could be analysed, is that of the resonant dipole antenna; this will be discussed first.

The calculation of the drive point impedance of an antenna is a two stage process. The current distribution on the surface of the antenna must first be found, and then assumed to flow as a filament along the axis of the cylindrical conductors. The field components due to this current distribution may then be calculated at an observation point so that the Poynting vector can be found. Integration of the normal component of the Poynting vector over the surface of the antenna gives the total real and imaginary power flow from the antenna. Then, if the antenna is assumed to be lossless, this may be equated to the power flowing into the antenna to yield the components of its drive point impedance.

The first successful method for the analysis of the resonant dipole antenna made the assumption that the antenna had a current distribution that was sinusoidally distributed, with a null at both ends of the antenna and a maximum at the central feed point. This model was based upon the idea that the antenna was simply a flared transmission line and would therefore have a similar current distribution. The current distribution on resonant dipoles becomes more sinusoidally distributed as they become thinner and so this method is more accurate for very thin antennas but not very accurate for antennas having diameters of practicable size. It is often called the applied EMF method and was developed by several authors during the late 1920s and 1930s [22], [23], [24], [25]. §2.2 shows how this method of analysis may be used to obtain the self impedance of, and mutual impedance between, resonant dipole antennas.

For a more accurate theory, it was necessary to obtain a better model of the current distribution on the resonant dipole antenna, and the solution of integral equations offered a method for achieving this. H. E. Pocklington developed an integral equation in 1897 [26] but it was the work of E. Hallèn and his integral equation, in 1938 [27], that led to the solutions that are used today. The integral equations could not be solved analytically and, before the advent of fast computers, it was difficult to solve them accurately. Solutions were based upon successive

approximations and series that were summed asymptotically; the most useful of these solutions was proposed by R. W. P. King in his *Theory of Linear Antennas* in 1956 [28].

The next significant development was the application of a numerical technique, known as the method of moments [29], to the solution of integral equations. This method offers a computationally efficient technique for solution of integral equations that describe electromagnetic scattering from conducting bodies. It has become the most widely accepted and most accurate mathematical technique for analysing general structures that can be expressed in terms of thin wires, and that have overall dimensions of up to several wavelengths. The method is discussed briefly in §2.4 and results are obtained using NEC [21], a software implementation of the method of moments.

All the above methods represent frequency domain methods of calculating the drive point impedance of the resonant dipole antenna, but integral equations may also be solved in the time domain. Fourier transformation can then give impedances as a function of frequency from a single simulation. Frequency domain simulations have to be run many times to obtain sufficient data points to plot impedance as a function of frequency. Suitable software was not available to obtain time domain solutions and so no work was performed in this thesis using that method.

Solution of Hallèn's integral equation allows the current distribution on a cylindrical dipole antenna to be calculated if the antenna is excited across an infinitesimally small gap at its centre. Real antennas are excited across finite gaps at their centres by transmission lines, therefore their excitation regions are not modelled very well by Hallèn's integral equation. In order to simulate a more realistic feed arrangement than an infinitesimal gap, it is necessary to solve a more general integral equation, such as Pocklington's equation.

## 2.2 The Applied EMF Method for Cylindrical Dipole Antennas

This section shows how the applied EMF method may be used to calculate the drive point impedance of a resonant dipole antenna. Definitions will be given of self and mutual impedances between antennas, and these used to show how the drive point impedance may be calculated for an antenna that is coupled to other antennas. The approach is general, in that it is for a dipole antenna with cylindrical arms that are not necessarily of exactly resonant length.

The applied EMF method does not attempt to calculate the current distribution on a cylindrical dipole antenna, but assumes that the current is distributed sinusoidally along the length of the antenna, as shown in figure 2.1 and defined by equation (2.1).

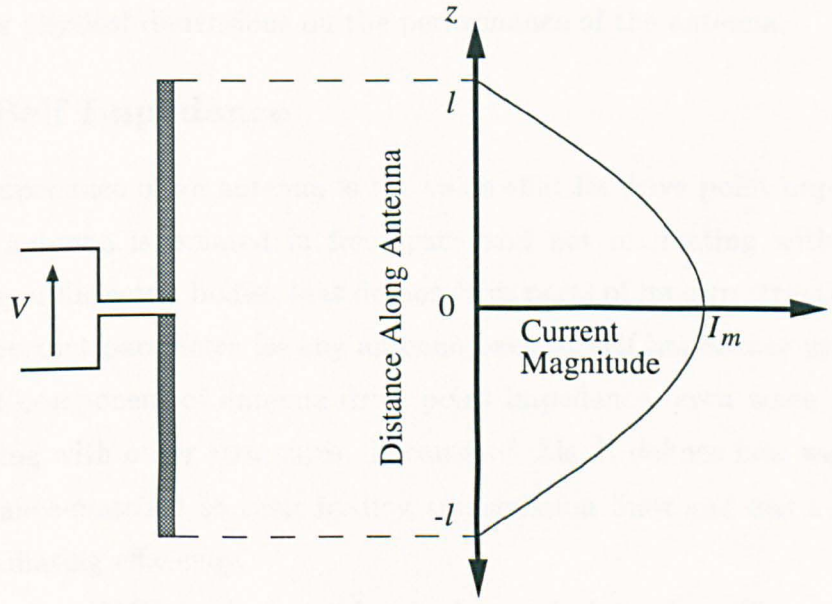


Figure 2.1: Sinusoidal current distribution on a resonant dipole antenna.

$$I(z) = \begin{cases} I_m \sin[\beta(l-z)] & z \geq 0 \\ I_m \sin[\beta(l+z)] & z \leq 0 \end{cases} \tag{2.1}$$

The length $l$ is the half-length of the antenna, the current, $I_m$ is the maximum value and $\beta$ is the phase propagation constant of the radiation, related to the wavelength, $\lambda$, by

$$\beta = \frac{2\pi}{\lambda} \tag{2.2}$$

The assumption that the currents on the cylindrical dipole antenna are sinusoidally distributed arises from the conceptual idea that the antenna is simply a flared transmission line and so will have a similar current distribution. It is known

that this assumption becomes more accurate for thinner antennas, but as King states [30]:

> A sinusoidal distribution of current is not possible even for an infinitely thin antenna if there is only a single generator at the center. A continuous distribution of generators along the entire antenna is required with emf's of proper amplitudes and phases.

The accuracy of the applied EMF method, for drive point impedance prediction, is discussed later in §2.5. Results from it are compared with measurements and predictions from the more accurate method of moments.

It is not necessary to reproduce the derivation of the expressions that result from the applied EMF method because it is a well established technique that is covered by many electromagnetics text books [31], [32]. However, graphs will be plotted to show how resonance arises in the cylindrical dipole antenna and the effect of its physical dimensions on the performance of the antenna.

### 2.2.1 Self Impedance

The self impedance of an antenna is the value that its drive point impedance has when the antenna is isolated in free space and not interacting with any other conducting or dielectric bodies that do not form parts of its own structure. This is a very important parameter for any antenna because self impedance usually forms the largest component of antenna drive point impedance, even when an antenna is interacting with other structures. Because of this, it defines how well antennas are impedance-matched to their feeding transmission lines and has a large effect on their radiating efficiency.

The applied EMF method can be used to calculate the self impedance of a cylindrical dipole, whose current is assumed to exist as a sinusoidally distributed filament along the central axis of the antenna. This filament is allowed to radiate so that the field it produces at the surface of the antenna sums with the scattered field to satisfy the boundary condition of vanishing tangential electric field at the surface of the antenna.

The resulting expressions for the resistive and reactive components of self impedance have appeared in many different forms, but the ones that were used in this thesis are given as follows: the self impedance of a cylindrical dipole antenna with a radius $a$ and a half-length $l$ is $Z_{11}$, and has resistive and reactive components $R_{11}$ and $X_{11}$, such that

$$Z_{11} = R_{11} + jX_{11} \tag{2.3}$$

The solutions for the resistive and reactive components are

$$R_{11} = \frac{Z_0}{4\pi \sin^2(\beta l)}\Big\{4\cos^2(\beta l)\mathrm{Cin}(2\beta l) - \cos(2\beta l)\mathrm{Cin}(4\beta l) + \sin(2\beta l)\Big[\mathrm{Si}(4\beta l) - 2\mathrm{Si}(2\beta l)\Big]\Big\} \quad (2.4)$$

$$X_{11} = \frac{Z_0}{4\pi \sin^2(\beta l)}\Big\{4\cos^2(\beta l)\mathrm{Si}(2\beta l) - \cos(2\beta l)\mathrm{Si}(4\beta l) + \sin(2\beta l)\Big[2\mathrm{Cin}(2\beta l) - \mathrm{Cin}(4\beta l) + 2\ln\left(\frac{a}{l}\right)\Big]\Big\} \quad (2.5)$$

The functions $\mathrm{Si}(x)$ and $\mathrm{Cin}(x)$ are integral functions that are defined in appendix B. They cannot be solved analytically but the appendix shows how they may be evaluated numerically by series summation and gives the Fortran subroutine that was used for this purpose.

### 2.2.2 Characteristics of the Cylindrical Dipole Antenna

Equations (2.4) and (2.5) give the resistive and reactive components of the self impedance of a cylindrical dipole antenna carrying a sinusoidal current distribution. Figure 2.2 shows the values of these components for a typical dipole antenna, with a radius of 5 mm and a half-length of 0.5 m, excited at frequencies up to 1 GHz.

Equations (2.4) and (2.5) show that the impedance components have a complicated dependence on the product $\beta l$, i.e. how long the antenna is as a fraction of a wavelength. The antenna used for the generation of the data in figure 2.2 was a half-wavelength long at 150 MHz, a whole wavelength long at 300 MHz etc. Hence the graph shows its self impedance at frequencies up to where it is just over three wavelengths long. At frequencies where the antenna length is much less than a half-wavelength the antenna is capacitive, but as the antenna length approaches a half-wavelength its self impedance becomes resistive, and then changes between resistive, inductive and capacitive behaviour as frequency continues to increase.

When a cylindrical dipole antenna is exactly a half-wavelength long, the applied EMF method gives the result that its self impedance is independent of the antenna radius and is

$$Z_{11} = (73 + j42.5)\,\Omega$$

### 2.2.3 Resonance

Figure 2.2 shows that there are several frequencies at which the reactive component of the self impedance of a resonant dipole antenna becomes equal to zero. These frequencies are the resonant frequencies of the antenna, and the resistive component

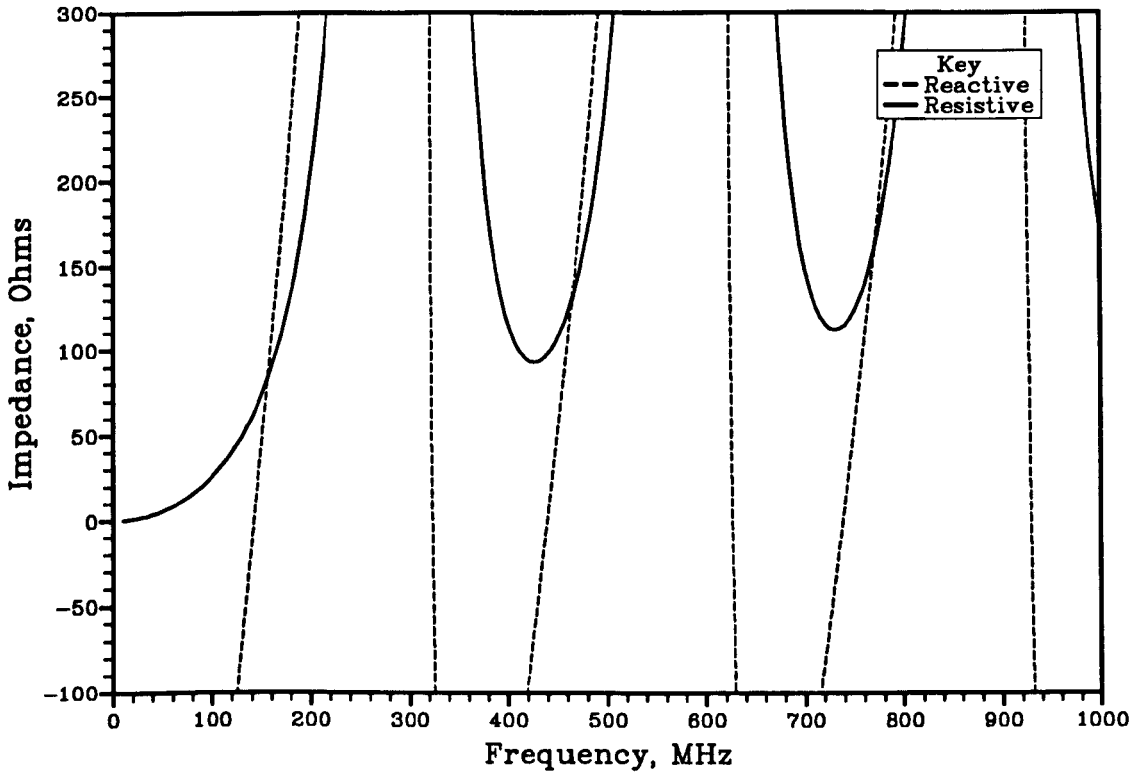


Figure 2.2: Self impedance of a cylindrical dipole antenna having a half-length of 0.5 m and a radius of 5 mm.

has alternately low and high values at successive resonances. Table 2.1 shows the values of the resistive component at the resonant frequencies.

| Frequency, MHz | 71.45 | 161.3 | 220.5 | 312.8 | 370.0 | 463.7 |
|---|---|---|---|---|---|---|
| Resistance, Ω | 63.60 | 3113 | 97.21 | 3101 | 113.01 | 3077 |

Table 2.1: Resonant frequencies for a dipole antenna.

The low resistance resonances have similar characteristics to series LCR networks, whilst the high resistance resonances, or antiresonances, have similar characteristics to parallel LCR networks. Q-factors may be found for the resonances, when the antenna is driven from a source, and it is these that define the bandwidth of the antenna when it is used for information transmission. It should be noted that the minimum standing wave ratio (SWR) of the cylindrical dipole antenna will occur at a frequency slightly below resonance, when driven from a 50 Ω transmission line.

Cylindrical dipole antennas are usually used at or near to their first resonance because their self impedance presents the best match to a 50 Ω transmission line at this frequency. The resonance occurs when the antenna has a length of slightly less than half a wavelength, its exact length being determined by the radius, as shown

by figure 2.3.

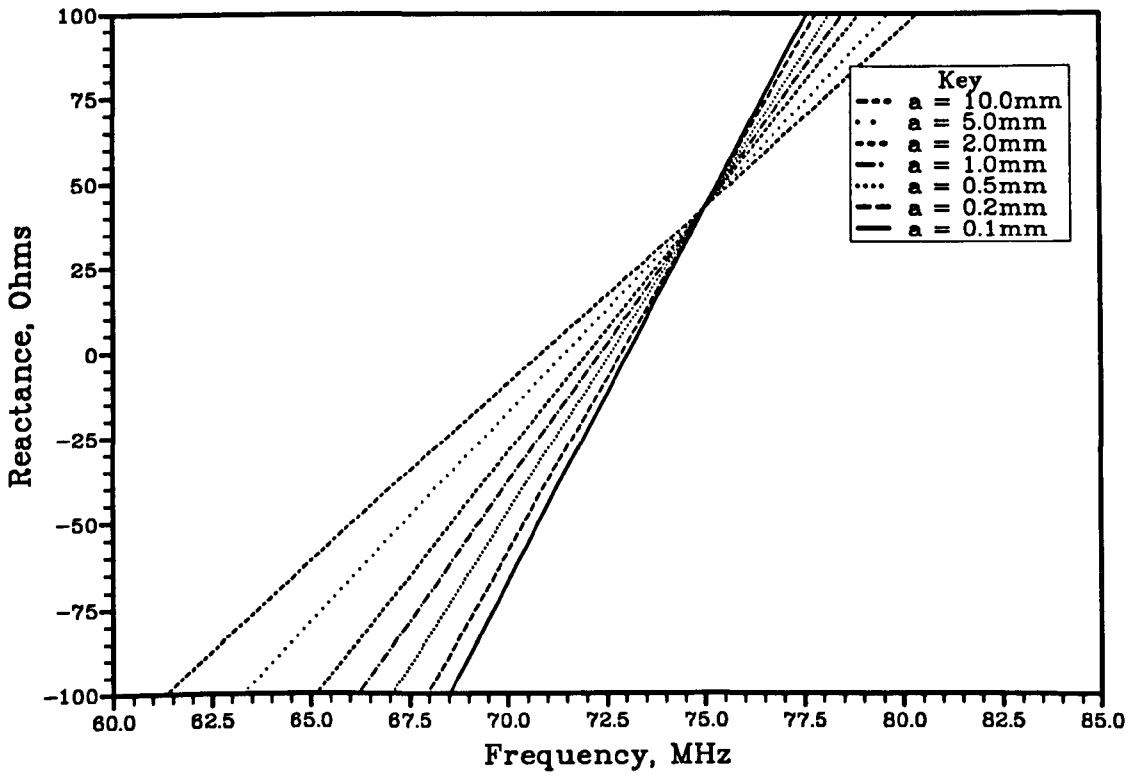


Figure 2.3: Effect of radius on self reactance.

The gradient with which the reactive component of the self impedance of a cylindrical dipole antenna passes through zero at its first resonance depends upon the radius of the arms of the antenna. The gradient is steepest for thin antennas, and they also resonate at frequencies where their lengths are closer to a half-wavelength. The gradient of the reactive component determines the Q-factor of the resonance and so fatter cylindrical dipole antennas have wider bandwidths.

### 2.2.4 Mutual Impedance

The applied EMF method can be expanded to allow analysis of the interactions between coupled cylindrical dipole antennas. This is achieved by use of the concept of mutual impedance between a pair of antennas [31] [32].

H. E. King [33] has derived expressions for the mutual impedance between parallel cylindrical dipole antennas by the applied EMF method. His expressions are general, in that they are for antennas of arbitrary different lengths in any parallel geometry. They have been modified for use in this thesis to represent a slightly different geometry, and also to be for equal length antennas.

The most general orientation of a pair of parallel cylindrical dipole antennas

is termed echelon configuration, and refers to the case where the antennas are offset from each other and not collinear. There are then two special cases of this, where the antennas are either collinear or parallel but not offset. All three of these configurations are shown in figure 2.4 together with the symbols that are used in this thesis to define the orientations. $d$ defines the perpendicular separation of the

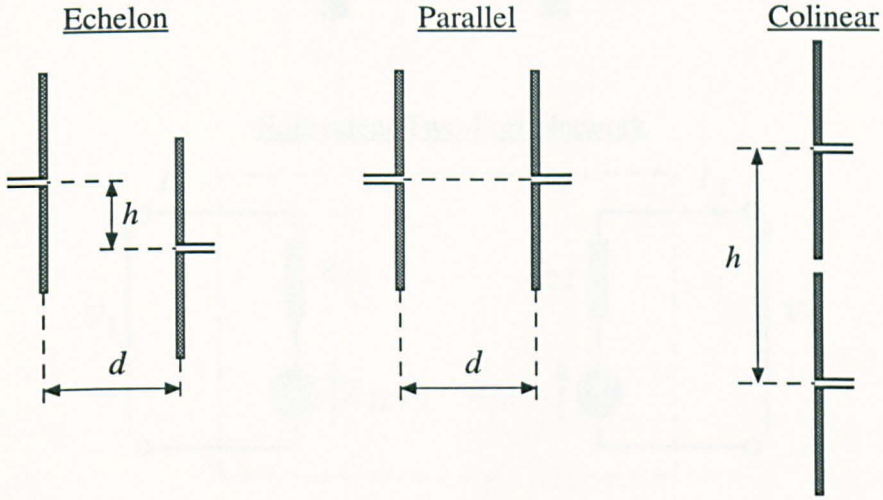


Figure 2.4: Different geometrical configurations of parallel cylindrical dipole antennas.

antennas and $h$ defines their collinear separation. $l$ and $a$ represent the half-length and radius of the antennas, respectively.

The expressions for the resistive and reactive components of mutual impedance are rather long and cumbersome and so they are given in appendix C.

### 2.2.5 Coupled Cylindrical Dipole Antennas

Earlier in this section the self impedance of, and mutual impedances between, cylindrical dipole antennas have been calculated by the applied EMF method. This subsection shows how these two parameters may be combined to analyse the situation of two coupled antennas, and how the analysis may be extended to cover multiple coupled antennas. A relationship between the drive point voltages and currents of the antennas is sought, so that the power coupled between them may be calculated.

The situation of two coupled antennas can be modelled as a two-port network, where the ports are the drive points of the antennas. Figure 2.5 shows two coupled antennas and an equivalent circuit showing the impedance parameters of the two-port network. The terminal voltage of antenna 1 is the sum of the voltage due to its own current flowing in its self impedance and the induced voltage due to the

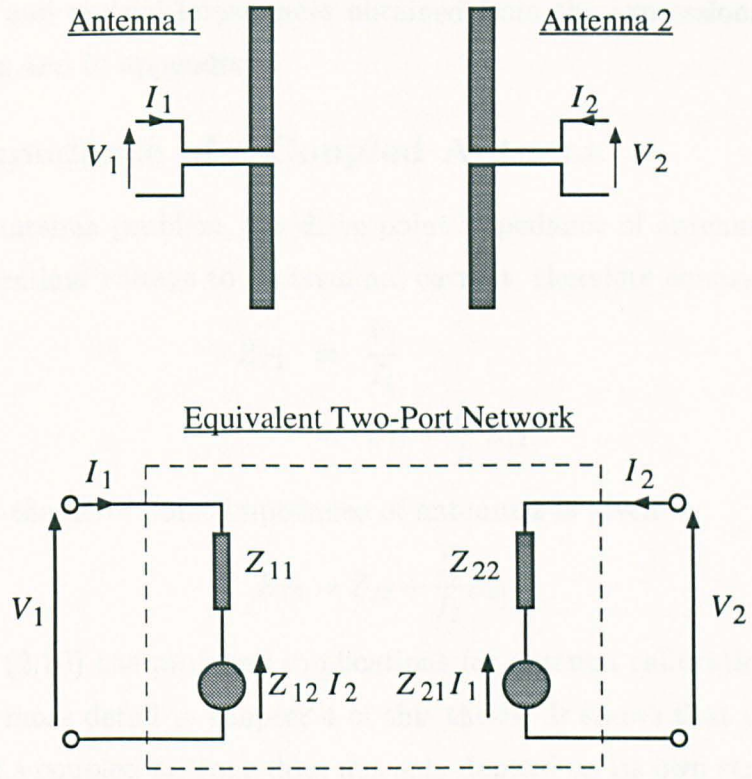


Figure 2.5: Two coupled cylindrical dipole antennas and their equivalent two-port network expressed in terms of impedance parameters.

second antenna's current flowing in their mutual impedance. i.e.

$$V_1 = Z_{11}I_1 + Z_{12}I_2 \tag{2.6}$$

A similar expression may be used to express the terminal voltage of the second antenna so that the coupling between both antennas can be described by the matrix equation (2.7).

$$\begin{bmatrix} V_1 \\ V_2 \end{bmatrix} = \begin{bmatrix} Z_{11} & Z_{12} \\ Z_{21} & Z_{22} \end{bmatrix} \cdot \begin{bmatrix} I_1 \\ I_2 \end{bmatrix} \tag{2.7}$$

$Z_{11}$ and $Z_{22}$ are the self impedances of antennas 1 and 2 respectively and, because all of the coupling antennas are linear and passive, the reciprocity principle applies so that the two mutual impedances, $Z_{12}$ and $Z_{21}$, are identical.

$$Z_{12} = Z_{21}$$

The above analysis can easily be expanded to cover $n$ coupled antennas, so the terminal voltage of the $i$th antenna is given by

$$V_i = \sum_{j=1}^{n} Z_{ij}I_j \tag{2.8}$$

The complete problem may be described by an $n \times n$ coupling matrix relating the voltage column vector to the current column vector in the same way as equation (2.7) does for the two antenna case. All that then remains is to fill the matrix

with the self and mutual impedances obtained from the expressions given earlier in this section and in appendix C.

### 2.2.6 Impedance of a Coupled Antenna

For the two antenna problem, the drive point impedance of antenna 1, $Z_{T1}$ is the ratio of its terminal voltage to its terminal current, therefore equation (2.7) gives

$$Z_{T1} = \frac{V_1}{I_1} \tag{2.9}$$

$$= Z_{11} + \frac{I_2}{I_1} Z_{12} \tag{2.10}$$

and similarly the drive point impedance of antenna 2 is given by

$$Z_{T2} = Z_{22} + \frac{I_1}{I_2} Z_{21} \tag{2.11}$$

Equation (2.10) has profound implications for antenna calibration that will be developed in more detail in chapter 4 of this thesis. It shows that the drive point impedance of a coupled antenna does not only depend on its own structure, i.e. its self impedance, but that it also depends on any other antenna or current carrying structure in the vicinity of the antenna.

### 2.2.7 Symmetrical and Antisymmetrical Impedances

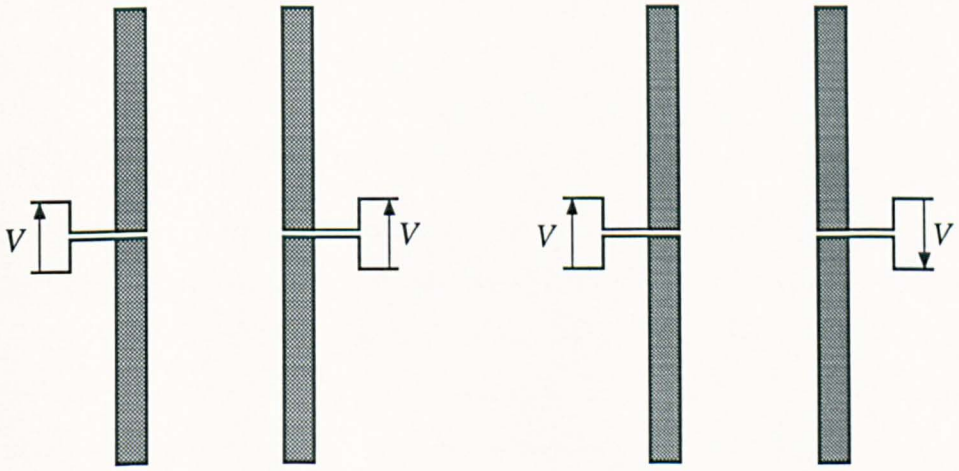


Figure 2.6: Symmetrically and antisymmetrically fed cylindrical dipole antennas.

If two identical parallel and not offset antennas are excited by voltages of equal magnitudes and phases, so that $I_2 = I_1$, their drive point impedances will be the same. This impedance is known as the symmetrical impedance, $Z_S$, and equation (2.10) shows that this is given by

$$Z_S = Z_{11} + Z_{12} \tag{2.12}$$

If two similarly arranged antennas are excited by voltages of equal magnitudes but 180° out of phase, so that $I_2 = -I_1$, their drive point impedances will also be the same. This impedance is known as the antisymmetrical impedance, $Z_A$, and (2.10) shows that this is given by

$$Z_A = Z_{11} - Z_{12} \tag{2.13}$$

Figure 2.6 shows the excitation voltages for both of these cases. Symmetrically and antisymmetrically fed impedances will be encountered later in this thesis because they are easier to calculate than mutual impedances from the integral equation based approaches to coupled antennas described in the rest of this chapter.

## 2.3 Integral Equation Models of the Current on Cylindrical Dipole Antennas

The applied EMF method of the previous section represents a quick and computationally simple method for obtaining the drive point impedances of isolated and coupled cylindrical dipole antennas. Unfortunately, the assumption that the current on the surface of a dipole antenna is sinusoidally distributed along the length of the antenna is not very accurate for antennas having radii of practical dimensions. The exact limitations to the accuracy of this method will be discussed in more detail in §2.5.

In order to develop a more accurate method for the calculation of the drive point impedances of cylindrical dipole antennas, it was necessary to have a better model of the current distribution on their conducting surfaces. This was accomplished by the derivation of Hallèn's Integral Equation for the current distribution on the cylindrical dipole antenna [27]. It is only in recent years that it has become practicable to solve this equation accurately with powerful computers using algorithms such as the method of moments; earlier solutions were approximations and required considerable mathematical effort in order to obtain useful degrees of accuracy.

In this section a brief derivation of Hallèn's integral equation is given, and then the work of Tai [34] is cited to show how a similar analysis to Hallèn's method may be used to analyse the coupled antenna problem.

### 2.3.1 Hallèn's Integral Equation

This section gives a brief derivation of Hallèn's integral equation as an example of a more rigorous approach to the determination of the current distribution on the cylindrical dipole antenna. A more detailed discussion of it is given in reference [35].

Consider a cylindrical dipole antenna, as shown in figure 2.7. The antenna is assumed to be thin so that current on its surface only flows in the $z$-direction and the vector potential $\mathbf{A}$ is therefore also $z$-directed. The antenna is assumed to be a perfectly conducting cylindrical surface, so the vector potential at its surface must satisfy the wave equation.

$$\frac{d^2 A_z}{dz^2} + \beta^2 A_z = 0 \tag{2.14}$$

The solution to this equation may be expressed as

$$A_z = \frac{-j}{c}\left[C_1 \cos(\beta z) + C_2 \sin(\beta |z|)\right] \tag{2.15}$$

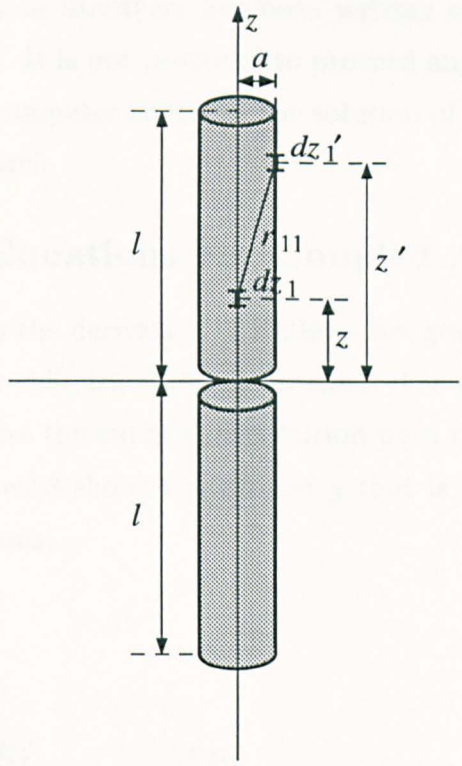


Figure 2.7: Geometry used for the derivation of Hallèn's integral equation for the current distribution on the cylindrical dipole antenna.

where $c$ is the velocity of light, and the constants $C_1$ and $C_2$ must be evaluated when the boundary conditions are imposed on the antenna.

One of the boundary conditions on the antenna is that it is excited by a voltage $V_s$ across an infinitesimal gap at its centre. This enables the constant $C_2$ to be evaluated to satisfy this discontinuity in the scalar potential.

$$C_2 = \frac{1}{2}V_s \tag{2.16}$$

The other constant, $C_1$, must be evaluated when the boundary condition that the current becomes zero at the ends of the antenna is imposed.

The current on the antenna is regarded as flowing as a filament along the $z$-axis, radiating onto the surface of the antenna. The vector potential due to such a filamentary current distribution is $z$-directed and can be expressed as

$$A_z = \frac{\mu_0}{4\pi}\int_{-l}^{l} I_z' \frac{e^{-j\beta r_{11}}}{r_{11}} dz' \tag{2.17}$$

Equating the vector potential given by equations (2.15) and (2.17) gives

$$\int_{-l}^{l} I_z' \frac{e^{-j\beta r_{11}}}{r_{11}} dz' = \frac{-j4\pi}{\eta}\left[C_1\cos(\beta z) + \frac{1}{2}V_s\sin(\beta|z|)\right] \tag{2.18}$$

This is Hallén's integral equation for the current distribution on a perfectly conducting cylindrical dipole antenna. Its solution is obtained by a complicated process,

and a substantial body of literature has been written on different numerical approaches to its solution. It is not proposed to proceed any further with its solution here, because existing computer codes for the solution of similar integral equations were used for this research.

### 2.3.2 Integral Equations For Coupled Antennas

By a similar analysis to the derivation of Hallèn's integral equation for the current distribution on a single cylindrical dipole antenna, it is possible to derive integral equations that determine the current distribution on a pair of coupled cylindrical dipole antennas. Figure 2.8 shows the geometry that is used for the development of these integral equations.

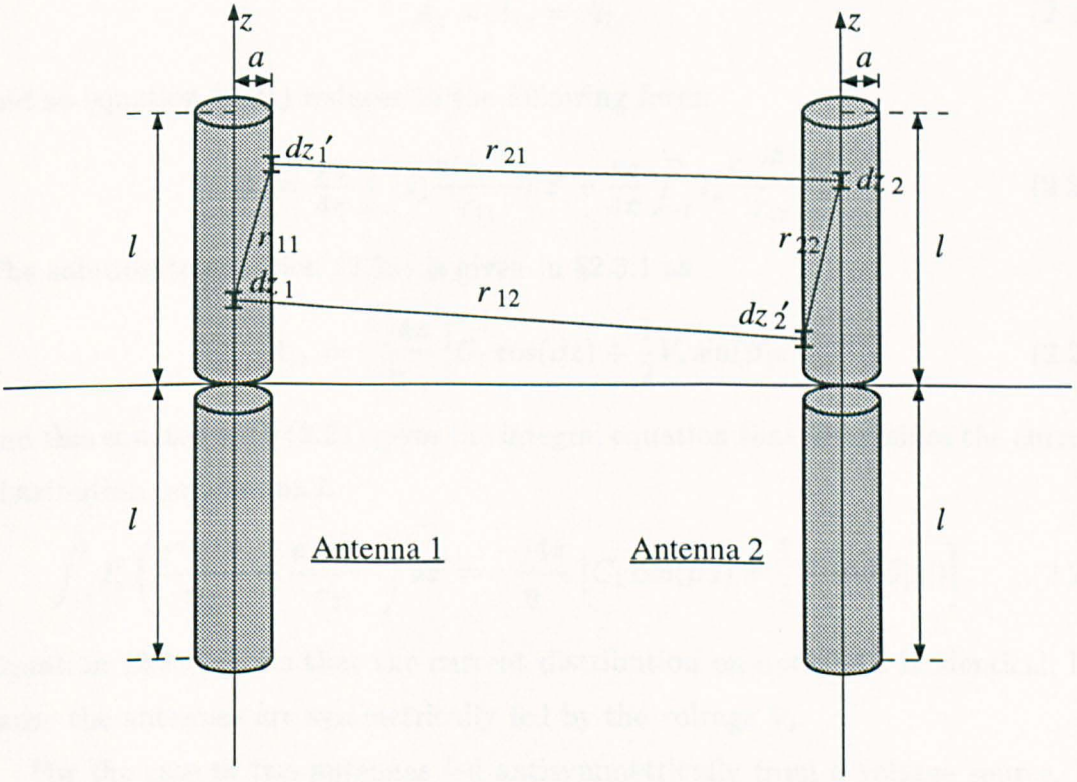


Figure 2.8: Geometry for the derivation of integral equations for the current distribution on a pair of coupled antennas.

The vector potential, **A**, at the perfectly conducting surface of each antenna is $z$-directed and satisfies the wave equations, (2.19) and (2.20).

$$\frac{d^2 A_{1z}}{dz^2} + \beta^2 A_{1z} = 0 \tag{2.19}$$

$$\frac{d^2 A_{2z}}{dz^2} + \beta^2 A_{2z} = 0 \tag{2.20}$$

The vector potential at the surface of each antenna is also given by the sum of the vector potentials due to its own current and the current on the other antenna. If

the current flowing on each antenna is regarded to flow as a filament along the axis of that antenna, the total vector potentials at the surface of each antenna are given by equations (2.21) and (2.22).

$$A_{1z} = \frac{\mu_0}{4\pi}\int_{-l}^{l} I'_{1z}\frac{e^{-j\beta r_{11}}}{r_{11}}dz' + \frac{\mu_0}{4\pi}\int_{-l}^{l} I'_{2z}\frac{e^{-j\beta r_{12}}}{r_{12}}dz' \tag{2.21}$$

$$A_{2z} = \frac{\mu_0}{4\pi}\int_{-l}^{l} I'_{2z}\frac{e^{-j\beta r_{22}}}{r_{22}}dz' + \frac{\mu_0}{4\pi}\int_{-l}^{l} I'_{1z}\frac{e^{-j\beta r_{21}}}{r_{21}}dz' \tag{2.22}$$

If two identical antennas are driven symmetrically by an excitation voltage $V_s$, they will have the same excitation currents and hence the same vector potentials at their surfaces, i.e.

$$I_z = I_{1z} = I_{2z} \tag{2.23}$$

$$A_z = A_{1z} = A_{2z} \tag{2.24}$$

and so equation (2.21) reduces to the following form:

$$A_z = \frac{\mu_0}{4\pi}\int_{-l}^{l} I'_{z}\frac{e^{-j\beta r_{11}}}{r_{11}}dz' + \frac{\mu_0}{4\pi}\int_{-l}^{l} I'_{z}\frac{e^{-j\beta r_{12}}}{r_{12}}dz' \tag{2.25}$$

The solution to equation (2.19) is given in §2.3.1 as

$$A_{1z} = \frac{-j4\pi}{\eta}\left[C_1\cos(\beta z) + \frac{1}{2}V_s\sin(\beta|z|)\right] \tag{2.26}$$

and this equated with (2.21) gives the integral equation that determines the current distribution on antenna 1.

$$\int_{-l}^{l} I'_z\left(\frac{e^{-j\beta r_{11}}}{r_{11}} + \frac{e^{-j\beta r_{12}}}{r_{12}}\right)dz' = \frac{-j4\pi}{\eta}\left[C_1\cos(\beta z) + \frac{1}{2}V_s\sin(\beta|z|)\right] \tag{2.27}$$

Equation (2.23) shows that the current distribution on antenna 2 is identical, because the antennas are symmetrically fed by the voltage $V_s$.

For the case of two antennas fed antisymmetrically from a voltage source, $V_s$, the derivation of the integral equation for the current on antenna 1 is similar except that the antenna currents, and hence their vector potentials, are 180° out of phase, i.e.

$$I_z = I_{1z} = -I_{2z} \tag{2.28}$$

$$A_z = A_{1z} = -A_{2z} \tag{2.29}$$

The resulting integral equation for the current distribution on antenna 1 in this case is

$$\int_{-l}^{l} I'_z\left(\frac{e^{-j\beta r_{11}}}{r_{11}} - \frac{e^{-j\beta r_{12}}}{r_{12}}\right)dz' = \frac{-j4\pi}{\eta}\left[C_1\cos(\beta z) + \frac{1}{2}V_s\sin(\beta|z|)\right] \tag{2.30}$$

Tai has derived an approximate solution to the integral equations (2.27) and (2.30) [34]. His solution is known as a first order solution and the accuracy of it is not clear from the solution method. It is not necessary to explain the derivation of the first order solution here, but the resulting expressions for the drive point impedances of symmetrically and antisymmetrically fed pairs of cylindrical dipole antennas are reproduced in appendix D. These expressions were built into a computer program that was used for antenna impedance prediction in the early stages of the work carried out in this thesis. The model was later abandoned due to its inaccuracy (see §2.5).

Self and mutual impedances can be found for the coupled antennas in this model by rearranging equations (2.12) and (2.13) in §2.2.6:

$$Z_{11} = \frac{1}{2}(Z_S + Z_A) \tag{2.31}$$

$$Z_{12} = \frac{1}{2}(Z_S - Z_A) \tag{2.32}$$

## 2.4 The Simulation of Wire Antennas using the Method of Moments

The method of moments is currently the most widespread approach to solving the integral equations that describe the current distributions on wire antenna structures. It reduces the integral equation to conventional integrations and a matrix inversion, of which both may readily be solved using a digital computer.

It is not within the scope of this thesis to include a detailed description of the method of moments because it is a well established numerical technique that is fully documented in the literature. The usual reference book on the method of moments, as applied to field computation, is reference [36], but a more brief and easily readable account of the technique is given in reference [37].

This section briefly describes the philosophy behind the method of moments and explains how an existing software implementation of it, known as Numerical Electromagnetics Code (NEC) [38], was used for the simulation of cylindrical dipole antennas. §2.6 and §2.7 describe how NEC was used to simulate another wire antenna known as the skeletal biconical antenna.

### 2.4.1 The Moment Method

The general form of integral equations such as (2.18), (2.23) and (2.30) is

$$F(g) = h \tag{2.33}$$

The function $F$ is a known linear integral operator, $h$ is a known excitation function and $g$ is the response function. The object is to determine $g$ from a knowledge of $F$ and $h$. It is not possible to solve the problem in closed form, but the linearity of $F$ means that $g$ can be expanded as a sum of $n$ chosen basis functions multiplied by the correct coefficients.

$$g(z) = c_1 g_1(z) + c_2 g_2(z) + \cdots + c_n g_n(z) \tag{2.34}$$

$$= \sum_{i=1}^{n} c_i g_i(z) \tag{2.35}$$

The linearity of the operator $F$ means that

$$\sum_{i=1}^{n} c_i F(g_i) = h \tag{2.36}$$

The basis functions $g_1 \cdots g_n$ are chosen so that each $F(g_i)$ can be evaluated, leaving only the coefficients $c_1 \cdots c_n$ to be found. On expansion, (2.36) is a single equation involving $n$ unknown constants: the coefficients $c_1 \cdots c_n$.

The method for obtaining the $n$ coefficients for the basis functions is known as point matching and involves applying boundary conditions at $n$ points. For an electromagnetic scattering problem, point matching involves enforcing the boundary condition of vanishing tangential electric field at $n$ points on the surface of a conducting body or antenna. Between these matching points, the field at the surface of the antenna is not guaranteed to become zero, and is termed a residual. A good choice of basis functions ensures smooth behaviour between the matching points and small residuals.

The basis functions must be chosen so that a small number of them can represent the function $g(z)$ accurately. In the case where g(z) represents the current distribution on a wire antenna, this is known to be of an essentially sinusoidal shape and so sinusoidal basis functions are usually used. A good explanation of the moment method, as applied specifically to the cylindrical dipole antenna, is given in reference [39].

### 2.4.2 The NEC Computer Code

A software implementation of the method of moments was available as a computer code known as Numerical Electromagnetics Code (NEC) [38]. NEC is a general purpose computer code intended for the analysis of electromagnetic scattering from arbitrary metallic structures with overall dimensions of up to several wavelengths. Its code contains two integral equations and their respective moment method solutions; an electric field integral equation is used to analyse scattering from thin wires and a magnetic field integral equation is used for scattering from surfaces [40]. These integral equations are solved to find the current distribution on a structure, and from this, parameters such as the radiation patterns and the drive point impedances of antennas may be found.

For input to NEC, a structure has to be specified as thin wires, divided into segments, and surface patches to represent the closed surfaces of broader scattering bodies. The structure may be in several disconnected parts to enable coupling between antennas to be studied, or it may be specified in free space or over a lossy or perfectly conducting ground plane. Voltage sources and load impedances may be placed at points on a wire structure to represent excitations and loading.

Excitation of a structure is accomplished either by illuminating it with a plane wave or by specifying voltage sources on certain wire segments of it. The impedances presented to voltage sources driving into a structure are calculated by NEC, and also the power dissipated in any load impedances so that antenna efficiencies

can be found.

NEC was used as a modelling tool to facilitate calculation of the drive point impedances of wire antennas used for the measurements described later in this thesis. Two types of wire antenna were used: the cylindrical dipole antenna and the skeletal biconical antenna. The cylindrical dipole antenna is a single straight wire and the skeletal biconical antenna is formed as a cage of thin wires, therefore both antennas are well suited to modelling with NEC.

For input to NEC, a wire structure must be divided into an appropriate number of segments. A wire is described by the coordinates of each end of it in cartesian space, and also by its radius, as shown in figure 2.9. The resonant dipole antenna is possibly the easiest structure to express in terms of wires, since it is simply a single straight wire element with a known length and radius. The only modelling problem is the choice of how many segments to divide the wire into; this is addressed in §2.4.3.

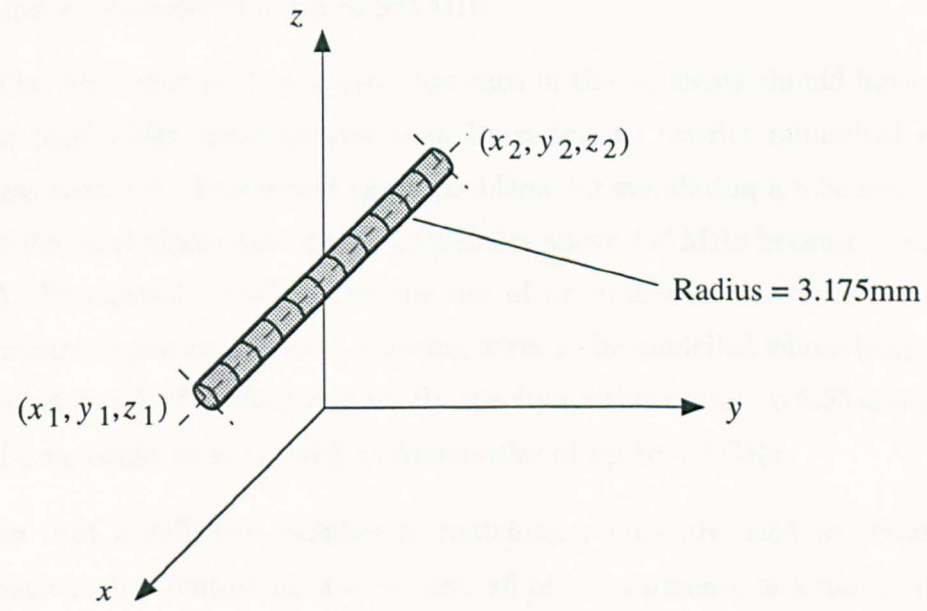


Figure 2.9: NEC representation of a cylindrical dipole antenna.

### 2.4.3 Segmentation for the Resonant Dipole Antenna

The choice of the correct number of segments required to model a resonant dipole antenna accurately is determined by numerical accuracy and the availability of computational resources such as memory and CPU time. Increasing the segmentation increases the number of matching points and basis functions that are used to represent the current distribution on the antenna and hence improves its resolution. From this it would appear that using as large a number of segments as possible

would be a good idea, but in fact this is not necessarily the case, for a variety of reasons that are explained in the modelling rules below.

The real resonant dipole antennas that were simulated using NEC were made from 6.35 mm diameter cylindrical brass rod and this section discusses the choice of appropriate segmentation for modelling them. Appropriate segmentation for the skeletal biconical antenna is discussed later in §2.6 and §2.7. The design rules below are developed for a half-wavelength dipole antenna but, because the length of the resonant dipole is only slightly less, the conclusions are the same for it.

1. The wires used to model a structure must be thin so that the assumption that no circumferential currents exist on the wires is valid. The NEC user guide [41] suggests that for this condition to be met no wire should have a radius greater that $0.16\lambda$ but more recent literature [42] suggests a more rigorous constraint that wire radii should be less than $0.01\lambda$. Under the latter constraint, a dipole antenna having a diameter of 6.35 mm may be considered thin at frequencies of up to 944 MHz.

2. The NEC user guide suggests that each of the segments should have a length at least eight times greater than its radius to restrict numerical errors to less than 1%. This would cause problems for simulating a 6.35 mm diameter cylindrical dipole antenna at frequencies above 295 MHz because of constraint 3. Fortunately NEC allows the use of an extended thin wire kernel in its integral equation solution, allowing wires to be modelled whose lengths are as short as a half of their radius. By specifying this option, a 6.35 mm diameter dipole could be simulated at frequencies of up to 4.7 GHz.

3. So that a sufficient number of matching points are used to represent the current distribution on a structure, all of the segments in a model should be significantly shorter than a wavelength. The NEC user guide states that no segment should be longer than $0.05\lambda$ for this constraint to be met. For a half-wavelength dipole antenna this means that at least 10 segments must be used to model it accurately.

4. Errors due to the numerical precision of the computer running NEC become apparent when segments become very short. This imposes the condition that no segment may be shorter than $0.001\lambda$ and so the maximum number of segments for acceptable modelling a half-wavelength dipole antenna is 500.

Design rules mentioned above impose limitations on the number of segments that can be used to simulate a 6.35 mm diameter half-wavelength dipole antenna

using NEC. Figure 2.10 shows the constraints imposed by rules 1 to 4 and the two shaded regions represent allowable segmentation with the normal integral equation kernel and with the extended thin wire kernel.

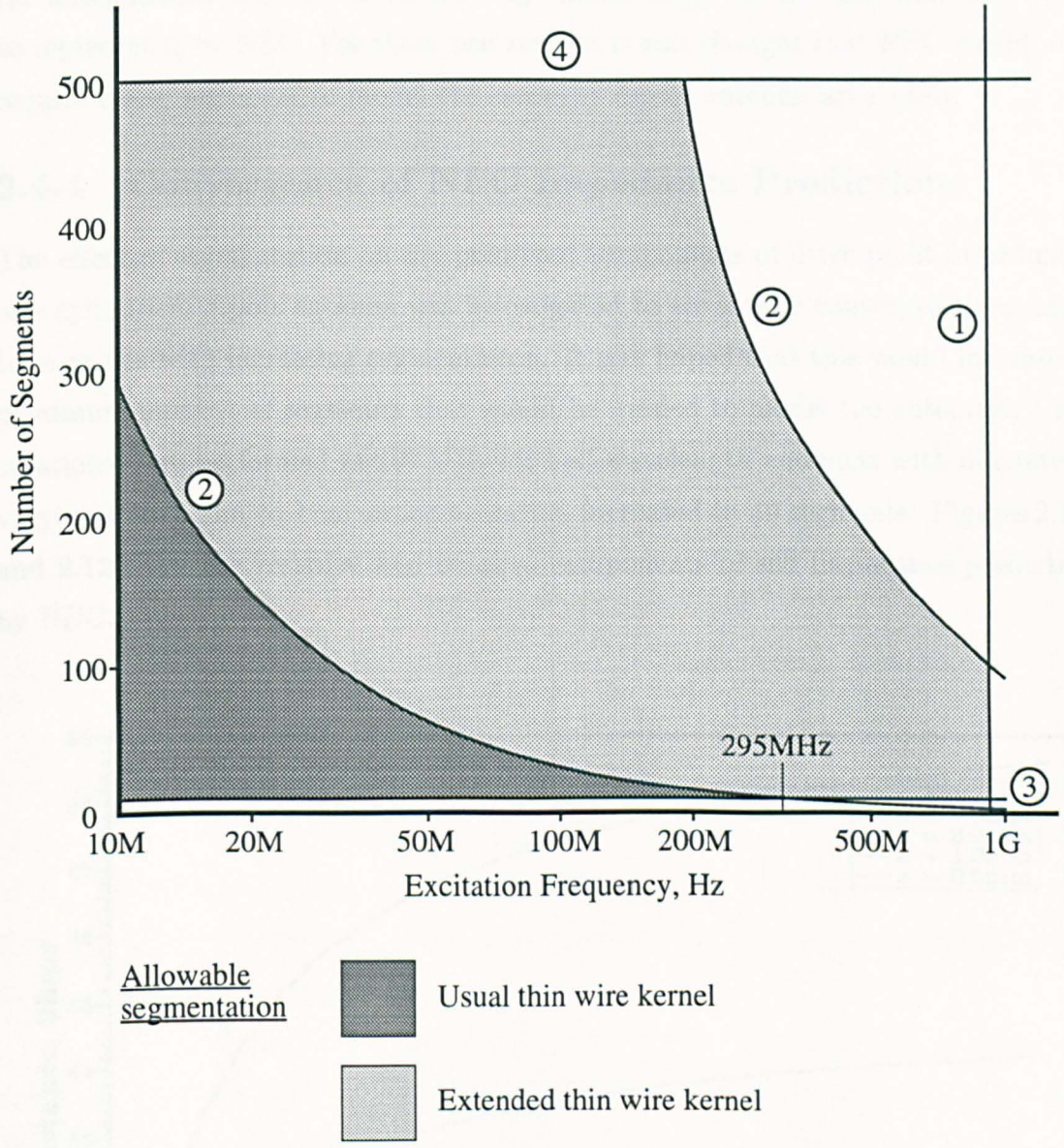


Figure 2.10: Allowable segmentation for a 6.35 mm diameter half-wavelength cylindrical dipole antenna.

The resonant dipole antennas simulated in this thesis had lengths that were slightly less than half a wavelength and were required to be simulated at frequencies between 20 MHz and 1 GHz. Figure 2.10 shows that there is no clear optimum number of segments to choose for modelling these antennas but that the extended thin wire kernel must be used above 295 MHz. The extended thin wire kernel was actually used for all the antennas simulated in this thesis because the extra computational time that it required was not a problem.

The resonance of the cylindrical dipole antenna has a relatively low Q-factor,

typically 3–4, and so there are no sharp changes in the magnitude and phase of its current distribution along the length of the antenna. The current distribution was also known to be approximately sinusoidally distributed along the length of the antenna and therefore to have a very similar shape to the basis functions used to represent it by NEC. For these two reasons it was thought that NEC would not require many segments to model the resonant dipole antenna accurately.

### 2.4.4 Convergence of NEC Impedance Predictions

The effect of segmentation on the predicted components of drive point impedance of a cylindrical dipole antenna was investigated to see if they converged to asymptotic values with increasing segmentation. It was hoped that this would indicate a maximum number of segments that would be needed to model the antennas. Calculations were performed at 100 MHz for half-wavelength antennas with diameters varying from 1 mm to 1 cm as segmentation increased to 49 segments. Figures 2.11 and 2.12 show the resistive and reactive components of self impedance predicted by NEC.

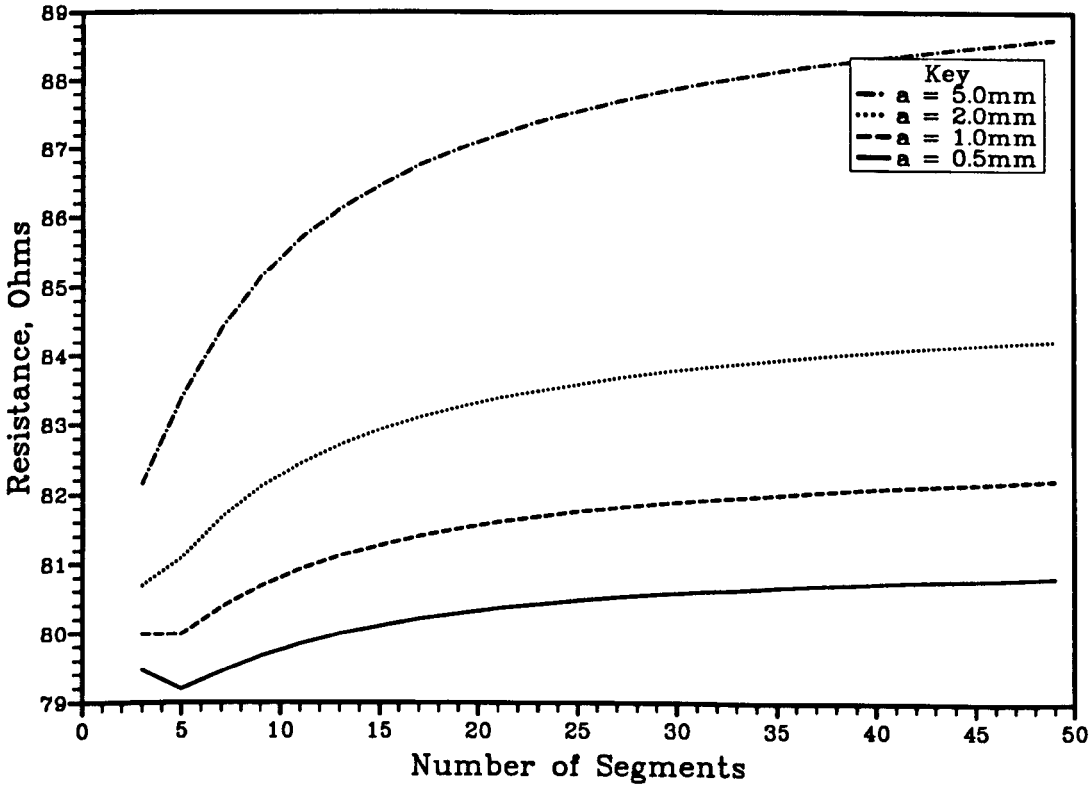


Figure 2.11: Effect of increasing segmentation on the predicted resistive component of the self impedance of half-wavelength dipole antennas of various radii.

Figures 2.11 and 2.12 show that both of the impedance components converge rapidly with increasing segmentation at first, but then the rate of convergence slows

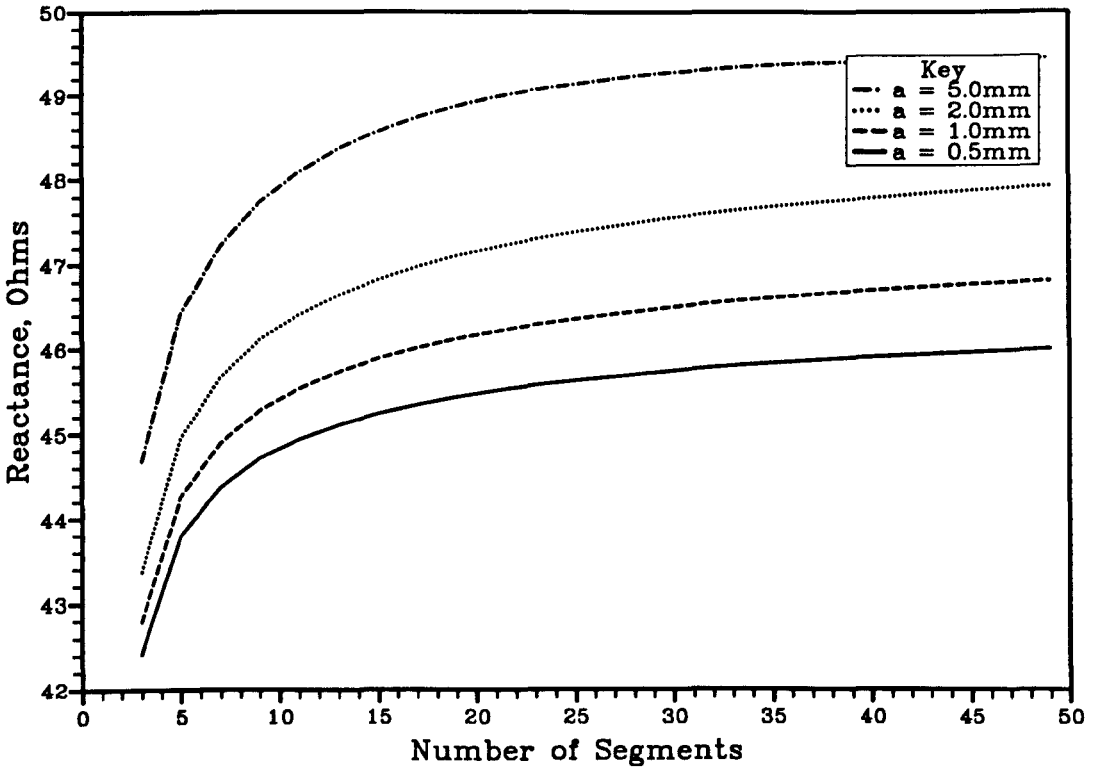


Figure 2.12: Effect of increasing segmentation on the predicted reactive component of the self impedance of half-wavelength dipole antennas of various radii.

down so that, even with 49 segments, the impedance components are slightly less than their fully converged values. The rate of convergence appears to be a function of the radius of the antenna in that it is more rapid for the thinner antennas, but even the impedance components of the 1 mm diameter antenna are a few ohms less than their fully converged values.

The slow convergence of the impedance values predicted by NEC was investigated further in order to try to determine the reasons for it. Initially it was thought that the criterion imposed in the modelling guidelines for wires to be thin was not stringent enough, but as NEC was to be used for modelling real 6.35 mm diameter antennas, the wires could not be made any thinner. Eventually it was accepted that NEC was not capable of returning clearer results and an attempt was made to determine how much less than their fully converged values the self impedance components of a 21 segment simulation of a dipole antenna would be. The calculations were performed for a half-wavelength antenna at 20 MHz with a variable number of segments up to its maximum allowable number of 500 (see figure 2.10). This gave the self impedance values shown in table 2.2.

Table 2.2 shows that with 499 segments the impedance components have converged to within three significant figures, and that the asymptotic value is (81.9 +

| Number of Segments | Self Impedance, Ω | |
|---|---|---|
| | Resistive | Reactive |
| 11 | 80.1819 | 45.1139 |
| 21 | 80.7419 | 45.7125 |
| 41 | 81.1558 | 46.1541 |
| 61 | 81.3373 | 46.3602 |
| 81 | 81.4446 | 46.4877 |
| 99 | 81.5068 | 46.5493 |
| 199 | 81.6866 | 46.7527 |
| 299 | 81.7635 | 46.8214 |
| 399 | 81.8081 | 46.8468 |
| 499 | 81.8382 | 46.8539 |

Table 2.2: Predicted self impedance from NEC as a function of segmentation, for a half-wavelength dipole antenna of diameter 6.35 mm at 20 MHz

$j46.9)\Omega$ . The predicted impedance with 21 segments is $(80.7 + j45.7)\Omega$ , and was judged to be sufficiently accurate for the later simulations in this thesis.

At frequencies higher than 20 MHz, dipole antennas become shorter and therefore proportionally less thin. It has been shown in figures 2.11 and 2.12 that the self impedance components of fatter antennas converge more slowly, and so their impedance components will be less converged with 21 segments than the 20 MHz dipole.

It was concluded that convergence testing would not give a very clear guide to the accuracy of NEC. In order to test the accuracy of any theory or computational model it is necessary to compare it with measurement; this is done in §2.5.

### 2.4.5 Source Modelling

The voltage source that was applied to the middle segment of the NEC representation of the cylindrical dipole antenna was of a type known as an applied electric field voltage source. This means that NEC models the source in the same way as it would model an applied electric field. If a structure is illuminated by a plane wave in NEC, the wave is resolved along each segment of the structure to calculate the voltage that is impressed over its length. Using an applied electric field voltage source, this field is only applied to the segment that has the voltage source on it. The field is set to the correct level to give the required voltage as a boundary condition between the ends of the segment.

It is not very easy to relate an applied electric field voltage source to any kind of real excitation of a practical antenna. The cylindrical dipole antenna developed in chapter 4 is excited across an 18 mm gap between its two arms by a balanced transmission line and so is quite different in nature. King [43] first investigated the

effect of a finite feed gap at the centre of a dipole antenna. He concluded that, for a half-wavelength antenna, a small gap would not affect the current distribution. Shelkunoff and Friis [44] also investigated the effect of the finite feed gap on the current distribution of various lengths of dipole antenna and concluded that it had negligible effect on antennas having lengths close to half a wavelength. From this information it was concluded that the NEC source model could be used to represent the excitation of the real cylindrical dipole antenna, described in chapter 4, provided that it was excited close to its resonant frequency.

## 2.5 Accuracy of Models of the Cylindrical Dipole Antenna

In the previous sections several different modelling approaches to determination of the drive point impedances of isolated and coupled cylindrical dipole antennas have been discussed. In this section the results from these models will be compared with each other, and with experimental measurements, in order to deduce the accuracy of each of them.

The ultimate test of accuracy for any theoretical model is comparison with experiment, and so an experiment was devised that allowed the accurate measurement of the self impedance of a dipole antenna. The NEC computer code employed the most accurate model of the current distribution on the cylindrical dipole antenna and so it was the first to be compared with the experiment. The applied EMF method results were then compared with both measurement and NEC.

### 2.5.1 Measurement of Self Impedance

The applied EMF method of §2.2 and the integral equations of §2.3 all assume that the cylindrical dipole antenna they are used to model is fed by a voltage source across an infinitesimally thin gap at the centre of the antenna. For this reason an experiment had to be devised that allowed the impedance of a cylindrical dipole antenna to be measured whilst excited in a comparable way. The feed region of a real dipole antenna consists of a balanced transmission line exciting the two halves of the antenna across a finite gap at its centre and so it does not have the same structure as these models. The applied electric field voltage source that was used for the NEC simulations in §2.4 cannot be related to a real excitation and so no attempt was made to devise an experimental structure equivalent to it.

Experimental apparatus was built that could be used to represent a cylindrical dipole antenna, excited across an infinitesimally small gap at its centre. This apparatus consisted of a coaxially fed monopole antenna at the centre of a 1.22 m square aluminium sheet and is shown in figure 2.13. A bulkhead BNC connector was mounted directly beneath the ground plane with its centre conductor connected to the monopole and its outer conductor connected to the ground plane.

The method of images (chapter 1) shows that the monopole antenna of figure 2.13, together with its image in the conducting metal ground plane, is equivalent to a dipole antenna of half-length equal to the height of the monopole. The excitation voltage of the equivalent dipole is twice that of the monopole but its current is the same, implying that the drive point impedance of the equivalent

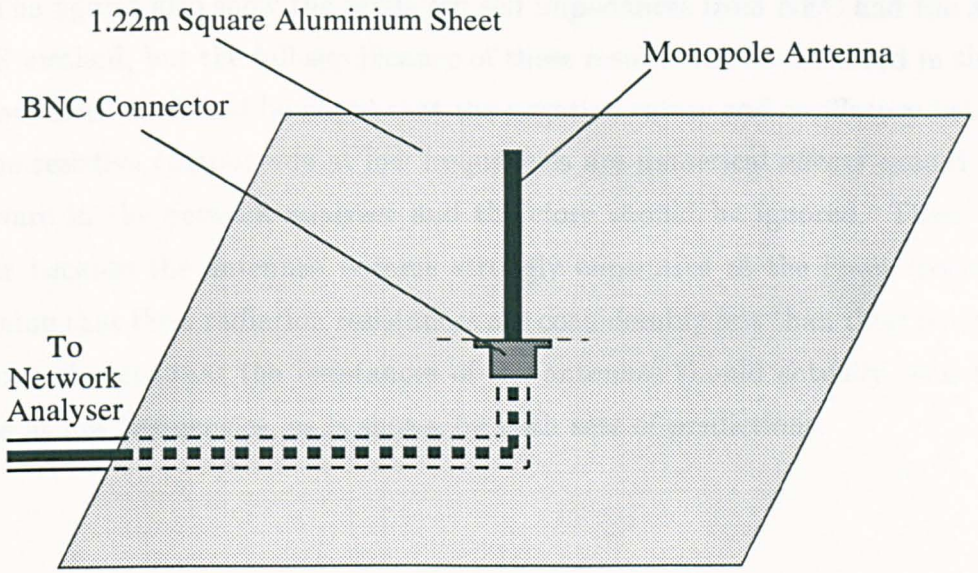


Figure 2.13: Measurement of the self impedance of a monopole antenna above a ground plane.

dipole is twice that of the monopole.

The impedance of the monopole antenna in figure 2.13 was measured with a network analyser by placing open, short and matched loads at the BNC connector to establish a reference plane at the base of the antenna, as described in chapter 4. Measurements of terminal impedances were made on antennas having various half-lengths, from 74 to 803 mm. All the monopole antennas had a diameter of 6.35 mm and their excitation frequencies were varied from 10 MHz up to just beyond where each of the antennas became resonant. The measured impedances were then doubled to give the self impedance of an equivalent dipole antenna and these values are shown in figures 2.14 to 2.19. In the keys of these graphs, "R" is used to denote a resistive component and "X" is used to denote a reactive component. The length of the monopole is also given in the key together with a three letter suffix to denote the source of the data.

The graphs show that dipole antennas that are significantly less than half a wavelength long have a predominantly negative reactive input impedance and so are capacitive. For electrically longer antennas the resistive component of self impedance rises from zero ohms at d.c. up to around 73 Ω at resonance, where the reactive component of self impedance passes through zero. The curves of measured impedance were plotted with 401 linearly spaced data points and a polynomial fit was then applied to determine the frequency of resonance. These frequencies are shown in the graphs and, together with the value of the resistance of the antenna at resonance, in table 2.3.

The figures also show the predicted self impedances from NEC and the applied EMF method, but the full significance of these results will be discussed in the next two sections. It should be noted that the negative values and oscillatory behaviour of the resistive components at low frequencies are numerical effects caused by the software in the network analyser and therefore should be ignored. These effects occur because the antennas become strongly capacitive at the lower frequencies, meaning that their radiation resistances are considerably less than their reactances. Theory dictates that the resistances of the antennas should actually tend to zero ohms at low frequencies, as is shown by both sets of predictions.

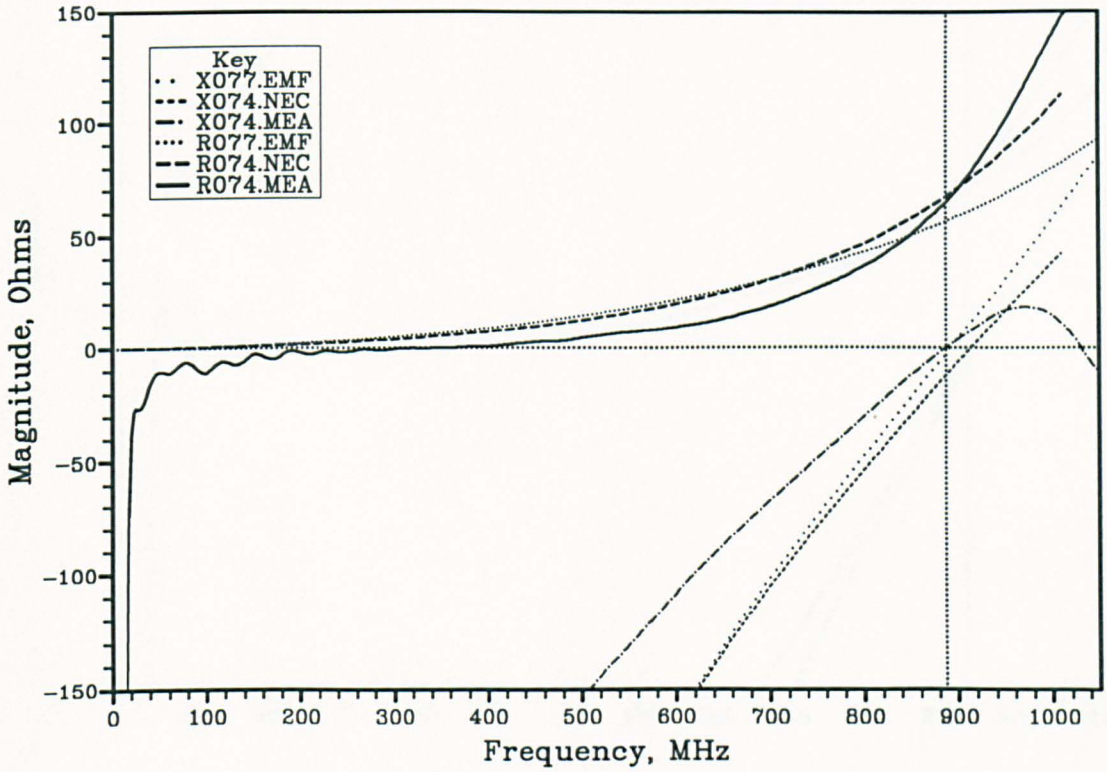


Figure 2.14: Measured self impedance components and predictions from NEC and the applied EMF method for a 74 mm half-length dipole.

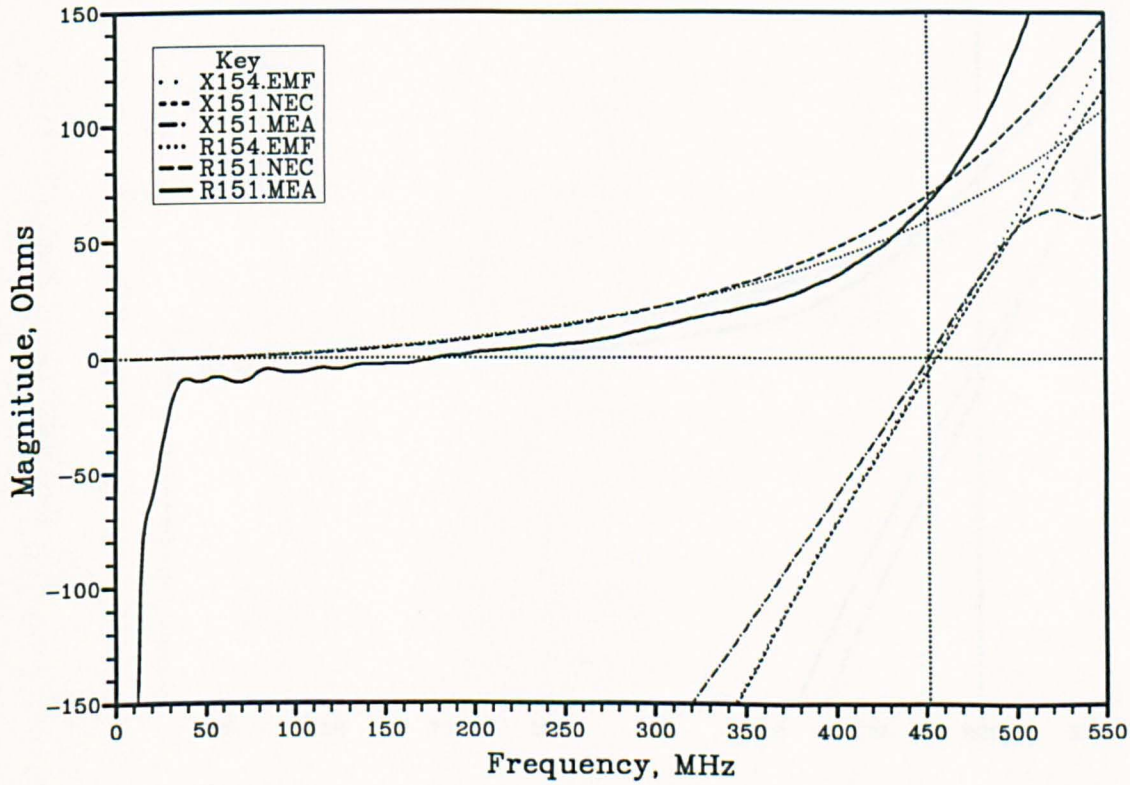


Figure 2.15: Measured self impedance components and predictions from NEC and the applied EMF method for a 151 mm half-length dipole.

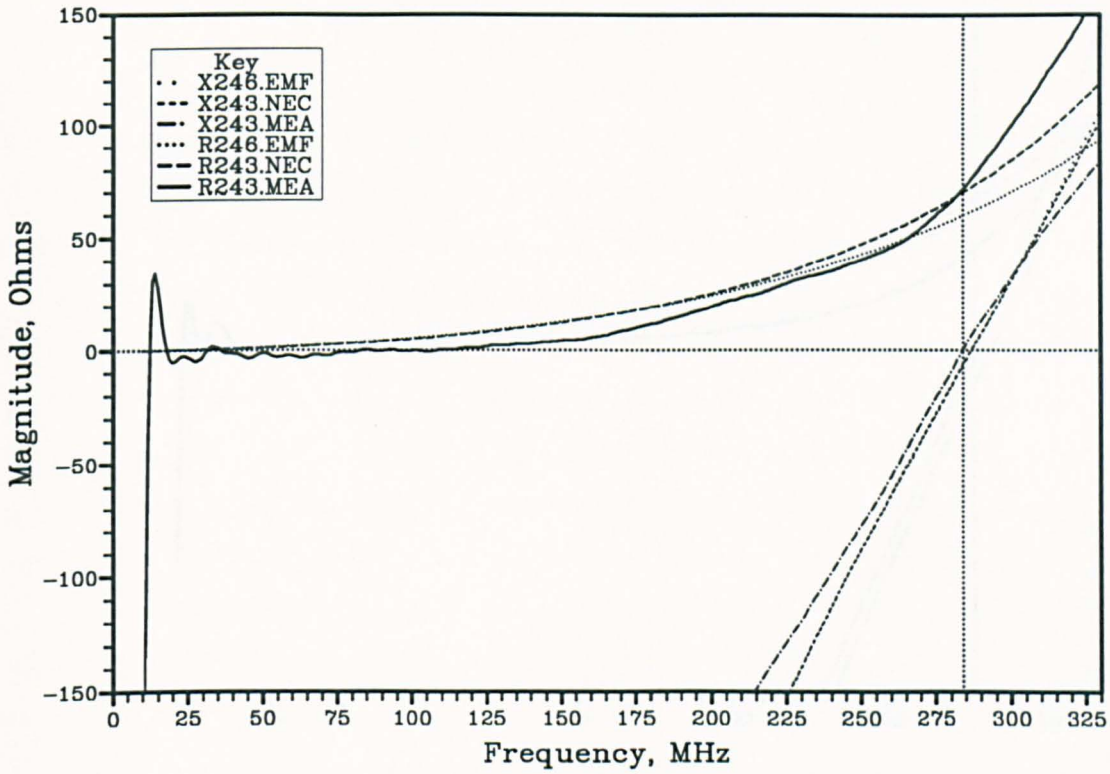


Figure 2.16: Measured self impedance components and predictions from NEC and the applied EMF method for a 243 mm half-length dipole.

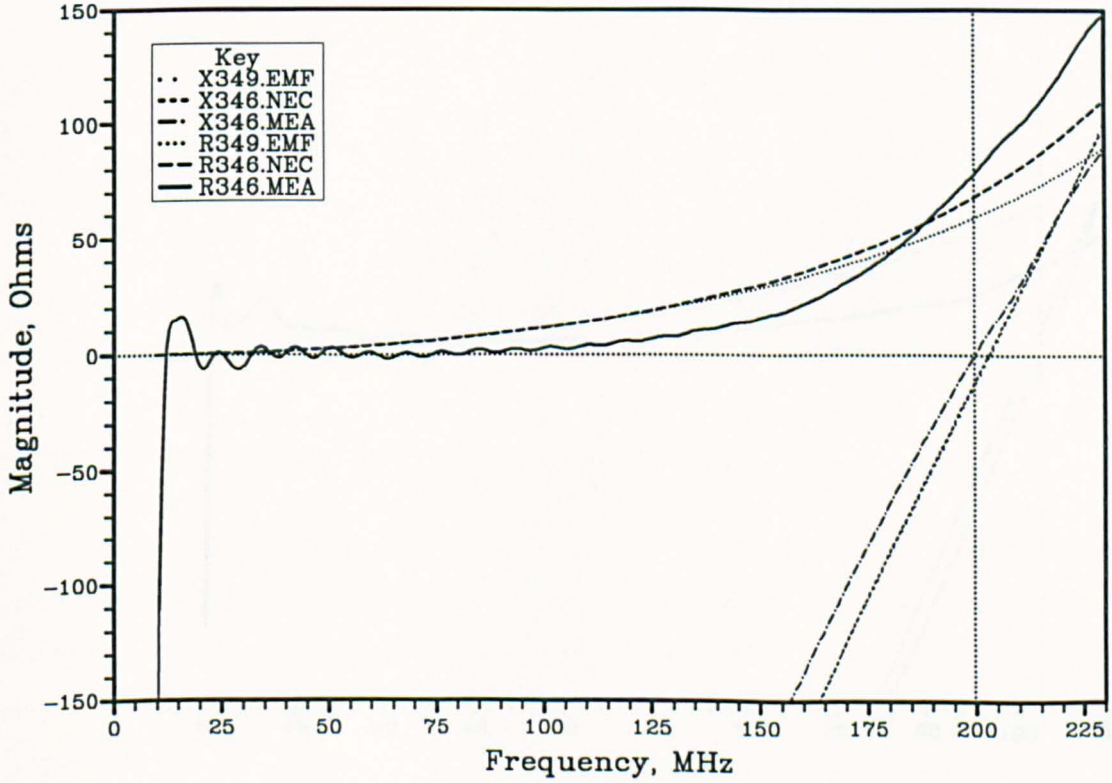


Figure 2.17: Measured self impedance components and predictions from NEC and the applied EMF method for a 346 mm half-length dipole.

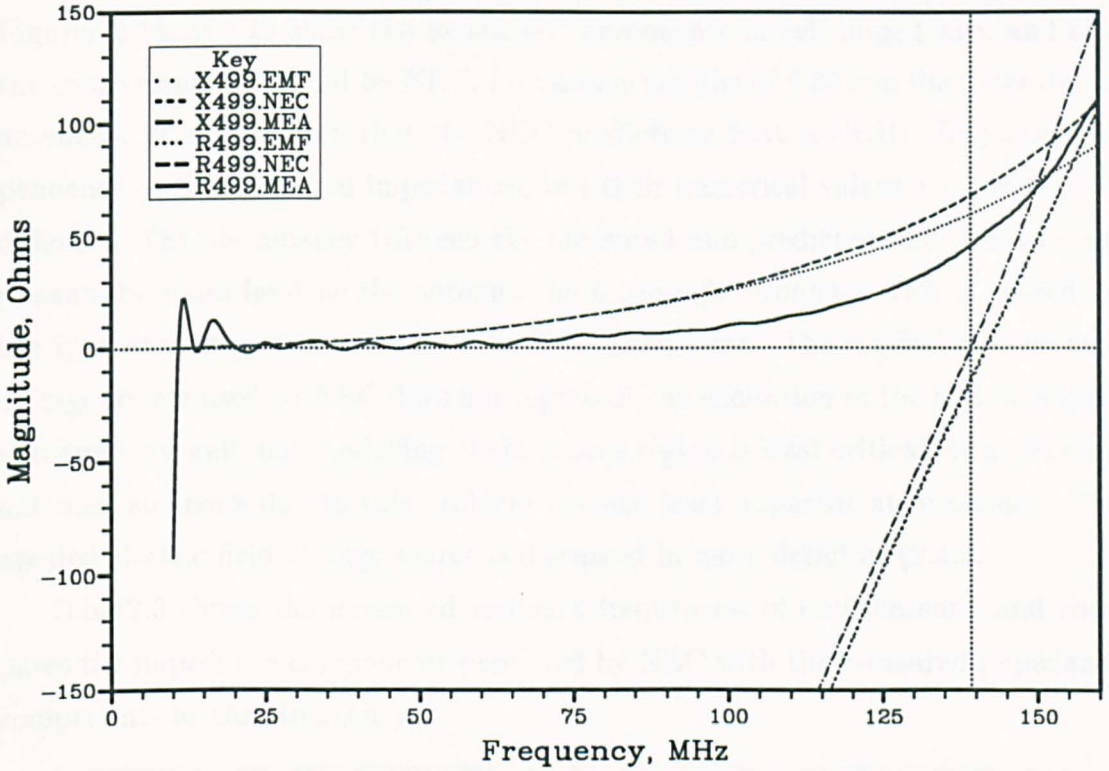


Figure 2.18: Measured self impedance components and predictions from NEC and the applied EMF method for a 499 mm half-length dipole.

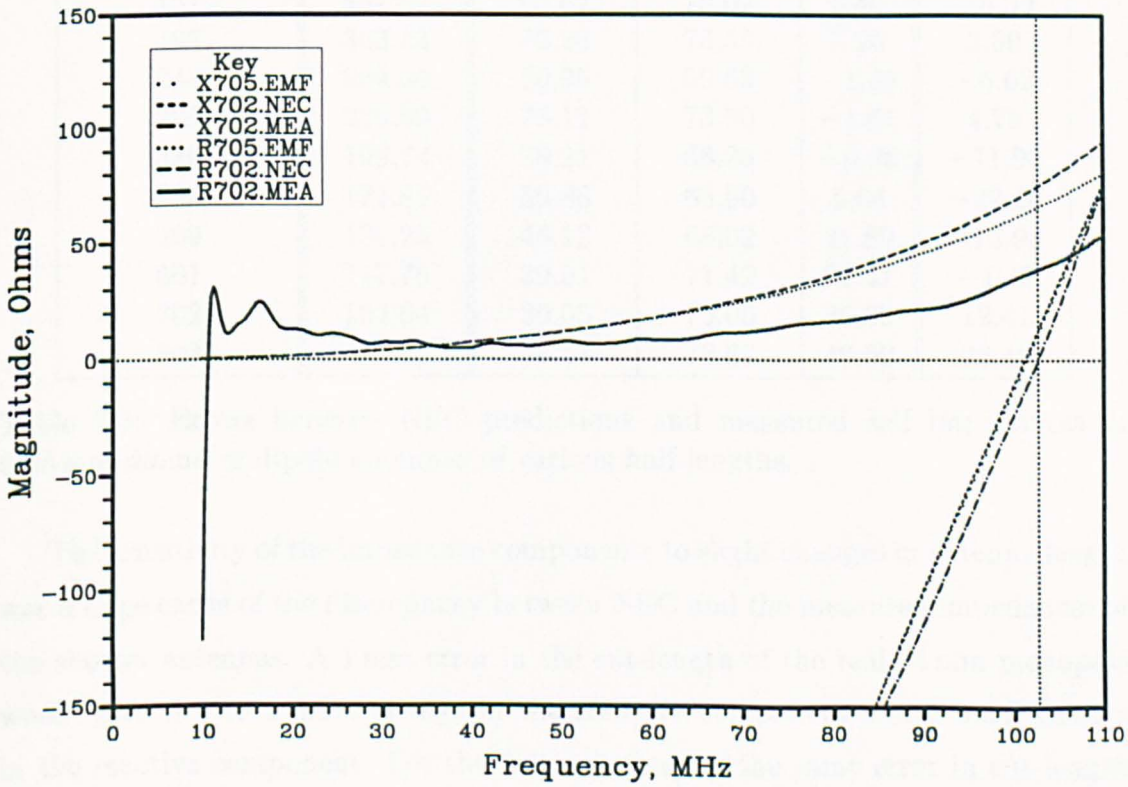


Figure 2.19: Measured self impedance components and predictions from NEC and the applied EMF method for a 702 mm half-length dipole.

### 2.5.2 Accuracy of NEC

Figures 2.14 to 2.19 show the measured components of self impedance, and also the components predicted by NEC, for various lengths of 6.35 mm diameter dipole antennas. It can be seen that the NEC predictions have a similar frequency dependence to the measured impedances, but their numerical values are appreciably different. The discrepancy between the measured and predicted impedances components becomes least as the antennas pass through resonance; this is caused by the type of voltage source used in the NEC simulation. The applied electric field voltage source used by NEC does not represent the excitation of the real monopole antenna very well, but modelling of the source region is least critical for a resonant antenna, so errors due to this problem become least apparent at resonance. The applied electric field voltage source is discussed in more detail in §2.4.5.

Table 2.3 shows the measured resonant frequencies of each antenna and compares the impedance components predicted by NEC with the measured impedance components at that frequency.

| Dipole antenna half-length mm | Resonant frequency MHz | Impedance / Ω | | | |
|---|---|---|---|---|---|
| | | Resistive | | | Reactive |
| | | Measured | Predicted | Error | Error |
| 74 | 886.73 | 64.30 | 66.80 | 2.50 | −12.43 |
| 109 | 622.00 | 67.84 | 71.15 | 3.31 | −3.68 |
| 151 | 451.87 | 66.62 | 70.02 | 3.40 | −5.59 |
| 192 | 363.13 | 70.26 | 73.55 | 3.29 | 3.50 |
| 243 | 284.06 | 70.95 | 69.69 | −1.26 | −6.62 |
| 295 | 238.89 | 78.11 | 73.50 | −4.61 | 4.78 |
| 346 | 199.74 | 78.21 | 68.25 | −9.96 | −11.90 |
| 398 | 171.85 | 59.86 | 65.50 | 5.64 | −22.20 |
| 499 | 139.25 | 46.12 | 68.02 | 21.89 | −13.93 |
| 601 | 117.76 | 39.01 | 71.42 | 32.41 | −1.42 |
| 702 | 102.64 | 39.05 | 75.06 | 36.00 | 12.41 |
| 803 | 91.22 | 38.17 | 78.67 | 40.50 | 26.40 |

Table 2.3: Errors between NEC predictions and measured self impedances of 6.35 mm diameter dipole antennas of various half-lengths.

The sensitivity of the impedance components to slight changes in antenna length was a large cause of the discrepancy between NEC and the measured impedances of the shorter antennas. A 1 mm error in the cut-length of the real 74 mm monopole would give rise to a 3.2 Ω change in the resistive component and a 5.3 Ω change in the reactive component. For the 803 mm antenna the same error in cut length would only introduce a 0.3 Ω change in the resistive component and a 1.2Ω change in the reactive component. The antennas that were used for these impedance

measurements were cut to within a tolerance of 1 mm and so it is not possible to comment on the accuracy of NEC to better than the above impedance tolerances.

The effect of the truncation of the ground plane, causing an incomplete image to be formed beneath the monopole, becomes apparent as its measured resistance becomes reduced at resonance for longer antennas. This occurs progressively more for antennas of heights greater than 300 mm and so it is difficult to use the results for antennas having greater lengths than this as an indication of the accuracy of NEC.

The two causes of error mentioned above have least effect on antennas of around 250 mm height, so the best agreement between measured and predicted impedances occurs for antennas of around this height. Typical errors from the 243, 295 and 346 mm monopoles are around 4 Ω in each impedance component, but NEC may still be more accurate than this as there may be errors in the measured impedances.

The convergence of NEC with increasing segmentation of a dipole antenna has been investigated in §2.4.4 and it has been concluded that a 21 segment model of a resonant dipole will result in predicted impedance values that are a certain amount less than their fully converged values. This amount increases as antennas become proportionally fatter and so also accounts for the large errors between NEC and measurement for the shorter antennas.

### 2.5.3 Accuracy of the Applied EMF Method

Values of the self impedance of a thin dipole antenna have been calculated by the applied EMF method of §2.2.2 and it has been explained that those predictions are likely to be significantly in error for antennas having diameters of practical sizes. Equations (2.4) and (2.5) were used to calculate the self impedance of the real dipole antenna in §2.5.1 at its measured resonant frequency. Table 2.4 shows these results.

Table 2.4 shows that the components of self impedance, predicted by the applied EMF method, were considerably in error. Both of the predicted components were less than the measured components by 10–15Ω and this appeared to suggest that the antenna length used for the applied EMF method calculations was too short. This was because the applied EMF method does not fully take account of the behaviour of the current distribution at the ends of the tubular brass arms of the antennas. As figure 2.20 shows, the current does not immediately go to zero at the ends of this type of antenna, but flows back down inside the tubular arms for a certain distance [45]. The NEC computer code accounts for this behaviour of

| Dipole antenna half-length mm | Resonant frequency MHz | Impedance / Ω | | | |
|---|---|---|---|---|---|
| | | Resistive | | | Reactive |
| | | Measured | Predicted | Error | Error |
| 74 | 886.73 | 64.30 | 50.36 | −13.94 | −19.75 |
| 109 | 622.00 | 67.84 | 54.99 | −12.85 | −12.34 |
| 151 | 451.87 | 66.62 | 55.96 | −10.66 | −14.58 |
| 192 | 363.13 | 70.26 | 59.38 | −10.88 | −5.18 |
| 243 | 284.06 | 70.95 | 57.76 | −13.19 | −14.99 |
| 295 | 238.89 | 78.11 | 61.18 | −16.93 | −3.21 |
| 346 | 199.74 | 78.21 | 57.95 | −20.26 | −19.39 |
| 398 | 171.85 | 59.86 | 56.32 | −3.54 | −29.24 |
| 499 | 139.25 | 46.12 | 58.83 | 12.71 | −20.47 |
| 601 | 117.76 | 39.01 | 61.92 | 22.91 | −7.63 |
| 702 | 102.64 | 39.05 | 65.13 | 26.08 | 6.54 |
| 803 | 91.22 | 38.17 | 68.28 | 30.11 | 20.78 |

Table 2.4: Errors between applied EMF method predictions and measurements of the self impedances of various lengths of 6.35 mm diameter dipole antennas at resonance.

current at free wire ends.

The tubular arms of the dipole antenna act as waveguides below their cutoff frequency and so the distance that current flows back into the ends of the antenna is similar to its radius, i.e. around 3 mm. This means that the half-length used in the applied EMF method models of a 6.35 mm diameter dipole antenna has to be approximately 3 mm longer than its physical length. The effect of adding a 3 mm correction to the lengths of the antennas simulated using the applied EMF method is shown in table 2.5. It shows that the reactive components now have very good agreement with the measured values, but the predicted resistive components are still 8–10Ω less than both NEC and measurement.

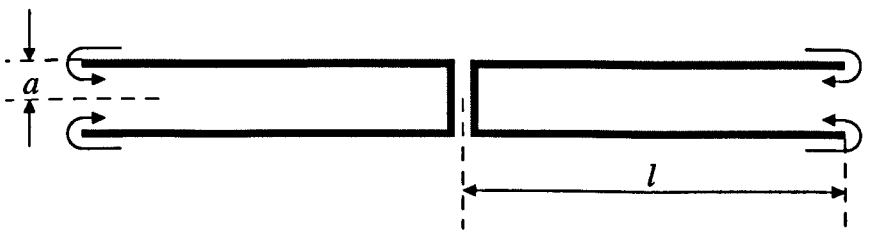


Figure 2.20: Behaviour of current at the ends of a cylindrical dipole antenna with tubular arms.

The applied EMF method uses a delta gap voltage source that is more representative of the excitation applied to the real antenna, therefore it was expected to be more accurate than NEC for antennas away from resonance. Figures 2.14 to 2.19 and table 2.5 show that this was not the case and that, for dipoles having half-lengths of less than an eighth of a wavelength, the NEC predictions and applied

| Dipole antenna half-length mm | Resonant frequency MHz | Impedance / Ω | | | |
|---|---|---|---|---|---|
| | | Resistive | | | Reactive |
| | | Measured | Predicted | Error | Error |
| 77 | 886.73 | 64.30 | 56.06 | −8.24 | −2.84 |
| 112 | 622.00 | 67.84 | 59.25 | −8.59 | 1.48 |
| 154 | 451.87 | 66.62 | 59.07 | −7.55 | −3.40 |
| 195 | 363.13 | 70.26 | 62.01 | −8.25 | 4.53 |
| 246 | 284.06 | 70.95 | 59.76 | −11.19 | −6.92 |
| 298 | 238.89 | 78.11 | 62.95 | −15.16 | 3.97 |
| 349 | 199.74 | 78.21 | 59.35 | −18.86 | −13.18 |
| 401 | 171.85 | 59.86 | 57.50 | −2.36 | −23.73 |
| 502 | 139.25 | 46.12 | 59.81 | 13.71 | −15.75 |
| 604 | 117.76 | 39.01 | 62.79 | 23.78 | −3.46 |
| 705 | 102.64 | 39.05 | 65.93 | 26.88 | 10.32 |
| 806 | 91.22 | 38.17 | 69.02 | 30.85 | 24.25 |

Table 2.5: Errors between Applied EMF Method predictions and measurements of the self impedances of various lengths of 6.35 mm diameter dipole antennas given a length 3 mm longer than the length at which their resonance was measured.

EMF method predictions were virtually the same. It was only as the antennas approached resonance that the predictions from these two methods started to diverge. As the antennas approached resonance, the reactive components predicted by both methods stayed very similar, but a discrepancy arose in the resistive components. The resistances predicted by the applied EMF method became 8–10Ω less than NEC predictions and measurements at resonance, indicating that the applied EMF method was less accurate than NEC.

In conclusion, it was found that NEC was accurate for calculating the self impedances of 6.35 mm diameter cylindrical dipole antennas at or close to resonance. The applied EMF method was no more accurate than NEC for antennas below resonance and considerably less accurate for modelling antennas at resonance. In particular, the resistive component predictions from the applied EMF method were in error by 8–10Ω at resonance, even with a length correction added to the antennas to account for the current distribution at their ends.

In order to calculate the self impedance accurately, NEC must have produced an accurate representation of the current distribution on a single dipole antenna and, because of this, it was assumed to be capable of similar accuracy when modelling coupled resonant antennas.

### 2.5.4 Limitations of Self and Mutual Impedances

The integral equations defining the current distribution on a pair of coupled cylindrical dipole antennas are given in §2.3.2, and appendix D gives the expressions of

an approximate solution developed by Tai [34]. This solution was used to calculate the symmetrically fed terminal impedances, $Z_S$, and the antisymmetrically fed terminal impedances, $Z_A$, of a pair of coupled half-wavelength dipole antennas as a function of their separation. Figure 2.21 shows the resulting resistive and reactive components of these impedances for a 6.35 mm diameter antenna at separations of up to a wavelength with an excitation frequency of 100 MHz.

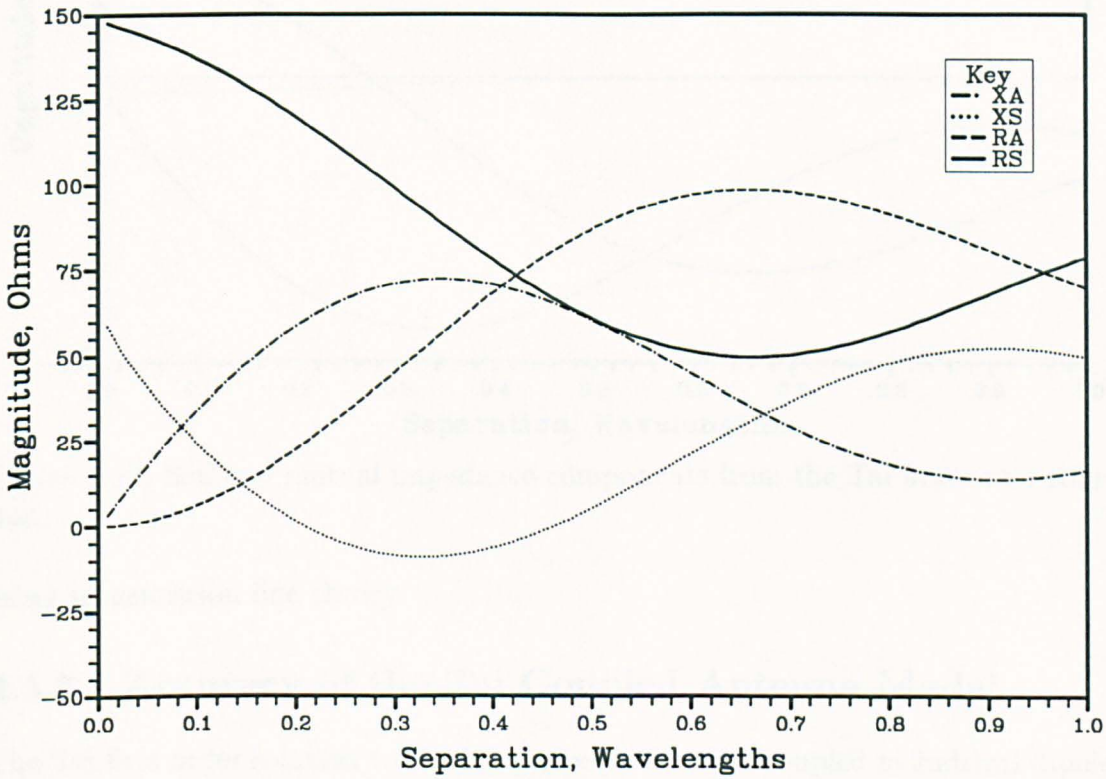


Figure 2.21: Symmetrically and antisymmetrically fed drive-point impedance components from the Tai first order solution.

Figure 2.21 shows that the components of $Z_S$ and $Z_A$ oscillate about each other with a decaying sinusoidal shape. Each symmetric component oscillates about the corresponding antisymmetric component and is 180° out of phase with it.

The symmetrical and antisymmetrical impedances were used to calculate the self and mutual impedances of the coupled antennas from equations (2.31) and (2.32). The resistive and reactive components of these are shown in figure 2.22. This shows that the self impedances of the antennas are a function of their separation and only have a constant value of $(74.34 + j33.26)\Omega$ for antenna separations of greater than half a wavelength. This shows that a self and mutual impedance based approach such as the applied EMF method becomes inaccurate for antennas that are less than half of a wavelength apart. Antennas more closely spaced than this behave similarly to a two conductor transmission line and so should be analysed

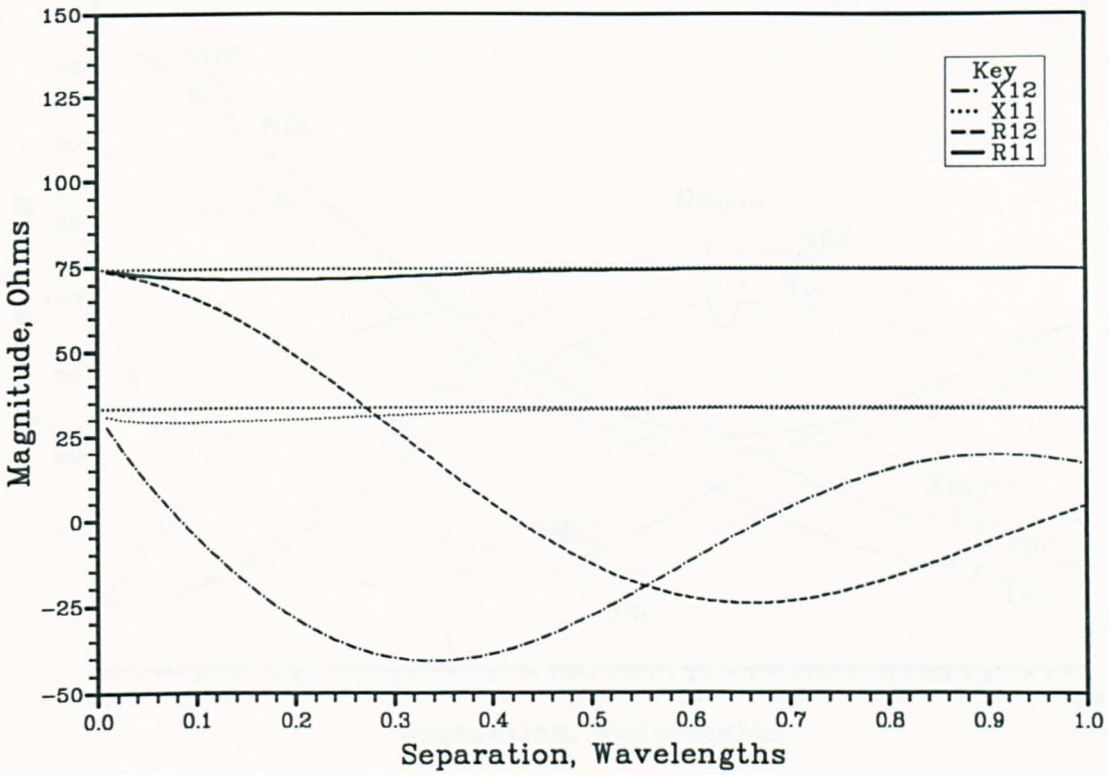


Figure 2.22: Self and mutual impedance components from the Tai first order solution.

using transmission line theory.

### 2.5.5 Accuracy of the Tai Coupled Antenna Model

The Tai first order solution to the integral equations for coupled cylindrical dipole antennas [34] has been mentioned in §2.3.2 and its expressions are reproduced in appendix D. In this section its drive point impedance predictions are compared with those from NEC in order to deduce the usefulness of the method for analysis of dipole antennas above a ground plane.

Two identical half-wavelength cylindrical dipole antennas were simulated first with NEC and then with the Tai model, at separations of up to one wavelength at a frequency of 100 MHz. The NEC simulation was performed with 21 segments and the dipole diameter was set to 6.35 mm. The results of these simulations are compared in figure 2.23.

Figure 2.23 shows that the predictions from the two different models are qualitatively the same but numerically rather different. All of the components predicted by the Tai model are a certain amount less than those predicted by NEC, although the exact amount varies with the antenna separation. Typical differences are around 30 Ω and there is no evidence of agreement between the two sets of predictions

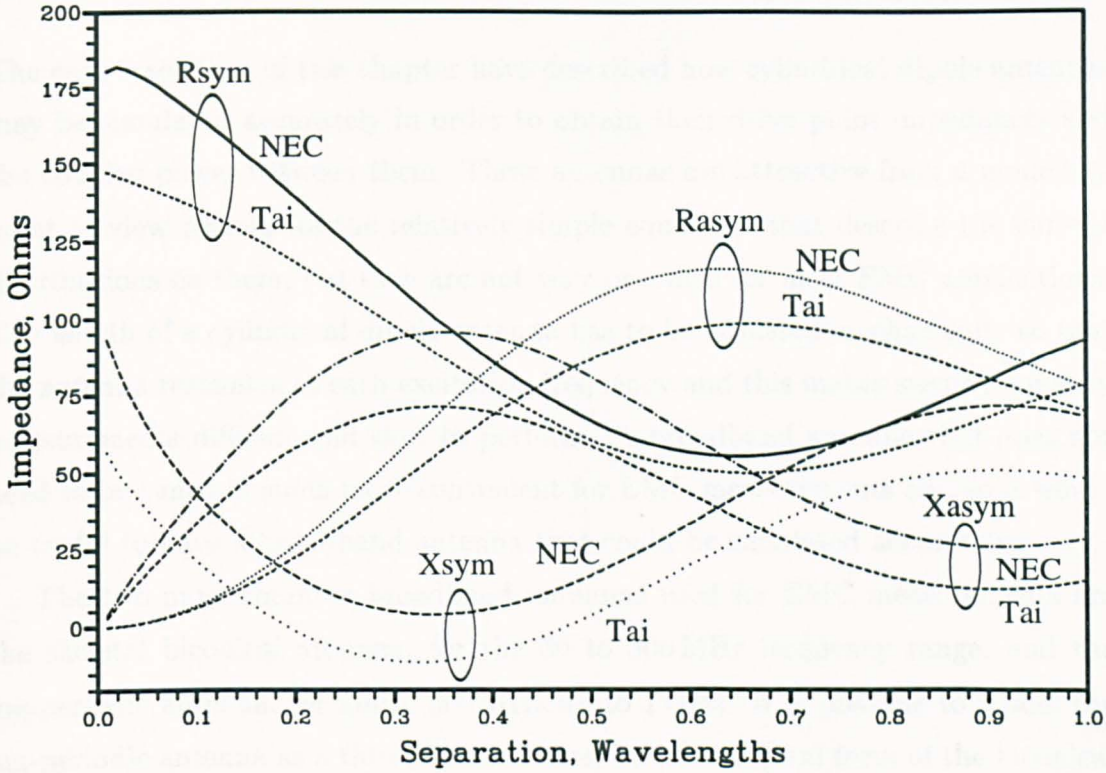


Figure 2.23: Comparison of symmetrically and antisymmetrically fed drive point impedance predictions from NEC and the Tai first order solution. Resistive and reactive components are shown as a function of separation for half-wavelength, 6.35 mm diameter, antennas at 100 MHz.

improving as antenna separation increases.

NEC has been found to be accurate to within a few ohms for this type of simulation and therefore it was concluded that the Tai model was considerably less accurate and of little use for simulating coupled resonant dipole antennas. It was not used for any of the later work in this thesis.

## 2.6 Simulation of Wire Biconical Antennas

The earlier sections of this chapter have described how cylindrical dipole antennas may be simulated accurately in order to obtain their drive point impedances and the coupled power between them. These antennas are attractive from a modelling point of view because of the relatively simple equations that describe the current distributions on them, but they are not very practical for most EMC applications. The length of a cylindrical dipole antenna has to be adjusted mechanically so that the antenna resonates at each excitation frequency and this makes swept frequency measurements difficult and slow to perform. A broadband antenna that does not need to be tuned is much more convenient for EMC measurements and so it would be useful to have a broadband antenna that could be simulated accurately.

The two most common broadband antennas used for EMC measurements are the skeletal biconical antenna, for the 30 to 300 MHz frequency range, and the log-periodic antenna, for above 300 MHz up to 1 GHz. It is possible to model the log-periodic antenna as a thin-wire structure, but the skeletal form of the biconical antenna is especially well suited to analysis using NEC. In this section a NEC model of the skeletal biconical antenna is developed and analysed to deduce the characteristics of the antenna. This model is optimised in §2.7 and used in chapter 4 to accurately calibrate the biconical antenna. It is also used in chapter 5 in order to calculate the coupled power between pairs of biconical antennas over a ground plane.

### 2.6.1 The Biconical Antenna

The infinite biconical antenna is a very attractive theoretical antenna because its self impedance is purely resistive and only dependent on the angle of its cones. Figure 2.24 shows the half-cone angle, $\theta_{hc}$, and equation (2.37) defines the radiation resistance of the antenna in terms of this angle [46].

$$R_{11} = \frac{\eta}{\pi} \ln \left[ \cot \left( \frac{\theta_{hc}}{2} \right) \right] \tag{2.37}$$

Equation (2.37) shows that the impedance of the infinite biconical antenna is independent of frequency, hence it achieves the same impedance mismatch at all frequencies when fed from a transmission line. The half-cone angle determines the value of the resistance of the antenna and an angle of 66.7° gives an exact impedance match to a 50 Ω transmission line.

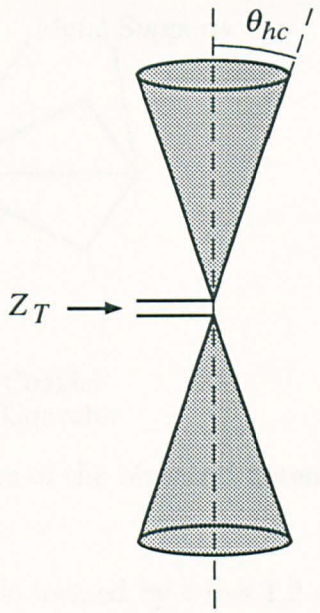


Figure 2.24: An infinite biconical antenna.

An antenna having infinite cones for its radiating structures is a very elegant theoretical structure but not very practical. The cones of any real biconical antenna must be truncated at some point and under these conditions its drive point impedance is not purely resistive and is difficult to calculate accurately. Most biconical antennas for the 30–300 MHz frequency range are truncated to give an antenna length of around 1.3 m, and have half-cone angles of 30° .

### 2.6.2 The Skeletal Biconical antenna

Conical arms are expensive to manufacture for commercially available biconical antennas and so a wire cage structure is generally used instead. It has been found that a sufficient electrical approximation to a cone can be achieved with six bent wires arranged as shown in figure 2.30. The wires are brought back together at the end of the conical part of the antenna in order to improve its rigidity, and a seventh wire is used for the same purpose along the centre of the cone.

As with commercially produced dipole antennas, the balun of the skeletal biconical antenna is included as an integral part of its structure and is mounted between the two radiators of the antenna. The effect of the balun on the performance of the antenna will be discussed in chapter 4.

### 2.6.3 NEC Model of the Biconical Antenna

The biconical antennas used for the measurements performed in this thesis were manufactured by Schwarzbeck with a model number of BBA9106. These antennas

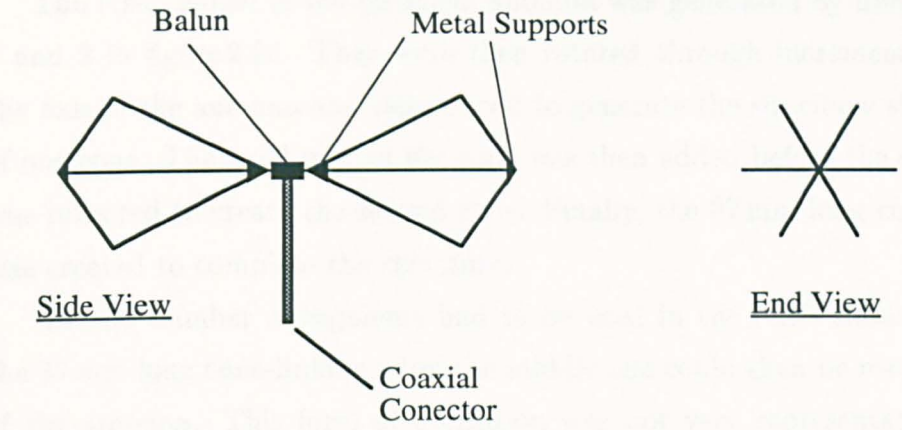


Figure 2.25: The skeletal form of the biconical antenna, as used for EMC measurements.

were built so that the triangle formed by wires 1,2 and 3 in figure 2.26 had angles of 30° at the centre of the antenna, 60° at the end of the antenna and 90° at the widest part of the antenna. Once this had been appreciated, only the three leading dimensions shown in figure 2.26 were required to define the entire structure of the antenna.

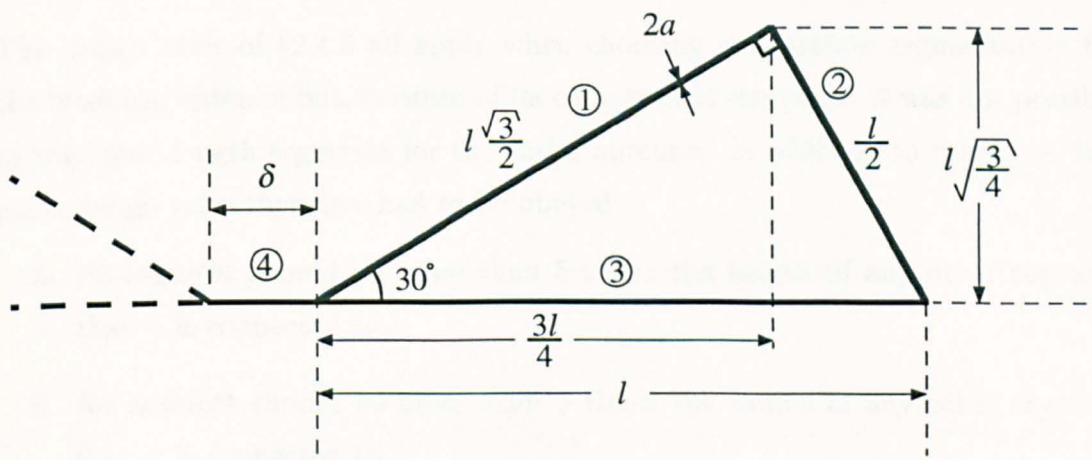


Figure 2.26: NEC model of a skeletal biconical antenna.

The radius of the wires was measured with a micrometer as 6 mm, but the other two leading dimensions could not be measured as accurately. The base of the cones, where the wires spread out, was encased in a solid metal support that made it difficult to determine the exact point of spreading. The feed point gap was measured to be 87 mm and the half-length of the antenna was measured as 647 mm, implying a cone length of 603.5 mm.

Cone Length, $l = 603.5\,\text{mm}$
Wire Radius, $a = 6.0\,\text{mm}$
Feed Gap, $\delta = 87\,\text{mm}$

The NEC model of the biconical antenna was generated by first creating wires 1 and 2 in figure 2.26. They were then rotated through increments of 60° about the axis of the antenna and reproduced to generate the six elbow shaped elements of one cone. The axial wire of the cone was then added before the entire structure was reflected to create the second cone. Finally, the 87 mm long cone-linking wire was created to complete the structure.

An odd number of segments had to be used in the NEC simulation to model the 87 mm long cone-linking wire; the middle one could then be used for excitation of the antenna. This form of excitation was not very representative of the feed region of the real biconical antenna, but it was the best that could be obtained using NEC. The real antenna was actually fed from a transmission line across a 40 mm gap between the cones, and within this gap region was a metal support at a balanced potential with respect to the cones. This metal support is shown in figure 2.25 and, because it was in the plane normal to the electric field of the antenna, it was assumed not to interact.

### 2.6.4 Segmentation for the Biconical Antenna

The design rules of §2.4.3 all apply when choosing appropriate segmentation for the biconical antenna but, because of its complicated structure, it was not possible to use equal length segments for the entire antenna. In addition to rules 1–4, two more design rules therefore had to be obeyed:

5. No segment should be more than 5 times the length of any other segment that it is connected to.

6. No segment should be more than 5 times the radius of any other segment that it is connected to.

The segment radius was set to its measured value of 6 mm for all of the wires in the simulation, including the hypothetical wire that was used to represent the excitation region. The lengths of the wires were also set to their measured values and therefore wires 1–4 of figure 2.26 were given the lengths shown in table 2.6.

It was undesirable to use more than 300 segments for the model of the biconical antenna because more segments would have required an excessive amount of computational time for simulation. It was decided that initially all of the segments would be chosen to have a length close to $\lambda/20$ and this segmentation scheme gave the numbers of segments for each wire shown in table 2.6. The total number of segments was 205 and solution time for the model was just less than one minute per excitation frequency.

| Wire No. | Length mm | No. of segments | Segment lengths /λ at 300 MHz |
|---|---|---|---|
| 1 | 522.646 | 10 | 0.0523 |
| 2 | 301.750 | 5 | 0.0604 |
| 3 | 603.500 | 11 | 0.0498 |
| 4 | 87.000 | 3 | 0.0290 |
| Total number of segments = 205 | | | |

Table 2.6: Initial segmentation scheme used for the skeletal biconical antenna.

A slightly different segmentation scheme was required for the excitation region because a single segment used to link the cones would have had a length of $\lambda/11.5$ and therefore been too long. The wire had to be formed with an odd number of segments in order to allow the antenna to be excited across a single segment at its centre, and so the cone-linking wire was modelled with 3 segments.

It was also a good idea to use three or more segments to model the cone linking wire because of the way that NEC allows the basis functions, used to model the current on a given segment, to flow onto the segments either side of it. To have the source segment joined directly to a junction of seven other wires might have caused NEC to form an inaccurate representation of the current on the antenna.

### 2.6.5 Self Impedance of the Biconical Antenna

The NEC model of §2.6.4 was used to return the drive point impedance of the skeletal biconical antenna at frequency intervals of 5 MHz from 30–300 MHz in free space. The resulting predictions for the resistive and reactive impedance components are shown in figure 2.27.

Figure 2.27 shows that the impedance of the antenna becomes purely resistive and equal to 26.97 Ω at 72.65 MHz. This is the resonance of the biconical antenna but, as with the resonant dipole antenna, it is not the exact frequency where minimum SWR occurs when driven from a 50 Ω transmission line.

At frequencies below its resonance the impedance of the biconical antenna becomes predominantly capacitive and mismatch losses rapidly reduce its radiating efficiency. Above resonance the antenna maintains a reasonable match to a 50 Ω transmission line, but the radiating properties of the antenna are discussed in more detail in chapter 4.

### 2.6.6 The Cone Resonance

A sharply tuned resonant feature was identified in the region of 278 MHz, from the self impedance predictions for the skeletal biconical antenna. More data points

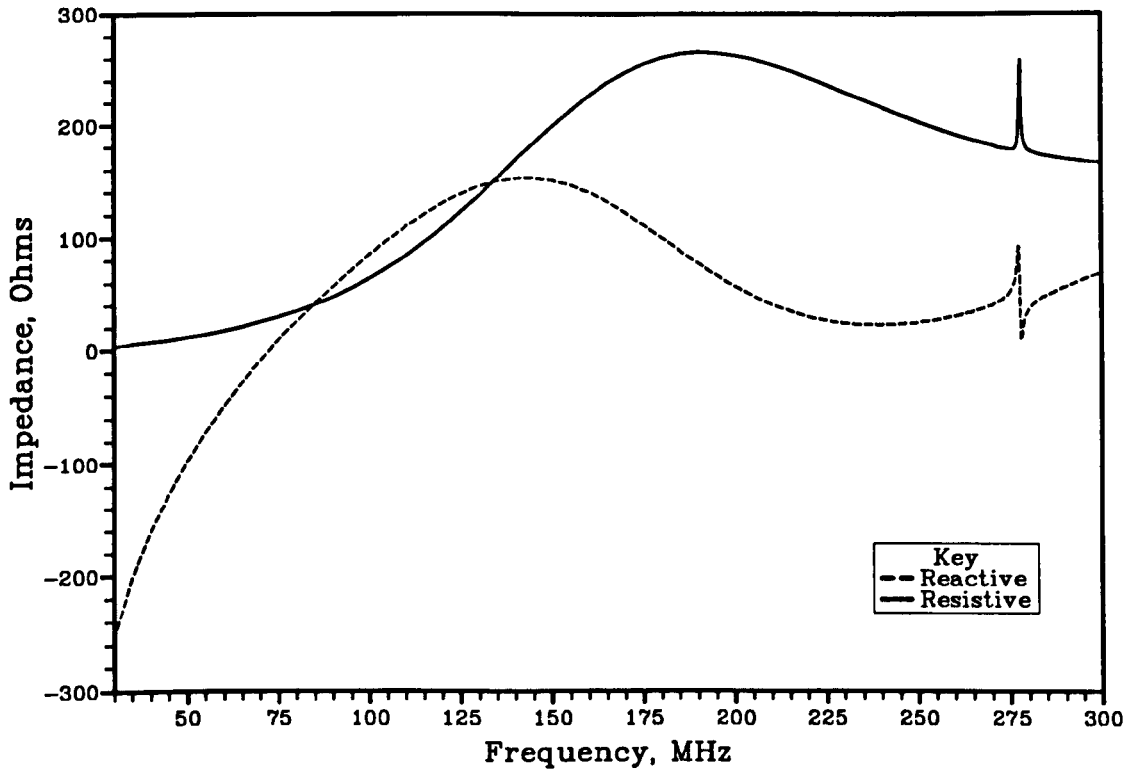


Figure 2.27: Self impedance components of the skeletal biconical antenna predicted using the 205 segment NEC model.

were calculated close to this frequency in order to reveal the shape of the resonance and the results are shown in figure 2.28.

Interpolating the resistive component through the region of the resonance shows that it is elevated from 175 Ω at the resonance to pass through a maximum value of 258 Ω at the centre frequency of 277.77 MHz. The interpolated value of the reactive component is 50 Ω in the region of the resonance and that is also its actual value at 277.77 MHz. It rises through a maximum of 91 Ω just below the resonant frequency, and then passes through a minimum of 8 Ω just above the resonant frequency.

The resonance only disturbs the impedance components significantly over a very narrow frequency range of around 2 MHz either side of 277.77 MHz. Over the range of 275–280 MHz this form of skeletal biconical antenna cannot, therefore, be accurately calibrated because its behaviour will change too rapidly as a function of frequency. Calibration of the skeletal biconical antenna will be discussed in more detail in chapter 4.

The origin of the resonance was investigated by plotting the current distribution on the wire at the centre of each cone as a function of frequency. Figure 2.29 shows that the current on the central cone wire is much greater at 277.77 MHz than it is at other frequencies. This shows that the resonance is associated with a standing

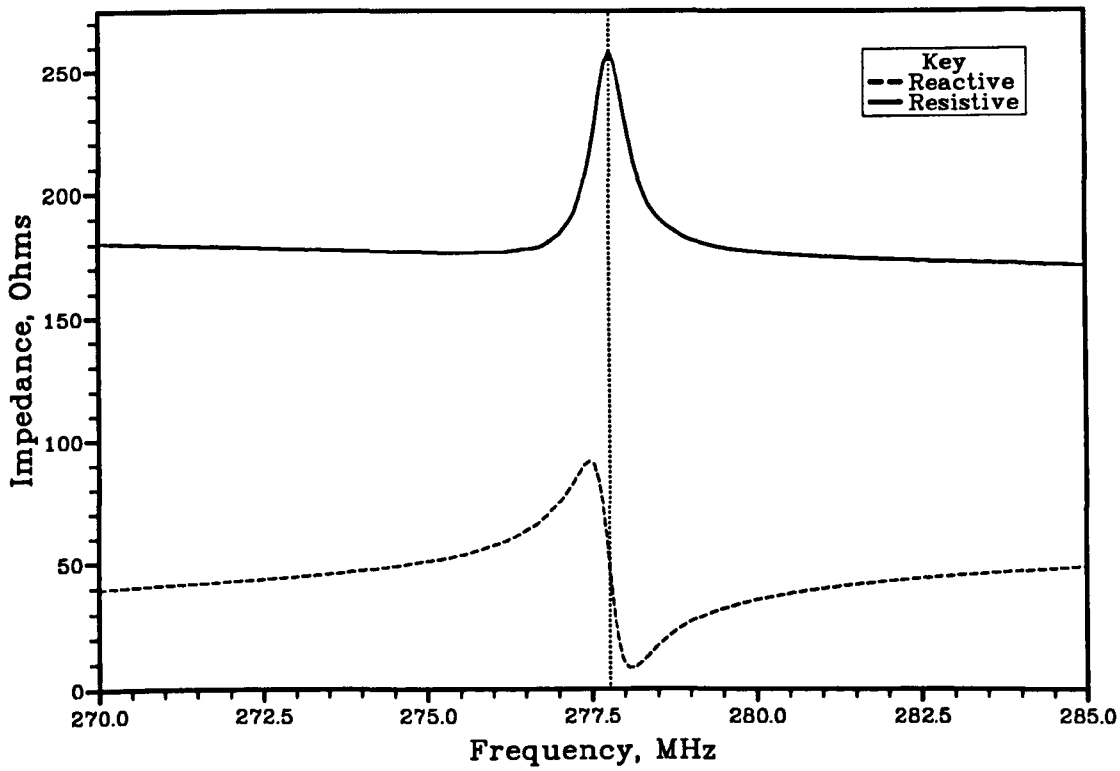


Figure 2.28: Cone resonance of the biconical antenna.

wave inside the cones of the antenna and that it is an internal resonance that cannot be used to aid the receiving and transmitting properties of the antenna.

There are two possible ways to remove the cone resonance from the skeletal biconical antenna; one is to add extra wires to the cones in a way that breaks up the standing waves inside them, and the other is simply to remove the central wire from the cone altogether. The first of these methods is the one employed by antenna manufacturers and the extra wire that they add to each cone connects from the central wire to one of the six bent wires that form each cone. The NEC model was modified, as shown in figure 2.30, in order to simulate this structure and the resulting predicted impedance components are shown in figure 2.31.

The other method for removing the cone resonance is not presently employed with real antennas but arises from the realisation that the cone resonance is associated with currents flowing on the central wire of each cone. Removing the central wire from each cone prohibits this current flow and therefore removes the resonance. The self impedance components resulting from antennas with the two modified cone structures are compared with those from more conventional cones in figure 2.31.

It can be seen from figure 2.31 that adding the extra wire to each cone removes the cone resonance at 278 MHz but introduces two smaller resonances at 221 MHz

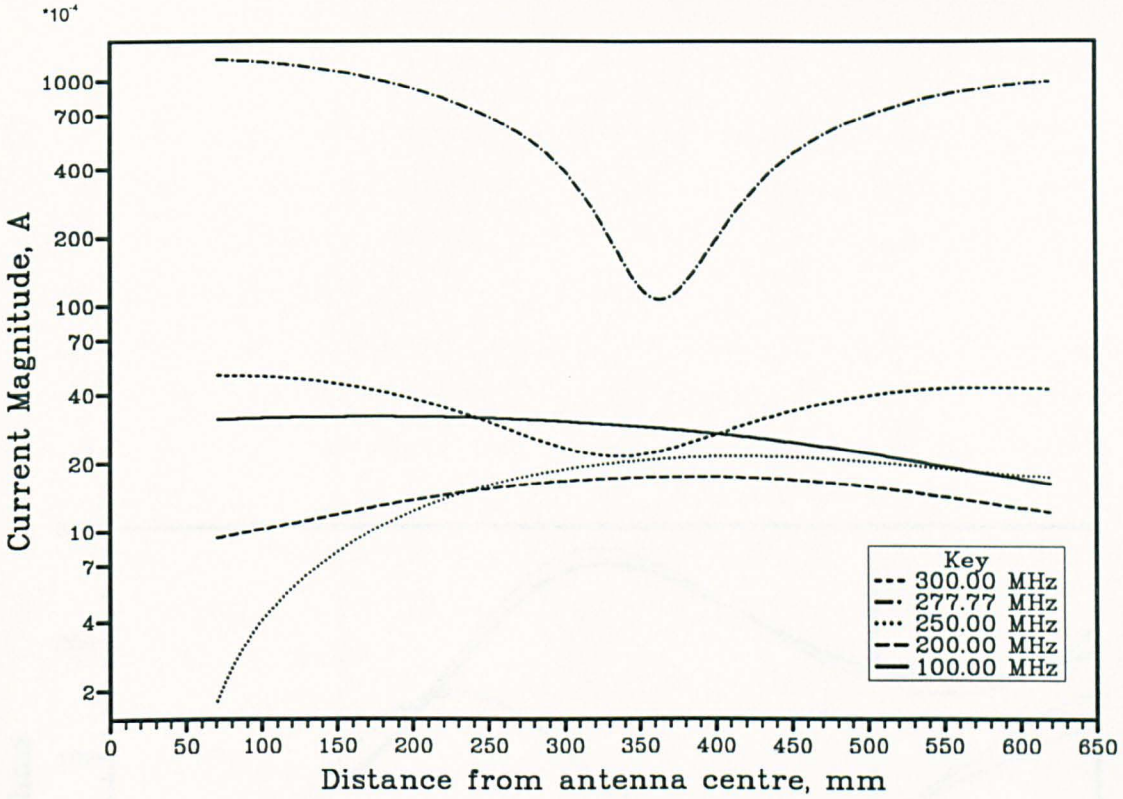


Figure 2.29: Current distribution on the central wire within one cone at excitation frequencies above, below and at resonance.

and 304 MHz. The first of these causes only very slight disturbances in the impedance components and is therefore not a problem for a practical antenna. The second resonance is slightly larger but lies out of the specified operating frequency range of the antenna, i.e. above 300 MHz. The cone structure with no centre wire gives only slightly different impedance curves to conventional cones, but they do not show any resonances. This would therefore appear to be the most effective modification to the skeletal biconical antenna structure for removing resonances due to standing waves in its cones.

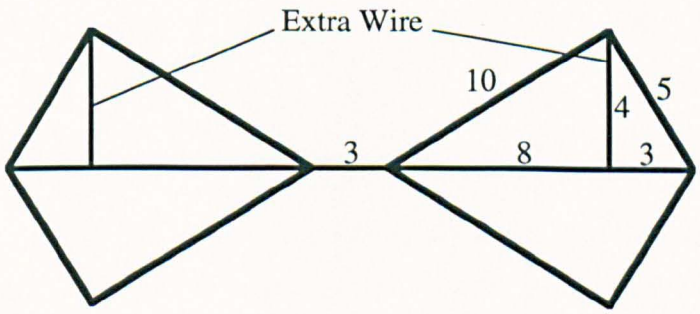


Figure 2.30: Extra wire applied to the cones of a skeletal biconical antenna and the segmentation scheme used to simulate it in NEC.

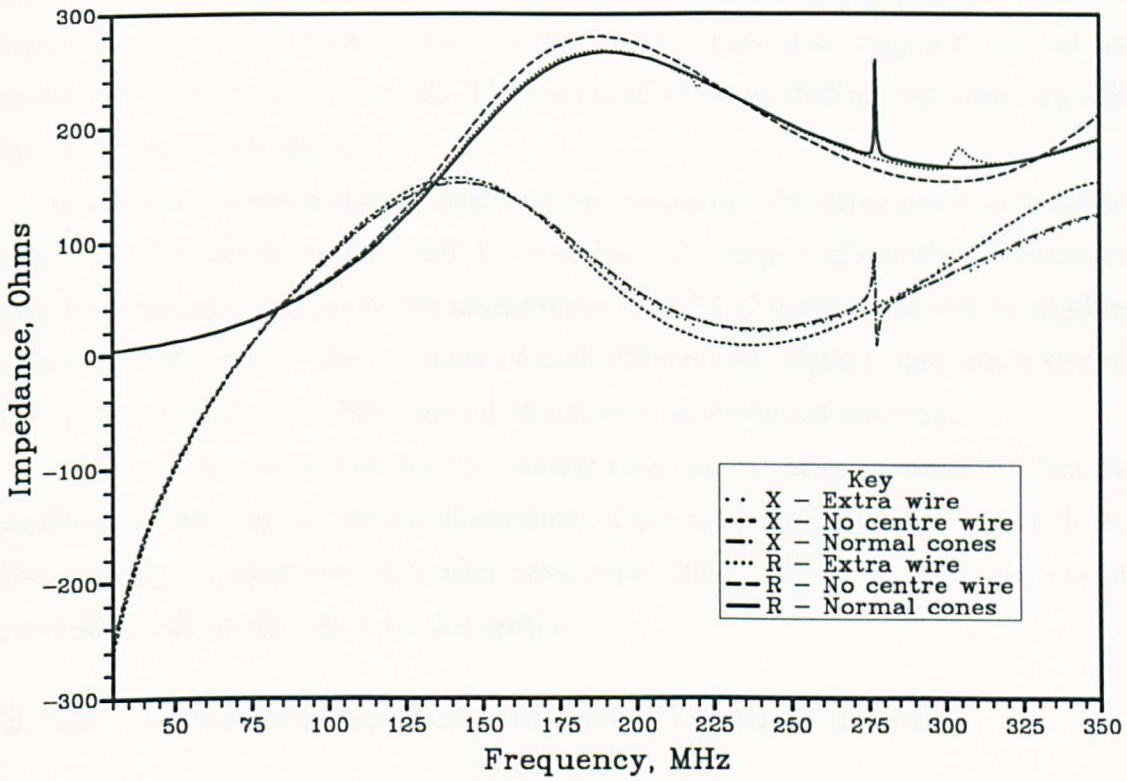


Figure 2.31: Comparison of impedance components from a skeletal biconical antenna with a conventional cone structure, cones with no central wire and cones with an extra wire used to break up the cone resonance.

## 2.7 An Optimal Model of the Skeletal Biconical Antenna

In §2.6 a NEC model of a Schwarzbeck BBA9106 skeletal biconical antenna was derived using its measured dimensions to develop wire cages equivalent to its cones. The two cones of the model were then joined by a wire, loaded with a voltage source, to represent the excitation region of the antenna.

The NEC model of a skeletal biconical antenna proposed in §2.6.4 did not have exactly the same structure as the real antenna because it was formed only from cylindrical wire elements. There were two main aspects in which the simulated antenna differed from the real antenna: it was not possible to fully model the solid metal supports at both ends of each cone, and the excitation region could not be modelled representatively at all. The effects of these modelling compromises will be discussed in this section.

In chapter 4 a method that was used for measuring the drive point impedance of a skeletal biconical antenna will be described. The degree of correlation between this measurement and predicted impedances from NEC simulations will be used in this section to deduce the accuracy of each different simulation, and hence derive the most representative NEC model of the skeletal biconical antenna.

There are two aspects of the NEC model that can be varied in order to affect its predictions: varying the actual dimensions of the model will affect its predictions, but varying segmentation will also have some effect. Both of these aspects of modelling will be discussed in this section.

### 2.7.1 Biconical Antenna above a Ground Plane

The drive point impedance of the skeletal biconical antenna was measured with the antenna horizontally polarised at a height of 1.542 m above the ground plane of the open-area test site described in chapter 1. A wooden tripod was used to support the antenna and was assumed not to interact with its fields so that, if the ground plane was assumed to be perfectly reflecting, NEC predictions could be compared with the measured impedances.

The first model of the skeletal biconical antenna to be compared with measurement was the 205 segment one, developed in §2.6.4 using the measured dimensions of the antenna. The NEC simulation of this antenna was performed with the antenna at a height of 1.542 m above a perfectly reflecting ground plane and the resulting predicted impedance components are compared with measured ones in figure 2.32.

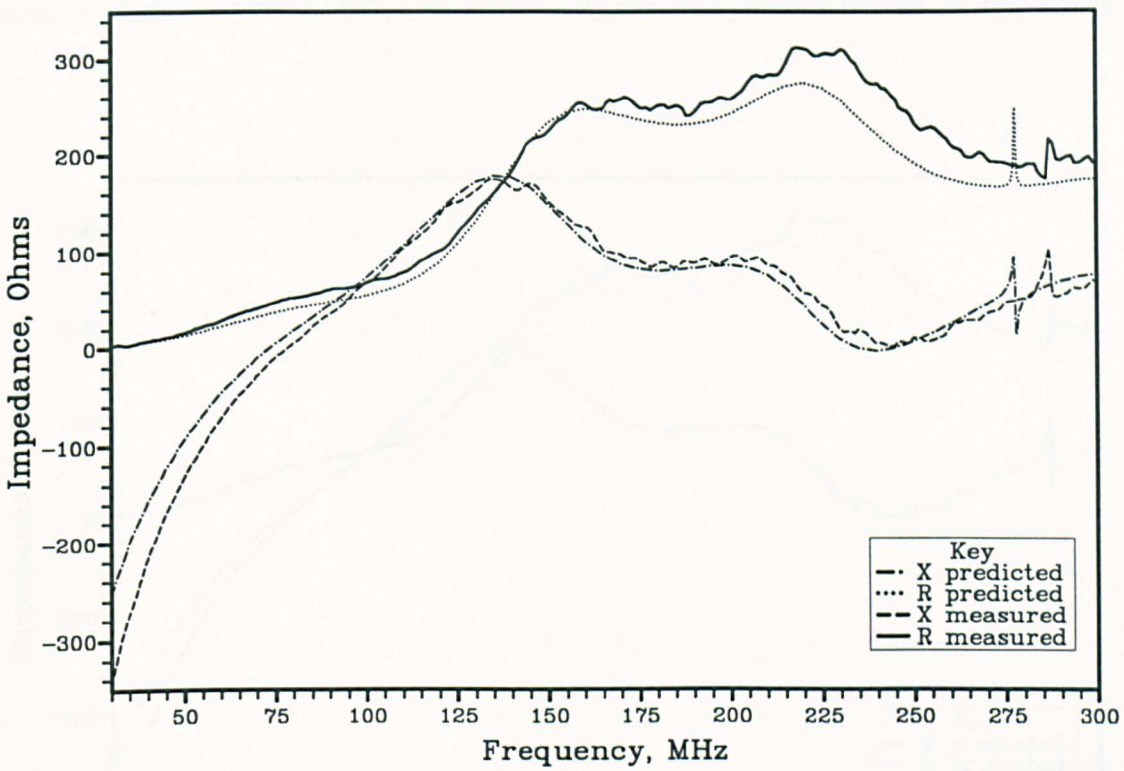


Figure 2.32: Comparison of measured and predicted drive point impedances of the skeletal biconical antenna at a height of 1.542 m above a perfectly reflecting ground plane.

The measured and predicted impedance components in figure 2.32 show good qualitative agreement but the quantitative agreement is not very good. In particular, the predicted resistive component is in error by as much as 40 Ω around 225 MHz and the reactive component is a similar amount in error below 70 MHz.

The measured cone resonance was at 287.3 MHz and not at the predicted frequency of 277.77 MHz. This difference was to prove an important clue to the reason for the inaccuracy of the NEC simulation.

### 2.7.2 Cone Shortening

The cone resonance of the skeletal biconical antenna has been explained in §2.6 to be a problem for antenna calibration, but it is a very useful aid to deriving an optimum NEC model of the antenna. The frequency of the cone resonance depends only on the dimensions of the cones of the antenna and not on its excitation region; it was therefore possible to change the cone length of the biconical antenna to bring the measured and predicted cone resonant frequencies into agreement.

The resonant frequency of the cones of the real antenna was measured as 287.3 MHz, whereas the predicted resonant frequency for a cone length of 603.5 mm

was 277.77 MHz. Shortening the simulated cone length to 585.275 gave a predicted cone resonance of 287.3 MHz and the impedance components shown in figure 2.33.

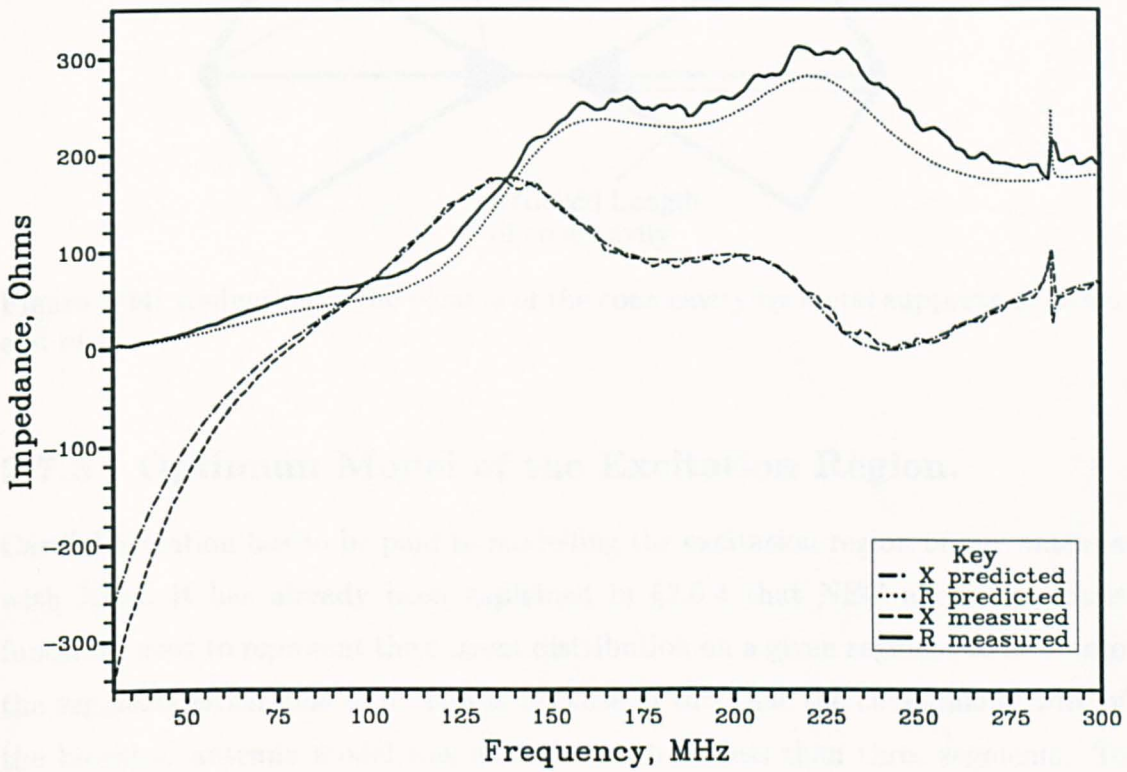


Figure 2.33: Comparison of the measured drive point impedance components of the skeletal biconical antenna with predictions from a model having a shortened cone length of 585.275 mm.

Shortening the cones has moved the maxima and minima in the predicted impedance curves to occur at the same frequencies as measurement; it has also resulted in a more accurate simulation than is shown in figure 2.32. The measured and predicted reactive components are in good agreement above 100 MHz, but the difference between them increases below this frequency to become as high as 80 Ω at 30 MHz. The real antenna is therefore less capacitive than the NEC model at low frequencies and the reasons for this will be discussed later in §2.7.4. The quantitative agreement between the resistive components in figure 2.33 is still not very good, with differences of up to 40 Ω.

The difference between the modelled cone length and the measured cone length was 18 mm, but the impedance components from the two were in good agreement. The reason for this was that the NEC model of the cones did not account for the volume occupied by the metal supports at either end of the cones. Figure 2.34 shows how they reduce the length of the cavity within the cones of the real antenna

by around 18 mm and hence this is the reason for the need to shorten the cones in the NEC model.

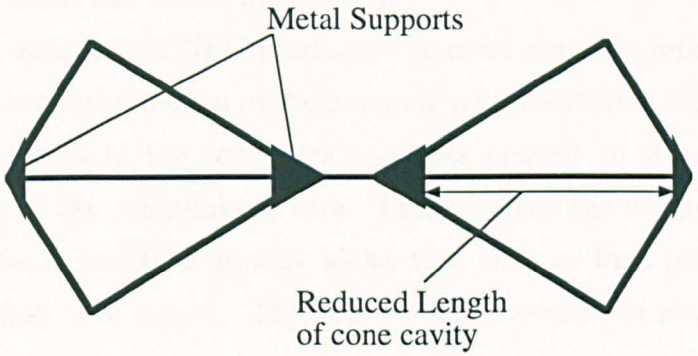


Figure 2.34: Reduction of the volume of the cone cavity by metal supports at either end of it.

### 2.7.3 Optimum Model of the Excitation Region.

Careful attention has to be paid to modelling the excitation region of any antenna with NEC. It has already been explained in §2.6.4 that NEC allows the basis functions used to represent the current distribution on a given segment to flow onto the segments either side of it. It was because of this that the cone-linking wire of the biconical antenna model was modelled with no less than three segments. To have used less would have required the source segment to be connected directly to the junction of the seven cone wires and may have caused inaccurate representation of the current by the basis functions.

An alternative modelling approach that has been used for the excitation region of the biconical antenna uses six individual voltage sources to feed pairs of cone wires separately as shown in figure 2.35. This model was proposed by Austin and

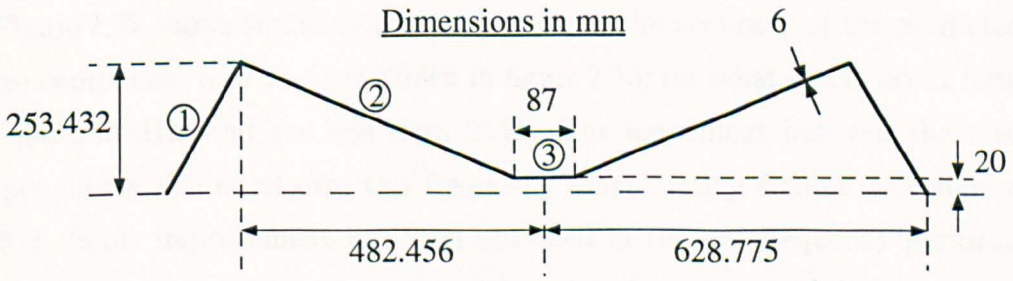


Figure 2.35: Alternative model for the excitation region of a skeletal biconical antenna.

Fourie [47] and must be used with great care because it is not representative of any real biconical antenna. It does not allow currents to flow from one wire of a cone to another at the feed of the antenna, and it does not model the central wire of

the cones at all. The close agreement between the impedance components of more representative models of the antenna and those measured suggests that there is no need to compromise the model in this way.

In order to ensure that NEC produced the most accurate representation of the current in the excitation region of the antenna, a segmentation scheme was devised that set the lengths of the cone wire segments nearest to the excitation region equal to those of the cone linking wire. This required the segments of each cone wire to increase in length gradually along that wire so that the correct number gave the required wire length. This segmentation scheme is shown in figure 2.36

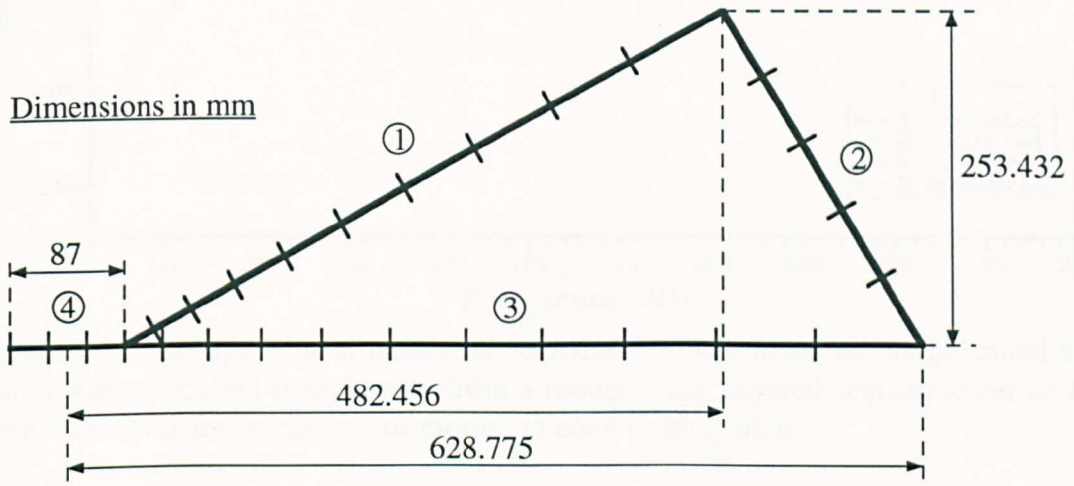


Figure 2.36: Modified segmentation scheme with three segments used to model the cone linking wire, and the segment lengths of the cone wires tapered to be equal to those of the cone linking wire where they joined it.

and simulations were performed with it as shown, and also with 5 and 7 segments used to model the cone linking wire. The best correlation between measured and predicted impedance components was obtained with 5 segments and these results are shown in figure 2.37.

Figure 2.37 shows significant improvement in the accuracy of the predicted resistive component over the one shown in figure 2.33; its worst errors occur between 225 and 250 MHz and are less than 25 Ω. The agreement between the reactive components is also worst over this frequency range, with a similar maximum error of 25 Ω. Some improvement has been obtained in the low frequency performance of the predicted reactive component, although it is still around 40 Ω greater than measurement at 30 MHz.

### 2.7.4 Cone Separation

All of the biconical antenna models mentioned so far in this chapter have predicted reactive impedance components that were slightly less negative than measured ones

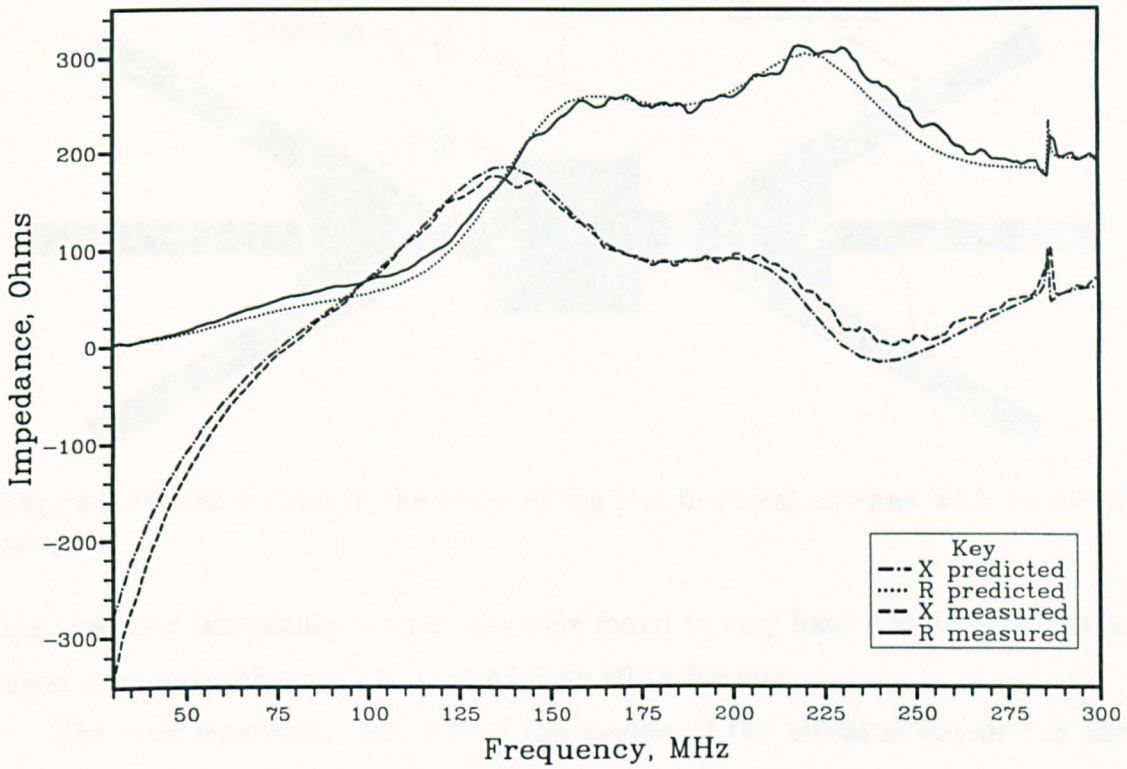


Figure 2.37: Comparison of measured impedance components of the biconical antenna with predicted components from a model using tapered segmentation on its cone wires and five segments to model its cone linking wire.

below 75 MHz. The biconical antenna is capacitive below 75 MHz and therefore the real antenna was slightly less capacitive than predicted. The real antenna had a capacitance of 15.39 pF at 30 MHz, whereas the predicted capacitance was 2.54 pF higher.

It has been noted in §2.5.2 that the structure of the excitation region of a cylindrical dipole antenna affects drive point impedance most significantly at frequencies where the antenna is electrically short, i.e. significantly less than half a wavelength long. The drive point impedance of the biconical antenna below 75 MHz is similar to that of a short dipole antenna in that both impedances are predominantly capacitive. This implies that the predicted impedance of the biconical antenna is also most sensitive to modelling of its feed region at frequencies below 75 MHz.

The NEC model of the biconical antenna does not account for the presence of the metal support, shown in figure 2.38, between the cones of the real biconical antenna. Interactions occur between the cones of the antenna and the support that are difficult to model and have most effect on the impedance of the antenna at frequencies below 75 MHz.

It was hoped that changing the length of the cone linking wire in the NEC model would give some improvement, but this was found not to be the case, and

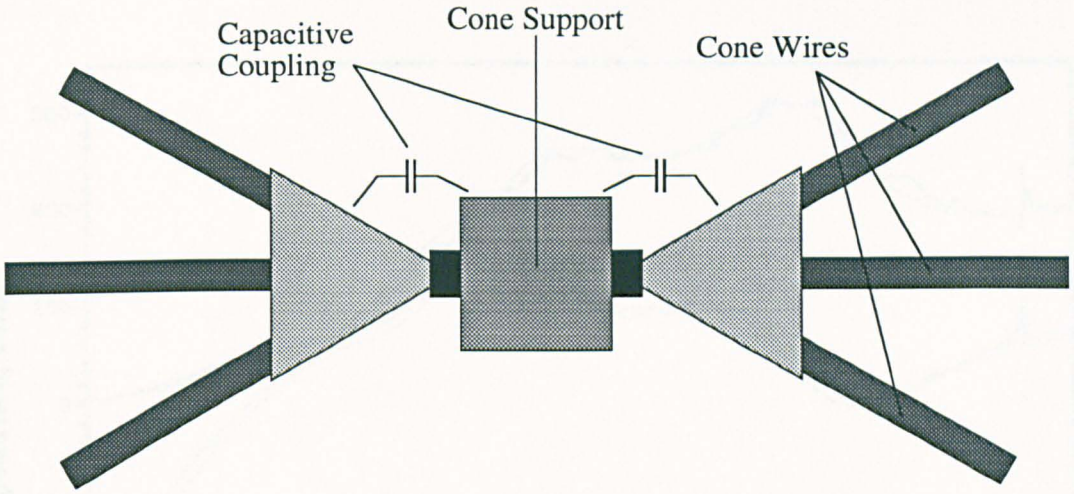


Figure 2.38: Interaction of the cones of the real biconical antenna with its metal support.

the predicted impedance components were found to only have a weak dependence upon cone separation as it was varied from 80 to 100 mm.

The cone separation used for all the models of the biconical antenna in the remainder of this thesis was 95 mm, and the resulting impedance curves from this model are compared with measurement in figure 2.39.

### 2.7.5 Minimum Segmentation

The final stage of optimising the NEC model was to reduce the number of segments as far as possible without compromising its accuracy. This was necessary to give a model with the fastest possible solution time.

As segmentation of the cone wires was reduced, segmentation in the excitation region was not changed; five segments were still used for the cone-linking wire and the segmentation of each cone wire was tapered so that its first segment was the same length as the segments of the cone-linking wire. The segmentation schemes that were used for the cone wires are shown in table 2.7 and the labelling scheme used for the wires is shown in figure 2.36.

| Model Number | Number of segments | | | | Cone resonant frequency / MHz |
|---|---|---|---|---|---|
| | Wire 1 | Wire 2 | wire 3 | Total | |
| 1 | 4 | 2 | 5 | 87 | 281.76 |
| 2 | 6 | 3 | 8 | 129 | 285.52 |
| 3 | 8 | 4 | 10 | 169 | 286.30 |
| 4 | 10 | 5 | 12 | 209 | 286.70 |
| 5 | 15 | 7 | 18 | 317 | 287.23 |

Table 2.7: Segmentation schemes used for the skeletal biconical antenna and their corresponding predicted cone resonant frequencies.

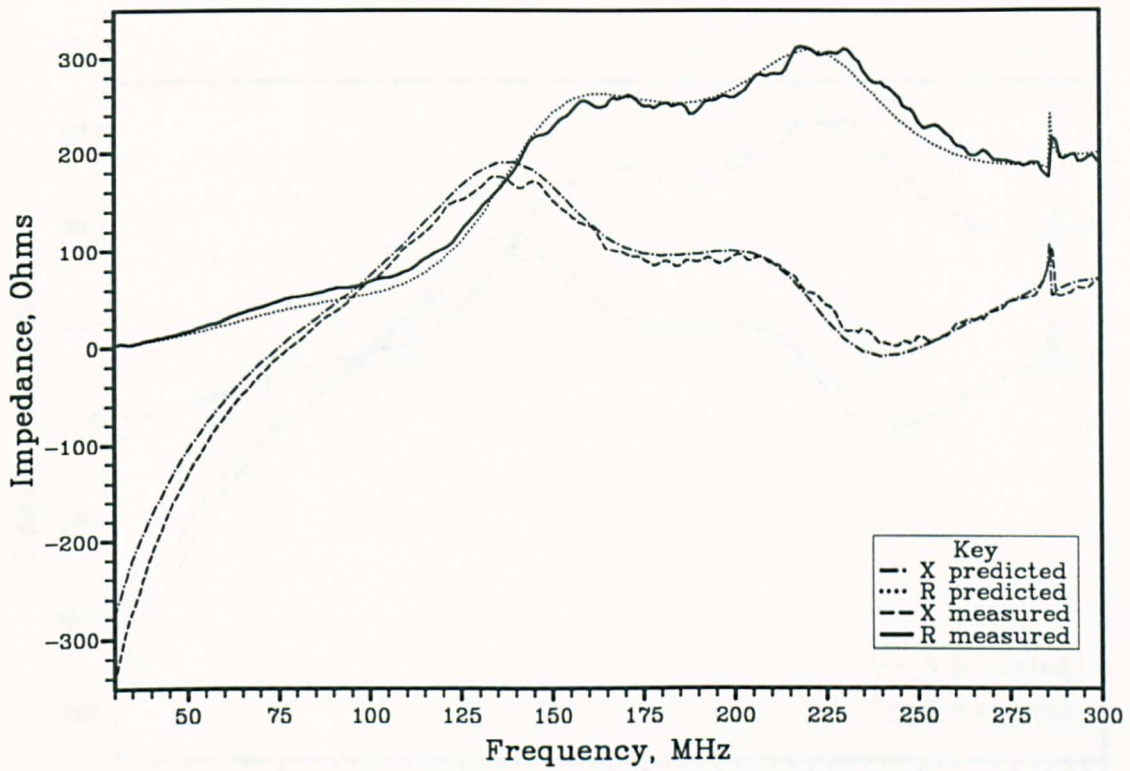


Figure 2.39: Comparison of measured drive point impedance impedance components of the biconical antenna with predicted ones from a 207 segment NEC model having five equal length segments in the source region and a 95 mm cone separation.

All of the segmentation schemes shown in table 2.7 gave predicted drive-point impedances that were almost identical, thus a segmentation scheme using as few as 87 segments could return excellent modelling results for the skeletal biconical antenna.

The only difference between the predictions with the different segmentation schemes was the predicted resonant frequency of the cones. This became lower as segmentation was reduced, particularly for models having less than 169 segments. This problem was due to under segmentation towards the ends of the antenna resulting from the segment tapering along the cone wires. Because the first segment of each cone wire was the same length as the segments of the cone linking wire, and a constant scaling factor was used between adjacent segment lengths, the last segment formed more than half the length of cone wires that were modelled using less than five or six segments.

It was decided to use the 169 segment model of the skeletal biconical antenna for all of the remaining work in this thesis because the cone resonance had not shifted appreciably with this segmentation and the solution time of the model was acceptable. The resulting predictions from this model are compared with

measurements in figure 2.40.

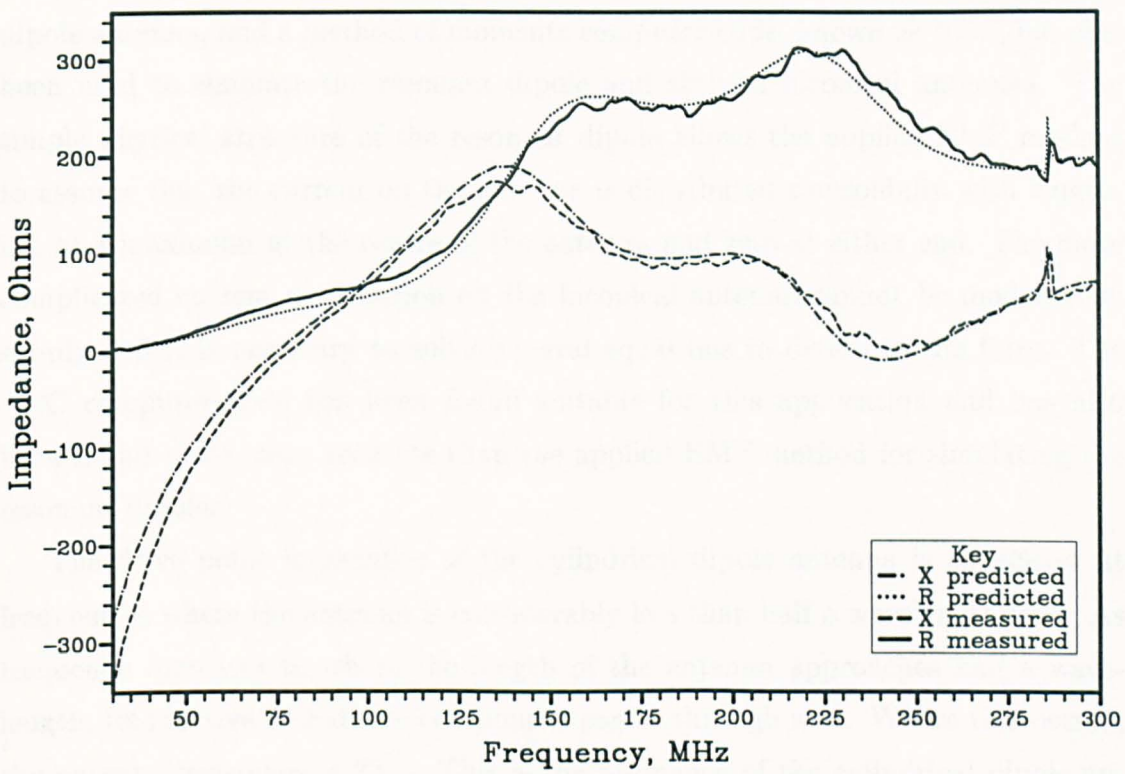


Figure 2.40: Comparison of measured impedance components with those predicted by the 169 segment, optimum NEC model of the skeletal biconical antenna.

## 2.8 Summary and Conclusions

In this chapter, the applied EMF method has been used to analyse the resonant dipole antenna, and a method of moments computer code, known as NEC, has also been used to simulate the resonant dipole and skeletal biconical antennas. The simple physical structure of the resonant dipole allows the applied EMF method to assume that the current on the antenna is distributed sinusoidally with length, i.e. at a maximum at the centre of the antenna and zero at either end. The more complicated current distribution on the biconical antenna cannot be modelled so simply and it is necessary to solve integral equations to determine its form. The NEC computer code has been found suitable for this application and has also been found to be more accurate than the applied EMF method for simulating the resonant dipole.

The drive point impedance of the cylindrical dipole antenna is capacitive at frequencies where the antenna is considerably less than half a wavelength long. As frequency increases to where the length of the antenna approaches half a wavelength, its reactive impedance component passes through zero. Where this occurs, the antenna resistance is 73 Ω. This is the resonance of the cylindrical dipole antenna and, at resonance, the precise shortening of the antenna length from half a wavelength is determined by its radius. Thinner antennas resonate where they are closer to half a wavelength long; typically, antennas resonate at between 46.5% and 48.5% of a wavelength. The bandwidth of a resonant dipole, driven from a transmission line and used for information transmission, is also determined by its radius. The thinner an antenna is, the steeper is the slope of its reactive component as it passes through zero, and therefore the narrower is the frequency range over which the antenna is well matched to its transmission line.

The applied EMF method can be extended to analyse coupled resonant dipoles through the concept of mutual impedance. The terminal voltages of an array of antennas are related to their terminal currents through an impedance matrix, whose diagonal terms are the self impedances of the antennas and whose non-diagonal terms are the mutual impedances between antennas. This method represents a mathematically simple way of analysing complex antenna interactions, but it has limitations that become apparent when more rigorous integral equation solutions are used to analyse coupled antennas. If a pair of antennas are very closely spaced, i.e. less than half a wavelength apart, their self and mutual impedances are not separable from symmetrically and antisymmetrically fed impedances. This is because the presence of a second antenna strongly affects the current distribution on the

other antenna. Under these conditions the coupled antennas form a transmission line and only a full integral equation solution approach is able to analyse them.

Predicted self impedances of a 6.35 mm diameter resonant dipole, obtained from a 21 segment NEC simulation and the applied EMF method, were compared with measurements in order to deduce the accuracy of each modelling approach. The predicted resistive and reactive impedance components from NEC were each found to be accurate to better than within 4 Ω at 300 MHz, but accuracy of the measured data limited the validation of NEC to better than this. Convergence testing the NEC model showed predictions from a 21 segment model to be within 1.2 Ω of a 499 segment model but the impedance components would be less converged at higher frequencies.

It is important to consider the behaviour of current at the free ends of tubular conductors when simulating antennas whose radii are not several orders of magnitude less than their lengths. The current does not immediately go to zero at these ends, but flows back down inside the tubes for a short distance comparable with the radius of the antenna. NEC accounts for this behaviour in its simulations, but the applied EMF method does not and therefore the accuracy of the applied EMF method is reduced for proportionally fatter antennas. The assumption of sinusoidally distributed current also becomes less accurate for antennas that are not thin. Predicted resistive and reactive impedance components were found to be 10–15 Ω less than those measured and this indicated the need to apply a length correction to account for the end effects. Adding 3 mm to the length of simulated antenna brought its predicted reactive component into agreement with NEC but the resistive component was still around 8 Ω less than NEC and measurement. This shortfall in predicted radiation resistance is the main limitation associated with using the applied EMF method to simulate resonant dipole antennas.

The impedance components of the skeletal biconical antenna, predicted by NEC, showed it to become increasingly capacitive below 70 MHz in a similar way to a short dipole antenna. At 73 MHz the impedance of the antenna is purely resistive and equal to 27 Ω. This is the resonant frequency of the antenna, but, at frequencies above 70 MHz, its impedance components are not as strongly frequency-dependent as those of the resonant dipole. Their magnitudes remain sufficiently small for the antenna to be reasonably matched to a 50 Ω transmission line at frequencies up to 300 MHz.

The cones of the skeletal biconical antenna have a sharply tuned resonance that affects the impedance of the antenna over a 3 MHz frequency range centred on 287 MHz. The resonance is associated with currents flowing on the central wire of

each cone and, because this wire is not part of the conical structure of the antenna, it may be removed without significantly altering the antenna performance. Certain antenna manufacturers break up the cone resonance with an extra wire in each cone but this does not remove the resonance; it moves it out of the normal operating frequency range of the antenna and above 300 MHz, but it also introduces another very small cone resonance at 225 MHz.

The solid metal supports at either end of both cones of the biconical antenna reduce the volume of the cavity within them and so a wire cage model of the cones, simulated with NEC and having the same dimensions as the real antenna, predicts a cone resonance at a lower frequency than that of the real antenna. Reducing the length of the simulated cones moves the predicted resonance to agree with measurement and also improves agreement between measured and predicted impedance components at all other frequencies.

Great care has to be taken when modelling the excitation region of the skeletal biconical antenna using NEC, because it cannot be modelled realistically as there is an eight-wire junction at either side of it. NEC allows the current basis functions on a given segment to flow onto one segment on either side of it, and to join the NEC source segment directly to a junction may result in inaccurate expansion of the basis functions. It was found best to use a five segment wire to model the 95 mm gap between the two cones, with its third segment used for excitation. Agreement between measured and predicted impedances was also enhanced by using a variable segmentation scheme for the seven wires of each cone that were joined to the excitation region. This scheme gave the first segment of each cone wire the same length as one segment of the cone-linking wire, and then progressively increased the length of the rest of the segments of that wire to give the correct total wire length.

Good agreement was achieved between the measured and predicted impedance components of the skeletal biconical antenna except in the region below 70 MHz where it is capacitive. This was because interactions occur between the cones of the real biconical antenna and its metal support that are not taken account of by the NEC simulation. The region between the cones of the real antenna was modelled with a 95 mm long wire having the same radius as the cone wire, but the real antenna had a 40 mm feed point gap containing a metal support at a balanced potential. The discrepancy between the measured and predicted capacitance at low frequencies was still less than 10% and so the NEC model of the biconical antenna was considered accurate enough for the remaining work in this thesis.

# Chapter 3

# Site Attenuation Theory

It has been explained in chapter 1 that the ideal open-area test site offers a convenient environment in which accurate and repeatable measurements of radiated emissions may be carried out. In order to show that any real open-area test site has propagation characteristics sufficiently close to those of an ideal test site, it is necessary to carry out measurements to validate that particular test site. These measurements are known as site attenuation measurements and the theoretical background to them is discussed in this chapter.

The possible methods that may be used to validate open-area test sites are discussed in §3.1 and it is shown that a comparison of the measured power coupled between a pair of antennas over the test site with a theoretical value, derived for an ideal site, is currently the most convenient one. A review of the necessary theoretical concepts concerned with this site attenuation measurement is given in §3.2, before the remaining sections of this chapter describe the different theoretical approaches that may be used to calculate the power loss between antennas over an ideal test site.

Current standard models for the calculation of site attenuation use geometrical optical theory and these are reviewed in §3.3. They are not very accurate because they do not consider the finite size of the antennas and also neglect mutual coupling effects. A better modelling approach, based upon the calculation of the self and mutual impedances between antennas, is described in §3.4, and it is shown how the applied EMF method may be used to calculate these and obtain theoretical values for site attenuation.

In §3.5 it is shown that even the approach of §3.4 is not an accurate method for calculating the coupled power between conventional commercially available EMC antennas and two more rigorous approaches to test site validation are proposed. These methods use NEC to calculate the scattering parameters of the two-port network formed between the drive-points of two antennas over an open-area test site.

Measurements of the scattering parameters of the baluns or connecting networks of the antennas are then combined with these to calculate predicted values of site attenuation or insertion loss measured with real antennas.

## 3.1 The Validation of Open-Area Test Sites

The radiation measured from an EUT on any specific open-area test site must be the same as that which would be measured from the same EUT on an ideal site to within known error bounds. The objective of a site validation procedure is to establish these error bounds for a real test site and to determine whether they are acceptably small.

The site validation procedure has to determine errors that occur when a test site is used for radiation measurement, therefore it has to be as similar to the radiation measurement procedure as possible. The simplest way of ensuring this is to replace the EUT with a standard source having known radiating properties and hence a calculable field strength at the receiving antenna of an ideal test site. The field strength from the source is measured on the test site under investigation and subtracted from its ideal value (in dB) to yield the site error. This procedure has to be performed at frequency intervals that are sufficiently close together that no features of the response of the test site are overlooked.

Current standard procedures for test site validation [48], [49] all use essentially the same method. That is to measure the attenuation between a pair of resonant dipole antennas and to compare the result with a theoretical value derived from a model of the propagation between the antennas. The later sections of this chapter are concerned with the development of such models but this section will briefly discuss some alternative approaches to test site validation.

### 3.1.1 Electrically Small Source

Typical items of equipment under test have dimensions of less than 1 m and therefore are electrically small at frequencies at least up to 150 MHz. Resonant dipoles are not electrically small and their resonant nature makes them much more sensitive to their environment than most EUTs. For this reason it is not sufficiently representative to use resonant dipoles to determine measurement errors that occur with real EUTs. An alternative site validation procedure could use an electrically small radiating source instead of a transmitting antenna in the way shown in figure 3.1.

The electrically small source would need to have a calculable field strength on an ideal test site so that the measured field strength on the real test site could be compared with it. Alternatively, if a very good test site were available, the measured field from the source on it could be compared with that on the site under test. The good site could then become a national standard to which all other sites would be traceable to.

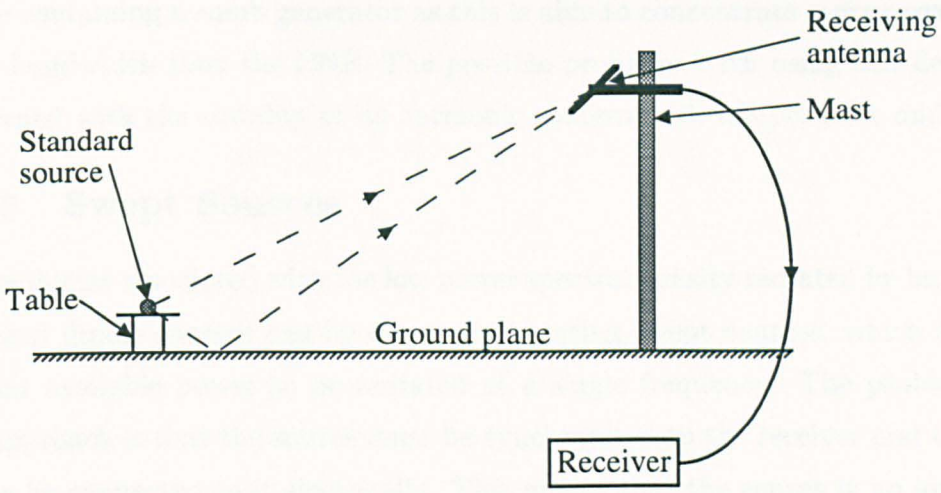


Figure 3.1: Electrically small standard source used for test site validation.

Suitable electrically small devices for this application would have to be either a self-contained broadband source or a fibre-optically fed swept source, as neither would need any connecting cables which its fields could interact with. One such device of the first type would be the Comparison Noise Emitter (CNE) used in chapter 1. It is a source of broadband radiation over the frequency range of 30 MHz to 1 GHz and has a stable radiated field strength. The problem with using this device is that, because its power is radiated over a broad spectrum, its radiated field is only around 10 dB above the noise floor of a 10 m test site. Use of a swept source would allow a much greater spectral power density and would therefore avoid this problem.

### 3.1.2 Spherical Dipole Sources

One particular class of source that would be very useful as a standard source for test site validation is the spherical dipole. This consists of two conducting hemispheres excited across a thin equatorial gap to give a spherical source. If the hemispheres are hollow, power supplies and circuits may be mounted inside them to give a self contained radiating source.

If the spherical dipole is electrically small, it has the radiating properties of an infinitesimal electric dipole. Therefore, if its dipole moment is known, the field produced by it at the receiving antenna of an ideal test site may be calculated from the expressions given in chapter 1. This field may be compared with a measured field to validate a given real test site.

Broadband noise sources such as the Comparison Noise Emitter have been built as 10 cm spherical dipoles but their radiated fields are so small that they can only be used on 3 m sites. Mantovani [50] has proposed the use of a spherical

dipole containing a comb generator as this is able to concentrate more power into a given bandwidth than the CNE. The possible problems with using this device are concerned with the stability of its harmonic content with temperature and ageing.

### 3.1.3 Swept Sources

The problems associated with the low power spectral density radiated by broadband spherical dipole sources can be overcome by using swept sources, which allow all of their available power to be radiated at a single frequency. The problem with this approach is that the source must be synchronised to the receiver and therefore has to be connected to it electrically. This means that the source is no longer self contained and must be fibre-optically driven to avoid problems with coupling to cables.

A fibre-optically driven spherical dipole swept emitter (SDSE) is manufactured by the York Electronics Centre [51]. It contains batteries and an amplifier to deliver the r.f. signal, modulated onto its fibre as a voltage across the two 10 cm hemispherical shells that form its case. The SDSE can be used for test site validation as shown in figure 3.2. A suitable receiver would be a spectrum analyser with a tracking generator. Once it has been calibrated to obtain its dipole moment,

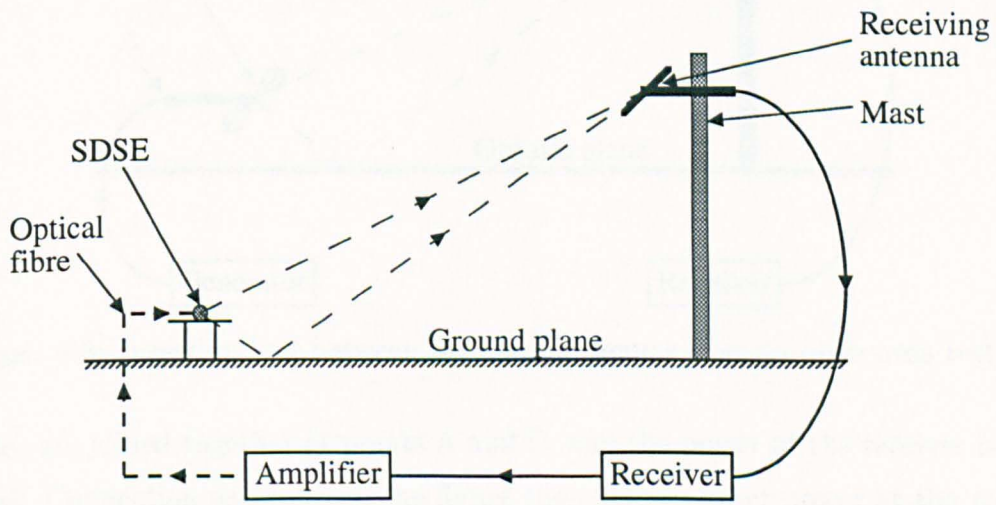


Figure 3.2: Use of a spherical dipole swept emitter for test site validation.

measured fields from the SDSE on a real site may be compared with calculated ones on an ideal test site.

The problem with the SDSE is that it only operates up to 250 MHz and, for it to operate up to higher frequencies, a more sophisticated fibre-optic link would be required. An alternative type of source would be a self-sweeping spherical dipole, however, a suitable self-locking receiver would be required to operate with it. This

type of source would have the advantage of being self-contained and not requiring a fibre-optic link to operate up to 1 GHz.

### 3.1.4 Loss between a Pair of Antennas

It has been shown above that one way to validate an open-area test site is to measure the field strength from a calibrated source and compare it with a theoretical value. If linear antennas are used for the source and receiver, the voltage at the terminals of the receiving antenna is proportional to the field strength illuminating it, and this is, in turn, proportional to the voltage at the transmitting antenna terminals. Hence, it is equally valid to assess the performance of a test site by comparing measurements of the insertion loss between two antennas over it with theoretical insertion losses over an ideal site.

All current standards for the validation of open-area test sites employ a measurement of the above type; figure 3.3 shows how it is performed. The antenna

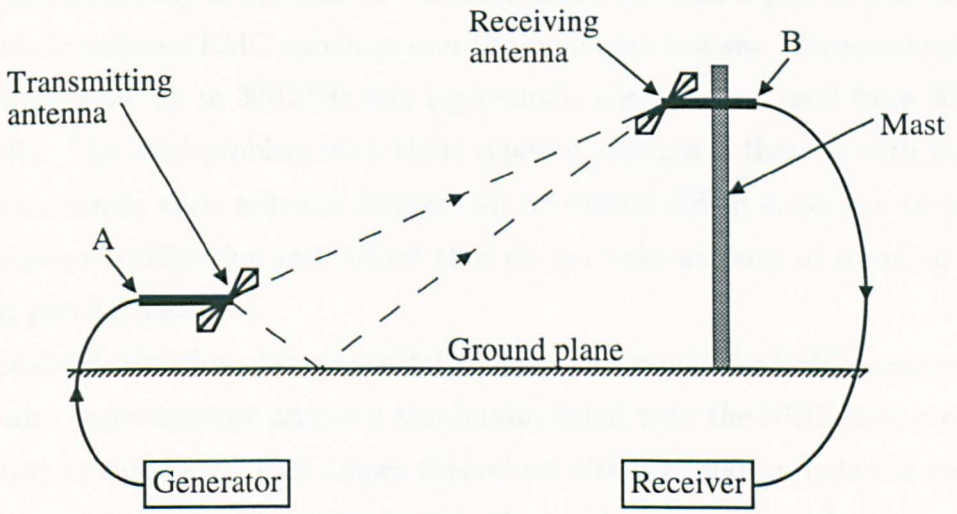


Figure 3.3: Insertion loss between a pair of antennas over an open-area test site.

cables are joined together at points A and B, and the power at the receiver is measured. Connection as shown in the figure then gives a lower power at the receiver and the ratio of these two powers is the site insertion loss.

#### Resonant Dipole Antennas

Current standard procedures for site validation [48], [49] use resonant dipoles for the transmitting and receiving antennas of a site attenuation measurement. These types of antennas have to be adjusted to a specific length at each measurement frequency and so are comparatively slow to use. This tuning process also means that it is not possible to automate the measurement by scanning frequency remotely.

Resonant dipole antennas are described in chapter 2 and have lengths that are slightly less than half a wavelength at each excitation frequency. They therefore have large physical sizes at the lower frequencies of test site operation (5 m at 30 MHz). For the reasons given in chapter 4, this results in a large amount of close coupling between these antennas and the ground plane of the test site, so calibration of them is a problem and their antenna factors tend to be particularly inaccurately known below 100 MHz. Fortunately it is not necessary to know the antenna factors of resonant dipole antennas in order to calculate theoretical site attenuation between them over an ideal test site. They can be simulated directly by a variety of computational techniques, described in chapter 2, and these methods fully account for any interactions between the antennas.

### Broadband Antennas

Of all the methods for site validation, the most attractive one with respect to speed and simplicity is to measure the attenuation between a pair of commercially available broadband EMC antennas over the open-area test site. Biconical antennas are usually used up to 300 MHz and log-periodic antennas are used from 300 MHz to 1 GHz. The chief problem with these types of antenna is that, as with resonant dipole antennas, their antenna factors can be several dB in error due to poor or inappropriate calibration procedures that do not take account of coupling to the ground plane (chapter 4).

The skeletal version of the biconical antenna that is used for EMC measurements has a wire cage structure and so it can be simulated with the NEC computer code, described in chapter 2. This allows theoretical site attenuation between biconical antennas over an ideal test site to be calculated accurately without the use of calibration data such as antenna factors. It would also be possible to use NEC to simulate log-periodic antennas over an ideal test site but this was not performed in this thesis.

## 3.2 Two-Port Network Insertion Loss Concepts

The arrangement of two antennas over an open-area test site can be regarded as a two-port network where the two ports are the drive-points of each antenna. For a measurement of site attenuation, this two-port network is inserted into a transmission line linking a generator to a load. This section will define the theoretical concepts necessary to understand the measurement.

Attenuation is a specific scientific term, with a rigid definition in terms of network theory, but it is often used inappropriately. For this reason, it and several other related terms will be defined in this section; expressions will also be given in terms of impedance and scattering parameters. A useful paper by Beatty [52] reviews many loss concepts, but the expressions given in it use scattering parameters that are not normalised to the characteristic impedance, whereas all of the scattering parameters used in this thesis are.

### 3.2.1 Insertion Loss

The most general loss concept is that of insertion loss. It is defined as the reduction in power dissipated in a load that results when a two-port network is connected into the transmission line between the load and the generator supplying it. Figure 3.4 illustrates this definition and defines the power dissipated in the load with it connected directly to the source as $P_1$, and the power dissipated in the load with connection via the two-port network as $P_2$. Insertion loss is then given by

$$\text{Insertion Loss, } IL = 10\log_{10}\left(\frac{P_1}{P_2}\right) \text{ dB}$$

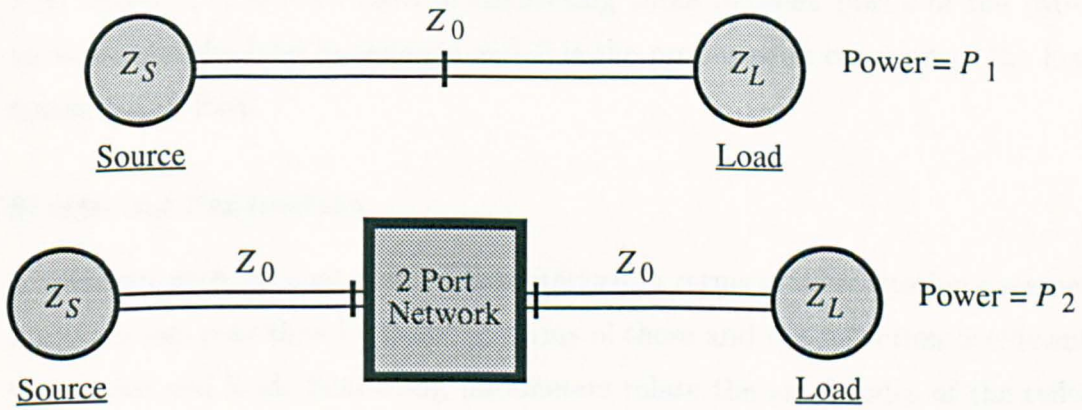


Figure 3.4: Definition of insertion loss.

The source has an output impedance of $Z_S$, the load impedance is $Z_L$, and the characteristic impedance of all the transmission lines is $Z_0$. Expressions for inser-

tion loss can be derived in terms of these impedances and the network parameters of the two-port network.

### Impedance Parameters

The impedance parameters of a two-port network relate the voltage at each of its ports to the currents at its ports through equation (3.1).

$$\begin{bmatrix} V_1 \\ V_2 \end{bmatrix} = \begin{bmatrix} Z_{11} & Z_{12} \\ Z_{21} & Z_{22} \end{bmatrix} \cdot \begin{bmatrix} I_1 \\ I_2 \end{bmatrix} \tag{3.1}$$

Insertion loss, $IL$, can be found in terms of these $Z$ parameters and equation (3.2) expresses it in decibels.

$$IL = 20 \log_{10} \left| \frac{(Z_{11} + Z'_S)(Z_{22} + Z'_L) - Z_{12}Z_{21}}{(Z'_S + Z'_L)Z_{21}} \right| \tag{3.2}$$

If the two-port network is both linear and passive, for example two antennas over an open-area test site, the reciprocity theorem applies. Therefore $Z_{12} = Z_{21}$ and equation (3.2) becomes

$$IL = 20 \log_{10} \left| \frac{(Z_{11} + Z'_S)(Z_{22} + Z'_L) - Z_{21}^2}{(Z'_S + Z'_L)Z_{21}} \right| \tag{3.3}$$

The terms $Z'_S$ and $Z'_L$ are not the $Z_S$ and $Z_L$ shown in figure 3.4. They are the source and load impedances transformed by their connecting transmission lines and referred to the ports of the two-port network.

$$Z'_S = Z_0 \frac{Z_S \cos \beta l_1 + j Z_0 \sin \beta l_1}{Z_0 \cos \beta l_1 + j Z_S \sin \beta l_1} \tag{3.4}$$

$$Z'_L = Z_0 \frac{Z_L \cos \beta l_2 + j Z_0 \sin \beta l_2}{Z_0 \cos \beta l_2 + j Z_L \sin \beta l_2} \tag{3.5}$$

where $l_1$ is the length of connecting cable between the source and port 1 of the two-port network, $l_2$ is the length of connecting cable between port 2 of the two-port network and the load impedance and $\beta$ is the propagation constant of the lossless transmission lines.

### Scattering Parameters

A two-port network may also be characterised in terms of its scattering parameters. Insertion loss may then be found in terms of these and the reflection coefficients of the source and load. Scattering parameters relate the amplitudes of the reflected waves from each of the ports, $b_1$ and $b_2$, to the waves incident at them, $a_1$ and $a_2$, via the matrix equation (3.6).

$$\begin{bmatrix} b_1 \\ b_2 \end{bmatrix} = \begin{bmatrix} S_{11} & S_{12} \\ S_{21} & S_{22} \end{bmatrix} \cdot \begin{bmatrix} a_1 \\ a_2 \end{bmatrix} \tag{3.6}$$

The source and load reflection coefficients, $\Gamma_S$ and $\Gamma_L$, are given from their impedances by equations (3.7) and (3.8).

$$\Gamma_S = \frac{Z_S - Z_0}{Z_S + Z_0} \tag{3.7}$$

$$\Gamma_L = \frac{Z_L - Z_0}{Z_L + Z_0} \tag{3.8}$$

The expression for the insertion loss of a two-port network in terms of its scattering parameters is

$$IL = 20\log_{10}\left|\frac{(1 - S_{11}\Gamma'_S)(1 - S_{22}\Gamma'_L) - S_{12}S_{21}\Gamma'_S\Gamma'_L}{S_{21}(1 - \Gamma'_S\Gamma'_L)}\right| \tag{3.9}$$

and, as with equation 3.2, if the network is linear passive, such as two antennas coupled together over a ground plane, the principle of reciprocity is obeyed so $S_{12} = S_{21}$ and equation (3.9) becomes

$$IL = 20\log_{10}\left|\frac{(1 - S_{11}\Gamma'_S)(1 - S_{22}\Gamma'_L) - S_{21}^2\Gamma'_S\Gamma'_L}{S_{21}(1 - \Gamma'_S\Gamma'_L)}\right| \tag{3.10}$$

The $\Gamma'_S$ and $\Gamma'_L$ terms are not the $\Gamma_S$ and $\Gamma_L$ of equations (3.7) and (3.8); they are the source and load reflection coefficients transformed by their connecting transmission lines and referred to the ports of the two-port network.

$$\Gamma'_S = \Gamma_S e^{-2j\beta l_1} \tag{3.11}$$

$$\Gamma'_L = \Gamma_L e^{-2j\beta l_2} \tag{3.12}$$

The effective source and load reflection coefficients can be related to the effective source and load impedances of equations (3.4) and (3.5).

$$\Gamma'_S = \frac{Z'_S - Z_0}{Z'_S + Z_0} \tag{3.13}$$

$$\Gamma'_L = \frac{Z'_L - Z_0}{Z'_L + Z_0} \tag{3.14}$$

### 3.2.2 Attenuation

Attenuation is a special case of insertion loss in which the generator and load impedances are matched to the characteristic impedances of their connecting transmission lines, i.e.

$$Z_S = Z_0$$

$$Z_L = Z_0$$

Under this condition equation (3.3) becomes

$$\text{Attenuation, } AL = 20\log_{10}\left|\frac{(Z_{11} + Z_0)(Z_{22} + Z_0) - Z_{21}^2}{2Z_0Z_{21}}\right| \tag{3.15}$$

and gives the expression for the attenuation of a reciprocal two-port network in terms of its $Z$ parameters.

It can be seen from equations (3.7) and (3.8) that, if the source and load impedances are both matched to the characteristic impedance of the connecting transmission lines, the source and load reflection coefficients become equal to zero. Equations (3.11) and (3.12) show that the effective source and load reflection coefficients are also zero and equation (3.9) reduces to

$$AL = 20\log_{10}\left|\frac{1}{S_{21}}\right| \tag{3.16}$$

### 3.2.3 Transducer Loss

Transducer loss is a different power ratio to insertion loss and attenuation. It is the ratio of the power developed in the load impedance, with connection via the two-port network, to the total power available from the source. The expression for the transducer loss of a reciprocal two port network in terms of its $Z$ parameters is

$$TL = 10\log_{10}\left(\left|\frac{(Z_{11}+Z'_S)(Z_{22}+Z'_L)-Z_{21}^2}{Z_{21}Z'_S}\right|^2 \cdot \frac{R'_L}{4R'_S}\right) \tag{3.17}$$

where $R'_S$ and $R'_L$ are the resistive components of $Z'_S$ and $Z'_L$ respectively. In terms of $S$ parameters, transducer loss is

$$TL = 10\log_{10}\left(\frac{|(1-S_{11}\Gamma'_S)(1-S_{22}\Gamma'_L)-S_{12}S_{21}\Gamma'_S\Gamma'_L|^2}{|S_{21}|^2(1-|\Gamma'_S|^2)(1-|\Gamma'_L|^2)}\right) \tag{3.18}$$

### 3.2.4 Classical Site Attenuation

The previous subsections have defined the three most common loss parameters that are considered when dealing with two-port networks. Attenuation has been defined in §3.2.2, hence site attenuation is:

> The minimum attenuation that occurs when a two-port network, formed by two antennas over an open-area test site, is inserted into a transmission line and the receiving antenna is scanned through its usual height range.

This definition is illustrated by figure 3.5.

$$SA = 10\log_{10}\left|\frac{P_1}{P_2}\right|_{min} \tag{3.19}$$

The power dissipated in the load for the directly connected case is $P_1$ and for the case of connection via the test site it is $P_2$. The power dissipated in the load impedance is proportional to the square of the voltage across it, and so equation (3.19)

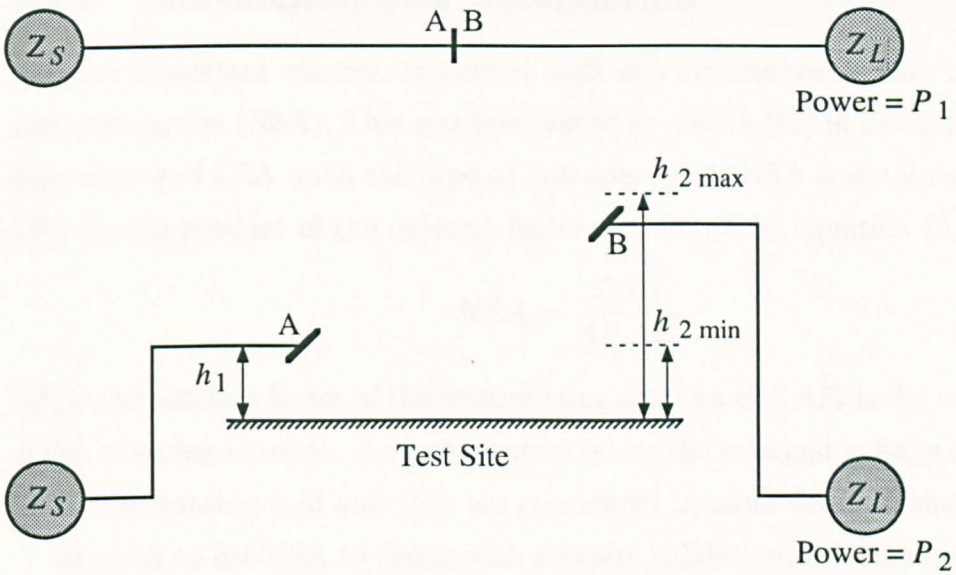


Figure 3.5: Definition of site attenuation.

may also be expressed as

$$SA = 20 \log_{10} \left| \frac{V_{L1}}{V_{L2}} \right|_{min} \tag{3.20}$$

where $V_{L1}$ is the voltage across the load for the directly connected case and $V_{L2}$ is the voltage across the load with connection via the site. The *min* subscript denotes the minimum value as the receiving antenna is scanned through its specified height range for the particular length of site.

In general, site attenuation depends upon:

- The site length.
- The transmitting antenna height.
- The limits of the receiving antenna height-scan range.
- The type of antennas used.
- The antenna polarisation.
- The characteristic impedance of the connecting transmission lines.
- The site propagation characteristics.

In order to calculate definitive values of site attenuation, all of above quantities must be defined. Classical site attenuation (CSA) is usually calculated for resonant dipole antennas fed from 50 Ω transmission lines.

### 3.2.5 Normalised Site Attenuation

Another important concept concerned with site attenuation is that of normalised site attenuation (NSA). This was introduced by Smith [53] in order to remove the dependence of CSA upon the type of antennas used. NSA is obtained by dividing CSA by the product of the antenna factors, as shown by equation (3.21).

$$NSA = \frac{CSA}{AF_t AF_r} \tag{3.21}$$

$AF_t$ is the antenna factor of the transmitting antenna and $AF_r$ is the antenna factor of the receiving antenna. Antenna factors relate the terminal voltage of an antenna to its illuminating field and they are considered in more detail in chapter 4.

In order to use NSA to accomplish test site validation, measured values of NSA are calculated by dividing measured CSA by the calibrated antenna factors; these are then compared with theoretical NSA. Several letters were exchanged between Smith and Bennett in the IEEE transactions [54] concerned with the limitations of NSA, but it has become widely accepted and is the most commonly used method for test site validation. This is because of the simple method shown in §3.3 for calculating theoretical values of NSA.

Antenna factors are discussed in more detail in chapter 4 and it is shown that they are not necessarily constant because antennas over a test site may be closely coupled to each other and to the ground plane. NSA can only be a valid concept if the antenna factors of both antennas on the test site are constant and equal to their calibrated values.

## 3.3 Models of Site Attenuation between Infinitesimally Small Antennas

The earliest and simplest models of the site attenuation measurement use geometrical optical theory to calculate site attenuation from purely radiative coupling between infinitesimally small antennas. The assumption that the antennas are small means that these models do not fully account for the interactions that occur between closely spaced antennas. In particular, mutual coupling effects are neglected and this leads to inaccuracy at the lower frequencies of test site operation where the antenna separations over an open-area test site become of the order of a wavelength.

In spite of the above mentioned inaccuracies, all standards advocating site validation by measurement of site attenuation use models of this kind in order to derive its theoretical values. Bennett [55] has written a paper reviewing several of the early models of site attenuation and in it he proposes a model for site attenuation between infinitesimal antennas that is formulated in terms of the gains of the antennas. Alternatively, Smith [53] has formulated a model in terms of the antenna factors, which forms the basis of the current FCC standard for open-area test site validation [49].

A debate ensued in the IEEE transactions [54] over the relative merits and shortcomings of the two models, but no clear conclusion was reached as to which model was most accurate; both authors claimed surprisingly good results for their models, even at low frequencies. In this section, the two models will be compared and contrasted in order to find an optimum model for site attenuation based on purely radiative coupling between infinitesimal antennas.

### 3.3.1 Field from an Infinitesimal Antenna

Figure 3.6 shows a point source isotropically radiating a total power of $P_t$. The

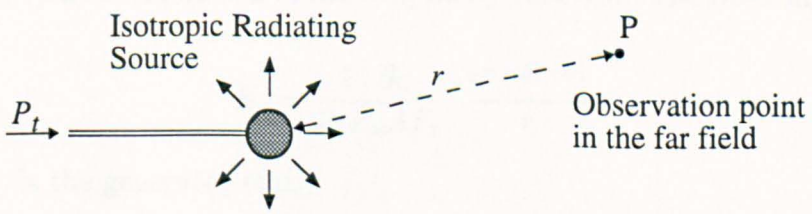


Figure 3.6: An isotropic radiating source.

power flux density at an observation point P, at a distance $r$ from the source and

in the far field, is given by

$$\frac{P_t}{4\pi r^2}$$

This power is radiated as an electric field of magnitude $E_r$ at the observation point therefore

$$\frac{P_t}{4\pi r^2} = \frac{E_r^2}{\eta} \tag{3.22}$$

where $\eta$ is the characteristic impedance of free space. If the transmitting antenna is not an isotropic radiator, but has a power gain of $G_t$ in the direction of the observation point equation (3.22) becomes

$$\frac{E_r^2}{\eta} = G_t\left(\frac{P_t}{4\pi r^2}\right) \tag{3.23}$$

and so the magnitude of the electric field at the observation point is given by

$$E_r = \sqrt{\frac{\eta P_t G_t}{4\pi r^2}} \tag{3.24}$$

If it is assumed that the wave is propagating in free space, the phase dependence of $E_r$ is of the form $e^{-j\beta r}$ therefore

$$E_r = \sqrt{\frac{\eta P_t G_t}{4\pi}} \cdot \frac{e^{-j(\beta r+\phi)}}{r} \tag{3.25}$$

where $\phi$ is an arbitrary phase angle. If $\eta$ is approximated to $120\pi$ and the $\phi$ is ignored, equation (3.25) takes the form of Bullington's expression [56] as quoted by both Smith and Bennett in their models.

$$E_r = \sqrt{30 P_t G_t}\frac{e^{-j\beta r}}{r} \tag{3.26}$$

It is proposed not to make this approximation throughout this analysis since it is unnecessarily imprecise and confuses the dimensions of the equations.

Smith derives an expression from equation (3.26) for $E_r$ in terms of the e.m.f. of the generator driving the transmitting antenna and the transmitting antenna's antenna factor by a consideration of the reciprocity theorem. The resulting expression is

$$E_r = \frac{V_S \beta \eta}{4\pi Z_S A F_t} \cdot \frac{e^{-j(\beta r+\phi)}}{r} \tag{3.27}$$

where $V_S$ is the generator emf,

$Z_S$ is the generator source impedance, equal to $50\,\Omega$, and

$AF_t$ is the antenna factor of the transmitting antenna.

This expression is in a slightly different form to the one derived by Smith because the numerical values of the constants have not been substituted into it.

### 3.3.2 Effect of a Ground Plane

The ground plane of an open-area test site is a reflecting surface and so introduces a second propagation path from the transmitting antenna to the receiving antenna as shown in figure 3.7. The path length of the direct wave is $r_1$ and the path length of the reflected wave is slightly longer and denoted by $r_2$. The total field at the

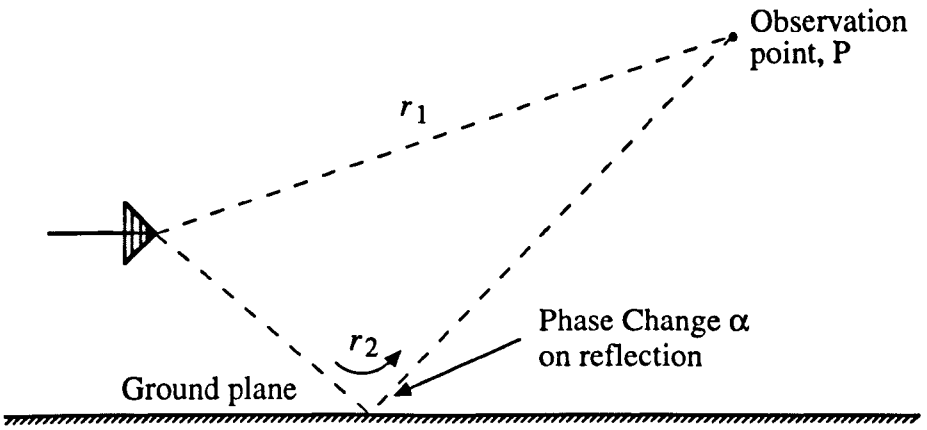


Figure 3.7: Direct and reflected waves on an open-area test site.

receiving antenna, situated at the observation point, is the sum of these two field components, i.e.

$$E_r = E_{r_1} + E_{r_2} \tag{3.28}$$

The reflected wave amplitude is multiplied by the reflection coefficient of the ground plane on reflection. For perfectly conducting ground planes the reflection coefficient has a magnitude of unity and a phase of $\alpha$, that is zero for vertically polarised waves and $\pi$ for horizontally polarised waves.

Bennett models the effect of the ground plane as a second gain term, $G_{t0}$ that is multiplied by $G_t$ in equation (3.25) in order to obtain the field at the receiving antenna with the ground plane present. His expression is formulated in terms of the two path lengths to the receiving antenna and the gain of the transmitting antenna in the direction of each wave.

$$G_{t0} = 1 + \frac{G_{t_2}}{G_{t_1}}\left(\frac{r_1}{r_2}\right)^2 + 2\sqrt{\frac{G_{t_2}}{G_{t_1}}}\left(\frac{r_1}{r_2}\right)\cos\left[\beta(r_1 - r_2) + \alpha\right] \tag{3.29}$$

$G_{t_1}$ is the transmitting antenna gain for the direct wave and $G_{t_2}$ is the gain in the direction of the reflected one. The deficiency of this approach lies in the specification of the receiving antenna's gain. Once the reflected wave has been combined with the direct wave into a gain term of this sort, it is not possible to account for the fact that the receiving antenna has a different gain for each component of the transmitted wave incident on it; Bennett ignores this fact.

Smith considers both waves and derives a formulation involving both waves considered separately for arbitrary ground plane reflection coefficients. This chapter is only concerned with perfectly reflecting ground planes and so it is proposed to modify his analysis accordingly. The geometry for Smith's analysis is shown in figure 3.8.

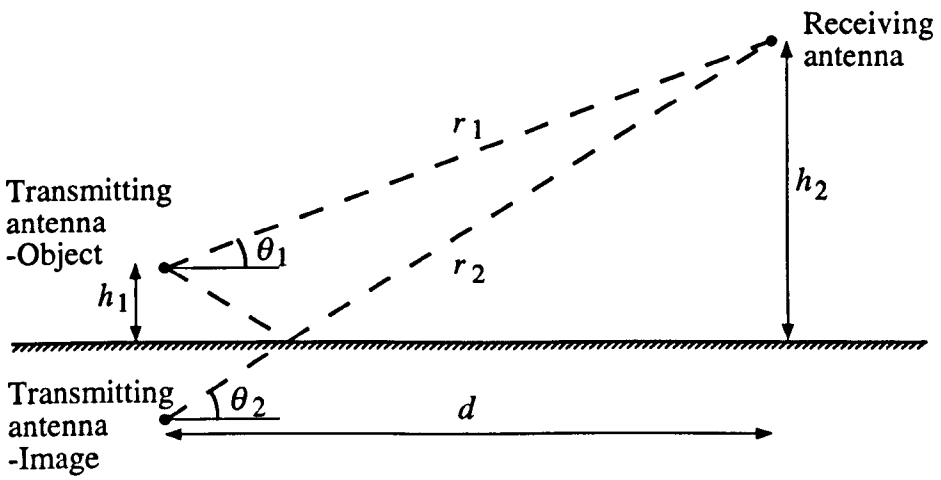


Figure 3.8: Propagation geometry for site attenuation between infinitesimal antennas.

### 3.3.3 Gains of EMC antennas

In order to formulate a model for site attenuation between infinitesimal antennas, it is necessary to make certain assumptions about their radiation patterns. Antennas are calibrated to give their gains in their direction of maximum radiation but in directions apart from this no information is given. In chapter 1 the radiated field components from real infinitesimal electric dipole antennas have been calculated and, if only the far field component of electric field is considered, the resulting expression is

$$E_\theta = \frac{j\eta\beta M_e}{4\pi} \sin\theta \frac{e^{-j\beta r}}{r} \tag{3.30}$$

where $M_e$ is the dipole moment of the electric dipole and is proportional to the

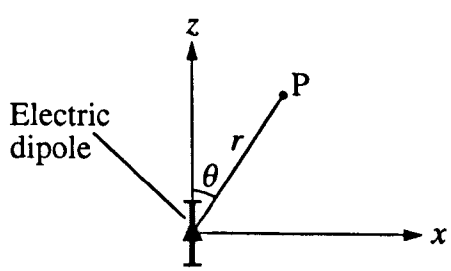


Figure 3.9: $\theta$-angle for antenna gains.

square root of its total radiated power.

Figure 3.9 shows the $\theta$-angle of equation (3.30) and it can be seen that the radiated field strength from the antenna is proportional to $\sin\theta$. The direction of maximum gain for the infinitesimal dipole antenna is therefore given by $\theta = 90°$. In order to formulate a site attenuation model, Smith assumes that the radiation patterns of EMC antennas have the same dependence on the $\theta$-angle.

### 3.3.4 Horizontally Polarised Site Attenuation

The gains of horizontally polarised dipole antennas are independent of the angle at which radiation is incident or scattered from them because of their cylindrical symmetry in the plane of propagation. The same will also be true for biconical antennas but the situation may be more complicated for log-periodic antennas. Smith states that because the gains of log-periodic antennas are small (typically around 6 dB), their antenna factors can also be considered independent of direction for this polarisation.

The field strength at the receiving antenna is the sum of the direct and reflected wave components travelling between the antennas, and so equation (3.27) gives

$$E_r = \frac{V_S \beta \eta}{4\pi A F_t Z_S}\left[\frac{e^{-j(\beta r_1+\phi)}}{r_1} - \frac{e^{-j(\beta r_2+\phi)}}{r_2}\right] \tag{3.31}$$

The negative sign applied to the reflected wave term accounts for the phase reversal on reflection that occurs for horizontally polarised waves. The field strength parallel to the receiving antenna is now given by the magnitude of equation (3.31).

$$E_H = \frac{V_S \beta \eta}{4\pi A F_t Z_S}\sqrt{\frac{r_1^2 + r_2^2 - 2r_1 r_2 \cos\beta(r_1 - r_2)}{r_1^2 r_2^2}} \tag{3.32}$$

The antenna factor of the receiving antenna is defined in terms of the magnitude of the voltage, $V_{L2}$, delivered to its 50 $\Omega$ load impedance, $Z_L$.

$$V_{L2} = \frac{E}{AF_r} \tag{3.33}$$

Substituting $E_H$ from equation (3.32) into (3.33) gives

$$V_{L2} = \frac{V_S \beta \eta}{4\pi A F_t A F_r Z_S}\sqrt{\frac{r_1^2 + r_2^2 - 2r_1 r_2 \cos\beta(r_1 - r_2)}{r_1^2 r_2^2}} \tag{3.34}$$

For the case where the generator is connected directly to the load impedance

$$V_{L1} = \frac{V_S}{2} \tag{3.35}$$

Classical site attenuation is defined by equation (3.20) in terms of the ratio of these two load voltages and so

$$CSA_H = 20\log_{10}\left|\frac{2\pi A F_t A F_r Z_S}{\beta\eta}\sqrt{\frac{r_1^2 r_2^2}{r_1^2 + r_2^2 - 2r_1 r_2 \cos\beta(r_1 - r_2)}}\right|_{min} \tag{3.36}$$

where the path lengths of the direct and reflected waves, $r_1$ and $r_2$, are given in terms of the site geometry shown in figure 3.8 as

$$r_1 = \sqrt{d^2 + (h_2 - h_1)^2} \tag{3.37}$$

$$r_2 = \sqrt{d^2 + (h_2 + h_1)^2} \tag{3.38}$$

Normalised attenuation is therefore simply equation (3.36) divided by the two antenna factors

$$NSA_H = 20\log_{10}\left|\frac{2\pi Z_S}{\beta\eta}\sqrt{\frac{r_1^2 r_2^2}{r_1^2 + r_2^2 - 2r_1 r_2\cos\beta(r_1 - r_2)}}\right|_{min} \tag{3.39}$$

### 3.3.5 Vertically Polarised Site Attenuation

The geometry for this case is also shown in figure 3.8 but the directional properties of vertically polarised antennas must be considered. These have been derived, in chapter 1, for real infinitesimal electric dipoles and Smith states that the antennas used for EMC measurements have a similar dependence on the $\theta$-angle shown in figure 3.8. The electric field parallel to a vertically polarised receiving antenna is therefore given from equation (3.27) as

$$E_r = \frac{V_S\beta\eta}{4\pi AF_t Z_S}\left[\frac{e^{-j\beta r_1+\phi}\cos^2\theta_1}{r_1} + \frac{e^{-j\beta r_2+\phi}\cos^2\theta_2}{r_2}\right] \tag{3.40}$$

The angles in equation (3.40) can be expressed in terms of the site geometry as

$$\cos\theta_1 = \frac{d}{r_1}$$

$$\cos\theta_2 = \frac{d}{r_2}$$

The magnitude of equation (3.40) is now the received field strength with these angles substituted.

$$E_V = \frac{V_S\beta\eta}{4\pi AF_t Z_S}d^2\sqrt{\frac{r_1^6 + r_2^6 + 2r_1^3 r_2^3\cos\beta(r_1 - r_2)}{r_1^6 r_2^6}} \tag{3.41}$$

A similar process to the derivation of equations (3.36) and (3.39) from equation (3.32) yields

$$CSA_V = 20\log_{10}\left|\frac{2\pi AF_t AF_r Z_S}{\beta\eta}\cdot\frac{1}{d^2}\sqrt{\frac{r_1^6 r_2^6}{r_1^6 + r_2^6 + 2r_1^3 r_2^3\cos\beta(r_1 - r_2)}}\right|_{min} \tag{3.42}$$

and

$$NSA_V = 20\log_{10}\left|\frac{2\pi Z_S}{\beta\eta}\cdot\frac{1}{d^2}\sqrt{\frac{r_1^6 r_2^6}{r_1^6 + r_2^6 + 2r_1^3 r_2^3\cos\beta(r_1 - r_2)}}\right|_{min} \tag{3.43}$$

### 3.3.6 Summary of Site Attenuation between Infinitesimal Antennas

In deriving the expressions (3.36) and (3.42) several assumptions have to be made about the antennas and the coupling between them. The assumptions have been indicated earlier in this section, but for clarity they are summarised here.

- The antennas are infinitesimally small.
- Only radiative coupling occurs between the antennas.
- The fields from the antennas have the same directional dependence as those from an infinitesimal electric dipole.
- The baluns of the antennas are lossless and provide conjugate matching between the antennas and their feeding transmission lines.

None of the above assumptions are particularly accurate, especially for frequencies below 100 MHz, but to see the limits to the accuracy of these models it is necessary to compare their results with more accurate models. This is performed in chapter 5.

## 3.4 Mutual Impedance Based Models of Site Attenuation

In models of this type the coupling between the antennas of the open-area test site is modelled as an impedance network so that the site attenuation can be formulated in terms of the self impedances of, and the mutual impedances between, the antennas by circuit analysis. All that then remains to be done is to calculate the mutual impedances and use the expressions of §3.2 to derive the insertion loss or attenuation of the site.

The earliest models for site attenuation in terms of mutual impedances were proposed by Kawana and Miyajima [57], [58] in the late 1970s. The first paper used an awkward hybrid application of impedance network theory and reflection coefficient theory to analyse the site attenuation measurement, and so unnecessarily assumed that the receiving antenna image could be neglected. The second paper defined site attenuation as the ratio of the power developed in the transmitting antenna to that developed in the load impedance. The resulting expression is accurate but represents none of the usual loss quantities defined in §3.2.

Smith [53] used a mutual impedance model in order to develop correction factors for normalised site attenuation, as derived from geometrical optics theory, but this approach is dangerously simplistic and ignores the different interactions that occur with closely spaced antennas other than cylindrical dipoles.

Several papers were presented by Maeda et al. during the mid 1980s [59], [60], [61] that calculated classical site attenuation from a rigorous mutual impedance based approach. They used the applied EMF method of chapter 2 to calculate self and mutual impedances between horizontally and vertically polarised resonant dipoles. In this way they calculated accurate values for classical site attenuation but did not address the problems associated with measuring it with real antennas.

Fitzgerrel [62] was the first author to consider the measurement of classical site attenuation with real antennas. He developed a specialised type of antenna with a balun that presented $50\,\Omega$ to the antenna drive-point and therefore allowed the measurement of classical site attenuation.

Recently Sugiura [63], [64] has concentrated on trying to relate classical site attenuation formulated in terms of mutual impedances to the formulations in terms of geometrical optics theory that are still used by EMC standards [49]. He has concluded that the concept of normalised site attenuation is only valid for antennas whose self impedances are significantly greater than the total mutual impedance component of their drive-point impedances.

In this section the derivation of site attenuation in terms of antenna self and mutual impedances will be presented and discussed in relation to the measurements performed in this thesis. This model was only used to predict site attenuation between resonant dipole antennas using the applied EMF method to calculate the impedances.

### 3.4.1 Four-Port Representation of an Open-Area Test Site

Image theory, as defined in chapter 1, is used to replace the ground plane by images of the transmitting and receiving antennas so that the ideal open-area test site can be considered as a coupling problem between four antennas in free space. Figure 3.10 shows this with horizontally polarised antennas. Antenna 1 is the transmitting antenna, antenna 2 is the receiving antenna and antennas 3 and 4 are the images in the ground plane of the transmitting and receiving antennas respectively.

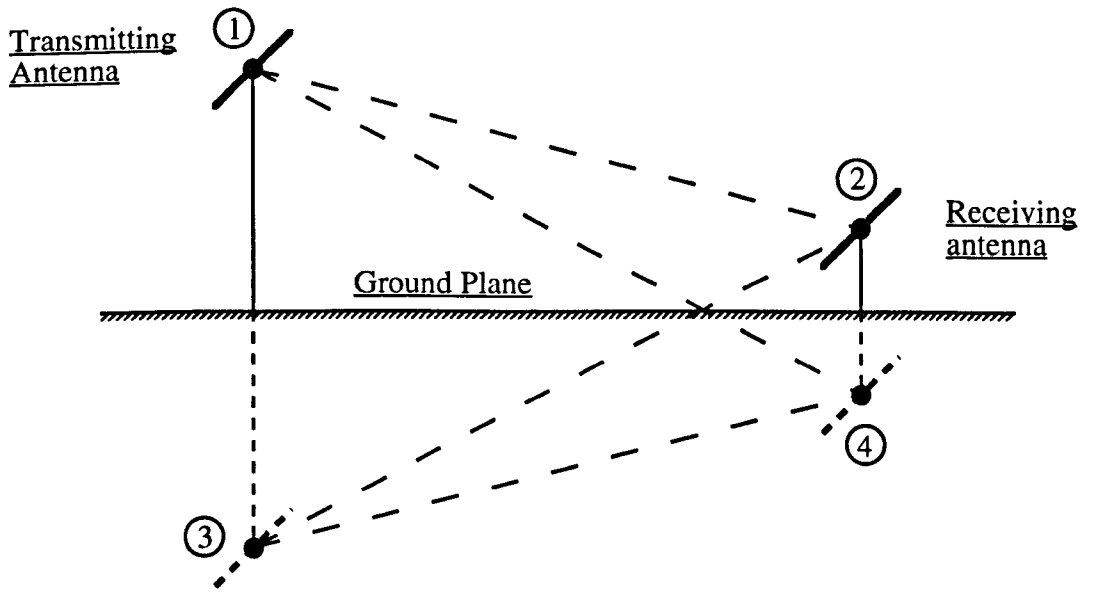


Figure 3.10: Arrangement of object and image antennas for mutual impedance formulation to describe coupled antennas over an open-area test site.

The coupling between the four antennas in figure 3.10 may be expressed in terms of their self and mutual impedances by the matrix equation (3.44).

$$\begin{bmatrix} V_1 \\ V_2 \\ V_3 \\ V_4 \end{bmatrix} = \begin{bmatrix} Z_{11} & Z_{12} & Z_{13} & Z_{14} \\ Z_{21} & Z_{22} & Z_{23} & Z_{24} \\ Z_{31} & Z_{32} & Z_{33} & Z_{34} \\ Z_{41} & Z_{42} & Z_{43} & Z_{44} \end{bmatrix} \cdot \begin{bmatrix} I_1 \\ I_2 \\ I_3 \\ I_4 \end{bmatrix} \tag{3.44}$$

This equation fully describes the site attenuation measurement and makes no assumptions about the size of the antennas or the coupling between them. Provided

the $Z$ terms that fill the matrix can be calculated accurately, it can be used to calculate parameters such as site attenuation and the drive-point impedances of the antennas.

### 3.4.2 Two-Port Representation of an Open-Area Test Site

Many of the terms in equation (3.44) are equivalent to each other and so it can be simplified considerably. The symmetry of the spatial arrangement of the antennas means that

$$Z_{12} = Z_{34}$$
$$Z_{14} = Z_{23}$$

Also, because the system is linear and contains only passive elements, it obeys the principle of reciprocity so that, in general,

$$Z_{mn} = Z_{nm}$$

This means that only the mutual impedances $Z_{12}$, $Z_{13}$, $Z_{14}$ and $Z_{24}$ need to be found, in addition to the two self impedances $Z_{11}$ and $Z_{22}$, in order to fill the matrix. Image theory gives the currents on the image antennas as those on the corresponding object antennas multiplied by the reflection coefficient of the ground plane, $\rho$.

$$I_3 = \rho I_1$$
$$I_4 = \rho I_2$$

This means that the matrix equation(3.44) reduces to the following two equations relating the terminal voltages and currents of antennas 1 and 2.

$$V_1 = I_1(Z_{11} + \rho_{11}Z_{13}) + I_2(Z_{12} + \rho_{12}Z_{14}) \quad (3.45)$$
$$V_2 = I_1(Z_{12} + \rho_{12}Z_{14}) + I_2(Z_{22} + \rho_{22}Z_{24}) \quad (3.46)$$

Under the conditions of a perfectly reflecting ground plane, all the $\rho$ parameters have a magnitude of unity and identical phases which depend upon the polarisation of the antennas. It is only necessary to consider generalised reflection coefficients, as shown, for partially reflecting ground planes and so equations (3.45) and (3.46) become

$$V_1 = I_1(Z_{11} + \rho Z_{13}) + I_2(Z_{12} + \rho Z_{14}) \quad (3.47)$$
$$V_2 = I_1(Z_{12} + \rho Z_{14}) + I_2(Z_{22} + \rho Z_{24}) \quad (3.48)$$

The reflection coefficient of a perfectly conducting ground plane depends upon the polarisation of the antennas above it, and is given by

$$\begin{aligned} \rho &= +1 \quad \text{in horizontal polarisation, and} \\ \rho &= -1 \quad \text{in vertical polarisation.} \end{aligned}$$

It is possible to replace the coefficients of the currents on the right hand side of equations (3.47) and (3.48) with $W$ terms defined as follows.

$$\begin{aligned} W_{11} &= Z_{11} + \rho Z_{13} \\ W_{12} &= Z_{12} + \rho Z_{14} \\ W_{21} &= Z_{21} + \rho Z_{23} \\ W_{22} &= Z_{22} + \rho Z_{24} \end{aligned} \tag{3.49}$$

The $W$ terms are the two-port impedance parameters that relate the terminal voltages of the object antennas to their terminal currents, and so equations (3.47) and (3.48) become

$$\begin{bmatrix} V_1 \\ V_2 \end{bmatrix} = \begin{bmatrix} W_{11} & W_{12} \\ W_{21} & W_{22} \end{bmatrix} \cdot \begin{bmatrix} I_1 \\ I_2 \end{bmatrix} \tag{3.50}$$

N.B. $W_{12} = W_{21}$ because of reciprocity.

### 3.4.3 Classical Site Attenuation

Site attenuation has already been given in terms of the two-port impedance parameters of the antennas over the open-area test site by equation (3.15) and so the expression for classical site attenuation, as defined in §3.2.4 is

$$CSA = 20 \log_{10} \left| \frac{(W_{11} + Z_0)(W_{22} + Z_0) - W_{21}^2}{2 Z_0 W_{21}} \right|_{min} \tag{3.51}$$

where $Z_0 = 50\,\Omega$.

This equation is exact and contains no assumptions about the antennas because it is only a model of the test site as an impedance network. The accuracy of theoretical classical site attenuation calculated in this way is determined only by the accuracy with which the self and mutual impedances can be calculated.

### 3.4.4 Calculation of Mutual Impedances

The self impedances of, and the mutual impedances between, antennas can be calculated or measured in a variety of ways depending upon the type of antenna that is used. Chapter 2 explains how the applied EMF method may be used to calculate self impedances and mutual impedances for cylindrical dipole antennas in a variety

of relative spatial configurations and this was the method used for the calculation of self and mutual impedances in this thesis. The more accurate moment method solutions were only used in scattering parameter based formulations of insertion loss and attenuation, although the two approaches are mathematically equivalent.

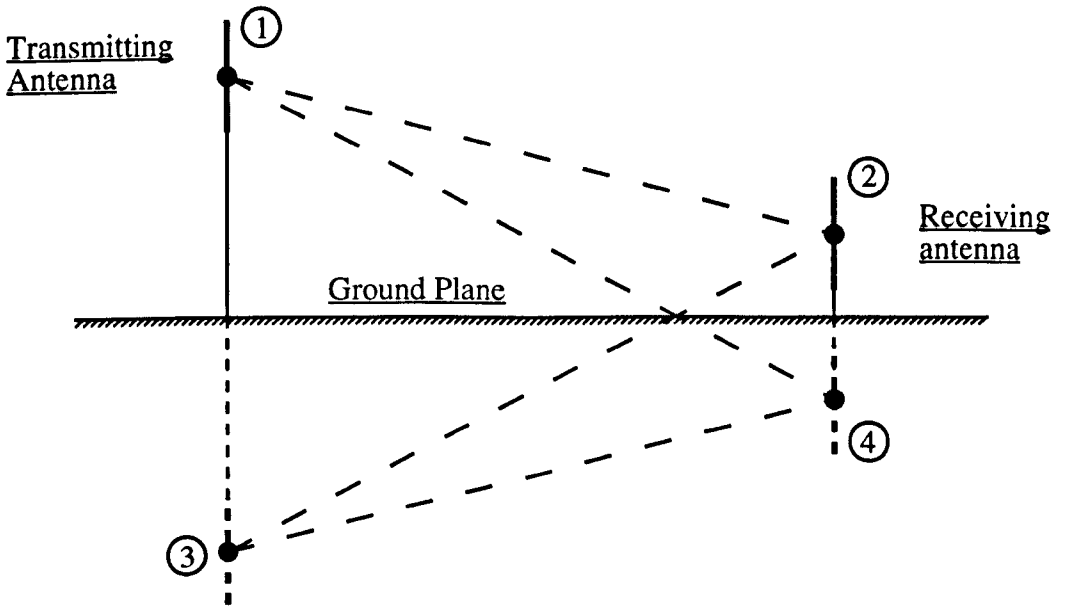


Figure 3.11: Arrangement of object and image antennas for vertically polarised excitation over an open-area test site.

There are several different ways in which coupled pairs of cylindrical dipole antennas may be aligned over the open-area test site according to their polarisation. Figure 3.10 shows that horizontally polarised antennas are all parallel and not offset but with vertically polarised antennas, as shown in figure 3.11, the situation is more complicated as some of the antenna pairs are collinear and others are in echelon (parallel but offset). The configurations for each of the mutual impedance parameters in equations (3.49) with both polarisations are shown in table 3.1.

| Component | Polarisation | |
|---|---|---|
| | Horizontal | Vertical |
| $Z_{11}$ | Self | Self |
| $Z_{12}$ | Parallel | Echelon |
| $Z_{13}$ | Parallel | Collinear |
| $Z_{14}$ | Parallel | Echelon |
| $Z_{22}$ | Self | Self |
| $Z_{24}$ | Parallel | Collinear |

Table 3.1: Orientation of antenna pairs for the calculation of the mutual impedances over an open-area test site.

## 3.5 Scattering Parameter based Formulations of Site Attenuation

In the previous section site attenuation models based upon a representation of the coupled antennas over an open-area test site as an impedance network have been described. The impedances of this network were calculated using the applied EMF method but they could also have been calculated more accurately from NEC simulations. An alternative formulation of the coupling between antennas over an ideal open-area test site is in terms of scattering parameters and this is the approach that was used with NEC. The approach has more convenient mathematics when dealing with cascaded two-port networks such as are considered in the site attenuation models of this section.

§3.5.1 shows how a NEC model of a pair of antennas above a perfectly reflecting ground plane was constructed. This was used to calculate the scattering parameters of the two-port network formed between the drive-points of the antennas and the mathematics involved are explained in §3.5.2.

The previous sections of this chapter have considered the coupling between antennas over the open-area test site in order to calculate classical site attenuation, but they have not addressed the problems associated with its measurement. These are outlined in §3.5.3 and it is shown that classical site attenuation cannot be measured with commercially available antennas calibrated in the usual way. This is because their baluns are included as an integral part of their structure and their connectors are not at the drive-point of the antennas.

When a measurement of site attenuation is performed with conventional EMC antennas, what is actually measured is the attenuation resulting from the cascade combination of the transmitting antenna balun, the antennas over the site and the receiving antenna balun. §3.5.4 shows how, if the scattering parameters of the two balun networks can be measured, predicted values of site attenuation may be calculated for comparison with measurement.

§3.5.5 shows how the resonant dipole antennas developed in chapter 4 may be used for test site validation. They have balanced feed networks and connectors at their drive-points so that site insertion loss may be measured with them. The effective source and load impedances presented to the antennas may be calculated and therefore predicted values of site insertion loss may be calculated for comparison with measurement.

### 3.5.1 NEC Model of Two Antennas over a Ground Plane

In chapter 2, accurate models have been developed of the resonant dipole and skeletal biconical antenna for simulation using the NEC computer code. Pairs of these antennas were simulated over a perfectly reflecting surface in order to model the coupling between real antennas over an ideal open-area test site.

Figure 3.12 shows a model of two horizontally polarised resonant dipole antennas on an ideal open-area test site. The transmitting antenna height is $h_1$, the receiving antenna height is $h_2$ and the site length is $d$. A perfectly reflecting surface in the xy-plane was used to represent an ideal ground plane.

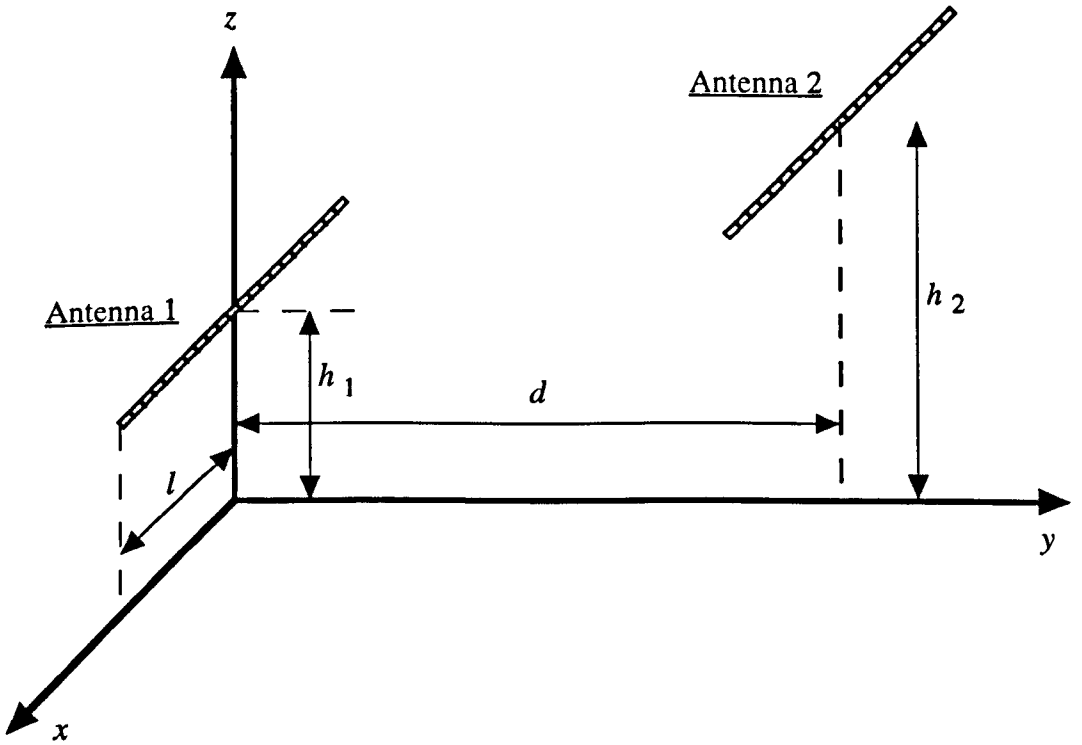


Figure 3.12: NEC model of two horizontally polarised cylindrical dipole antennas above a perfectly reflecting ground plane.

An equivalent two-port network can be used to describe the coupling between the antennas shown in figure 3.12 fully, and NEC was used to derive the scattering parameters of this network. The ports of the two-port network were defined as the drive-points of the antennas by loading the middle segment of each antenna with an impedance equal to the characteristic impedance of the port.

The transmitting antenna was excited with a voltage source and the results of the simulation then gave the drive-point impedance of the transmitting antenna and the current in the load of the receiving antenna.

### 3.5.2 Derivation of Scattering Parameters from the NEC Simulation

The NEC model of two coupled antennas over a ground plane, described in §3.5.1, has the equivalent circuit and $S$-parameter representation shown in figure 3.13. The excitation voltage of antenna 1 is $V_S$, and the source and load impedances are

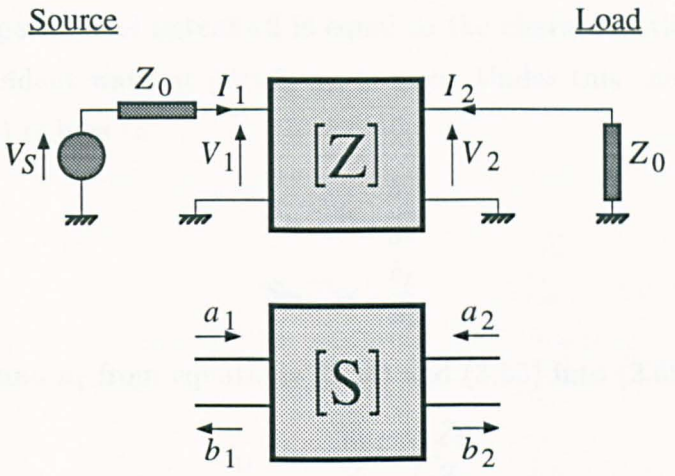


Figure 3.13: Equivalent circuit for NEC model of antennas over an open-field test site.

set to the characteristic impedance of the ports. Equations can then be deduced from figure 3.13 that relate the voltage to the current at each of the ports.

$$V_1 = V_S - I_1 Z_0 \tag{3.52}$$

$$V_2 = -I_2 Z_0 \tag{3.53}$$

Hayward [65] gives expressions for the incident and reflected waves at each of the ports in terms of the voltages and currents at that port.

$$a_1 = \frac{V_1 + I_1 Z_0}{2\sqrt{Z_0}} \tag{3.54}$$

$$b_1 = \frac{V_1 - I_1 Z_0}{2\sqrt{Z_0}} \tag{3.55}$$

$$a_2 = \frac{V_2 + I_2 Z_0}{2\sqrt{Z_0}} \tag{3.56}$$

$$b_2 = \frac{V_2 - I_2 Z_0}{2\sqrt{Z_0}} \tag{3.57}$$

The definition of the scattering parameters of a general two-port network is given in equation (3.6) and implies

$$S_{11} = \left.\frac{b_1}{a_1}\right|_{a_2=0} \tag{3.58}$$

$$S_{12} = \left.\frac{b_2}{a_1}\right|_{a_2=0} \tag{3.59}$$

$$S_{21} = \left.\frac{b_1}{a_2}\right|_{a_1=0} \tag{3.60}$$

$$S_{22} = \left.\frac{b_2}{a_2}\right|_{a_1=0} \tag{3.61}$$

The notation in equations (3.58) to (3.61) is such that equation (3.58) states that $S_{11}$ is the ratio of $b_1$ to $a_1$ under the condition that $a_2$ is equal to zero.

The load impedance of antenna 2 is equal to the characteristic impedance and therefore the incident wave at port 2, $a_2$, is zero. Under this condition equations (3.58) and (3.60) reduce to

$$S_{11} = \frac{b_1}{a_1} \tag{3.62}$$

$$S_{21} = \frac{b_2}{a_1} \tag{3.63}$$

Substituting $b_1$ and $a_1$ from equations (3.54) and (3.55) into (3.62) gives

$$\begin{aligned} S_{11} &= \frac{V_1 - I_1 Z_0}{V_1 + I_1 Z_0} \\ &= \frac{Z_{T1} - Z_0}{Z_{T1} + Z_0} \end{aligned} \tag{3.64}$$

where $Z_{T1}$ is the drive-point impedance of antenna 1 and is returned directly from the NEC simulation. Substitution of $b_2$ and $a_1$ from equations (3.54) and (3.57) into (3.63) gives

$$S_{21} = \frac{V_2 - I_2 Z_0}{V_1 + I_1 Z_0} \tag{3.65}$$

Equation (3.52) shows that the denominator of equation (3.65) is equal to the source voltage, $V_S$. Also, substituting $V_2$ from equation (3.53) gives

$$S_{21} = \frac{-2 I_2 Z_0}{V_S} \tag{3.66}$$

$V_S$ was set equal to $(1 + j0)$ Volts and the current $I_2$ was returned from the NEC simulation.

Calculation of $S_{12}$ and $S_{22}$ is not possible from the the same simulation as $S_{11}$ and $S_{21}$ because of the requirement that $a_1 = 0$ for equations (3.60) and (3.61) to reduce to

$$S_{22} = \frac{b_2}{a_2} \tag{3.67}$$

$$S_{12} = \frac{b_1}{a_2} \tag{3.68}$$

A second simulation was performed with the voltage source moved from the centre segment of antenna 1 to the centre segment of antenna 2. This simulation returned the drive-point impedance of antenna 2 and the load current of antenna 1. The

remaining scattering parameters were then derived, similarly to equations (3.64) and (3.66), as

$$S_{22} = \frac{Z_{T2} - Z_0}{Z_{T2} + Z_0} \tag{3.69}$$

$$S_{12} = \frac{-2I_1 Z_0}{V_S} \tag{3.70}$$

A check was made that $S_{12} = S_{21}$ to ensure that reciprocity was obeyed and the simulation had been run correctly.

By use of this method, employing two simulations using NEC, the scattering parameters of the two-port network formed between the drive-points of two antennas over a perfectly conducting ground plane were calculated. It was possible to calculate classical site attenuation directly from $S_{21}$ using equation (3.16) but this would not have been representative of the measured attenuation with real antennas for the reasons explained in the next subsection.

### 3.5.3 Problems with the Measurement of Site Attenuation

The structure of commercially available EMC antennas is such that their coaxial connectors are not at the drive-points of the antennas. There is a two-port network between the connector and the drive-point that consists of a length of transmission line and a balun. Because of this, when a measurement of site attenuation is made with this type of antenna, what is actually measured is the attenuation due to the three cascaded two-port networks shown in figure 3.14.

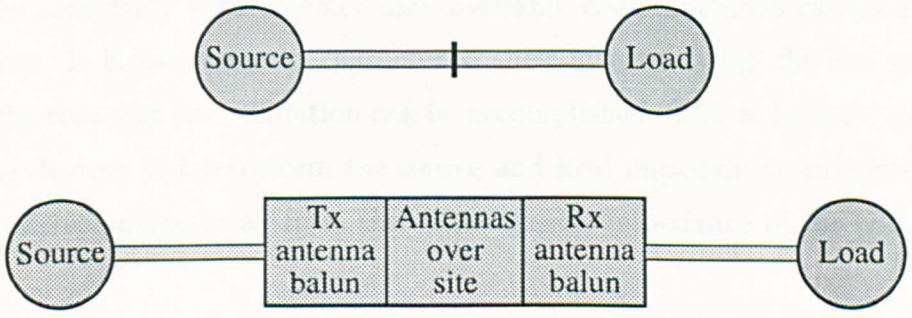


Figure 3.14: Site attenuation measurement with commercially available EMC antennas.

Classical site attenuation cannot be measured directly because the balun networks are integral parts of each antenna. This would not be a problem if the baluns could be made lossless and to behave as 1 : 1 impedance transformers over the entire operating frequency range of each antenna, but this would be very difficult to achieve.

Manufacturers of commercially available EMC antennas do not supply the full scattering parameters of the baluns of their antennas, but simply quote a vague loss value in dB. The source and load impedances presented to the balun while this parameter was measured are not stated and so, when the variable impedance of the antenna is presented to the balun, it is naive to assume a constant loss for the balun. This means that it is not possible to carry out a rigorous comparison between measured and theoretical attenuations with antennas calibrated in this way.

If the scattering parameters of the balun of each antenna can be measured, an alternative approach to test site validation that does not make any assumptions about balun behaviour becomes possible. This is to calculate the theoretical attenuation due to the three cascaded two-port networks in figure 3.14 with the measured attenuation with the real antennas. Chapter 4 explains how the scattering parameters of the baluns of the Schwarzbeck BBA9106 biconical antennas were measured in order to facilitate test site validation in this way.

In order to calculate predicted site attenuation between pairs of real antennas, it is necessary to combine the three scattering parameter matrices representing the balun of the transmitting antenna, the antennas over the site and the balun of the receiving antenna, into a single matrix, S′. Appendix E describes how this is accomplished and equation (3.16) then gives predicted attenuation from $S'_{21}$.

### 3.5.4 Use of Insertion Loss for Site Validation

The previous subsection has explained that it is not possible to validate open-area test sites accurately with commercially available EMC antennas calibrated in the usual way. It is necessary to characterise their integral balun devices separately before rigorous test site validation can be accomplished. This is because the baluns are lossy devices and transform the source and load impedances, presented at the antenna drive-points, away from the characteristic impedance of the transmission lines.

If an antenna could be designed with a balanced feed arrangement and connectors at its drive-point, it would be possible to measure the effective source or load impedance presented at its drive-point. It would then be possible to calculate predicted values for insertion loss between a pair of the antennas and these could be compared with measured insertion loss values in order to accomplish test site validation.

A specialised type of resonant dipole antenna was developed for the above

application and it is described in chapter 4. Figure 3.15 shows the feed network for the antenna and how a pair of antennas were used to perform an insertion loss measurement. The connecting network between each antenna and its source

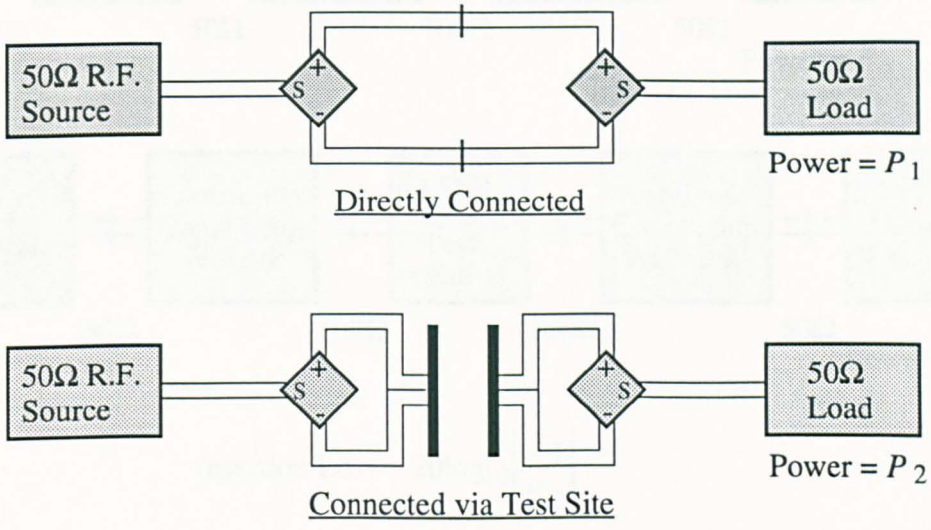


Figure 3.15: Measurement of site insertion loss.

or load was a three port network containing a Minicircuits ZFSCJ-2-1 180° phase splitting device used instead of a balun. The two antiphase ports of this device were connected to the antenna drive-point via a balanced screened twin coaxial transmission line.

The connecting network between each antenna and its generator or load was a three-port network, and its scattering parameters were measured with an HP8753A network analyser. The two antiphase ports were then modelled as a single combined port and the three-port scattering parameters were transformed to an equivalent two-port representation. The insertion loss measurement with the antennas could then be regarded as the cascade of two-port networks shown in figure 3.16. The measurements and transformations associated with obtaining the two-port scattering parameters of each connecting network are described in chapter 4.

The characteristic impedance of the twin-port of each connecting network was twice that of a single port, i.e. it was equal to 100 Ω in the 50 Ω coaxial system. The scattering parameters of the resonant dipoles over the test site therefore also had to be calculated normalised to 100 Ω.

The effective source reflection coefficient presented at the drive-point of the transmitting antenna is related to the actual source reflection coefficient and the scattering parameters of the coupling network, $\mathbf{T}$ by

$$\Gamma'_S = T_{11} + \frac{T_{12}T_{21}\Gamma_S}{1 - T_{22}\Gamma_S} \tag{3.71}$$

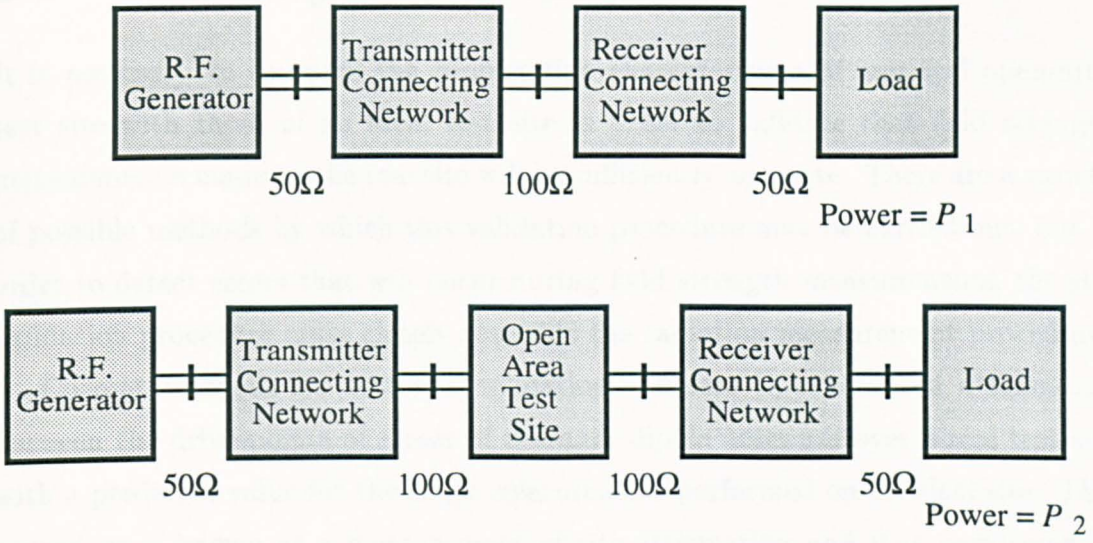


$$\text{Insertion Loss} = 20\log_{10}\left|\frac{P_1}{P_2}\right|$$

Figure 3.16: Two-port networks associated with site insertion loss measurement showing the characteristic impedance of each port.

where port 1 of the connecting network is connected to the antenna. A similar expression was used to calculate the effective load reflection coefficient presented at the receiving antenna and then equation 3.10 was used to calculate the predicted site insertion loss.

## 3.6 Summary and Conclusions

It is necessary to compare the propagation characteristics of any real open-area test site with those of an ideal test site in order to validate that field strength measurements made on the real site will be sufficiently accurate. There are a variety of possible methods by which this validation procedure may be carried out, but in order to detect errors that will occur during field strength measurements, the site validation procedure must closely resemble the radiation measurement procedure.

Current methods for test site validation compare the measured attenuation between the drive-points of a pair of resonant dipole antennas over a real test site with a predicted value for the same measurement performed on an ideal site. This procedure is known as a measurement of site attenuation and it is performed at frequency intervals that are sufficiently close together that none of the features of the response of a site are overlooked.

A measurement of site attenuation with a pair of resonant dipole antennas is not entirely representative of the field strength measurement procedure on an open-area test site. This is because typical items of equipment under test are electrically small up to 100–200 MHz and broadband antennas tend to be used to measure field strength. The use of resonant dipoles for test site validation will tend to exaggerate site propagation non-idealities and it would therefore be better to use an electrically small standard radiating source and a broadband receiving antenna. Resonant dipole antennas are also undesirable for test site validation because they have to be mechanically tuned to every excitation frequency.

In order to use measurements of site attenuation to validate a given test site it is necessary to obtain predicted values of site attenuation measured with the same antennas over an ideal test site. The predicted values of site attenuation must be considerably more accurate than the tolerance that a test site is to be validated to, e.g. if it is required to show that the propagation characteristics of a given site are within 1 dB of ideal, it is necessary to obtain measured values of site attenuation within 0.5 dB of predicted values, if the predicted values are only accurate to 0.5 dB.

The models that are used by EMC standards to derive predicted site attenuation between resonant dipoles are unnecessarily simplistic and likely to be prone to error. They neglect to consider the finite size of real antennas and assume that purely radiative coupling occurs between them over an open-area test site. These assumptions are made in order to facilitate the calculation of normalised site attenuation and the use of antennas that have been calibrated to obtain their antenna

factors.

The use of normalised site attenuation is unnecessary for test site validation and only serves to introduce errors into predicted site attenuations. It is possible to use the applied EMF method to calculate predicted site attenuation between resonant dipoles, or NEC for more general wire antennas. Both of these approaches account for the finite size of the real antennas and also the mutual coupling effects that occur between closely spaced antennas.

It is difficult to obtain predicted values of site attenuation measured with conventional EMC antennas because there is usually an uncalibrated two-port network between the connector of each real antenna and its drive-point. This network contains the balun of the antenna and a length of transmission line. In order to calculate predicted values of site attenuation with these antennas it is necessary to obtain the two-port network parameters of the connecting networks inside each antenna.

The NEC computer code may be used to calculate the scattering parameters of the two-port network formed between the drive-points of two skeletal biconical antennas over an ideal open-area test site. The scattering matrices of the baluns of these two antennas can then be cascaded with the site matrix in order to calculate predicted site attenuation. As there is no need to tune skeletal biconical antennas, swept frequency measurements of site attenuation can then be made to give a much greater degree of resolution than is practical with resonant dipole antennas.

# Chapter 4

# Construction and Calibration of Standard Antennas

Antennas designed for EMC applications are usually calibrated by measuring their performance parameters directly. This approach is prone to error and requires very expensive test facilities, but an alternative approach to antenna calibration is based upon computer simulation. In this chapter the design and calibration of real antenna structures, based upon the resonant dipole and the skeletal biconical antenna, is described. The approach builds upon the theoretical work of chapter 2.

A standard antenna is an antenna that has been characterised sufficiently accurately that it may be used as a primary standard that other antennas and test facilities may be calibrated against. The computer models used in this chapter are intended to be sufficiently accurate for both the resonant dipole antenna and the skeletal biconical antenna to be used as standard antennas.

Antenna factor is defined in §4.1, and the techniques that may be used to obtain it are also described, before theoretical antenna factors are derived for the resonant dipole and skeletal biconical antennas in §4.2. It is shown in §4.3 that the concept of antenna factor has to be used carefully when antennas are closely coupled to the ground plane of an open-area test site. The interactions between antennas and ground planes are analysed in detail in order to derive correction factors and uncertainty limits for their calibrations.

The ground plane reflection coefficient measurements of chapter 6 required a resonant dipole antenna whose drive-point impedance could be both measured and predicted accurately. Commercially available antennas were found to be unsuitable for this application because their structures incorporated an integral balun that formed an uncalibrated two-port network between their radiating structure and coaxial connector. In §4.4 a specialised resonant dipole antenna is described that was designed and built for this application. §4.6 shows how the parasitic effects associated with the drive-point of this real antenna were measured and taken

account of in simulations.

§4.5 describes the techniques that were used for measurement of the impedance of antennas. The unusual feed arrangement of the resonant dipole antenna necessitated a novel calibration procedure for the network analyser, and measurement of the impedance of the skeletal biconical antenna required the construction of specialised calibration tools.

A technique is described in §4.7 that was used to measure the scattering parameters of the balun network of the biconical antenna. These were combined with a NEC model of the antenna in order to calibrate it for use as a standard antenna. The predicted antenna factors from this model are compared with measured antenna factors in order to deduce their accuracy.

This chapter is summarised and conclusions are drawn from it in §4.8. Both of the antennas calibrated are used in chapter 5 for measurements of site attenuation. The results are used there to deduce confidence limits for the predicted antenna factors and the performance of the open-area test site at the University of York.

## 4.1 Calibration of Antennas for EMC Applications

The calibration of a receiving antenna for EMC applications involves the determination of the relationship between its illuminating field and the power delivered to its load impedance. This relationship is often described by an antenna factor, and the most general definition of antenna factor is given in the IEEE standard dictionary of terms [66] as:

> That factor which, when properly applied to the voltage at the input terminals of the measuring instrument, yields the electric field strength in volts per meter and the magnetic field strength in amperes per meter.

The above definition is not very useful because it does not depend only upon the measuring antenna; it also depends on the connecting cables and the calibration of the receiver. A more useful definition is given by Paul [67]:

> The ratio of the incident field at the surface of the measurement antenna to the received voltage at the antenna terminals.

For antenna factor to be defined rigorously it is necessary to specify the load impedance applied to the antenna which, for EMC applications, is usually 50 Ω. In order to specify the illuminating field, it is also necessary for the antenna to be uniformly illuminated and this is discussed in §4.1.1. Figure 4.1 illustrates the definition of antenna factor.

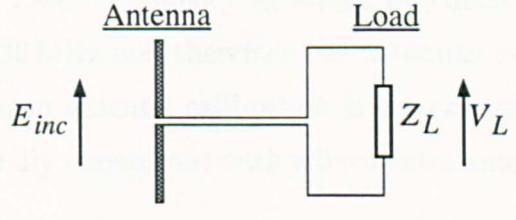


Figure 4.1: Definition of the antenna factor of a receiving antenna.

If an antenna is illuminated by an electric field strength of magnitude $E_{inc}$, the voltage delivered to its load impedance is $V_L$. The antenna factor is then given in decibels by equation (4.1).

$$AF_r = 20 \log_{10} \left| \frac{E_{inc}}{V_L} \right| \tag{4.1}$$

In a 50 Ω transmission line system, the load voltage, $V_L$, is developed across a 50 Ω impedance.

There are essentially three methods by which antenna factors may be measured and these are described in §4.1.2 to §4.1.4. All of these methods involve measurements of the coupled power between two antennas above the ground plane of an open-area test site and so are closely related to the site attenuation measurements of chapter 3. The major difference between antenna calibration and site attenuation is that it is possible to derive expressions for the attenuation between antennas that are closely spaced but calibration requires the antennas to be sufficiently far apart for the receiving antenna to be uniformly illuminated. The conditions for this uniform illumination are given in §4.1.1.

### 4.1.1 Conditions for Uniform Illumination

A uniformly illuminated antenna has the same parallel component of electric field over its entire length; a plane electromagnetic wave is required to achieve this. No real source can radiate a plane-wave, but provided that the separation between the source and the receiving antenna is significantly greater than either of their physical sizes, a good approximation to plane-wave illumination will result. This is the Rayleigh far field criterion, that the antenna separation, $r$, must satisfy

$$r > \frac{2D^2}{\lambda} \tag{4.2}$$

where $D$ is the maximum physical dimension of the transmitting antenna and $\lambda$ is the wavelength.

Typical antennas used over open-area test sites have lengths that are less than $\lambda/2$, and so the Rayleigh far field criterion implies that they should be separated by at least $\lambda/2$. The lowest frequency at which antennas are calibrated over an open-area test site is 30 MHz and therefore the antennas must be separated by at least 5 m. For this reason antenna calibration is not carried out on 3 m open-area test sites, and it is usually carried out with a horizontal antenna separation of 10 m or 30 m.

Antenna calibration is carried out over a reflecting surface that forms the ground plane of an open-area test site and, from the theory explained in chapter 1, there will be certain antenna heights at which the direct and reflected waves cancel out to produce minima. Any calibration carried out in the vicinity of these minima will be subject to large errors and so the receiving antenna height must be scanned to eliminate the nulls in the same way as it is when performing a radiation measurement. This means that the antenna factors may be measured with radiation paths that are significantly off axis and, for antennas that have narrow main beams, this will cause inaccuracy. Use of a 30 m test site ensures that the geometric ray paths

between the antennas are not more than 15° off axis but they may be as much as 27° off axis on a 10 m site.

For EMC measurements, antenna factors are assumed to be constant, irrespective of the height of an antenna above a ground plane. In §4.2 it will be shown that this assumption is not always true for the antennas used on an open-area test site. The remainder of this section will briefly outline some methods that are used for the measurement of antenna factors.

### 4.1.2 Standard Field Method

The first method that can be used to determine the antenna factors of a receiving antenna involves using a calibrated transmitting antenna to establish a known field strength at an observation point, as shown in figure 4.2. Once the field has been

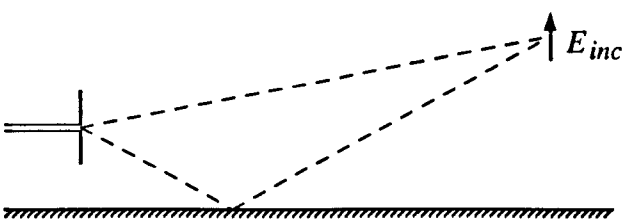


Figure 4.2: Standard field method for antenna calibration.

calculated at the observation point the receiving antenna is placed there and the voltage delivered from it to a matched load is measured. Then equation (4.1) can be used to calculate the antenna factor.

This experiment can also form the basis of a computer simulation to derive theoretical antenna factors for certain types of antennas. It will be used to determine predicted antenna factors for the cylindrical dipole antenna and the skeletal biconical antenna in §4.2.

### 4.1.3 Standard Antenna Method

This method of antenna calibration requires an antenna whose antenna factor is already known, in addition to an uncalibrated transmitting antenna and the antenna that is to be calibrated. The method is shown in figure 4.3.

The transmitting antenna is supplied with the same excitation voltage in both of the cases shown in figure 4.3 so that each receiving antenna is illuminated by the same field strength. Under this condition the antenna factor of the uncalibrated antenna, $AF_{uncal}$, is defined in terms of the measured load voltages and the calibrated antenna factor, $AF_{cal}$, as

$$AF_{uncal} = AF_{cal} + V_{L1} - V_{L2} \tag{4.3}$$

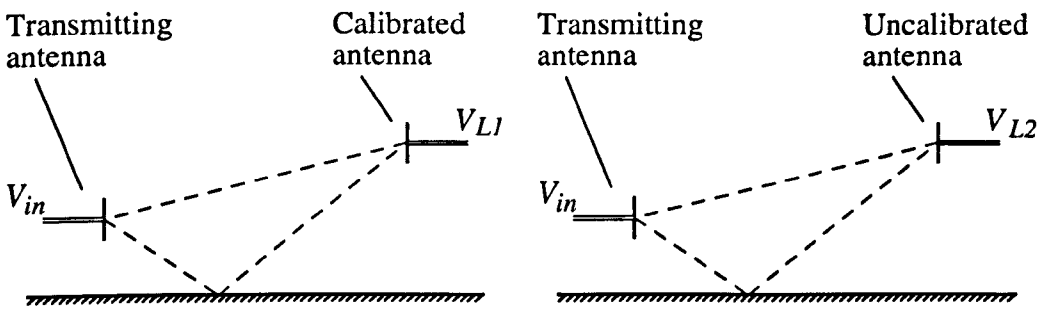


Figure 4.3: Standard antenna method for antenna calibration.

where all of the quantities are in dB.

### 4.1.4 Standard Site Method

The standard site, or three antenna, method for antenna calibration [68] uses theoretical values of normalised site attenuation and measured values of classical site attenuation, as defined in chapter 3, to calculate the antenna factors of three uncalibrated antennas simultaneously.

Normalised site attenuation is equal to the classical site attenuation between two antennas divided by the two antenna factors, i.e.

$$CSA = AF_t + AF_r + NSA \tag{4.4}$$

where all of the quantities are in decibels. A measurement of classical site attenuation is performed between each of the three possible pairings of antennas to give

$$CSA_1 = AF_2 + AF_3 + NSA \Big|_{\text{antennas 2 and 3}} \tag{4.5}$$

$$CSA_2 = AF_1 + AF_3 + NSA \Big|_{\text{antennas 1 and 3}} \tag{4.6}$$

$$CSA_3 = AF_1 + AF_2 + NSA \Big|_{\text{antennas 1 and 2}} \tag{4.7}$$

Equations (4.5) to (4.7) can be solved to give expressions for each antenna factor in terms of the three measured classical site attenuations and normalised site attenuation.

$$AF_1 = \frac{-NSA - CSA_1 + CSA_2 + CSA_3}{2} \tag{4.8}$$

$$AF_2 = \frac{-NSA + CSA_1 - CSA_2 + CSA_3}{2} \tag{4.9}$$

$$AF_3 = \frac{-NSA + CSA_1 + CSA_2 - CSA_3}{2} \tag{4.10}$$

Antenna factors must be known accurately, and so this method requires a high quality of open-area test site that has propagation characteristics close to those

of an ideal test site. The validation procedure for a test site used for antenna calibration by this method has to be very stringent and errors between theoretical and measured classical site attenuations should be less than 1 dB [69].

This calibration method also relies on the validity of the concept of normalised site attenuation and the constancy of antenna factor. Later in this chapter it will be shown that antenna factor is not always a constant, but can vary if an antenna is closely coupled to its surrounding environment. The implications of this are that under certain conditions antenna factor has to be specified as a function of height and the three antenna calibration method does not account for this.

## 4.2 Theoretical Antenna Factors

Antenna factors are usually obtained by one of the measurement procedures described in §4.1, but they may also be derived from a theoretical basis for certain types of antenna. By developing expressions for the antenna factor of a general receiving antenna, the relationship between it and antenna parameters such as gain and impedance can be studied.

### 4.2.1 A General Receiving Antenna

Consider a general receiving antenna illuminated by a plane electromagnetic wave, as shown in figure 4.4. The parallel component of electric field is $E_{inc}$, and the antenna delivers a voltage, $V_L$, to its load impedance. The antenna may be modelled

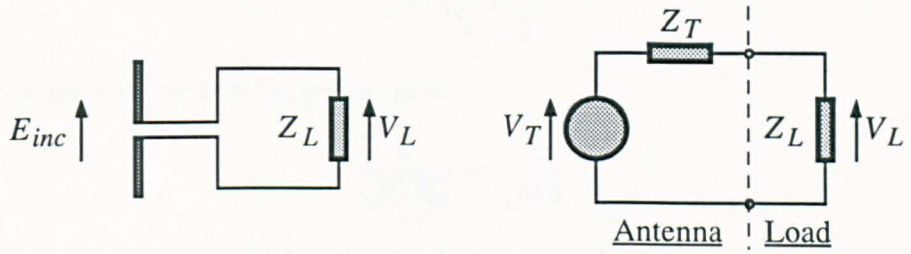


Figure 4.4: A general receiving antenna illuminated by a plane electromagnetic wave and its equivalent Thèvenin voltage source.

as an equivalent Thèvenin voltage source having an excitation voltage of $V_T$, equal to the EMF developed in the antenna, and an impedance $Z_T$, equal to the drive-point impedance of the antenna.

The maximum power available from a Thèvenin voltage source is the power that would be dissipated in a load impedance conjugately matched to the source impedance, and is therefore given by

$$\begin{aligned} P_{max} &= \frac{|V_T|^2}{4\Re\{Z_T^*\}} \\ &= \frac{|V_T|^2}{4R_T} \end{aligned} \tag{4.11}$$

where $R_T$ is the real part of the conjugate source impedance, $Z_T^*$.

The power $P_{max}$ is equal to the power flux density illuminating the antenna multiplied by the size of its maximum effective aperture. The maximum effective aperture, $A_{em}$, is related to the antenna gain, $G$, by equation (4.12),

$$A_{em} = \frac{G\lambda^2}{4\pi} \tag{4.12}$$

therefore

$$P_{max} = \frac{|E_{inc}|^2}{\eta} \cdot \frac{G\lambda^2}{4\pi} \tag{4.13}$$

By equating (4.11) and (4.13) an expression for the EMF developed at the drive-point of the antenna can be derived in terms of the illuminating field.

$$|V_T| = |E_{inc}|\lambda\sqrt{\frac{GR_T}{\pi\eta}} \tag{4.14}$$

The ratio of the EMF induced in the antenna to the illuminating field has the dimension of length and is often referred to as the effective length or effective height of the antenna, $l_e$. It will be referred to as effective length in this thesis, since height is used to describe the position of an antenna in relation to a ground plane. Equation (4.14) gives effective length as

$$l_e = \lambda\sqrt{\frac{GR_T}{\pi\eta}} \tag{4.15}$$

This equation can be rearranged to give

$$\frac{l_e}{\sqrt{GR_T}} = \frac{\lambda}{\sqrt{\pi\eta}} \tag{4.16}$$

All of the terms on the right hand side of equation (4.16) are constant and therefore it follows that the ratio of $l_e/\sqrt{GR_T}$ is constant for any antenna at a given frequency. This was first observed by Bennett [70] and has profound implications for antenna calibration as a function of height, as investigated in §4.3.

The EMF developed in a receiving antenna is applied across its drive-point impedance in series with its load impedance. The voltage across the load impedance is therefore given by

$$V_L = \frac{V_T Z_L}{Z_T + Z_L} \tag{4.17}$$

Taking the magnitude of each side of equation (4.17) and substituting $|V_T|$ from (4.14) yields an expression for the voltage developed across the load impedance in terms of the incident field.

$$|V_L| = |E_{inc}|\lambda\sqrt{\frac{GR_T}{\pi\eta}}\left|\frac{Z_L}{Z_T + Z_L}\right| \tag{4.18}$$

Equation (4.1) defines antenna factor as the ratio of incident electric field to load voltage, therefore equation (4.18) implies

$$AF = \frac{1}{\lambda}\sqrt{\frac{\eta\pi}{GR_T}}\left|1 + \frac{Z_T}{Z_L}\right| \tag{4.19}$$

or alternatively,

$$AF = \frac{1}{l_e}\left|1 + \frac{Z_T}{Z_L}\right| \tag{4.20}$$

Equation (4.19) shows that the antenna factor of a receiving antenna is inversely proportional to the wavelength and the square root of the antenna gain. There is also a complicated dependence on the drive-point impedance of the antenna and the full significance of this will be discussed in §4.3.

It should be noted that in the above analysis, the ohmic resistance of the conductors of an antenna has been assumed to be negligible in comparison to the radiation resistance. This assumption is valid because typical antennas used for EMC applications all have appreciable electrical size.

### 4.2.2 The Resonant Dipole Antenna

Equation 4.19 gives antenna factor in terms of the wavelength of the illuminating field and the gain and impedance of a general antenna. If these parameters are known, the antenna factor of any specific antenna may be found. The gain and impedance of the resonant dipole antenna can be calculated by a variety of theoretical approaches described in chapter 2 and theoretical values for its antenna factor may then be found.

If a resonant dipole antenna is assumed to be thin and exactly half of a wavelength long, its current distribution can be assumed to be a sinusoidally distributed filament along the axis of the antenna. Under these conditions its gain and impedance have the following values [71].

$$\begin{aligned} G &= 1.64 \\ Z_T &= 73\,\Omega \end{aligned}$$

The impedance is purely resistive because the antenna is at resonance. If these values are substituted into equation (4.17) and the wavelength is expressed as $300/f_M$, where $f_M$ is the frequency in MHz, the antenna factor of the resonant dipole antenna driving into a $50\,\Omega$ load is

$$AF_r = \left(20\log_{10}(f_M) - 31.77\right)\ \text{dB} \tag{4.21}$$

Equation (4.21) is a simple formula for the antenna factor of the resonant dipole antenna, but it only gives an approximate value, based upon the assumption of a sinusoidal current distribution. In order to determine the antenna factor more accurately it is necessary to find a better representation for the current distribution.

In chapter 2 it has been shown that the NEC computer code can be used to simulate the resonant dipole antenna accurately. The NEC model was used to obtain the resonant lengths for cylindrical dipole antennas and then their corresponding

antenna factors. Table 4.1 shows the predicted resonant lengths for cylindrical dipole antennas having radii of 1, 2, 5 and 10 mm respectively, at frequencies in the range of 30 MHz to 1 GHz. The table shows the result, also obtained from the

| Frequency | Antenna Radius / mm | | | |
|---|---|---|---|---|
| MHz | 1 | 2 | 5 | 10 |
| 30 | 2416.635 | 2406.919 | 2389.464 | 2370.813 |
| 50 | 1445.825 | 1438.797 | 1425.785 | 1411.623 |
| 80 | 900.792 | 895.486 | 885.427 | 874.551 |
| 120 | 598.586 | 594.369 | 586.295 | 577.899 |
| 180 | 397.519 | 394.139 | 387.733 | 381.659 |
| 250 | 285.157 | 282.325 | 277.131 | 272.975 |
| 350 | 202.782 | 200.431 | 196.408 | |
| 500 | 141.162 | 139.266 | 136.487 | |
| 700 | 100.216 | 98.714 | | |
| 1000 | 69.633 | 68.539 | | |

Table 4.1: Resonant lengths for various radii of cylindrical dipole antennas.

applied EMF method in chapter 2, that the resonant lengths of antennas become shorter as their radii increase. Resonant lengths are not given for the antennas in the lower right-hand corner of table 4.1 because the lengths of these antennas are not sufficiently greater than their radii for the antennas to be considered thin.

NEC was used to simulate each of the resonant dipole antennas illuminated by a $1\,\mathrm{Vm}^{-1}$ plane electromagnetic wave and loaded with $50\,\Omega$. The resulting voltages across the load impedance were substituted into equation (4.1) to find the antenna factor. Table 4.2 shows a comparison of the predicted antenna factors from NEC with those of the simple formula of equation (4.21).

| Frequency | Antenna Radius / mm | | | | Simple |
|---|---|---|---|---|---|
| MHz | 1 | 2 | 5 | 10 | formula |
| 30 | −2.233 | −2.232 | −2.231 | −2.231 | −2.228 |
| 50 | 2.205 | 2.205 | 2.206 | 2.208 | 2.209 |
| 80 | 6.287 | 6.288 | 6.289 | 6.292 | 6.292 |
| 120 | 9.809 | 9.810 | 9.813 | 9.817 | 9.814 |
| 180 | 13.332 | 13.333 | 13.337 | 13.344 | 13.335 |
| 250 | 16.186 | 16.187 | 16.193 | 16.204 | 16.189 |
| 350 | 19.109 | 19.111 | 19.119 | | 19.111 |
| 500 | 22.208 | 22.211 | 22.224 | | 22.209 |
| 700 | 25.132 | 25.137 | | | 25.132 |
| 1000 | 28.232 | 28.240 | | | 28.230 |

Table 4.2: Antenna factors of various radii of resonant dipole antennas.

Table 4.2 shows that the antenna factor of the resonant dipole antenna does not vary significantly as a function of the antenna radius. It also shows that there

is no need for a full method of moments solution to obtain the antenna factor of a resonant dipole antenna under plane-wave illumination. The simple formula of equation (4.21) gives errors of less than 0.02 dB and so is perfectly adequate.

### 4.2.3 The Skeletal Biconical Antenna

It is not possible to determine the drive-point impedance or the gain of the skeletal biconical antenna from a simple analytical approach because of its complicated structure; it is, however, possible to use the NEC computer code. In chapter 2, an optimal NEC model of a skeletal biconical antenna has been derived and this was used to calculate its antenna factor.

The NEC model was illuminated by a $1\text{Vm}^{-1}$ plane-wave and driven into a $50\,\Omega$ load impedance so that the current in the load impedance could be obtained. The load voltage was then calculated and equation (4.1) was used to calculate the antenna factor.

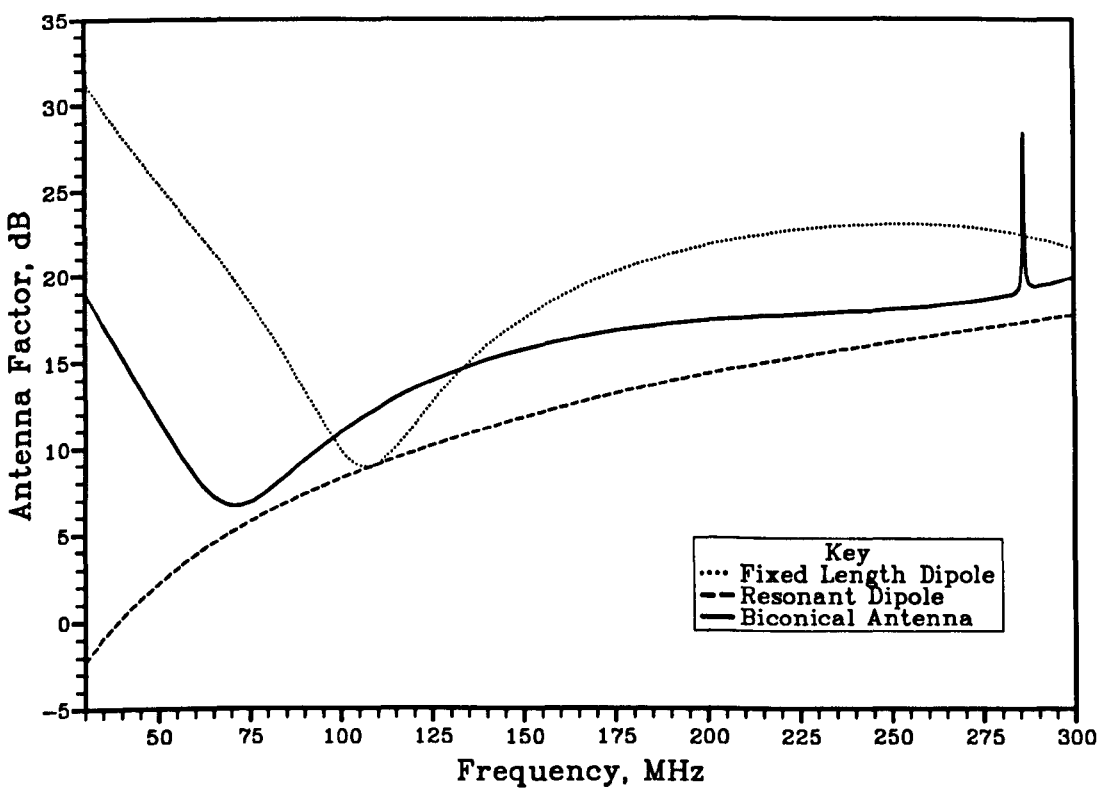


Figure 4.5: Theoretical antenna factor of a 1.3 m skeletal biconical antenna, a 1.3 m dipole antenna and a resonant dipole antenna.

Figure 4.5 shows that the antenna factor of the skeletal biconical antenna increases sharply below 70 MHz and therefore the antenna becomes progressively less sensitive. The small electrical size of the biconical antenna causes it to become capacitive below 70 MHz and this results in a poor impedance match to its $50\,\Omega$

transmission line. Therefore it extracts progressively less power from an illuminating field below this frequency.

The biconical antenna is most sensitive at 71 MHz, where its antenna factor is 6.8 dB. Above this frequency, its antenna factor rises gently but remains less than 20 dB up to 300 MHz.

The cone resonance of the biconical antenna is shown at its predicted antenna factor at 286.3 MHz. It can be seen that the antenna becomes desensitised at this frequency as its antenna factor is elevated by 9 dB. The disturbance is most pronounced from 285–288 MHz and does not significantly affect the antenna outside this frequency range.

### 4.2.4 Comparison of Dipole and Biconical Antennas

The total length of the biconical antenna was 1.3 m and figure 4.5 shows its antenna factor together with the antenna factors of a fixed length dipole antenna and a resonant dipole antenna. The fixed length dipole antenna was given a length of 1.3 m, i.e. equal to that of the biconical antenna, and its radius was 3.175 mm.

It is shown in chapter 2 that the impedance of a resonant dipole is 73 Ω, whereas the impedance of the biconical antenna is complex and generally of a somewhat greater magnitude. Figure 4.5 shows that above 70 MHz the biconical antenna extracts between 2 dB and 5 dB less power than the resonant dipole from a given illumination. This is because of its poorer impedance match to the 50 Ω load.

The antenna factor of the fixed length dipole has a similar frequency dependence to that of the biconical antenna in that its antenna factor passes through a minimum at a resonant frequency and rises either side of this. The resonance of the dipole is at 107 MHz, i.e. at a higher frequency than the biconical antenna, which resonates at 71 MHz. Both of the antennas have the same lengths, but this is a consequence of the broader nature of the biconical antenna. It is shown in chapter 2 that increasing the radii of resonant dipole antennas causes a similar reduction in their resonant frequencies.

Below their resonant frequencies the fixed length dipole and biconical antennas are capacitive and their antenna factors rise at 40 dB per decade. The fact that the resonant frequency of the biconical antenna is 36 MHz lower than that of the dipole allows it to be usable at frequencies down to 36 MHz below the minimum usable frequency of the dipole.

The antenna factor of the biconical antenna is always less than that of the fixed length dipole except over a 30 MHz interval about the resonance of the dipole. This

shows that the biconical antenna has a better broadband response.

## 4.3 Antenna Factor as a Function of Height

Equation (4.20) in §4.2.2 shows that antenna factor depends upon the effective length, $l_e$, and the drive-point impedance, $Z_T$, of an antenna.

$$AF = \frac{1}{l_e}\left|1 + \frac{Z_T}{Z_L}\right| \tag{4.22}$$

$Z_L$ is the load impedance that the antenna drives into. For antenna factor to be regarded as a constant during measurements, neither the effective length nor the drive-point impedance of an antenna must vary significantly from their values when the antenna was calibrated.

It has been shown in chapter 2 that, when an antenna is above a ground plane, its drive-point impedance may be significantly different to that of the antenna under plane wave illumination. This is because, when an antenna is closely coupled to a perfect ground plane, its drive-point impedance is not equal to its self impedance, but is given by

$$Z_T = Z_{11} + \rho Z_{12} \tag{4.23}$$

$Z_{11}$ is the self impedance of the antenna and $Z_{12}$ is the mutual impedance between the antenna and its image below the ground plane. $\rho$ is the reflection coefficient of the perfect ground plane and is equal to $+1$ for a vertically polarised antenna and $-1$ for a horizontally polarised antenna. The mutual impedance will vary as a function of height and, if its magnitude is not considerably less than the self impedance, drive-point impedance will vary significantly as a function of height.

The drive-point impedance of an antenna under plane wave illumination is equal to its self impedance and therefore its plane wave antenna factor is given by

$$AF_0 = \frac{1}{l_{e0}}\left|1 + \frac{Z_{11}}{Z_L}\right| \tag{4.24}$$

where $l_{e0}$ is the plane-wave effective length of the antenna. Antenna factor at a general height is given by equation (4.22) and therefore the change in antenna factor from its plane-wave value is given by

$$\begin{aligned} \Delta AF &= \frac{AF}{AF_0} \\ &= \frac{l_{e0}}{l_e}\left|\frac{Z_T + Z_L}{Z_{11} + Z_L}\right| \end{aligned} \tag{4.25}$$

This equation may also be represented by

$$\Delta AF = \frac{\Delta M}{\Delta l_e} \tag{4.26}$$

where $\Delta M = \left|\frac{Z_{11}+Z_L}{Z_T+Z_L}\right|$, the change in impedance mismatch between the antenna and its load impedance. The change in the effective length of an antenna from its plane wave value is $\Delta l_e$, where $\Delta l_e = \frac{l_e}{l_{e0}}$.

It is possible to use the applied EMF method to calculate the variation in the drive-point impedance of a resonant dipole antenna above a ground plane, however, in chapter 2 this approach has been shown to give limited accuracy. For variations in the impedance of more general antennas, or accurate analysis of the resonant dipole, it is necessary to use a computer code such as NEC. Variations in effective length cannot be calculated by any simple method, but NEC can also be used for their calculation.

Several authors have computed variations in the antenna factors of resonant dipoles purely from variations in their drive-point impedances [72], [73]. The authors do not give justification for assuming a constant effective length and the validity of this assumption will be determined in this section. NEC models will be used to calculate variations in effective length and the antenna factors of skeletal biconical and resonant dipole antennas at various heights above a ground plane and at various excitation frequencies.

### 4.3.1 NEC Model of a Uniformly Illuminated Antenna above a Ground Plane

Plane-wave illumination of an antenna is not possible unless the antenna is isolated in free space; for this reason, plane-wave antenna factors cannot be measured on an open-area test site. It is, however, possible to illuminate an antenna uniformly above a ground plane and this is the only condition required to define its antenna factor.

A NEC model was developed that allowed uniform illumination of model antennas above a ground plane. It is shown in figure 4.6 and was used to investigate the variation of effective length and antenna factor as functions of height and frequency.

A short, $\lambda/20$, dipole was placed 30 m away from the antenna under test at a height of 2 m above the ground plane. Use of a short dipole to provide illumination resulted in less mutual coupling between it and the antenna under test, but shorter antennas than $\lambda/20$ were found to give insufficient illuminating field. The radius of this antenna was set to $\lambda/2000$ and 11 segments were used to model it.

With a horizontally polarised illuminating source and antenna under test, this model achieved a field uniformity to within better than 0.12 dB over the length of a 6.35 mm diameter resonant dipole at 30 MHz. At higher frequencies the resonant

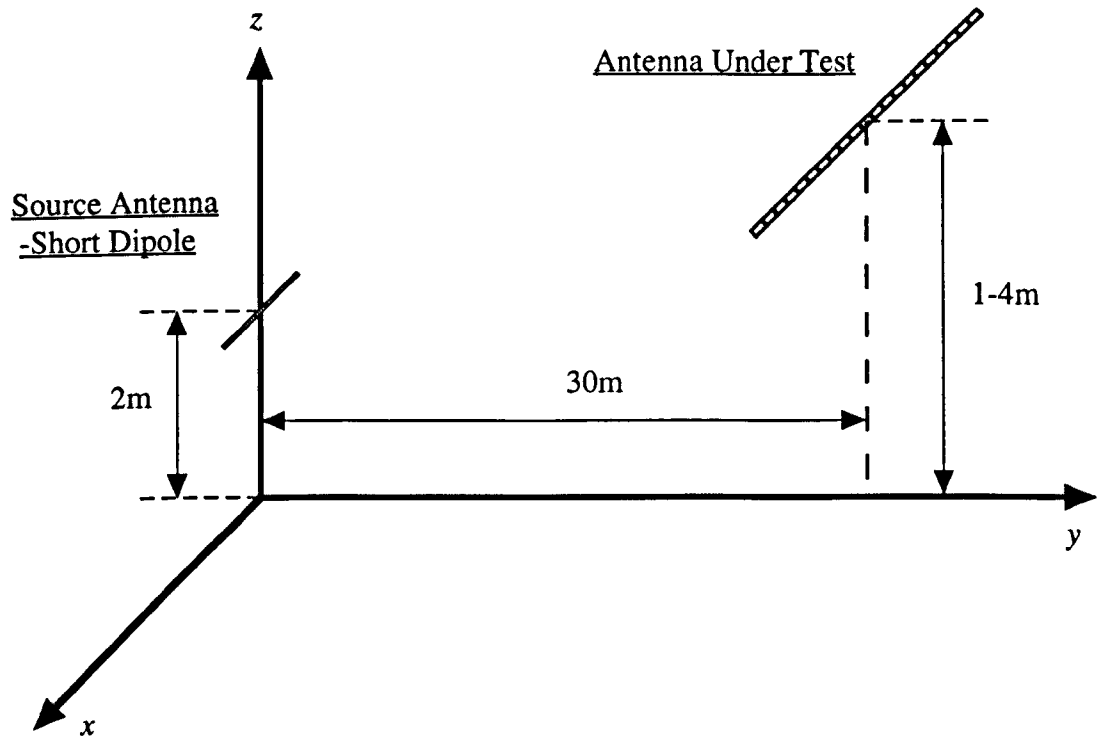


Figure 4.6: NEC model used to predict variations in antenna factor with height and frequency.

dipole was shorter and hence its illumination was more uniform; above 100 MHz the field uniformity was better than 0.01 dB and above 300 MHz it was better than 0.001 dB. The horizontally polarised biconical antenna had a field uniformity of better than 0.01 dB over its length but only had a field uniformity of 0.3 dB across the widest point of its cones. Horizontally polarised field uniformity was found to have negligible dependence on antenna height.

The model was only used with horizontally polarised antennas because it was difficult to illuminate vertically polarised antennas uniformly at general heights. This was because minima were formed at certain receiving antenna heights, where the direct and reflected waves from the source antenna arrived in antiphase. The magnitude of the illuminating field varied rapidly with height in the vicinity of these minima and therefore it was difficult to illuminate an antenna of appreciable length uniformly.

### 4.3.2 Variation of Antenna Factors

Investigations were performed using the NEC model of §4.3.1 in order to predict the variation of the antenna factors of the resonant dipole and skeletal biconical antennas with height and frequency. Simulations were performed to return the current delivered by each antenna to a 50 Ω load and the illuminating field at its

centre. The load voltage was then calculated so that equation (4.1) could be used to calculate the antenna factor. The uniformly illuminated antenna factors were normalised to the plane-wave antenna factors of §4.2 in order to yield the variations.

### The Resonant Dipole

Figure 4.7 shows the variation of the antenna factor of a 6.35 mm diameter horizontally polarised resonant dipole antenna. The variation is shown as a function of frequency at the four fixed heights of 1, 2, 3 and 4 m. The antenna factor of a

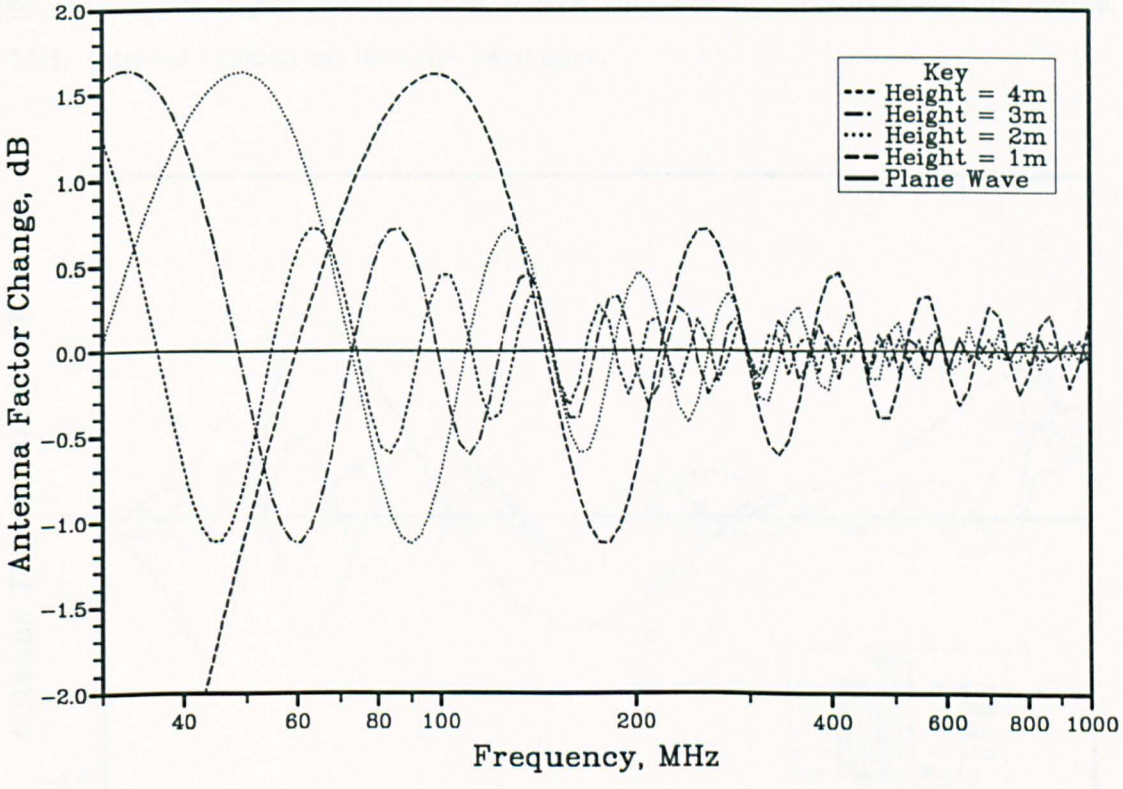


Figure 4.7: Variation of the antenna factor of a horizontally polarised resonant dipole antenna above a ground plane as a function of its height and excitation frequency.

resonant dipole above a ground plane oscillates about its plane-wave value with a decreasing amplitude as frequency increases. The amplitude of the oscillations is greater for lower antenna heights and is considerably greater at 1 m height than at 2 m height. The antenna factor of a resonant dipole at 1 m height falls by more than 2 dB below 45 MHz and is reduced by 4.5 dB at 30 MHz. Under these conditions it would be very difficult to calibrate the antenna because of the strong dependence of its antenna factor upon height.

The antenna factor of a resonant dipole used above 2 m height and below 100 MHz will vary between −1.2 dB and +1.7 dB about its plane wave value. Above

100 MHz these limits fall to ±1.0 dB and above 200 MHz they are less than ±0.6 dB. These limits represent the accuracy to which field strength measurements can be made if plane wave antenna factors are used uncorrected.

### The Skeletal Biconical Antenna

Figure 4.8 shows the variation of the antenna factor of a skeletal biconical antenna from its plane-wave value at heights of 1, 2, 3 and 4 m above a ground plane. The data is plotted as a linear function of frequency from 30MHz to 300 MHz in 5 MHz steps. This did not provide a sufficient resolution to show the cone resonance at 286.3 MHz, but it has already been shown that the antenna is unusable over a 3 MHz interval centred on its cone resonance.

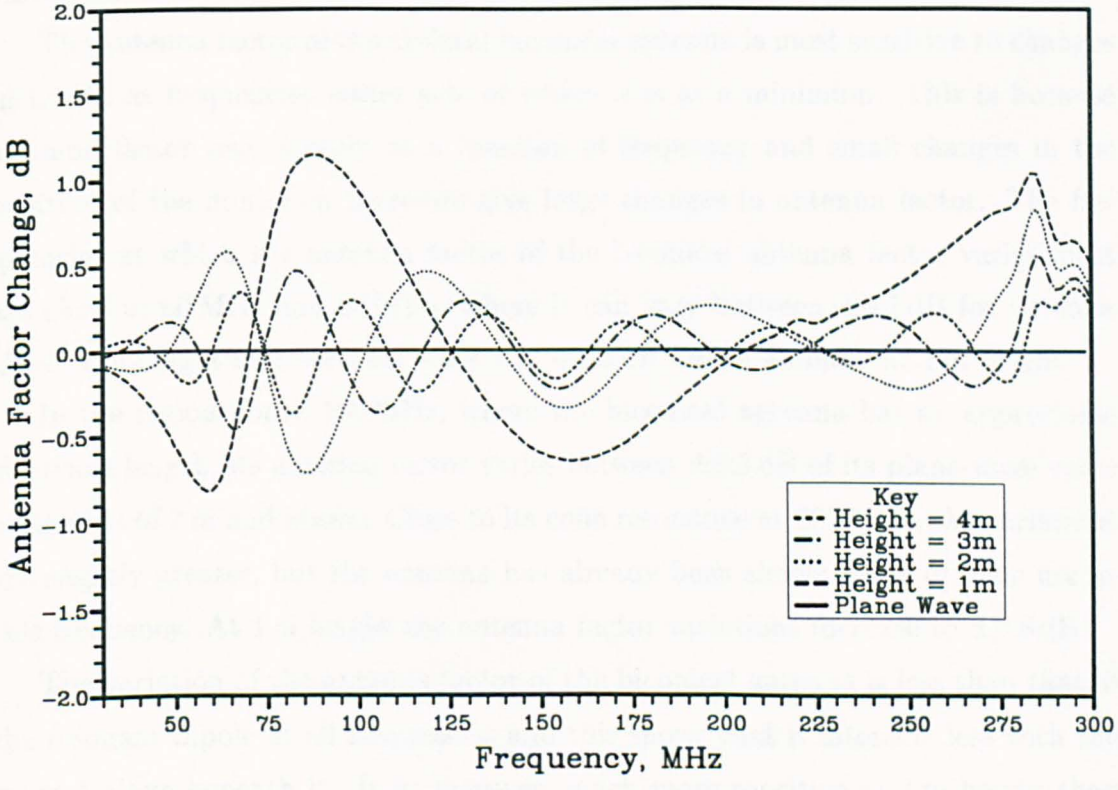


Figure 4.8: Variation of the antenna factor of a horizontally polarised biconical antenna above a ground plane as a function of its height and excitation frequency.

The antenna factor of the skeletal biconical antenna oscillates about its plane wave value but, unlike the antenna factor of the resonant dipole, the amplitude and the periodicity of the oscillations do not change steadily as functions of frequency. The impedance of a resonant dipole is, by definition, resistive, but the biconical antenna has fixed physical dimensions and thus an impedance whose phase changes with frequency. The antenna factor of the biconical antenna can be seen to vary

differently in each of the different regions of antenna behaviour.

As the biconical antenna becomes increasingly capacitive below 70 MHz, the variations in its antenna factor become less and at 30 MHz they have fallen to less than ±0.1 dB. The antenna is considerably shorter than a wavelength in this region and this shows how an electrically short antenna interacts much less with its environment than an antenna of appreciable electrical length.

The impedance of the biconical antenna becomes purely resistive close to 71 MHz and figure 4.5 shows that its antenna factor passes through a broad minimum at 73 MHz. This is where the antenna presents its best impedance match to a 50 Ω load and delivers most power from a given field. When the antenna is above a ground plane the depth of the minimum in its antenna factor does not change significantly but the centre frequency shifts slightly; this causes the antenna factor variations of antennas above 2 m height to become small at 73 MHz.

The antenna factor of the skeletal biconical antenna is most sensitive to changes in height at frequencies either side of where it is at a minimum. This is because antenna factor rises steeply as a function of frequency and small changes in the position of the minimum therefore give large changes in antenna factor. The frequencies at which the antenna factor of the biconical antenna factor varies most are close to 60 MHz and 80 MHz, where it can vary between ±0.7 dB for antenna above 2 m height and between −0.8 and +1.2 dB for an antenna at 1 m height.

In the region above 100 MHz, where the biconical antenna has an appreciable electrical length, its antenna factor varies between ±0.5 dB of its plane-wave value at heights of 2 m and above. Close to its cone resonance at 287 MHz, the variations are slightly greater, but the antenna has already been shown to be of little use at this frequency. At 1 m height the antenna factor variations increase to ±0.8 dB.

The variation of the antenna factor of the biconical antenna is less than that of the resonant dipole at all frequencies and this shows that it interacts less with the ground plane beneath it. It is, however, much more sensitive at 1 m height than at 2 m and this indicates that it should not be calibrated by measurements at 1 m height.

### 4.3.3 Variation of Effective Length

The NEC simulations described so far in this section have returned the field strength illuminating an antenna and the current delivered by the antenna to a 50 Ω load. These parameters have been used to calculate the antenna factor, but in order to calculate the effective length of the antenna, it was necessary to obtain

the EMF developed at the drive-point of the antenna. A further NEC simulation was performed with the same geometry as figure 4.6, but with the antenna under test driven into a 100 Ω load. This returned the current delivered by the antenna to the load and it was then possible to use the approach of §4.7.1 to obtain the EMF developed in the antenna and also its drive-point impedance.

The effective length of the antenna was calculated as the ratio of the EMF developed at its drive-point to the illuminating field. It was calculated as a function of frequency with the antenna at heights of 1, 2, 3 and 4 m above a ground plane. The results were normalised to the effective length of the antenna under plane-wave illumination and they are shown for the resonant dipole in figure 4.9.

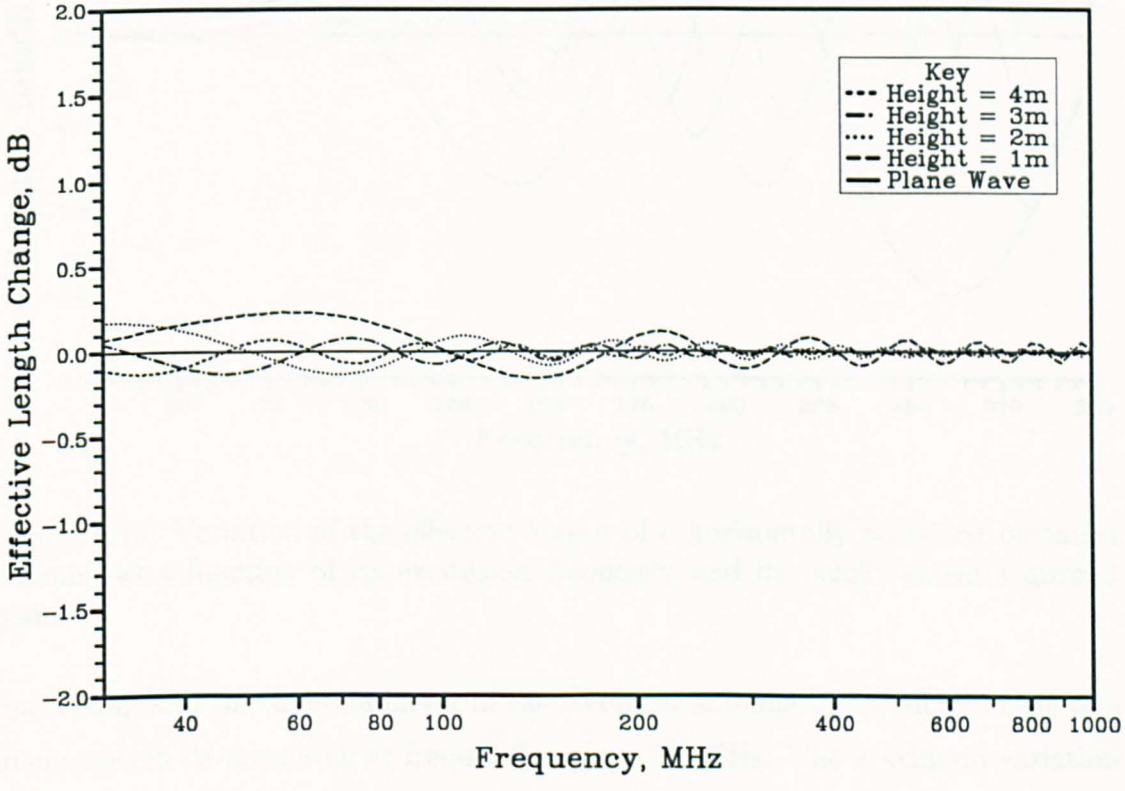


Figure 4.9: Variation of the effective length of a horizontally polarised resonant dipole antenna as a function of its excitation frequency and height above a ground plane.

Comparison of figure 4.9 with figure 4.7 shows that the effective length of the resonant dipole antenna varies much less than its antenna factor as a function of height. This indicates that changes in the antenna factor of a resonant dipole are predominantly due to changes in the mismatch between the antenna and its load.

Variations in effective length are greatest at lower antenna heights but, even at 1 m height, effective length only changes between +0.23 dB and −0.16 dB from its plane-wave value. These are the maximum errors that could ever result if changes

in the antenna factor of a resonant dipole were assumed to be due only to changes in its mismatch.

Figure 4.10 shows the effective length change of the skeletal biconical antenna as a function of its height and excitation frequency. Comparison with figure 4.8 shows

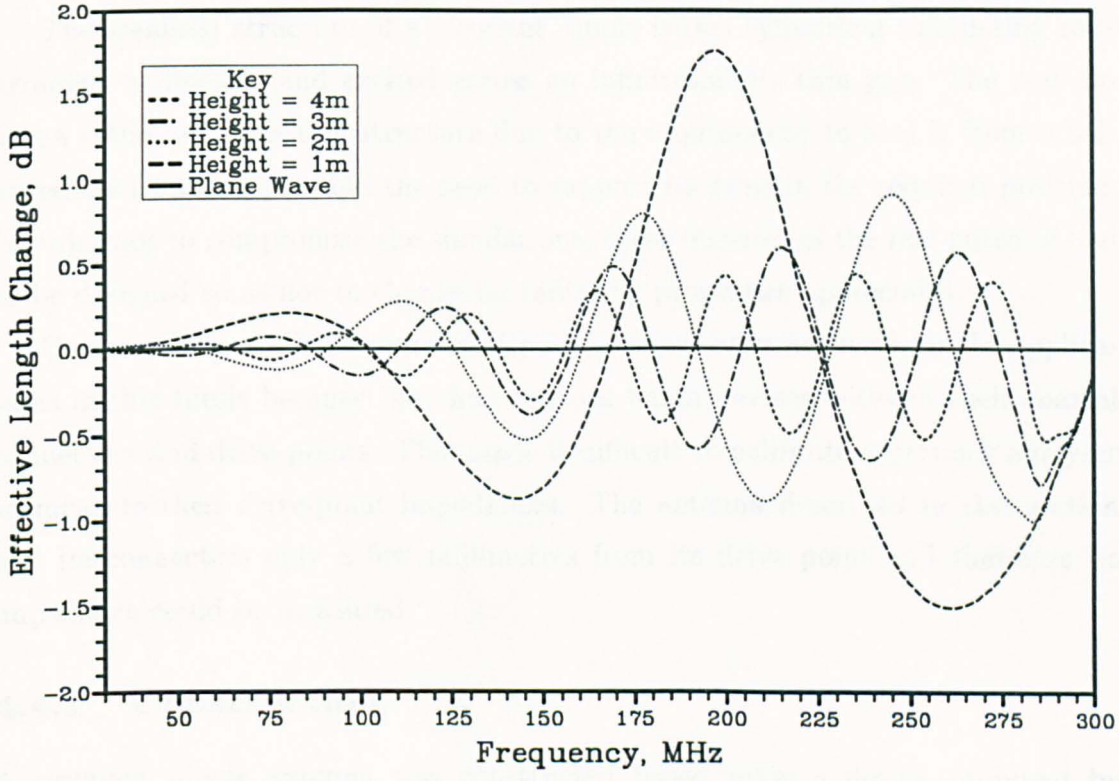


Figure 4.10: Variation of the effective length of a horizontally polarised biconical antenna as a function of its excitation frequency and its height above a ground plane.

that changes in the antenna factor of the biconical antenna are predominantly due to changes in its mismatch at frequencies up to 100 MHz. The maximum variation of effective length over this frequency range is $\pm 0.2$ dB and occurs at the resonant frequency of 75 MHz.

At frequencies above 100 MHz, changes in the effective length of the biconical antenna become progressively larger and they must be taken account of in any predictions of antenna factor variations. The variations in effective length actually become slightly greater than the variations in antenna factor, showing that there is a tendency for variations in antenna factor due to changes in effective length to be offset by variations due to changes in mismatch.

## 4.4 A Standard Resonant Dipole Antenna

A resonant dipole antenna that could be simulated accurately was required in order to model the measurements in chapters 5 and 6 of this thesis. This section describes the design of such an antenna and the approaches that were used to simulate it are described in chapter 2.

The idealised structure of a resonant dipole is two cylindrical conducting rods arranged collinearly and excited across an infinitesimally thin gap. The real antenna could not have this structure due to the requirement to feed it from a balanced transmission line and the need to support its arms in the required position. In order not to compromise the simulations, these features of the real antenna had to be designed so as not to change its radiating properties appreciably.

Commercially available resonant dipole antennas were not used for the applications in this thesis because they had integral balun devices between their coaxial connectors and drive-points. This made it difficult to calibrate a network analyser to measure their drive-point impedances. The antenna described in this section had its connectors only a few millimetres from its drive point and therefore its impedance could be measured.

### 4.4.1 Construction

A resonant dipole antenna was constructed based upon a design proposed by Fitzgerrel [74] and shown in figure 4.11. The antenna consisted of a pair of cylindrical metal arms held in a nylon support and fed from a balanced transmission line.

Models of the feed points of cylindrical dipole antennas assume that they are excited across an infinitesimally small gap at their feed point. No real antenna can have this structure and the antenna shown in figure 4.11 has a gap of 18 mm where it is fed from a twin coaxial transmission line. It has been explained in chapter 2 that small feed point gaps do not affect the impedance of a cylindrical dipole antenna at resonance and an 18 mm gap would not have significantly affected the impedance of this antenna up to 1 GHz.

It was necessary to support the arms of the dipole antenna and enable connection to them at the drive-point in a way that would interact minimally with the fields of the antenna. This was achieved with a 10 cm length of 25 mm diameter cylindrical nylon rod machined as shown in figure 4.11. The effect of this nylon support on the drive-point impedance of the antenna is measured in §4.6.

Two SMA connectors were mounted in the nylon support at a separation of

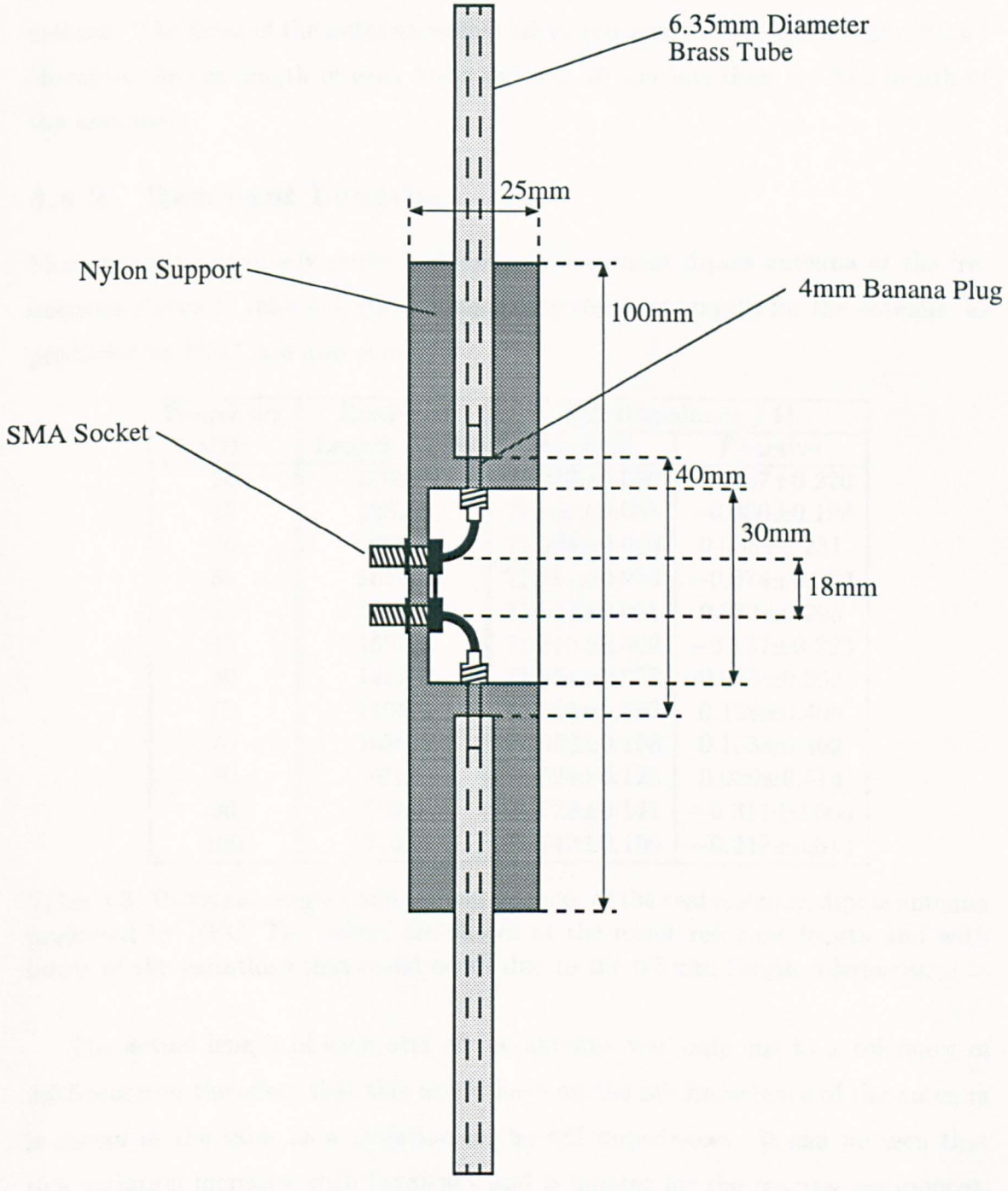


Figure 4.11: Practical implementation of a cylindrical dipole antenna.

18 mm and it was via these that the antenna was excited from its twin coaxial transmission line. The wires connecting from the SMA connectors to the 4 mm plugs were as short as possible in order to minimise parasitics.

Measurements were made with this antenna at the lowest excitation frequency first and its arms were then trimmed to maintain resonance as frequency was increased. The arms of the antenna were held 40 mm apart in the nylon support and therefore the cut length of each brass rod was 20 mm less than the half-length of the antenna.

### 4.4.2 Resonant Lengths

Measurements were only performed using the resonant dipole antenna at the frequencies shown in table 4.3; the corresponding resonant lengths for the antenna, as predicted by NEC, are also shown.

| Frequency | Resonant | Self Impedance / Ω | |
|---|---|---|---|
| MHz | Length / mm | Resistive | Reactive |
| 20 | 3609.0 | 71.918±0.030 | −0.007±0.226 |
| 25 | 2882.5 | 71.882±0.038 | −0.080±0.198 |
| 30 | 2399.0 | 71.887±0.046 | 0.035±0.231 |
| 35 | 2053.5 | 71.852±0.053 | −0.074±0.262 |
| 40 | 1795.0 | 71.872±0.061 | 0.083±0.293 |
| 45 | 1593.5 | 71.816±0.069 | −0.137±0.323 |
| 50 | 1433.0 | 71.854±0.077 | 0.078±0.352 |
| 60 | 1192.0 | 71.854±0.092 | 0.128±0.408 |
| 70 | 1020.0 | 71.852±0.108 | 0.153±0.462 |
| 80 | 891.0 | 71.824±0.125 | 0.059±0.514 |
| 90 | 790.5 | 71.729±0.141 | −0.311±0.565 |
| 100 | 710.5 | 71.742±0.156 | −0.248±0.613 |

Table 4.3: Resonant lengths and self impedances of the real resonant dipole antenna predicted by NEC. The values are shown at the exact resonant length and with limits of the variations that could occur due to the 0.5 mm length tolerances.

The actual length of each arm of the antenna was only cut to a tolerance of ±0.5 mm and the effect that this would have on the self impedance of the antenna is shown in the table as a variation in the self impedances. It can be seen that this variation increases with frequency and is greater for the reactive component. The maximum possible variation in any impedance component at frequencies up to 100 MHz is only 0.613 Ω and therefore it was concluded that differences between the lengths of the real and simulated antennas would not cause significant inaccuracy.

### 4.4.3 Balanced Connecting Networks

The transmission line used to feed the antenna shown in figure 4.11 was of an unusual type as it consisted of two 50 Ω coaxial cables. The centre conductor of each cable fed one arm of the antenna and the two outer conductors were joined together at the drive-point of the antenna. Together, the two 50 Ω coaxial cables formed a balanced, screened 100 Ω transmission line, and figure 4.12 shows how a Minicircuits ZFSCJ-2-1 phase splitting device was used to drive it from a single balanced 50 Ω coaxial transmission line.

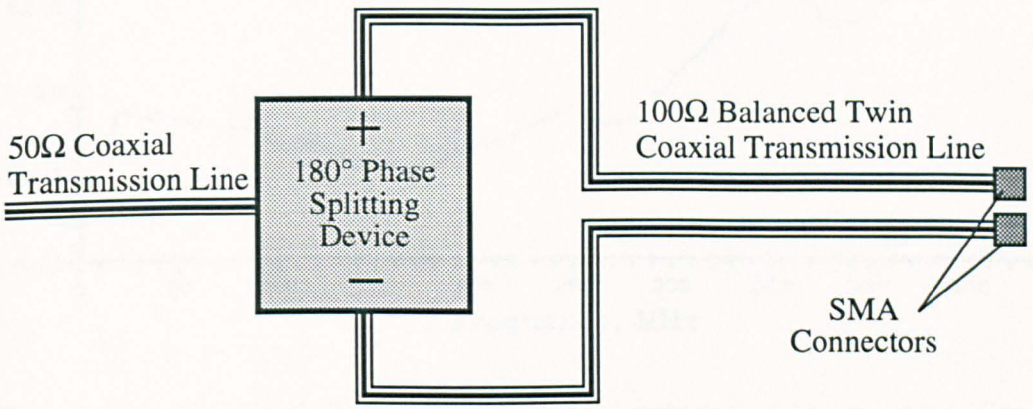


Figure 4.12: Balanced feed network for the resonant dipole.

The baluns of antennas intended for EMC applications are usually mounted between the arms of the antennas as integral parts of their structure. The feed arrangement shown in figure 4.12 offers several advantages that become particularly apparent when it is necessary to design an antenna that can be computer simulated. The balun can be a significant distance away from the antenna and so it can be a much larger device of better quality. This will enable the gap between the arms of the antenna to be much smaller so that the antenna structure will behave more closely to the theoretical models of antennas which have infinitesimally small feed point gaps.

The currents at the antenna feed point must be of equal magnitude and exactly 180° out of phase for the antenna to be perfectly balanced. This required a high quality phase splitting device and a pair of phase matched cables to form the twin coaxial transmission line. The Minicircuits phase splitter was connected to two 2 m lengths of cable and the resulting feed network gave the magnitude and phase imbalances shown in figures 4.13 and 4.14.

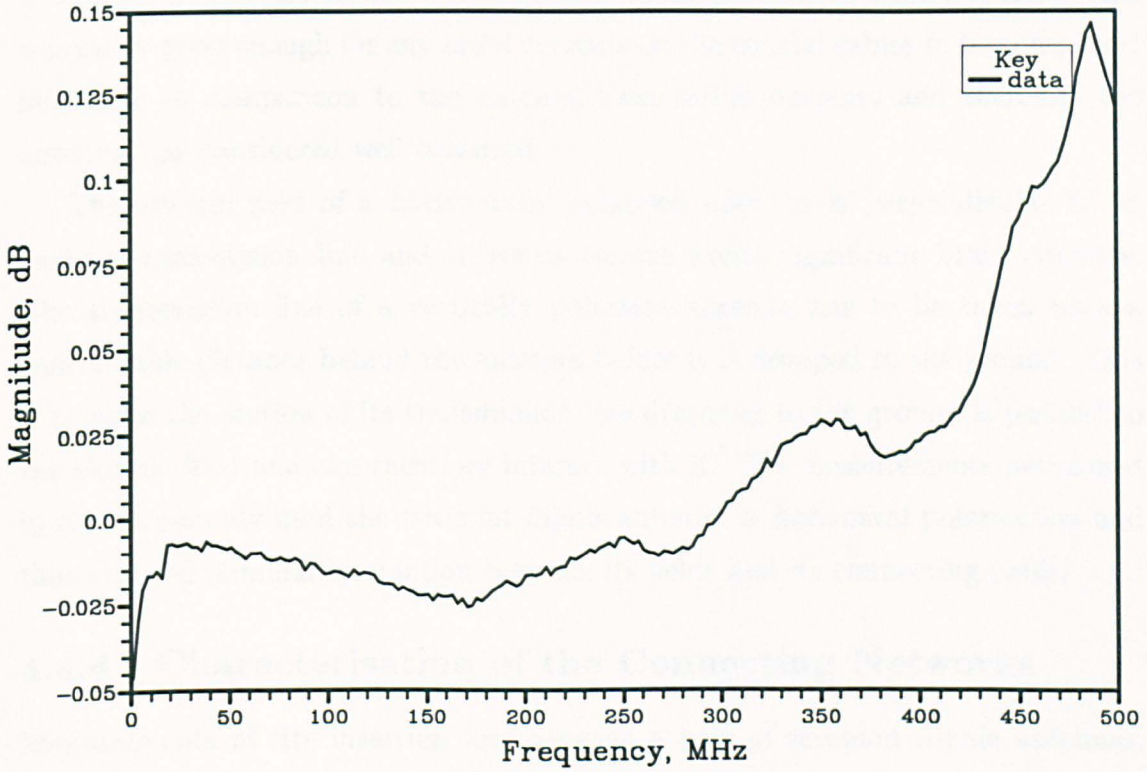


Figure 4.13: Magnitude imbalance of the feed network of the resonant dipole.

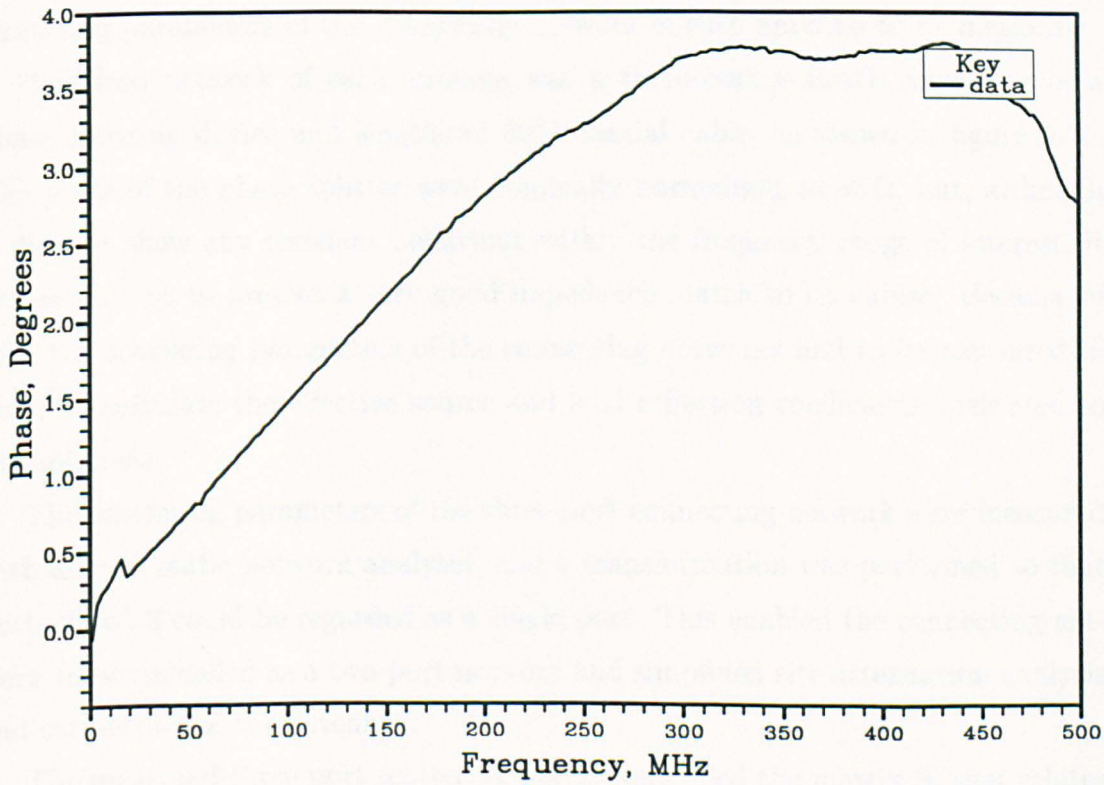


Figure 4.14: Phase imbalance of the feed network of the resonant dipole.

The graphs show magnitude imbalances of less than 0.01 dB and phase errors of less than 1.5° over the 20–100 MHz frequency range that the antenna was used. This was easily good enough for any braid currents on the coaxial cables to be considered negligible in comparison to the antenna's excitation currents and therefore the antenna was considered well balanced.

The electric field of a horizontally polarised antenna is perpendicular to its feeding transmission line and therefore cannot excite significant braid currents. The transmission line of a vertically polarised antenna has to be taken back a considerable distance behind the antenna before it is dropped to the ground. This is because the section of its transmission line dropping to the ground is parallel to the electric field and can therefore interact with it. The measurements performed in this thesis only used the resonant dipole antenna in horizontal polarisation and thus ensured minimal interaction between its fields and its connecting cable.

### 4.4.4 Characterisation of the Connecting Networks

Measurements of site insertion loss between a pair of resonant dipole antennas, of the type described in this section, are described in chapter 5. The theory of chapter 3 shows that, in order to use NEC to calculate predicted values of site insertion loss between these antennas, it is necessary to know the effective source and load reflection coefficients presented to their drive-points. This required the scattering parameters of the connecting network of each antenna to be measured.

The feed network of each antenna was a three-port network consisting of a phase splitting device and lengths of 50 Ω coaxial cable, as shown in figure 4.15. The ports of the phase splitter were nominally normalised to 50 Ω, but, although it did not show any resonant behaviour within the frequency range of interest, it was found not to present a very good impedance match to its cables. Because of this, the scattering parameters of the connecting networks had to be measured in order to calculate the effective source and load reflection coefficients presented to the antennas.

The scattering parameters of the three-port connecting network were measured with an automatic network analyser, and a transformation was performed so that ports 2 and 3 could be regarded as a single port. This enabled the connecting network to be modelled as a two-port network and simplified site attenuation analysis and calibration of the antennas.

The measured three port scattering parameters filled the matrix **S**, that relates

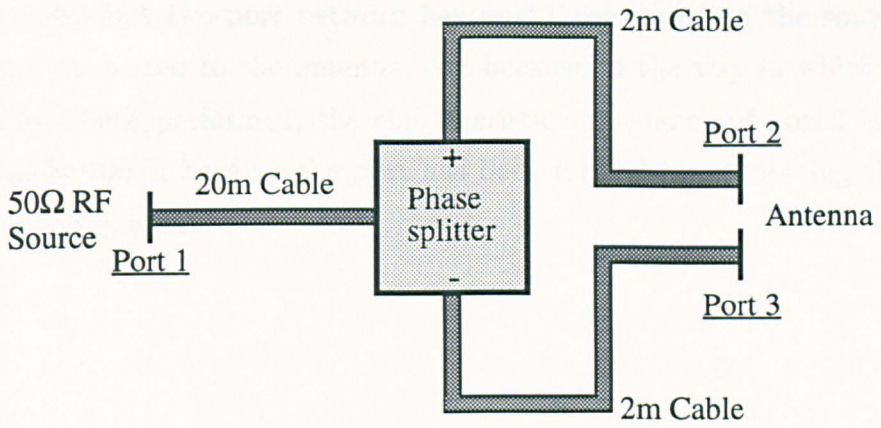


Figure 4.15: Three-port connecting network between a resonant dipole antenna and its source or load.

the scattered waves from each of the three ports to the incident waves.

$$b_1 = S_{11}a_1 + S_{12}a_2 + S_{13}a_3 \tag{4.27}$$

$$b_2 = S_{21}a_1 + S_{22}a_2 + S_{23}a_3 \tag{4.28}$$

$$b_3 = S_{31}a_1 + S_{32}a_2 + S_{33}a_3 \tag{4.29}$$

The scattered and incident waves at ports 2 and 3 are in antiphase with each other, i.e.

$$b_3 = -b_2 \tag{4.30}$$

$$a_3 = -a_2 \tag{4.31}$$

Subtracting equation (4.29) from (4.28) and substituting $a_3$ and $b_3$ from equations (4.30) and (4.31) gives

$$(2b_2) = [S_{21} - S_{31}]\, a_1 + \left[\frac{S_{22} + S_{33} - S_{23} - S_{32}}{2}\right](2a_2) \tag{4.32}$$

Substituting $a_3$ from equation (4.31) into (4.27) gives

$$b_1 = [S_{11}]\, a_1 + \left[\frac{S_{12} - S_{13}}{2}\right](2a_2) \tag{4.33}$$

Equations (4.32) and (4.33) show that the three port connecting network may be modelled as an equivalent two-port network having incident waves, $a_1$ and $2a_2$, and scattered waves, $b_1$ and $2b_2$, at its ports. The scattering parameters that fill the two-port matrix, $\mathbf{S}'$, are defined as follows:

$$S'_{11} = S_{11} \tag{4.34}$$

$$S'_{12} = \frac{S_{12} - S_{13}}{2} \tag{4.35}$$

$$S'_{21} = S_{21} - S_{31} \tag{4.36}$$

$$S'_{22} = \frac{S_{22} + S_{33} - S_{23} - S_{32}}{2} \tag{4.37}$$

The equivalent two-port network has port 1 connected to the source or load and port 2 connected to the antenna, but because of the way in which the above analysis has been performed, the characteristic impedance of port 2 is not $50\,\Omega$; it is actually $100\,\Omega$, because the port has been formed by connecting the original ports 2 and 3 in series.

## 4.5 Measurement of Antenna Impedance

The measurements of ground plane reflection coefficients in chapter 6 require the accurate measurement of the drive-point impedance of a horizontally polarised resonant dipole antenna above the ground plane of an open-area test site. The drive-point impedance of a skeletal biconical antenna also had to be measured in order to validate its NEC simulation. Both of these antenna impedances were measured with a Hewlett Packard 8753A Automatic Network Analyser (ANA) and the procedures used are described in this section.

### 4.5.1 General Approach to Impedance Measurement

Consider a transmission line fed from a source and terminated at an antenna whose impedance is to be measured, as shown in figure 4.16. There are two waves propa-

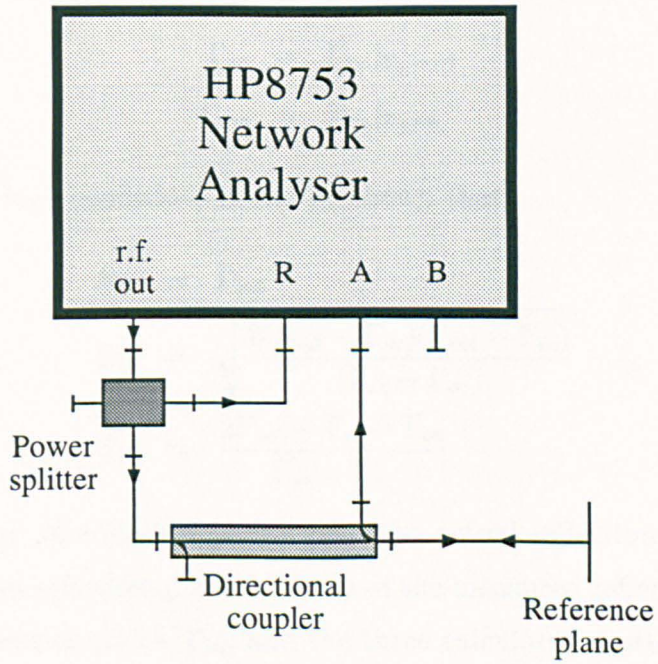


Figure 4.16: Use of a network analyser for impedance measurements.

gating on the transmission line; one towards the antenna in the forward direction, and the other away from the antenna in the reverse direction. The ratio of the amplitude of the reverse wave to the amplitude of the forward wave is equal to the reflection coefficient of the antenna, if both waves are measured at the drive-point of the antenna. Elsewhere on the transmission line, the wave amplitude ratio is still related to the reflection coefficient of the antenna, but a two-port network can be regarded to exist between the measurement position and the desired reference plane at the antenna. To perform an impedance measurement with a network analyser it is necessary to find the scattering parameters of this intervening two-port

network and calibrate to move the reference plane to the antenna drive-point.

Consider a two-port network with port 2 connected to a load of reflection coefficient $\Gamma_L$. The input reflection coefficient at port 1 is $\Gamma_{in}$ and is related to $\Gamma_L$, by

$$\Gamma_{in} = S_{11} + \frac{S_{12}^2 \Gamma_L}{1 - S_{22}\Gamma_L} \tag{4.38}$$

where $S_{11}$, $S_{12}$ and $S_{22}$ are the scattering parameters of the two-port network

If three known loads can be connected in place of the unknown load, $\Gamma_L$, it is possible to deduce the scattering parameters of the two-port network from the three measurements of $\Gamma_{in}$. The three known reflection coefficients that are usually placed at the reference plane are open, short and matched loads to establish reflection coefficients of $+1$, $-1$ and 0 respectively. The measured values of $\Gamma_{in}$ for these three load conditions are then

$$\Gamma_{oc} = \Gamma_{in}|_{\Gamma_L=+1} \tag{4.39}$$

$$\Gamma_{sc} = \Gamma_{in}|_{\Gamma_L=-1} \tag{4.40}$$

$$\Gamma_{mt} = \Gamma_{in}|_{\Gamma_L=0} \tag{4.41}$$

Under the three load conditions it can be shown that

$$S_{11} = \Gamma_{mt} \tag{4.42}$$

$$S_{12} = \sqrt{\frac{2(\Gamma_{mt} - \Gamma_{oc})(\Gamma_{mt} - \Gamma_{sc})}{(\Gamma_{sc} - \Gamma_{oc})}} \tag{4.43}$$

$$S_{22} = \frac{2\Gamma_{mt} - \Gamma_{sc} - \Gamma_{oc}}{\Gamma_{sc} - \Gamma_{oc}} \tag{4.44}$$

Rearrangement of equation (4.38) gives the actual reflection coefficient of the load at the desired reference plane in terms of the measured reflection coefficient at the arbitrary reference plane, $\Gamma_{in}$, and the three calculated scattering parameters.

$$\Gamma_L = \frac{S_{11} - \Gamma_{in}}{S_{22}(S_{11} - \Gamma_{in}) - S_{12}^2} \tag{4.45}$$

The impedance of the load antenna is then calculated from

$$Z_L = Z_0 \frac{1 + \Gamma_L}{1 - \Gamma_L} \tag{4.46}$$

### 4.5.2 The Cylindrical Dipole Antenna

The impedance of an antenna must be measured at its drive-point, which, for the cylindrical dipole antenna shown in figure 4.11, is the exact position where its transmission line bifurcates into the arms of the antenna. The network analyser had to be calibrated to establish a reference plane at this point and, due to the

unusual transmission line feed arrangement, appropriate standard loads had to be made. These were made from female SMA connectors identical to those mounted in the antenna support and are shown in figure 4.17.

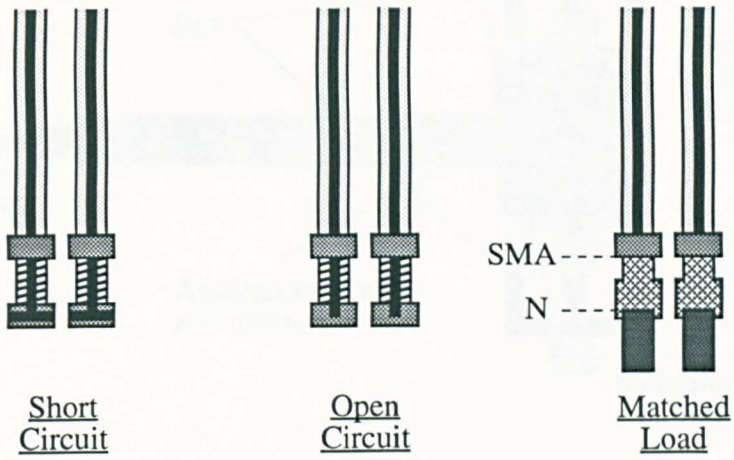


Figure 4.17: Standard loads for calibration of the network analyser to measure the impedance of the cylindrical dipole antenna.

Two of each type of load were required to establish the reflection coefficients of $+1$, $-1$ and 0 in the $100\,\Omega$ twin coaxial transmission line system. The short and open-circuits were made from SMA sockets and the matched loads were formed from SMA to N-type converters followed by commercially available N-type $50\,\Omega$ loads. Due to the fact that this calibration was carried out in a transmission line having a characteristic impedance of $100\,\Omega$, the measured impedances with the $50\,\Omega$ network analyser had to be multiplied by two.

The amplitudes of the reflected waves from the matched loads were at least 40 dB less than the amplitudes of the incident waves; thus they were judged to be of sufficient quality. Care was taken to establish a planar termination inside the short-circuit loads and the inner conductor of the open-circuit loads was terminated at the same position inside their SMA sockets. Fringing capacitance can be a problem with open-circuit loads and this makes it difficult to define the exact point of termination. At frequencies up to 100 MHz the wavelength in the transmission lines was greater than 2 m and so a positional error of 2 mm in the reference plane of the open-circuit load would have caused a negligible phase shift of less than 0.5°.

### 4.5.3 The Skeletal Biconical Antenna

The construction of the skeletal biconical antenna was such that it was not possible to connect standard loads to its feeding transmission line at the drive-point of the antenna. Figure 4.18 shows how a pair of jigs was used to mount N-type connectors on each side of the head of the of the antenna support. By connecting pairs of

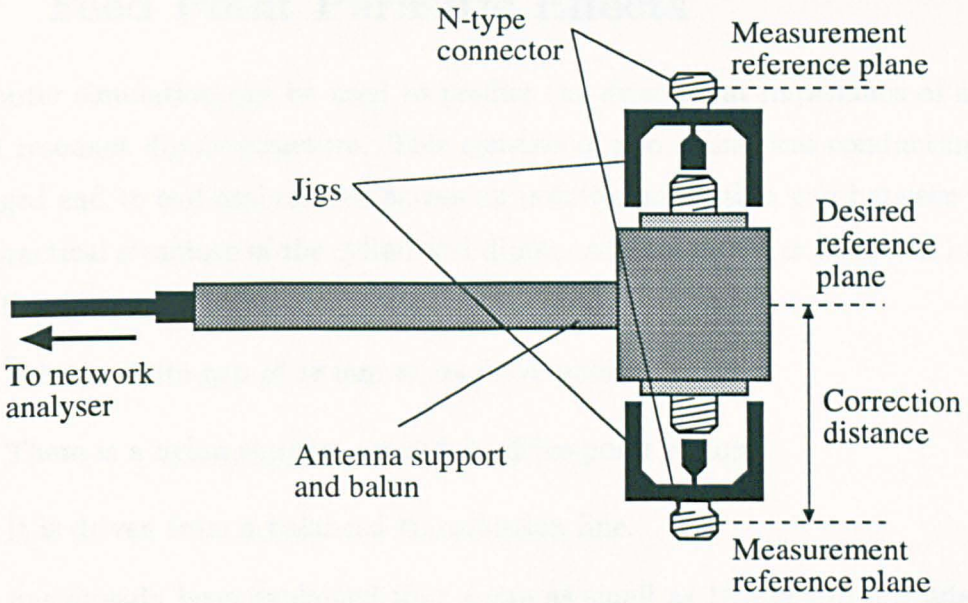


Figure 4.18: Measurement of the impedance of the skeletal biconical antenna.

open, short and matched loads to the N-type connectors, the network analyser was calibrated for an impedance measurement between the twin measurement reference planes shown in figure 4.18.

The physical distance between the measurement reference plane and the desired reference plane was 75 mm, but 28 mm of this transmission line was filled with a PTFE dielectric having a velocity factor of 0.67. It was calculated that the equivalent free space distance between the reference planes was 89 mm and so all of the measured reflection coefficients were corrected for this before calculation of the antenna impedance took place. This correction is described in §4.7.2.

The maximum frequency at which the impedance of the skeletal biconical antenna was measured was 300 MHz, corresponding to a wavelength of 1 m. With a wavelength as large as this, any errors associated with the distance through which the reference plane was moved would have been small.

## 4.6 Feed Point Parasitic Effects

Computer simulation can be used to predict the drive-point impedance of an idealised resonant dipole structure. This consists of two cylindrical conducting rods arranged end to end and excited across an infinitesimally thin gap between them. The practical structure of the cylindrical dipole antenna shown in figure 4.11 differs from this in several ways:

1. It has a finite gap of 18 mm at its drive-point.
2. There is a nylon support around its drive-point region.
3. It is driven from a balanced transmission line.

It has already been explained that a gap as small as 18 mm will not affect the impedance of a resonant antenna and, provided that the transmission line leaves in the plane that is normal to the electric field from the antenna, it should also not affect the antenna significantly. The effect of the nylon support upon the impedance of the antenna is not as clear, and experiments that were carried out to assess its effect are described in this section.

### 4.6.1 Effect of the Nylon Support

The dipole antenna shown in figure 4.11 uses a length of cylindrical nylon rod as a support, and this material does not have the same electrical properties as free space. Nylon has a dielectric constant of 3.8 and will therefore modify the fields from the antenna in the support region. This will cause the measured antenna drive-point impedance to deviate from the theoretical one.

Since the resonant dipole antenna is close to half a wavelength long, the 10 cm nylon support at its centre covers less than 7% of its total length for frequencies of up to 100 MHz. For this reason it was hoped to model the effect of the dielectric sleeve as a single lumped parasitic impedance, $Z_P$, in parallel with the antenna's drive-point impedance, $Z_T$. Figure 4.19 shows how this was done. The measured antenna impedance is $Z_M$ and is given by

$$Z_M = Z_T \parallel Z_P \tag{4.47}$$

Equation (4.47) can be rearranged to obtain the true drive-point impedance of the antenna in free space from its measured drive-point impedance.

$$Z_T = \frac{Z_P Z_M}{Z_P - Z_M} \tag{4.48}$$

Consequently, if a value for $Z_P$ can be found, $Z_M$ can then be corrected to $Z_T$.

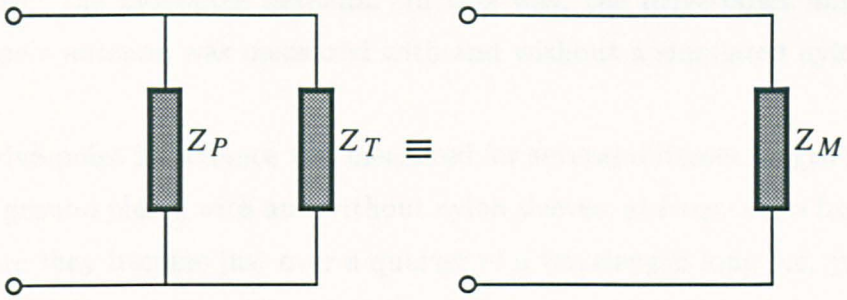


Figure 4.19: Modelling of the nylon support as a parasitic impedance in parallel with the antenna drive-point impedance.

### 4.6.2 Measurement of The Parasitic Impedance

In order to measure the parasitic impedance, $Z_P$, an antenna structure had to be devised that was self supporting and whose drive-point impedance could be measured with and without a nylon support. Figure 4.20 shows the experimental apparatus that was used. It was difficult to build a self supporting dipole structure

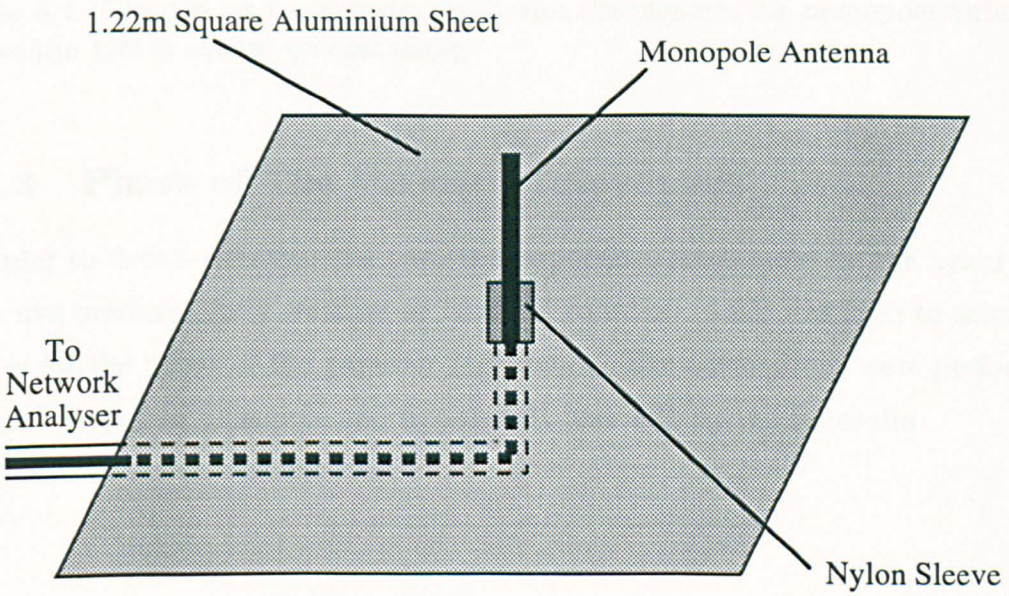


Figure 4.20: Measurement of the parasitic impedance.

and so the experimental apparatus was built in the form of a monopole antenna above 1.22 m square aluminium sheet used as a ground plane. In this way an image of the monopole antenna was created below it so that the combined structure would have similar electrical characteristics to a dipole antenna.

A BNC connector was mounted beneath the ground plane with its centre terminal feeding the monopole. Standard loads could be substituted in place of the antenna enabling calibration of the network analyser for a measurement of the drive-point impedance of the monopole. A 5 cm length of 25 mm diameter nylon sleeve was then cut to represent half the support of the dipole antenna when it

was slid over the monopole antenna. In this way, the drive-point impedance of the monopole antenna was measured with and without a simulated nylon support around it.

The drive-point impedance was measured for several different length monopoles above the ground plane, with and without nylon sleeves, at frequencies from 10 MHz up to where they became just over a quarter of a wavelength long, i.e. just beyond their resonant frequencies. These lengths and maximum excitation frequencies are shown in table 4.4.

| Length mm | Frequency MHz | Length mm | Frequency MHz |
|---|---|---|---|
| 74 | 1050 | 346 | 230 |
| 109 | 750 | 398 | 200 |
| 151 | 550 | 499 | 160 |
| 192 | 440 | 601 | 130 |
| 243 | 330 | 702 | 110 |
| 295 | 270 | 803 | 100 |

Table 4.4: Lengths and maximum excitation frequencies for monopole antennas above the 1.22 m square ground plane.

### 4.6.3 Phase of The Parasitic Impedance

In order to deduce whether the parasitic impedance introduced by the nylon support was predominantly resistive or reactive, equation (4.48) was used to calculate values for the phase of the parasitic impedance. The calculations were performed for each length of monopole and figures 4.21 and 4.22 show the results

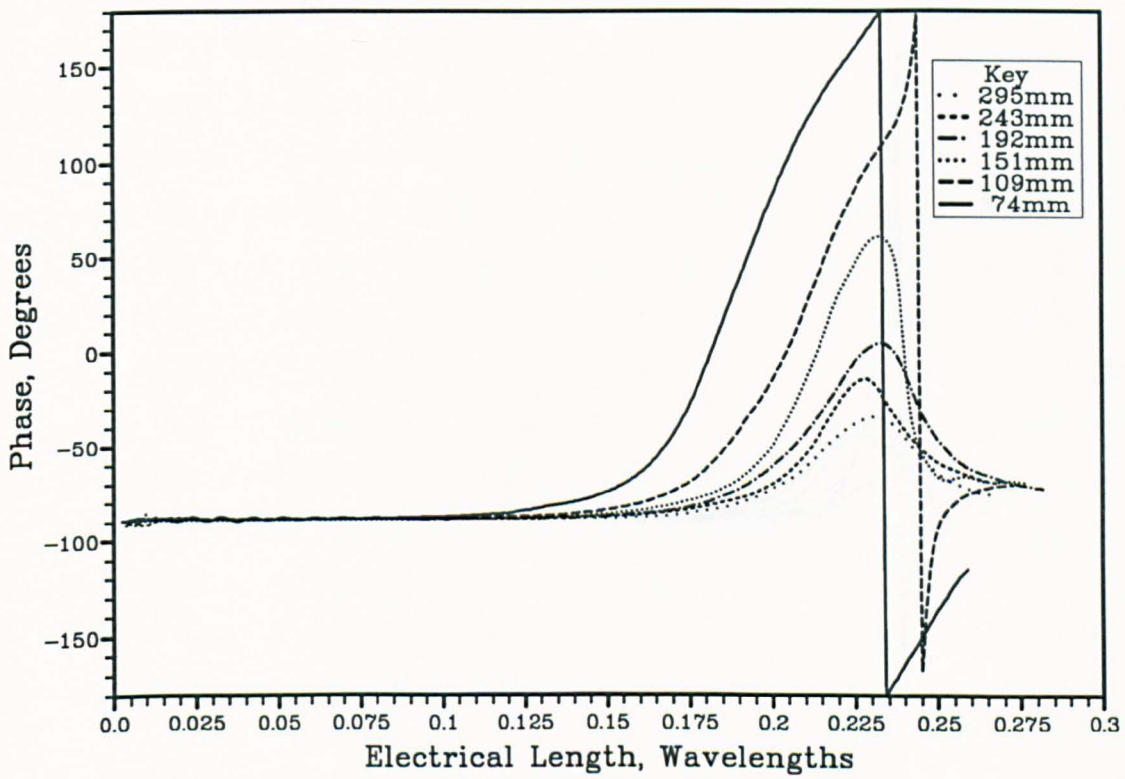


Figure 4.21: Phase of the parasitic impedance introduced by the nylon sleeve as a function of electrical length of the antenna.

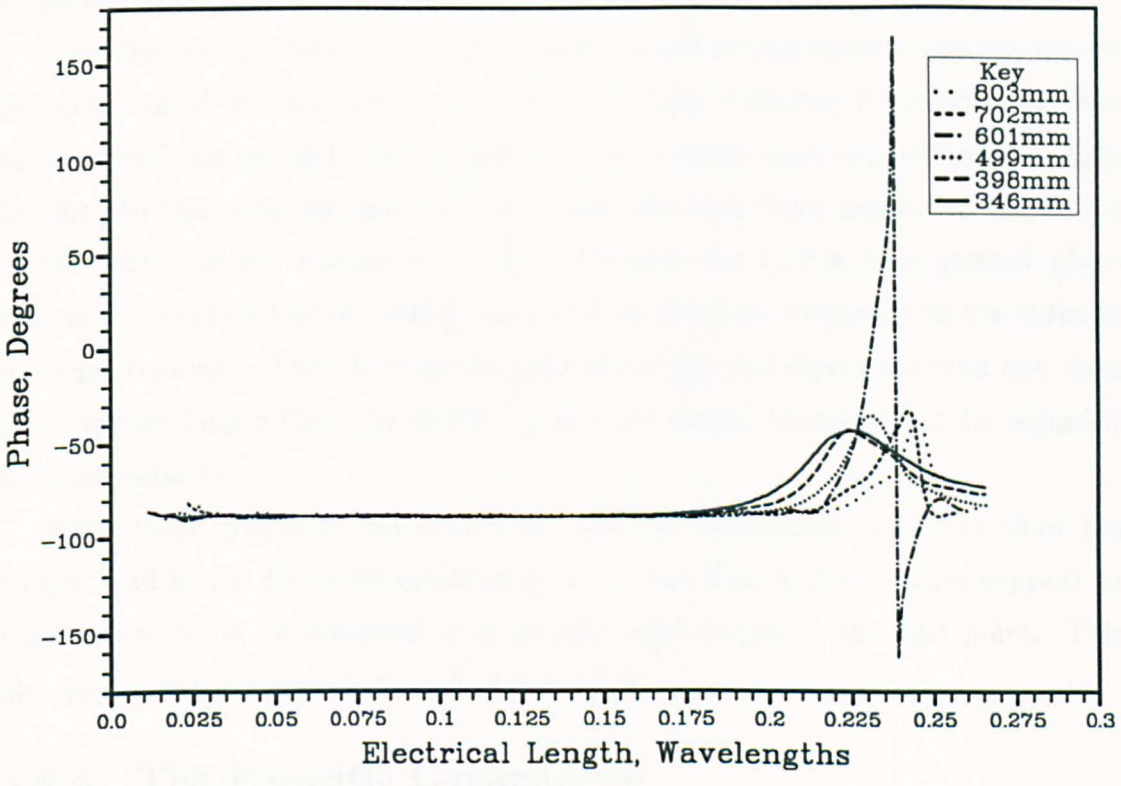


Figure 4.22: Phase of the parasitic impedance introduced by the nylon sleeve as a function of electrical length of the antenna.

Figures 4.21 and 4.22 show that that the phases of the parasitic impedances introduced by the nylon sleeve are equal to $-90°$ at frequencies below those where each of the antennas approaches resonance. This indicates that the parasitic impedance is predominantly capacitive for antennas that are electrically short. At frequencies where the antennas approach resonance, the phases of the parasitic impedances rise and then return to $-90°$ , to indicate capacitive behaviour at frequencies above resonance. The extent of this excursion from capacitive behaviour as the antenna passes through resonance is a function of its length. For the longer antennas, the excursion is small, and for antennas of length significantly greater than the support, the parasitic impedance can be regarded as capacitive at all frequencies.

The effect of the truncation of the ground plane becomes apparent on the results for antennas of 499 mm length and greater. Their resonant frequencies become elevated and the parasitic impedances cease to become more capacitive. The data for the 601 mm antenna shows a very large excursion from capacitive behaviour in the region of the resonance. This is because the 1.22 m wide ground plane beneath it becomes half of a wavelength wide at the same frequency as the antenna becomes resonant. This effect is not present for the real dipole antenna and data for antennas longer than the 499 mm monopole should therefore not be regarded as representative.

From these graphs it was concluded that, for monopoles of greater than 1 m length, and hence dipole antennas of greater than 2 m, a 10 cm nylon support at their centre could be modelled as a parallel capacitance at the feed point. This also supports the theoretical work of King [75].

### 4.6.4 The Parasitic Capacitance

It has been explained earlier in this section that the nylon support at the centre of the resonant dipole antenna can be modelled as a parasitic capacitance in parallel with the drive-point of the antenna. The values of this capacitance for the antennas in table 4.4 are shown in figures 4.23 and 4.24.

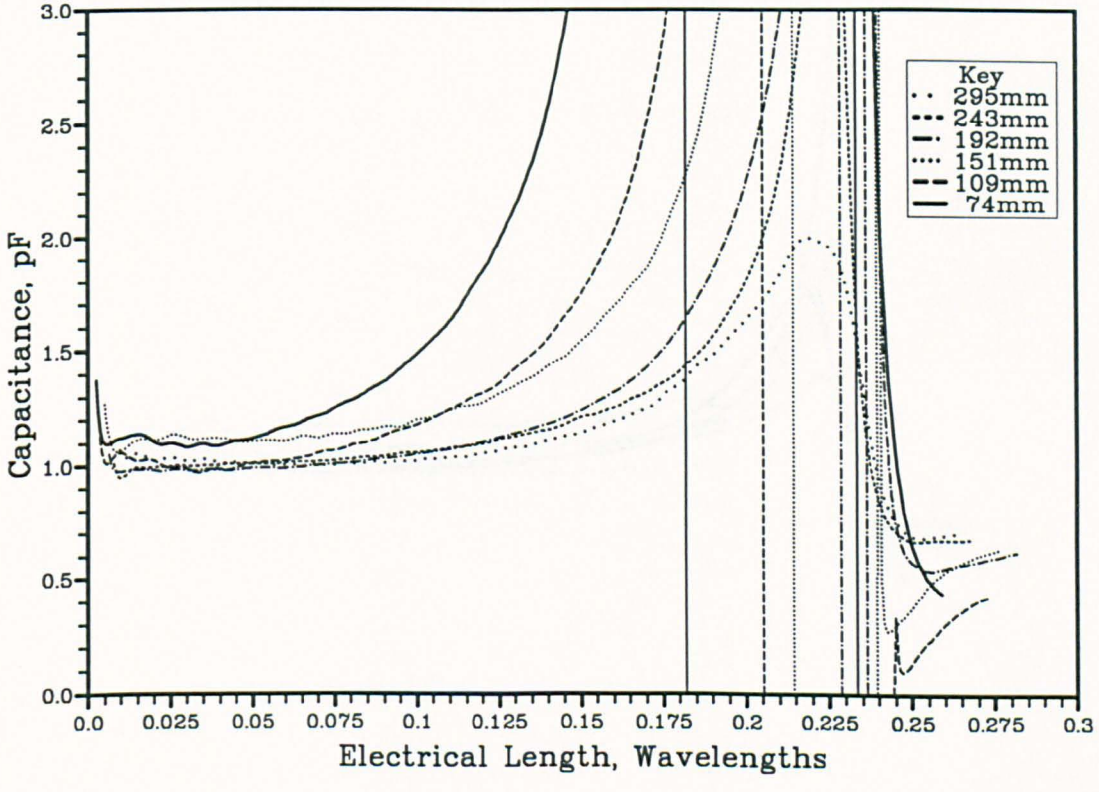


Figure 4.23: Parasitic capacitance introduced by the nylon sleeve as a function of the electrical length of the antenna.

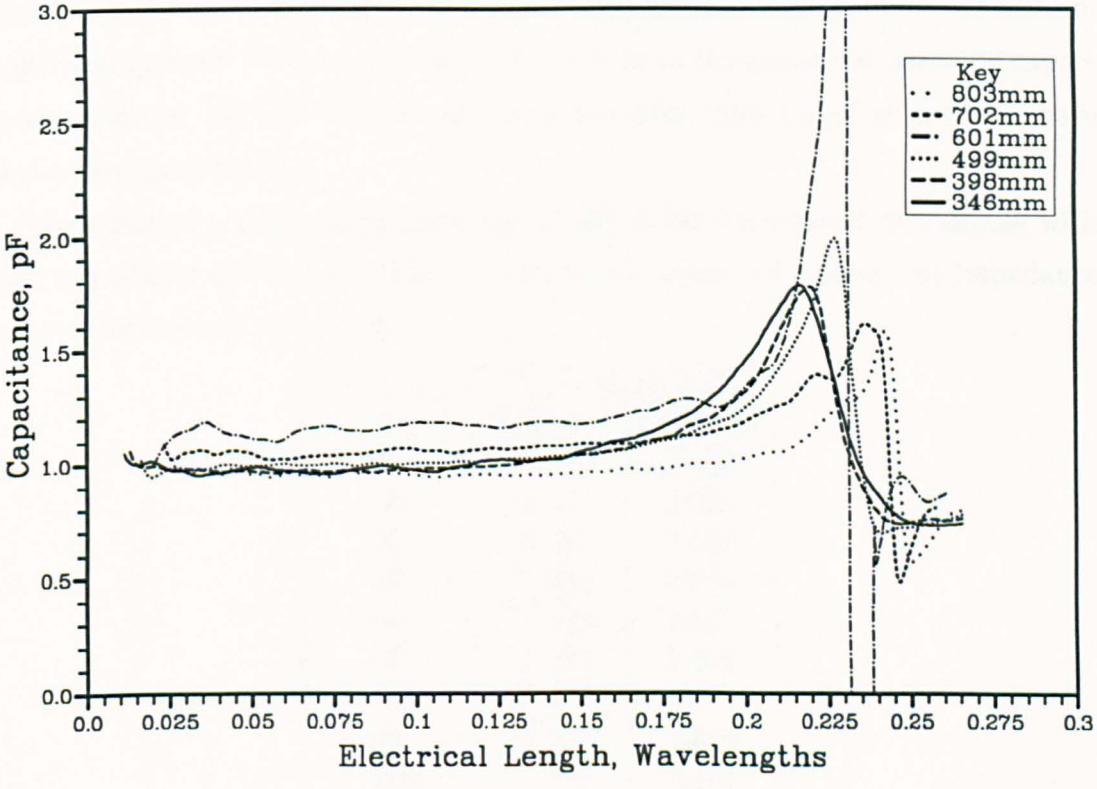


Figure 4.24: Parasitic capacitance introduced by the nylon sleeve as a function of the electrical length of the antenna.

Figures 4.23 and 4.24 show that the capacitance is constant for frequencies below those where the antennas start to become resonant but that it increases as they pass through resonance. The exact amount of this increase depends upon how much longer the antenna is than its nylon sleeve, and if the antenna is greater than 1 m high, the parasitic capacitance may be regarded as a constant value of 1.0 pF for all antenna lengths and excitation frequencies. This is the value of the parasitic capacitance for the monopole, but for an equivalent dipole its value, $C_P$, would be half of this.

$$C_P = 0.5\,\text{pF}$$

The effect of the truncation of the ground plane has been found to cause the results to become unrepresentative of a real dipole antenna for monopoles of 499 mm length and greater. This is apparent in figure 4.24 as the measured parasitic capacitance with the 499 and 702 mm antennas increases from 1.0 pF where they have shorter electrical lengths.

The effect of a shunt capacitance of 0.5 pF at the drive-point of a dipole with a self impedance of $(73 + j0)\,\Omega$ is to translate its measured drive-point impedance to the values shown in table 4.5.

| Frequency | Impedance / Ω | |
|---|---|---|
| MHz | Resistive | Reactive |
| 10 | 73.000 | 0.167 |
| 20 | 73.002 | 0.335 |
| 30 | 73.003 | 0.502 |
| 40 | 73.006 | 0.670 |
| 50 | 73.010 | 0.837 |
| 60 | 73.014 | 1.005 |
| 70 | 73.019 | 1.172 |
| 80 | 73.025 | 1.340 |
| 90 | 73.031 | 1.507 |
| 100 | 73.038 | 1.675 |

Table 4.5: Effect of a parallel parasitic capacitance of 0.5pF on the measured drive-point impedance of a dipole antenna having a self impedance of 73 Ω .

Table 4.5 shows that the presence of a nylon support does not have a significant effect on the measured resistive component of the antennas drive-point impedance, but that it does slightly increase the reactive component. This causes the antenna to resonate at a slightly shorter length than would otherwise be expected. The change in the reactive component is limited to 1.675 Ω at 100 MHz, but for antennas of this type used at higher frequencies, the effect of the support would be progressively greater. Also, a more complicated model of the support than a simple parallel capacitance would be required for dipole antennas to be used at

frequencies above 100 MHz, because they would not be appreciably longer than their supports. Alternatively, the support dimensions could be scaled with the arm lengths of the antenna so that they would remain appreciably shorter than the length of the antenna.

Although the electrical behaviour of the nylon support has been examined here, the measurements were performed on a monopole antenna with no gap at its feed point. The dipole antenna that was used did have a gap of 18 mm at its drive-point and this may have resulted in a slightly different parasitic capacitance to the one measured here. However, it has been shown that the effect of the nylon support is sufficiently small at frequencies of up to 100 MHz for this not to be a problem.

## 4.7 A Standard Biconical Antenna

A NEC model of the skeletal biconical antenna has been proposed in chapter 2 and this was used in §4.2.3 to determine its theoretical antenna factor. This antenna factor was derived assuming that the drive-point of the antenna was connected directly to a 50 Ω load. This approach was useful for determining the properties of the radiating structures in isolation, but was not very representative of the real antenna. The radiating structure of the real antenna was not connected directly to the coaxial connector, but was connected via a two-port network contained in the antenna support and shown in figure 4.25.

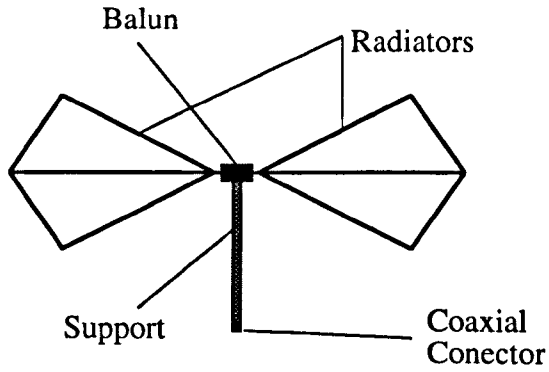


Figure 4.25: Physical structure of the real skeletal biconical antenna.

The two-port network in the antenna support consisted of a balun transformer and a length of coaxial cable. In order to obtain a useful antenna factor for comparison with the manufacturers' quoted antenna factors, and for use with measurements, it was necessary to take account of this network and derive the antenna factor in terms of the voltage delivered to a matched load at the coaxial connector of the antenna.

In this section the theoretical antenna factor of the skeletal biconical antenna is calculated from the NEC simulation of its radiating structure and the measured scattering parameters of its support and balun.

### 4.7.1 Equivalent Voltage Source

The NEC model of the skeletal biconical antenna was illuminated twice by a 1 $\mathrm{Vm}^{-1}$ plane-wave, each time with the antenna connected to a different load impedance, as shown in figure 4.26. The resulting output currents for the two different load conditions were then used to obtain the Thévenin source parameters of the antenna from equations (4.49) and (4.50).

$$V_T = \frac{I_{L1} I_{L2} (Z_{L2} - Z_{L1})}{I_{L1} - I_{L2}} \tag{4.49}$$

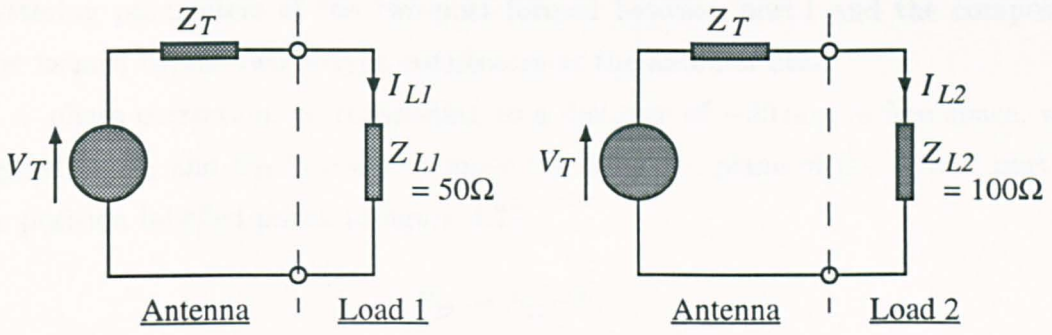


Figure 4.26: Use of NEC to determine Thévenin voltage source equivalent to an antenna under plane-wave illumination.

$$Z_T = \frac{I_{L2}Z_{L2} - I_{L1}Z_{L1}}{I_{L1} - I_{L2}} \tag{4.50}$$

The source parameters of the antenna were obtained at frequency intervals of 5 MHz throughout its specified operating range of 30–300 MHz.

### 4.7.2 Characterisation of the Balun

An experiment was devised to measure the scattering parameters of the two-port network between the coaxial connector of the real biconical antenna and its radiating structure. Figure 4.20 shows how the measurement was performed. Two jigs

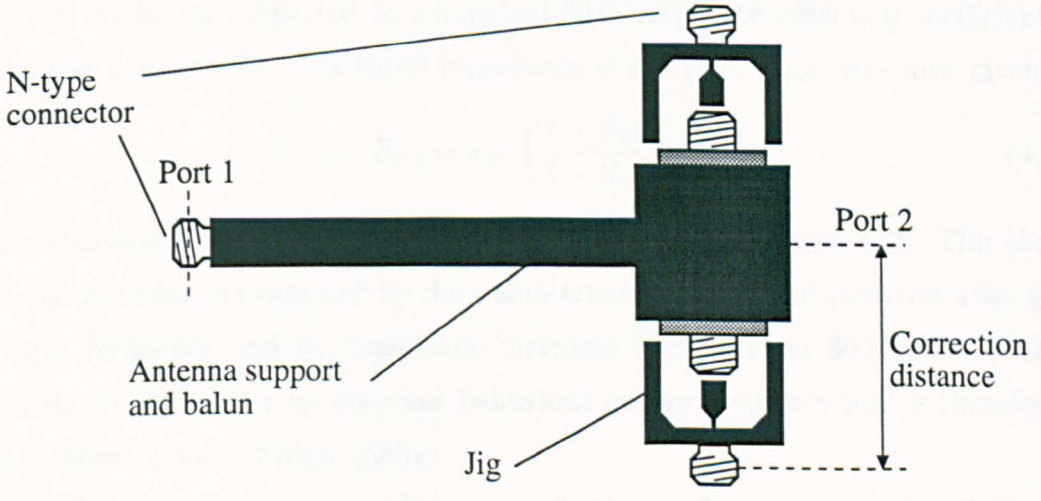


Figure 4.27: Measurement of balun scattering parameters.

were built to allow N-type connectors to be mounted in place of the cones of the antenna so that loads having known reflection coefficients could be mounted at the head of the antenna support.

Pairs of open, short, and matched loads were connected at the antenna head to establish reflection coefficients of +1, −1 and 0 respectively. Under these three loading conditions the measured reflection coefficients at port 1 were $\Gamma_{oc}$, $\Gamma_{sc}$ and $\Gamma_{mt}$. Equations (4.42) to (4.44) in §4.5.1 could then be used to calculate the

scattering parameters of the two-port formed between port 1 and the composite port formed by the two N-type connectors at the antenna head.

A phase correction, corresponding to a distance of −89 mm in free space, was applied to $S_{12}$ and $S_{22}$ in order to move the reference plane of the second port to the position labelled port 2 in figure 4.27.

$$S_{12} \rightarrow S_{12}e^{j\phi}$$
$$S_{22} \rightarrow S_{22}e^{j\phi}$$

where the phase correction, $\phi$, was given by

$$\phi = \frac{2\pi}{\lambda} \times -0.089$$

It should be noted that, because of the way in which the S-parameters were measured, the characteristic impedance of port 2, $Z_{02}$, was 100 Ω, whereas that of port 1, $Z_{01}$, was 50 Ω.

### 4.7.3 Optimal Balun Design

The measured scattering parameters of the balun were used to calculate the impedance presented by it to the radiating structure of the biconical antenna. With port 1 of the balun connected to a matched 50 Ω cable, the reflection coefficient of port 2 was equal to $S_{22}$. The input impedance of the port, $Z_{in2}$, was then given by

$$Z_{in2} = Z_{02}\left(\frac{1 + S_{22}}{1 - S_{22}}\right) \tag{4.51}$$

The resistive and reactive components of $Z_{in2}$ are shown in figure 4.28. This shows that the impedance presented by the balun transformer to the radiators rises gently with frequency and its magnitude increases from 55 Ω at 30 MHz to 95 Ω at 300 MHz. It also shows no resonant behaviour at any frequency and is therefore a well behaved device of high quality.

The balun acts as an impedance transformer and its turns ratio affects the impedance that it presents to the antenna. Careful design of the balun will result in a good match between $Z_{in2}$ and the drive-point impedance of an antenna and ideally they should be complex conjugates. Conjugate matching is very difficult to establish over a broad frequency range, such as the 30–300 MHz range that the skeletal biconical antenna is used over, but turns ratio can still have a large effect on the performance of a broadband antenna.

The self impedance of the radiators of the biconical antenna has been calculated in chapter 2 and this was used to deduce their efficiency when connected to the real

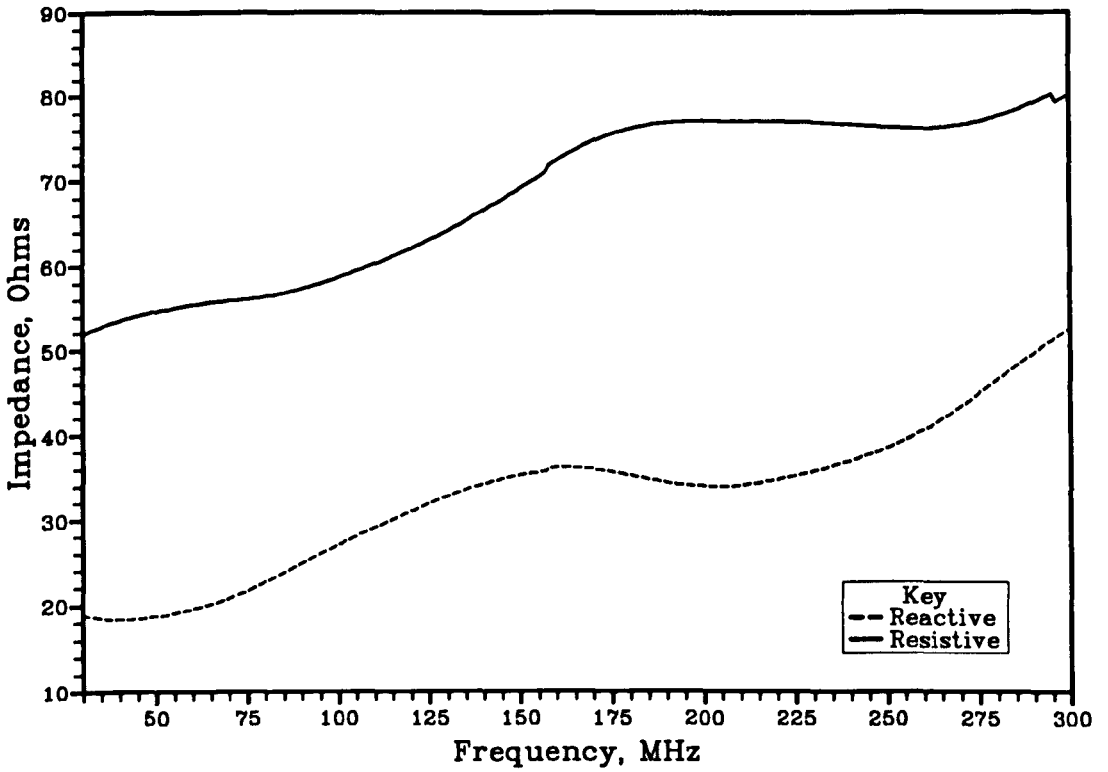


Figure 4.28: The impedance presented to the radiating structure of the skeletal biconical antenna by its balun.

balun and several fixed load impedances. The maximum power available from the radiators to the balun is $P_{max}$ and this is delivered when the balun has an input impedance equal to the complex conjugate of the impedance of the radiators. This maximum power is therefore given by

$$P_{max} = \left|\frac{V_T}{2Z_T}\right|^2 \cdot \Re\{Z_T^*\} \tag{4.52}$$

The power delivered to a general load impedance, $Z_L$, is $P_{load}$ and is given by

$$P_{load} = \left|\frac{V_T}{Z_T + Z_L}\right|^2 \cdot \Re\{Z_L\} \tag{4.53}$$

The ratio of these two powers gives the efficiency of the radiators of the biconical antenna when driven into the load $Z_L$.

$$\text{Efficiency} = \frac{P_{load}}{P_{max}} \tag{4.54}$$

Figure 4.29 shows the efficiency of the radiators when connected to the balun and when connected to baluns having input impedances of 50, 100 and 150 $\Omega$. The efficiency of the real antenna is closest to that of a 50 $\Omega$ fixed load and therefore it is probable that the turns ratio of the real balun is 1:1. This is however not necessarily an optimal turns ratio because it only gives an antenna efficiency of

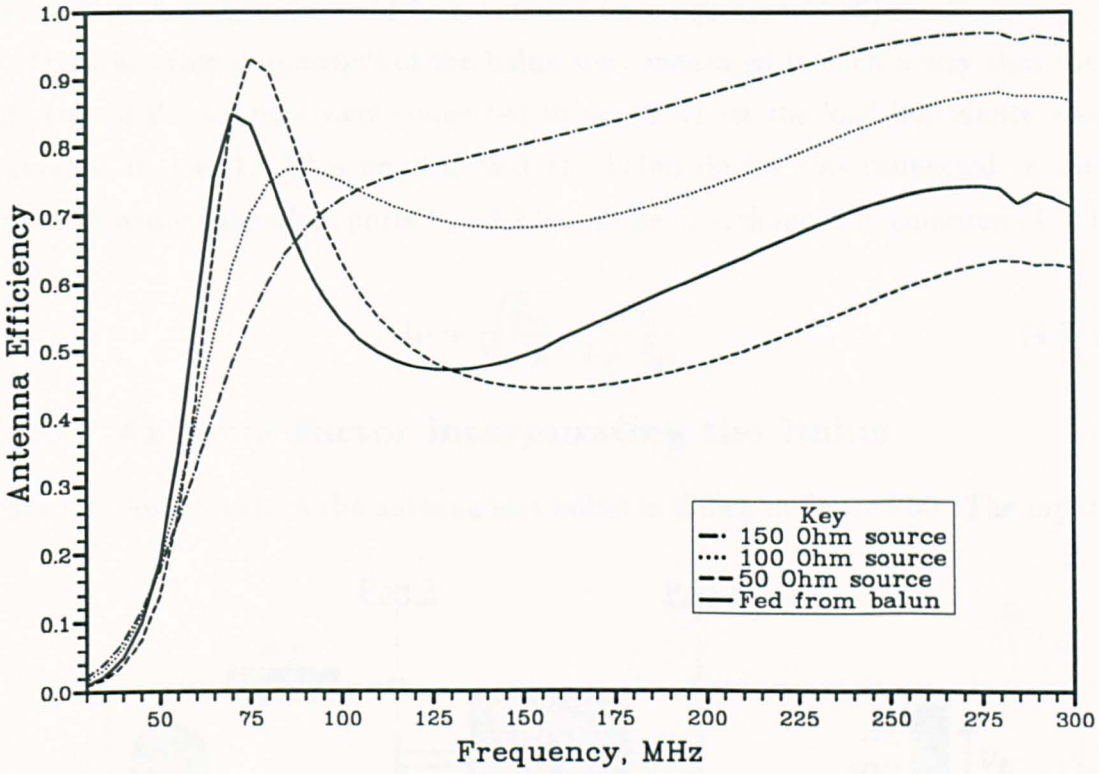


Figure 4.29: Efficiency of the skeletal biconical antenna when driven into various theoretical load impedances and when driven into the actual impedance presented by its balun.

between 50% and 70% over the majority of the frequency range. A turns ratio of $\sqrt{2}:1$ would present an impedance of $100\,\Omega$ to the radiators and give an efficiency of over 70% above 75 MHz.

The efficiency of the biconical antenna is very poor below 50 MHz with all of the impedances presented to it. This is because is becomes capacitive and it would be very difficult to develop a broadband balun capable of extracting significant power below this frequency.

### 4.7.4 Voltage Gain of the Balun

The voltage gain of a general two-port network can be calculated from signal flow graph theory in terms of its scattering parameters.

$$A_V = \sqrt{\frac{Z_{02}}{Z_{01}}} \cdot \frac{S_{21}(1-\Gamma_L)}{(1+S_{11})(1-S_{22}\Gamma_L)+S_{12}S_{21}\Gamma_L} \tag{4.55}$$

Under the conditions of a matched load impedance, so that $\Gamma_L = 0$, and a reciprocal network, so that $S_{12} = S_{21}$, equation (4.55) reduces to

$$A_V = \sqrt{\frac{Z_{02}}{Z_{01}}} \cdot \frac{S_{21}}{1+S_{11}} \tag{4.56}$$

The balun of the skeletal biconical antenna satisfied the conditions specified above, therefore its voltage gain could be calculated from equation (4.56).

The scattering parameters of the balun were measured in such a way that the radiators of the antenna were connected to port 2 whilst the load impedance was connected to port 1. This implied that the balun device was connected in the reverse direction, therefore ports 1 and 2 had to be interchanged in equation (4.56) to give

$$A_V = \sqrt{\frac{Z_{01}}{Z_{02}}} \cdot \frac{S_{12}}{1 + S_{22}} \tag{4.57}$$

### 4.7.5 Antenna Factor incorporating the Balun

The equivalent circuit of the antenna and balun is shown in figure 4.30. The input

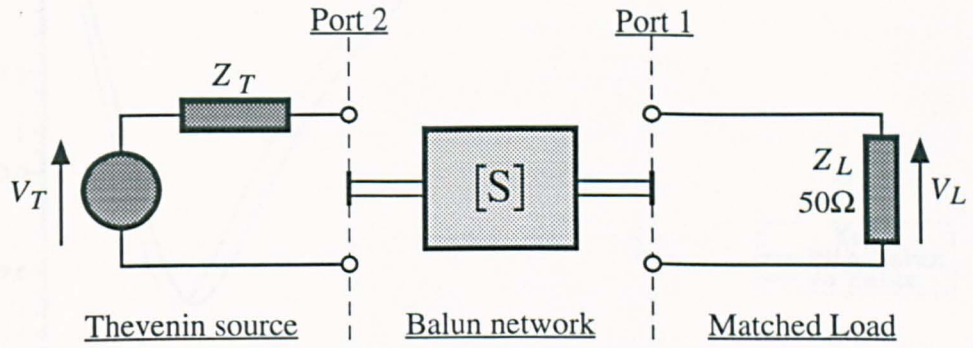


Figure 4.30: Equivalent circuit of the radiators and balun of the skeletal biconical antenna.

impedance of port 2 of the balun was calculated from equation (4.51). The input voltage at port 2 was then given by

$$\begin{aligned} V_{in2} &= \frac{V_T Z_{in2}}{Z_T + Z_{in2}} \\ &= \frac{V_T Z_{02}(1 + S_{22})}{Z_T(1 - S_{22}) + Z_{02}(1 + S_{22})} \end{aligned} \tag{4.58}$$

The output voltage from port 1, i.e. the load voltage, was given by the input voltage multiplied by the voltage gain of the balun, given by equation (4.57).

$$V_L = \frac{V_T \sqrt{Z_{01} Z_{02}} S_{12}}{Z_T(1 - S_{22}) + Z_{02}(1 + S_{22})} \tag{4.59}$$

Substituting $V_L$ into equation (4.1) gave the antenna factor as

$$AF_r = 20 \log_{10} \left| \frac{E}{V_T} \cdot \frac{Z_T(1 - S_{22}) + Z_{02}(1 + S_{22})}{S_{12}\sqrt{Z_{01} Z_{02}}} \right| \tag{4.60}$$

$E$, $V_T$ and $Z_T$ were obtained from the NEC simulation, $S_{12}$ and $S_{22}$ were the measured scattering parameters of the balun and the characteristic impedances, $Z_{01}$ and $Z_{02}$, were equal to 50 Ω and 100 Ω respectively.

### 4.7.6 Effect of the Balun

Predicted antenna factors were obtained from equation (4.60) with the antenna under plane-wave illumination. Figure 4.31 compares these antenna factors with those calculated in §4.2.3 for the radiators of the antenna with no balun.

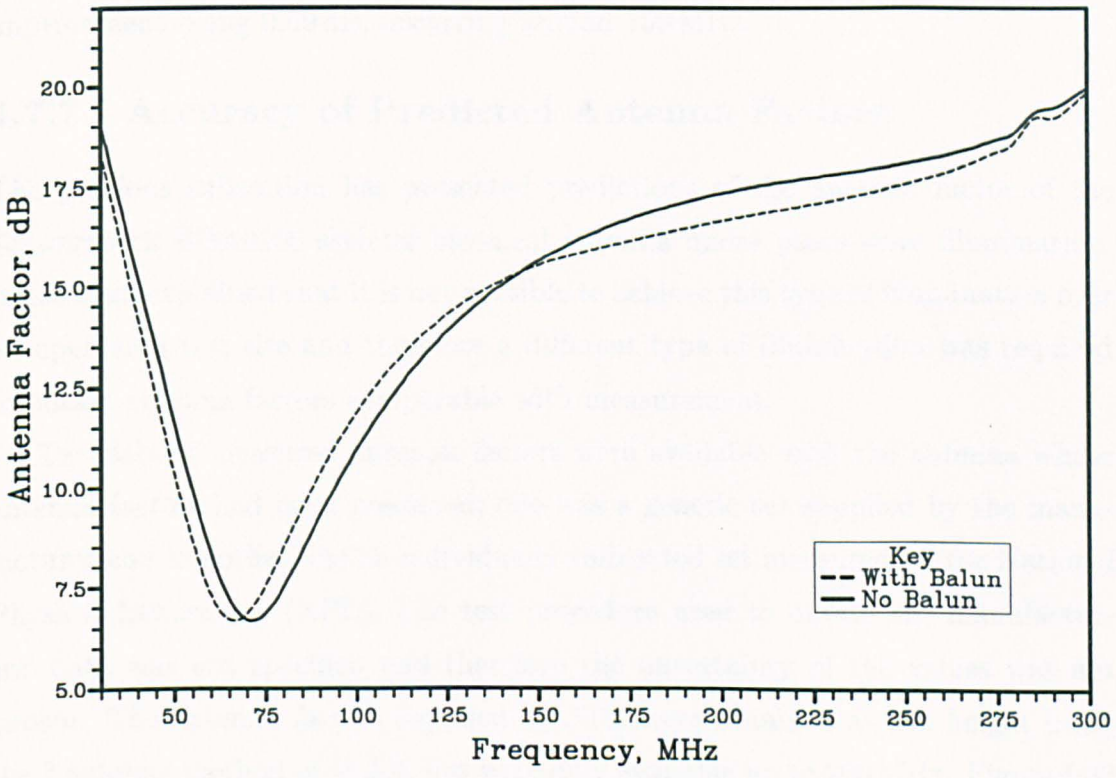


Figure 4.31: Predicted plane-wave antenna factors for the skeletal biconical antenna with and without its balun.

Figure 4.31 shows that the balun not only provides a balanced to unbalanced transformation at the feed to the antenna but that it also modifies the antenna factor appreciably. This is because the balun acts as an impedance transformer, and it has been shown in §4.7.3 that the balun of the Schwarzbeck BBA9106 antenna generally increases the impedance presented at the drive-point of that antenna from the transmission line impedance of 50 Ω.

The presence of a balun device in the feed network of a biconical antenna can either increase or reduce the antenna factor, whereas the balun of the resonant dipole antenna generally introduces a small loss at all frequencies. This is because the impedance of the biconical antenna varies as a function of frequency much more than that of the resonant dipole. It indicates that manufacturers' balun loss data should not be used to correct antenna factors obtained from simulation of the biconical antenna.

Below 69 MHz the antenna factor of the biconical antenna is reduced by the

presence of its balun and this indicates an improvement in sensitivity. The greatest improvement in sensitivity is 1.24 dB and occurs at frequencies around 50 MHz. Between 69 MHz and 145 MHz the sensitivity of the antenna is reduced, with the largest degradation in antenna factor being 1.07 dB, around 200 MHz. This is not a problem because the antenna factor is still reasonably small, i.e. less than 15 dB. Above 145 MHz the sensitivity of the antenna is improved, with the greatest improvement being 0.69 dB, occurring around 150 MHz.

### 4.7.7 Accuracy of Predicted Antenna Factors

The previous subsection has presented predictions of the antenna factor of the Schwarzbeck BBA9106 skeletal biconical antenna under plane-wave illumination. It has been explained that it is not possible to achieve this type of illumination over an open-area test site and therefore a different type of illumination was required to obtain antenna factors comparable with measurement.

Two sets of measured antenna factors were available with the antenna whose antenna factors had been predicted; one was a generic set supplied by the manufacturer and the other was an individually calibrated set measured by the National Physical Laboratory (NPL). The test procedure used to obtain the manufacturers' data was not specified and therefore the uncertainty of the values was not known. The antenna factors supplied by NPL were obtained at 2 m height using the 3 antenna method of §4.1.4, but were only available up to 200 MHz. Figure 4.32 compares both of these sets of measured antenna factors with values predicted at 2 m height using the simulations described in §4.3.

The predicted antenna factor at 2 m height is within 1 dB of the NPL measurement except between 80 and 140 MHz, where it differs by up to 1.9 dB. This is because the minimum antenna factor is predicted at a slightly different frequency to that where it is measured and the antenna factor characteristic rises steeply just outside this minima. Agreement between the two sets of data would be better, and calibration reliability thus improved, if a biconical antenna could be designed whose antenna factor did not have such a pronounced minimum.

The three antenna method for antenna calibration relies upon the use of predicted values of normalised site attenuation. These are liable to be inaccurate because they cannot properly account for the interactions that occur between closely spaced antennas. It is difficult to calculate precise uncertainty limits for antenna factors calculated by the three antenna method, but they are around 1 dB above 100 MHz, and could be up to 2 dB below 100 MHz. It is, therefore, not possible to

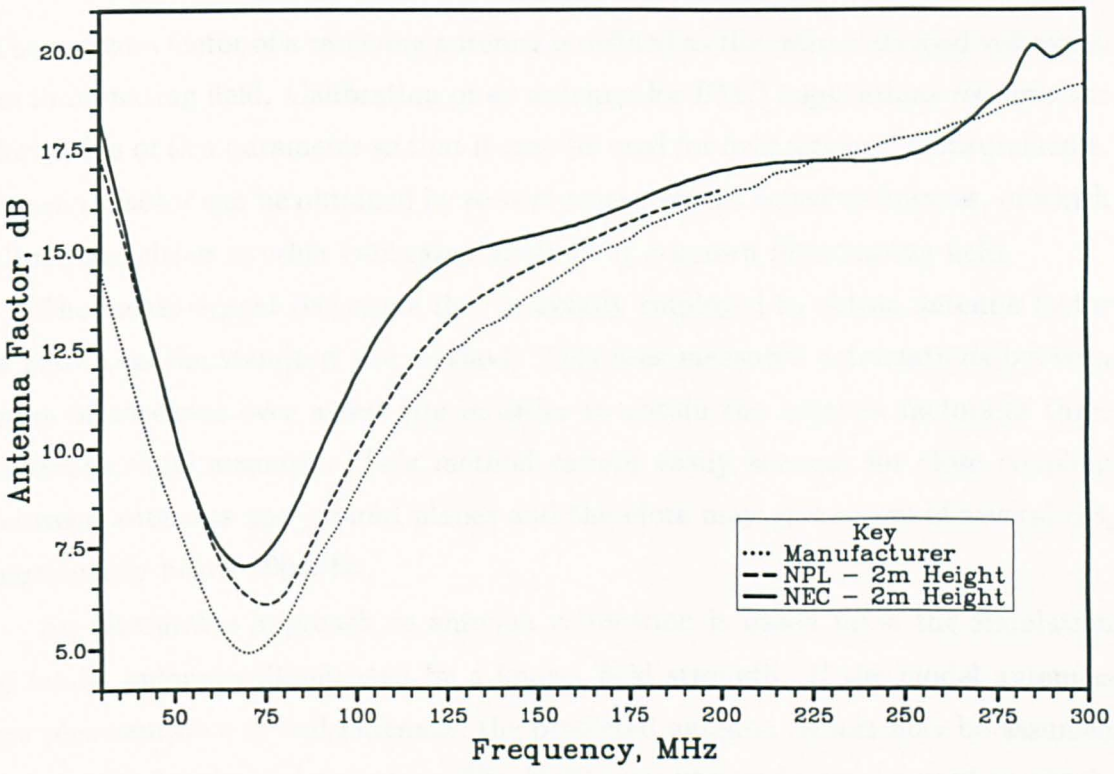


Figure 4.32: Predicted antenna factors at 2 m height compared with antenna factors measured by NPL and supplied by the manufacturer of the biconical antenna.

state that the NEC simulation is more accurate than within 2 dB.

The antenna factors provided by the manufacturer are lower than those measured by NPL and those predicted by NEC. They therefore claim that the antenna is more sensitive than it actually is. The practical implication of this is that, if the manufacturers' antenna factors are used to calculate fields illuminating the antenna, the radiation from items of equipment under test will be underestimated. This is very undesirable from an EMC point of view and therefore these antenna factors should not be used.

## 4.8 Summary and Conclusions

The antenna factor of a receiving antenna is defined as the ratio of its load voltage to its illuminating field. Calibration of an antenna for EMC applications requires the derivation of this parameter so that it may be used for field strength measurements. Antenna factor can be obtained by several measurement based techniques, of which all require either another calibrated antenna or a known illuminating field.

The measurement technique that is usually employed to obtain antenna factor is known as the standard site method. This uses measured attenuations between pairs of antennas over a test site in order to obtain the antenna factors of three antennas simultaneously. This method cannot easily account for close coupling between antennas and ground planes and therefore may give errors of several dB, particularly below 100 MHz.

An alternative approach to antenna calibration is based upon the simulation of model antennas illuminated by a known field strength. If the model antennas are representative of real antennas, the predicted antenna factors may be assumed to be valid for the real antennas. The NEC computer code can be used to obtain predicted antenna factors for wire antennas such as the resonant dipole and skeletal biconical antennas.

One advantage that computer simulation has over measurement methods is that it permits a more carefully controlled illumination of an antenna than is possible on most open-area test sites. This is because the simulations may be performed with ideal test site environments or even in free space. When an antenna is in free space, it may be illuminated with a plane electromagnetic wave in order to return its plane-wave antenna factor.

The antenna factor of a resonant dipole antenna is proportional to frequency and rises from $-2.3$ dB at 30 MHz to 17.3 dB at 300 MHz. Over the same frequency range, the behaviour of a skeletal biconical antenna is more complicated because its electrical size changes considerably. Below 70 MHz, the biconical antenna is electrically short and its impedance is capacitive. Its antenna factor therefore increases rapidly as frequency decreases due to poor matching between its impedance and a 50 $\Omega$ resistive load. Above 70 MHz, the antenna factor of the skeletal biconical antenna rises gently and is between 2 dB and 4 dB greater than that of a resonant dipole.

The effective length of an antenna is defined as the ratio of the EMF developed at its drive-point to the illuminating field strength. Antenna factor therefore depends upon both effective length and the mismatch between the drive-point

impedance of an antenna and its load. When an antenna is above a ground plane, both of these quantities may vary as functions of height. Care must be taken that, when using antennas above a ground plane, any variation in their antenna factors due to effective length or drive-point impedance changes is either insignificant or accounted for.

The NEC computer code can be used to calculate variations in the effective length and the drive-point impedance of an antenna above a ground plane. These quantities can then be used to calculate variations in the antenna factor. The antenna factor of a resonant dipole varies more at lower heights and with lower excitation frequencies. It may vary between −1.2 dB and +1.7 dB from its plane-wave value at heights above 2 m and at 1 m height above 45 MHz. At 1 m height, with excitation frequencies below 45 MHz, the antenna interacts very heavily with the ground plane and its antenna factor becomes drastically reduced. Resonant dipoles should not therefore be used below 2 m height at frequencies less than 45 MHz.

The antenna factor of the skeletal biconical antenna varies rather less than that of the resonant dipole because it is electrically short at lower frequencies. At 1 m height, the antenna factor of a horizontally polarised biconical antenna varies between −0.8 dB and +1.2 dB from its plane-wave value. At heights of 2 m and above, the antenna factor variations fall to between −0.7 dB and +0.6 dB. The antenna factor of the skeletal biconical antenna varies most at frequencies just above and below where its minimum value occurs, i.e. 75 MHz. This is because the position of the minimum shifts slightly and, if a biconical antenna could be designed with a shallower minimum in its antenna factor, the variations would be reduced.

As a horizontally polarised resonant dipole antenna is scanned from 1–4 m height above a ground plane with excitation frequencies down to 30 MHz, its effective length varies between −0.16 dB and +0.23 dB from its plane-wave value. Because these limits are so small, it is possible to calculate variations in the antenna factors of resonant dipoles purely from variations in their drive-point impedances. The effective length of the skeletal biconical antenna varies more significantly than that of the resonant dipole and the variations in its effective length are of the same order as the variations in its antenna factor. For this reason, variations in the antenna factors of skeletal biconical antennas should not be calculated purely from variations in their drive-point impedances.

Commercially available antennas intended for EMC applications do not have their connectors at their drive-points. It is not possible to electrically connect to

their drive-points and there is a two-port network containing their balun between their connectors and drive-points. It is therefore difficult to calibrate a network analyser in order to measure their drive-point impedances. An alternative design of antenna can have connectors at its drive-point if its feeding transmission line is balanced, e.g. if it is of a twin coaxial type fed from a phase splitter. A network analyser can be calibrated to measure the impedance of such an antenna at its drive-point.

If computer simulation is to be used to calibrate real antennas, the model antennas used must be representative of the real antennas. It is particularly difficult to model the feed regions of real antennas and therefore these must be designed to be as easy to simulate as possible. The resonant dipole antenna, described in this chapter, has a 10 cm long, 25 mm diameter nylon support sleeve at its drive-point. The presence of this sleeve can be modelled as a 0.5 pF capacitance in parallel with the drive-point, provided that it covers less than 10% of the total length of the antenna. The effect of such a parasitic element increases with frequency, but even at 100 MHz the self impedance of a resonant dipole is only changed from 73 Ω to $(73.038 + j1.675)\,\Omega$.

With certain types of antenna, it is possible to measure the scattering parameters of the two-port network between their connectors and their drive-points. This is only possible if their radiators can be removed and a reference plane for calibration of a network analyser can be defined in place of them. In this chapter, such a procedure was used to measure the scattering parameters of the balun of the Schwarzbeck BBA9106 biconical antenna. These were then combined with a NEC simulation of its radiators in order to calculate the plane-wave antenna factor of the complete antenna.

The balun of an antenna acts as an impedance transformer and modifies the impedance presented to the drive-point of an antenna from that of its feeding transmission line. This can have a large effect on the efficiency of an antenna and therefore also a large effect on its antenna factor. The drive-point impedance of the skeletal biconical antenna varies as a function of frequency and, to extract maximum power from it, its balun should present a conjugate impedance match at all frequencies. This would be very difficult to achieve in practice and it is more realistic to define an optimal turns ratio for the balun transformer. This appears to be around $\sqrt{2}:1$ in order to present 100 Ω to the drive-point of the antenna.

In order to have confidence in any computer model, it must be validated against measurement, but measurements themselves have associated errors. Comparison of predicted antenna factors with ones obtained using the three antenna calibration

method showed them to be accurate to within 2 dB, however the inaccuracy of the measured antenna factors was only to within 2 dB. The predicted antenna factors could therefore be more accurate than this. The antenna factors supplied by the manufacturer of this antenna were found to be considerably different to those measured or predicted, this indicates that they are inaccurate and should not be used.

An indirect method of determining the accuracy of the predicted antenna factors of a pair on Schwarzbeck biconical antennas is carried out in chapter 5. This is a comparison between measured and predicted attenuations between the antennas over an open-area test site. Unfortunately, the test site used for the measurements was not of sufficient quality to validate the antenna models to better than within 2 dB.

# Chapter 5

# Site Attenuation Results

Three different theoretical approaches to deriving predicted values of site attenuation are described in chapter 3. In this chapter, the results from these approaches are compared with each other and with measurements made on the open-area test site at the University of York in order to deduce their respective limitations and accuracies.

The simplest model used for the calculation of site attenuation, neglects the finite size of real antennas and only considers radiative coupling between them. The applied EMF method offers improvement over this by assuming the current distribution on resonant dipole antennas to be sinusoidally distributed along their lengths. This allows it to consider mutual coupling effects between real antennas, but it cannot analyse antennas other than resonant dipoles. The most rigorous site attenuation model employed the NEC computer code to calculate site attenuation between pairs of resonant dipoles and skeletal biconical antennas. NEC numerically solves integral equations to calculate a representation of the current distribution on antennas, it was therefore assumed to yield the most accurate predicted values of site attenuation.

In §5.1, predicted values of classical site attenuation are calculated for resonant dipole antennas using the NEC computer code. The results are presented graphically for 3 m and 10 m test sites with transmitting antenna heights of 1 m and 2 m and both horizontally and vertically polarised antennas. The form of each of the graphs is discussed in terms of interfering direct and reflected waves travelling over the test site and close coupling effects between the antennas and the ground plane.

NEC was the most rigorous of the approaches used to calculate predicted values of site attenuation. §5.2 compares predictions from NEC with predictions from the two simpler models in chapter 3. The differences between the models are discussed and used to deduce limits to the accuracy of each model for the different site configurations.

Experimentally measured classical site attenuation is compared with predictions from NEC in §5.3 and the correlation between the two data sets is used to assess the performance of the York open-area test site. The antennas used for the measurement were of a commercially available resonant dipole type, having telescopic arms. The baluns of these antennas were integral parts of their structures and prevented a rigorous comparison between measured and predicted site attenuations because they were not appropriately calibrated.

A more rigorous comparison of measured test site propagation characteristics with predicted ones is performed in §5.4. A specialised type of resonant dipole antenna was used for these measurements and is described in chapter 4. It had a balanced feed network and terminals at its drive-point so that measured and predicted site insertion losses between pairs of such antennas could be compared.

In §5.5, a swept measurement of site attenuation from 30–300 MHz is performed with horizontally polarised biconical antennas over 3 m and 10 m test sites. The results are compared with theoretical values obtained from NEC so that the detailed behaviour of the York open-area test site can be examined over a continuous frequency range. The results are used to deduce the effect of peripheral buildings on the performance of the test site.

§5.6 discusses normalised site site attenuation and argues its limitations as tool for test site validation, before §5.7 summarises the conclusions of this chapter.

## 5.1 Classical Site Attenuation between Resonant Dipoles

In this section, definitive values of classical site attenuation between resonant dipole antennas are calculated using the NEC computer code. The data are calculated for all of the spatial geometries usually used with 3 m and 10 m test sites, i.e. transmitting antenna heights of both 1 m and 2 m and both horizontally and vertically polarised antennas. The results are explained in terms of the coupling between the pairs of object and image antennas above and below the ground plane.

It is usual to calculate site attenuation at around thirty frequencies that are spread approximately logarithmically from 30 MHz to 1 GHz. This is not a sufficient number of data points to give continuous theoretical curves and so the data presented in this chapter have been calculated at 100 frequencies, with correct logarithmic spacing over the frequency range. This implied a scaling ratio of

$$e^{\frac{1}{99}\ln\left(\frac{1000}{30}\right)} = 1.036054529$$

between adjacent frequency points.

Although the data presented in this section have not been calculated at the usual frequencies specified in EMC standards, a suitable interpolation algorithm can give site attenuation at any required frequency.

### 5.1.1 Resonant Lengths

Before site attenuation could be calculated, it was necessary to determine the resonant length of a dipole antenna at each of the 100 excitation frequencies. The calculations were performed for a 6.35 mm diameter dipole, although it has been shown in chapter 4 that the impedance and antenna factor of a dipole at resonance are not significant functions of its radius. This means that site attenuation results calculated for the 6.35 mm dipole are equally valid for resonant dipoles having other radii of practical dimensions.

The impedance of the dipole was calculated at ten lengths between $0.85\lambda/2$ and $\lambda/2$ at each frequency. This gave values of the reactive component of antenna impedance in the region that passed through zero. Applying a polynomial fit, and solving for zero reactance, then gave the resonant length of the antenna at each frequency. This procedure is illustrated by figure 5.1.

The data of resonant length at each of the 100 excitation frequencies were written to a file that was accessed by the NEC simulations, described in the next section. They are also given in appendix F.

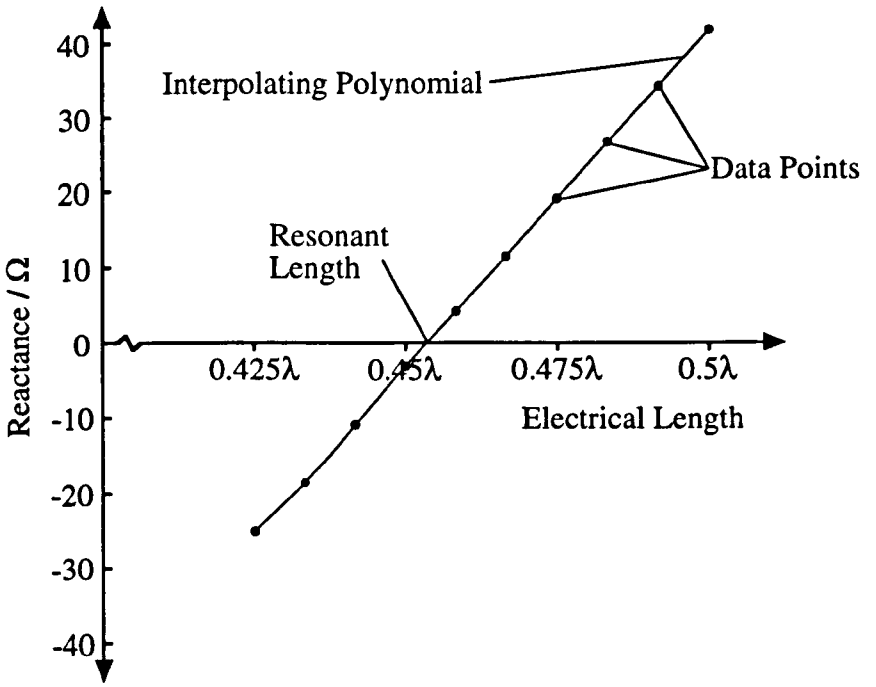


Figure 5.1: Use of polynominal curve fit to determine the exact resonant length of a dipole antenna from its reactance at several lengths close to resonance.

### 5.1.2 Calculation of Site Attenuation

The details of the NEC simulation are described in chapter 3 and so do not need repeating here. It was performed for a pair of resonant dipole antennas over a perfectly reflecting ground plane, fed from matched 50 Ω transmission lines, in order to give the classical site attenuation.

Attenuation data were generated for the 3 m and 10 m test site, with the transmitting antenna at a height of 1 m and 2 m above the ground plane, and both horizontally and vertically polarised antennas, i.e. eight data sets in all. The receiving antenna was scanned from 1 m to 4 m in increments of 2 cm so that each of the data sets contained 15100 attenuation values (151 receiving antenna heights for each of the 100 frequencies). Each of these data sets was then stored as a site transfer file.

Site attenuation was calculated for each site configuration as the minimum value of attenuation present within the receiving antenna height scan range at every frequency. The attenuation varied sufficiently gently as a function of mast height that scanning the receiving antenna in 2 cm increments did not give more than 0.05 dB of error from the minima that would have been predicted by a smooth scan. The predicted results for site attenuation are shown in figures 5.2 and 5.3 for the site configurations with horizontally and vertically polarised antennas respectively.

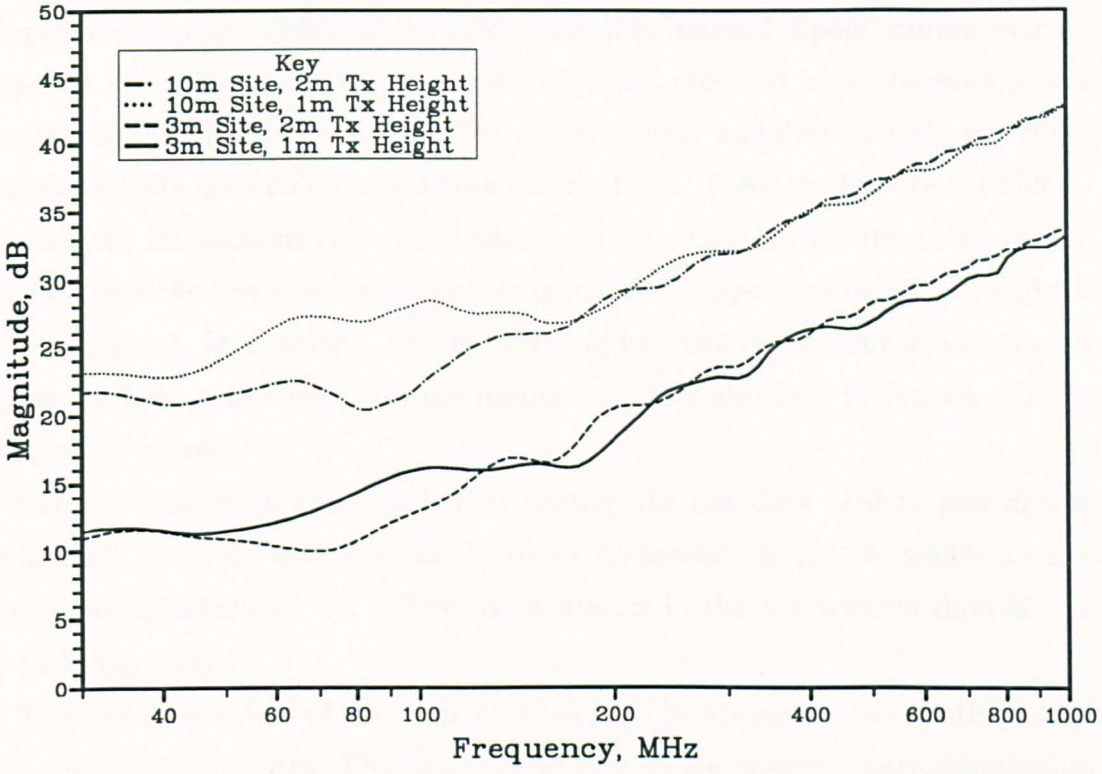


Figure 5.2: Horizontally polarised classical site attenuation between resonant dipole antennas predicted using NEC.

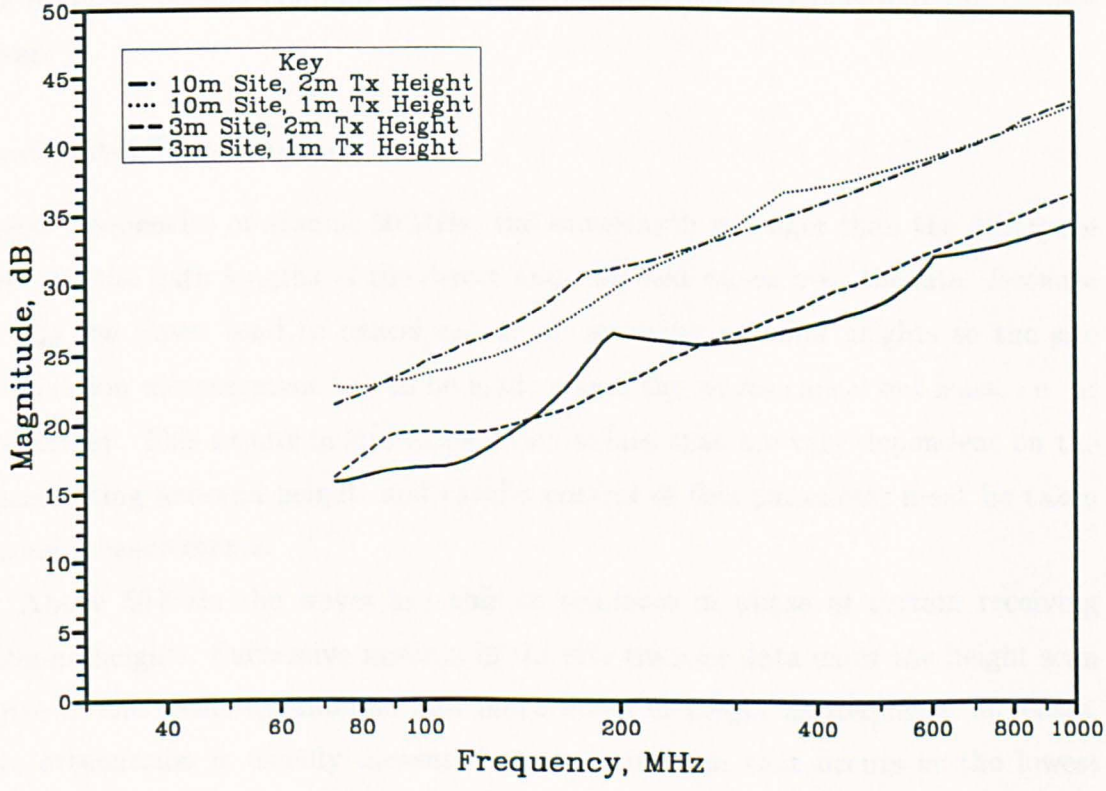


Figure 5.3: Vertically polarised classical site attenuation between resonant dipole antennas predicted using NEC.

### 5.1.3 Interpretation of the Site Attenuation Results

Chapter 1 describes models of the fields from infinitesimal dipole sources over an ideal test site. These models show how direct and reflected waves between a pair of antennas over a test site can interfere constructively and destructively according to the exact site geometry and antenna polarisations. These models are not able to consider the interactions that occur when real antennas, having finite size, couple together over the test site, but do enable many of the aspects of figures 5.2 and 5.3 to be explained. In chapter 4, mutual coupling between real antennas and ground planes has been considered, and the results from this also help to explain the site attenuation curves.

Tables are given in appendix F that contain the raw data used to plot figures 5.2 and 5.3. Data are also given of the receiving antenna heights at which the site attenuation is measured, i.e. where the minimum in the site transfer data occurs for each frequency.

The site attenuation of the 10 m sites tends to be approximately 10 dB greater than that of the 3 m sites. This is a consequence of the inverse square relationship of coupled power with the separation distance of antennas.

Above 200 MHz the results for the 1 m and 2 m transmitting antenna heights are very similar, but they are markedly different below that frequency because of the different mutual couplings that occur between the antennas and the ground plane.

#### Horizontal Polarisation

Below frequencies of around 50 MHz, the wavelength is longer than the difference between the path lengths of the direct and reflected waves over the site. Because of this the waves tend to cancel out at all receiving antenna heights so the site attenuation measurement has to be made where the waves cancel out least, i.e. at 4 m height. This results in site attenuation values that are very dependent on the transmitting antenna height, and careful control of this parameter must be taken during measurements.

Above 50 MHz the waves are able to reinforce in phase at certain receiving antenna heights. Successive minima in the site transfer data enter the height scan range of the receiving antenna and move down in height as frequency increases. Site attenuation is usually measured at the minimum that occurs at the lowest height because the path lengths are shortest, and therefore the field strengths are greatest, at the lower heights.

At certain frequencies a minimum in the site transfer function occurs just below 1 m height, with the next minimum being higher up the mast. Under these conditions the measurement tends to be made at 1 m height.

Below 200 MHz and above 50 MHz there is a tendency for the 10 m site measurements to be made at 4 m height rather than at a minimum. This is because the minimum that does occur at a lower height is more shallow due to the influence of mutual coupling effects between the receiving antenna and the ground plane.

### Vertical Polarisation

Measurements with vertically polarised resonant dipole antennas cannot be made below 75 MHz because the antenna tips will be in collision with the ground plane. No data are therefore shown in figure 5.3 below 75 MHz.

The reflected wave does not suffer a phase inversion on reflection with vertically polarised antennas, and therefore the first maximum in field strength occurs with a receiving antenna height at ground plane level, i.e. outside the usual scan range of 1–4 m. Because of this there is a tendency for measurements to be made on the edge of this maximum, at 1 m height, particularly at lower frequencies where no other maxima exist within the scan range. The mutual coupling between the receiving antenna and the ground plane is strongest at lower frequencies and tends to offset the tendency to perform a measurement at 1 m height. The minimum attenuation between vertically polarised antennas therefore occurs at somewhat greater than 1 m height below 120 MHz.

Above 200 MHz further attenuation minima start to move down in mast height so that, as for the horizontal polarisation case, measurements tend to be performed at the minimum that occurs at the lowest height within the scan range.

The cusps in the curves, that are particularly apparent for the 3 m site with a 1 m transmitting antenna height, occur where the measurement height changes from an attenuation minimum at one height to one at a very different height. Usually, one of these measurement positions is at 1 m height and the other is towards the top end of the receiving antenna height scan range, so they both give a larger attenuation than would result from a measurement at a true minimum at a lower height.

## 5.2 Comparison of Site Attenuation Models

In chapter 3, three different modelling approaches are described for the calculation of classical site attenuation between resonant dipole antennas. The Smith model uses geometric optical theory to calculate site attenuation with purely radiative coupling between infinitesimally small antennas. This is clearly not very representative of a site attenuation measurement carried out with resonant dipole antennas, but the accuracy of the model and the limits to the validity of its assumptions are not immediately clear.

A more rigorous model for site attenuation between resonant dipoles is based upon the applied EMF method, that assumes a sinusoidally distributed current along the length of each antenna. This model does fully account for the interactions that occur between antennas of finite size but the implications for accuracy of using a simplified current distribution are not clear.

In this section the two simpler models mentioned above will be compared with the more accurate results from the NEC computer code in order to deduce their usefulness for test site validation. Figures 5.4 to 5.7 show the results of this comparison. Each graph shows the data for both the 3 m and 10 m sites with one of the transmitting antenna heights and antenna polarisations.

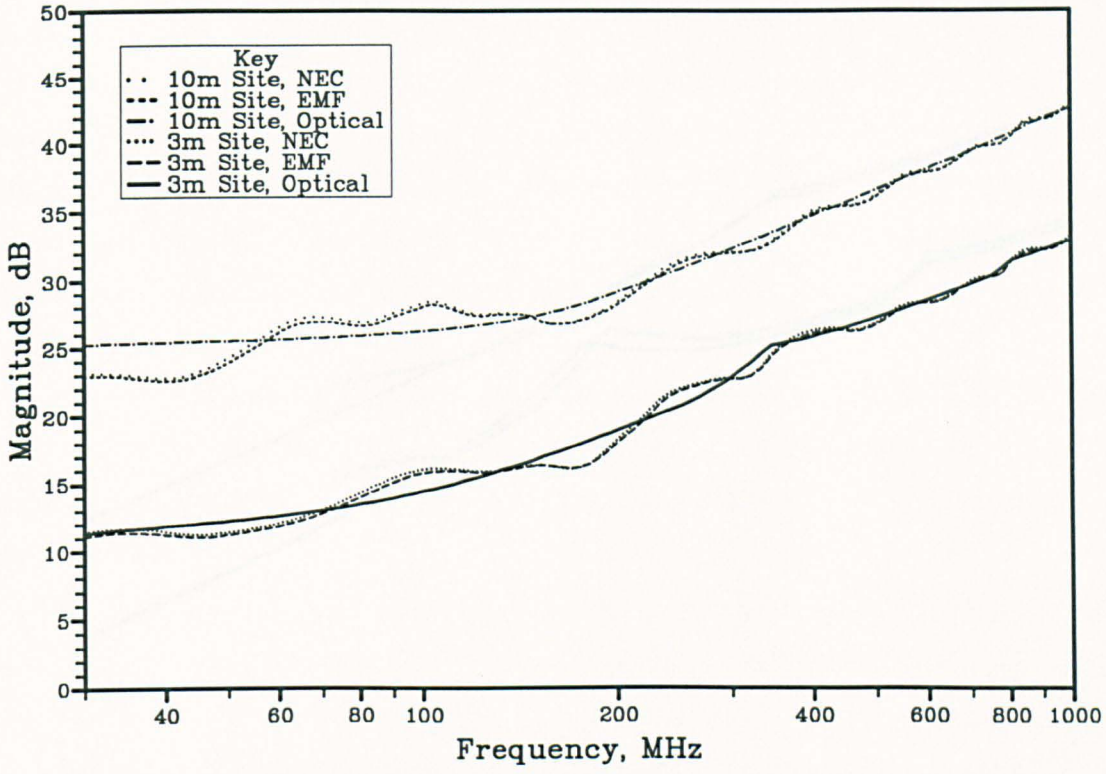


Figure 5.4: Comparison of horizontally polarised classical site attenuation predictions. 3 m and 10 m sites with a 1 m transmitting antenna height.

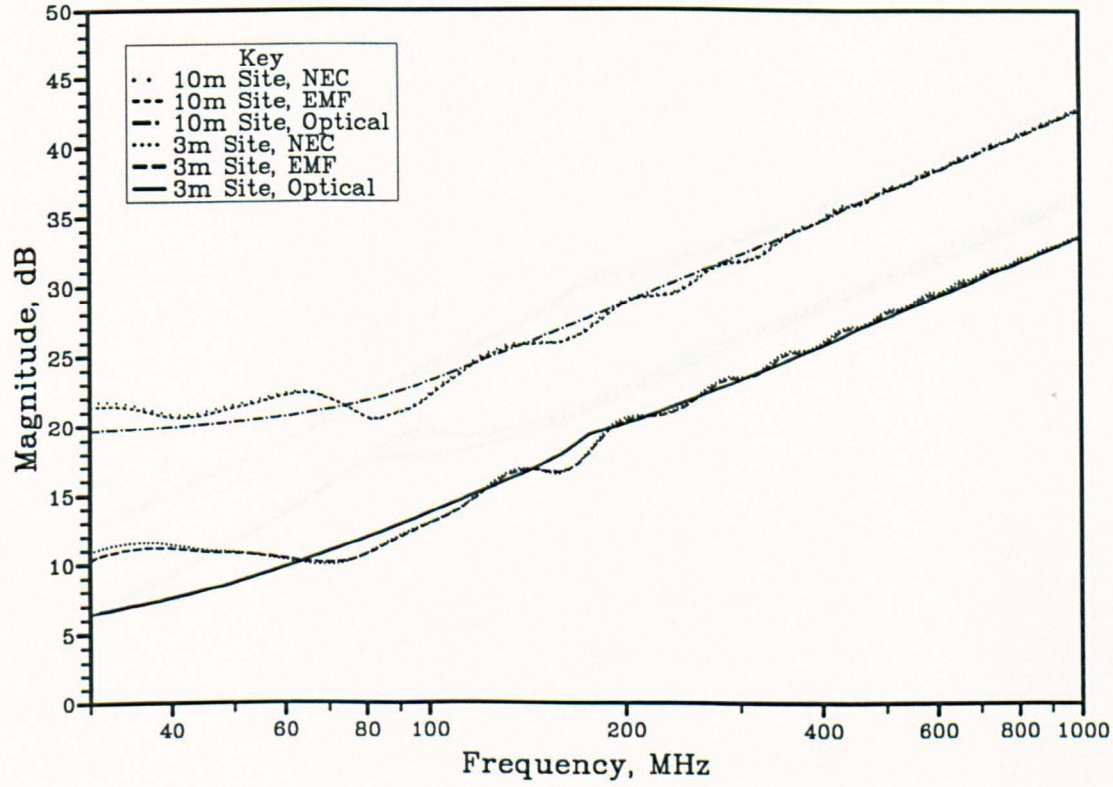


Figure 5.5: Comparison of horizontally polarised classical site attenuation predictions. 3 m and 10 m sites with a 2 m transmitting antenna height.

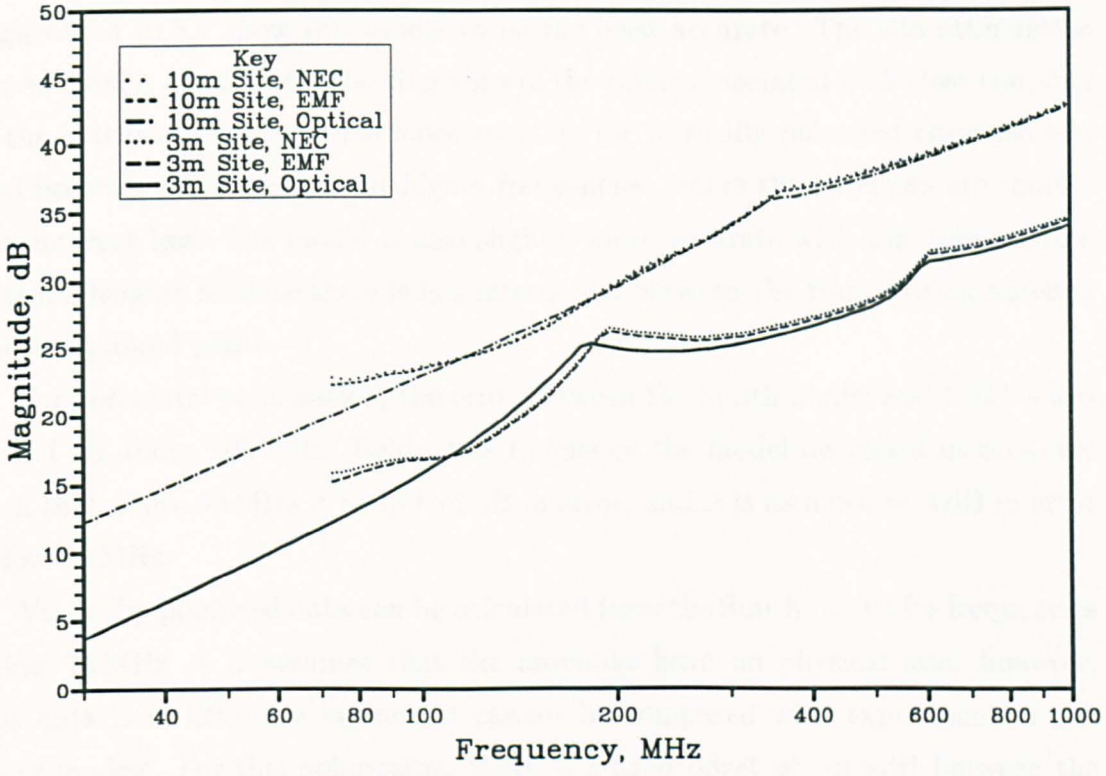


Figure 5.6: Comparison of vertically polarised classical site attenuation predictions. 3 m and 10 m sites with a 1 m transmitting antenna height.

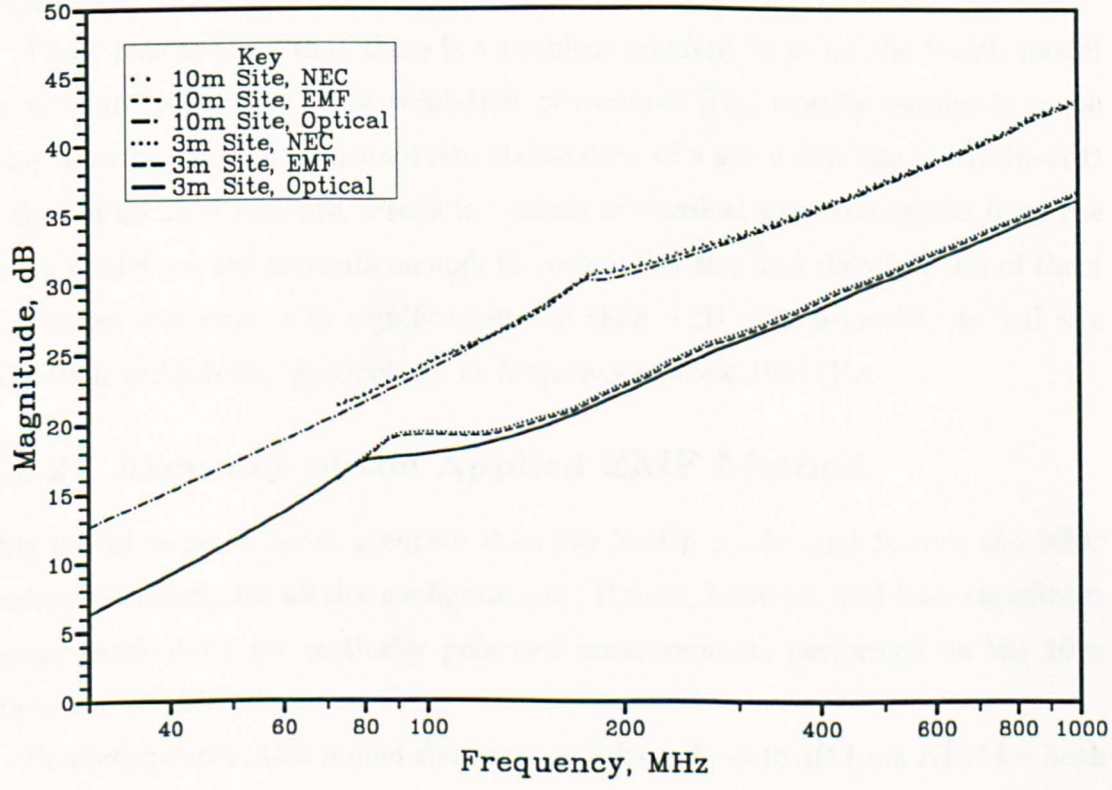


Figure 5.7: Comparison of vertically polarised classical site attenuation predictions. 3 m and 10 m sites with a 2 m transmitting antenna height.

### 5.2.1 Accuracy of the Smith Model

Figures 5.4 to 5.7 show this model to be the least accurate. The site attenuation curves from it are smooth, showing none of the ripple associated with close coupling of the antennas. The model is more accurate for vertically polarised antennas and also becomes more accurate at higher frequencies, where the antennas are smaller and interact less. The model is also slightly more accurate with 2 m transmitting antenna heights because there is less interaction between the transmitting antenna and the ground plane.

For horizontal polarisation, the error between the Smith model and NEC is less than 1 dB above 200 MHz. Below this frequency the model decreases in accuracy such that above 60 MHz it is up to 2 dB in error, and it is as much as 4 dB in error below 60 MHz.

Vertically polarised data can be calculated from the Smith model for frequencies below 75 MHz as it assumes that the antennas have no physical size; however, this data is of little use because it cannot be compared with experiment or the other models. For this polarisation there is a fixed offset of −0.5 dB between the Smith model and NEC, superimposed on a ripple that becomes less with increasing frequency. Numerically the discrepancy between this model and NEC is less than 1 dB above 300 MHz, less than 1.5 dB above 100 MHz and up to 3.5 dB at the lowest frequencies.

These results show that there is a problem inherent in using the Smith model for test site validation. Site validation procedures [76], usually require it to be demonstrated that the measured site attenuation of a given test site is within 4 dB of that of an ideal test site. Predicted values of classical site attenuation from the Smith model are not accurate enough to accomplish this and therefore use of them may cause test sites with significantly less than 4 dB of non-ideality to fail site validation procedures, particularly at frequencies below 100 MHz.

### 5.2.2 Accuracy of the Applied EMF Method

This model is much more accurate than the Smith model and follows the NEC predictions closely for all site configurations. It does, however, still have significant errors, particularly for vertically polarised measurements performed on the 10 m site below 100 MHz.

Predictions from this model show a fixed offset of −0.18 dB from NEC for both polarisations, upon which a ripple is superimposed. The reason for this is associated with the inaccuracy of the self impedances predicted by the applied EMF method.

This gives antenna self impedances of between 55 Ω and 65 Ω instead of the correct value of 73 Ω . Consequently, the antennas are predicted to be better matched to their 50 Ω transmission lines than is actually the case, and therefore less attenuation is predicted.

With horizontally polarised antennas, the total error is less than 0.25 dB above 250 MHz, less than 0.4 dB above 40 MHz and 0.6 dB at the lowest frequencies. With a better self impedance calculation, these errors could be reduced by a further 0.15 dB.

Errors are slightly smaller for the vertical polarisation and again are dominated by the 0.18 dB offset. If this is ignored, vertically polarised errors are less than 0.1 dB above 100 MHz. Below this frequency the data with 2 m transmitting antenna heights are still within 0.1 dB, but the total error with 1 m height increases to 0.6 dB. The reasons for this were investigated by plotting the current distribution on a vertically polarised resonant dipole antenna at a low height and with a low excitation frequency.

NEC was used to simulate a resonant dipole antenna at 1 m height above a ground plane. An excitation frequency of 72.725 MHz was chosen to give an antenna half-length of 981.192 mm (appendix 6) and the antenna radius was set to 3.175 mm. 21 segments were used to model the antenna and the middle segment was excited by a voltage of 1 V. The predicted currents on all the segments were normalised to the current on the centre segment and figure 5.8 compares this actual distribution with the assumed sinusoidal distribution of the applied EMF method.

Figure 5.8 shows that the current distribution on the antenna has become asymmetric with its maximum no longer occurring at the centre of the antenna. This is because there is a large amount of interaction between the antenna and the ground plane and causes the sinusoidal current distribution assumed by the applied EMF method to become less representative of the current on the real antenna.

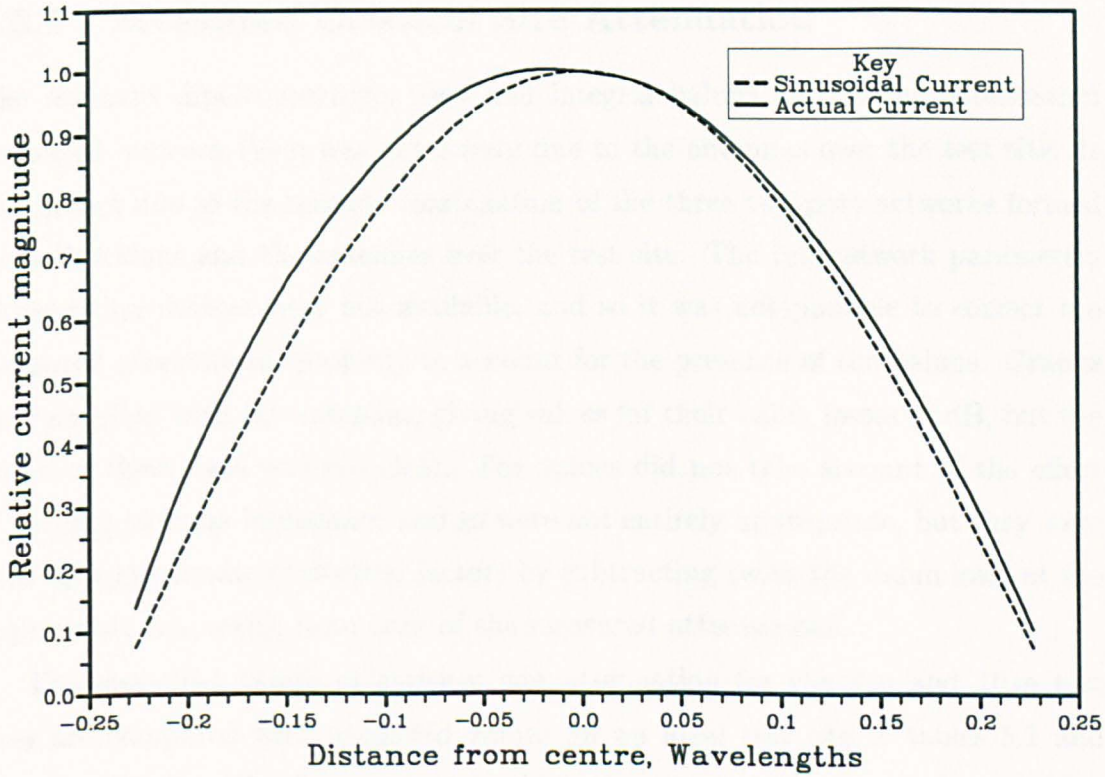


Figure 5.8: Asymmetry of the current distribution of a vertically polarised resonant dipole antenna at 1 m height above a ground plane and with an excitation frequency of 72.725 MHz.

## 5.3 Test Site Validation using Classical Site Attenuation

As part of a programme to obtain NAMAS accreditation for the open-area test site facility at the University of York, its site attenuation was measured with a pair of commercially available resonant dipole antennas with conventional telescopic arms. Measurements were only made with horizontally polarised antennas and a transmitting antenna height of 2 m. In this section, the measurements of site attenuation are compared with predicted values from NEC in order to deduce the quality of the York open-area test site.

### 5.3.1 Measured Classical Site Attenuation

The resonant dipole antennas used had integral baluns and so the attenuation measured between them was not purely due to the antennas over the test site. It was in fact due to the cascade combination of the three two-port networks formed by both baluns and the antennas over the test site. The full network parameters of the balun devices were not available, and so it was not possible to correct the measured attenuations properly to account for the presence of the baluns. Graphs were supplied with the antennas, giving values for their balun losses in dB, but the origin of these data was not clear. The values did not take account of the effect of varying antenna impedance and so were not entirely appropriate, but they were used as approximate correction factors by subtracting twice the balun loss, at the appropriate frequency, from each of the measured attenuations.

The measured values of classical site attenuation for the 3 m and 10 m test sites are compared with predicted values for an ideal test site in tables 5.1 and 5.2 respectively. The frequencies at which the comparisons are made are those specified in EMC standards [77] and are assumed to be sufficiently close together to indicate any site imperfections.

| Frequency MHz | Balun Loss dB | Site Attenuation / dB | | | |
|---|---|---|---|---|---|
| | | Measured | Corrected | NEC | Error |
| 30 | 0.3 | 9.2 | 8.6 | 10.9 | 2.3 |
| 40 | 0.5 | 12.0 | 11.0 | 11.4 | 0.4 |
| 50 | 0.8 | 11.4 | 9.8 | 10.8 | 1.0 |
| 60 | 1.0 | 11.8 | 9.8 | 10.3 | 0.5 |
| 70 | 0.3 | 9.8 | 9.2 | 9.9 | 0.7 |
| 80 | 0.3 | 9.8 | 9.2 | 10.7 | 1.5 |
| 90 | 0.5 | 12.2 | 11.2 | 12.0 | 0.8 |
| 100 | 0.6 | 12.4 | 11.2 | 12.9 | 1.7 |
| 125 | 1.0 | 16.4 | 14.4 | 15.8 | 1.4 |
| 150 | 0.4 | 17.4 | 16.6 | 16.6 | 0.0 |
| 175 | 0.2 | 18.0 | 17.6 | 17.9 | 0.3 |
| 200 | 0.2 | 19.4 | 19.0 | 20.5 | 1.5 |
| 225 | 0.2 | 21.6 | 21.2 | 20.8 | −0.4 |
| 250 | 0.3 | 21.2 | 20.6 | 21.6 | 1.0 |
| 275 | 0.3 | 22.2 | 21.6 | 23.0 | 1.4 |
| 300 | 0.3 | 23.4 | 22.8 | 23.5 | 0.7 |
| 350 | 0.4 | 25.8 | 25.0 | 25.2 | 0.2 |
| 400 | 0.7 | 27.2 | 25.8 | 25.9 | 0.1 |
| 450 | 0.3 | 27.0 | 26.4 | 27.1 | 0.7 |
| 500 | 0.3 | 29.4 | 28.8 | 28.2 | −0.6 |
| 550 | 0.4 | 29.0 | 28.2 | 28.7 | 0.5 |
| 600 | 0.4 | 32.4 | 31.6 | 29.6 | −2.0 |
| 650 | 0.7 | 32.4 | 31.0 | 30.4 | −0.6 |
| 700 | 0.7 | 31.4 | 30.0 | 30.8 | 0.8 |
| 750 | 0.5 | 33.0 | 32.0 | 31.4 | −0.6 |
| 800 | 0.6 | 33.6 | 32.4 | 32.0 | −0.4 |
| 850 | 1.0 | 33.8 | 31.8 | 32.3 | 0.5 |
| 900 | 0.5 | 33.8 | 32.8 | 32.8 | −0.1 |
| 950 | 0.6 | 34.2 | 33.0 | 33.6 | 0.4 |
| 1000 | 1.3 | 37.0 | 34.4 | 33.7 | −0.8 |

Table 5.1: Comparison of site attenuation measured with commercially available resonant dipoles and NEC predictions for the 3 m test site at the University of York with horizontally polarised antennas and a transmitting antenna height of 2 m.

| Frequency MHz | Balun Loss dB | Site Attenuation / dB | | | |
|---|---|---|---|---|---|
| | | Measured | Corrected | NEC | Error |
| 30 | 0.3 | 20.8 | 20.2 | 21.7 | 1.5 |
| 40 | 0.5 | 23.2 | 22.2 | 20.9 | −1.3 |
| 50 | 0.8 | 22.2 | 20.6 | 21.5 | 0.9 |
| 60 | 1.0 | 23.4 | 21.4 | 22.3 | 0.9 |
| 70 | 0.3 | 22.0 | 21.4 | 22.0 | 0.6 |
| 80 | 0.3 | 22.2 | 21.6 | 20.5 | −1.1 |
| 90 | 0.5 | 21.6 | 20.6 | 21.0 | 0.4 |
| 100 | 0.6 | 23.0 | 21.8 | 22.1 | 0.3 |
| 125 | 1.0 | 26.2 | 24.2 | 25.3 | 1.1 |
| 150 | 0.4 | 26.4 | 25.6 | 26.0 | 0.4 |
| 175 | 0.2 | 26.8 | 26.4 | 26.9 | 0.5 |
| 200 | 0.2 | 29.2 | 28.8 | 28.9 | 0.1 |
| 225 | 0.2 | 31.4 | 31.0 | 29.4 | −1.6 |
| 250 | 0.3 | 31.6 | 31.0 | 30.0 | −1.0 |
| 275 | 0.3 | 31.2 | 30.6 | 31.5 | 0.9 |
| 300 | 0.3 | 33.8 | 33.2 | 31.9 | −1.3 |
| 350 | 0.4 | 35.2 | 34.4 | 33.6 | −0.8 |
| 400 | 0.7 | 34.4 | 33.0 | 34.8 | 1.8 |
| 450 | 0.3 | 36.2 | 35.6 | 36.0 | 0.4 |
| 500 | 0.3 | 37.0 | 36.4 | 37.1 | 0.7 |
| 550 | 0.4 | 38.4 | 37.6 | 37.6 | 0.0 |
| 600 | 0.4 | 38.0 | 37.2 | 38.4 | 1.2 |
| 650 | 0.7 | 40.4 | 39.0 | 39.3 | 0.3 |
| 700 | 0.7 | 39.4 | 38.0 | 39.7 | 1.7 |
| 750 | 0.5 | 40.8 | 39.8 | 40.4 | 0.6 |
| 800 | 0.6 | 39.0 | 37.8 | 41.0 | 3.2 |
| 850 | 1.0 | 39.8 | 37.8 | 41.4 | 3.6 |
| 900 | 0.5 | 42.2 | 41.2 | 41.9 | 0.7 |
| 950 | 0.6 | 42.2 | 41.0 | 42.7 | 1.7 |
| 1000 | 1.3 | 45.6 | 43.0 | 42.8 | −0.2 |

Table 5.2: Comparison of site attenuation measured with commercially available resonant dipoles and NEC predictions for the 10 m test site at the University of York with horizontally polarised antennas and a transmitting antenna height of 2 m.

### 5.3.2 Interpretation of Results

The results for both lengths of test site show very good correlation between measured and theoretical site attenuations, although the results for the 3 m test site are slightly better. The average error magnitudes are 0.8 dB for the 3 m site and 1.0 dB for the 10 m site across the frequency range but typical errors are even smaller than this because certain isolated data points are significantly more in error than the majority.

Both lengths of test site show unusually large errors at 30 MHz. This was because of the large physical length of the arms of the antennas at lower frequencies caused them to bend downwards due to their weight. The NEC simulation did not account for this and is therefore only valid for straight antennas. §5.4 describes measurements performed with supported antennas and those measurements show much smaller errors at 30 MHz.

The 600 MHz data point of the 3 m site shows an error of −2.0 dB that may indicate a problem with the test site and so must be investigated further; however, this may simply be a bad measurement due to inaccurate mechanical tuning of the antenna. This was the worst case error and, it and the 30 MHz data point aside, propagation over the 3 m site was within 1.7 dB of theory.

Propagation over the 10 m site was also found to be within 1.7 dB of theory except at 800 MHz and 850 MHz, where errors were found of 3.2 and 3.6 dB respectively. This was due to precipitation causing the antennas to become damp and, as the antennas were hired, it was not possible to remeasure the data. The measurements must be repeated in order to draw conclusions about the test site.

It is difficult to specify the exact source of the errors found for each test site because the validity of using the single dB loss value to represent the effect of the baluns is not known. Also the data is not sufficiently continuous for any frequency dependence of the errors to emerge. Later in this chapter more rigorous approaches to test site validation, that do not simplify the balun effects, will be presented and these will be shown to give more reliable information about test site performance.

## 5.4 The use of Insertion Loss Measurements for Test Site Validation

In the previous section, test site validation was carried out by comparison of the measured and theoretical attenuations resulting from the insertion of three cascaded two-port networks into a matched 50 Ω transmission line. The first and third networks were antenna baluns and the second network was a pair of antennas over a test site. The baluns were not properly characterised resulting in unnecessary uncertainties in the theoretical attenuation values. In order to avoid this problem the full two-port network parameters of the balun of each antenna have to be known.

The cylindrical dipole antennas designed in chapter 2 and characterised in chapter 4 have separate balun devices that form part of their feeding networks. These devices have been fully characterised so that the effective source and load reflection coefficients presented to the antennas are known and insertion loss measurements with these antennas may be used for test site validation. The procedure is described in chapter 3 and only the results will be discussed here.

The measurements, and therefore the predictions, in this section were obtained from 3 m and 9 m test sites rather than the usual 3 m, and 10 m test sites. This was because the presence of a fixed plastic enclosure on the ground plane of the test site at the University of York prevented antennas of greater than 2 m length being mounted in the usual EUT position.

### 5.4.1 Measurement Method

Data of measured insertion loss were gathered at frequencies between 20 MHz and 50 MHz in 5 MHz steps, and then in further steps of 10 MHz up to 100 MHz, for 3 m and 9 m site lengths with both 1 m and 2 m transmitting antenna heights. The physical size of the antennas over this frequency range precluded vertically polarised measurements and so only horizontally polarised ones were made. Also, the drive-point impedances of the antennas vary most below 100 MHz, and so any problems associated with the use of the scalar balun loss in dB are most pronounced in this frequency range.

The large physical length of the antennas required several physical support structures to maintain their horizontality and prevent them drooping whilst the measurements were performed. Five thin wooden trestles used to support the transmitting antenna, although only three were used above 30 MHz and one above 50 MHz. The receiving antenna was mounted on a mast and supported by an ar-

rangement of string and wooden supports that allowed it to be scanned through the usual 1–4 m height range in 2 cm increments. This support structure is illustrated in more detail in chapter 6.

### 5.4.2 Results

The measured and theoretical minimum insertion loss values throughout the receiving antenna height scan range are compared in tables 5.3 to 5.6. Theoretical values of attenuation are also given in the tables to show the effect of the unmatched source and load impedances.

For the reasons explained in chapter 4, the ports of the networks used to feed the antennas had a characteristic impedance of 100 Ω, hence the measured and theoretical values given in tables 5.3 to 5.6 are different to those that would be obtained with a 50 Ω system. The transformation that was used to convert test site scattering parameters from the 50 Ω system to the 100 Ω one is given in appendix G.

| Frequency MHz | Attenuation dB | Insertion Loss / dB | | |
|---|---|---|---|---|
| | | Measurement | Theoretical | Error |
| 20 | 11.7 | 14.0 | 10.4 | 3.6 |
| 25 | 11.9 | 13.6 | 11.5 | 2.1 |
| 30 | 12.1 | 13.0 | 12.3 | 1.7 |
| 35 | 11.9 | 13.6 | 13.5 | 0.1 |
| 40 | 11.7 | 13.6 | 11.9 | 1.7 |
| 45 | 11.6 | 12.3 | 11.3 | 1.0 |
| 50 | 11.8 | 13.0 | 12.2 | 0.8 |
| 60 | 12.3 | 13.5 | 12.4 | 1.1 |
| 70 | 13.1 | 13.3 | 14.5 | −1.2 |
| 80 | 14.1 | 13.9 | 13.8 | 0.1 |
| 90 | 15.0 | 16.0 | 15.1 | 0.9 |
| 100 | 15.6 | 15.2 | 15.4 | −0.2 |

Table 5.3: Horizontally polarised attenuation and insertion loss between resonant dipole antennas over a 3 m test site with a transmitting antenna height of 1 m and a 100 Ω transmission line system.

| Frequency MHz | Attenuation dB | Insertion Loss / dB | | |
|---|---|---|---|---|
| | | Measurement | Theoretical | Error |
| 20 | 8.0 | 10.6 | 7.4 | 3.2 |
| 25 | 9.0 | 10.6 | 9.1 | 1.5 |
| 30 | 9.9 | 10.7 | 9.9 | 0.8 |
| 35 | 10.4 | 12.2 | 11.1 | 1.1 |
| 40 | 10.6 | 12.7 | 10.5 | 2.2 |
| 45 | 10.6 | 10.8 | 10.5 | 0.3 |
| 50 | 10.7 | 11.2 | 11.3 | −0.1 |
| 60 | 10.7 | 11.6 | 10.5 | 1.1 |
| 70 | 10.7 | 11.5 | 12.1 | −0.6 |
| 80 | 11.2 | 10.5 | 11.3 | −0.8 |
| 90 | 12.2 | 12.9 | 12.3 | 0.6 |
| 100 | 13.2 | 13.1 | 12.9 | 0.2 |

Table 5.4: Horizontally polarised attenuation and insertion loss between resonant dipole antennas over a 3 m test site with a transmitting antenna height of 2 m and a 100 Ω transmission line system.

| Frequency MHz | Attenuation dB | Insertion Loss / dB | | |
|---|---|---|---|---|
| | | Measurement | Theoretical | Error |
| 20 | 22.1 | 24.0 | 20.8 | 3.2 |
| 25 | 22.4 | 22.4 | 22.5 | −0.1 |
| 30 | 22.4 | 21.9 | 22.4 | −0.5 |
| 35 | 22.2 | 24.6 | 23.8 | 0.8 |
| 40 | 21.9 | 23.7 | 22.1 | 1.6 |
| 45 | 22.0 | 21.9 | 21.7 | 0.2 |
| 50 | 22.8 | 24.8 | 23.4 | 1.4 |
| 60 | 24.5 | 25.2 | 24.7 | 0.5 |
| 70 | 25.2 | 27.1 | 26.0 | 1.1 |
| 80 | 25.0 | 24.6 | 24.8 | −0.2 |
| 90 | 25.5 | 27.9 | 25.5 | 2.4 |
| 100 | 26.3 | 26.6 | 26.2 | 0.4 |

Table 5.5: Horizontally polarised attenuation and insertion loss between resonant dipole antennas over a 9 m test site with a transmitting antenna height of 1 m and a 100 Ω transmission line system.

| Frequency MHz | Attenuation dB | Insertion Loss / dB | | |
|---|---|---|---|---|
| | | Measurement | Theoretical | Error |
| 20 | 18.3 | 20.3 | 17.8 | 2.5 |
| 25 | 19.2 | 18.9 | 19.6 | −0.7 |
| 30 | 19.6 | 19.0 | 19.2 | −0.2 |
| 35 | 19.6 | 22.2 | 20.4 | 1.8 |
| 40 | 19.3 | 20.9 | 19.3 | 1.6 |
| 45 | 19.2 | 18.9 | 19.2 | −0.3 |
| 50 | 19.8 | 21.1 | 20.7 | 0.4 |
| 60 | 20.6 | 21.1 | 20.4 | 0.7 |
| 70 | 20.7 | 22.7 | 21.4 | 1.4 |
| 80 | 20.0 | 18.6 | 20.0 | −1.4 |
| 90 | 20.3 | 22.9 | 20.3 | 2.6 |
| 100 | 21.4 | 21.9 | 21.1 | 0.8 |

Table 5.6: Horizontally polarised attenuation and insertion loss between resonant dipole antennas over a 9 m test site with a transmitting antenna height of 2 m and a 100 Ω transmission line system.

### 5.4.3 Interpretation of Results

Tables 5.3 to 5.6 show that the theoretical values of attenuation and insertion loss between resonant dipole antennas are not the same. The average difference is 0.4 dB, but the worst case differences are up to 1.6 dB. This shows that the effective source and load impedances presented to the antennas used for a site attenuation measurement can have a significant effect. If the balun design is such that these are not equal to the transmission line characteristic impedances, a simple calculation of attenuation will give errors between measurement and theoretical losses that are not due to site imperfections.

The measured and theoretical insertion loss values show agreement to within 2 dB at all but a few frequencies. The resonant dipoles become longer as frequency is reduced and, for frequencies below 40 MHz, this results in the antenna being longer than the width of the metallised portion of the ground plane. The effect of this is particularly clear at 20 MHz with up to 3.6 dB more attenuation being measured than is predicted. This problem is not present on the 10 m site for frequencies of 30 MHz and above, but extends up to 30 MHz on the 3 m site.

There are two other frequencies where large differences are present between measured and theoretical insertion loss. At 90 MHz up to 2.6 dB of error was found for the 10 m site, although this frequency was not a problem for the 3 m site. The earlier measurements in §5.3 do not show a problem at 90 MHz and so further investigation is necessary. The other possible problem frequency was 40 MHz, where differences of up to 2.2 dB were found. This may be due to the truncation of the metal portion of the ground plane and could indicate a problem with the design of the test site.

Correlation between measurement and theory with this rigorous model was found to be no better than that found in §5.2 using telescopic dipoles and assuming that their balun effects could be described by a simple dB loss factor. The reason for this was that the repeatability of the measurements was of the same order as the errors that were measured in both cases, and more repeatable measurements would be needed to compare the models. A detailed study of repeatability of site attenuation measurements was not carried out, but repetition of several of the measurements indicated a typical repeatability of 0.5 dB. The reason for poor repeatability below 100 MHz was that the large degree of mutual coupling present in this frequency range gave measurements that were very sensitive to antenna position and the experimental equipment used only gave positional accuracy to within 5–10 cm.

These results indicate that the open-area test site has site insertion loss to within the ±4 dB required by site attenuation standards, over the frequency range of 20–100 MHz. However, they do show that there is possibly a problem with the ground plane design that may give errors of up to 2 dB around 40 MHz.

## 5.5 Site Attenuation between Biconical Antennas

Earlier in this chapter, methods for the validation of open-area test sites have been discussed that involve measurements of insertion loss and attenuation between resonant dipole antennas over the test site. The use of resonant dipoles is undesirable from a practical point of view because of their large physical size at frequencies below 100 MHz, and because of the requirement to adjust their length as frequency is scanned. A more attractive method of site validation would involve an attenuation measurement performed using a pair of broadband antennas, such as biconical antennas over the frequency range of 30–300 MHz and log-periodic antennas from 300 MHz to 1 GHz.

In this section the NEC computer code is used to derive values of classical site attenuation between a pair of biconical antennas. These values are compared with measurements performed over the open-area test site at the University of York in order to determine the performance of the test site and the accuracy of the simulation used to obtain the theoretical values.

### 5.5.1 Measurement of Site Attenuation

A pair of Schwarzbeck BBA9106 biconical antennas, as described in chapters 2 and 4, were used for the measurement of site attenuation on the open-area test site. The data were gathered for 3 m and 10 m sites with horizontally polarised antennas and a single transmitting antenna height of 1.26 m. The measurement apparatus is illustrated in figure 5.9.

The HP8753 network analyser was calibrated to perform an attenuation measurement between the terminals of the two antennas over their full specified frequency range of 30–300 MHz. 1 MHz frequency steps were found to provide adequate resolution to show all the features of the response of the test site.

Attenuation was measured as a function of frequency at receiving antenna heights from 1 m to 4 m in 10 cm steps. The resulting 31 data files were then analysed to determine the minimum attenuation that occurred within the height scan range at each excitation frequency. Figure 5.10 shows these measurements for the 3 m and 10 m test sites, and compares them with predicted values calculated in §5.5.2.

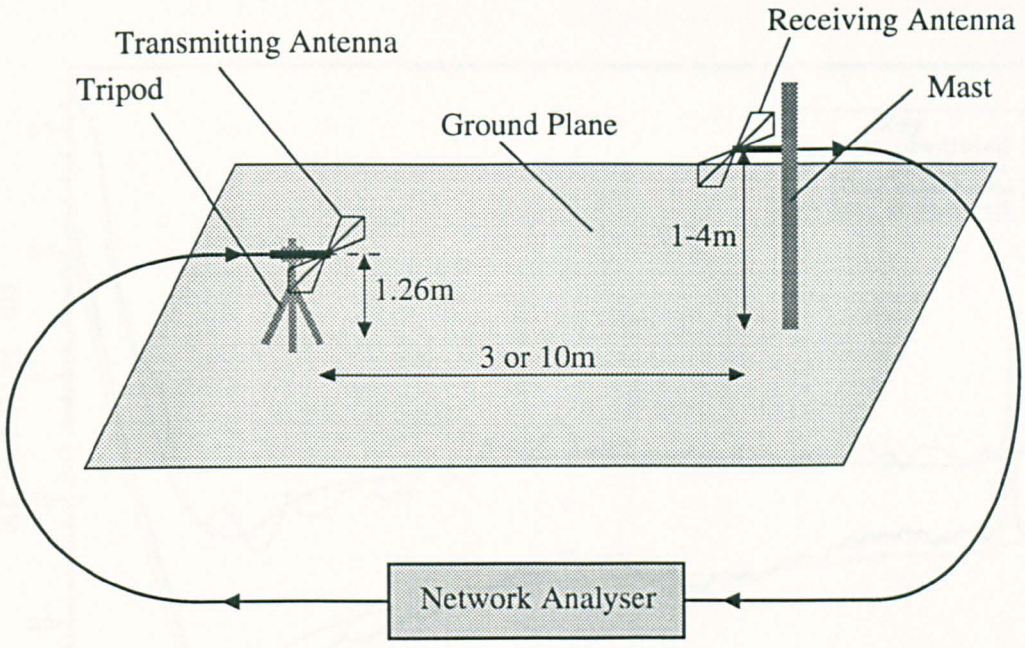


Figure 5.9: Apparatus used for the measurement of site attenuation with biconical antennas.

### 5.5.2 Calculation of Predicted Site Attenuation

The Schwarzbeck BBA9106 biconical antennas used had integral balun devices contained within their supports and because of this the measured attenuation with these antennas was not the classical site attenuation. The measured attenuation was due to the cascade combination of the transmitting antenna balun connected via the radiators of the antennas over the test site to the receiving antenna balun.

The NEC model that was used to simulate the radiators of a pair of skeletal biconical antennas above a ground plane is discussed in chapter 3. It returned the scattering parameters of the two-port network formed between the drive points of these two antennas with a particular relative geometry above the ground plane of an ideal test site.

To obtain the site scattering parameters required a very large amount of CPU time because of the complexity of the structure. For this reason, data were only calculated in 10 MHz frequency steps and 10 cm receiving antenna height steps. The data were calculated with horizontally polarised antennas over 3 m and 10 m sites with a transmitting antenna height of 1.26 m, chosen to be the same as the experimental height of §5.5.1.

In chapter 4, a method that was used to measure the scattering parameters of the balun of each antenna has been described. By concatenating the three scattering parameter matrices of balun-site-balun into a single matrix, it was possible to derive theoretical attenuation values between a pair of the complete antennas.

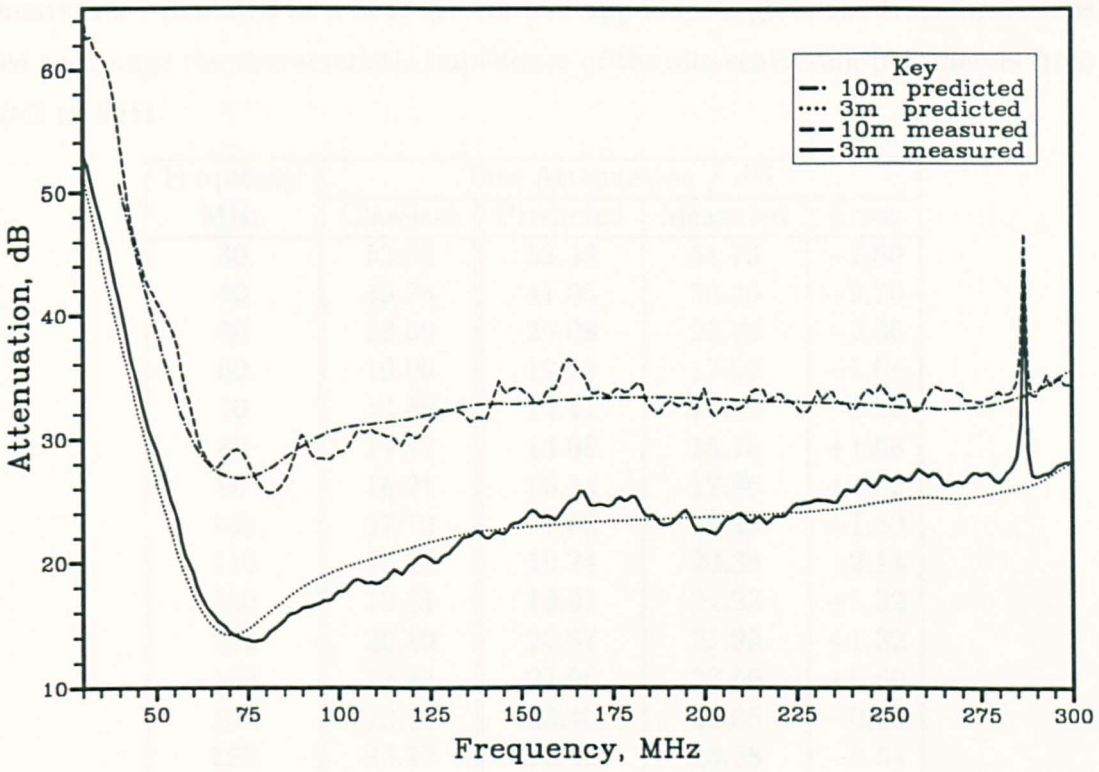


Figure 5.10: Measured and predicted site attenuations between biconical antennas.

The mathematics associated with this concatenation are described in appendix E.

The predicted values are correct only for measurements made with a transmitting antenna height of 1.26 m, and with a pair of the Schwarzbeck biconical antennas. No attempt has been made in this thesis to calculate definitive values of classical site attenuation between arbitrary biconical antennas because their different cone dimensions will each require a separate NEC simulation. They will also have different balun scattering parameters that must be measured and taken account of.

### 5.5.3 Results

Tables 5.7 and 5.8, and also figure 5.10, compare the measured values of site attenuation with predicted values for the 3 m and 10 m test sites. The tables also give values of predicted classical site attenuation that would be measured with the antennas over an ideal test site if their baluns behaved as 1 : 1 impedance transformers.

The procedure used to measure the scattering parameters of the balun of each antenna resulted in a characteristic impedance of 100 Ω at the port that was connected to the radiators of each antenna. Because of this, the site scattering parameters, calculated from NEC, were normalised to 100 Ω and it was necessary to

transform them in order to calculate classical site attenuation. Classical site attenuation is calculated in a 50 Ω system and appendix G gives the transformations used to change the characteristic impedance of the site scattering parameters from 100 Ω to 50 Ω.

| Frequency | Site Attenuation / dB | | | |
|---|---|---|---|---|
| MHz | Classical | Predicted | Measured | Error |
| 30 | 52.65 | 53.33 | 51.73 | −1.60 |
| 40 | 39.74 | 41.06 | 38.36 | −2.70 |
| 50 | 28.56 | 29.08 | 26.72 | −2.36 |
| 60 | 19.05 | 19.16 | 17.52 | −1.64 |
| 70 | 13.88 | 14.41 | 14.19 | −0.22 |
| 80 | 14.17 | 14.08 | 15.76 | +1.68 |
| 90 | 16.21 | 16.34 | 17.96 | +1.62 |
| 100 | 17.73 | 17.62 | 19.42 | +1.80 |
| 110 | 18.77 | 18.24 | 20.38 | +2.14 |
| 120 | 19.81 | 19.91 | 21.23 | +1.32 |
| 130 | 20.89 | 20.67 | 21.99 | +1.32 |
| 140 | 21.85 | 21.96 | 22.56 | +0.60 |
| 150 | 22.60 | 23.40 | 22.85 | −0.55 |
| 160 | 23.17 | 23.62 | 23.08 | −0.54 |
| 170 | 23.67 | 24.60 | 23.31 | −1.29 |
| 180 | 24.03 | 25.36 | 23.40 | −1.96 |
| 190 | 24.33 | 23.04 | 23.52 | +0.48 |
| 200 | 24.51 | 22.67 | 23.67 | +1.00 |
| 210 | 24.57 | 23.93 | 23.78 | −0.15 |
| 220 | 24.67 | 23.71 | 23.96 | +0.25 |
| 230 | 24.73 | 25.02 | 24.16 | −0.86 |
| 240 | 24.94 | 25.74 | 24.53 | −1.21 |
| 250 | 25.24 | 26.72 | 24.99 | −1.73 |
| 260 | 25.52 | 27.10 | 25.30 | −1.80 |
| 270 | 25.36 | 26.43 | 25.22 | −1.21 |
| 280 | 25.67 | 26.46 | 25.70 | −0.76 |
| 290 | 26.20 | 26.88 | 26.40 | −0.48 |
| 300 | 27.60 | 28.28 | 28.14 | −0.14 |

Table 5.7: Measured and predicted attenuations of a 3 m test site with horizontally polarised biconical antennas and a transmitting antenna height of 1.26 m.

### 5.5.4 Discussion of Results

The objective of the measurements and simulations described in this section was to analyse the performance of the test site at the University of York and to validate the NEC simulation of the biconical antenna by demonstrating close correlation between measured and predicted site attenuations.

The curves of measured site attenuation shown in figure 5.10 follow the predicted

| Frequency MHz | Site Attenuation / dB | | | |
|---|---|---|---|---|
| | Classical | Predicted | Measured | Error |
| 30 | | 64.60 | | |
| 40 | 52.11 | 54.23 | 50.65 | −3.58 |
| 50 | 40.64 | 41.27 | 38.79 | −2.48 |
| 60 | 31.29 | 31.94 | 29.88 | −2.06 |
| 70 | 26.72 | 28.72 | 26.96 | −1.76 |
| 80 | 25.98 | 25.79 | 27.43 | +1.64 |
| 90 | 27.68 | 30.31 | 29.41 | −0.90 |
| 100 | 29.22 | 28.96 | 30.79 | +1.83 |
| 110 | 29.73 | 30.54 | 31.21 | +0.67 |
| 120 | 30.35 | 30.27 | 31.66 | +1.39 |
| 130 | 31.28 | 32.30 | 32.32 | +0.02 |
| 140 | 32.13 | 31.52 | 32.79 | +1.27 |
| 150 | 32.61 | 33.99 | 32.82 | −1.17 |
| 160 | 33.22 | 34.46 | 33.06 | −1.40 |
| 170 | 33.67 | 33.61 | 33.24 | −0.37 |
| 180 | 33.93 | 33.95 | 33.31 | −0.64 |
| 190 | 34.02 | 32.86 | 33.29 | +0.43 |
| 200 | 33.95 | 34.00 | 33.21 | −0.79 |
| 210 | 33.81 | 32.50 | 33.11 | +0.61 |
| 220 | 33.59 | 33.50 | 32.97 | −0.53 |
| 230 | 33.40 | 33.15 | 32.90 | −0.25 |
| 240 | 33.18 | 32.36 | 32.77 | +0.41 |
| 250 | 32.91 | 33.46 | 32.57 | −0.89 |
| 260 | 32.68 | 33.12 | 32.42 | −0.70 |
| 270 | 32.58 | 33.45 | 32.44 | +1.01 |
| 280 | 32.78 | 33.71 | 32.82 | −0.89 |
| 290 | 33.67 | 33.36 | 33.82 | +0.46 |
| 300 | 35.01 | 34.73 | 35.54 | +0.81 |

Table 5.8: Measured and predicted attenuations of a 10 m test site with horizontally polarised biconical antennas and a transmitting antenna height of 1.26 m.

curves generally but they do also show several differences that are due to the non-ideality of the test site.

The 10 m data, and also the 3 m data to a lesser extent, show a ripple having a periodicity of 25 MHz. This is due to a stray reflection from the workshop building along one side of the test site (see figure in chapter 1). This undesired reflected wave travels a path length of an extra 12 m compared to the direct wave from the transmitting antenna to the receiving antenna and this distance is equal to one wavelength at 25 MHz. The effect of the workshop on the site performance can be found by determining the envelope of the 25 MHz ripple and this is greatest for the 10 m site at ±2 dB for frequencies of up to 200 MHz. At higher frequencies the ripple becomes less pronounced and it is also less than ±1 dB for the 3 m site because of its shorter desired path lengths.

The cone resonance of the antennas is also evident at 287 MHz although the predicted data do not show it because it falls between the 280 and 290 MHz data points. The resonance is very sharply tuned, with a Q-factor of 1100, and therefore slight differences between the measured and predicted resonant frequency will cause very large differences between measured and predicted attenuations close to the resonance. For this reason no conclusions may be drawn from the data about test site performance between 280 and 295 MHz.

The differences between the measured and predicted attenuations are given in tables 5.7 and 5.8 at 10 MHz intervals throughout the frequency range. Aside from the ripple mentioned earlier, the data for the 10 m site show smaller errors than those from the 3 m site. This is thought to be due to inaccurate positioning of the receiving antenna due to a slightly off-vertical mast. This would have a larger effect on the path lengths of shorter test sites, particularly with the greater mast heights.

The 10 m test site data are within 1 dB of prediction at frequencies above 160 MHz and are still within 2 dB down to 60 MHz. Below this frequency the biconical antenna is strongly capacitive and the NEC simulation of it has already been shown to be inaccurate in chapter 4. The 3 m site data is only within 2 dB of prediction at frequencies down to 60 MHz but, for the reason given above, this is a problem with the measured data.

Comparison of the classical site attenuation with the predicted attenuation shows the effect of the balun device on the measurement. Although the balun has been shown to introduce a slight loss for resonant dipole antennas, its effect on broadband antennas is more complicated. The impedance of the biconical antenna varies much more than that of the resonant dipole, so the balun can improve matching between it and its transmission line and actually give gain rather than loss under certain conditions. Because of this a simple balun loss in dB may not be used with broadband antennas and the full scattering parameters of their balun devices must be accounted for.

## 5.6 Normalised Site Attenuation

Normalised site attenuation (NSA) is defined as classical site attenuation (CSA) divided by the product of the antenna factors of the antennas used for a site attenuation measurement. It is used in the three antenna method for antenna calibration [78] and also for test site validation according to the standard ANSI C63 [79].

Antenna parameters such as gain and balun loss are accounted for in antenna factors and therefore dividing CSA by the antenna factors is intended to remove the dependence of the site attenuation measurement upon the type of antennas that are used. NSA is assumed to be a fundamental constant for a given test site length irrespective of the antennas used.

The disadvantage of using NSA is that the concept of antenna factor is only meaningful for antennas that are uniformly illuminated, and even the antenna factors of uniformly illuminated antennas may vary because of the mutual coupling effects described in chapter 4. Accounting for this variation in antenna factor is very difficult with NSA and a variety of approaches to the derivation of correction factors can be found in the literature [80], [81]. All of these corrections are specific to one particular type of antenna, thus having to employ them negates any advantage that NSA has over CSA for test site validation.

In this section theoretical values of NSA will be derived for coupling between resonant dipole antennas. These will be discussed and compared with measurements in order to deduce their usefulness for test site validation.

### 5.6.1 Measurement of NSA

Measurements of CSA between horizontally polarised resonant dipole antennas, over 3 m and 10 m test sites, are given in §5.3. Antenna factors, obtained by the three antenna calibration method, were provided with these antennas and they were used to calculate the measured NSA. Table 5.9 shows how this was performed by subtracting both of the antenna factors from the classical site attenuation values in decibels.

It is interesting to note that the two antenna factors, $AF_1$ and $AF_2$, are not the same, even though the antennas are structurally identical. The differences are most pronounced at low frequencies and are up to 1.5 dB at 30 MHz. The reason for this is associated with the inability of the three antenna calibration method to properly account for close coupling effects between antennas and ground planes. This problem has been discussed in chapter 4.

| Frequency | 3 m Site | | | | 10 m site | | | |
|---|---|---|---|---|---|---|---|---|
| MHz | CSA | AF1 | AF2 | NSA | CSA | AF1 | AF2 | NSA |
| 30 | 9.2 | −2.2 | −0.7 | 12.1 | 20.8 | −1.1 | 1.4 | 20.5 |
| 40 | 12.0 | 1.2 | 0.4 | 10.4 | 23.2 | 1.5 | 2.2 | 19.5 |
| 50 | 11.4 | 2.6 | 2.5 | 6.3 | 22.2 | 5.1 | 4.2 | 12.9 |
| 60 | 11.8 | 4.0 | 5.1 | 2.7 | 23.4 | 5.5 | 8.0 | 9.9 |
| 70 | 9.8 | 5.1 | 5.5 | −0.8 | 22.0 | 5.4 | 6.6 | 10.0 |
| 80 | 9.8 | 7.0 | 7.2 | −4.4 | 22.2 | 7.1 | 6.7 | 8.4 |
| 90 | 12.2 | 8.2 | 8.4 | −4.4 | 21.6 | 7.3 | 7.3 | 7.0 |
| 100 | 12.4 | 9.5 | 9.5 | −6.6 | 23.0 | 8.4 | 8.1 | 6.5 |
| 125 | 16.4 | 10.5 | 10.6 | −4.7 | 26.2 | 11.1 | 10.7 | 4.4 |
| 150 | 17.4 | 12.6 | 12.1 | −7.3 | 26.4 | 12.3 | 12.2 | 1.9 |
| 175 | 18.0 | 13.4 | 13.1 | −8.5 | 26.8 | 13.6 | 13.4 | −0.2 |
| 200 | 19.4 | 14.9 | 14.3 | −9.8 | 29.2 | 14.4 | 15.0 | −0.2 |
| 225 | 21.6 | 16.2 | 15.9 | −10.5 | 31.4 | 15.5 | 15.8 | 0.1 |
| 250 | 21.2 | 17.4 | 17.0 | −13.2 | 31.6 | 16.6 | 16.5 | −1.5 |
| 275 | 22.2 | 18.2 | 17.7 | −13.7 | 31.2 | 17.8 | 17.6 | −4.2 |
| 300 | 23.4 | 18.5 | 18.1 | −13.2 | 33.8 | 18.7 | 18.1 | −3.0 |
| 350 | 25.8 | 19.7 | 19.2 | −13.1 | 35.2 | 20.1 | 20.1 | −5.0 |
| 400 | 27.2 | 21.6 | 21.7 | −16.1 | 34.4 | 21.6 | 21.5 | −8.7 |
| 450 | 27.0 | 21.9 | 22.0 | −16.9 | 36.2 | 21.9 | 21.4 | −7.1 |
| 500 | 29.4 | 22.7 | 23.5 | −16.8 | 37.0 | 23.1 | 22.6 | −8.7 |
| 550 | 29.0 | 23.9 | 24.0 | −18.9 | 38.4 | 23.9 | 23.1 | −8.6 |
| 600 | 32.4 | 24.2 | 24.9 | −16.7 | 38.0 | 25.1 | 24.5 | −11.6 |
| 650 | 32.4 | 25.7 | 25.6 | −18.9 | 40.4 | 25.8 | 25.4 | −10.8 |
| 700 | 31.4 | 25.8 | 25.8 | −20.2 | 39.4 | 26.5 | 25.9 | −13.0 |
| 750 | 33.0 | 26.7 | 26.1 | −19.8 | 40.8 | 27.0 | 26.3 | −12.5 |
| 800 | 33.6 | 27.2 | 26.8 | −20.4 | 39.0 | 27.4 | 27.6 | −16.0 |
| 850 | 33.8 | 28.4 | 28.1 | −22.7 | 39.8 | 27.5 | 27.9 | −15.6 |
| 900 | 33.8 | 28.6 | 27.8 | −22.6 | 42.2 | 28.0 | 28.2 | −14.0 |
| 950 | 34.2 | 28.7 | 29.3 | −23.8 | 42.2 | 28.7 | 29.8 | −16.3 |
| 1000 | 37.0 | 31.0 | 31.1 | −25.1 | 45.6 | 30.1 | 31.1 | −15.6 |

Table 5.9: Calculation of measured NSA on 3 m and 10 m test sites with horizontally polarised resonant dipole antennas and a transmitting antenna height of 2 m.

### 5.6.2 Predictions of NSA

In order to calculate theoretical values for NSA, it is necessary to have theoretical values for CSA and each of the antenna factors. Accurate values of CSA have been calculated for resonant dipole antennas in §5.1, and a simple formula is given in chapter 4 for the plane wave antenna factor of a resonant dipole. These two sets of data were used to calculate the normalised site attenuation curves shown in figures 5.11 and 5.12.

The plane wave antenna factors that are used for the calculation of NSA in this section are not equivalent to those that would be obtained from a three antenna method of calibration. This is because they do not account for deviations in the antenna factors that occur due to close coupling to the ground plane. It would be possible to calculate theoretical antenna factors equivalent to those from the three antenna method, however there would be little merit in performing this calculation because those antenna factors would still not be correct due to the problems with the three antenna method outlined in chapter 4.

An alternative approach used for the calculation of NSA involves the Smith formulas, derived from geometrical optical theory and given in chapter 3. The expressions for classical site attenuation obtained from this approach are proportional to the antenna factors, which may therefore be eliminated to yield theoretical NSA. This is apparently an advantage over the NEC approach to obtaining theoretical values of NSA because it avoids the need to use antenna factors that would be obtained from a three antenna calibration. The problem is that the simple theory used to derive the CSA expressions is the Smith model for CSA (see §5.2) and consequently has all of its accuracy limitations.

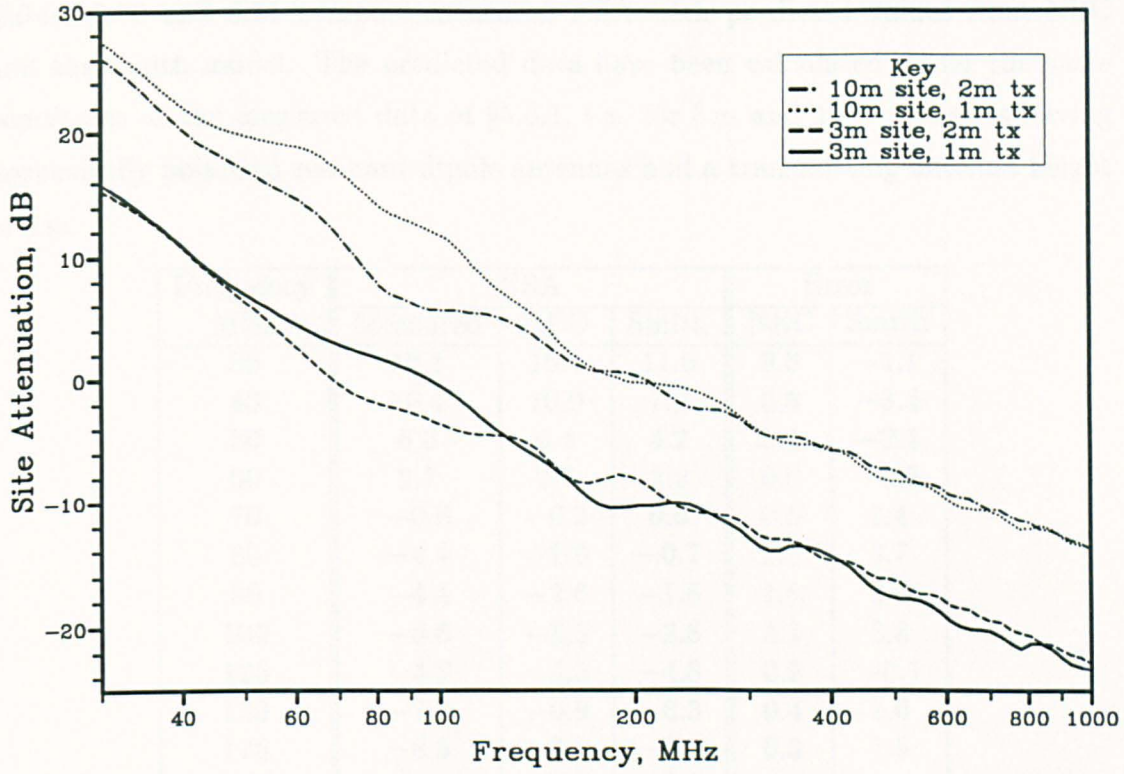


Figure 5.11: Predicted values of horizontally polarised normalised site attenuation for the 3 m site, calculated with the NEC computer code.

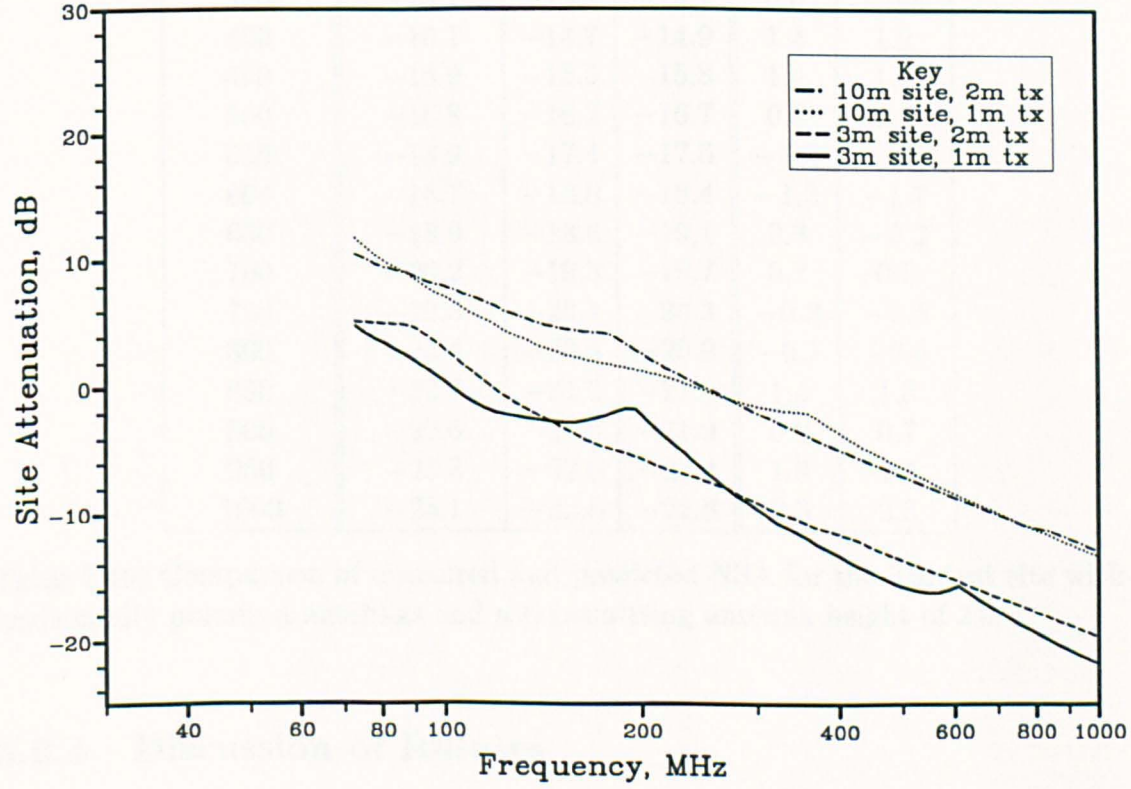


Figure 5.12: Predicted values of vertically polarised normalised site attenuation for the 10 m site, calculated with the NEC computer code.

### 5.6.3 Results

Tables 5.10 and 5.11 compare measured NSA with predicted values from NEC and the Smith model. The predicted data have been calculated under the same conditions as the measured data of §5.6.1, i.e. for 3 m and 10 m test sites having horizontally polarised resonant dipole antennas and a transmitting antenna height of 2 m.

| Frequency | NSA | | | Error | |
|---|---|---|---|---|---|
| MHz | Measured | NEC | Smith | NEC | Smith |
| 30 | 12.1 | 15.4 | 11.0 | 3.3 | −1.1 |
| 40 | 10.4 | 10.9 | 7.0 | 0.5 | −3.4 |
| 50 | 6.3 | 6.4 | 4.2 | 0.1 | −2.1 |
| 60 | 2.7 | 2.7 | 2.2 | 0.0 | −0.5 |
| 70 | −0.8 | −0.3 | 0.6 | 0.5 | 1.4 |
| 80 | −4.4 | −1.9 | −0.7 | 2.5 | 3.7 |
| 90 | −4.4 | −2.6 | −1.8 | 1.8 | 2.6 |
| 100 | −6.6 | −3.5 | −2.8 | 3.1 | 3.8 |
| 125 | −4.7 | −4.5 | −4.8 | 0.2 | −0.1 |
| 150 | −7.3 | −6.9 | −6.3 | 0.4 | 1.0 |
| 175 | −8.5 | −8.2 | −7.0 | 0.3 | 1.5 |
| 200 | −9.8 | −8.0 | −8.4 | 1.8 | 1.4 |
| 225 | −10.5 | −9.8 | −9.6 | 0.7 | 0.9 |
| 250 | −13.2 | −10.8 | −10.6 | 2.4 | 2.6 |
| 275 | −13.7 | −11.0 | −11.5 | 2.7 | 2.2 |
| 300 | −13.2 | −12.0 | −12.3 | 1.2 | 0.9 |
| 350 | −13.1 | −13.1 | −13.7 | 0.0 | −0.6 |
| 400 | −16.1 | −14.7 | −14.9 | 1.4 | 1.2 |
| 450 | −16.9 | −15.5 | −15.8 | 1.4 | 1.1 |
| 500 | −16.8 | −16.2 | −16.7 | 0.6 | 0.1 |
| 550 | −18.9 | −17.4 | −17.6 | −1.5 | 1.3 |
| 600 | −16.7 | −18.0 | −18.4 | −1.3 | −1.7 |
| 650 | −18.9 | −18.6 | −19.1 | 0.3 | −0.2 |
| 700 | −20.2 | −19.5 | −19.7 | 0.7 | 0.5 |
| 750 | −19.8 | −20.1 | −20.3 | −0.3 | −0.5 |
| 800 | −20.4 | −20.5 | −20.9 | −0.1 | −0.5 |
| 850 | −22.7 | −21.3 | −21.4 | 1.4 | 1.3 |
| 900 | −22.6 | −21.8 | −21.9 | 0.8 | 0.7 |
| 950 | −23.8 | −22.0 | −22.4 | 1.8 | 1.4 |
| 1000 | −25.1 | −22.8 | −22.8 | 2.3 | 2.3 |

Table 5.10: Comparison of measured and predicted NSA for the 3 m test site with horizontally polarised antennas and a transmitting antenna height of 2 m.

### 5.6.4 Discussion of Results

It can be seen from tables 5.10 and 5.11 that the predicted values of NSA from the Smith model and NEC are slightly different to each other. The difference increases

| Frequency MHz | NSA | | | Error | |
|---|---|---|---|---|---|
| | Measured | NEC | Smith | NEC | Smith |
| 30 | 20.5 | 26.2 | 24.1 | 5.7 | 3.6 |
| 40 | 19.5 | 20.3 | 19.4 | 0.8 | −0.1 |
| 50 | 12.9 | 17.1 | 15.9 | 4.2 | 3.0 |
| 60 | 9.9 | 14.7 | 13.1 | 4.8 | 3.2 |
| 70 | 10.0 | 11.7 | 10.9 | 1.7 | 0.9 |
| 80 | 8.4 | 8.0 | 9.2 | −0.4 | 0.8 |
| 90 | 7.0 | 6.4 | 7.8 | −0.6 | 0.8 |
| 100 | 6.5 | 5.7 | 6.7 | −0.8 | 0.2 |
| 125 | 4.4 | 4.9 | 4.6 | 0.5 | 0.2 |
| 150 | 1.9 | 2.5 | 2.9 | 0.6 | 1.0 |
| 175 | −0.2 | 0.7 | 1.5 | 0.9 | 1.7 |
| 200 | −0.2 | 0.4 | 0.3 | 0.6 | 0.5 |
| 225 | 0.1 | −1.2 | −0.8 | −1.3 | −0.9 |
| 250 | −1.5 | −2.3 | −1.7 | −0.8 | −0.2 |
| 275 | −4.2 | −2.5 | −2.6 | 1.7 | 1.6 |
| 300 | −3.0 | −3.7 | −3.3 | −0.7 | −0.3 |
| 350 | −5.0 | −4.6 | −4.7 | 0.4 | 0.3 |
| 400 | −8.7 | −5.7 | −5.8 | 3.0 | 2.9 |
| 450 | −7.1 | −6.6 | −6.7 | 0.5 | 0.4 |
| 500 | −8.7 | −7.3 | −7.6 | 1.4 | 1.1 |
| 550 | −8.6 | −8.5 | −8.5 | 0.1 | 0.1 |
| 600 | −11.6 | −9.1 | −9.3 | 2.5 | 2.3 |
| 650 | −10.8 | −9.7 | −10.0 | 1.1 | 0.8 |
| 700 | −13.0 | −10.6 | −10.7 | 2.4 | 2.3 |
| 750 | −12.5 | −11.1 | −11.3 | 1.4 | 1.2 |
| 800 | −16.0 | −11.6 | −11.8 | 4.4 | 4.2 |
| 850 | −15.6 | −12.3 | −12.4 | 3.3 | 3.2 |
| 900 | −14.0 | −12.7 | −12.9 | 1.3 | 1.1 |
| 950 | −16.3 | −12.9 | −13.4 | 3.4 | 2.9 |
| 1000 | −15.6 | −13.7 | −13.8 | 1.9 | 1.8 |

Table 5.11: Comparison of measured and predicted NSA for the 10 m test site with horizontally polarised antennas and a transmitting antenna height of 2 m.

towards the lower frequencies, where mutual coupling effects are more significant.

Both of the models show a similar level of correlation with the measured data but neither of them correlates as well as the earlier measurements of CSA in §5.3. This is because neither of the models fully accounts for the coupling between the antennas: the Smith model neglects mutual coupling and the NEC model assumes plane wave antenna factors.

Above 100 MHz, the two sets of predicted NSA are within 1 dB of each other. This shows the diminishing effect of mutual coupling and indicates that NSA can give acceptable results above 100 MHz, provided it is not required to validate a test site to within a greater accuracy than 1 dB.

## 5.7 Summary and Conclusions

The NEC computer code can be used to calculate predicted values of CSA between resonant dipole antennas with an accuracy of significantly better than 0.5 dB over the frequency range of 30 MHz to 1 GHz. Unfortunately a good enough test site was not available for this work in order to carry out validation of NEC to a greater degree of accuracy.

NEC represents the most accurate approach to the calculation of predicted site attenuation between resonant dipole antennas. Use of the more conventional Smith model to calculate CSA can introduce errors of up to 4 dB below 60 MHz, 2 dB from 60 MHz to 200 MHz and 1 dB above 200 MHz and up to 1 GHz. The applied EMF method is much more accurate and always within 1 dB of NEC. For this reason it is suitable for the validation procedure of test sites for EMC measurements, that requires their measured site attenuations to be within 4 dB of theoretical predictions. The Smith model is insufficiently accurate and should not be used below 200 MHz.

The 30 frequencies at which site attenuation is usually measured are not sufficiently closely spaced to enable a continuous site attenuation characteristic to be plotted for a given site. The implication of this is that certain features of the response of a site may be overlooked, leading to inaccurate measurements being made at other frequencies. Use of broadband antennas constructed from thin wires, such as skeletal biconical antennas, allows a swept measurement of CSA to be performed and NEC to be used to obtain predicted values of CSA. This approach is computationally expensive but massively reduces the amount of time that has to be spent on measurements.

Care has to be taken in accounting for the baluns of antennas used for a site attenuation measurement. With resonant dipoles, whose impedance does not vary significantly from 73 Ω, it appears that the manufacturers' balun loss figures in dB may be used successfully. Broadband antennas, such as the biconical antenna, have an impedance that varies strongly as a function of frequency and the full scattering parameters of their baluns must be accounted for in the calculation of predicted site attenuation.

The use of NSA for test site validation introduces unnecessary errors because it relies on antenna calibrations from the standard site method. The standard site method, and hence NSA, does not properly account for mutual coupling between closely spaced antennas and ground planes and therefore introduces errors between measured and predicted NSA that are not due to the site. These errors are suffi-

ciently large below 100 MHz that a good test site may not fall within the ±4 dB tolerance allowed between its measured site attenuation and prediction.

Below 60 MHz it is difficult to perform accurate test site validation. The NEC model of the biconical antenna has been shown to become less accurate below this frequency and the arms of resonant dipole antennas tend to droop. This means that it is difficult to calculate accurate predicted values of site attenuation. Accurate test site validation below 60 MHz should be performed with resonant dipoles, although they must be supported so that they do not droop. The full scattering parameters of their baluns must also be accounted for because the antenna impedances will not be close to 73 Ω.

The buildings around the test site at the University of York introduce a ripple whose amplitude is not greater 2 dB onto its 10 m site attenuation characteristic. The 3 m site is less affected and only suffers a ripple of 1 dB. The test site may therefore be used to perform radiation measurements to within these confidence levels over the frequency range of 30–300 MHz. Above this frequency the measured site attenuation data is not continuous and has only been taken at 50 MHz intervals with commercially available resonant dipole antennas. These results indicate that the ripple becomes less as frequency increases and that the site is still within 2 dB of prediction.

# Chapter 6

# Open-Area Test Site Characterisation by the Measurement of Ground Plane Reflection Coefficients

In chapter 1, theory has been developed to describe the fields that are set up by dipole sources above the ground plane of an open-area test site. This has shown that there are two propagation paths by which waves may travel between a pair of antennas above such a ground plane; the first is a direct path and the second involves reflection from the ground plane.

The ground plane of an ideal open-area test site is infinite in extent, perfectly flat and infinitely conducting; therefore it acts as a perfect reflector. The ground planes of real open-area test sites are intended to be as close to perfectly reflecting as possible, but they cannot be of infinite size or perfectly flat. Non-ideality of ground planes causes the reflected waves on different test sites to have slightly different amplitudes and phases at the respective receiving antennas. Because of this, measurements of the radiation from a standard item of equipment under test (EUT) are slightly different when performed on different test sites using the same measurement geometry.

In this chapter, a method is described that was used to measure the reflection coefficient of the ground plane of the real open-area test site at the University of York. The structure of this ground plane is described in chapter 1 and the procedures described in this chapter were devised to provide a means of assessing how close to perfectly reflecting it was.

§6.1 defines the reflection coefficient of a perfect ground plane and discusses the considerations that affect the reflection coefficient of a real ground plane. Aspects such as inhomogeneity of ground planes and finite conductivity of their construction materials are considered.

The measurement procedures described in this chapter can be used to calculate the reflection coefficient of a ground plane from the drive-point impedance of an antenna above the ground plane. §6.2 gives the theory that was used to calculate the reflection coefficients in this way. It also explains how simulations using the NEC computer code were performed as part of the calculation.

A complicated support arrangement was required to hold resonant dipole antennas at defined heights above a ground plane whilst their drive-point impedances were measured. These structures are described in §6.3 together with the instrumentation that was used for the measurements. §6.4 presents the results of the measurements and §6.5 summarises and draws conclusions from the work in this chapter.

## 6.1 Ground Plane Reflection Coefficients

The measurements of ground plane reflection coefficients presented in this chapter were performed in order to show how closely the ground plane of a real open-area test site approximated to an ideal one. This section defines the reflection coefficient of a perfect ground plane and explains the factors that affect the reflection coefficient of a real ground plane.

Reflection coefficient theory is usually developed for plane waves incident upon infinite, flat, homogeneous ground planes, but this is not representative of the measurement procedures of this chapter. The reflection coefficients were calculated from measurements of the drive-point impedances of horizontally polarised resonant dipole antennas and this section explains the special considerations that are necessary to interpret the results of measurements performed in this way.

### 6.1.1 Perfect Ground Plane

A perfectly reflecting ground plane reflects all power that is incident upon it, therefore its reflection coefficient has a magnitude of unity. The phase of the reflection coefficient depends upon the polarisation of the incident wave and is derived to satisfy the boundary condition that the electric field parallel to the ground plane must be zero at the surface.

Chapter 1 has shown how image theory can be used to satisfy the boundary conditions at the surfaces of ground planes with infinitesimal dipole sources above them. This shows that waves with their electric fields perpendicular to their plane of incidence, such as those originating from horizontally polarised antennas, undergo phase inversions on reflection, whereas waves from vertically polarised sources suffer no phase inversion.

The work in this chapter uses horizontally polarised antennas to measure the reflection coefficient of a real ground plane. It would therefore be expected to yield reflection coefficients of $-1$ at all frequencies if the ground plane had ideal behaviour.

### 6.1.2 Real Ground Plane

It has been explained in chapter 1 that the ground plane of a real open-area test site cannot be of infinite extent but, provided that it covers an area significantly larger than the first Fresnel zone, it will appear infinite. When considering coupling between two antennas above a ground plane, the three Fresnel zones shown in figure 6.1 must be considered. If the ground plane is perfect, all three reflection

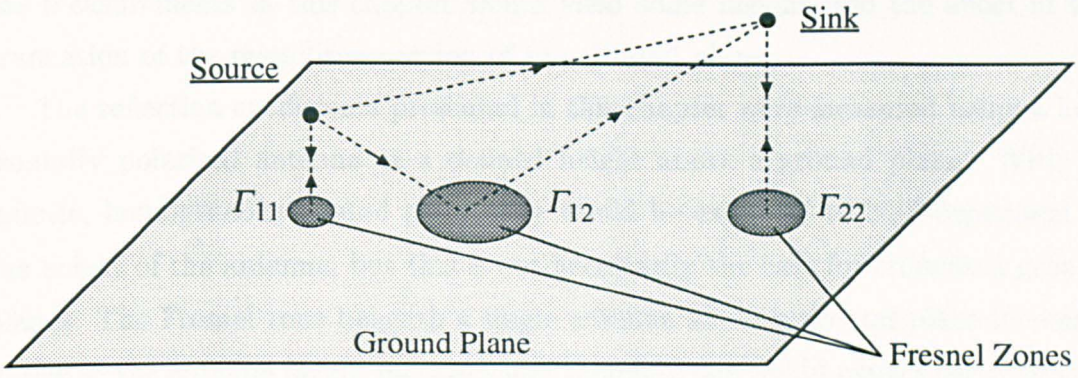


Figure 6.1: Fresnel zones affecting the reflected waves on an open-area test site.

coefficients, $\Gamma_{11}$, $\Gamma_{12}$ and $\Gamma_{22}$, shown in the figure will be equal, but with any other type of ground plane they will not be equal.

The circular Fresnel zones that are shown beneath each antenna in figure 6.1 affect the ground plane reflection coefficients, $\Gamma_{11}$ and $\Gamma_{22}$, experienced by waves that propagate from each antenna to the ground plane and then back to the same antenna. With an infinite, flat but partially reflecting ground plane, they will be identical, but not equal to $\Gamma_{12}$. This is because the wave affected by $\Gamma_{12}$ is not incident upon the ground plane normally.

The three Fresnel zones increase in size as the height of each antenna increases, and also as frequency is reduced. In order for the rectangular ground plane of a 10 m test site to extend beyond the first Fresnel zones at 30 MHz, with transmitting and receiving antenna heights of 2 m and 4 m respectively, it would need to have a minimum length of 18.1 m and a minimum width of 13.1 m. The grassed area of ground plane of the test site at the University of York is illustrated by a figure in chapter 1. It has dimensions larger than those required by the the CISPR ellipse, i.e. 20×17.3 m, therefore it extends beyond the first Fresnel zones under all conditions.

### 6.1.3 Inhomogeneous Ground Plane

The previous subsection has explained that the grassed area of the ground plane of the test site at the University of York is of sufficient size for it to act as a perfect reflector, however grassed earth is not a sufficiently good conductor for the ground plane to be a perfectly reflecting surface. It has been explained in chapter 1 that a metallic plate of dimensions 19.6×3.8 m lies over the central portion of the ground plane of this test site in order to improve the reflectivity of the ground plane.

Although this plate is sufficiently long to cover the first Fresnel zones, it is not sufficiently wide to cover the first Fresnel zones of the 10 m site at frequencies up to 1 GHz, or those of the 3 m site at frequencies below 380 MHz. It was hoped that

the measurements in this chapter would yield some insight into the effect of the truncation of the metallised portion of this ground plane.

The reflection coefficients presented in this chapter were measured using a horizontally polarised antenna at a defined height above a ground plane. With an infinite, homogeneous ground plane they would be expected to be independent of the height of the antenna, but this is not necessarily the case for truncated ground planes. The Fresnel zone beneath a single antenna above a ground plane increases in size as the antenna height increases and therefore one would expect the reflection coefficient of a truncated ground plane to become degraded as antenna height increases. A similar effect could also occur with an unhomogeneous ground plane and it was hoped to demonstrate it with the measurements performed in this chapter.

### 6.1.4 Effective Reflection Coefficient

Another important aspect in which a real open-area test site differs from an ideal one is that its ground plane may not be the only cause of the reflected wavefront. Buildings surrounding the test site will introduce specular reflections that will sum together with the wave reflected from the ground plane to give a total reflected wave due to the entire ground environment of the test site. It is difficult to separate these elements of the reflected wave and therefore it is difficult to analyse reflection from a ground plane in isolation.

It is possible to model the entire reflected wave on a given test site as if it had arisen purely from a reflection via the ground plane; this process gives rise to effective reflection coefficients. All of the reflection coefficients measured in this chapter are effective reflection coefficients.

The effective reflection coefficient is a function of height because the effect of stray reflections from buildings will become more significant as the antenna becomes further away from the ground plane. Also because of this, an effective reflection coefficient will tend towards the actual reflection coefficient of a ground plane as antenna height is reduced.

## 6.2 Reflection Coefficient in terms of Antenna Impedance

This section shows how image theory can be used to express the reflection coefficient of a ground plane in terms of the drive-point impedance of an antenna above the ground plane. The work in this chapter was performed using horizontally polarised resonant dipole antennas, although the approach taken may be extended to more general antenna structures and polarisations.

In order to calculate the reflection coefficient of a ground plane from the drive-point impedance of an antenna, it was also necessary to obtain the theoretical drive-point impedances of symmetrically and antisymmetrically fed antennas. These were calculated using NEC models that are described in this section.

### 6.2.1 Antenna above a Ground Plane

Consider a horizontally polarised resonant dipole antenna at a height, $h$, above a conducting ground plane, as shown in figure 6.2. The drive-point impedance of

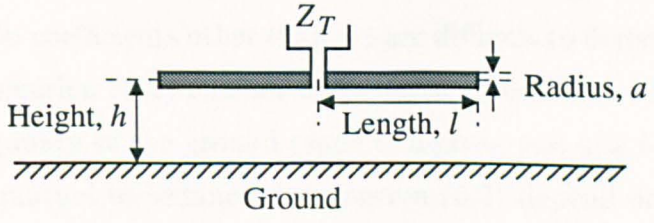


Figure 6.2: A horizontally polarised resonant dipole antenna above a conducting ground plane.

the antenna, $Z_T$, depends upon its own structure, i.e. its self impedance, and the coupling between the antenna and the ground plane. If the ground plane is a good conductor, its skin depth will be significantly less than the height of the antenna above it. Image theory may then be used to replace the ground plane by an image antenna, as shown in figure 6.3. The image antenna has the same physical dimensions as the object antenna and is separated from it by a distance of $2h$.

The drive-point impedance of the object antenna shown in figure 6.3 is given by the sum of its self impedance, $Z_{11}$, and the ground plane reflection coefficient, $\Gamma$, multiplied by the mutual impedance between the object and image antennas, $Z_{12}$, i.e.

$$Z_T = Z_{11} + \Gamma Z_{12} \tag{6.1}$$

From equation (6.1) it follows that the ground plane reflection coefficient may be

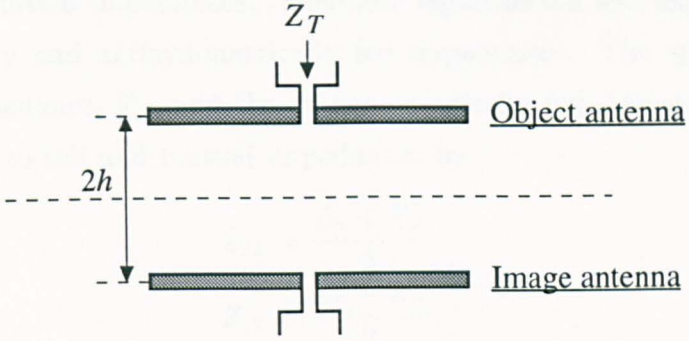


Figure 6.3: Pair of coupled antennas equivalent to a single horizontally polarised resonant dipole antenna above a conducting ground plane.

expressed as,

$$\Gamma = \frac{Z_T - Z_{11}}{Z_{12}} \tag{6.2}$$

Equation (6.2) implies that, if $Z_T$ can be measured and $Z_{11}$ and $Z_{12}$ can be calculated, the ground plane reflection coefficient may be determined.

It is important to realise that reflection coefficients calculated from equation (6.2) are only strictly correct for a perfectly reflecting ground plane. Such a ground plane is required for image theory to be exact and it would give $\Gamma = -1$. Therefore, although reflection coefficients other than $-1$ are difficult to derive any quantitative meaning from, equation (6.2) enables frequencies where $\Gamma \neq -1$ to be identified. This allows the quality of the ground plane of a given test site to be deduced.

The self and mutual impedances in equation (6.2) depend only upon the excitation frequency and the spatial geometry of the antennas, i.e. their length, radius and separation. They can be calculated directly using the NEC computer code but a slightly different approach was used and is described below.

### 6.2.2 Symmetrical and Antisymmetrical Impedances

The self impedance in equation 6.2 could have been calculated directly from a NEC simulation of a single antenna in free space and the mutual impedance could then have been deduced from a simulation of a pair of coupled antennas. It has been shown in chapter 2 that self and mutual impedances of resonant dipole antennas deduced from the impedances of symmetrically and antisymmetrically fed pairs of antennas are in error for antenna separations of less than half a wavelength. The 20 MHz dipole used for this work was used as close as 1.2 m, i.e.$\lambda/13$, from its image and therefore the mutual impedance calculated by this method would have been inaccurate.

The drive-point impedance of a horizontally polarised antenna closely coupled to a ground plane is better calculated as an antisymmetrically fed impedance than

from self and mutual impedances. Therefore equation 6.2 was expressed in terms of symmetrically and antisymmetrically fed impedances. The symmetrically fed drive-point impedance, $Z_S$, and the antisymmetrically fed drive-point impedance, $Z_A$, are related to self and mutual impedances by

$$Z_{11} = \frac{Z_S + Z_A}{2} \tag{6.3}$$

$$Z_{12} = \frac{Z_S - Z_A}{2} \tag{6.4}$$

These may be substituted into equation (6.2) to obtain

$$\Gamma = \frac{2Z_T - (Z_S + Z_A)}{(Z_S - Z_A)} \tag{6.5}$$

This equation was used to calculate the effective reflection coefficient of a ground plane from measurements of the drive-point impedance of an antenna above the ground plane and predictions of the drive-point impedances of pairs of symmetrically and antisymmetrically fed antennas.

### 6.2.3 NEC Model

In chapter 2, NEC has been used to simulate a resonant dipole antenna. The model that was used consisted of a single straight wire element divided into 21 equal length segments and with excitation applied across the middle segment. For the calculation of symmetrically and antisymmetrically fed drive-point impedances, two such model antennas were placed side by side as shown in figure 6.4.

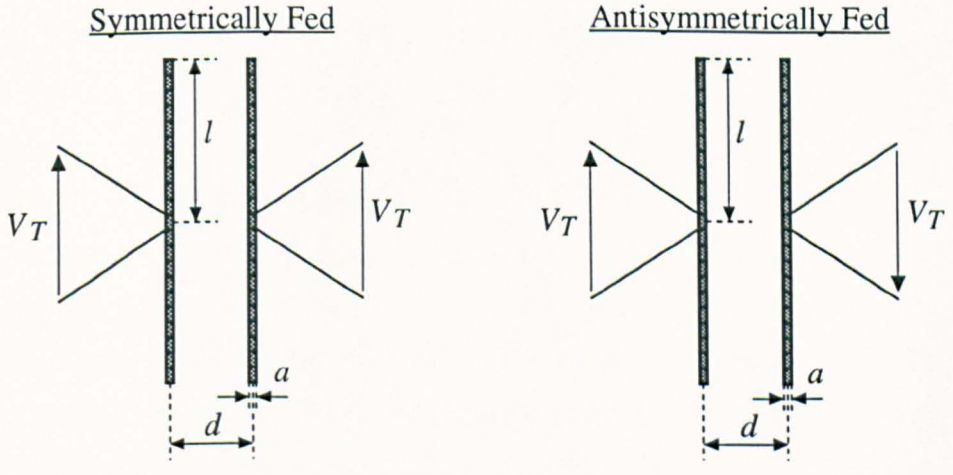


Figure 6.4: NEC models of pairs of symmetrically and antisymmetrically fed resonant dipole antennas.

Both of the antennas of each pair shown in figure 6.4 were driven by voltages whose magnitudes were the same but whose relative phases were determined by the impedance to be investigated. The drive-point voltages were in phase for the

calculation of symmetrically fed drive-point impedances and 180° out of phase for the calculation of antisymmetrically fed drive-point impedances.

The NEC simulations returned the drive-point impedances of the antennas directly and, since these were not affected by the magnitude of the excitation voltage, $V_T$, it was set arbitrarily to 1 Volt.

The diameter of each model antenna was equal to that of the real antennas used for the measurements in §6.3, i.e. 6.35 mm, and the lengths of the model antennas were set equal to the physical lengths of the real antennas.

The separations of the model antennas were twice the height of the real antenna above the ground plane. This was because one of the antennas of each pair was used to represent an image antenna the same distance below the ground plane as the object antenna was above.

## 6.3 Experimental Equipment

It was required to support a horizontal resonant dipole antenna above the ground plane of the test site at the University of York and to scan the height of the antenna while its drive-point impedance was measured. This section describes the structures that were used to provide support and the measurement and data acquisition equipment that were also used.

The measurements in this chapter were performed in order to determine the reflection coefficient of the ground plane and therefore deduce the effect of the truncation of the metallised portion of the ground on the performance of the test site. §6.1 has explained that this effect was expected to be most pronounced at the lower frequencies of test site operation and therefore drive-point impedance was measured over the 20–100 MHz frequency range, in 5 MHz steps up to 50 MHz and 10 MHz steps above 50 MHz.

### 6.3.1 Antenna Support Structures

Resonant dipole antennas have lengths from 7 m down to 1.5 m over the 20–100 MHz frequency range. The ones used for the measurements in this thesis had a diameter of 6.35 mm and therefore they had to be supported at several points over their lengths in order to prevent them from drooping. The support equipment that was used for this is shown in figure 6.5.

An EMCO antenna positioning mast was used to control the height of the antenna above the ground plane and a frame was built around the antenna in order to keep it horizontal while its height was scanned. The frame consisted of two wooden struts supporting a string tetrahedron across the bottom of which the antenna was mounted.

The minimum amount of material was used for the support structures in order to minimise their interaction with the antenna. Care was taken to ensure that both the wood and string used were dry so that they had good insulating properties.

The mast was used to vary the height of the antenna between 60 cm and 400 cm in 2 cm steps. Drive-point impedance was measured at each of these 171 heights at the 12 excitation frequencies. The accuracy to which the height of the antenna could be set was determined by the slight elasticity of the nylon rope that was used to hoist the antenna up and down. The height of the antenna could not be set with greater accuracy than ±4 cm with the EMCO mast.

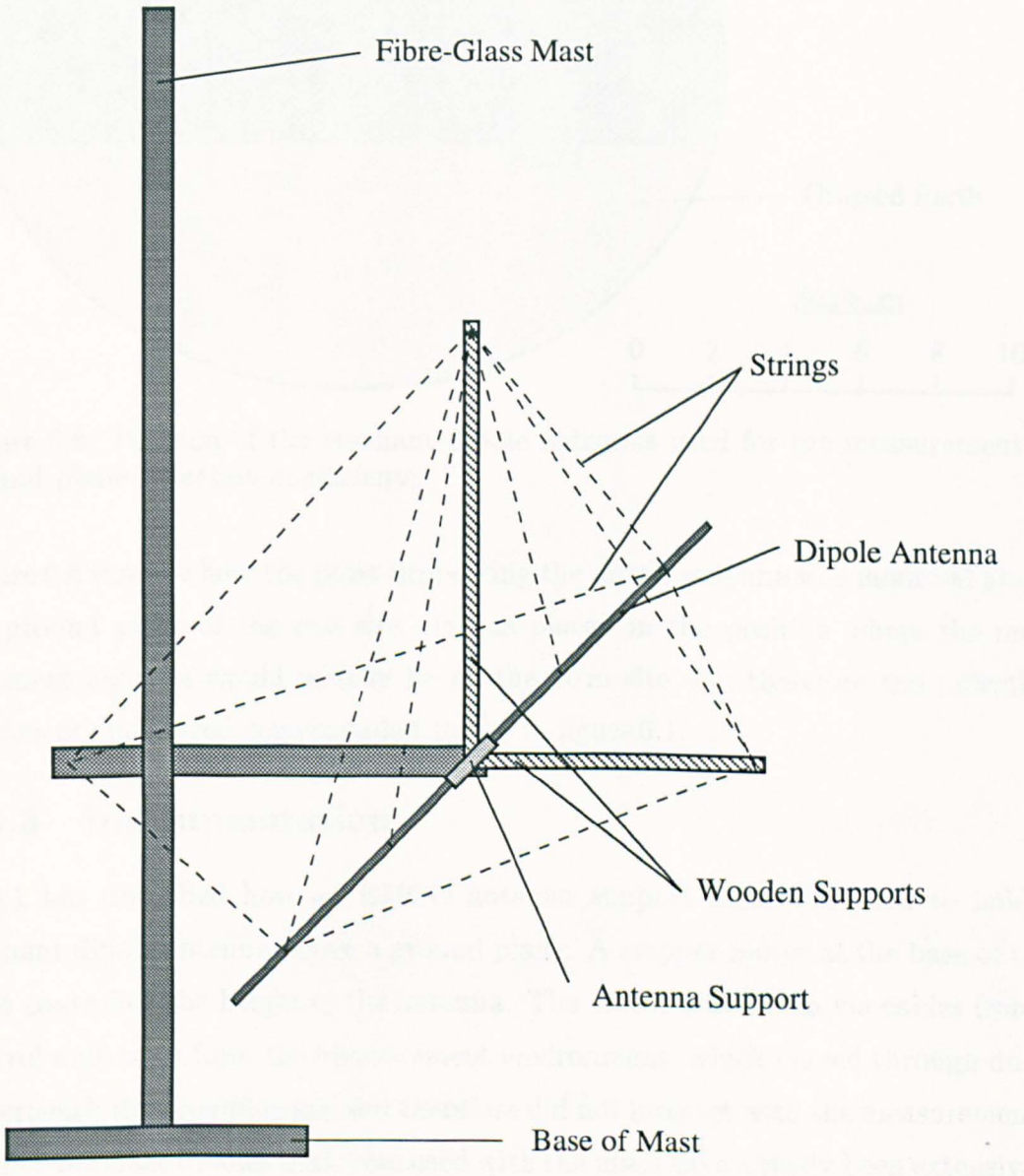


Figure 6.5: Support structures for the horizontal dipole antenna on the mast.

### 6.3.2 Antenna Position

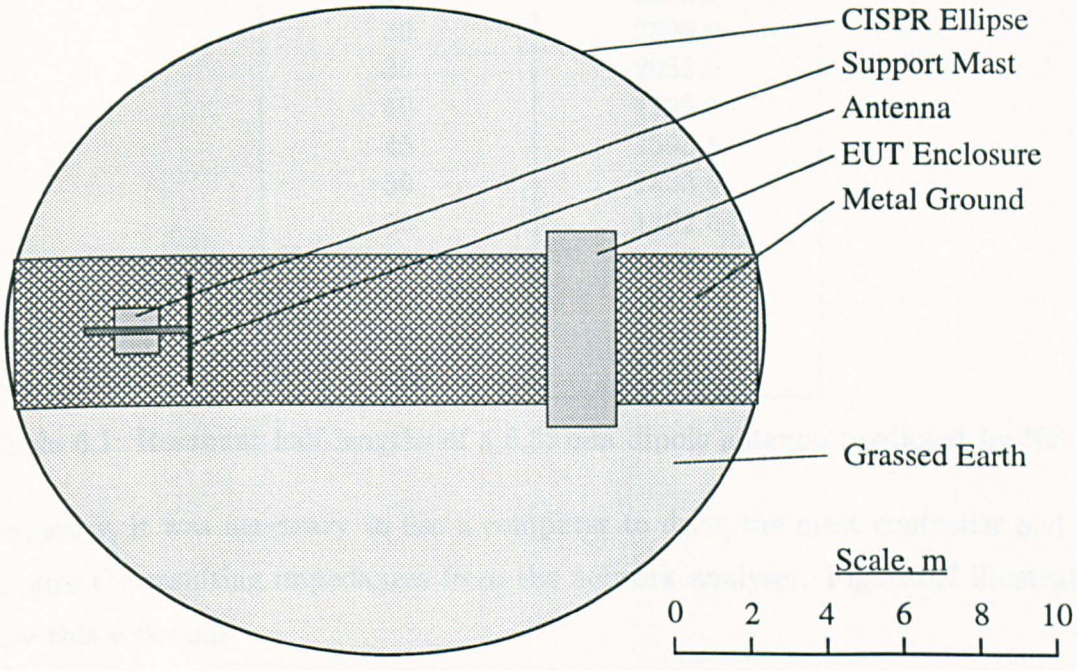


Figure 6.6: Position of the resonant dipole antennas used for the measurement of ground plane reflection coefficients.

Figure 6.6 shows where the mast supporting the dipole antenna was mounted above the ground plane of the test site. It was placed in the position where the measurement antenna would usually be on the 10 m site and therefore the reflection coefficients measured corresponded to $\Gamma_{11}$ in figure 6.1.

### 6.3.3 Instrumentation

§6.3.1 has described how an EMCO antenna support mast was used to hold a resonant dipole antenna above a ground plane. A stepper motor at the base of this mast controlled the height of the antenna. The motor was driven via cables from a control unit away from the measurement environment, which passed through ducts underneath the ground plane and therefore did not interact with the measurements.

The resonant dipoles that were used with the mast have already been extensively described in chapter 4, where their lengths have been calculated. The antennas had cylindrical arms of 6.35 mm diameter and their resonant lengths are repeated in table 6.1 for convenience. The antennas used for the experiments in this section were all cut to their resonant lengths except for the 20 MHz one, which was cut to a half-length of 3519 mm because this was the maximum length of brass rod available.

In order to generate a data file of antenna impedance against height at a fixed

| Frequency / MHz | Half-Length / mm |
|---|---|
| 20 | 3609.0 |
| 25 | 2882.5 |
| 30 | 2399.0 |
| 35 | 2053.5 |
| 40 | 1795.0 |
| 45 | 1593.5 |
| 50 | 1433.0 |
| 60 | 1192.0 |
| 70 | 1020.0 |
| 80 | 891.0 |
| 90 | 790.5 |
| 100 | 710.5 |

Table 6.1: Resonant half-lengths of a 6.35 mm dipole antenna predicted by NEC.

frequency, it was necessary to use a computer to drive the mast controller and to acquire the resulting impedances from the network analyser. Figure 6.7 illustrates how this was done.

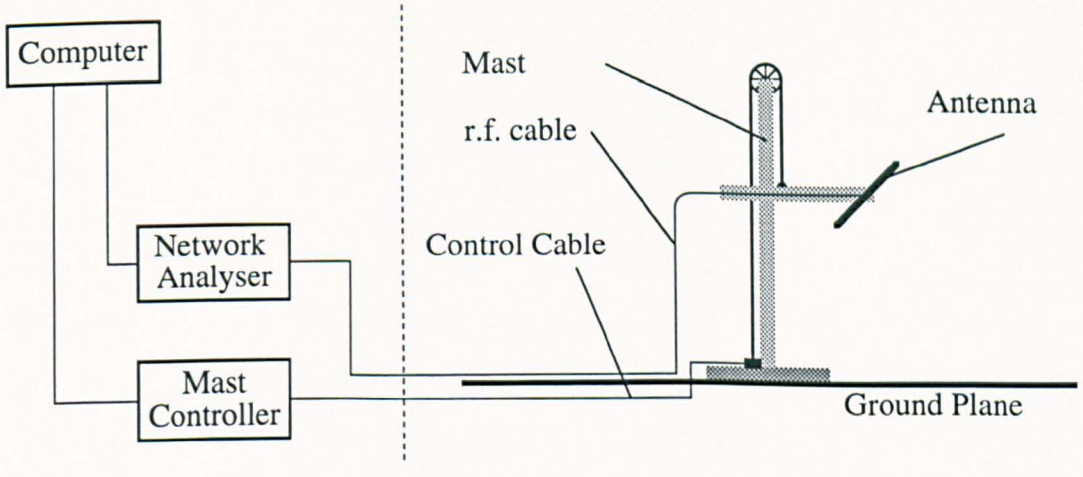


Figure 6.7: Instrumentation used for the measurement of the drive-point impedance of an antenna as a function of its height above a ground plane.

### 6.3.4 Measurement of Drive-Point Impedance

In order to measure the impedance of an antenna it is necessary to calibrate a network analyser to establish a reference plane at the drive-point of the antenna. An HP8753A network analyser with an HP85046A two-port test set was used for the measurements in this chapter and the procedures used for its calibration are described in chapter 4.

In chapter 4 it has been explained that the measured impedance of the antenna, $Z_M$, is given by the parallel combination of the idealised drive-point impedance of the antenna, $Z_T$, and a parasitic capacitance of 0.5 pF that can be used to model

the effect of the nylon support in the feed region of the antenna. An expression was derived to correct the measured impedances and this is repeated as equation (6.6).

$$Z_T = \frac{Z_M}{1 - j\omega C Z_M} \tag{6.6}$$

## 6.4 Results

Measurements of $Z_M$ were made at the frequencies shown in table 6.1 and these were corrected to $Z_T$ using equation (6.6). The resulting measurements are shown as functions of antenna height in figures 6.8 to 6.19. Also shown by these graphs are the predicted symmetrically and antisymmetrically fed impedances corresponding to each measurement. Equation (6.5) was used to calculate the effective ground plane reflection coefficients and their real and imaginary components are shown in figures 6.20 to 6.31.

### 6.4.1 Measured Drive-Point Impedances

The graphs of measured drive-point impedances show the behaviour expected from the self and mutual impedance theory of chapter 2, in that the resistive and reactive components oscillate above the self impedance as functions of height. The self impedance of all the antennas is close to $(73 + j0)\,\Omega$ except for that of the 20 MHz dipole. This antenna was slightly shorter than its resonant length and is therefore slightly capacitive.

The periodicity of the oscillations is a function of the wavelength, so there is only half a cycle between 60 and 400 cm height at 20 MHz, whereas there are four and a half cycles at 100 MHz. The oscillations are periodic in half-wavelengths, i.e. whole wavelengths of the object and image separations.

Under most conditions the measured impedances closely follow the antisymmetrical impedances, indicating close to ideal ground plane behaviour. As height increases, particularly above 2 m, the measured impedances begin to diverge from the antisymmetrical impedances and the reasons for this will be explained in §6.4.2.

### 6.4.2 Reflection Coefficients

The real and imaginary components of the reflection coefficients show smooth behaviour that has progressively less dependence upon height towards lower antenna heights. As height increases, the reflection coefficients show an increasing oscillatory height dependence with the same period as their corresponding impedances. This behaviour is not a property of the ground plane of the test site but is caused by the buildings surrounding it.

It was found that constant offsets of a few ohms in the measured impedances could cause oscillatory behaviour in the resulting reflection coefficients and therefore a cause of such offsets was searched for. The structure of the test site at the University of York is shown by a figure in chapter 1. This figure shows that behind

the antenna, at a distance of 7.5 m, was a building capable of introducing a stray reflection. The separation of the antenna from this building was 7.5 m irrespective of antenna height, therefore at lower heights a reflection from the ground plane dominated the drive-point impedance but towards 4 m height, the reflections from the ground plane and from the building were significant.

The reflection coefficients at frequencies up to 60 MHz are smooth functions of height and show only a single ripple component due to the stray reflection, but above this frequency the data becomes degraded. A problem with the network analyser gave small steps in the measured impedances that are particularly visible on the real reflection coefficient data at 90 MHz and 100 MHz. These two data sets also show more noise than the others due to the concentration of ambients associated with the VHF radio band. The 70MHz data have an anomalous form that is thought to be due to a bad connection or incorrectly cut antenna length.

### 6.4.3 Reflection Coefficients at Low Heights

It has been explained that the effective reflection coefficients in figures 6.20 to 6.31 are not purely due to the ground reflection because stray reflections from buildings around the test site also affect the antenna impedance. At lower heights the reflection from the ground plane dominates the antenna impedance and so at zero height the effective reflection coefficients tend to the actual reflection coefficient of the ground plane.

An algorithm was desired that could be used to extrapolate the reflection coefficient curves shown in the figures to determine their values at zero height. Extrapolation of curves is a mathematically dangerous operation and is only reliable for certain types of data. It can be performed successfully with curves that are very smooth and have no high frequency oscillations, such as the reflection coefficient data for frequencies up to 60 MHz.

A Linear Prediction routine was taken from a Numerical Recipes text book [82] and was used to determine the reflection coefficients at zero height. The results are shown in table 6.2.

Table 6.2 shows that the ground plane acts as a perfect reflector at 60 MHz but its performance degrades progressively at lower frequencies. The ground plane is a 70% reflector at 20 MHz, but its lowest usual frequency of illumination, i.e. 30 MHz, it is still a 90% reflector. The reflection coefficient at 50 MHz is the only one that does not follow the general trend and has the impossible value of 1.08. This is clearly wrong and visual inspection of the data indicates that the extrapolation

| Frequency MHz | Reflection Coefficient | | | |
|---|---|---|---|---|
| | Real | Imaginary | Magnitude | Phase |
| 20 | −0.69 | 0.21 | 0.72 | 163 |
| 25 | −0.80 | 0.10 | 0.81 | 172 |
| 30 | −0.89 | 0.10 | 0.90 | 174 |
| 35 | −0.95 | 0.05 | 0.95 | 174 |
| 40 | −0.97 | 0.05 | 0.97 | 178 |
| 45 | −0.97 | 0.06 | 0.98 | 177 |
| 50 | −1.07 | −0.03 | 1.08 | 178 |
| 60 | −1.00 | 0.03 | 1.00 | 180 |

Table 6.2: Ground plane reflection coefficient data extrapolated to zero antenna height.

routine may not have given an accurate value.

Although table 6.2 shows that ground plane performance becomes slightly degraded at frequencies approaching 30 MHz, it is important to consider the fact that the measurement antenna was far from physically small at these frequencies. At 30 MHz it was 7.0 m long and protruded beyond the edges of the metallised portion of ground plane. This would have given rise to degraded reflection coefficients, but with EUTs and measurement antennas of more realistic dimensions, i.e. less than 2 m, it is unlikely that the ground plane reflection coefficient would be degraded.

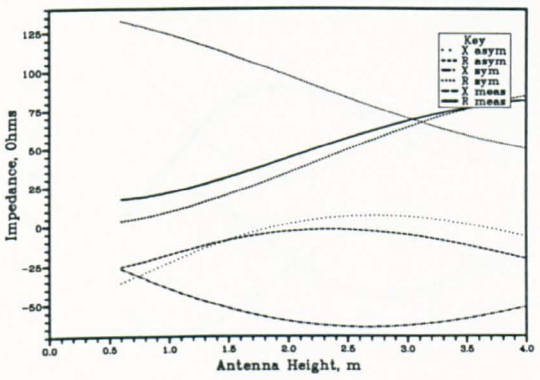


Figure 6.8: The resistive and reactive components of measured drive-point impedance and predicted symmetrically and antisymmetrically fed impedances at 20 MHz.

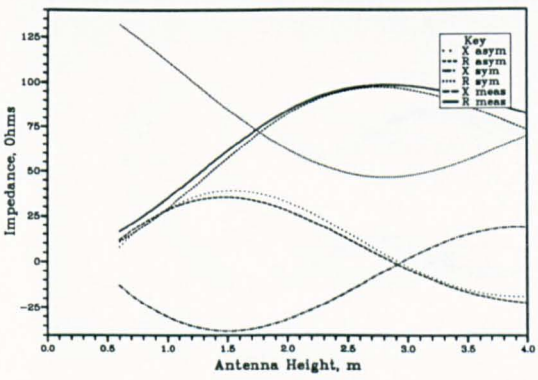


Figure 6.11: The resistive and reactive components of measured drive-point impedance and predicted symmetrically and antisymmetrically fed impedances at 35 MHz.

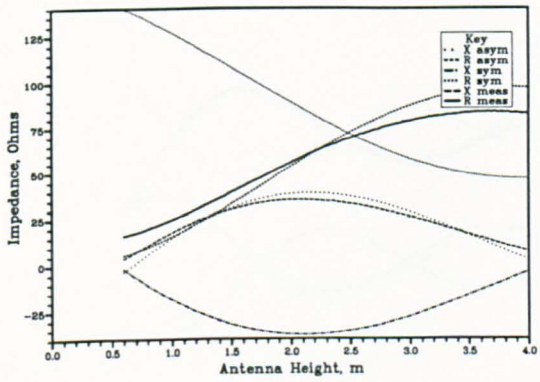


Figure 6.9: The resistive and reactive components of measured drive-point impedance and predicted symmetrically and antisymmetrically fed impedances at 25 MHz.

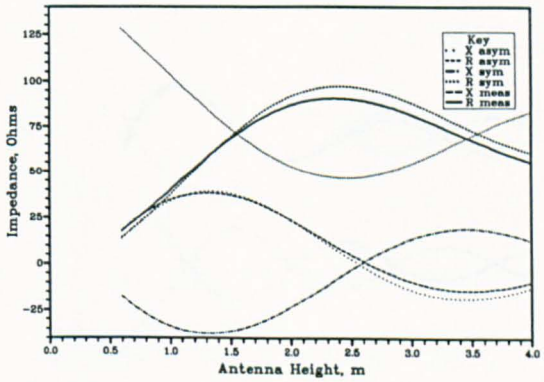


Figure 6.12: The resistive and reactive components of measured drive-point impedance and predicted symmetrically and antisymmetrically fed impedances at 40 MHz.

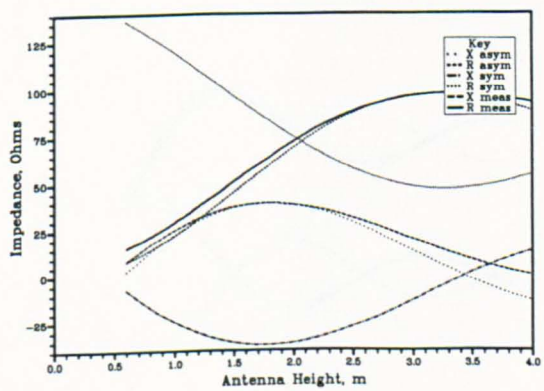


Figure 6.10: The resistive and reactive components of measured drive-point impedance and predicted symmetrically and antisymmetrically fed impedances at 30 MHz.

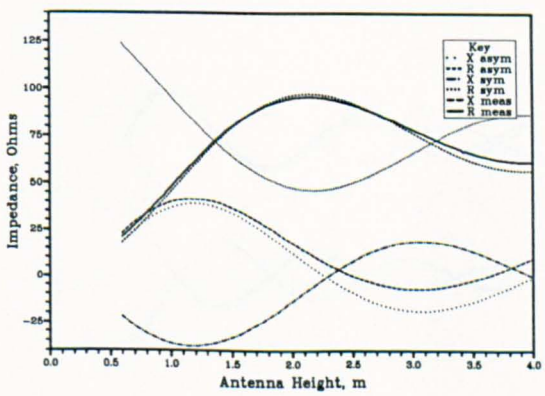


Figure 6.13: The resistive and reactive components of measured drive-point impedance and predicted symmetrically and antisymmetrically fed impedances at 45 MHz.

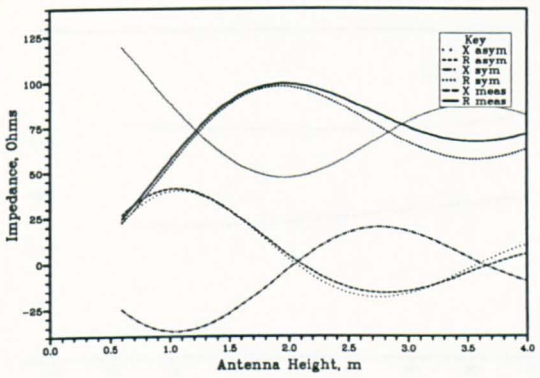


Figure 6.14: The resistive and reactive components of measured drive-point impedance and predicted symmetrically and antisymmetrically fed impedances at 50 MHz.

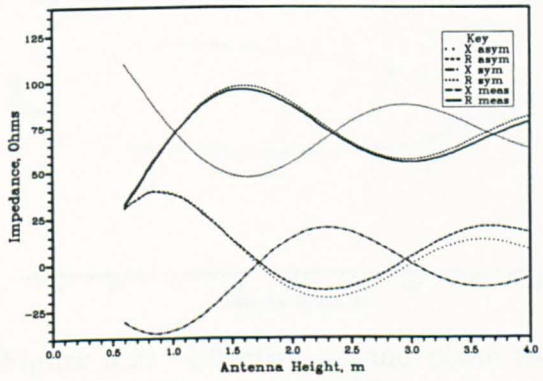


Figure 6.15: The resistive and reactive components of measured drive-point impedance and predicted symmetrically and antisymmetrically fed impedances at 60 MHz.

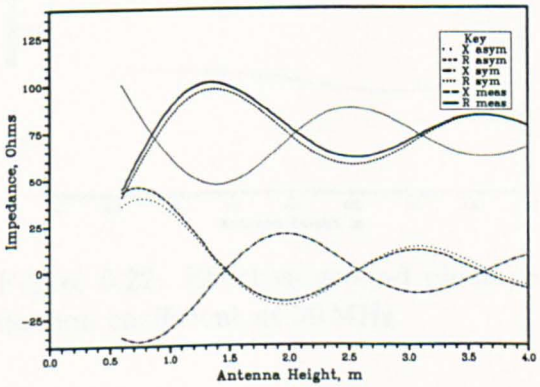


Figure 6.16: The resistive and reactive components of measured drive-point impedance and predicted symmetrically and antisymmetrically fed impedances at 70 MHz.

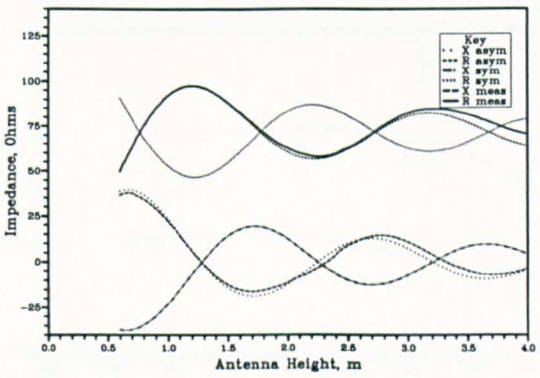


Figure 6.17: The resistive and reactive components of measured drive-point impedance and predicted symmetrically and antisymmetrically fed impedances at 80 MHz.

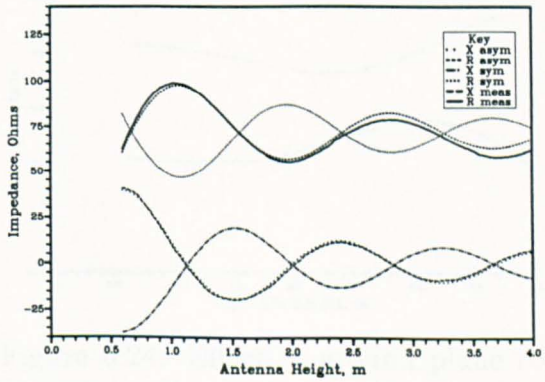


Figure 6.18: The resistive and reactive components of measured drive-point impedance and predicted symmetrically and antisymmetrically fed impedances at 90 MHz.

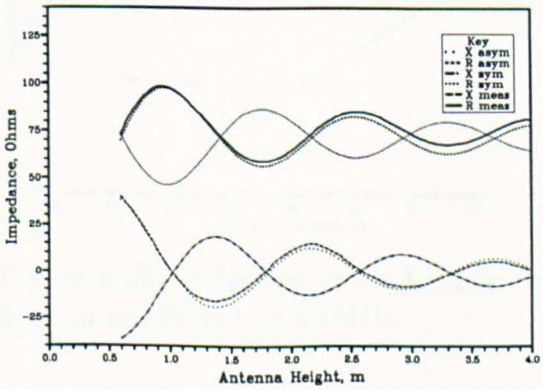


Figure 6.19: The resistive and reactive components of measured drive-point impedance and predicted symmetrically and antisymmetrically fed impedances at 100 MHz.

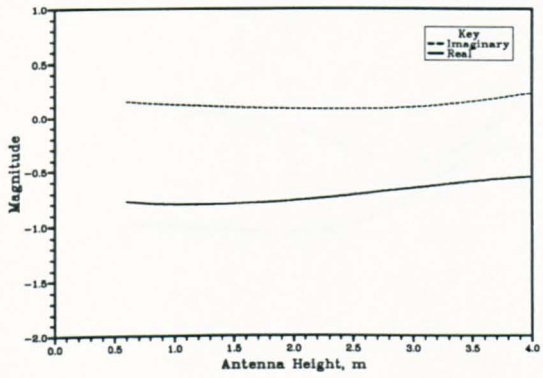


Figure 6.20: Effective ground plane reflection coefficient at 20 MHz.

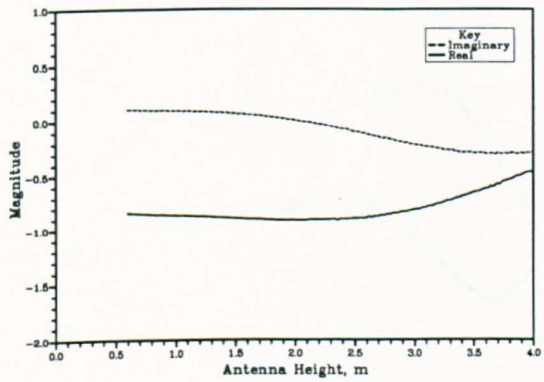


Figure 6.21: Effective ground plane reflection coefficient at 25 MHz.

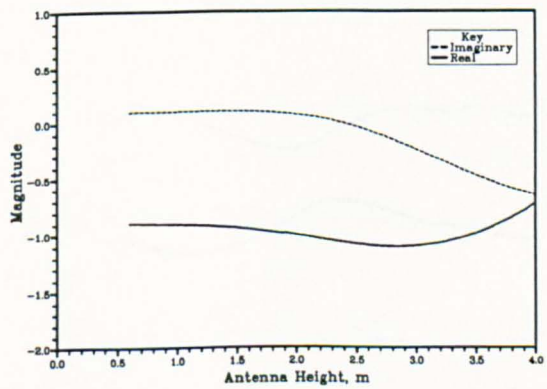


Figure 6.22: Effective ground plane reflection coefficient at 30 MHz.

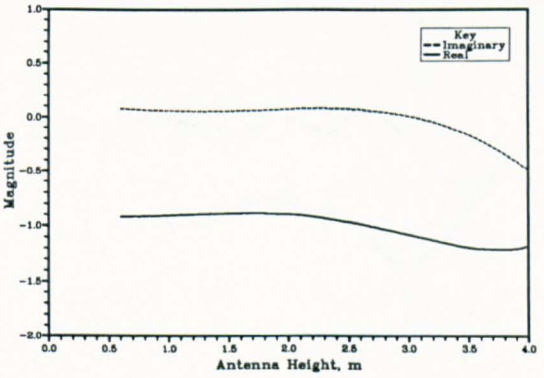


Figure 6.23: Effective ground plane reflection coefficient at 35 MHz.

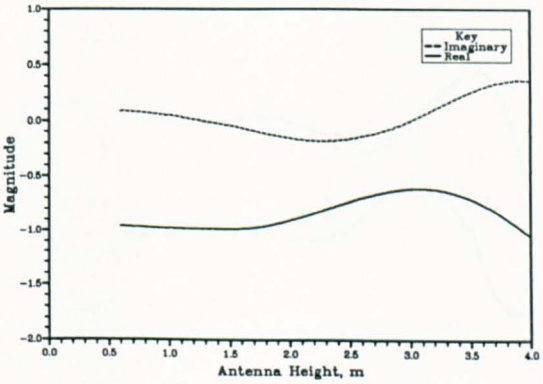


Figure 6.24: Effective ground plane reflection coefficient at 40 MHz.

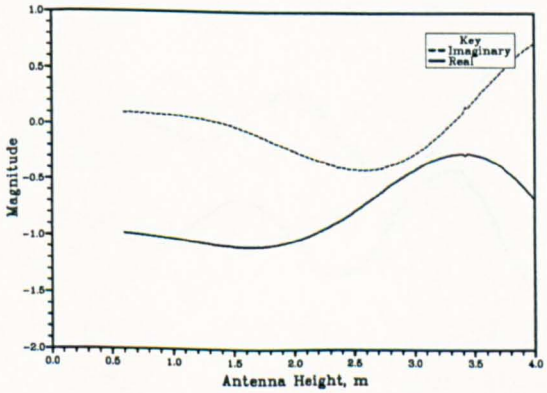


Figure 6.25: Effective ground plane reflection coefficient at 45 MHz.

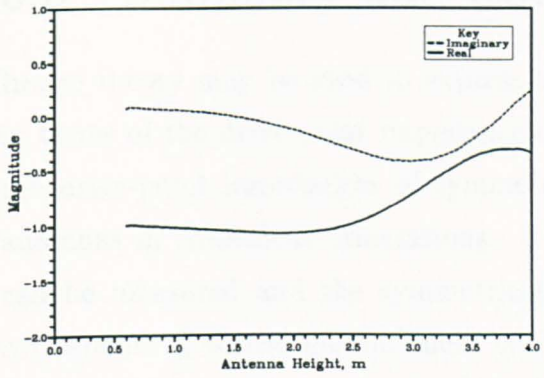


Figure 6.26: Effective ground plane reflection coefficient at 50 MHz.

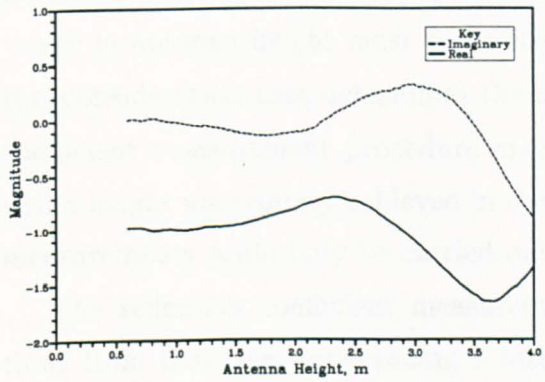


Figure 6.27: Effective ground plane reflection coefficient at 60 MHz.

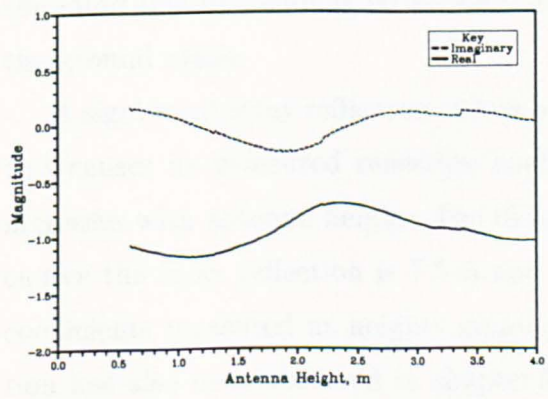


Figure 6.28: Effective ground plane reflection coefficient at 70 MHz.

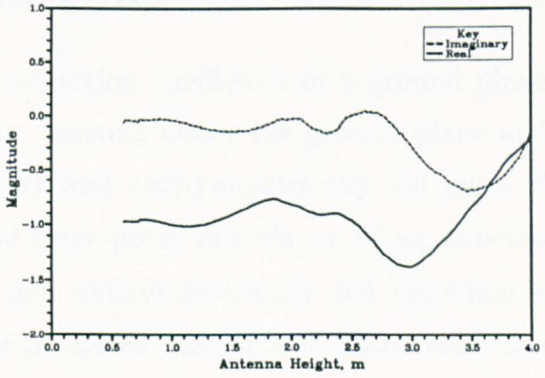


Figure 6.29: Effective ground plane reflection coefficient at 80 MHz.

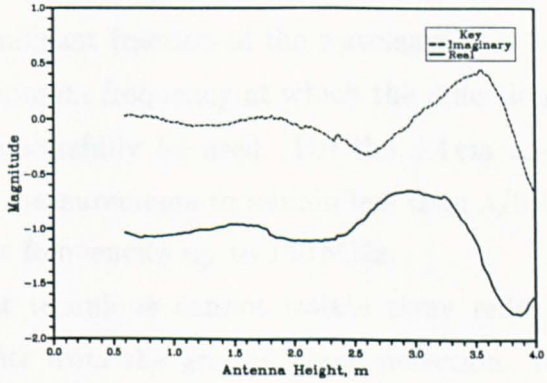


Figure 6.30: Effective ground plane reflection coefficient at 90 MHz.

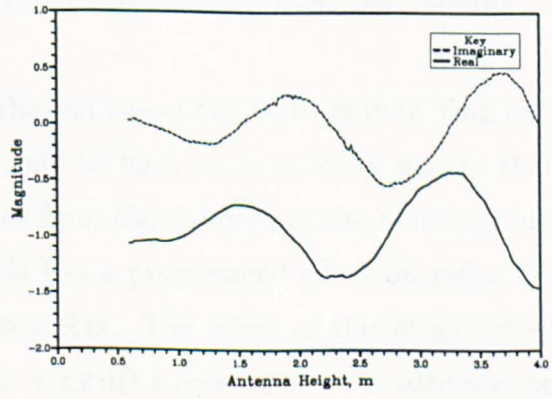


Figure 6.31: Effective ground plane reflection coefficient at 100 MHz.

## 6.5 Summary and Conclusions

Image theory may be used to express the reflection coefficient of a ground plane in terms of the drive-point impedance of an antenna above the ground plane and the drive-point impedances of symmetrically and antisymmetrically fed pairs of antennas in equivalent orientations. If the drive-point impedance of an antenna can be measured and the symmetrically and antisymmetrically fed impedances corresponding to the measurement can be predicted, the ground plane reflection coefficient may then be calculated.

The resistive and reactive components of the impedance of an antenna above a ground plane oscillate about the self impedance as functions of height. The period of these oscillations is equal to half a wavelength and therefore any uncertainty in antenna height must be an insignificant fraction of the wavelength. It is this consideration that determines the maximum frequency at which the reflection coefficient measurement procedure may successfully be used. For the $\pm 4$ cm antenna height uncertainty achieved in these measurements to remain less than $\lambda/50$, measurements could only be carried out at frequencies up to 150 MHz.

The reflection coefficient measurement technique cannot isolate stray reflections from buildings surrounding a test site from the ground plane reflection. If significant stray reflections occur on a given test site, the measurements must be performed with sufficiently low antenna heights that the reflection from the ground plane will dominate, i.e. the distance from the measurement antenna to any surrounding building should be at least ten times the distance from the antenna to the ground plane.

A significant stray reflection occurs on the test site at the University of York and this causes its measured reflection coefficients to have an oscillatory nature that increases with antenna height. The distance from the antenna to the building that causes the stray reflection is 7.5 m and this has a pronounced effect on reflection coefficients measured at heights greater than 2 m. The effect of this stray reflection has also been observed in chapter 5 as a $\pm 2$ dB ripple on the site attenuation characteristic of the 10 m site.

The metallised portion of the ground plane of the York test site has slightly degraded reflecting properties at the lowest frequencies of test site operation. This is because it is only 3.8 m wide and therefore is not wide enough to cover the first Fresnel zones. Fortunately the grassed earth around the metal area is a sufficiently good reflector for the degradation not to have a significant effect on EMC measurements. The ground plane has a reflection coefficient of $0.89\angle 174°$ at 30 MHz,

which is the lowest usual frequency of operation of an open-area test site, but at 20 MHz it has a reflection coefficient of $0.72\angle 163°$.

The reflection coefficients in this chapter were measured with resonant dipole antennas and therefore are not entirely representative of those that would be perceived by broadband antennas or items of equipment under test. These have typical dimensions of less than 1.5 m, whereas the resonant dipoles had lengths of 7.0 m at 20 MHz and 4.8 m at 30 MHz. The degraded reflection coefficients were partly caused by the resonant dipole antennas protruding beyond the edges of the metal ground plane, but this would not occur with broadband antennas or EUTs, which would experience reflection coefficients closer to unity.

The measured reflection coefficients of the ground plane of the York test site have been explained to be worse than those that would be achieved when making a radiation measurement because resonant dipoles are considerably larger than broadband antennas or items of equipment under test. They are, however, representative of the reflection coefficients that would be perceived when using resonant dipole antennas for a measurement of site attenuation. In chapter 5, no degradation has been found in the agreement between measured and theoretical site attenuations until 20 MHz. This indicates that the reflection coefficient measurement procedure is more sensitive than a site attenuation measurement to ground plane non-ideality at low frequencies.

# Chapter 7

# Conclusions

The primary objective of this thesis was to characterise the open-area test site facility at the University of York and determine the factors affecting the accuracy of radiation measurements performed using it. In order to achieve this aim, theory was developed to describe the performance of an ideal open-area test site. Results from the York test site were compared with this in order to deduce how close its propagation characteristics were to those of an ideal test site. Predictions for the performance of non-ideal test sites were used to explain any differences between the propagation characteristics of the York test site and the theoretical ideal one.

Two basic approaches were used to characterise the York test site; the first was a measurement of the effective reflection coefficient of its ground plane and the second was a more conventional site attenuation measurement. Both of these techniques required accurately characterised antennas and therefore the initial work of this thesis was concerned with the development of such antennas.

For clarity, the conclusions of this thesis have been divided into five main areas. The first three sections of this chapter present conclusions derived from modelling work that was carried out on resonant dipole and skeletal biconical antennas. §7.1 and §7.2 concentrate on the electrical characteristics of these antennas and the development of suitable models for their simulation using the NEC computer code. §7.3 extends the modelling work to antenna calibration and derives corrections to account for the presence of ground planes beneath each type of antenna.

Several different variations on the site attenuation method for test site validation were used in this thesis and considerable shortcomings were found with the measurement techniques advocated by EMC standards. §7.4 summarises the findings of this work and suggests a novel technique for rigorous test site validation using broadband antennas. §7.5 presents the conclusions about test site design that were derived from theory and contrasts them with the results obtained for the York test site. Finally §7.6 is a further work section that describes useful extensions that

could be carried out to the work in this thesis.

## 7.1 The Resonant Dipole Antenna

The resonant dipole is the simplest and best understood practical antenna. Its idealised structure consists of two equal-length cylindrical rods arranged collinearly and excited across an infinitesimally thin gap. It is possible to derive integral equations to describe the current distribution on this antenna and they may be solved using a method of moments computer code such as NEC. The self impedance of the antenna may then be found, or a similar approach may be used to analyse the interactions between several antennas.

An alternative method of analysis for the resonant dipole is based upon the realisation that its current distribution has an essentially sinusoidal shape, with a maximum at the centre of the antenna and nulls at either end. If the current distribution of the antenna is assumed to have this form, the applied EMF method can be used to calculate its self impedance, or the mutual impedance between pairs of such antennas. Impedance predictions from the NEC computer code and the applied EMF method have been compared with measurements of self impedance in this thesis.

### 7.1.1 Electrical Characteristics

The self impedance of a cylindrical dipole antenna is capacitive at frequencies where the antenna is significantly shorter than half a wavelength. As the length of the antenna approaches half a wavelength, the resistive component of the antenna impedance becomes significant and the reactive component passes through zero. The frequency at which this occurs is known as the resonant frequency of the antenna and the resistance is equal to $73\,\Omega$ at this frequency.

The precise length at which a dipole antenna resonates is determined by its radius; thinner antennas resonate where their lengths are closer to half a wavelength. The gradient of the reactive impedance component as it passes through zero controls the frequency range over which the antenna maintains a good match to a $50\,\Omega$ transmission line. This gradient is steeper for thinner antennas and therefore they have less bandwidth than proportionally fatter antennas.

### 7.1.2 Accuracy of Models

The modelling results showed NEC to be capable of predicting self impedance components of a resonant dipole within $4\,\Omega$ of measurement, however limited measurement accuracy meant that NEC was probably more accurate than this. The applied EMF method was found to be significantly less accurate than NEC and

gave resistive and reactive components that were around 10–15 Ω less than measured values.

One reason for the inaccuracy of the applied EMF method was associated with the modelling of currents at the free ends of an antenna. The current on the model antenna was assumed to become zero immediately at its ends, whereas that of the real antenna flowed for a short distance back inside the tubular arms. This resulted in model antennas whose lengths were electrically shorter than those of the real ones. Adding a 3 mm length correction to the model antennas brought their reactances into good agreement with NEC, but the resistive components were still 8–10 Ω less than NEC. This shortfall in predicted radiation resistance is the main limitation of the applied EMF method.

There are two approaches that may be used to model the interactions between coupled cylindrical dipole antennas; one is to use a complete integral equation formulation to solve for all the interactions between the antennas, and the other is to solve a matrix containing the self and mutual impedances of the antennas. The latter approach is the only one possible for the applied EMF method and its mathematical simplicity also makes it attractive for integral equation solutions for coupling between more than two antennas.

A technique was used to separate self and mutual impedances from the drive-point impedances of pairs of symmetrically and antisymmetrically fed antennas. Self impedances obtained from NEC simulations in this way were found to be equal to ones obtained from a simulation of a single antenna, provided that the separations of the coupled antennas were greater than half of a wavelength. For smaller separations, self and mutual impedances deduced from coupled impedances become inaccurate, therefore care should be taken when analysing closely coupled antennas by an impedance matrix based approach.

### 7.1.3 Practical Considerations

Two different practical implementations of resonant dipoles were used for the measurements in this thesis. A set of commercially available EMCO resonant dipoles were used, but because their structures contained integral balun devices that were uncalibrated, problems were found deducing predictions that were equivalent to measurements made with them. The other type of resonant dipole antennas overcame this problem by having balanced feed networks and connectors at their drive-points to facilitate calibration of a network analyser.

NEC was used to simulate both of the above antennas, but because their struc-

tures differed from the idealised structures of the model antennas, corrections had to be derived. It has been explained that the integral balun of the first antenna caused problems for accurate simulation of the antenna. The manufacturers of these antennas supplied loss factors in dB for their baluns and these were used as corrections.

The resonant dipoles that were constructed differed from the model antennas in three ways:

1. They had a finite gap of 18 mm at their drive-points.

2. They were fed from balanced transmission lines.

3. Their drive-points were encased in a nylon support.

Small gaps at the drive-points of cylindrical dipole antennas do not affect their impedances provided that the antenna is at resonance, therefore the first consideration was not a problem. The transmission lines feeding the antennas left the measurement environments in the plane normal to the electric fields and therefore could be assumed not to interact.

An experiment was devised to measure the effect of the nylon support. It was found that it could be modelled as a parasitic capacitance in parallel with the drive-point, provided that it did not cover an appreciable fraction of the length of the antenna. The 100 mm support of the real antenna was equivalent to a capacitance of 0.5 pF at frequencies up to 100 MHz. This parasitic capacitance had negligible effect on site attenuation measurements made with the antennas, but slightly affected their impedances. A correction was applied to the measured impedances of the antennas in order to account for this when calculating ground plane reflection coefficients.

## 7.2 The Skeletal Biconical Antenna

A commercially available broadband skeletal biconical antenna was calibrated and used for measurements of site attenuation in this thesis. It was manufactured by Schwarzbeck, model no. BBA9106, and had a total length of 1.3 m. This antenna had an integral balun device, but a technique was developed by which the radiators of the antenna could be removed whilst the scattering parameters of its balun were measured. These measurements were combined with a NEC simulation of the radiators in order to derive predicted antenna factors.

The two cones of the antenna were each formed from six elbow-shaped wires and a central straight wire. The triangle formed by one elbow-shaped wire and the central wire had an angle of 30° at the middle of the antenna and 90° at the widest point of the antenna, thus the entire structure of a cone could be defined by one length. The only other dimensions of the antenna required to simulate its radiators were the cone separation and the wire radius. The measured dimensions were:

Cone length = 603.5 mm
Cone separation = 87 mm
Wire radius = 6 mm

NEC can only model structures made from thin wires and therefore it was not possible to model the feed region of the real antenna representatively. The feed region consisted of a 40 mm gap containing the metal antenna support, but this was modelled by an 87 mm cone-linking wire that was given the same radius as the other wires, i.e. 6 mm. The middle segment of this wire was used to excite the model. Simulations were performed using this model to deduce the drive-point impedance and other performance parameters of the real antenna.

### 7.2.1 Electrical Characteristics

At frequencies where the length of the biconical antenna is considerably shorter than half a wavelength, i.e. below 60 MHz, it has similar characteristics to a cylindrical dipole antenna, in that its impedance is capacitive. Mismatch between the antenna and a 50 Ω transmission line therefore reduces its efficiency at low frequencies. At 73 MHz the impedance of the biconical antenna is purely resistive and equal to 27 Ω ; this is its resonant frequency, although the impedance is rather less than the 73 Ω of the resonant dipole antenna. Above 73 MHz the impedance is

complex but its magnitude remains sufficiently small for the antenna to maintain a reasonable match to a 50 Ω transmission line.

Over a very narrow frequency range of 3 MHz centred on 277.8 MHz, the self impedance components of the biconical antenna show a sharply tuned resonant feature. This is the cone resonance of the antenna and is associated with standing waves inside its cones. It is not possible to calibrate the antenna reliably at frequencies close to this resonance and so some manufacturers add an extra wire to each cone of their antennas to break up the standing waves. This moves the resonance up in frequency and above the 300 MHz maximum operating frequency of the antenna. A more effective modification would be to remove the central wire from each cone; this removes the resonance and only slightly changes the drive-point impedance of the antenna.

### 7.2.2 Optimum NEC Model

A network analyser was calibrated to perform an impedance measurement at the drive-point of the real skeletal biconical antenna. The antenna was then mounted above the ground plane of an open-area test site and its measured impedance was compared with the predicted impedance of the model antenna. Various parameters of the model antenna were adjusted in order to achieve the best possible agreement between its predicted and measured impedances. It was assumed that if a NEC model of the antenna gave the correct drive-point impedance, it must have a representative current distribution and would therefore give equally good results for radiated fields and power coupled to other antennas.

The predicted cone resonance of the model antenna was 277.8 MHz, whereas the cone resonance of the real antenna was at 287.3 MHz. The frequency of this resonance depended only upon the cone length and it was found that reducing this to 585.275 mm brought the predicted cone resonant frequency into agreement with measurement. It also improved the agreement between the measured and predicted impedance components at all other frequencies.

The reason for the need to shorten the cones of the model antenna by 18 mm was that the NEC model was a wire cage representation of the real cones. It did not account for the presence of solid metal supports at either end of the cones, or the radius of curvature of the elbow shaped wires at the widest points of the cones. These features of the real antenna reduce the volume of the cavities inside its cones and therefore increase their resonant frequency.

Segmentation of wires close to the drive-point of the model antenna was found

to have a considerable effect upon its drive-point impedance predictions. It was found best to use five segments for the cone-linking wire and also to taper the lengths of the segments of the cone wires so that they had the same lengths as the segments of the cone-linking wire where they joined it. Segmentation of the cone wires was then reduced until the predicted impedances started to diverge appreciably. This occurred when less than eight segments were used for the cone wires and so the optimum NEC model of the biconical antenna used for the work in this thesis had 169 segments.

The NEC model was found to be slightly inaccurate at the low frequencies where the biconical antenna was capacitive. The real antenna had a capacitance of 15.4 pF, whereas the model antenna had a capacitance of 17.9 pF and this was believed to be due to the previously mentioned problems of developing a realistic NEC model of the feed region of the real antenna.

## 7.3 Antenna Calibration

Antennas designed for EMC applications are usually calibrated by the standard site, or three antenna, method. This method calculates the antenna factors of three antennas simultaneously from site attenuation measurements between the three possible pairs of antennas and theoretical values of normalised site attenuation calculated by the Smith method.

Normalised site attenuation cannot fully account for the interactions between closely spaced antennas on an open-area test site, as it is derived from a purely radiative model of the coupling. If normalised site attenuation is used uncorrected for antenna calibration, the resulting antenna factors of resonant dipoles may be in error by up to 4 dB below 60 MHz, up to 2 dB from 60–200 MHz and by up to 1 dB above 200 MHz.

An alternative approach to antenna calibration is based upon the simulation of model antennas. If the model antennas are representative of the real antennas, their predicted antenna factors will be valid for the real antennas. This calibration method permits a more carefully controlled illumination than is possible on a real test site, and it is possible to illuminate antennas in ideal test site environments or in free space. Illumination of an antenna in free space gives its plane wave antenna factor, which can then be corrected to take account of variations due to the presence of a ground plane beneath the antenna.

### 7.3.1 Antennas above Ground Planes

Interactions between an antenna and a ground plane cause its antenna factor to vary as a function of height because of changes in the following two parameters:

**Effective length** — the EMF induced at the antenna drive-point by a given uniform illuminating field.

**Drive-point impedance** — the mismatch between the antenna and its connecting network.

The three antenna method cannot easily account for these variations because one antenna is scanned in height whilst each of the three attenuation measurements is performed.

The effective length of a horizontally polarised resonant dipole varies very little as a function of its height above a ground plane. At heights above 1 m and frequencies above 30 MHz, it varies between −0.16 dB and +0.23 dB from its plane-wave

value. Variations in the antenna factor of the resonant dipole can therefore be calculated purely from variations in its drive-point impedance. The effective length of the biconical antenna varies much more than that of the resonant dipole and therefore variations in its antenna factor may not be calculated purely from variations in its drive-point impedance.

The antenna factor of a horizontally polarised resonant dipole varies between $-1.2\,\mathrm{dB}$ and $+1.7\,\mathrm{dB}$ from its plane-wave value at heights above 2 m and frequencies above 30 MHz. The same limits apply with the antenna at 1 m height for frequencies above 45 MHz. At frequencies below 45 MHz the antenna factor of a resonant dipole becomes drastically reduced at 1 m height and therefore it should not be used under these conditions. The variations in the antenna factor of the horizontally polarised skeletal biconical antenna are less than those of the resonant dipole. At 1 m height its antenna factor varies between $-0.8\,\mathrm{dB}$ and $+1.2\,\mathrm{dB}$ from its plane wave value, but at 2 m height these variations are reduced to between $-0.7\,\mathrm{dB}$ and $+0.6\,\mathrm{dB}$.

### 7.3.2 Performance of Antenna Baluns

It is possible to combine the measured scattering parameters of the balun network of a practical EMC antenna with a NEC simulation of its radiators in order to obtain the antenna factors of a complete practical antenna. This has been performed for a skeletal biconical antenna in this thesis, and should be possible for any antenna with a balun whose scattering parameters can be measured and whose radiators have a suitable structure that can be modelled with NEC.

The Schwarzbeck BBA9106 biconical antenna is unusual amongst EMC antennas in that its structure allows calibration of a network analyser in order to measure the scattering parameters of its balun. This is not possible for the majority of antennas because their baluns are contained in plastic supports rather than metal ones, making it very difficult to define reference planes for the calibration of a network analyser. It would therefore be useful if antenna manufacturers would not produce such antennas.

The drive-point impedance of a resonant dipole antenna above the ground plane of an open-area test site varies significantly from its self impedance of $73\,\Omega$ at frequencies below 60 MHz. It appears that above 60 MHz, these variations are sufficiently small that the behaviour of a transformer balun used with the antenna can be characterised by a simple loss value in dB. It is, therefore, not necessary to know the full scattering parameters of their baluns above 60 MHz. It is always necessary to know the full scattering parameters of the baluns of broadband antennas because

their drive-point impedances vary much more as functions of frequency than those of resonant dipoles.

## 7.4 Site Attenuation

Site attenuation measurements are used to validate real open-area test sites by showing that their propagation characteristics are sufficiently close to those of an ideal site. The procedure compares measurements of the radiation from an EUT on the real site with predictions of the radiation that would be measured from the same EUT on an ideal site. The procedure requires a standard EUT with known radiating characteristics and also a calibrated receiving antenna.

Current EMC standards specify that resonant dipole antennas should be used for both the standard EUT and the receiving antenna. This is because the plane-wave antenna factor of a resonant dipole can be calculated accurately from a theoretical basis. Resonant dipole antennas are very inconvenient to use because their lengths have to be mechanically tuned to each frequency of excitation, also they are not particularly representative of real EUTs or measurement antennas because of their large physical size at low frequencies.

The concept of normalised site attenuation was introduced to facilitate the use of broadband antennas such as the skeletal biconical antenna and the log-periodic antenna for test site validation. However, there are several problems associated with this approach to test site validation:

1. The antenna factors of the real antennas used for the measurement are obtained by the three antenna calibration method and may therefore be inaccurate.

2. The model used for the calculation of theoretical site attenuation is the Smith model, that neglects close coupling effects between the antennas and the ground plane.

Since it is usually desired to show that the propagation characteristics of a given test site are within 4 dB of those of an ideal site, the results from a normalised site attenuation based site validation procedure are more likely to show the above two causes of error than to reveal propagation problems with the test site.

The test site validation procedures used in this thesis are based upon classical site attenuation because this enables a more rigorous comparison between measured and predicted quantities to be carried out than can be performed using normalised site attenuation.

### 7.4.1 Predictions of Classical Site Attenuation

Predicted values of classical site attenuation can be obtained using the Smith model, however this is insufficiently accurate for test site validation and is in error by up to 4 dB below 60 MHz. A more accurate model is based upon the use of the applied EMF method to formulate site attenuation in terms of the self and mutual impedances between resonant dipoles. This method gives predictions within 1 dB of NEC and is therefore sufficiently accurate for test site validation.

NEC can be used to obtain accurate values for classical site attenuation between resonant dipole antennas, but it can also be used for more general wire antenna structures including the broadband skeletal biconical antenna. Measurements of site attenuation with these types of antennas can be performed at much smaller frequency separations than are practical with tunable resonant dipoles.

A measurement of classical site attenuation performed with real EMC antennas is not a measurement of the attenuation due purely to the radiators of the antennas coupling over the site. It is actually a measurement of the attenuation due to three cascaded two port networks corresponding to the balun of the transmitting antenna, followed by the radiators over the test site, followed by the receiving antenna balun. The predicted values of site attenuation must include the effects of both balun devices. The baluns of EMC antennas are supplied with loss values quoted in dBs. It appears that these are sufficiently accurate for resonant dipoles above 60 MHz, but with resonant dipoles below 60 MHz or with skeletal biconical antennas at any frequency, it is necessary to account for the full scattering parameters of each balun.

## 7.5 Test Site Design

There are two aspects of the design of an open-area test site that were considered in this thesis. These were the construction of a practical ground plane to act as a perfect reflector and the effect of surrounding buildings on site propagation characteristics. Both of these aspects of the design of the open-area test site at the University of York have been considered theoretically and by measurement in this thesis

### 7.5.1 Area of Flat Ground Plane

There are three waves reflected from the ground plane of an open-area test site; a wave propagates from each antenna to the ground plane and then back to the same antenna whilst a third wave propagates between the antennas with a reflection from the ground plane. The ground plane must be of sufficient size for it to appear perfectly reflecting for all three reflected waves.

Geometrical optical theory defines the area of a reflecting surface that is primarily responsible for the reflected wave as the first Fresnel zone. Fresnel zones on an open-area test site are largest with the greatest antenna heights and lowest excitation frequencies, i.e. with antenna heights of 2 m and 4 m and an excitation frequency of 30 MHz. Under these conditions the minimum area of ground plane that a 10 m test site should be centred upon is approximately an ellipse with a major axis of 18.1 m and a minor axis of 13.1 m. EMC standards specify the CISPR ellipse as an appropriate area of flat ground plane and this has dimensions of 20×17.3 m for a 10 m site. The CISPR ellipse therefore extends beyond the first Fresnel zones of a 10 m open-area test site and represents a sufficient area for a flat ground plane.

### 7.5.2 Degree of Flatness

The ground plane of an open-area test site has to obey the Rayleigh criterion for optical flatness. This requires any spurious phase shifts experienced by elements of the reflected wavefronts to correspond to less than a quarter of a wavelength. The shortest wavelengths over an open-area test site occur at 1 GHz and therefore the ground plane is required to be flattest over the area of its first Fresnel zones at 1 GHz. This results in circular areas of 1.2 m radius below the transmitting antenna and 1.6 m radius beneath the receiving antenna that are required to be flat to within 3.8 cm. The elliptical zone affecting the reflected wave between the

antennas is required to be flat to within 4.4 cm on a 3 m site and 7.3 cm on a 10 m site.

In order for the central portion of a ground plane to be sufficiently flat to achieve the above tolerances, it has to be formed from a metal mesh or plate laid over flat concrete or asphalt. A suitable rectangular flat strip at the centre of a 10 m test site would have dimensions of at least $5.7 \times 13.2$ m.

### 7.5.3 Ground Plane Materials

The ground plane is required to act as a perfect reflector and therefore it must be formed from a highly conductive metallic material. From the arguments of the size of ground plane required, the metallised area of a ground plane should should cover an ellipse with a major axis of 18.1 m and a minor axis of 13.1 m for a 10 m site. The metallised portion of the ground plane of the test site at the University of York is rather smaller than this, with rectangular dimensions of $19.6 \times 3.8$ m. It has been found to have a slightly degraded reflection coefficient of $0.89\angle 174$ at 30 MHz for a horizontally polarised resonant dipole. For practical broadband antennas and EUTs, which are smaller, it would appear closer to a perfect reflector. No degradation has been found between measured and predicted site attenuations of this test site at low frequencies and therefore it appears that a $19.6 \times 3.8$ m metal ground is adequate for a 10 m site.

### 7.5.4 Surrounding Buildings

Buildings surrounding a test site introduce unwanted reflections, but it is difficult to analyse numerically the effect of a general building in a general location. This is because it will only be partially reflecting and certain objects, such as parked cars, tend to move. The effect of surrounding buildings can be deduced from differences between the measured and predicted site attenuations of a real test site.

The rigorous measurements and predictions of classical site attenuation that were performed using the open-area test site at the University of York showed that surrounding buildings can be important causes of measurement uncertainties. The buildings surrounding the York test site introduce a ripple of $\pm 2$ dB onto its 10 m site attenuation characteristic and $\pm 1$ dB onto its 3 m site attenuation characteristic. These uncertainties must be added to any uncertainties in antenna factors when performing radiation measurements using the site.

## 7.6 Future Work

The work in this thesis has shown that it is possible to use NEC simulations and measurements of the scattering parameters of the baluns of real antennas to obtain accurate predicted values of classical site attenuation. This has only been performed using Schwarzbeck BBA9106 biconical antennas over the frequency range of 30–300 MHz, but could be extended up to 1 GHz if accurate NEC models could be developed of real log-periodic antennas.

The NEC model of the Schwarzbeck biconical antenna has been found to be inaccurate below 60 MHz because of problems forming a realistic model of its feed point. It is possible that an equivalent circuit containing parasitic circuit elements could be used to model the feed region and improve the simulation.

Much of the data in this thesis could be obtained more accurately by more careful control of antenna position. Control of antenna height has a critical effect on the reflection coefficient measurement procedure, and mast angle also has a large effect on the measurements of site attenuation for the 3 m site.

For the work in this thesis to become a practical site validation procedure it would be necessary to develop standard NEC models for various manufactured antennas and supply pairs of them with their predicted site attenuations. The only alternative to this would be to compare the measured attenuation between a pair of antennas on a national standard site with attenuation between the same antennas on a site under test.

Current test site validation procedures are not rigorous enough to be able to deduce information about the propagation characteristics of test sites. The Smith model must be abandoned and a return must be made to classical site attenuation. This could only be carried out with resonant dipoles if simulations of the type proposed in this thesis were not used.

# Appendix A

# Casey's Model of Reflection from a Wire-Mesh Screen

The equations in this section are taken from reference [16] in chapter 1. Figure A.1 shows the physical dimensions of a portion of an infinite planar wire mesh.

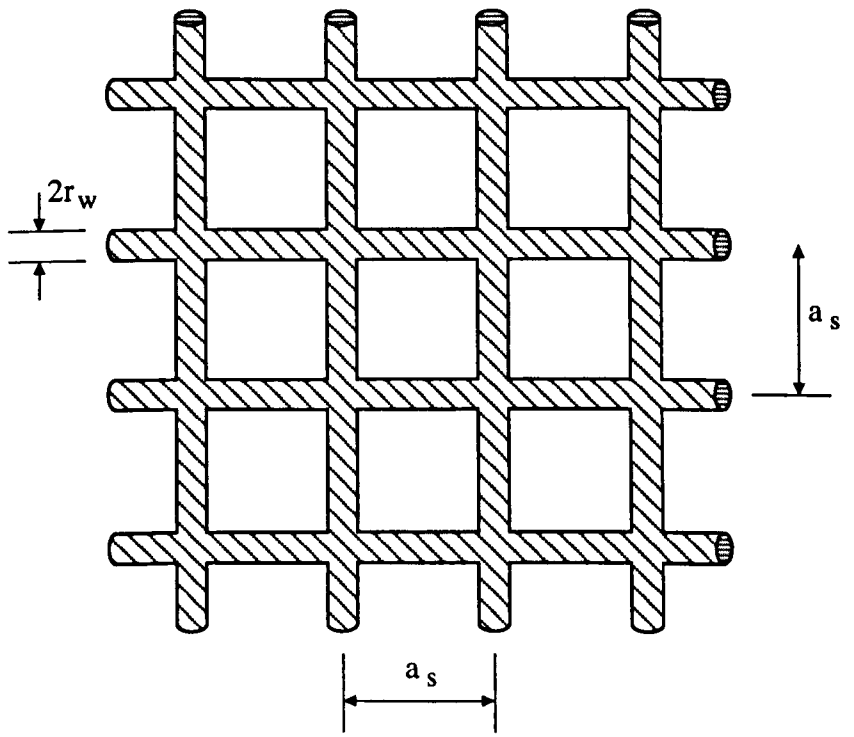


Figure A.1: Geometry of the wire mesh.

The sheet inductance parameter for the mesh, $L_s$, is given by

$$L_s = \frac{\mu_0 a_s}{2\pi} \ln(1 - e^{\frac{-2\pi r_w}{a_s}})^{-1} \tag{A.1}$$

where $r_w$ is the radius of the cylindrical wires in the mesh and $a_s$ is their separation. The internal impedance of the wires per unit length, $Z'_w$, is

$$Z'_w = R'_w \frac{\sqrt{j\omega\tau_w} I_0(\sqrt{j\omega\tau_w})}{2I_1(\sqrt{j\omega\tau_w})} \tag{A.2}$$

where $R'_w = (\pi r_w^2 \sigma_w)^{-1}$ and is the d.c. resistance per unit length of the wires, $\tau_w = \mu_w \sigma_w r_w^2$ is the diffusion time constant and $I_n(\cdot)$ denotes the modified Bessel function of the first kind of order $n$. $\sigma_w$ and $\mu_w$ denote the conductivity and permeability of the wire material respectively.

The effective surface impedance of the mesh for a plane wave having an electric field perpendicular to the plane of incidence is

$$Z_{s1} = Z'_w a_s + j\omega L_s \tag{A.3}$$

and for a plane wave having an electric field parallel to the plane of incidence,

$$Z_{s2} = Z'_w a_s + j\omega L_s \left(1 - \frac{1}{2}\sin^2\theta\right) \tag{A.4}$$

where $\theta$ is the angle between the plane of incidence and the normal to the mesh surface.

The reflection coefficients are therefore, for perpendicular polarisation,

$$R_1 = \frac{-Z_0}{Z_0 + 2Z_{s1}\cos\theta} \tag{A.5}$$

and for parallel polarisation,

$$R_2 = \frac{Z_0 \cos\theta}{2Z_{s2} + Z_0 \cos\theta} \tag{A.6}$$

$Z_0$ is the characteristic impedance of free space, given by $Z_0 = \sqrt{\mu_0/\epsilon_0}$.

For the calculations involving the mesh ground plane of the open-area test site at the University of York,

$$\begin{aligned} a_s &= 1.5\,\text{mm} \\ r_w &= 34.28\,\text{mm} \\ \sigma_w &= 3.54 \times 10^7 (\text{Aluminium}) \\ \mu_w &= 1.0 \\ \theta &= 59^\circ \end{aligned}$$

Equations (A.1) to (A.6) were incorporated into a computer program to determine how the reflection coefficient of the mesh varied as a function of frequency.

# Appendix B

# Evaluation of Trigonometric Integral Functions

The trigonometric integral functions referred to in chapter 2 have the following definitions

$$\mathrm{Si}(x) = \int_0^x \frac{\sin u}{u} du \tag{B.1}$$

$$\mathrm{Ci}(x) = \int_\infty^x \frac{\cos u}{u} du \tag{B.2}$$

$$\mathrm{Cin}(x) = \int_0^x \frac{1-\cos u}{u} du \tag{B.3}$$

The sine and cosine functions in these formulae can be expressed as series of ascending powers of $u$ so that (B.1) and (B.3) can be evaluated as the following power series

$$\mathrm{Si}(x) = x - \frac{x^3}{3!3} + \frac{x^5}{5!5} - \frac{x^7}{7!7} + \cdots \tag{B.4}$$

$$\mathrm{Cin}(x) = 1 - \frac{x^2}{2!2} + \frac{x^4}{4!4} - \frac{x^6}{6!6} + \cdots \tag{B.5}$$

(B.2) cannot be evaluated directly by this method but $\mathrm{Ci}(x)$ is related to $\mathrm{Cin}(x)$ by

$$\mathrm{Ci}(x) = \ln(x) + U - \mathrm{Cin}(x) \tag{B.6}$$

where $U$ is Euler's constant given by $U = 0.57721665$

The power series (B.4) and (B.5) are evaluated by adding terms progressively until they became negligibly small. The following table shows how many terms are required to converge $\mathrm{Si}(x)$ until terms become less than a part in $10^{10}$ of the total sum to that point in the series.

| x | 5 | 10 | 15 | 20 | 25 | 30 | 35 | 40 | 45 | 50 |
|---|---|---|---|---|---|---|---|---|---|---|
| No. | 13 | 20 | 27 | 34 | 41 | 48 | 54 | 61 | 68 | 75 |

Each term in the series is obtained by multiplying the previous term by a scaling factor and so numerical errors introduced by rounding-off become progressively

worse in successive terms of each series. For this reason an alternative series expansion, as employed by Dawood [83], was used for calculation of the functions for larger values of $x$. Two series are defined

$$P(x) = \frac{1}{x} - \frac{2!}{x^3} + \frac{4!}{x^5} - \frac{6!}{x^7} + \cdots \tag{B.7}$$

$$Q(x) = \frac{1}{x^2} - \frac{3!}{x^4} + \frac{5!}{x^6} - \frac{7!}{x^8} + \cdots \tag{B.8}$$

and the integral functions are defined in terms of these

$$\mathrm{Si}(x) = \frac{\pi}{2} - P(x)\cos(x) - Q(x)\sin(x) \tag{B.9}$$

$$\mathrm{Ci}(x) = P(x)\sin(x) - Q(x)\cos(x) \tag{B.10}$$

$$\mathrm{Cin}(x) = \ln(x) + U - \mathrm{Ci}(x) \tag{B.11}$$

The number of terms required to converge these series to a part in $10^6$ is

| x | 50 | 45 | 40 | 35 | 30 | 25 | 20 | 15 | 10 | 5 |
|---|---|---|---|---|---|---|---|---|---|---|
| No. | 3 | 3 | 4 | 4 | 4 | 5 | 7 | | | |

This algorithm requires far less terms to be summed together than the first algorithm in order to calculate the integral functions accurately but it breaks down for $x < 20$ due to numerical problems. For this reason a program was written to calculate the integral functions using the first algorithm for $x < 20$ and the second algorithm for $x > 20$. This program was written in VAX FORTRAN and the source is given below.

```
      SUBROUTINE TRIGINTEGRALS(X,S,C,CIN)
      REAL*8  X                          ! Input  : x
      REAL*8  S,C,CIN                    ! Output : Sine and Cosine integrals.
      REAL*8  HP,U                       ! Constants.
      REAL*8  XSQ,M1,M2
      REAL*16 SSUM,CSUM,STERM,CTERM
      REAL*16 PSUM,QSUM,PTERM,QTERM
      INTEGER NSTO,NPTO
      HP  = 1.570796327                  ! Pi/2.
      U   = 0.577215665                  ! Eulers Constant.
      XSQ = X*X
      IF (X.LT.20) THEN
          GOTO 10
      ELSE
          GOTO 20
      ENDIF
10    STERM = X                                    ! First term of Si(x) series
      CTERM = XSQ/4                                ! First term of Cin(x) series
      SSUM  = STERM
      CSUM  = CTERM
      NSTO  = 3                                    ! Order of next Sine term
11    STERM = -XSQ*STERM * (NSTO-2)/NSTO * 1/((NSTO-1)*NSTO)     ! Next term
      CTERM = -XSQ*CTERM * (NSTO-1)/(NSTO+1) * 1/(NSTO*(NSTO+1)) ! Next term
      SSUM  = SSUM + STERM
      CSUM  = CSUM + CTERM
      M1    = ABS(STERM/SSUM)
      M2    = ABS(CTERM/CSUM)
      IF ((M1.LT.1E-10).AND.(M2.LT.1E-10)) THEN    ! Terminating Condition
          S   = SSUM
          CIN = CSUM
          C   = U + LOG(X) - CIN
          GOTO 30
      ELSE
          NSTO  = NSTO+2
          GOTO 11
      ENDIF
20    PTERM = 1/X                                  ! First term of P(x) series
      QTERM = 1/XSQ                                ! First term of Q(x) series
      PSUM  = PTERM
      QSUM  = QTERM
      NPTO  = 3                                    ! Order of next Pterm
21    PTERM = -PTERM/XSQ * (NPTO-1)*(NPTO-2)
      QTERM = -QTERM/XSQ * NPTO*(NPTO-1)
      PSUM  = PSUM + PTERM
      QSUM  = QSUM + QTERM
      M1    = ABS(PTERM/PSUM)
      M2    = ABS(QTERM/QSUM)
      IF ((M1.LT.1E-6).AND.(M2.LT.1E-6)) THEN      ! Terminating Condition
          S     = HP - PSUM*COS(X) - QSUM*SIN(X)
          C     = PSUM*SIN(X) - QSUM*COS(X)
          CIN   = LOG(X) + U - C
          GOTO 30
      ELSE
          NPTO  = NPTO + 2
          GOTO 21
      ENDIF
30    CONTINUE
      RETURN
      END
```

# Appendix C

# Evaluation of the Mutual Impedances between Parallel Cylindrical Dipole Antennas by the Applied EMF Method

In chapter 2, the mutual impedance between a pair of arbitrary antennas was defined. If the current on cylindrical dipole antennas is assumed to be distributed sinusoidally along their lengths, the applied EMF method may be used to calculate the mutual impedance between a pair of them. This appendix summarises the equations that were used for the work in thesis to calculate mutual impedances by the applied EMF method.

The equations listed here are based upon reference [33] in chapter 2. The symbols used in this thesis to describe the spatial orientation of the antennas are slightly different to those in the reference and so the equations have a slightly different form. Also, the equations in the reference are developed for the mutual impedance between two antennas of unequal length, but they were simplified for equal length antennas in this thesis.

## C.1 Echelon Antennas

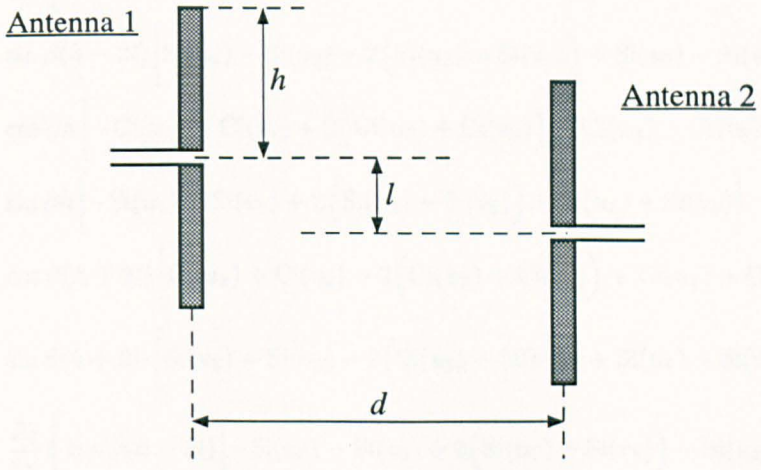


Figure C.1: Parallel cylindrical dipole antennas in echelon.

This is the most general orientation of a pair of parallel cylindrical dipole antennas and it is shown in figure C.1. The symbols used to represent the geometry are

| | |
|---|---|
| $l$ | Half-length of each antenna. |
| $d$ | Perpendicular separation of the antenna mid points. |
| $h$ | Axial separation of the antenna mid points |

The mutual impedance between the antennas is $Z_{12}$ and has resistive and reactive components of $R_{12}$ and $X_{12}$ such that

$$Z_{12} = R_{12} + jX_{12} \tag{C.1}$$

These components are given by equations (C.2) to (C.13).

$$u_0 = \beta\left(\sqrt{d^2+(h-2l)^2}+(h-2l)\right) \tag{C.2}$$

$$v_0 = \beta\left(\sqrt{d^2+(h-2l)^2}-(h-2l)\right) \tag{C.3}$$

$$u_1 = \beta\left(\sqrt{d^2+(h-l)^2}+(h-l)\right) \tag{C.4}$$

$$v_1 = \beta\left(\sqrt{d^2+(h-l)^2}-(h-l)\right) \tag{C.5}$$

$$u_2 = \beta\left(\sqrt{d^2+h^2}+h\right) \tag{C.6}$$

$$v_2 = \beta\left(\sqrt{d^2+h^2}-h\right) \tag{C.7}$$

$$u_3 = \beta\left(\sqrt{d^2+(h+l)^2}+(h+l)\right) \tag{C.8}$$

$$v_3 = \beta\left(\sqrt{d^2+(h+l)^2}-(h+l)\right) \tag{C.9}$$

$$u_4 = \beta\left(\sqrt{d^2+(h+2l)^2}+(h+2l)\right) \tag{C.10}$$

$$v_4 = \beta\left(\sqrt{d^2+(h+2l)^2}-(h+2l)\right) \tag{C.11}$$

$$
\begin{aligned}
R_{mn} &= \frac{Z_0}{8\pi}\Big\{ \cos\beta(h-2l)\Big[\mathrm{Ci}(u_0)+\mathrm{Ci}(v_0)-2\Big(\mathrm{Ci}(u_1)+\mathrm{Ci}(v_1)\Big)+\mathrm{Ci}(u_2)+\mathrm{Ci}(v_2)\Big] \\
&+ \sin\beta(h-2l)\Big[\mathrm{Si}(u_0)-\mathrm{Si}(v_0)-2\Big(\mathrm{Si}(u_1)-\mathrm{Si}(v_1)\Big)+\mathrm{Si}(u_2)-\mathrm{Si}(v_2)\Big] \\
&+ \cos\beta h\Big[-\mathrm{Ci}(u_1)-\mathrm{Ci}(v_1)+2\Big(\mathrm{Ci}(u_2)+\mathrm{Ci}(v_2)\Big)-\mathrm{Ci}(u_3)-\mathrm{Ci}(v_3)\Big] \\
&+ \sin\beta h\Big[-\mathrm{Si}(u_1)+\mathrm{Si}(v_1)+2\Big(\mathrm{Si}(u_2)-\mathrm{Si}(v_2)\Big)-\mathrm{Si}(u_3)+\mathrm{Si}(v_3)\Big] \\
&+ \cos\beta(h+2l)\Big[\mathrm{Ci}(u_2)+\mathrm{Ci}(v_2)-2\Big(\mathrm{Ci}(u_3)+\mathrm{Ci}(v_3)\Big)+\mathrm{Ci}(u_4)+\mathrm{Ci}(v_4)\Big] \\
&+ \sin\beta(h+2l)\Big[\mathrm{Si}(u_2)-\mathrm{Si}(v_2)-2\Big(\mathrm{Si}(u_3)-\mathrm{Si}(v_3)\Big)+\mathrm{Si}(u_4)-\mathrm{Si}(v_4)\Big]\Big\} \qquad \text{(C.12)}
\end{aligned}
$$

$$
\begin{aligned}
X_{mn} &= \frac{Z_0}{8\pi}\Big\{ \cos\beta(h-2l)\Big[-\mathrm{Si}(u_0)-\mathrm{Si}(v_0)+2\Big(\mathrm{Si}(u_1)+\mathrm{Si}(v_1)\Big)-\mathrm{Si}(u_2)-\mathrm{Si}(v_2)\Big] \\
&+ \sin\beta(h-2l)\Big[\mathrm{Ci}(u_0)-\mathrm{Ci}(v_0)-2\Big(\mathrm{Ci}(u_1)-\mathrm{Ci}(v_1)\Big)+\mathrm{Ci}(u_2)-\mathrm{Ci}(v_2)\Big] \\
&+ \cos\beta h\Big[\mathrm{Si}(u_1)+\mathrm{Si}(v_1)-2\Big(\mathrm{Si}(u_2)+\mathrm{Si}(v_2)\Big)+\mathrm{Si}(u_3)+\mathrm{Si}(v_3)\Big] \\
&+ \sin\beta h\Big[-\mathrm{Ci}(u_1)+\mathrm{Ci}(v_1)+2\Big(\mathrm{Ci}(u_2)-\mathrm{Ci}(v_2)\Big)-\mathrm{Ci}(u_3)+\mathrm{Ci}(v_3)\Big] \\
&+ \cos\beta(h+2l)\Big[-\mathrm{Si}(u_2)-\mathrm{Si}(v_2)+2\Big(\mathrm{Si}(u_3)+\mathrm{Si}(v_3)\Big)-\mathrm{Si}(u_4)-\mathrm{Si}(v_4)\Big] \\
&+ \sin\beta(h+2l)\Big[\mathrm{Ci}(u_2)-\mathrm{Ci}(v_2)-2\Big(\mathrm{Ci}(u_3)-\mathrm{Ci}(v_3)\Big)+\mathrm{Ci}(u_4)-\mathrm{Ci}(v_4)\Big]\Big\} \qquad \text{(C.13)}
\end{aligned}
$$

## C.2 Parallel Antennas

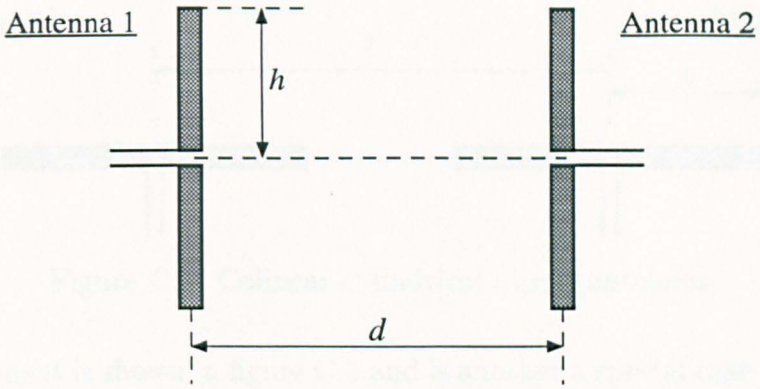


Figure C.2: Parallel cylindrical dipole antennas.

Figure C.2 shows the arrangement of the antennas in this case and it can be seen to be equivalent to the echelon configuration under the condition that $h = 0$. Equations (C.2) to (C.13) simplify, under this condition, to the following

$$u_0 = \beta\left(\sqrt{d^2+4l^2}-2l\right) \tag{C.14}$$

$$u_1 = \beta\left(\sqrt{d^2+l^2}-l\right) \tag{C.15}$$

$$u_2 = \beta d \tag{C.16}$$

$$u_3 = \beta\left(\sqrt{d^2+l^2}+l\right) \tag{C.17}$$

$$u_4 = \beta\left(\sqrt{d^2+4l^2}+2l\right) \tag{C.18}$$

$$\begin{aligned} R_{mn} &= \frac{Z_0}{8\pi}\Big\{\cos 2\beta l\Big[\mathrm{Ci}(u_0)-2\Big(\mathrm{Ci}(u_1)-\mathrm{Ci}(u_2)+\mathrm{Ci}(u_3)\Big)+\mathrm{Ci}(u_4)\Big] \\ &+ \sin 2\beta l\Big[-\mathrm{Si}(u_0)+2\Big(\mathrm{Si}(u_1)-\mathrm{Si}(u_3)\Big)+\mathrm{Si}(u_4)\Big] \\ &+ 2\Big[-\mathrm{Ci}(u_1)+2\mathrm{Ci}(u_2)-\mathrm{Ci}(u_3)\Big]\Big\} \end{aligned} \tag{C.19}$$

$$\begin{aligned} X_{mn} &= \frac{Z_0}{8\pi}\Big\{\cos 2\beta l\Big[-\mathrm{Si}(u_0)+2\Big(\mathrm{Si}(u_1)-\mathrm{Si}(u_2)+\mathrm{Si}(u_3)\Big)-\mathrm{Si}(u_4)\Big] \\ &+ \sin 2\beta l\Big[-\mathrm{Ci}(u_0)+2\Big(\mathrm{Ci}(u_1)-\mathrm{Ci}(u_3)\Big)+\mathrm{Ci}(u_4)\Big] \\ &+ 2\Big[\mathrm{Si}(u_1)-2\mathrm{Si}(u_2)+\mathrm{Si}(u_3)\Big]\Big\} \end{aligned} \tag{C.20}$$

## C.3 Colinear Antennas

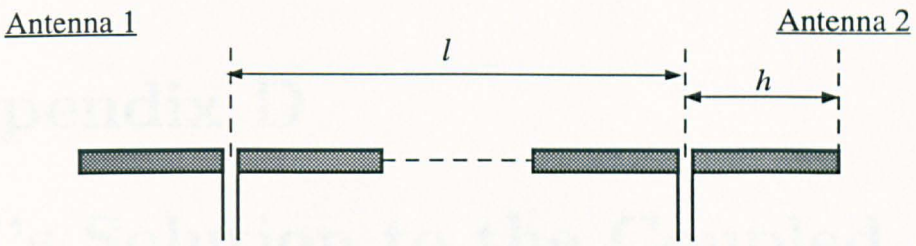


Figure C.3: Colinear cylindrical dipole antennas.

This arrangement is shown in figure C.3 and is another a special case of the echelon configuration. In this case $d = 0$ in equations (C.2) to (C.13) which reduce to

$$u_0 = 2\beta(h - 2l) \tag{C.21}$$
$$u_1 = 2\beta(h - l) \tag{C.22}$$
$$u_2 = 2\beta h \tag{C.23}$$
$$u_3 = 2\beta(h + l) \tag{C.24}$$
$$u_4 = 2\beta(h + 2l) \tag{C.25}$$

$$\begin{aligned} R_{mn} = \frac{Z_0}{8\pi}\Bigg\{ & \cos\beta(h-2l)\left[\mathrm{Ci}(u_0) - 2\mathrm{Ci}(u_1) + \mathrm{Ci}(u_2) + \ln\left(\frac{l^2 - 2lh + h^2}{l^2 - 2lh}\right)\right] \\ & + \sin\beta(h-2l)\left[\mathrm{Si}(u_0) - 2\mathrm{Si}(u_1) + \mathrm{Si}(u_2)\right] \\ & + 2\cos\beta h\left[-\mathrm{Ci}(u_1) + 2\mathrm{Ci}(u_2) - \mathrm{Ci}(u_3) + \ln\left(\frac{l^2 - h^2}{l^2}\right)\right] \\ & + 2\sin\beta h\left[-\mathrm{Si}(u_1) + 2\mathrm{Si}(u_2) - \mathrm{Si}(u_3)\right] \\ & + \cos\beta(h+2l)\left[\mathrm{Ci}(u_2) - 2\mathrm{Ci}(u_3) + \mathrm{Ci}(u_4) + \ln\left(\frac{l^2 + 2lh + h^2}{l^2 + 2lh}\right)\right] \\ & + \sin\beta(h+2l)\left[\mathrm{Si}(u_2) - 2\mathrm{Si}(u_3) + \mathrm{Si}(u_4)\right]\Bigg\} \end{aligned} \tag{C.26}$$

$$\begin{aligned} X_{mn} = \frac{Z_0}{8\pi}\Bigg\{ & \cos\beta(h-2l)\left[-\mathrm{Si}(u_0) + 2\mathrm{Si}(u_1) - \mathrm{Si}(u_2)\right] \\ & + \sin\beta(h-2l)\left[\mathrm{Ci}(u_0) - 2\mathrm{Ci}(u_1) + \mathrm{Ci}(u_2) - \ln\left(\frac{l^2 - 2lh + h^2}{l^2 - 2lh}\right)\right] \\ & + 2\cos\beta h\left[\mathrm{Si}(u_1) - 2\mathrm{Si}(u_2) + \mathrm{Si}(u_3)\right] \\ & + 2\sin\beta h\left[-\mathrm{Ci}(u_1) + 2\mathrm{Ci}(u_2) - \mathrm{Ci}(u_3) - \ln\left(\frac{l^2 - h^2}{l^2}\right)\right] \\ & + \cos\beta(h+2l)\left[-\mathrm{Si}(u_2) + 2\mathrm{Si}(u_3) - \mathrm{Si}(u_4)\right] \\ & + \sin\beta(h+2l)\left[\mathrm{Ci}(u_2) - 2\mathrm{Ci}(u_3) + \mathrm{Ci}(u_4) - \ln\left(\frac{l^2 + 2lh + h^2}{l^2 + 2lh}\right)\right]\Bigg\} \end{aligned} \tag{C.27}$$

# Appendix D

# Tai's Solution to the Coupled Antenna Problem

This appendix contains the expressions of Tai's first order iterative solution to the integral equations describing the current distribution of coupled cylindrical dipole antennas. The equations are taken from reference [34] and are used in chapter 2.

The drive-point impedances of symmetrically and antisymmetrically fed coupled antennas, $Z_S$ and $Z_A$, are given by

$$Z_S = \frac{-jZ_0\Psi_s}{2\pi} \times \left[ \frac{\cos\beta l + \frac{1}{\Psi_s}[F_s(l) + P(l)]}{\sin\beta l + \frac{1}{\Psi_s}\{[F_s(0) + P(0)]\sin\beta l - [G_s(0) + Q(0)]\cos\beta l + [G_s(l) + Q(l)]\}} \right] \tag{D.1}$$

$$Z_A = \frac{-jZ_0\Psi_a}{2\pi} \times \left[ \frac{\cos\beta l + \frac{1}{\Psi_a}[F_a(l) - P(l)]}{\sin\beta l + \frac{1}{\Psi_a}\{[F_a(0) - P(0)]\sin\beta l - [G_a(0) - Q(0)]\cos\beta l + [G_a(l) - Q(l)]\}} \right] \tag{D.2}$$

The functions referred to in (D.1) and (D.2) have the following definitions

$$F_s(z) = \Psi_s[\cos\beta z - \cos\beta l] - C_a(z) + E_a(z)\cos\beta l \tag{D.3}$$

$$F_a(z) = \Psi_a[\cos\beta z - \cos\beta l] - C_a(z) + E_a(z)\cos\beta l \tag{D.4}$$

$$G_s(z) = \Psi_s[\sin\beta|z| - \sin\beta l] - S_a(z) + E_a(z)\sin\beta l \tag{D.5}$$

$$G_a(z) = \Psi_a[\sin\beta|z| - \sin\beta l] - S_a(z) + E_a(z)\sin\beta l \tag{D.6}$$

$$P(z) = -C_b(z) + E_b(z)\cos\beta l \tag{D.7}$$

$$Q(z) = -S_b(z) + E_b(z)\sin\beta l \tag{D.8}$$

$$\psi_s(z) = \frac{[C_a(z) + C_b(z)]\sin\beta l - [S_a(z) + S_b(z)]\cos\beta l}{\sin\beta(l - |z|)} \tag{D.9}$$

$$\psi_a(z) = \frac{[C_a(z) - C_b(z)]\sin\beta l - [S_a(z) - S_b(z)]\cos\beta l}{\sin\beta(l - |z|)} \tag{D.10}$$

$$\Psi_s = \begin{cases} |\psi_s(0)| & \text{For} \beta l \leq \frac{\pi}{2} \\ |\psi_s(l - \frac{\lambda}{4})| & \text{For } \beta l \geq \frac{\pi}{2} \end{cases} \tag{D.11}$$

$$\Psi_a = \begin{cases} |\psi_a(0)| & \text{For} \beta l \leq \frac{\pi}{2} \\ |\psi_a(l - \frac{\lambda}{4})| & \text{For } \beta l \geq \frac{\pi}{2} \end{cases} \tag{D.12}$$

The equations (D.3) to (D.12) are defined in terms of six functions: $S_a$, $C_a$, $E_a$, $S_b$, $C_b$ and $E_b$. The first three of these are defined below in terms of the antenna half length and radius

$$S_a(l,z) = \int_0^l \sin\beta z' \left( \frac{e^{-j\beta R_1}}{R_1} + \frac{e^{-j\beta R_2}}{R_2} \right) dz' \tag{D.13}$$

$$C_a(l,z) = \int_0^l \cos\beta z' \left( \frac{e^{-j\beta R_1}}{R_1} + \frac{e^{-j\beta R_2}}{R_2} \right) dz' \tag{D.14}$$

$$E_a(l,z) = \int_0^l \left( \frac{e^{-j\beta R_1}}{R_1} + \frac{e^{-j\beta R_2}}{R_2} \right) dz' \tag{D.15}$$

where $R_1$ and $R_2$ are defined by equations (D.21) and (D.22). The final three functions, $S_b$, $C_b$ and $E_b$, are defined similarly, but with the radius dimension, $a$, replaced by the antenna separation, $d$. These functions can be integrated numerically or expanded into the following form.

$$\begin{aligned} S_a(l,z) = {} & \frac{1}{2}\cos\beta z \Big[ \mathrm{Si}\beta(R_2+\mu_2) + \mathrm{Si}\beta(R_1+\mu_1) + \mathrm{Si}\beta(R_2-\mu_2) \\ & + \mathrm{Si}\beta(R_1-\mu_1) - 2\mathrm{Si}\beta(R_0+z) - 2\mathrm{Si}\beta(R_0-z) \\ & + j\mathrm{Ci}\beta(R_2+\mu_2) + j\mathrm{Ci}\beta(R_1+\mu_1) + j\mathrm{Ci}\beta(R_2-\mu_2) \\ & + j\mathrm{Ci}\beta(R_1-\mu_1) - 2j\mathrm{Ci}\beta(R_0+z) - 2j\mathrm{Ci}\beta(R_0-z) \Big] \\ - {} & \frac{1}{2}\sin\beta z \Big[ \mathrm{Ci}\beta(R_2+\mu_2) - \mathrm{Ci}\beta(R_1+\mu_1) - \mathrm{Ci}\beta(R_2-\mu_2) \\ & + \mathrm{Ci}\beta(R_1-\mu_1) - 2\mathrm{Ci}\beta(R_0+z) - 2\mathrm{Ci}\beta(R_0-z) \\ & - j\mathrm{Si}\beta(R_2+\mu_2) + j\mathrm{Si}\beta(R_1+\mu_1) + j\mathrm{Si}\beta(R_2-\mu_2) \\ & - j\mathrm{Si}\beta(R_1-\mu_1) + 2j\mathrm{Si}\beta(R_0+z) - 2j\mathrm{Si}\beta(R_0-z) \Big] \end{aligned} \tag{D.16}$$

$$\begin{aligned} C_a(l,z) = {} & \frac{1}{2}\cos\beta z \Big[ \mathrm{Ci}\beta(R_2+\mu_2) + \mathrm{Ci}\beta(R_1+\mu_1) - \mathrm{Ci}\beta(R_2-\mu_2) \\ & - \mathrm{Ci}\beta(R_1-\mu_1) - j\mathrm{Si}\beta(R_2+\mu_2) - j\mathrm{Si}\beta(R_1+\mu_1) \\ & + j\mathrm{Si}\beta(R_2-\mu_2) + j\mathrm{Si}\beta(R_1-\mu_1) \Big] \\ + {} & \frac{1}{2}\sin\beta z \Big[ \mathrm{Si}\beta(R_2+\mu_2) - \mathrm{Si}\beta(R_1+\mu_1) + \mathrm{Si}\beta(R_2-\mu_2) \\ & - \mathrm{Si}\beta(R_1-\mu_1) + j\mathrm{Ci}\beta(R_2+\mu_2) - j\mathrm{Ci}\beta(R_1+\mu_1) \\ & + j\mathrm{Ci}\beta(R_2-\mu_2) - j\mathrm{Ci}\beta(R_1-\mu_1) \Big] \end{aligned} \tag{D.17}$$

$$E_a(l,z) = \mathrm{Suv}(\beta\mu_2) + \mathrm{Cuv}(\beta\mu_1) - j\mathrm{Suv}(\beta\mu_2) - j\mathrm{Suv}(\beta\mu_1) \tag{D.18}$$

Where:

$$\mu_2 = l + z \tag{D.19}$$

$$\mu_1 = l - z \tag{D.20}$$

$$R_2 = \sqrt{{\mu_2}^2 + a^2} \tag{D.21}$$

$$R_1 = \sqrt{{\mu_1}^2 + a^2} \tag{D.22}$$

$$R_0 = \sqrt{z^2 + a^2} \tag{D.23}$$

and the integral functions are defined by:

$$\mathrm{Si}(x) = \int_0^x \frac{\sin u}{u} du \tag{D.24}$$

$$\mathrm{Ci}(x) = \int_\infty^x \frac{\cos u}{u} du \tag{D.25}$$

$$\mathrm{Suv}(x) = \int_0^x \frac{\sin\sqrt{u^2+v^2}}{\sqrt{u^2+v^2}} du \tag{D.26}$$

$$\mathrm{Cuv}(x) = \int_0^x \frac{\cos\sqrt{u^2+v^2}}{\sqrt{u^2+v^2}} du \tag{D.27}$$

where $v = \beta a$

The integrals (D.24) and (D.25) were evaluated by series summation in appendix B and integrals (D.26) and (D.27) were evaluated by Gaussian quadrature. Software was written to implement equations D.1 to D.27 and hence return symmetrical and antisymmetrical impedances for any combination of antenna lengths, radii and separations at any frequency.

# Appendix E

# Concatenation of Three Scattering Matrices into a Single Matrix

The scattering parameter representation of a two-port network relates the amplitudes of the waves scattered from its ports to the waves incident at its ports via equation (E.1).

$$\begin{bmatrix} b_1 \\ b_2 \end{bmatrix} = \begin{bmatrix} S_{11} & S_{12} \\ S_{21} & S_{22} \end{bmatrix} \begin{bmatrix} a_1 \\ a_2 \end{bmatrix} \tag{E.1}$$

An alternative representation of the same two-port network is in terms of its transmission parameters. These fill the matrix **T** and relate the scattered and incident waves at port 2 to the incident and scattered waves at port 1 via equation (E.2)

$$\begin{bmatrix} b_2 \\ a_2 \end{bmatrix} = \begin{bmatrix} T_{11} & T_{12} \\ T_{21} & T_{22} \end{bmatrix} \begin{bmatrix} a_1 \\ b_1 \end{bmatrix} \tag{E.2}$$

The T-parameters of the network are related to its scattering parameters by the following equations.

$$T_{11} = S_{21} - \frac{S_{11}S_{22}}{S_{12}} \tag{E.3}$$

$$T_{12} = \frac{S_{22}}{S_{12}} \tag{E.4}$$

$$T_{21} = -\frac{S_{11}}{S_{12}} \tag{E.5}$$

$$T_{22} = \frac{1}{S_{12}} \tag{E.6}$$

Consider three cascaded two-port networks, described in terms of their T-parameters, as shown in figure E.1. The waves at port 2 of the third network are related to the waves at port 1 of the first network by

$$\begin{bmatrix} b_{23} \\ a_{23} \end{bmatrix} = \begin{bmatrix} T3_{11} & T3_{12} \\ T3_{21} & T3_{22} \end{bmatrix} \begin{bmatrix} T2_{11} & T2_{12} \\ T2_{21} & T2_{22} \end{bmatrix} \begin{bmatrix} T1_{11} & T1_{12} \\ T1_{21} & T1_{22} \end{bmatrix} \begin{bmatrix} a_{11} \\ b_{11} \end{bmatrix} \tag{E.7}$$

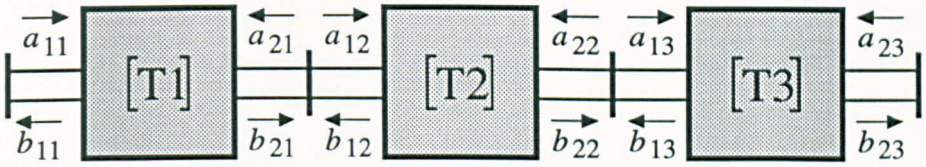


Figure E.1: Three cascaded two-port networks.

therefore the three concatenated two-port networks can be described in terms of an overall transmission matrix, $\mathbf{T}'$, that is formed from multiplying the three individual transmission matrices together.

$$\begin{bmatrix} T'_{11} & T'_{12} \\ T'_{21} & T'_{22} \end{bmatrix} = \begin{bmatrix} T3_{11} & T3_{12} \\ T3_{21} & T3_{22} \end{bmatrix} \begin{bmatrix} T2_{11} & T2_{12} \\ T2_{21} & T2_{22} \end{bmatrix} \begin{bmatrix} T1_{11} & T1_{12} \\ T1_{21} & T1_{22} \end{bmatrix} \begin{bmatrix} a_{11} \\ b_{11} \end{bmatrix} \tag{E.8}$$

The elements of $\mathbf{T}'$ are therefore given by

$$T'_{11} = T3_{11}T2_{11}T1_{11} + T3_{11}T2_{12}T1_{21} + T3_{12}T2_{21}T1_{11} + T3_{12}T2_{22}T1_{21} \tag{E.9}$$
$$T'_{12} = T3_{11}T2_{11}T1_{12} + T3_{11}T2_{12}T1_{22} + T3_{12}T2_{21}T1_{12} + T3_{12}T2_{22}T1_{22} \tag{E.10}$$
$$T'_{21} = T3_{21}T2_{11}T1_{11} + T3_{21}T2_{12}T1_{21} + T3_{22}T2_{21}T1_{11} + T3_{22}T2_{22}T1_{21} \tag{E.11}$$
$$T'_{22} = T3_{21}T2_{11}T1_{12} + T3_{21}T2_{12}T1_{22} + T3_{22}T2_{21}T1_{12} + T3_{22}T2_{22}T1_{22} \tag{E.12}$$

The transmission parameters given by equations (E.9) to (E.12) can be converted to scattering parameters in order to give the matrix $\mathbf{S}'$. This matrix is the scattering parameter matrix that describes the composite two-port network formed from the three cascaded individual two-port networks.

$$S'_{11} = \frac{-T'_{21}}{T'_{22}} \tag{E.13}$$
$$S'_{12} = \frac{1}{T'_{22}} \tag{E.14}$$
$$S'_{21} = T'_{11} - \frac{T'_{12}T'_{21}}{T'_{22}} \tag{E.15}$$
$$S'_{22} = \frac{T'_{12}}{T'_{22}} \tag{E.16}$$

# Appendix F

# Classical Site Attenuation Data for Resonant Dipole Antennas

This appendix gives site attenuation data calculated using the NEC computer code. The data is for resonant dipole antennas in horizontal and vertical polarisations above 3 m and 10 m test sites with transmitting antenna heights of 1 m and 2 m above the ground plane.

The resonant dipoles were 6.35 mm diameter and were modelled with 21 equal length segments. The centre segment of both antennas was used to specify a voltage source or load impedance in order to calculate classical site attenuation in a 50 Ω transmission line system. The extended thin wire kernel was used for all of the simulations.

The first table in this appendix gives the resonant lengths that were predicted by NEC and used for the antennas at each of the 100 excitation frequencies. The following four tables give the site attenuation predictions; the first two specify the receiving antenna heights at which the minimum in the site transfer function occurs and the second two give the values of classical site attenuation at that height.

| Frequency MHz | Half-Length mm | Frequency MHz | Half-Length mm |
|---|---|---|---|
| 30.000 | 2398.925 | 176.300 | 399.564 |
| 31.082 | 2314.736 | 182.660 | 385.409 |
| 32.202 | 2233.636 | 189.240 | 371.770 |
| 33.363 | 2155.283 | 196.060 | 358.604 |
| 34.566 | 2079.654 | 203.130 | 345.893 |
| 35.812 | 2006.713 | 210.460 | 333.622 |
| 37.104 | 1936.206 | 218.040 | 321.804 |
| 38.441 | 1868.326 | 225.910 | 310.378 |
| 39.827 | 1802.743 | 234.050 | 299.373 |
| 41.263 | 1739.451 | 242.490 | 288.749 |
| 42.751 | 1678.355 | 251.230 | 278.503 |
| 44.292 | 1619.444 | 260.290 | 268.613 |
| 45.889 | 1562.563 | 269.680 | 259.068 |
| 47.544 | 1507.646 | 279.400 | 249.869 |
| 49.258 | 1454.690 | 289.470 | 240.995 |
| 51.034 | 1403.575 | 299.910 | 232.428 |
| 52.874 | 1354.251 | 310.720 | 224.168 |
| 54.780 | 1306.669 | 321.930 | 216.194 |
| 56.756 | 1260.693 | 333.530 | 208.511 |
| 58.802 | 1216.381 | 345.560 | 201.092 |
| 60.922 | 1173.611 | 358.020 | 193.938 |
| 63.118 | 1132.353 | 370.930 | 187.037 |
| 65.394 | 1092.508 | 384.300 | 180.383 |
| 67.752 | 1054.062 | 398.150 | 173.966 |
| 70.195 | 1016.963 | 412.510 | 167.772 |
| 72.725 | 981.192 | 427.380 | 161.801 |
| 75.347 | 946.654 | 442.790 | 156.041 |
| 78.064 | 913.312 | 458.760 | 150.484 |
| 80.879 | 881.139 | 475.300 | 145.127 |
| 83.795 | 850.102 | 492.430 | 139.963 |
| 86.816 | 820.155 | 510.190 | 134.979 |
| 89.946 | 791.256 | 528.580 | 130.177 |
| 93.189 | 763.367 | 547.640 | 125.544 |
| 96.549 | 736.454 | 567.380 | 121.078 |
| 100.030 | 710.485 | 587.840 | 116.771 |
| 103.640 | 685.407 | 609.030 | 112.620 |
| 107.370 | 661.266 | 630.990 | 108.618 |
| 111.240 | 637.941 | 653.740 | 104.759 |
| 115.250 | 615.428 | 677.310 | 101.040 |
| 119.410 | 593.677 | 701.730 | 97.455 |
| 123.720 | 572.693 | 727.030 | 94.000 |
| 128.180 | 552.470 | 753.250 | 90.669 |
| 132.800 | 532.956 | 780.400 | 87.460 |
| 137.590 | 514.115 | 808.540 | 84.367 |
| 142.550 | 495.948 | 837.690 | 81.386 |
| 147.690 | 478.410 | 867.900 | 78.513 |
| 153.010 | 461.508 | 899.190 | 75.746 |
| 158.530 | 445.173 | 931.610 | 73.079 |
| 164.240 | 429.435 | 965.200 | 70.509 |
| 170.160 | 414.243 | 999.996 | 68.034 |

Table F.1: Resonant lengths of the dipole antennas used for the calculations of predicted classical site attenuations.

| Frequency MHz | Horizontal Polarisation | | | | Vertical Polarisation | | | |
|---|---|---|---|---|---|---|---|---|
| | 3 m Site | | 10 m Site | | 3 m Site | | 10 m Site | |
| | 1 m Tx | 2 m Tx | 1 m Tx | 2 m Tx | 1 m Tx | 2 m Tx | 1 m Tx | 2 m Tx |
| 30.000 | 4.00 | 4.00 | 4.00 | 4.00 | | | | |
| 31.082 | 4.00 | 4.00 | 4.00 | 4.00 | | | | |
| 32.202 | 4.00 | 4.00 | 4.00 | 4.00 | | | | |
| 33.363 | 4.00 | 4.00 | 4.00 | 4.00 | | | | |
| 34.566 | 4.00 | 4.00 | 4.00 | 4.00 | | | | |
| 35.812 | 4.00 | 4.00 | 4.00 | 4.00 | | | | |
| 37.104 | 4.00 | 4.00 | 4.00 | 4.00 | | | | |
| 38.441 | 4.00 | 4.00 | 4.00 | 4.00 | | | | |
| 39.827 | 4.00 | 4.00 | 4.00 | 4.00 | | | | |
| 41.263 | 4.00 | 4.00 | 4.00 | 4.00 | | | | |
| 42.751 | 4.00 | 4.00 | 4.00 | 4.00 | | | | |
| 44.292 | 4.00 | 4.00 | 4.00 | 4.00 | | | | |
| 45.889 | 4.00 | 4.00 | 4.00 | 4.00 | | | | |
| 47.544 | 3.94 | 3.98 | 4.00 | 4.00 | | | | |
| 49.258 | 3.80 | 3.82 | 4.00 | 3.94 | | | | |
| 51.034 | 3.64 | 3.68 | 3.84 | 3.78 | | | | |
| 52.874 | 3.52 | 3.52 | 3.72 | 3.68 | | | | |
| 54.780 | 3.38 | 3.36 | 3.62 | 3.56 | | | | |
| 56.756 | 3.24 | 3.24 | 3.46 | 3.44 | | | | |
| 58.802 | 3.14 | 3.08 | 3.38 | 3.30 | | | | |
| 60.922 | 3.00 | 2.94 | 3.28 | 3.18 | | | | |
| 63.118 | 2.88 | 2.82 | 4.00 | 3.10 | | | | |
| 65.394 | 2.76 | 2.68 | 4.00 | 3.00 | | | | |
| 67.752 | 2.66 | 2.54 | 4.00 | 4.00 | | | | |
| 70.195 | 2.56 | 2.42 | 4.00 | 4.00 | | | | |
| 72.725 | 2.46 | 2.34 | 4.00 | 4.00 | 1.36 | 1.70 | 1.84 | 1.64 |
| 75.347 | 2.36 | 2.22 | 4.00 | 4.00 | 1.30 | 1.66 | 1.74 | 1.60 |
| 78.064 | 2.28 | 2.12 | 4.00 | 4.00 | 1.30 | 1.62 | 1.68 | 1.56 |
| 80.879 | 2.20 | 2.06 | 4.00 | 4.00 | 1.28 | 1.56 | 1.66 | 1.50 |
| 83.795 | 2.14 | 2.00 | 4.00 | 4.00 | 1.24 | 1.52 | 1.60 | 1.44 |
| 86.816 | 2.06 | 1.96 | 3.98 | 3.88 | 1.18 | 1.48 | 1.54 | 1.42 |
| 89.946 | 2.02 | 1.88 | 3.88 | 3.76 | 1.18 | 2.74 | 1.48 | 1.38 |
| 93.189 | 1.96 | 1.86 | 3.76 | 3.64 | 1.12 | 2.76 | 1.42 | 1.30 |
| 96.549 | 1.90 | 1.78 | 3.64 | 3.50 | 1.12 | 2.76 | 1.38 | 1.24 |
| 100.030 | 1.84 | 1.74 | 3.50 | 3.36 | 1.06 | 2.74 | 1.34 | 1.22 |
| 103.636 | 1.80 | 1.66 | 3.36 | 3.24 | 1.04 | 2.70 | 1.32 | 1.18 |
| 107.373 | 1.76 | 1.60 | 4.00 | 3.16 | 1.00 | 2.66 | 1.26 | 1.12 |
| 111.244 | 1.70 | 1.52 | 4.00 | 3.02 | 1.00 | 2.58 | 1.20 | 1.10 |
| 115.255 | 1.64 | 1.46 | 4.00 | 2.92 | 1.00 | 2.52 | 1.18 | 1.06 |
| 119.411 | 1.56 | 1.40 | 4.00 | 2.82 | 1.00 | 2.48 | 1.14 | 1.02 |
| 123.716 | 1.52 | 1.34 | 4.00 | 2.72 | 1.00 | 2.40 | 1.10 | 1.00 |
| 128.176 | 1.44 | 1.30 | 3.84 | 2.64 | 1.00 | 2.32 | 1.06 | 1.00 |
| 132.798 | 1.38 | 1.26 | 3.74 | 2.54 | 1.00 | 2.26 | 1.02 | 1.00 |
| 137.586 | 1.34 | 1.22 | 3.60 | 2.46 | 1.00 | 2.20 | 1.00 | 1.00 |
| 142.546 | 1.28 | 1.18 | 3.48 | 2.36 | 1.00 | 2.14 | 1.00 | 1.00 |
| 147.686 | 1.24 | 1.14 | 4.00 | 2.28 | 1.00 | 2.08 | 1.00 | 1.00 |
| 153.010 | 1.22 | 1.10 | 4.00 | 2.20 | 1.00 | 2.00 | 1.00 | 1.00 |
| 158.527 | 1.18 | 1.04 | 4.00 | 2.12 | 1.00 | 1.96 | 1.00 | 1.00 |
| 164.243 | 1.14 | 1.02 | 3.90 | 2.06 | 1.00 | 1.88 | 1.00 | 1.00 |
| 170.164 | 1.10 | 1.00 | 3.76 | 1.98 | 1.00 | 1.82 | 1.00 | 1.00 |

Table F.2: Receiving antenna heights at which classical site attenuation is measured.

| Frequency MHz | Horizontal Polarisation | | | | Vertical Polarisation | | | |
|---|---|---|---|---|---|---|---|---|
| | 3 m Site | | 10 m Site | | 3 m Site | | 10 m Site | |
| | 1 m Tx | 2 m Tx | 1 m Tx | 2 m Tx | 1 m Tx | 2 m Tx | 1 m Tx | 2 m Tx |
| 176.300 | 1.06 | 1.00 | 3.62 | 1.92 | 1.00 | 1.74 | 1.00 | 1.00 |
| 182.656 | 1.02 | 1.00 | 3.50 | 1.86 | 1.00 | 1.68 | 1.00 | 4.00 |
| 189.241 | 1.00 | 2.52 | 4.00 | 1.78 | 1.00 | 1.62 | 1.00 | 4.00 |
| 196.064 | 1.00 | 2.44 | 3.98 | 1.72 | 2.32 | 1.54 | 1.00 | 4.00 |
| 203.133 | 1.00 | 2.34 | 3.88 | 1.66 | 2.26 | 1.50 | 1.00 | 3.86 |
| 210.457 | 1.00 | 2.26 | 3.72 | 1.60 | 2.20 | 1.44 | 1.00 | 3.74 |
| 218.045 | 1.00 | 2.16 | 3.60 | 1.54 | 2.12 | 1.38 | 1.00 | 3.60 |
| 225.907 | 1.00 | 2.06 | 3.46 | 1.50 | 2.08 | 1.32 | 1.00 | 3.46 |
| 234.052 | 1.34 | 2.00 | 3.34 | 1.44 | 2.02 | 1.28 | 1.00 | 3.32 |
| 242.490 | 1.30 | 1.92 | 3.22 | 1.40 | 1.96 | 1.22 | 1.00 | 3.24 |
| 251.233 | 1.26 | 1.84 | 3.12 | 1.34 | 1.92 | 1.18 | 1.00 | 3.12 |
| 260.291 | 1.20 | 1.76 | 3.00 | 1.30 | 1.86 | 1.14 | 1.00 | 2.98 |
| 269.676 | 1.16 | 1.70 | 2.90 | 1.26 | 1.80 | 1.08 | 1.00 | 2.88 |
| 279.399 | 1.12 | 1.62 | 2.80 | 1.20 | 1.74 | 2.20 | 1.00 | 2.78 |
| 289.473 | 1.08 | 1.56 | 2.70 | 1.16 | 1.68 | 2.10 | 1.00 | 2.70 |
| 299.909 | 1.04 | 1.50 | 2.60 | 1.12 | 1.64 | 2.04 | 1.00 | 2.60 |
| 310.723 | 1.00 | 1.44 | 2.52 | 1.08 | 1.58 | 1.94 | 1.00 | 2.50 |
| 321.925 | 1.00 | 1.38 | 2.44 | 1.04 | 1.52 | 1.86 | 1.00 | 2.40 |
| 333.532 | 1.00 | 2.34 | 2.34 | 1.02 | 1.46 | 1.80 | 1.00 | 2.32 |
| 345.558 | 1.00 | 2.24 | 2.26 | 1.00 | 1.42 | 1.72 | 1.00 | 2.24 |
| 358.017 | 2.58 | 2.16 | 2.18 | 1.00 | 1.38 | 1.66 | 1.00 | 2.16 |
| 370.925 | 2.16 | 2.06 | 2.10 | 1.00 | 1.32 | 1.58 | 4.00 | 2.08 |
| 384.298 | 2.08 | 1.98 | 2.04 | 1.22 | 1.28 | 1.52 | 3.98 | 2.02 |
| 398.154 | 2.00 | 1.90 | 1.96 | 1.16 | 1.22 | 1.46 | 3.84 | 1.94 |
| 412.509 | 1.92 | 1.82 | 1.90 | 1.12 | 1.20 | 1.40 | 3.72 | 1.88 |
| 427.382 | 1.84 | 1.74 | 1.84 | 2.86 | 1.14 | 2.14 | 3.58 | 1.80 |
| 442.791 | 1.78 | 1.68 | 1.76 | 2.76 | 1.10 | 2.06 | 3.46 | 1.74 |
| 458.756 | 1.72 | 1.60 | 1.70 | 2.66 | 1.06 | 1.96 | 3.36 | 1.68 |
| 475.296 | 1.64 | 2.28 | 1.64 | 2.56 | 1.02 | 1.88 | 3.22 | 1.62 |
| 492.432 | 1.60 | 2.18 | 1.58 | 2.46 | 1.00 | 1.80 | 3.08 | 1.56 |
| 510.187 | 1.54 | 2.10 | 1.54 | 2.38 | 1.00 | 1.74 | 2.98 | 1.50 |
| 528.581 | 1.48 | 2.00 | 1.48 | 2.30 | 1.00 | 1.66 | 2.90 | 1.46 |
| 547.639 | 1.42 | 1.92 | 1.42 | 2.22 | 1.00 | 1.60 | 2.76 | 1.40 |
| 567.384 | 1.38 | 1.84 | 1.38 | 2.14 | 1.00 | 1.54 | 2.70 | 1.36 |
| 587.840 | 1.32 | 1.18 | 1.32 | 2.06 | 1.00 | 1.48 | 2.60 | 1.30 |
| 609.035 | 1.28 | 1.14 | 1.28 | 1.98 | 1.72 | 1.98 | 2.50 | 1.26 |
| 630.993 | 1.22 | 2.18 | 1.24 | 1.92 | 1.66 | 1.88 | 2.42 | 1.22 |
| 653.743 | 1.18 | 1.06 | 1.20 | 1.84 | 1.60 | 1.82 | 2.34 | 1.18 |
| 677.314 | 1.14 | 1.02 | 1.16 | 1.78 | 1.52 | 1.74 | 2.26 | 1.14 |
| 701.734 | 1.10 | 1.42 | 1.12 | 1.72 | 1.46 | 1.66 | 2.18 | 1.10 |
| 727.035 | 1.06 | 1.36 | 1.08 | 2.72 | 1.40 | 1.60 | 2.08 | 1.06 |
| 753.247 | 1.02 | 1.30 | 1.04 | 2.62 | 1.36 | 1.54 | 2.02 | 1.02 |
| 780.405 | 1.00 | 1.26 | 1.00 | 2.54 | 1.30 | 1.90 | 1.96 | 1.00 |
| 808.543 | 1.68 | 1.20 | 1.00 | 2.44 | 1.26 | 1.82 | 1.88 | 1.00 |
| 837.694 | 1.52 | 1.16 | 2.74 | 2.36 | 1.20 | 1.76 | 1.82 | 1.86 |
| 867.897 | 1.46 | 1.12 | 2.64 | 2.28 | 1.16 | 1.68 | 1.74 | 1.78 |
| 899.188 | 1.40 | 1.08 | 2.54 | 2.20 | 1.10 | 1.62 | 1.68 | 1.72 |
| 931.608 | 1.34 | 1.04 | 2.46 | 2.12 | 1.06 | 1.92 | 1.62 | 1.66 |
| 965.197 | 1.30 | 1.00 | 2.38 | 2.04 | 1.02 | 1.84 | 1.58 | 1.60 |
| 999.996 | 1.26 | 1.26 | 2.30 | 1.96 | 1.00 | 1.76 | 1.52 | 1.54 |

Table F.3: Receiving antenna heights at which classical site attenuation is measured.

| Frequency MHz | Horizontal Polarisation | | | | Vertical Polarisation | | | |
|---|---|---|---|---|---|---|---|---|
| | 3 m Site | | 10 m Site | | 3 m Site | | 10 m Site | |
| | 1 m Tx | 2 m Tx | 1 m Tx | 2 m Tx | 1 m Tx | 2 m Tx | 1 m Tx | 2 m Tx |
| 176.300 | 16.20 | 18.12 | 27.04 | 27.01 | 24.11 | 21.63 | 28.22 | 30.63 |
| 182.656 | 16.56 | 19.01 | 27.29 | 27.60 | 25.00 | 22.02 | 28.65 | 30.94 |
| 189.241 | 17.14 | 19.91 | 27.69 | 28.15 | 25.88 | 22.40 | 29.13 | 31.00 |
| 196.064 | 17.84 | 20.36 | 28.00 | 28.69 | 26.44 | 22.72 | 29.57 | 31.11 |
| 203.133 | 18.52 | 20.63 | 28.55 | 29.03 | 26.29 | 22.99 | 30.01 | 31.26 |
| 210.457 | 19.15 | 20.73 | 29.08 | 29.29 | 26.16 | 23.25 | 30.43 | 31.41 |
| 218.045 | 19.82 | 20.73 | 29.67 | 29.34 | 26.06 | 23.57 | 30.82 | 31.58 |
| 225.907 | 20.58 | 20.76 | 30.18 | 29.38 | 26.00 | 23.96 | 31.19 | 31.77 |
| 234.052 | 21.22 | 20.93 | 30.70 | 29.41 | 25.94 | 24.38 | 31.54 | 31.98 |
| 242.490 | 21.69 | 21.25 | 31.11 | 29.66 | 25.87 | 24.75 | 31.87 | 32.21 |
| 251.233 | 22.00 | 21.68 | 31.48 | 30.10 | 25.79 | 25.08 | 32.21 | 32.45 |
| 260.291 | 22.20 | 22.19 | 31.74 | 30.68 | 25.72 | 25.41 | 32.53 | 32.66 |
| 269.676 | 22.38 | 22.74 | 31.92 | 31.26 | 25.70 | 25.79 | 32.88 | 32.90 |
| 279.399 | 22.57 | 23.22 | 32.02 | 31.63 | 25.75 | 25.97 | 33.25 | 33.11 |
| 289.473 | 22.68 | 23.49 | 32.04 | 31.81 | 25.83 | 26.19 | 33.64 | 33.34 |
| 299.909 | 22.67 | 23.51 | 32.04 | 31.85 | 25.90 | 26.43 | 34.08 | 33.59 |
| 310.723 | 22.62 | 23.52 | 32.07 | 31.91 | 25.97 | 26.65 | 34.56 | 33.84 |
| 321.925 | 22.84 | 23.88 | 32.17 | 32.21 | 26.09 | 26.92 | 35.07 | 34.10 |
| 333.532 | 23.49 | 24.46 | 32.41 | 32.76 | 26.28 | 27.25 | 35.59 | 34.37 |
| 345.558 | 24.45 | 25.02 | 32.83 | 33.37 | 26.48 | 27.58 | 36.14 | 34.63 |
| 358.017 | 25.14 | 25.31 | 33.37 | 33.91 | 26.63 | 27.86 | 36.68 | 34.88 |
| 370.925 | 25.58 | 25.36 | 33.96 | 34.26 | 26.78 | 28.16 | 36.82 | 35.14 |
| 384.298 | 25.93 | 25.45 | 34.52 | 34.43 | 26.98 | 28.54 | 36.92 | 35.41 |
| 398.154 | 26.17 | 25.81 | 34.97 | 34.73 | 27.18 | 28.89 | 37.04 | 35.69 |
| 412.509 | 26.34 | 26.35 | 35.27 | 35.30 | 27.33 | 29.22 | 37.17 | 35.97 |
| 427.382 | 26.42 | 26.87 | 35.43 | 35.80 | 27.51 | 29.58 | 37.31 | 36.24 |
| 442.791 | 26.34 | 27.12 | 35.46 | 35.97 | 27.76 | 29.82 | 37.47 | 36.51 |
| 458.756 | 26.22 | 27.13 | 35.48 | 36.00 | 27.98 | 30.05 | 37.66 | 36.80 |
| 475.296 | 26.29 | 27.40 | 35.59 | 36.31 | 28.20 | 30.32 | 37.86 | 37.09 |
| 492.432 | 26.58 | 27.97 | 35.92 | 36.89 | 28.50 | 30.63 | 38.07 | 37.38 |
| 510.187 | 27.00 | 28.32 | 36.44 | 37.25 | 28.82 | 30.92 | 38.29 | 37.65 |
| 528.581 | 27.57 | 28.36 | 37.03 | 37.30 | 29.23 | 31.23 | 38.51 | 37.94 |
| 547.639 | 28.04 | 28.64 | 37.53 | 37.52 | 29.77 | 31.58 | 38.71 | 38.23 |
| 567.384 | 28.29 | 29.20 | 37.83 | 38.09 | 30.38 | 31.91 | 38.92 | 38.53 |
| 587.840 | 28.38 | 29.57 | 37.93 | 38.43 | 31.22 | 32.26 | 39.14 | 38.81 |
| 609.035 | 28.37 | 29.58 | 37.94 | 38.47 | 32.12 | 32.52 | 39.38 | 39.10 |
| 630.993 | 28.49 | 29.95 | 38.08 | 38.85 | 32.22 | 32.79 | 39.63 | 39.40 |
| 653.743 | 28.91 | 30.46 | 38.51 | 39.37 | 32.31 | 33.09 | 39.89 | 39.70 |
| 677.314 | 29.48 | 30.54 | 39.10 | 39.47 | 32.43 | 33.38 | 40.14 | 39.99 |
| 701.734 | 29.99 | 30.82 | 39.60 | 39.73 | 32.56 | 33.71 | 40.39 | 40.29 |
| 727.035 | 30.20 | 31.34 | 39.83 | 40.26 | 32.70 | 34.04 | 40.63 | 40.59 |
| 753.247 | 30.24 | 31.40 | 39.86 | 40.36 | 32.87 | 34.38 | 40.89 | 40.88 |
| 780.405 | 30.43 | 31.70 | 39.97 | 40.67 | 33.06 | 34.65 | 41.17 | 41.21 |
| 808.543 | 31.48 | 32.13 | 40.60 | 41.13 | 33.27 | 34.94 | 41.45 | 41.63 |
| 837.694 | 32.07 | 32.16 | 41.49 | 41.20 | 33.47 | 35.25 | 41.72 | 42.12 |
| 867.897 | 32.30 | 32.64 | 41.83 | 41.70 | 33.68 | 35.56 | 41.98 | 42.40 |
| 899.188 | 32.28 | 32.85 | 41.87 | 41.92 | 33.91 | 35.90 | 42.25 | 42.68 |
| 931.608 | 32.30 | 33.10 | 41.95 | 42.20 | 34.14 | 36.20 | 42.54 | 42.97 |
| 965.197 | 32.68 | 33.49 | 42.42 | 42.60 | 34.39 | 36.49 | 42.83 | 43.25 |
| 999.996 | 33.20 | 33.68 | 42.96 | 42.77 | 34.66 | 36.81 | 43.11 | 43.55 |

Table F.5: Classical site attenuation data calculated using NEC.

# Appendix G

# Transformation of the Characteristic Impedance of the Scattering Parameter Representation of a Two-Port Network

Consider a two-port network, described by scattering parameters normalised to a particular characteristic impedance, as shown in figure G.1

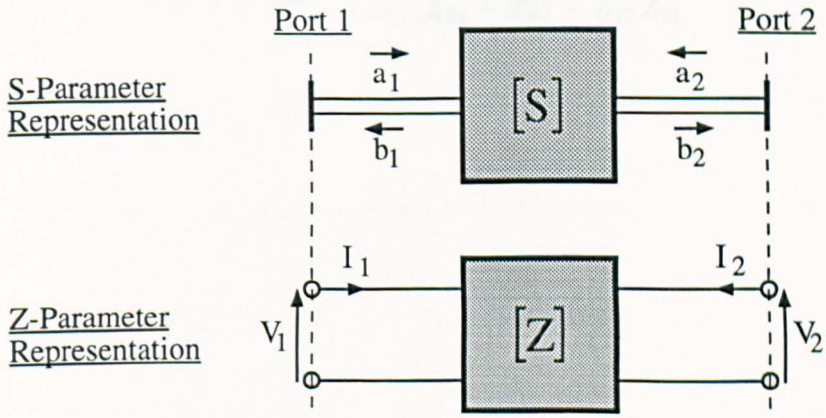


Figure G.1: Scattering parameter and impedance parameter representations of a two-port network.

In order to convert scattering parameters normalised to one characteristic impedance into scattering parameters normalised to a different characteristic impedance, it is necessary to transform to a parameter set that does not depend on the characteristic impedance. Impedance parameters are one such parameter set.

Equations (G.1) to (G.4) can be used to convert scattering parameters normalised to a characteristic impedance, $Z_0$, into impedance parameters.

$$Z_{11} = \frac{(1+S_{11})(1-S_{22})+S_{12}S_{21}}{(1-S_{11})(1-S_{22})+S_{12}S_{21}}Z_0 \quad \text{(G.1)}$$

$$Z_{12} = \frac{2S_{12}}{(1-S_{11})(1-S_{22})+S_{12}S_{21}}Z_0 \quad \text{(G.2)}$$

$$Z_{21} = \frac{2S_{21}}{(1-S_{11})(1-S_{22})+S_{12}S_{21}}Z_0 \quad \text{(G.3)}$$

$$Z_{22} = \frac{(1-S_{11})(1+S_{22})+S_{12}S_{21}}{(1-S_{11})(1-S_{22})+S_{12}S_{21}}Z_0 \quad \text{(G.4)}$$

The impedance parameters can then be transformed back to scattering parameters normalised to a different characteristic impedance, $Z_0'$. Equations (G.5) to (G.8) give this transformation.

$$S'_{11} = \frac{(Z_{11}-Z'_0)(Z_{22}+Z'_0)-Z_{12}Z_{21}}{(Z_{11}+Z'_0)(Z_{22}+Z'_0)-Z_{12}Z_{21}} \quad \text{(G.5)}$$

$$S'_{12} = \frac{2Z_{12}Z'_0}{(Z_{11}+Z'_0)(Z_{22}+Z'_0)-Z_{12}Z_{21}} \quad \text{(G.6)}$$

$$S'_{21} = \frac{2Z_{21}Z'_0}{(Z_{11}+Z'_0)(Z_{22}+Z'_0)-Z_{12}Z_{21}} \quad \text{(G.7)}$$

$$S'_{22} = \frac{(Z_{11}+Z'_0)(Z_{22}-Z'_0)-Z_{12}Z_{21}}{(Z_{11}+Z'_0)(Z_{22}+Z'_0)-Z_{12}Z_{21}} \quad \text{(G.8)}$$

# References


[1] W.S. Bennett. Ground plane effects on far-field EMI measurements. In *Proc. IEEE Int. Symp. EMC, San Diego CA*, pages 365–368, October 1979.

[2] T. Dvorak and G. Meyer. Influence of ground reflection in open site measurements of broadband interference. In *Proc. IEEE Int. Symp. EMC, San Diego CA*, pages 369–374, October 1979.

[3] R. F. German. On radiated EMI measurement in the VHF/UHF frequency range. In *Proc. IEEE Int. Symp. EMC, Baltimore MD*, pages 91–97, OA1980.

[4] T. J Dvorak and G. V. Meyer. Field patterns at an IEC 3 m radiation measuring site. In *Proc. IEEE Int. Symp. EMC, Baltimore MD*, pages 101–106, 1980.

[5] T. J. Dvorak. Polarisation error in field strength measurements. In *Proc. IEEE Int. Symp. EMC, Santa Clara*, pages 134–139, 1982.

[6] W. S. Bennett. Far-field conditions for radiated emissions measurements. In *Proc. IEEE Int. Symp. EMC*, pages 391–395, August 1983.

[7] C. A. Balanis. *Antenna Theory Analysis and Design*, chapter 4, pages 100–103. Wiley, New York, 1982.

[8] C. A. Balanis. *Antenna Theory Analysis and Design*, chapter 5, pages 164–169. Wiley, New York, 1982.

[9] C. A. Balanis. *Antenna Theory Analysis and Design*, chapter 4, pages 133–135. Wiley, New York, 1982.

[10] P. R. Bannister. Image theory results for the mutual impedance of crossing earth return circuits. *IEEE Trans. EMC*, 15(4):158–160, November 1973.

[11] International Special Committee on Radio Interference (CISPR). *Limits and Methods of Measurement of Radio Interference Characteristics of Information Technology Equipment.* Geneva, Switzerland. Publication No. 22.

[12] K. F. Sander. *Transmission and Propagation of Electromagnetic Waves*, chapter 8, pages 369–371. Cambridge Univ. Press, London, England, 1986.

[13] American National Standards Institute. American national standard guide for construction of open area test sites for performing radiated emission measurements, C63.7. In *Electromagnetic Compatibility, C63.* IEEE, December 1989.

[14] P. Beckmann and A. Spizzichino. *The Scattering of Electromagnetic Waves From Rough Surfaces.* Mac-Millan, Pergamon Press, New York, 1963.

[15] British Standards Institute. *Limits and Methods of Measuremennts of Radio Interference Characteristics of Information Technology Equipment*, 1988. BS6527.

[16] K. F. Casey. Electromagnetic behaviour of wire mesh screens. *IEEE Trans. EMC*, 30(3):298–306, August 1988.

[17] W. S. Bennett and H. E. Taggart. Characterisation of a CISPR/VDE far-field EMI test-site with ground screen. In *Proc. 3rd EMC Symp. Rotterdam*, pages 507–513, May 1979.

[18] A. A. Smith *et al.* Calculation of site attenuation from antenna factors. *IEEE Trans. EMC*, 24(3):301–316, August 1982.

[19] A. C. Marvin and J. Ahmadi. Comparison of open-field test sites used for radiated emission measurements. *Proc. IEE, part A*, 139(7), January 1993.

[20] C. A. Balanis. *Antenna Theory Analysis and Design*, chapter 4, page 105. Wiley, New York, 1982.

[21] G. J. Burke and A. J. Poggio. Numerical Electromagnetics Code (NEC) — method of moments. Technical report, Lawrence Livermore National Laboratory, January 1981. Report UICD-18834.

[22] A. A. Pistolkers. The radiation resistance of beam antennas. *Proc. IRE*, 17:562–579, March 1929.

[23] R. Benchman. On the calculation of radiation resistance of antennas and antenna combinations. *Proc. IRE*, 19:461–466, March 1931.

[24] P.S. Carter. Circuit relations in radiating systems and applications to antenna problems. *Proc. IRE*, 20:1004–1041, June 1932.

[25] G. H. Brown and R. King. High frequency models in antenna investigations. *Proc. IRE*, 22(4):457–480, April 1934.

[26] H. C. Pocklington. Electrical oscillations in wire. *Cambridge Philosophical Society Proceedings, London, England*, 9:324–332, 1897.

[27] E. Hallèn. Theoretical investigations into the transmitting and receiving qualities of antennae. *Nova Acta Regiae Soc. Sci. Upsaliensis*, 11(4):1–44, 1938.

[28] R. W. P. King. *The Theory of Linear Antennas.* Harvard Univ. Press, Cambridge, Massachusetts, 1956.

[29] R.F. Harrington. *Field Computation by Moment Methods.* Macmillan, New York, 1968.

[30] R. W. P. King. *The Theory of Linear Antennas*, chapter II.17, page 87. Harvard Univ. Press, Cambridge, Massachusetts, 1956.

[31] C. A. Balanis. *Antenna Theory Analysis and Design*, chapter 7, pages 285–304. Wiley, New York, 1982.

[32] J. D. Kraus. *Antennas*, chapter 10, pages 251–278. McGraw-Hill, New York, 1950.

[33] H. E. King. Mutual impedance of unequal length antennas in echelon. *IEEE Trans. Antennas and Propagation*, 5:306–313, July 1957.

[34] C. T. Tai. Coupled antennas. *Proc. IRE*, 36:487–500, 1948.

[35] R. W. P. King. *The Theory of Linear Antennas*, chapter II.11–II.14, pages 69–81. Harvard Univ. Press, Cambridge, Massachusetts, 1956.

[36] R. F. Harrington. *Field Computation by Moment Methods.* Macmillan, New York, 1968.

[37] C. A. Balanis. *Advanced Engineering Electromagnetics*, chapter 12, pages 670–730. Wiley, New York, 1990.

[38] G. J. Burke and A. J. Poggio. Numerical Electromagnetics Code (NEC) — method of moments. Technical report, Lawrence Livermore National Laboratory, January 1981. Report UICD-18834.

[39] C. A. Balanis. *Antenna Theory Analysis and Design*, chapter 7, pages 304–317. Wiley, New York, 1982.

[40] G. J. Burke and A. J. Poggio. Numerical Electromagnetics Code (NEC) — program description, theory. Technical report, Lawrence Livermore National Laboratory, January 1981. Report UICD-18834, vol. 1, part I.

[41] G. J. Burke and A. J. Poggio. Numerical Electromagnetics Code (NEC) — program description, user's guide. Technical report, Lawrence Livermore National Laboratory, January 1981. Report UICD-18834.

[42] C. W. Trueman and S. J. Kubina. Verifying wire-grid model integrity with program "check". *American Computational Electromagnetics Society (ACES)*, 5(2):17–42, Winter 1990.

[43] R. W. P. King. *The Theory of Linear Antennas*, chapter II.32, page 193. Harvard Univ. Press, Cambridge, Massachusetts, 1956.

[44] S. K. Shelkunoff and H. T. Friis. *Antennas: Theory and Practice*, pages 229–244, 351–353. Wiley, New York, 1952.

[45] R. W. P. King. *The Theory of Linear Antennas*, chapter II.11, page 70. Harvard Univ. Press, Cambridge, Massachusetts, 1956.

[46] J. D. Kraus. *Antennas*, chapter 8, pages 217–229. McGraw-Hill, New York, 1950.

[47] B. A. Austin and A. P. C. Fourie. Computer modelling of field strength measuring antennas. Univ. of Liverpool, Department of Electrical Engineering and Electronics, Report on University Contract 460416 for the Department of Trade and Industry, Radio Technology Laboratory, Whyteleafe, Surrey.

[48] Measurement of radio interferences, measurement of radio interference field strength, February 1985. VDE0877, part 2.

[49] American National Standards Institute. American national standard methods of measurement of radio-noise emissions from low-voltage electrical and electronic equipment in the range of 10 KHz to 1 GHz, C63.4. In *Electromagnetic Compatibility, C63.* IEEE, December 1988.

[50] J. C. Mantovani. A spherical dipole source for use as a transfer standard between radiated emission test sites. In *Proc. IEEE Int. Symp. EMC, Tokyo, Japan*, pages 583–588, 1984.

[51] York Electronics Centre. *The Spherical Dipole Swept Emitter.* University of York, Heslington, York, U.K.

[52] R. W. Beatty. Insertion loss concepts. *Proc. IEEE*, 52:663–671, June 1964.

[53] A. A. Smith *et al.* Calculation of site attenuation from antenna factors. *IEEE Trans. EMC*, 24(3):301–316, August 1982.

[54] W. S. Bennett. Comment on "calculation of site attenuation from antenna factors". *IEEE Trans. EMC*, 22(2):121–124, May 1983.

[55] W. S. Bennett. A comparison of open-field test site qualification procedures. In *Proc. IEEE Int. Symp. EMC*, pages 396–402, August 1983.

[56] K. Bullington. Radio propagation at frequencies above 30 megacycles. *Proc. IRE*, pages 1122–1136, October 1947.

[57] T. Kawana and S. Miyajima. Theoretical investigations on site attenuation — propagation characteristics inside the measuring site for the radio interference. *Jour. Radio Research Laboratories, Tokyo, Japan*, 25(117 and 118):105–115, July and November 1978.

[58] T. Kawana and S. Miyajima. Theoretical investigations of site attenuation by means of mutual impedance between antennas. In *Proc. 3rd Symp. Tech. Exhibit. EMC, Rotterdam*, pages 83–88, May 1979.

[59] S. Takeya and A. Maeda. New correction factor for high-precision open site attenuation calculation. In *Proc. IEEE Int. Symp. EMC, Tokyo*, October 1984.

[60] S. Takeya and A. Maeda. New correction factor for high-precision open site attenuation calculation. In *Proc. IEEE Int. Symp. EMC, Boston*, pages 183–187, August 1985.

[61] S. Takeya and A. Maeda. New correction factor for high-precision open site attenuation calculation. In *Proc. IEEE Int. Symp. EMC, San Diego*, pages 354–361, 1986.

[62] R. G. Fitzgerrell. Site attenuation. *IEEE Trans. EMC*, 28(1):38–40, February 1986.

[63] A. Sugiura and M. Okamura. Correction factors for the normalised site attenuation. In *Proc. IEEE Int. Symp. EMC, Nagoya, Japan*, pages 29–34, 1989.

[64] A. Sugiura. Formulation of normalised site attenuation in terms of antenna impedances. *IEEE Trans. EMC*, 32(4):257–263, November 1990.

[65] W. H. Hayward. *Introduction to Radio Frequency Design*, chapter 5, pages 191–201. Prentice Hall, New Jersey, 1982.

[66] F. Jay. *IEEE Standard Dictionary of Electrical and Electronics Terms.* IEEE, New York, 1977. ANSI/IEEE Standard, 100-1977.

[67] C. R. Paul. *Introduction to Electromagnetic Compatibility*, chapter 5, page 202. Wiley, New York, 1992.

[68] A. A. Smith *et al.* Standard site method for antenna calibration. *IEEE trans. EMC*, 24(3):301–316, August 1982.

[69] M. J. Salter and M. J. Alexander. Emc antenna calibration and the design of an open-field test site. *Proc. IEE, part A*, 139(7):510–519, January 1993.

[70] W. S. Bennett. A comparison of open-field test site qualification procedures. In *Proc IEEE Int. Symp. EMC*, pages 396–402, August 1983.

[71] C. A. Balanis. *Antenna Theory, Analysis and Design*, chapter 4, pages 130–132. Wiley, New York, 1982.

[72] W. S. Bennett. Antenna factors in EMC measurements. In *Proc. IEEE Int. Symp. EMC,*, pages 34–37, August 1983.

[73] J. DeMarinis. Antenna calibration as a function of height. In *Proc. IEEE Int. Symp. EMC, Atlanta, Georgia*, pages 107–114, August 1987.

[74] R. G. Fitzgerrel. Standard linear antennas, 30 MHz to 1000 MHz. In *Proc. 5th IEE Int. Conf. EMC, Univ. of York*, pages 147–154, October 1986.

[75] R. W. P. King. *The Theory of Linear Antennas*, chapter II.37, page 221. Harvard Univ. Press, Cambridge, Massachusetts, 1956.

[76] E. L. Bronaugh. Derivation of the ±4 db criterion for site attenuation on open-area test sites. In *Proc. 8th IEE Int. Conf. EMC, Herriot-Watt Univ.*, pages 160–163, September 1992.

[77] American National Standards Institute. American national standard methods of measurement of radio-noise emissions from low-voltage electrical and electronic equipment in the range of 10 KHz to 1 GHz, C63.4. In *Electromagnetic Compatibility, C63.* IEEE, December 1988.

[78] A. A. Smith *et al.* Standard site method for antenna calibration. *IEEE trans. EMC*, 24(3):301–316, August 1982.

[79] American National Standards Institute. American national standard methods of measurement of radio-noise emissions from low-voltage electrical and electronic equipment in the range of 10 KHz to 1 GHz, C63.5. In *Electromagnetic Compatibility, C63.* IEEE, December 1988.

[80] A. Sugiura *et al.* Correction factors for normalised site attenuation. *IEEE trans. EMC*, 34(4):461–470, November 1992.

[81] R. A. McConnell. A derivation of the normalised site attenuation mutual coupling correction factor and an improved method of antenna factor determination. In *Proc. IEEE Int. Symp. EMC, Anaheim, CA*, pages 407–411, August 1992.

[82] W. H. Press *et al. Numerical Recipies*, chapter 12, pages 444–449. Cambridge Univ. Press, London, England, 1989.

[83] M. M. Dawood. *A new approach to wideband and superdirective array antennas by Incorporating Microwave Transistors.* PhD thesis, Univ. of Sheffield, U.K., 1973. Appendix A.

# THE MEASUREMENT AND USE OF GROUND PLANE REFLECTION COEFFICIENTS FOR IMPROVING THE ACCURACY OF RADIATION MEASUREMENTS USING OPEN-FIELD TEST SITES

S. M. Mann and A. C. Marvin

University of York, England

## INTRODUCTION

Open-Field Test Sites [1] have become the most widely accepted environments that are used for the measurement of radio frequency emissions from electronic equipment within the frequency range from 30 MHz to 1 GHz. This is because they enable a more accurate and repeatable measurement to be performed than some other measurement environments, such as screened rooms, and cost considerably less than anechoic chambers of practical size. Unfortunately open-field test sites do require a large area of land for their installation and this can represent a major problem for some companies and hence lead to design compromises, the results of which tend not to be well understood. This paper aims to consider the question of ground plane design for open-field test sites and show how different designs can affect the reflected wave and hence measurements performed on the sites.

## OPEN-FIELD TEST SITES

An ideal test site consists of the infinite, obstruction free half-space over a flat perfectly conducting ground plane. In this half space is the equipment under test (EUT) at a set height above the ground, usually 80 cm, and the receiving antenna used to measure the radiation. A direct wave propagates from the EUT to the receiving antenna but there is also a reflected wave from the image of the EUT in the ground plane. Measurements are performed by scanning the receiving antenna through a specified height range to obtain the maximum field strength at every frequency of interest. Infinite half spaces are difficult to make in practice and so an acceptable compromise has to be used instead. The CISPR ellipse [2] is the recommended flat area by European and American standards and it is chosen so that all elements of the reflected wave front from the ground plane that have travelled a path length up to twice the site length have a defined amplitude and phase. Typical site lengths are 3,10 and 30 m giving the following major and minor axes for the CISPR ellipse.

| Site Length | Ellipse Axis | |
|---|---|---|
| | Major | Minor |
| 3 | 6 | 5.2 |
| 10 | 20 | 17.3 |
| 30 | 60 | 52.0 |

Within the flat elliptical area the ground is normally concrete or earth and so is not perfectly conducting and hence not a perfect reflector. For this reason an area at the centre of the ellipse is usually covered with a metal plate of solid or mesh form to improve the reflectivity of the ground plane. Due to its truncated nature edge scattering effects can occur that may even degrade the site at low frequencies as this paper aims to show.

The test site on which the measurements in this paper were performed is located at the University of York and is owned by The York Electronics Centre. It has the ground plane structure shown in figure 1 consisting of an aluminium mesh of electrically small holes laid over a concrete area at the centre of the site and grassed earth towards its periphery. The

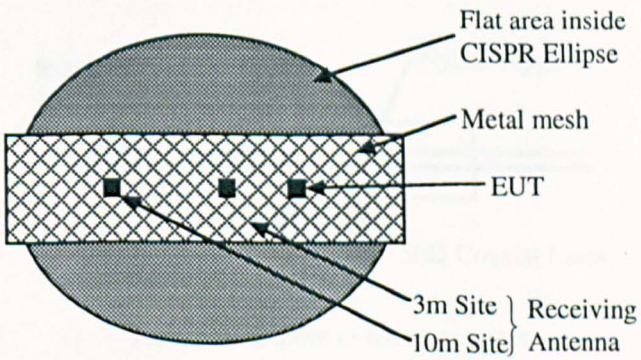


Figure 1: Typical OFTS ground plane structure

metalised portion of the ground plane has dimensions of 19.6 m by 3.8 m and so it is two wavelengths long at 30 MHz but only a third of a wavelength wide. This means it will scatter waves incident on it although the exact amount of scattering will depend on the connection between the metal mesh and the bulk earth surrounding it. A method for measuring the effective reflection coefficient of the ground plane has been devised as a means for examining

the properties of the ground plane and determining how much scattering is occurring. It may be possible to use the reflection coefficients to determine correction factors for the test site so that the ground plane is no longer a cause of inaccuracy.

## CALCULATION OF REFLECTION COEFFICIENTS

The method devised for evaluating ground plane performance involves a frequency domain measurement of its effective refection coefficient as a function of antenna height above it. It combines image theory with the use of an antenna analysis program known as NEC (Numerical Electromagnetics Code) [3] to calculate the reflection coefficient from terminal impedance measurements on a resonant dipole antenna over the ground plane. Scattering effects cause this effective reflection coefficient to be a height dependent quantity and so data was gathered for antenna heights between 60 cm and 400 cm.

Consider a cylindrical dipole antenna horizontally polarised above a ground plane as shown in figure 2. This is equivalent to the situation of two coupled antennas where the second antenna is the image of the first antenna in the ground and the reflection coefficient is the scaling factor between the object and image antenna currents. Consider the matrix

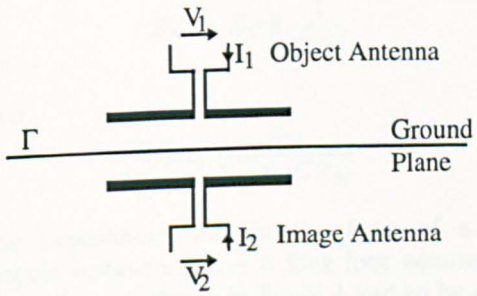


Figure 2: Single antenna above a ground plane

describing the coupling between the two antennas

$$\begin{bmatrix} V_1 \\ V_2 \end{bmatrix} = \begin{bmatrix} Z_{11} Z_{12} \\ Z_{21} Z_{22} \end{bmatrix} \cdot \begin{bmatrix} I_1 \\ I_2 \end{bmatrix} \quad (1)$$

but as $I_2 = \Gamma I_1$ and $Z_T = \frac{V_1}{I_1}$ it can be seen that

$$Z_T = Z_{11} + \Gamma Z_{12} \quad (2)$$

Where $Z_{11}$ is the self impedance of the transmitting antenna, $Z_{12}$ is the mutual impedance between it and the image antenna, $\Gamma$ is the ground plane reflection coefficient and $Z_T$ is the terminal impedance of the object antenna.

When two coupled antennas are fed by the same magnitude and phase voltages their terminal impedances are the symmetrical impedance $Z_S$ and where two antennas are fed by the same magnitude voltages but 180° out of phase their terminal impedances are the antisymmetrical impedance $Z_A$. When $\Gamma = +1$,

$$Z_T = Z_S = Z_{11} + Z_{12} \quad (3)$$

and when $\Gamma = -1$

$$Z_T = Z_A = Z_{11} - Z_{12} \quad (4)$$

Hence $Z_{11} = \frac{Z_S + Z_A}{2}$
$Z_{12} = \frac{Z_S - Z_A}{2}$

and so substituting in equation 2 gives

$$\Gamma = \frac{2Z_T - (Z_S + Z_A)}{Z_S - Z_A} \quad (5)$$

The value of $Z_T$ is obtained by measurement for each antenna height and the values of $Z_S$ and $Z_A$ are obtained by computer simulations of the experimental arrangement under the symmetrical and antisymmetrical excitation conditions using the NEC computer code.

## MEASUREMENT OF ANTENNA TERMINAL IMPEDANCES

The cylindrical dipole antennas used for this measurement are similar to the ones used by Fitzgerrel [4] in that they consisted of quarter inch brass tubes held in a 10 cm long support of one inch diameter nylon rod as shown in figure 3. The SMA con-

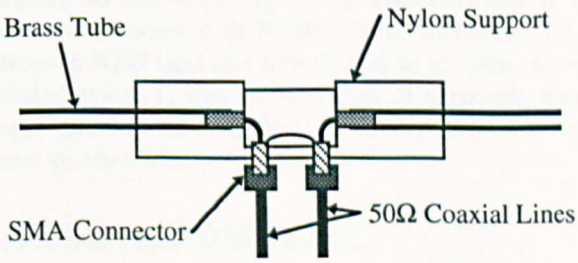


Figure 3: Dipole antenna support

nectors each join to equal length 50Ω coaxial lines which between them form a 100Ω balanced screened transmission line. The other ends of these coaxial lines are connected to the output ports of a 180° phase splitting device to act as a balun. Computer simulation using NEC was employed to predict the half-lengths shown in table 1 for a resonant dipole of 6.35 mm diameter at frequencies between 20 and 100 MHz.

The SMA connectors at the antenna feed allow open and short circuit loads to be connected

| Frequency MHz | Half Length mm |
|---|---|
| 20 | 3609.0 |
| 25 | 2882.5 |
| 30 | 2399.0 |
| 35 | 2053.5 |
| 40 | 1795.0 |
| 45 | 1593.5 |
| 50 | 1433.0 |
| 60 | 1192.0 |
| 70 | 1020.0 |
| 80 | 891.0 |
| 90 | 790.5 |
| 100 | 710.5 |

Table 1: Resonant half lengths for a 6.35 mm diameter cylindrical dipole antenna

at the ends of the transmission line in place of the antenna so that the HP8753 network analyser can be calibrated to measure antenna drive point impedance, $Z_M$, directly. $Z_M$ is not the ideal terminal impedance of the antenna, $Z_T$, because of parasitic effects associated with the nylon support [5]. These can be modelled in the form of a lumped capacitance in parallel with the antenna feed and so an experiment was devised to measure it so that it could be calibrated out using equation 7.

$$Z_M = Z_T \parallel \frac{1}{j\omega C} \tag{6}$$

and so

$$Z_T = \frac{Z_M}{1 - j\omega C Z_M} \tag{7}$$

The experiment was in the form of a short monopole antenna above a four foot square sheet of aluminium as shown in figure 4 and so by sliding a 5 cm nylon sleeve over the antenna the corresponding increase in capacitance could be measured with a bridge. This was found to be constant at 1.0 pF for antennas appreciably longer than the support and so for the case of a dipole antenna the parasitic capacitance was taken to be half of this value i.e. 0.5 pF.

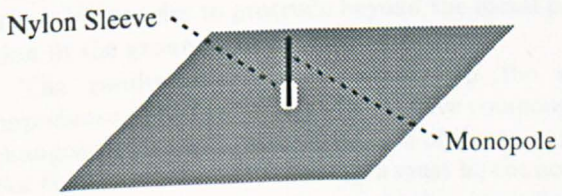


Figure 4: Experiment to measure parasitic C

## CALCULATION OF SYMMETRICAL AND ANTISYMMETRICAL IMPEDANCES

Many computer packages are available for the computation of the terminal impedances of coupled and isolated dipole antennas but for this work a method of moments based package called NEC was used was used because it was known to be fairly accurate and was already available at the University of York of availability. There are more accurate codes for impedance prediction and these may be able to give better results but work is continuing to evaluate the sensitivity of this measurement to impedance errors.

For input to the NEC computer code an antenna problem has to be expressed in the form of thin cylindrical wires and as such a cylindrical dipole is simply expressed as one wire. The wire is segmented into sections and the code calculates the current at the centre of each of these segments i.e increasing the number of segments increases the resolution and hence accuracy of the predicted current distribution. The maximum number of segments that a wire can be broken up into is determined by the need for each segment to be "thin" and a segment is usually taken to be "thin" if it has a length greater than about eight times its radius. The excitation for the antenna is specified in the form of a potential difference across the ends of the centre segment.

Another limitation to the number of segments is set by the availability of computational resources as the required CPU time rises with the square of the number of segments and memory requirements rise similarly. This means that there is an optimum number of segments for structures. For structures such as dipole antennas the current distribution is known to converge rapidly as segmentation is increased because it is formed from sinusoidal functions in NEC that are very similar to its own current distribution. It was decided that 21 segments was a reasonable number for both accuracy and CPU time and so that number was used.

## RESULTS AND DISCUSSION

Measurements of $Z_M$ were made at the frequencies shown in table 1 and they were corrected to $Z_T$ using equation 7. The resulting measurements are shown together with their corresponding symmetrical and antisymmetrical impedances at the end of this paper. Graphs are also presented of the resulting reflection coefficients. An infinite and perfectly reflecting ground plane will give a reflection coefficient of -1+j0 at all heights above it but the theoretical behaviour of a truncated one is more complicated. It would be expected that as the antenna is moved away from the truncated ground plane, the reflection coefficient would slowly change from that of the

truncated ground to that of the surrounding earth as the antenna became a lot further away than the truncated ground planes own dimensions. In addition to this any scattering effects would cause further height dependences in the reflection coefficient.

These results are preliminary and further analysis is currently under way to interpret them more fully but at this stage some conclusions can already be drawn from the graphs. For an ideal reflector the measured terminal impedance components should be the same as the antisymmetric predicted ones and any differences between them will give rise to $\Gamma \neq -1 + \mathrm{j}0$. The closest to ideal result appears to be at 90 MHz but towards the greater mast heights the antisymmetrical and measured components start to diverge. Most of the other results also appear to do this and it is thought to be due to an interaction between the antenna and the face of a building that is 3 m from the CISPR ellipse giving rise to a second image antenna. As the antenna becomes further above the ground plane the relative contribution of this image increases with respect to the one in the ground and so deviations in $\Gamma$ occur. At the lower mast heights the reflection coefficients appear to reach the asymptotic values shown in table 2

| Frequency | Reflection Coefficient, $\Gamma$ | | | |
|---|---|---|---|---|
| | $\Re\{\Gamma\}$ | $\Im\{\Gamma\}$ | $\lvert\Gamma\rvert$ | $\angle\Gamma$ |
| 20 | -0.69 | 0.19 | 0.72 | 164 |
| 25 | -0.81 | 0.12 | 0.83 | 172 |
| 30 | -0.88 | 0.09 | 0.90 | 174 |
| 35 | -0.93 | 0.11 | 0.93 | 176 |
| 40 | -0.92 | 0.12 | 0.96 | 175 |
| 45 | -0.93 | 0.12 | 0.95 | 173 |
| 50 | -0.95 | 0.11 | 0.98 | 173 |
| 60 | -0.96 | 0.12 | 0.98 | 173 |
| 70 | | | | |
| 80 | -0.97 | -0.12 | 0.98 | -173 |
| 90 | -1.00 | -0.04 | 1.00 | -178 |
| 100 | -0.96 | -0.08 | 0.96 | -179 |

Table 2: Zero height asymptote for reflection coefficients

This shows a reflection coefficient of falling magnitude below 60 MHz which is thought to be due to the antenna arms becoming sufficiently long at the lower frequencies to protrude beyond the metal portion of the ground plane.

The results are very dependent on the self impedance of the antenna as its reactive component changes very rapidly with the length of the antenna. For this reason the antenna length must be cut accurately to be the same as the one in the simulations. At 100 MHz a 1 mm error in the length of the antenna arms will give up to 1.4 ohms error in the self reactance and hence a bad result. It appears that the 45 MHz result is bad for this reason probably because the antenna arms were not inserted fully into the support.

## FUTURE WORK

These measurements will be used in a site attenuation model based on mutual impedances [6] in order to verify them by an improved correlation between measurement and theory than for the case for $\Gamma$ being assumed to be $-1 + j0$.

## REFERENCES


[1] American National Standards Institute *American National Standard Guide for Construction of Open Area Test Sites for Performing Radiated Emission Measurements* ANSI C63.7-1988, IEEE, New York, USA

[2] International Special Committee on Radio Interference *Limits and Methods of Measurement of Radio Interference Characteristics of Information Technology Equipment*, CISPR, Publication no. 22, Geneva, Switzerland

[3] G. J. Burke and A. J. Poggio *Numerical Electromagnetics Code (NEC) - Method of Moments* Lawrence Livermore Laboratory, Livermore, California, USA

[4] R. G. Fitzgerrel *Standard Linear Antennas, 30MHz to 1000MHz*, 5th IEE International Conference on EMC, 1986, University of York, England

[5] R. W. P. King *The Theory of Linear Antennas*, Harvard University Press, Cambridge, Massachusetts, USA, 1956

[6] T. Kawana and S. Miyajima *Theoretical investigations on Site Attenuation by means of Mutual Impedance Between Antennas*, 3rd International Technical Exhibition on EMC, Rotterdam, May 1-3, 1979, pp 83-88

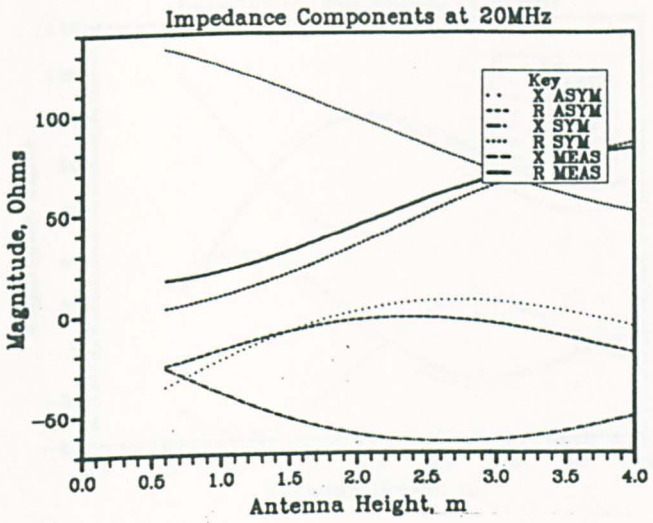
Impedance Components at 20MHz
Key
X ASYM
R ASYM
X SYM
R SYM
X MEAS
R MEAS
Magnitude, Ohms
Antenna Height, m

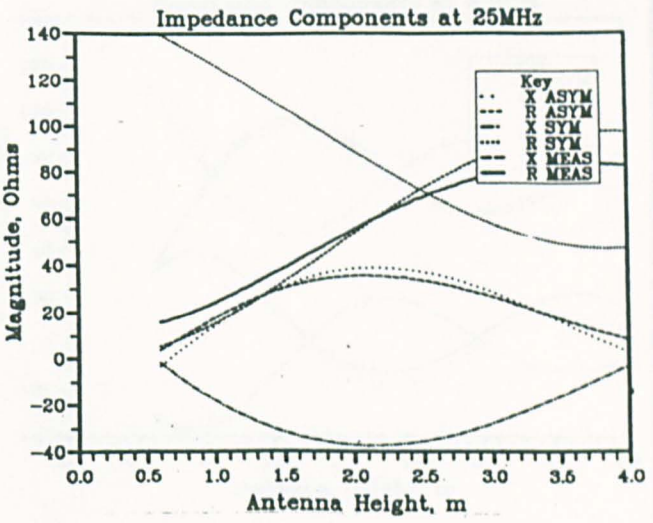
Impedance Components at 25MHz
Key
X ASYM
R ASYM
X SYM
R SYM
X MEAS
R MEAS
Magnitude, Ohms
Antenna Height, m

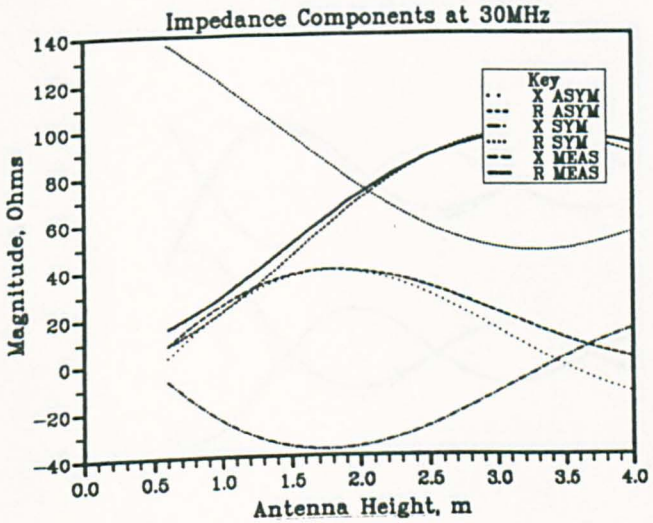
Impedance Components at 30MHz
Key
X ASYM
R ASYM
X SYM
R SYM
X MEAS
R MEAS
Magnitude, Ohms
Antenna Height, m

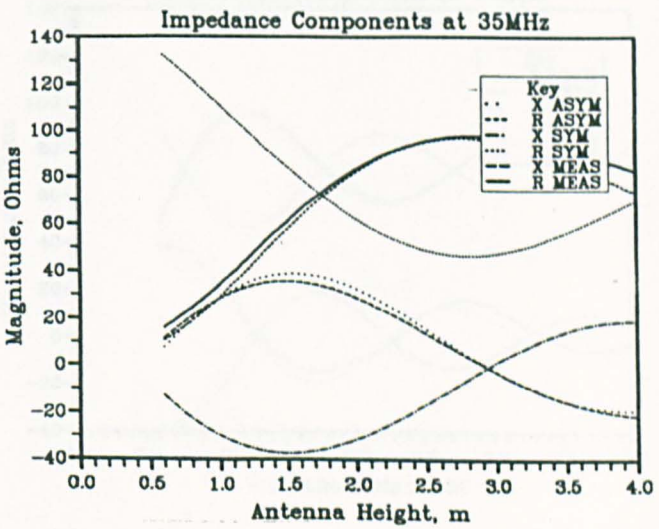
Impedance Components at 35MHz
Key
X ASYM
R ASYM
X SYM
R SYM
X MEAS
R MEAS
Magnitude, Ohms
Antenna Height, m

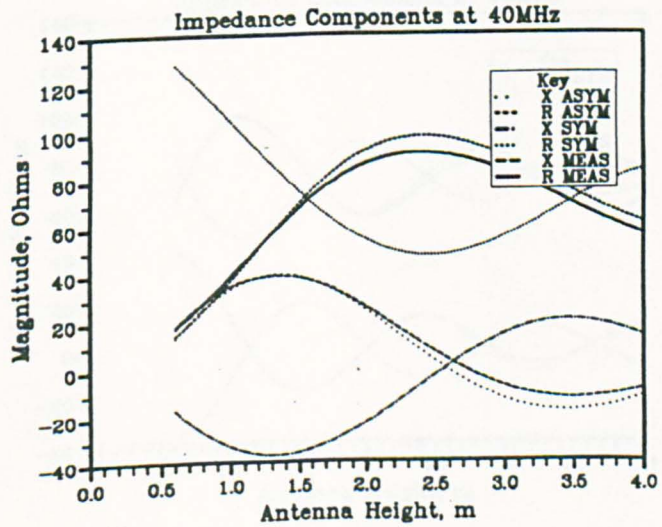
Impedance Components at 40MHz
Key
X ASYM
R ASYM
X SYM
R SYM
X MEAS
R MEAS
Magnitude, Ohms
Antenna Height, m

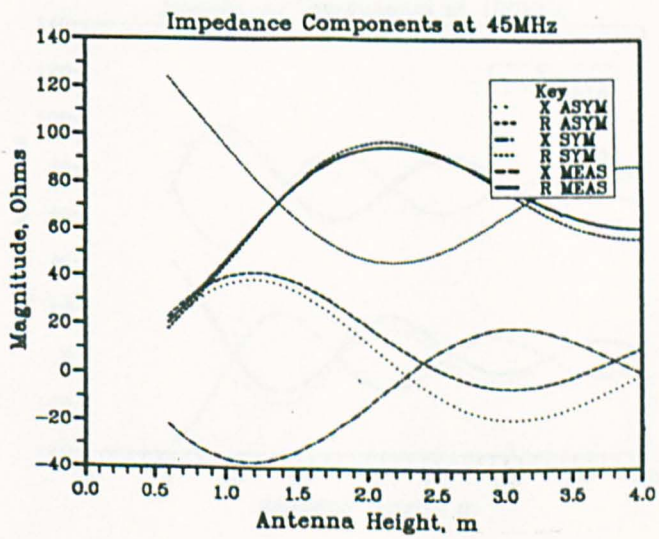
Impedance Components at 45MHz
Key
X ASYM
R ASYM
X SYM
R SYM
X MEAS
R MEAS
Magnitude, Ohms
Antenna Height, m

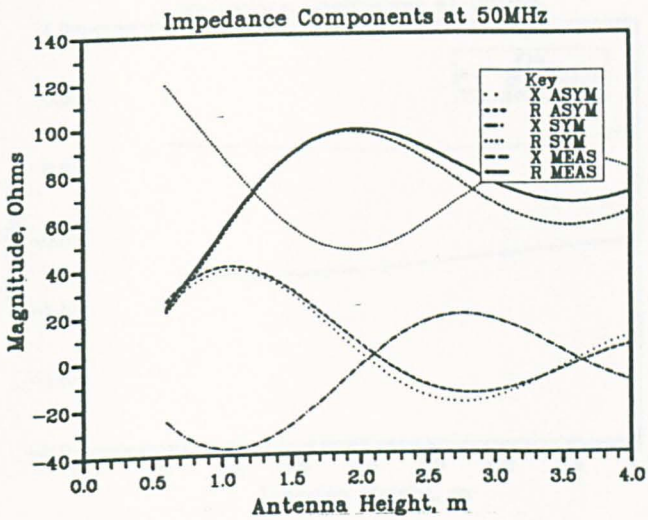
Impedance Components at 50MHz
Key
X ASYM
R ASYM
X SYM
R SYM
X MEAS
R MEAS
Magnitude, Ohms
Antenna Height, m

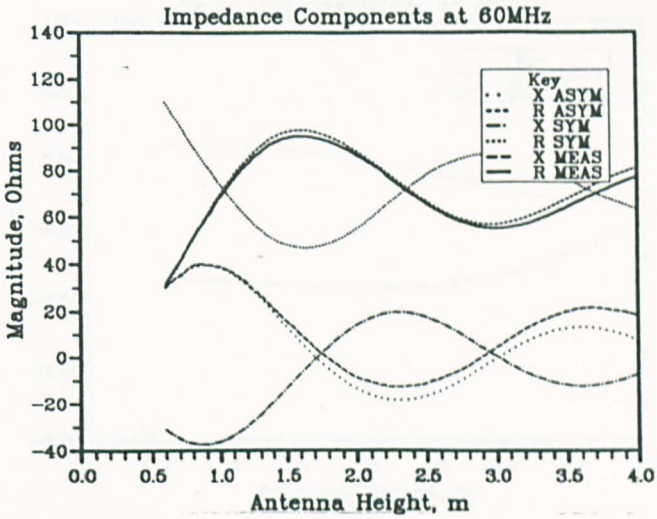
Impedance Components at 60MHz
Key
X ASYM
R ASYM
X SYM
R SYM
X MEAS
R MEAS
Magnitude, Ohms
Antenna Height, m

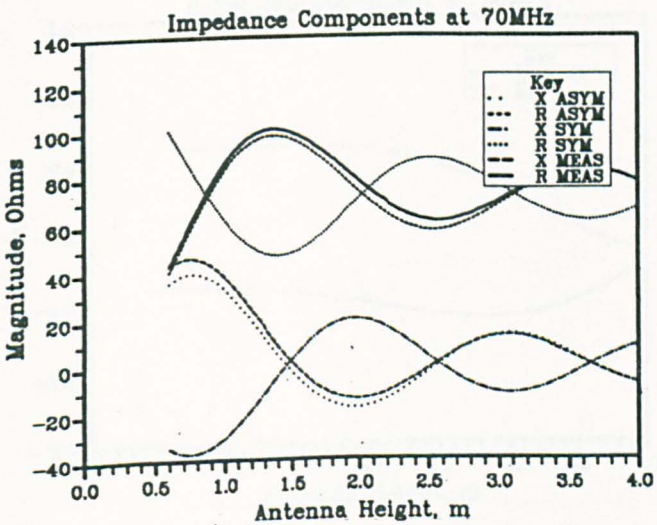
Impedance Components at 70MHz
Key
X ASYM
R ASYM
X SYM
R SYM
X MEAS
R MEAS
Magnitude, Ohms
Antenna Height, m

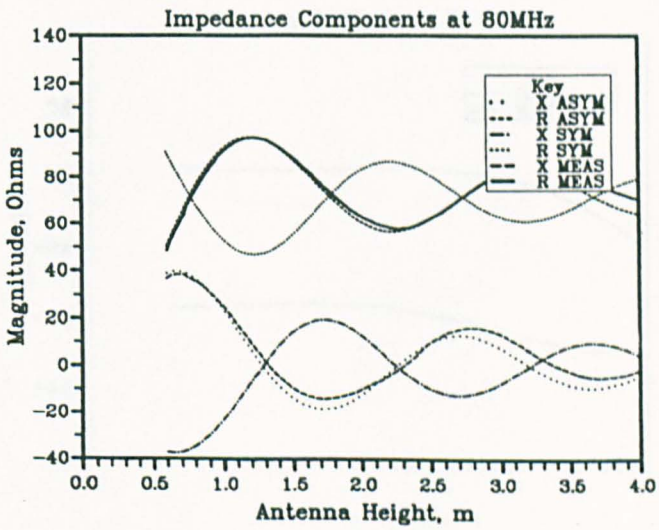
Impedance Components at 80MHz
Key
X ASYM
R ASYM
X SYM
R SYM
X MEAS
R MEAS
Magnitude, Ohms
Antenna Height, m

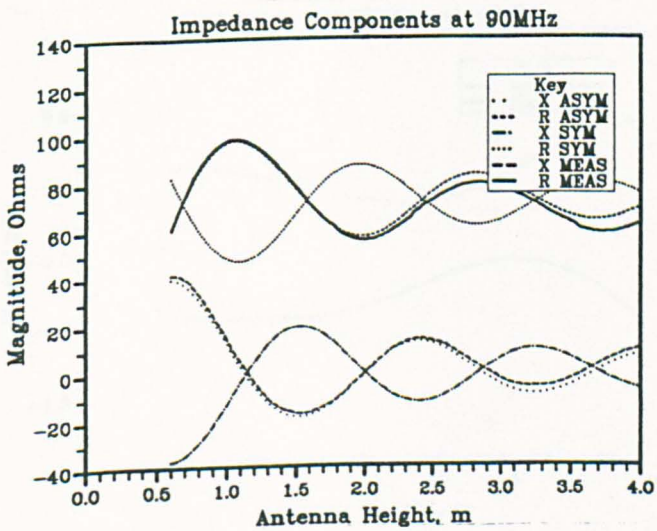
Impedance Components at 90MHz
Key
X ASYM
R ASYM
X SYM
R SYM
X MEAS
R MEAS
Magnitude, Ohms
Antenna Height, m

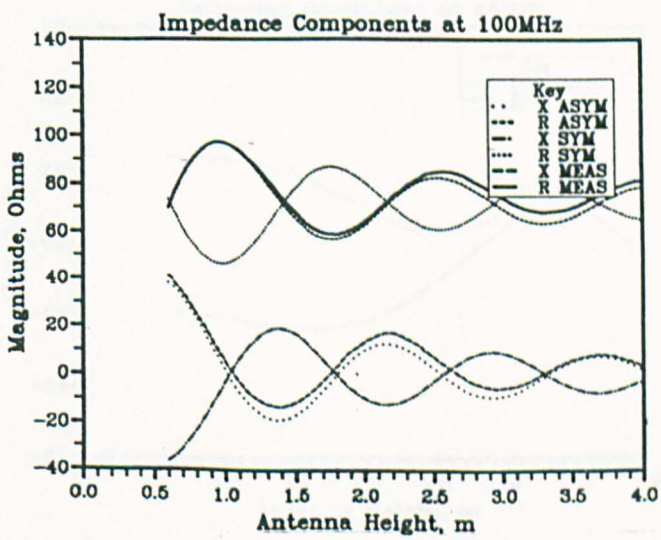
Impedance Components at 100MHz
Key
X ASYM
R ASYM
X SYM
R SYM
X MEAS
R MEAS
Magnitude, Ohms
Antenna Height, m

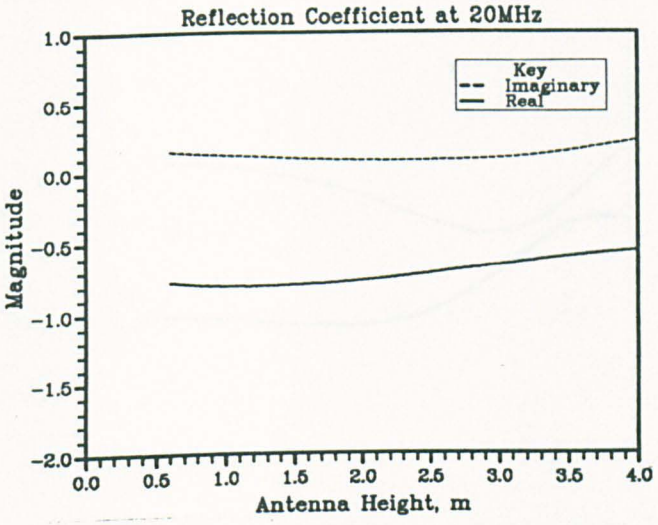
Reflection Coefficient at 20MHz
Key
Imaginary
Real
Magnitude
Antenna Height, m

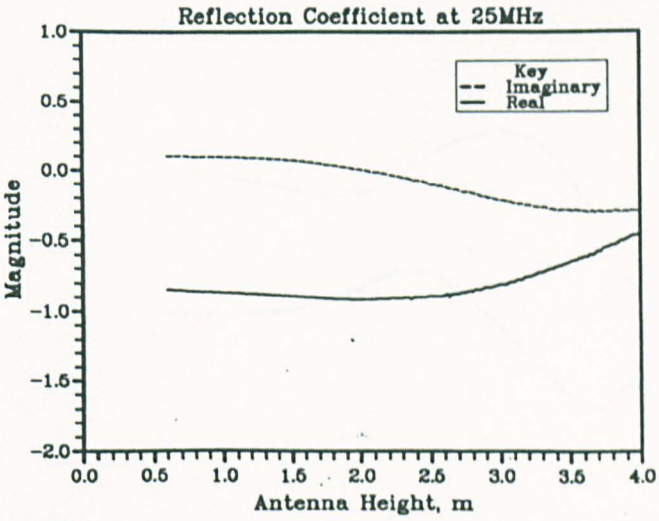
Reflection Coefficient at 25MHz
Key
Imaginary
Real
Magnitude
Antenna Height, m

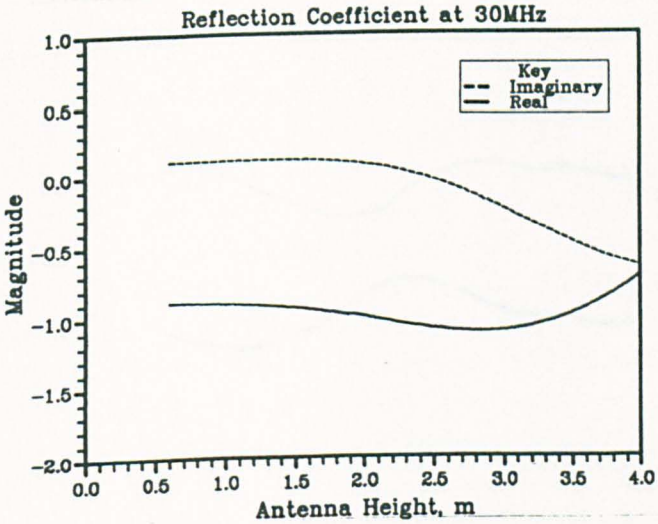
Reflection Coefficient at 30MHz
Key
Imaginary
Real
Magnitude
Antenna Height, m

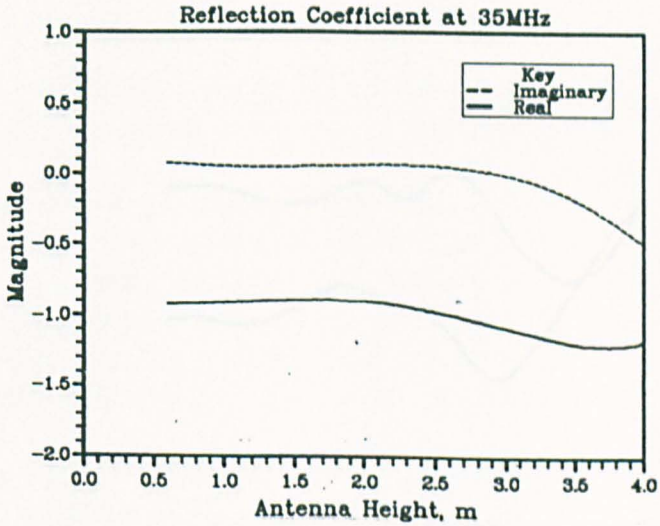
Reflection Coefficient at 35MHz
Key
Imaginary
Real
Magnitude
Antenna Height, m

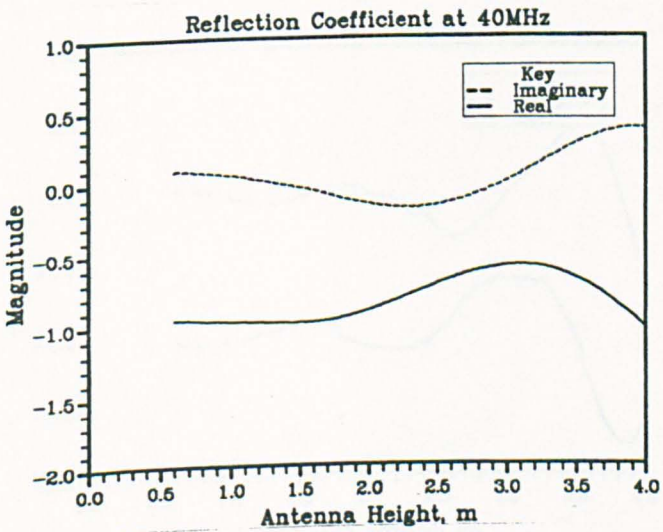
Reflection Coefficient at 40MHz
Key
Imaginary
Real
Magnitude
Antenna Height, m

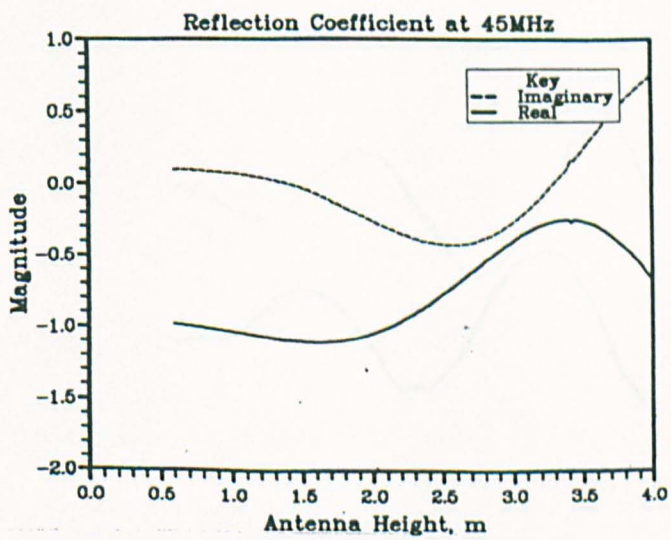
Reflection Coefficient at 45MHz
Key
Imaginary
Real
Magnitude
Antenna Height, m

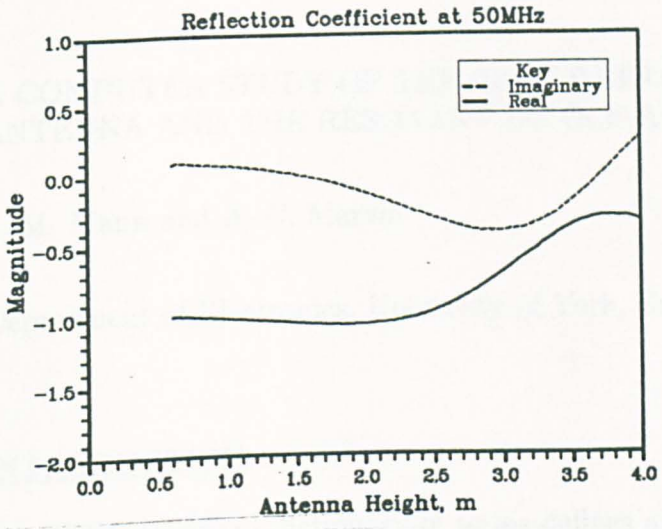
Reflection Coefficient at 50MHz
Key
Imaginary
Real
Magnitude
Antenna Height, m

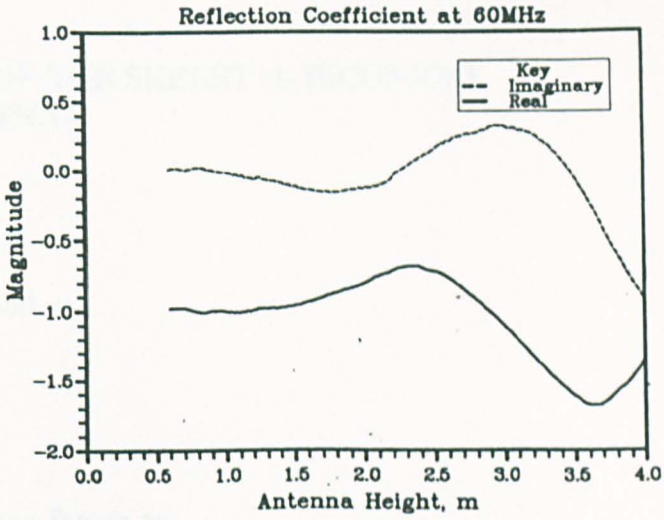
Reflection Coefficient at 60MHz
Key
Imaginary
Real
Magnitude
Antenna Height, m

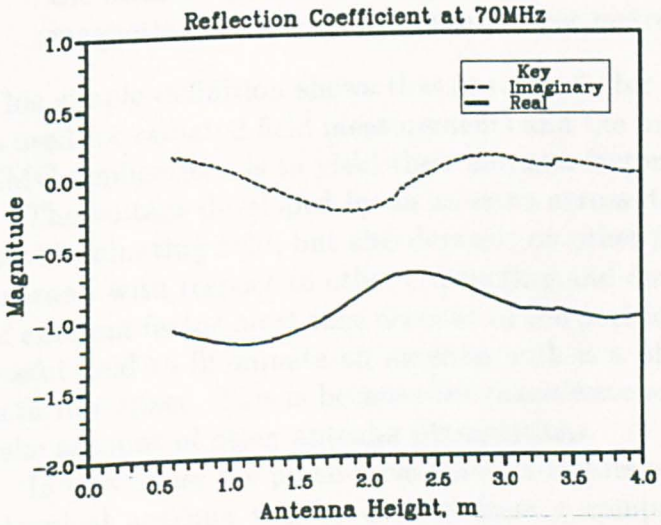
Reflection Coefficient at 70MHz
Key
Imaginary
Real
Magnitude
Antenna Height, m

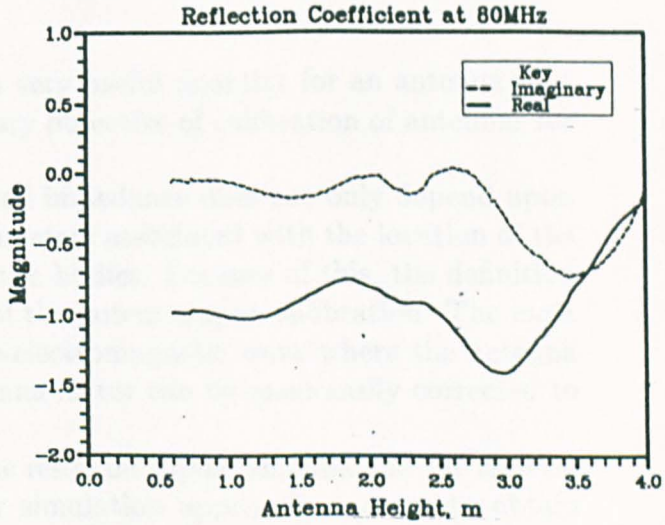
Reflection Coefficient at 80MHz
Key
Imaginary
Real
Magnitude
Antenna Height, m

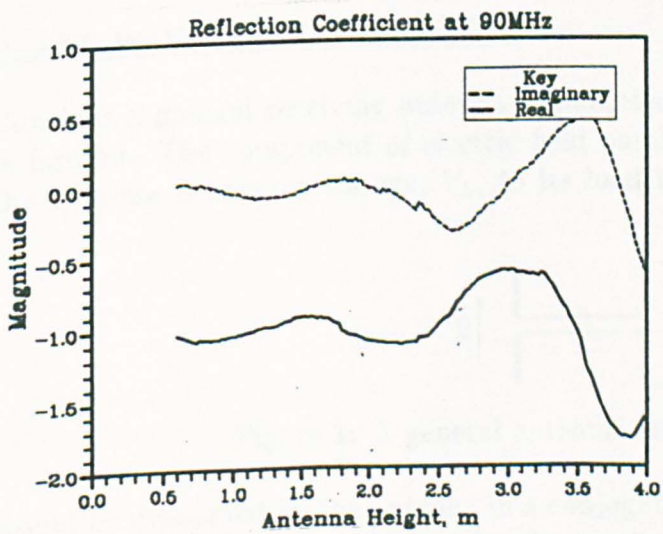
Reflection Coefficient at 90MHz
Key
Imaginary
Real
Magnitude
Antenna Height, m

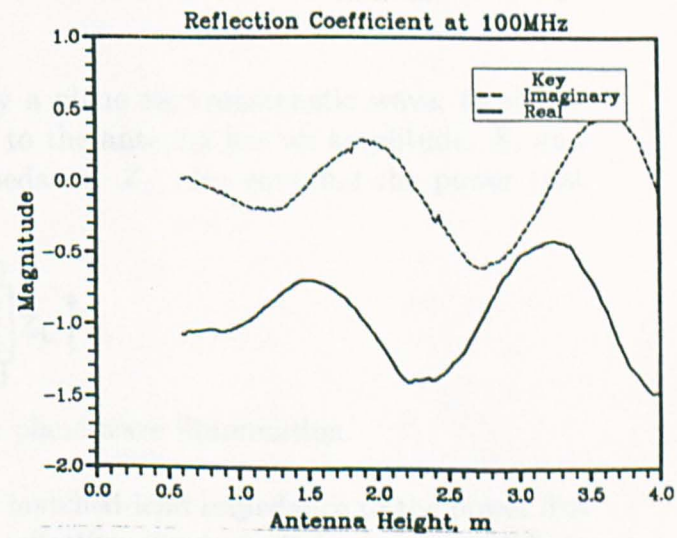
Reflection Coefficient at 100MHz
Key
Imaginary
Real
Magnitude
Antenna Height, m

# A COMPUTER STUDY OF THE CALIBRATION OF THE SKELETAL BICONICAL ANTENNA AND THE RESONANT DIPOLE ANTENNA

S. M. Mann and A. C. Marvin

Department of Electronics, University of York, England

## INTRODUCTION

The IEEE standard dictionary of terms defines antenna factor as:

> That factor which, when properly applied to the voltage at the input terminals of the measuring instrument, yields the electric field strength in volts per meter and the magnetic field strength in amperes per metre.

This simple definition shows that antenna factor is a very useful quantity for an antenna that is used for radiated field measurements and the primary objective of calibration of antennas for EMC applications is to yield their antenna factors.

The voltage developed by an antenna across its load impedance does not only depend upon the illuminating field, but also depends on other parameters associated with the location of the antenna with respect to other conducting and dielectric bodies. Because of this, the definition of antenna factor must take account of the position of the antenna upon calibration. The most useful field to illuminate an antenna with is a plane-electromagnetic wave where the antenna is in free space. This is because the plane-wave antenna factor can be most easily corrected to take account of other antenna illuminations.

In this paper the plane-wave antenna factors of the resonant dipole antenna and the skeletal biconical antenna will be derived from a computer simulation approach in order to obtain accurate values. The method for calibration of the skeletal biconical antenna will also show how the effects of a balun may be incorporated into a theoretical antenna factor.

## PLANE-WAVE ANTENNA FACTOR

Consider a general receiving antenna illuminated by a plane electromagnetic wave, as shown in figure 1. The component of electric field parallel to the antenna has an amplitude, $E$, and the antenna delivers a voltage, $V_L$, to its load impedance, $Z_L$. By equating the power that

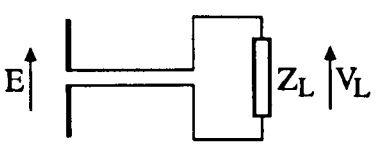


Figure 1: A general antenna under plane-wave illumination.

would be dissipated by the antenna in a conjugately matched load impedance to the power flux density illuminating it multiplied by the maximum effective aperture, it becomes possible to calculate the emf developed in the antenna. The antenna can then be modelled as an equivalent

Thévenin voltage source to calculate the voltage delivered to the actual load impedance. The expression for the antenna factor of a general receiving antenna is then,

$$AF_r = \left|\frac{E}{V_L}\right| \quad (1)$$

$$= \frac{1}{\lambda}\sqrt{\frac{\eta\pi}{G_r R_S}}\left|1+\frac{Z_S}{Z_L}\right| \quad (2)$$

$\eta$ is the characteristic impedance of free space, $G_r$ is the antenna gain and $Z_S$, the impedance of the antenna, has resistive and reactive components of $R_S$ and $X_S$ respectively. This equation shows that antenna factor is only a constant if both the terminal impedance and gain of an antenna do not vary significantly from their values when the antenna was initially calibrated.

It must be noted that the ohmic losses of the antenna structure have been neglected in the above analysis and so equation (2) is only valid for antennas whose radiation resistance dominates their ohmic losses. The skeletal biconical antenna and the resonant dipole antenna have sufficient electrical size to justify this assumption.

## THE RESONANT DIPOLE ANTENNA

If the current distribution on the resonant dipole antenna is assumed to be a sinusoidally distributed filament along the length of the antenna, and the antenna is assumed to be exactly half of a wavelength long, it can be shown that [1],

$$G_r = 1.64$$
$$R_s = 73\,\Omega$$

The antenna is at resonance so that its terminal impedance is purely resistive and $Z_S = R_S$. If the wavelength is replaced by $300/f_M$, where $f_M$ is the frequency in MHz, and the above values are substituted into equation (2), the theoretical antenna factor of a resonant dipole antenna driving into a $50\,\Omega$ load impedance is,

$$AF_r = \left(20\log_{10}(F_M) - 31.77\right)\text{dB} \quad (3)$$

The above formula is an approximation based upon the assumption of a sinusoidally distributed current on the antenna. In order to determine the antenna factor more accurately it is necessary to derive a more accurate representation of the current distribution on the antenna.

The method of moments is a numerical technique that can be used to solve the integral equations that determine the scattered fields from structures such as certain types of antennas. A software implementation of the method of moments, known as NEC [2], was used for this work. It contained a solution to an integral equation that was especially suited to determining the current distribution on structures that are made up of thin wires.

For input to NEC, the dipole antenna was represented by a single straight wire composed of 21 equal length segments. First, a voltage source was placed on the middle segment and NEC simulations were used to determine the length where the reactive component of the impedance of the antenna became equal to zero, i.e. the resonant length of the antenna. Next, the middle segment of the model was loaded with a $50\,\Omega$ resistance and the structure was illuminated with a $1\text{Vm}^{-1}$ plane-wave. The voltage that appeared across the load impedance was then substituted into equation (1) to calculate the the antenna factor of the resonant dipole.

The NEC computer code was used to simulate resonant dipole antennas and to determine their theoretical antenna factors with radii of 1, 2, 5 and 10 mm and at frequencies in the range of 30 MHz to 1 GHz. The results are shown in table 1, together with predictions from the simple theory of equation (2).

| Frequency MHz | Receiving Antenna Factor / dB | | | | |
|---|---|---|---|---|---|
| | Results from NEC | | | | Simple Theory |
| | 1 mm | 2 mm | 5 mm | 10 mm | |
| 30 | -2.232 | -2.232 | -2.232 | -2.230 | -2.228 |
| 50 | 2.205 | 2.205 | 2.206 | 2.208 | 2.209 |
| 80 | 6.287 | 6.288 | 6.289 | 6.292 | 6.292 |
| 120 | 9.809 | 9.810 | 9.813 | 9.817 | 9.814 |
| 180 | 13.332 | 13.333 | 13.336 | 13.344 | 13.335 |
| 250 | 16.186 | 16.187 | 16.192 | 16.204 | 16.189 |
| 500 | 22.208 | 22.212 | 22.224 | – | 22.209 |
| 800 | 26.293 | 26.298 | – | – | 26.292 |
| 1000 | 28.231 | 28.238 | – | – | 28.230 |

Table 1: Comparison of antenna factors for various radii of resonant dipole antennas calculated from NEC, and antenna factors calculated from the simple formula.

The results in table 1 show that the antenna factor of resonant dipole antennas varies by less than 0.01 dB as a function of the radius of the antenna. The approximate formula is very accurate and so can be used to determine the theoretical antenna factor of resonant dipole antennas for EMC applications.

## THE SKELETAL BICONICAL ANTENNA

It has been shown above that a simple formula can be used to determine the theoretical antenna factor of the resonant dipole antenna, but other antennas, such as the biconical antenna and the logarithmic-periodic antenna, cannot be analysed so easily. The skeletal form of the biconical antenna that is used for EMC applications is made from thin, wire elements and so is suitable for analysis using NEC.

A 205 segment model of the biconical antenna was developed for input to NEC and the simulation was run to obtain a Thévenin voltage source equivalent to the antenna under illumination by a $1 Vm^{-1}$ plane-wave. The dimensions of the cones of the antenna simulated are shown in figure 2. The wires labelled 1, 2, 4 and 5 were duplicated about the axis XX′ in

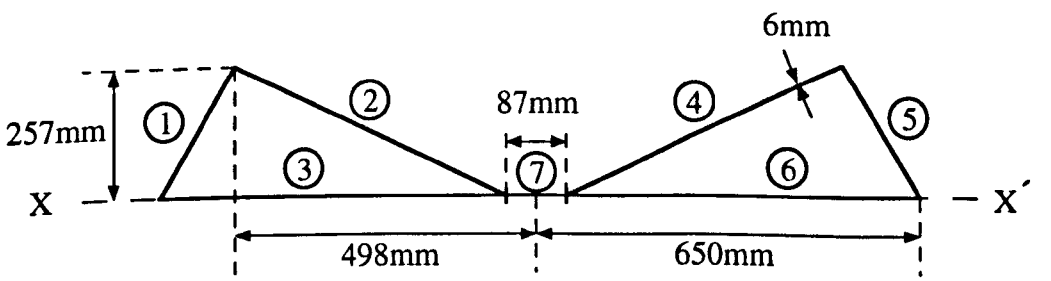


Figure 2: The skeletal biconical antenna.

increments of 60° to generate the six elbow shaped wires that formed each cone.

The source parameters of the antenna were obtained at frequency intervals of 5 MHz throughout its specified operating range of 30–300 MHz. This data revealed a sharply tuned resonant feature at 277 MHz and more data points were obtained to reveal its shape. Figure 3 shows the predicted components of self impedance.

From the Thévenin source model of the skeletal biconical antenna it was possible to calculate its theoretical antenna factors, driving directly into a 50 Ω load impedance, but these would not

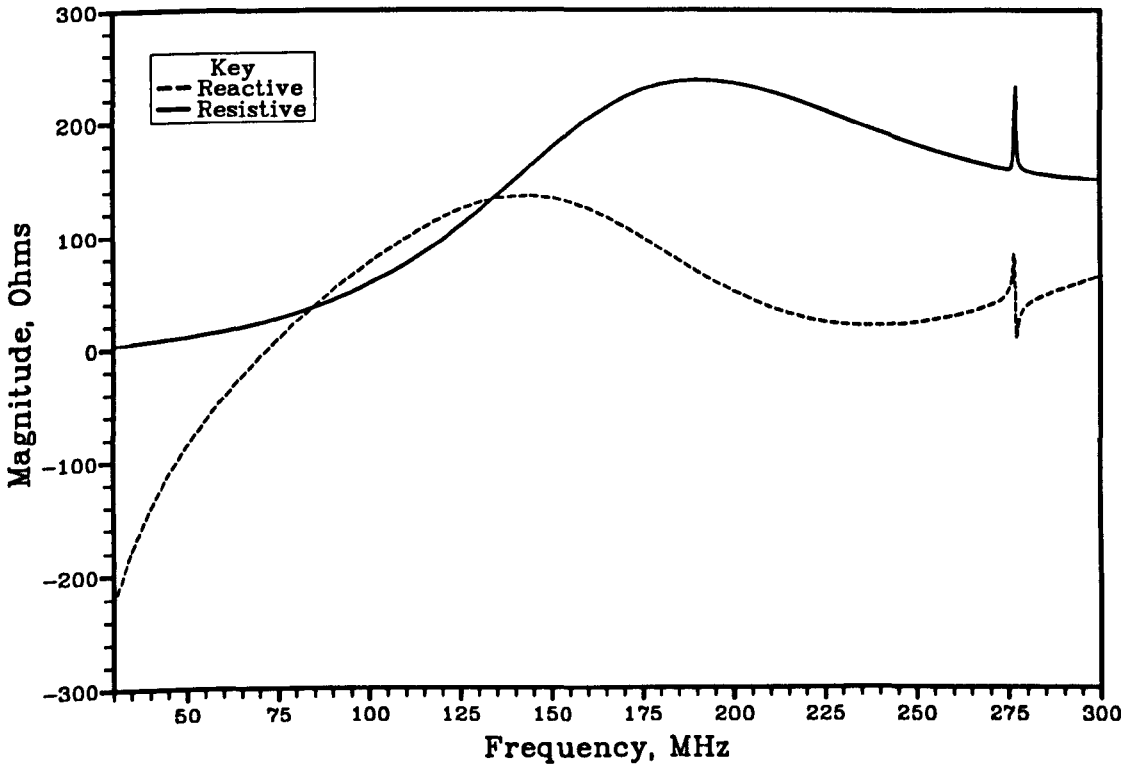


Figure 3: Predicted self impedance components for the skeletal biconical antenna.

have been very useful. The real biconical antenna was not connected directly to a 50 Ω load, but had a two-port network, consisting of the balun and a length of transmission line, between its radiating structure and its coaxial connector. In order to obtain theoretical antenna factors for comparison with those quoted by the manufacturer it was necessary to take account of this two-port connecting network.

## OPTIMAL BALUN DESIGN

The balun transformer of a biconical antenna should be such that the antenna is presented with a good impedance match throughout its operating frequency range to result in a low SWR. From the predicted components of self impedance it was possible to derive the SWR that would result with the biconical antenna connected to various load impedances. These results are shown in figure 4 for impedances of 50, 100, 150, 200 and 250 Ω .

A balun transformer having a 1 : 1 turns ratio would nominally present 50 Ω to the antenna, and so result in a high SWR throughout most of the frequency range. Increasing the impedance presented to the antenna reduces the SWR over most of the frequency range but produces degradation at the lower frequencies. An optimal impedance seems to be around 100 Ω and so the balun should have a turns ratio of $\sqrt{2}:1$.

## CHARACTERISATION OF THE BALUN

An experiment was devised to measure the scattering parameters of the two-port network between the coaxial connector of the real biconical antenna and its radiating structure. Figure 5 shows how the measurement was performed. Two jigs were built to allow N-type connectors to be mounted in place of the cones of the antenna. Pairs of open, short, and matched loads

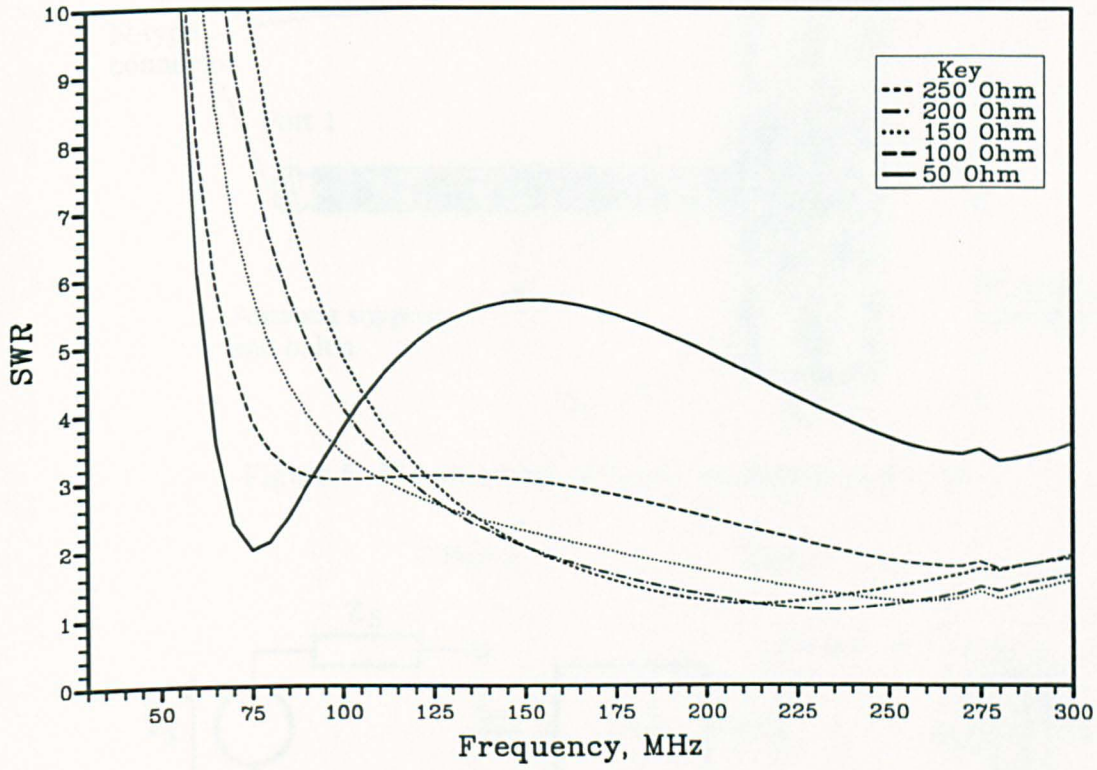


Figure 4: SWR of biconical antenna driving into various load impedances.

were then connected to establish reflection coefficients, $\Gamma_L$, of $+1$, $-1$ and 0 respectively at the connectors. The measured reflection coefficient at port 1 was then related to each of the load reflection coefficients by

$$\Gamma_{measured} = S_{11} + \frac{S_{12}S_{21}\Gamma_L}{1 - S_{22}\Gamma_L} \tag{4}$$

A phase correction corresponding to 89 mm in free space was then applied to each of the measured reflection coefficients at port 1 to move the reference plane to the position labelled port 2 in figure 5. They were then denoted by $\Gamma_{oc}$, $\Gamma_{sc}$ and $\Gamma_{mt}$.

Equation (4) gave expressions that were solved to obtain the scattering parameters of the antenna connecting network in terms of the corrected measured reflection coefficients at port 1.

$$\begin{aligned} S_{11} &= \Gamma_{mt} \\ S_{22} &= \frac{2\Gamma_{mt} - \Gamma_{sc} - \Gamma_{oc}}{\Gamma_{sc} - \Gamma_{oc}} \\ S_{12} &= \sqrt{\frac{2(\Gamma_{mt} - \Gamma_{oc})(\Gamma_{mt} - \Gamma_{sc})}{\Gamma_{sc} - \Gamma_{oc}}} \\ S_{21} &= S_{12} \text{ because of reciprocity.} \end{aligned}$$

It should be noted that, because of the way the S-parameters were measured, the characteristic impedance of port 2 was 100 Ω whereas that of port 1 was 50 Ω .

The resulting scattering parameters showed that the balun transformer had a turns ratio of 1 : 1 and 1–2 dB of loss.

## ANTENNA FACTOR INCORPORATING BALUN EFFECTS

The equivalent circuit of the antenna and balun is shown in figure 6. Port 1 of the balun is

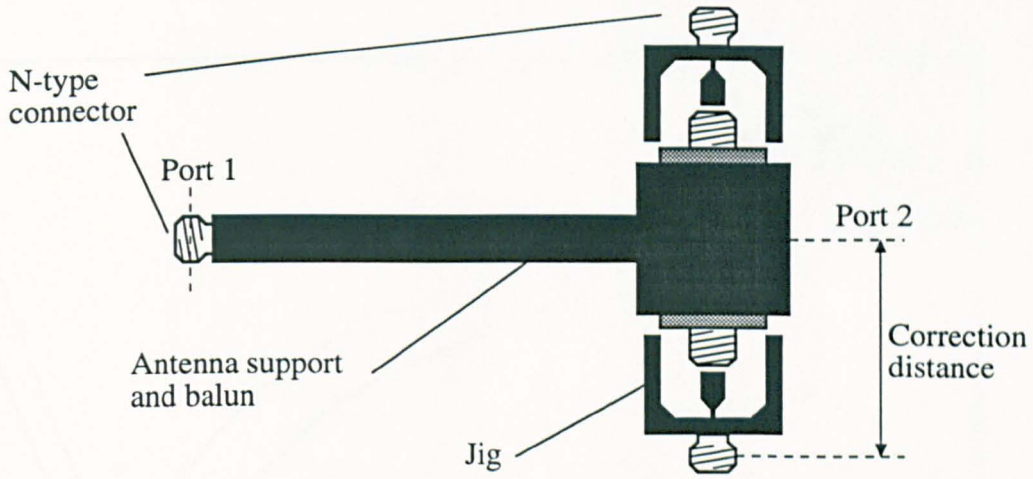


Figure 5: Measurement of balun scattering parameters.

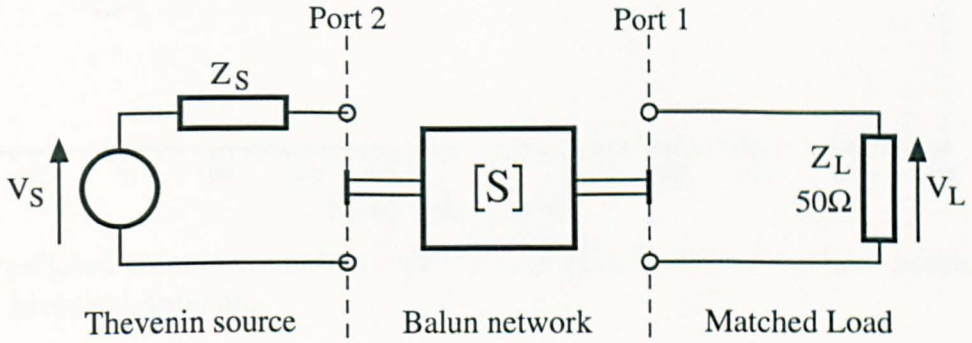


Figure 6: Equivalent circuit of antenna and balun.

terminated in a matched load so that the reflection coefficient at port 2 is simply $S_{22}$. From this, the input impedance of port 2 was determined and hence its input voltage was also found. Multiplying the input voltage by the voltage gain of the two-port network, enabled an expression for the load voltage, $V_L$, to be derived in terms of the equivalent source parameters of the antenna and the scattering parameters of the balun network. Substituting this into equation (1) then gave the antenna factor as

$$AF_r = 20\log_{10}\left|\frac{E}{V_S}\cdot\frac{Z_S(1-S_{22})+Z_{02}(1+S_{22})}{S_{12}\sqrt{Z_{01}Z_{02}}}\right| \tag{5}$$

The characteristic impedance of port 1, $Z_{01}$, was equal to 50 Ω , but the characteristic impedance of port 2, $Z_{02}$, was twice this because of the way the scattering parameters were measured. The illuminating electric field, $E$, was set to $1\,\mathrm{Vm}^{-1}$ in the NEC simulation and thus it was possible to evaluate equation (5).

Figure 7 shows that the predicted antenna factors are significantly different from those quoted by the manufacturer. Typical errors were around 2 dB but the worst error of 3.7 dB occurred at 75 MHz.

## DISCUSSION

The computer simulation approach to antenna calibration has several advantages over conventional measurement based methods for determining antenna factor.

1. Antennas can be illuminated with a plane-electromagnetic wave.

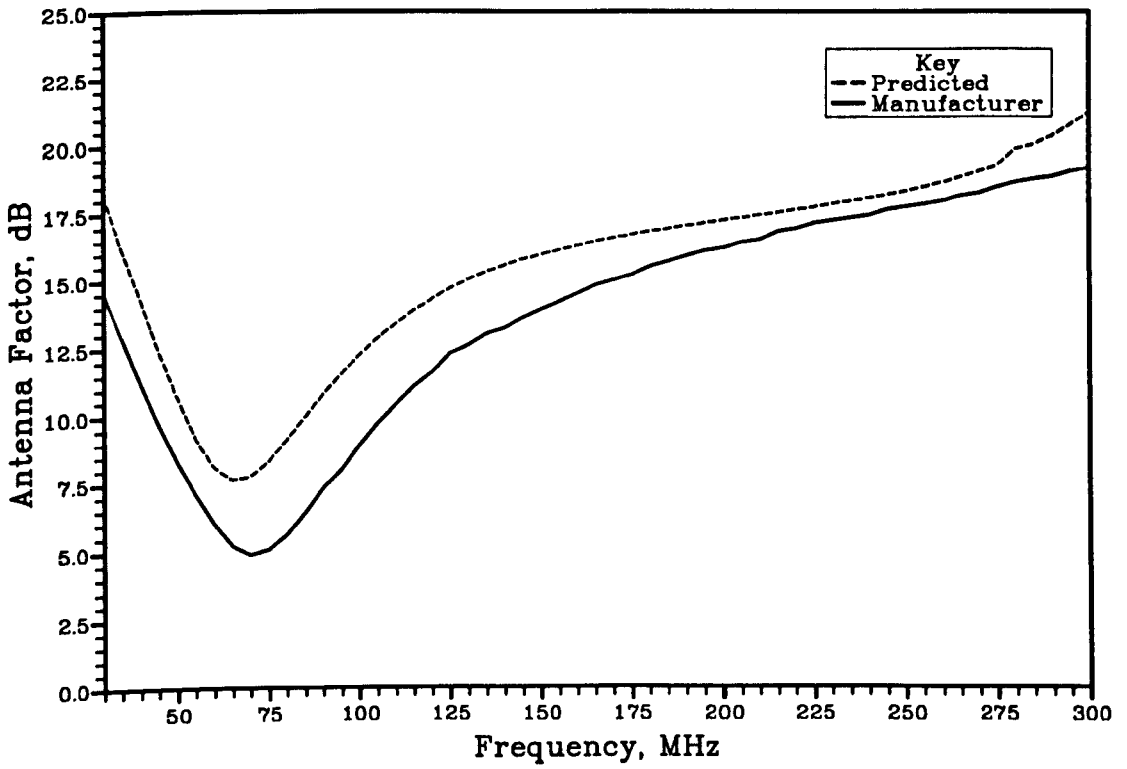


Figure 7: Predicted plane-wave antenna factors and manufacturers quoted antenna factors for the skeletal biconical antenna.

2. Interactions between antennas and ground planes may be eliminated.

3. Illumination by a single electromagnetic wave in the direction of boresight is possible.

In order to have confidence in any computer model, it must be validated against measurement, but measurements have errors associated with them. It is very difficult to measure plane-wave antenna factor accurately, but it is possible to measure the insertion loss between a pair of biconical antennas over a ground plane. This process is equivalent to a measurement of site attenuation as usually used for the validation of open-area test sites.

Measurements of insertion loss between biconical antennas were performed on the open-area test site at the University of York. This test site was not designed for antenna calibration and it was estimated that measurements made on it were subject to 1–2 dB of error. Agreement between measurement and the NEC simulation was typically to within 2 dB, but measurements must be performed on a better test site to further validate the NEC model.

In conclusion, it does appear that the manufacturers antenna factors for the skeletal biconical antenna are significantly in error, and the computer simulation represents a more accurate calibration.

## REFERENCES

[1] C. A. Balanis *Antenna Theory, Analysis and Design*, Wiley, New York, 1982, pp. 130-132.

[2] G. J. Burke and A. J. Poggio *Numerical Electromagnetics Code (NEC) - Method of Moments, User's Guide*, Lawrence Livermore National Laboratory, Report UICD-18834, January 1981.

# A STATISTICAL DESCRIPTION OF FIELD UNIFORMITY AND ITS EFFECT ON THE MEASURED IMMUNITY OF EQUIPMENT UNDER TEST

L. Dawson*, S. M. Mann# and A. C. Marvin#

#Department of Electronics, University of York, England
* York Electronics Centre, University of York, England

## INTRODUCTION

During radiated susceptibility measurements the equipment under test (EUT) is exposed to field strengths of up to several volts per metre. These high field levels cannot be radiated in unbounded test environments, such as open-area test sites, and so a variety of screened room and absorber lined chamber environments are used instead. The screened rooms form resonant cavities and absorber material is not very efficient, in the frequency range from 30-200 MHz, so that the field that illuminates EUTs in these environments is far from uniform. The objective of this project was to measure the field uniformity within typical radiated susceptibility testing environments and to assess its effect on the repeatability of measurements performed within them.

## EXPERIMENTAL METHOD

The principle of reciprocity was applied to the process of field measurement so that a spherical dipole radiating source (SDSE) could be allowed to radiate at a measurement point, and the normal transmitting antenna be allowed to receive the field from it. Figure 1 shows this reciprocal field measurement process. A reference measurement was performed by connecting

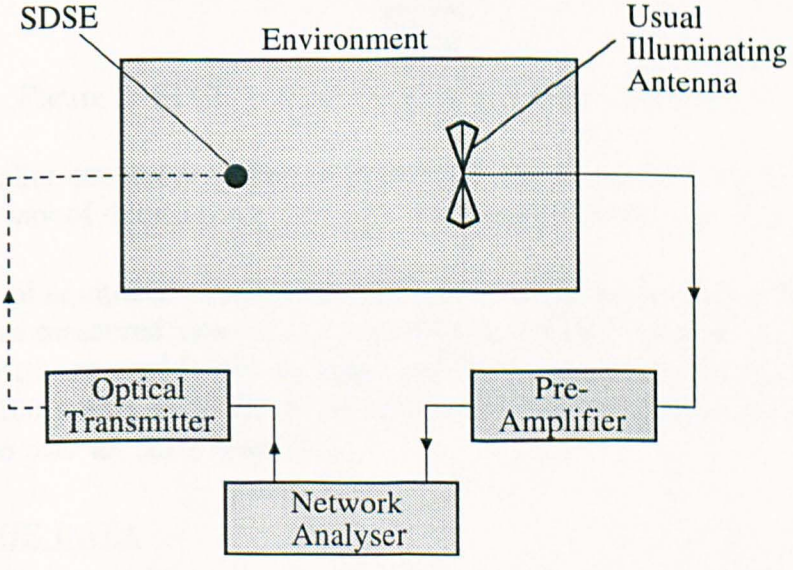


Figure 1: Reciprocal field measurement with the SDSE.

the cables together at points A and B in the figure and so the insertion gain of the SDSE and the usual illumination source in the measurement environment was found.

This work was concerned with the determination of the field uniformity, rather than the absolute field levels, within the measurement environments and so no attempt was made to convert the insertion gain values into effective field strengths at the SDSE. Instead, the insertion gain was assumed to be proportional to the effective field strength at the SDSE, and all the mathematical analysis was conducted on these values.

The frequency range of interest was 30-230 MHz and field measurements were made at 1 MHz intervals throughout this range. It was found that that this spacing was only just close enough to follow peaks in the response of the more resonant environments, but perfectly adequate for damped and well behaved environments. Use of more data points would have created data storage problems with the computational resources available.

## THE VOLUME UNDER TEST

A standard size of volume under test (VUT) was defined over which the field uniformity measurements were made in each measurement environment. This volume was a cube of 50 cm side length in order to have similar dimensions to the volume occupied by a typical EUT. The SDSE was placed at 343 points located on a 7x7x7 grid within the VUT, and the insertion gain was measured throughout the frequency range at each point. The diameter of the SDSE was 10 cm and so the measurement positions overlapped as shown in fig. 2. This particular array of data

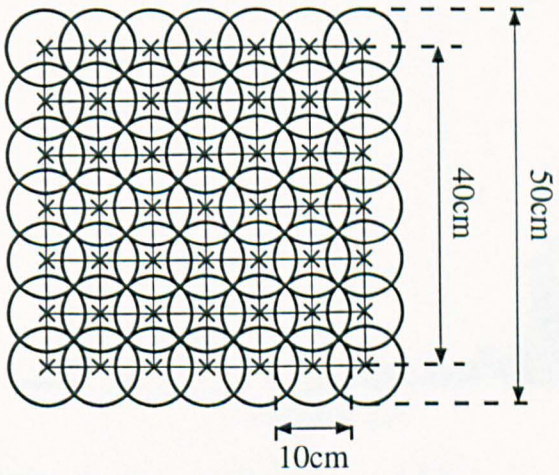


Figure 2: SDSE positions within one layer of the VUT.

points allowed smaller concentric cubes of 3x3x3 and 5x5x5 points within the volume to also be examined as a way of determining how field uniformity varied with the overall dimensions of the VUT.

A dummy item of equipment under test (DEUT) was placed at the centre of the VUT and field uniformity was measured close to it around three orthogonal rings as shown in fig. 3. 40 measurement points were used in the xy-plane and 30 points were used in each of the xz- and yz-planes, giving 100 points in total. Field uniformity was measured in each of these planes separately and also over all three together.

## ANALYSIS OF THE DATA

The the data array of insertion gains for each environment was very large, comprising of 201 frequency points at 343 positions in the empty VUT and data from 100 positions around the DEUT. A statistical method was needed to extract meaningful information from this data so that the field uniformity in each of the environments could be compared.

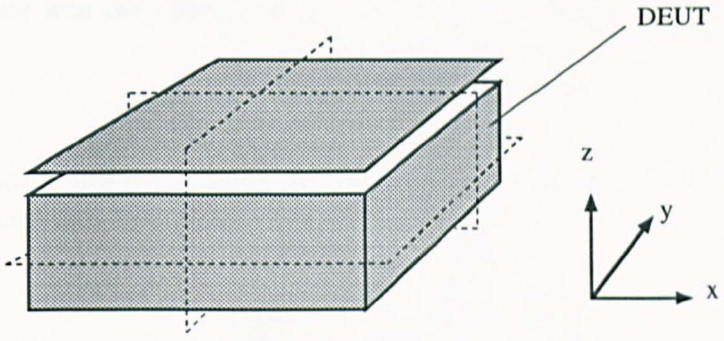


Figure 3: SDSE positions around the DEUT.

The first quantity of interest was the maximum variation of the fields over the empty VUT, and this was obtained by subtracting the minimum insertion gain from the maximum insertion gain present at each measurement frequency within the 7x7x7 array.

A typical histogram of field values within one of the environments, at a single frequency, is shown in figure 4. The majority of the field values are close together but that a few are

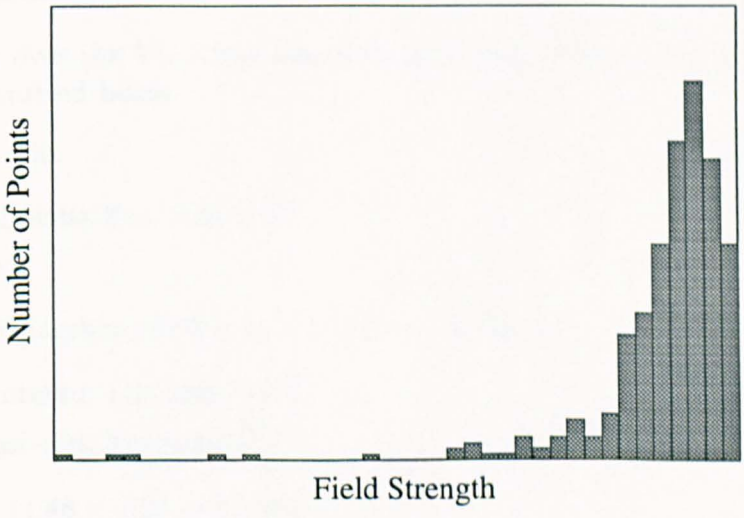


Figure 4: Typical Histogram of Field Values.

significantly different to the others. For this reason the values of absolute field variation were overly pessimistic and what was needed was a quantity that could be used to represent more typical field uniformity over the whole volume. The standard deviation of the field values was determined to be suitable.

Several similar histograms to figure 4 were plotted and it was found that there was no general shape to them and they could not be related to any of the classical probability distributions. This was because the fields at the measurement points were not statistically independent, but were all related to each other by the solutions of Maxwell's equations for that particular environment. For this reason the standard deviation of the fields could not be used to assign exact confidence levels that the fields within any of the environments would be below a particular level.

Before the standard deviation or the average value of the field within the volume could be calculated, the data had to be transformed to a linear magnitude scale. This was performed by dividing each insertion gain value by 20 and taking its base 10 inverse-logarithm. The average

field at each frequency was then given by,

$$\overline{x} = \frac{1}{N}\sum_{i=1}^{N} x_i \tag{1}$$

where $N$ was the total number of points i.e. $N = 343$ for the 7x7x7 VUT array. The standard deviation of the $N$ insertion loss values was then given by,

$$\sigma = \sqrt{\frac{1}{N-1}\left[\left(\sum_{i=1}^{N} x_i^2\right) - N\overline{x}^2\right]} \tag{2}$$

This value of standard deviation was then divided by the average field over the VUT and converted back to decibels to obtain a quantity known as normalised standard deviation (NSD). NSD was used, together with absolute field bounds, to specify the uniformity of the field in each of the environments.

The above statistical treatment was used to find absolute field bounds and standard deviations for the fields around the DEUT.

## THE ENVIRONMENTS

The field uniformity over the VUT was measured in eleven different environments whose characteristics are summarised below.

1. Open-area test site.
   (a) biconical antenna 3 m from VUT.
   (b) stripline cell.
2. Semi-anechoic Chamber (8.60 × 4.64 × 3.60) m (L,W,H)
   (a) biconical antenna 1 m from VUT.
   (b) biconical antenna 3 m from VUT.
3. Screened room (4.48 × 2.24 × 2.24) m.
   (a) illuminated with biconical antenna.
      i. undamped.
      ii. damped with carbon loaded foam.
      iii. damped with ferrite tiles.
   (b) illuminated with stripline cell.
      i. undamped.
      ii. damped with carbon loaded foam.
4. Screened room (6.35 × 3.05 × 3.05) m. Biconical antenna.
   (a) undamped.
   (b) damped with carbon loaded foam.

The smaller screened room and open-area test site were at the University of York and the larger screened room and anechoic chamber were provided by RFI Investigations Limited. It is not possible to give precise diagrams showing the layout of all of the above environments but they will be described in the presentation.

## RESULTS

The results for the field uniformity over the cubic volume for frequencies between 30 and 200 MHz are summarised in table 1.

| Environment | DIF dB | LIM dB | NSD dBav |
|---|---|---|---|
| 1a | 2 | 5 (9) | -19 (-13) |
| 1b | 0.5 | 5 (7) | -22 (-18) |
| 2a | 1 | 6 (15) | -18 (-7) |
| 2b | 3 | 6 (13) | -14 (-6) |
| 3ai | 2 (31) | 8 (56) | -14 (-1) |
| 3aii | 2 (5) | 13 (62) | -14 (-3) |
| 3aiii | 2 (14) | 11 (46) | -14 (-3) |
| 3bi | 2 (13) | 11 (56) | -18 (-3) |
| 3bii | 2 (6) | 10 (36) | -18 (-6) |
| 4a | 2 (15) | 10 (53) | -17 (-2) |
| 4b | 1 (18) | 13 (46) | -13 (-4) |

Table 1: Results of measured field uniformity over the empty VUT.

The environments are denoted by their labels from the listing in the previous section and the three righthand columns give different parameters that were used to describe the field uniformity. DIF is the difference between the average field calculated over the total volume and the average field calculated over the two smaller concentric cubic volumes within it. LIM is the absolute field variation over the total volume, i.e. the difference between the maximum and minimum field within it, and NSD is the standard deviation of the fields over the volume normalised to the mean.

The resonances of the screened room environments caused field uniformity within them to be much worse at their resonant frequencies. It was difficult to define typical field uniformity values within these environments across the whole frequency range, hence a typical value between resonances is given in table 1 together with a worst case figure, at resonance, in brackets.

The results from the larger screened room indicated a slightly smaller absolute variation of its fields than those in the smaller room, but that its fields were subject to high uncertainty over a much larger proportion of the frequency range. This was due to its larger volume resulting in a greater mode density and lower cutoff frequencies for all of the propagating modes.

The results for the stripline cell in the non-resonant environments showed that the field within it was much more uniform than that field generated by the biconical antenna. This advantage over the biconical antenna was also clear in the small screened room damped with carbon loaded foam.

Both the ferrite tile and carbon loaded foam damping techniques had a smaller effect on the fields with the biconical antenna in the screened rooms than was expected. The reasons for this have to be investigated further and better damping techniques need to be developed. The damping with carbon loaded foam caused a very noticeable improvement in the field uniformity inside the stripline cell in the small screened room. This shows that the technique of building a wall of absorber around the cell is very effective.

The results for the field uniformity measured along the three concentric rings around the DEUT showed greater field variations and worse normalised standard deviations than did the corresponding measurements on the empty VUT. This was because the SDSE was closely coupled to the DEUT, as would any other field probe be. The field components parallel to the conducting surfaces of the DEUT were effectively shorted out close to it so that when the

SDSE was moved up the sides of the DEUT parallel to the z-axis (figure 3) very low fields were measured. This gave rise to apparently greater field variation in the xz- and yz-planes than in the xy-plane.

## CONCLUSIONS

The results of this work show that, even in nominally well behaved environments such as semi anechoic chambers, the field uniformity levels, and hence the repeatability of radiated susceptibility measurements may not be as good as expected. Semi-anechoic chambers are the best environments to use but, when they are not available, similar uniformity levels can be obtained with stripline cells in damped screened rooms.

It appears that lightly damping screened rooms only creates a modest improvement in field uniformity and so must be approached with caution. Also the use of large screened rooms is not a good idea because the increased number of propagating modes inside them causes their fields to be less uniform than those in smaller rooms.

There is also a fundamental misconception associated with measuring the field illuminating an EUT close to it in the measurement environment. The measured field in this case is not the illuminating field but is the sum of the illuminating and the scattered fields from the EUT and so will inevitably be less uniform. For this reason it is the average field over the volume occupied by the EUT before it is placed into the environment that should be measured and used as the illuminating field.

# SOME MEASUREMENTS OF FIELD UNIFORMITY WITHIN COMMONLY USED ENVIRONMENTS FOR RADIATED SUSCEPTIBILITY MEASUREMENTS

L. Dawson*, S. M. Mann# and A. C. Marvin#

#Department of Electronics, University of York, England
*York Electronics Centre, University of York, England

## ABSTRACT

Measurements of field strength are made in a 7x7x7 array of positions within a 50 cm cubic volume, in eleven environments that are commonly used for radiated susceptibility testing. The average value, absolute variation and standard deviation of the fields are analysed to deduce the field uniformity levels in each environment for the frequency range of 30-230 MHz. A simulated item of equipment under test is also used to assess the suitability of each environment for making repeatable measurements. It is concluded that semi-anechoic chambers offer the best environment in which to perform susceptibility measurements, but that stripline cells used in small damped screened rooms can offer a similar level of repeatability. A criterion, that the standard deviation of the fields over the volume occupied by the equipment under test should be at least 13 dB down from the mean field, is proposed for a general environment to provide repeatable measurements.

## INTRODUCTION

Specifications for radiated immunity testing are written with the implicit assumption that the threat field to which an equipment under test (EUT) is exposed to during normal operation is a uniform plane wave. The test procedures attempt to replicate this situation so that the tolerance of an EUT to plane wave illumination may be measured at any frequency. The uniformity of the field illuminating the EUT in a radiated susceptibility environment is verified by measurement in one of two ways: by measuring the field over the empty volume that would be occupied by the EUT, or by measuring the field around the EUT during the test.

The field levels to which EUTs are exposed during immunity measurements are very high and so cannot be radiated in an unbounded environment, such as an open-area test site. For this reason, testing is usually carried out in a variety of anechoic chamber and screened room environments where the energy can be contained. Screened room environments are resonant cavities and so the field that illuminates the EUT in these environments bears little resemblance to a plane wave; also the absorber material lining the anechoic chambers is not very effective towards the lower end of the 30-200 MHz frequency range over which measurements are carried out.

Damping materials such as ferrite tiles and carbon loaded foam are often used in screened room environments to increase the field uniformity, but it is known that the fields within these environments are far from uniform even with damping. This paper reports the results from the first part of a three stage investigation to measure the field uniformity in different environments, derive mathematical models for the environments and develop test procedures that will give the best uniformity levels achievable in each of the environments.

## INSTRUMENTATION

Instrumentation was developed to measure the fields present in each of the environments and to determine the effect of non-uniform illumination on EUTs. This instrumentation had to be electrically self-contained, with only optical fibre connections to the outside world, because any cabling would disturb the fields present in an uncontrolled way. Two items of specialist equipment were developed and are briefly described here.

The first item was an electrically small radiating source, known as the spherical dipole swept emitter (SDSE). It was used for the measurements of field uniformity and consisted of an optical demodulator, an rf amplifier and their power supply contained within a 10 cm diameter spherical shell. This shell was formed from two brass hemispheres separated by an insulating washer so that the rf signal on the fibre could be applied as a voltage across the two halves. The resulting structure was electrically small over the frequency range used and so had the radiating properties of an infinitesimal electric dipole.

A dummy item of equipment under test (DEUT) was also needed to act as a victim for the illuminating fields so that their effect on a real EUT could be assessed. This was in the form of a 48.4 cm square and 20.8 cm deep brass box as shown in figure 1. The DEUT had several slots and gaps that could be opened on its structure to enable it to simulate different types of victim circuits although only one of these modes was used. The DEUT was used with its top plate raised 4 cm above the rest of its body

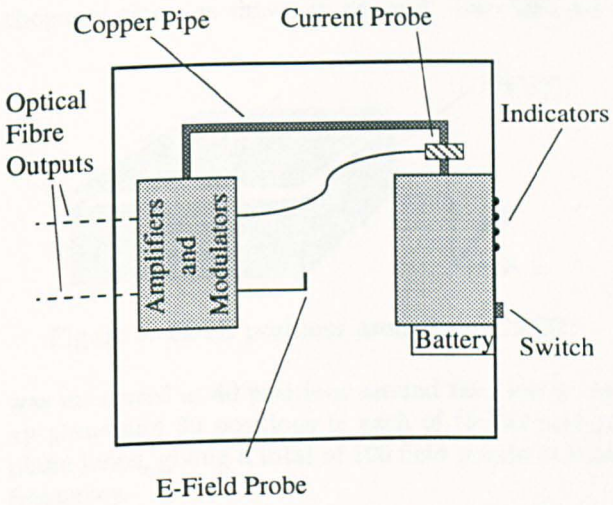


Figure 1: The dummy equipment under test (DEUT).

by nylon struts to allow the fields to penetrate it. Inside the DEUT were sensors for internal electric field and current induced on a copper pipe designed to simulate a cabling harness. The signals from these two sensors were used to assess the affect that the illuminating fields had on the DEUT.

## EXPERIMENTAL METHOD

In order to determine the overall field uniformity, it was necessary to measure the field at many points within a radiated susceptibility testing environment. This required the use of a small field probe that would interact minimally with the fields to be measured, and could be swept in frequency, but no such device was available. By assuming that the coupling between the illuminating source and the field probe was reciprocal it became possible to use the SDSE to generate the field at the measurement point and receive it with the usual radiating antenna as shown in figure 2.

Points A and B in figure 2 were connected directly together provide a reference measurement so that the insertion gain between points A and B could be measured. This was a negative value in decibels and was used to represent the measured field. No attempt was made to convert the insertion gain to actual field strength because it was the uniformity of the fields over the volume that was being analysed rather than the actual field levels.

The frequency range of interest was 30 MHz to 230 MHz and field measurements were made at 1 MHz intervals within this range. It was found that this spacing was only just close enough to follow peaks in the response of the more resonant environments but perfectly adequate for damped and well behaved environments. Use of more data points would have created data storage problems with the

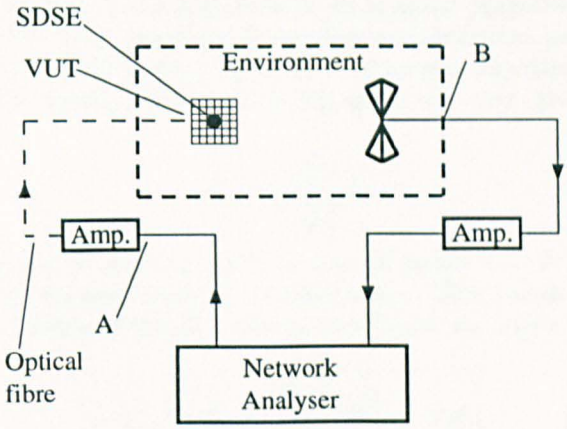


Figure 2: Reciprocal field measurement with the SDSE.

computational resources available.

A standard size of volume under test (VUT) was defined over which the field uniformity measurements were performed within each measurement environment. This volume was a cube of 50 cm side length in order to have similar dimensions to the volume occupied by a typical item of equipment under test. The SDSE was placed at 343 points, each located on a 7x7x7 grid within the VUT, and the insertion gain was measured throughout the frequency range at each point. The diameter of the SDSE was 10 cm and so the measurement points overlapped as shown in figure 3. This particular array of data points al-

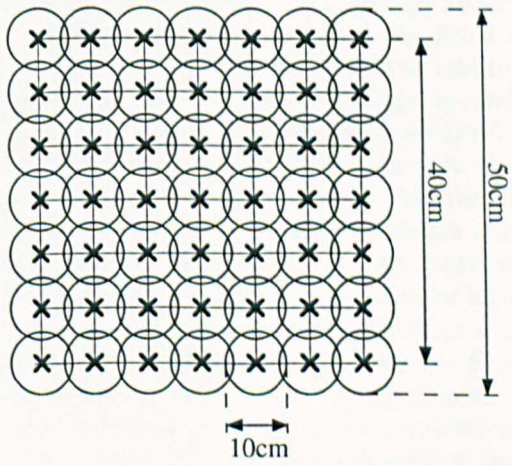


Figure 3: SDSE positions within one layer of VUT.

lowed smaller concentric cubes of 3x3x3 and 5x5x5 points within the volume to also be examined as a way of determining how field uniformity varied with the overall dimensions of the VUT.

In addition to the above described measurements of field uniformity over the empty VUT a similar measurement was made of field uniformity around the DEUT inside the VUT. For this measurement the DEUT was positioned at the centre of the VUT and field measurements were made around three or-

thogonal rings, as shown in figure 4. Insertion gain

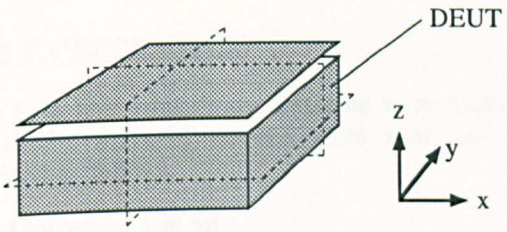


Figure 4: SDSE positions around the DEUT.

was measured at 40 positions around the loop in the xy-plane and 30 positions in each of the xz and yz plane loops, giving a total of 100 field points at each frequency.

The field pickup from the electric field (E) and induced current (H) sensors inside the DEUT was also measured for comparison with the field over the VUT and field around the DEUT.

## ANALYSIS OF DATA

The values of insertion gain for the measurement points were manipulated to obtain several useful quantities which were used for determination of the field uniformity within each measurement environment. The first quantity of interest was the absolute variation of the fields within the VUT, this was obtained by subtracting the minimum insertion gain value from the maximum insertion gain value present within the VUT at each frequency.

A typical histogram of field values within one of the environments at one frequency is shown in figure 5. This shows that the majority of the field values are close together but that a few are significantly different from the others. For this reason the values of absolute field variation were overly pessimistic and what was needed was a quantity that could be used to represent more typical field uniformity over the whole volume. The standard deviation of the field values was determined to be suitable for this.

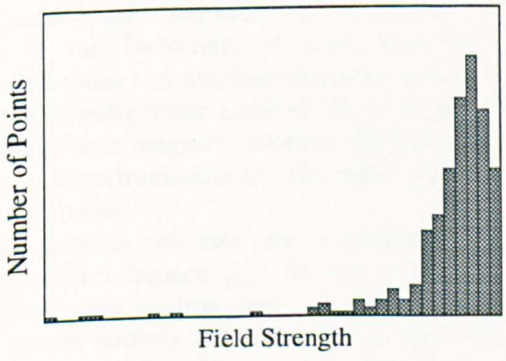


Figure 5: Typical histogram of field values.

Before the standard deviation or the average value of the field within the volume could be calculated, the data had to be transformed to a linear magnitude scale. This was done by dividing each insertion gain value by 20 and taking its base 10 inverse-logarithm. The average field at each frequency was then given by,

$$\overline{x} = \frac{1}{N}\sum_{i=1}^{N} x_i \qquad (1)$$

where $N$ was the total number of points i.e. $N = 343$ for the 7x7x7 VUT field array. The standard deviation of the $N$ insertion loss values was given by

$$\sigma = \sqrt{\frac{1}{N-1}\left[\left(\sum_{i=1}^{N} x_i^2\right) - N\overline{x}^2\right]} \qquad (2)$$

This value of standard deviation was then divided by the average field in the environment and converted back to decibels to obtain a quantity known as the normalised standard deviation (NSD). NSD was used together with absolute field limits to specify the uniformity of the field in each of the environments.

The normalised standard deviation is a somewhat unusual unit and so, in order to gain an idea of what it represents, certain properties of it will be mentioned here. NSD is a negative value in decibels and a value of -20 dBav (decibels relative to the average) would correspond to a typical field variation of 10% i.e. $1\,\mathrm{Vm}^{-1}$ in an average field of $10\,\mathrm{Vm}^{-1}$. An NSD of $-\infty$ dBav corresponds to a totally uniform field and so the more negative a value of NSD is, the more uniform is the field it describes.

The same mathematical approach as above was used to analyse the uniformity of the fields measured around the DEUT, except that in addition to analysing the data for the three rings around the DEUT together, they were also each analysed individually to give the field uniformity in each plane.

The reciprocal excitation method with the SDSE, as described above, was not used to obtain the field pickup signals from the DEUT at the centre of the VUT in each environment. The stripline or biconical antenna was driven in the usual way from a power amplifier and the pickup signals from the E and H field sensors inside the DEUT were measured. They were normalised to the average field measured over the entire empty VUT, the field measured at the centre of the empty VUT and also the field measured around the DEUT in the VUT.

It is shown later in this paper that the field generated within a stripline cell on an open-area test site is very uniform and as ideal as can be obtained. For this reason the normalised pickup signals from the DEUT in this environment were treated as its ideal response to a plane wave illumination. The normalised pickup signals from the DEUT in all other environments were compared with this ideal response so that the usefulness of the field measurements over the empty volumes and around the DEUT could be

assessed as a measurement of the DEUT response to an effective field.

## THE ENVIRONMENTS

The field uniformity measurements were performed on eleven different environments that are summarised as follows.

1. Open-area test site.
   (a) biconical antenna 3 m from VUT.
   (b) stripline cell.
2. Semi-anechoic Chamber (8.60 × 4.64 × 3.60) m (L,W,H)
   (a) biconical antenna 1 m from VUT.
   (b) biconical antenna 3 m from VUT.
3. Screened room (4.48 × 2.24 × 2.24) m.
   (a) illuminated with biconical antenna.
      i. undamped.
      ii. damped with carbon loaded foam.
      iii. damped with ferrite tiles.
   (b) illuminated with stripline cell.
      i. undamped.
      ii. damped with carbon loaded foam.
4. Screened room (6.35 × 3.05 × 3.05) m. Biconical antenna.
   (a) undamped.
   (b) damped with carbon loaded foam.

The smaller screened room and open-area test site were at the University of York and the larger screened room and anechoic chamber were provided by RFI Investigations Limited. It is not possible to enclose precise diagrams showing the layout of all of the above environments but the main points will be outlined below.

The stripline cell used was constructed in accordance with reference [1]. It was centred in the screened room environments, as shown in figure 6, and placed midway along the site axis on the 10 m open-area test site. The damping that was used in the smaller screened room was in the form of 16 blocks of carbon loaded foam that were built into a wall, 2 blocks high, around the stripline cell at a distance of 30 cm as shown in the figure.

Excitation with the biconical antenna was conducted with the horizontal separation between it and the front of the VUT as defined in the above list and with the antenna mounted on a tripod at a height of 1.26 m. The VUT was placed above a wooden table with its base at a height of 1 m above the floor of each environment and, as with all of the measurements in this paper, the antenna and SDSE were both vertically polarised. A typical arrangement that was used in the screened rooms is shown in figure 7. A minimal amount of damping material was used in both rooms in accordance with the mode suppression technique proposed in [2]. The arrangement of the six carbon loaded blocks that were used in the small screened room is shown in figure 7; a larger number of blocks were used in the same relative positions in the larger screened room.

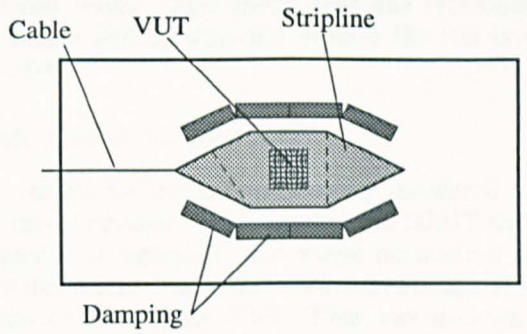


Figure 6: Excitation with stripline in screened room damped with carbon loaded foam.

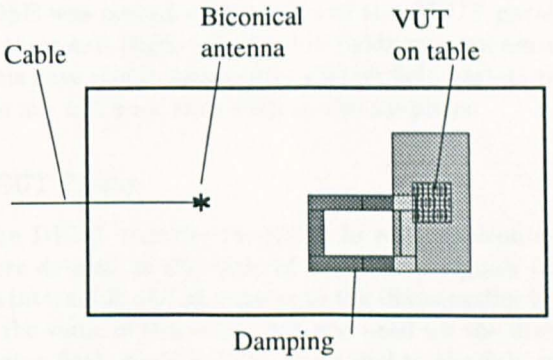


Figure 7: Excitation with biconical antenna in screened room damped with carbon loaded foam.

The damping with ferrite tiles was also a minimal damping technique [2] and involved placing the tiles in specified positions on the floor and walls of the room in order to extract maximum energy from the lower order modes.

## RESULTS

A vast amount of data was gathered during this project and it would be impossible to present all of it in this paper but instead it will be summarised here and the general results commented upon.

### Fields Over the Empty Volume

The results for the field uniformity over the cubic volume for frequencies between 30 and 200 MHz are summarised in table 1. The environments are de-

| Environment | DIF dB | LIM dB | NSD dBav |
|---|---|---|---|
| 1a | 2 | 5 (9) | -19 (-13) |
| 1b | 0.5 | 5 (7) | -22 (-18) |
| 2a | 1 | 6 (15) | -18 (-7) |
| 2b | 3 | 6 (13) | -14 (-6) |
| 3ai | 2 (31) | 8 (56) | -14 (-1) |
| 3aii | 2 (5) | 13 (62) | -14 (-3) |
| 3aiii | 2 (14) | 11 (46) | -14 (-3) |
| 3bi | 2 (13) | 11 (56) | -18 (-3) |
| 3bii | 2 (6) | 10 (36) | -18 (-6) |
| 4a | 2 (15) | 10 (53) | -17 (-2) |
| 4b | 1 (18) | 13 (46) | -13 (-4) |

Table 1: Results of measured field uniformity over the empty VUT.

noted by their labels from the listing in the previous section and the three righthand columns give different parameters that were used to describe the field uniformity. DIF is the difference between the average field calculated over the total volume and the average field calculated over the two smaller concentric cubic volumes within it. LIM is the absolute field variation over the total volume, i.e. the difference between the maximum and minimum field within it, and NSD is the standard deviation of the fields over the volume normalised to the mean.

The screened room environments, 3 and 4, are highly resonant and so the field uniformity within them was far worse at their resonant frequencies. This made it difficult to define typical field uniformity values for them across the whole frequency range and so a typical value between resonances is given in table 1 together with a worst case figure at resonance in brackets.

The results from the larger screened room indicated a slightly smaller absolute variation of its fields than those in the smaller room, but that its fields were subject to high uncertainty over a much larger proportion of the frequency range. This is due to its larger volume resulting in a greater mode density and lower cutoff frequencies for all of the propagating modes.

The results for the stripline cell in the non-resonant environments show that the field within it is much more uniform than the field generated by the biconical antenna. This advantage over the biconical antenna is also clear in the small screened room damped with carbon loaded foam.

Both the ferrite and carbon loaded foam damping techniques had a smaller effect on the fields with the biconical antenna in the screened rooms than was expected. The reasons for this have to be investigated further and better damping techniques need to be developed. The damping with carbon loaded foam caused a very noticeable improvement in the field uniformity inside the stripline cell in the small screened room. This shows that the technique of building a wall of absorber around the cell is very effective.

### Fields Around the DEUT

The results for the field uniformity measured along the three concentric rings around the DEUT showed greater field variations and worse normalised standard deviations than did the corresponding measurements on the empty VUT. This was because the SDSE was closely coupled to the DEUT, as would any other field probe be. The field components parallel to the conducting surfaces of the DEUT were effectively shorted out close to it so that when the SDSE was moved up the sides of the DEUT parallel to the z-axis (figure 4) very low fields were measured. This gave rise to apparently greater field variation in the xz- and yz-planes than in the xy-plane.

### DEUT Pickup

The DEUT transfer functions in each environment were defined as the ratio of the pickup signals from its internal **E** and **H** sensors to the illuminating field. If the value of the value that was used for the illuminating field over the VUT was equal to the field perceived by the DEUT, these transfer functions should have been the same in each environment. The value of the average field over the empty VUT yielded more consistent transfer functions for the environments than did using the field at the centre of the VUT or the average field measured around the DEUT.

Having determined that the field perceived by the DEUT was not exactly the same as the field measured over the VUT in all of the environments, it was necessary to determine the **E** and **H** transfer functions for plane wave illumination. This would enable the representability of the average fields over the VUTs for describing the perceived field illuminating the DEUT to be assessed. It was not possible to achieve plane wave illumination of the DEUT, but the field within the stripline cell on the open area test site had already been found to be considerably more uniform than that in any of the other environments. Hence, the **E** and **H** transfer functions in this environment were treated as the response of the DEUT to plane wave illumination.

The transfer functions of the DEUT pickups to the average fields in each of the other environments were normalised to the one for the DEUT in the stripline cell on the open area test site. From this the representability of average field for describing the perceived field illuminating the DEUT in each environment was found. The results are shown in table 2.

Table 2 gives the average errors that resulted from using the average field over the VUT to describe the field illuminating the DEUT in each environment;

| Environment | E | H |
|---|---|---|
| 1a | 3 (17) | 3 (12) |
| 1b | | |
| 2a | 3 (11) | 4 (13) |
| 2b | 3 (11) | 3 (12) |
| 3ai | 3 (13) | 5 (37) |
| 3aii | 3 (20) | 5 (26) |
| 3aiii | 3 (19) | 4 (23) |
| 3bi | 5 (22) | 5 (25) |
| 3bii | 3 (10) | 3 (11) |
| 4a | 10 (38) | 10 (36) |
| 4b | 7 (28) | 8 (23) |

Table 2: Limits of the representability of the average field over the VUT for describing the perceived field by the DEUT.

a worst case figure is also given in brackets. The results show that average field over the VUT is a good measure of field illuminating the DEUT in the anechoic chamber and adequate for describing it in the damped smaller screened room with illumination from a biconical antenna. The results from the larger screened room are considerably worse than the other environments, even with damping, and so there are serious problems with this environment. The result for the stripline cell in the smaller screened room is particularly good and indicates that this environment is as good as the semi anechoic chamber.

An attempt was made to relate the normalised standard deviation values of the fields within each VUT to the results in table 2, and it was found that as NSD became greater, the volume fields became less representative of the perceived illuminating field. As a rough guide it was found that NSD should be less than -13 dBav for the field to be sufficiently uniform for average field over the VUT to be used to describe it.

## CONCLUSIONS

The results of this work show that, even in nominally well behaved environments such as semi anechoic chambers, the field uniformity levels, and hence the repeatability of radiated susceptibility measurements may not be as good as expected. Semi anechoic chambers are still the best environments to use but, when they are not available, similar uniformity levels can be obtained with stripline cells in damped screened rooms.

It appears that lightly damping screened rooms only creates a modest improvement in field uniformity and so must be approached with caution. Also the use of large screened rooms is not a good idea because the increased number of propagating modes inside them causes their fields to be less uniform than those in smaller rooms.

There is also a fundamental misconception associated with measuring the field illuminating an EUT close to it in the measurement environment. The measured field in this case is not the illuminating field but is the sum of the illuminating and the scattered fields from the EUT and so will inevitably be less uniform. For this reason it is the average field over the volume occupied by the EUT before it is placed into the environment that should be measured and used as the illuminating field.

The standard deviation of the fields over the volume must also be measured for any environment that is used for susceptibility measurements to verify that it is at least 13 dB down from the mean field in the volume. Use of environments that do not satisfy this criterion will result in unrepeatable measurements that have little meaning.

## ACKNOWLEDGEMENT

The authors would like to thank the DTI for their generous support of this project and also to thank RFI Investigations Ltd for the use of their test facilities.

## REFERENCES

[1] British Standards Institution, Electromagnetic Compatibility for Industrial-Process Measurement and Control Equipment, BS 6667, part 3, 1985.

[2] L. Dawson *New Techniques for the Measurement of Radiated Emissions in a Screened Room for Frequencies up to 200 MHz*, Uni. of York, D. Phil. Thesis, Dep't of Electronics, 1989.

# COMPUTER AIDED DESIGN FOR RADIO-FREQUENCY INTERFERENCE REDUCTION

A. C. Marvin, J. M. Tealby, T. J. F. Carr-Brion, S. J. Porter and S. M. Mann

University of York, England

## ABSTRACT

This paper describes the requirements for a Computer Aided Design (CAD) package to predict radiated emissions from electronic equipment and to aid their reduction. Input for the package is obtained from a suite of CAD tools covering electrical and mechanical aspects of electronic equipment design. An electromagnetic solver using a Method of Moments technique is described and its current performance is indicated. The methods and problems of interfacing the package with the existing CAD packages are described, as are some of the challenges facing future users of integrated packages of this type.

## INTRODUCTION

The current trends towards the use of microprocessor based equipment in commercial and domestic environments for many forms of information processing and storage, and the use of many more types of radio systems for personal communications and some control systems have led to an increase in interference problems. As a result the European Community has produced the infamous Electromagnetic Compatibility (EMC) Directive and part of the minds of electronic equipment designers are now concentrated on problems associated with the reduction and control of interference.

For many designers this is a new area of concern and the level of knowledge is relatively low. Electromagnetics was never a popular subject with engineering students, the perceived conceptual difficulties being only matched by the quality of teaching of the subject in many institutions. Continuing education, in various forms, is attempting to overcome the knowledge gap, but the imminence of 1992 and the limited event horizons of much of industry have caused many of the courses to be oriented towards the quick-fix and recipe approach rather than a prescriptive philosophy for EMC. Thus there is a need for Computer Aided Design (CAD) tools to incorporate EMC considerations along with other design aspects. This paper describes our philosophy and approach to the production of such a CAD tool.

## THE PROBLEM

An electronic instrument is a complex device with many aspects to its design – it is seldom that one designer is responsible for the entire design. The electronic design may be undertaken with no reference to the mechanical design of the equipment enclosure, nor to the eventual circuit layout. The enclosure design may be done at a later stage than the electronic design and circuit layout, when the thermal properties of the electronic design are known. In each design activity several designers may be involved. If EMC is not a consideration then this design activity separation is possible because, with the exception of thermal design, the different performance aspects do not interact. The gain of an amplifier is not dependent on the equipment enclosure material or the orientation and position of the amplifier on the circuit card. For thermal analysis the interaction can be unilateral – once the thermal requirements of the electronics are known, the enclosure and cooling equipment can be designed to cope.

The EMC aspects of the design do not respect such design-process demarcation. The radiated emission performance of a design depends on the logic family used in implementation, the circuit card layout, its orientation within the enclosure and the enclosure material and construction. Power and interconnection cables are critical, with the conducted emissions also being part of the problem. The immunity of a design is also of concern. It should be noted that the principle of reciprocity applies only to the electromagnetic aspects of the design. If low emissions are a consequence of good screening then the design is likely to have good immunity; if low emissions are a consequence of a low power logic family then the design may have poor immunity. All the electromagnetic aspects of the design interact.

Good design, incorporating EMC considersations, should therefore involve considerable interaction between all the design stages. Such interaction, if it is among the designers themselves, presupposes a common body of knowledge of electromagnetics among the designers which is unlikely to exist. It also constrains the timing of the various design activities. If an integrated CAD package were to exist which brings together all the relevant aspects of design for EMC, then many of the problems could be solved.

However, the design and implementation of such a package is not straight forward. Assuming that the electromagnetic problems can be solved with sufficient accuracy within an acceptable time, the problems of communication between the package and the designers still remain. In what forms are the outputs from the package required, and at what stage of the design process are they required? How do the outputs help the design process? How do they influence the individual designers, and the design team as a whole? The outputs must be in a form that is comprehensible to all the users whatever their engineering background. The use of such a package may force some re-training of the users so that they can make use of the output.

It can be seen that the production of an integrated CAD package to assist in the design of electronic equipment raises problems that have not been apparent to the same extent in other CAD packages for the electronics industry. Potentially the most intractable of the problems are not the electromagnetic ones but those associated with the use of the package and the mis-match in expertise that may exist between the users. In this respect any such package will be unusual as most CAD packages only address one aspect of design whereas the EMC package must make use of information associated with all aspects of the design. It must also be used in a way that the source of the information, for instance a mechanical design package concerned with the enclosure, may not be configured for.

## SOLUTION OF THE ELECTROMAGNETIC PROBLEM

The package under development is designed to produce an estimate of the radiated emissions from electronic equipment. Packages with similar aims have been developed in the past, but these only operate at circuit card level and do not take into account the rest of the equipment structure. The frequency range of interest covers not only the conventional 30MHz to 1GHz range of EMC radiated emissions concern, but also lower frequencies, for example those of interest for magnetic field hazard assessment. Thus the size of the equipment is comparable to that of the wavelength at the higher frequencies and negligible compared to the wavelength at the lower frequencies. The type of field solution employed then depends on the frequency, the higher frequencies requiring a more complex solution. In our implementation of the solution we have used a Method of Moments approach for the radiation solution in the 30MHz to 1GHz range while a simpler assessment of dipole moments will be used for lower frequencies.

Both the electromagnetic solutions mentioned above are frequency domain approaches and thus the electromagnetic solutions have to be repeated for each spectral component of the radiation. In the case of the Method of Moments solution, the segmentation of the structure can be the same over a substantial frequency range, with the whole range split into two or more sub-ranges with finer segmentation for the higher frequency range. If $n$ is the number of segments then the solution time for each frequency is proportional to $n^3$ for large numbers of segments. A possible time reduction for multiple frequency solutions with relatively small frequency increments may be obtained by using an iterative approach, the first estimate for a solution being the solution from the previous frequency. In the case of the low frequency dipole solution the computation is much simpler, requiring only the frequency and current magnitude information.

The number of solution-frequencies required depends on the equipment circuit architecture. Digital circuits, controlled by a clock, have well defined line spectra associated with the clock frequency harmonics with intermediate spectral components at subharmonic intervals defined by data word-lengths. When information is processed a continuous background spectrum is present between the clock harmonics. In general it is observed that the clock harmonics are the dominant signals in radiated emission measurements and so the emission profile can be sufficiently well defined by these alone. This is shown in figure 1 which shows part of the emission spectrum from a computing audio spectrum-analyser. It can be seen that the regularly spaced clock spectral lines are dominant in both housekeeping and data-processing modes.

In most devices, such as VDU's or workstations, analogue signals in the form of video information are restricted in bandwidth to below 100MHz. However, the majority of the energy is still associated with line spectra as most video displayed consists of alpha-numerics with a fixed spatial periodicity on the screen translating through the raster scan to time-periodic waveforms. The raster scan waveforms are also rich in harmonics of the line rate, but mainly fall in the lower frequency dipole solution range, as do keyboard scanning signals.

For the Method of Moments solution the circuits within the equipment form the sources exciting the structure of the equipment. Two excitation routes are possible. On circuit cards without ground and supply planes the tracks carrying clock signals can interact with the other conductors in the structure in the inductive or radiative manner accounted for by the Method of Moments. Shielded cards will excite the structure through radiation from the currents on the conductors connecting them to other parts of the equipment, this mechanism also being

the case with unshielded cards.

The major aim of this work is to predict the performance of equipment which is not housed in a shielded enclosure. Much equipment is housed in non-metallic cases with poor shielding effectiveness and which have large apertures for displays. A substantial part of the research is concentrating on the interaction between dielectric bodies with partial conductivity and the primary conducting structure of the equipment. This work is described in [1].

The overall solution attempts to predict a radiated emission profile of the equipment on an open-field test site. As the operating environment of each item of equipment cannot be defined, the EMC standards require testing to specifications the physical layout of which mimic in a simplified way an average environment. Since the equipment will only be tested on an open-field site, the radiated emission computation will be performed assuming that the equipment is on a perfect example of such a site as defined in CISPR-16. Were the solution of the computation perfectly accurate, then the error between the simulation and the measured performance would be limited by the permissible site imperfections. The type of solution outlined here accounts for the interactions of the site groundplane with the equipment. Also any power and signal cables connected to the equipment will be accounted for. The solution for the complete structure has a current distribution which is a function of the equipment construction and layout. This includes cables and site groundplanes which have to be defined in a standard form in the CAD package. The sources in the equipment then excite the whole structure.

Work on a parallel processing technique for a Method of Moments solution is also underway [2]. The computational speed advantages of such a technique may make it worthwhile implementing a separate multi-processor add-on machine, hosted by the CAD workstation, solely for the electromagnetic solution. Processor efficiencies of greater than 90% have been obtained for preliminary problems on 5 – 128 node machines, which would mean that an add-on solver with $N$ nodes would achieve a factor $0{\cdot}9N$ saving in computational time. For example, for a 5 node machine, $N = 5$, the solution would take only $0{\cdot}22$ of the time taken by a single processor. The multi-processor machine may also be applicable to thermal analysis problems.

## INPUTS AND OUTPUTS

The data input files to the EMC CAD package are to be obtained from existing Mentor Graphics circuit design packages (NETED, MSPICE, QUICKSIM and LAYOUT) and 3D mechanical modelling package (PACKAGE), all running on Apollo 3550 workstations. Output from the schematic editor tool, NETED, and from the analogue and digital simulation tools, MSPICE and QUICKSIM respectively, defines the necessary electrical information for all the PCB's. This is then combined with the physical geometry information from the placement and layout tool, LAYOUT, to give a complete definition of all the required properties of the PCB's. The 3D mechanical package then shows how each board is oriented in space and gives the positions of all the interconnections, casing, etc., completing the description of the entire piece of equipment.

The level of detail required in both the mechanical description and electrical excitation will be determined by the desired accuracy of the solution and the speed of solution. Our current Method of Moments solver takes 3·5 hours to solve a 600 segment structure. While this segmentation level may be appropriate for a complete device at the highest frequencies, substantially smaller segmentation levels will be appropriate for the lower frequencies – the eventual segmentation complexity and solution accuracy need only match the precision of the EMC tests themselves. Open-field site specifications require the measured site attenuation to be within ±4 dB of the theoretical value for a perfect site. A reasonable level of accuracy for the predictions of radiated emissions would match this figure. Currently, our predictions for trial structures are all within 10 dB of values measured on the York open-field site. Our predictions of field values compared to NEC3 are within 1%.

This part of the package design lends itself to the application of an "expert system" approach. For example, the segmentation details should only be derived from the 3D package with no operator interaction, although it may be desirable for the operator to be presented with the information for verification purposes. Similarly, if the circuit simulation packages produce a pulse train with a null in the spectrum envelope at one of the clock harmonic frequencies, then the solution for that frequency would not be required.

The outputs of the package are in two forms. An emission profile is the ultimate output which shows a prediction of the fields radiated by the equipment as measured on a perfect open-field test site. This can then be compared with the appropriate specification. The intermediate output, of more use for diagnostics, is a mapping of the set of most significant currents and fields giving rise to radiation from the equipment. The designers would use this to experiment with the positioning and orientation of sub-systems within the equipment, and also the design and construction of partial shields around the equipment. At this stage in the design of the total package, the final details of the outputs are yet to

be decided. Collaboration with the research sponsors through experimentation with different output formats will determine the final form of the output.

## CONCLUSIONS

We have described the philosophy adopted for the implementation of a CAD package to be used in conjunction with other CAD packages for the prediction of the radio-frequency radiated emissions generated by electronic equipment. In principle the package could also produce a conducted emission profile. We have not, however, addressed the problems of conducted and radiated immunity at this stage in the research. Much work remains to be done on the implementation of the package, in particular on the extraction of data files from the existing packages.

We foresee possible problems for the users. For example, a number of designers who do not share a common expertise base may be required to use the package for the design of the equipment. However, this enforced co-operation is likely in time to lead to better overall design.

Designing to achieve EMC is an example of the increasing complexity of the design process, and the use of CAD packages of the type described here is certain to increase in the future.

## ACKNOWLEDGEMENTS

This work is being funded by Lynwood Scientific Developments Limited in collaboration with the DTI.

## REFERENCES

[1] Carr-Brion, T.J.F. and Porter, S.J., *Prediction of PCB Radiation in the Presence of Scattering Bodies*, These proceedings.

[2] Chege, G.W., Taylor, R.W. and Tealby, J.M., *Parallel Modelling of Electromegnetic Field Radiation and Scattering for Coupled Antenna-Dielectric Systems*, 6th Annual Review of Progress in Applied Computational Electromagnetics, To be published.

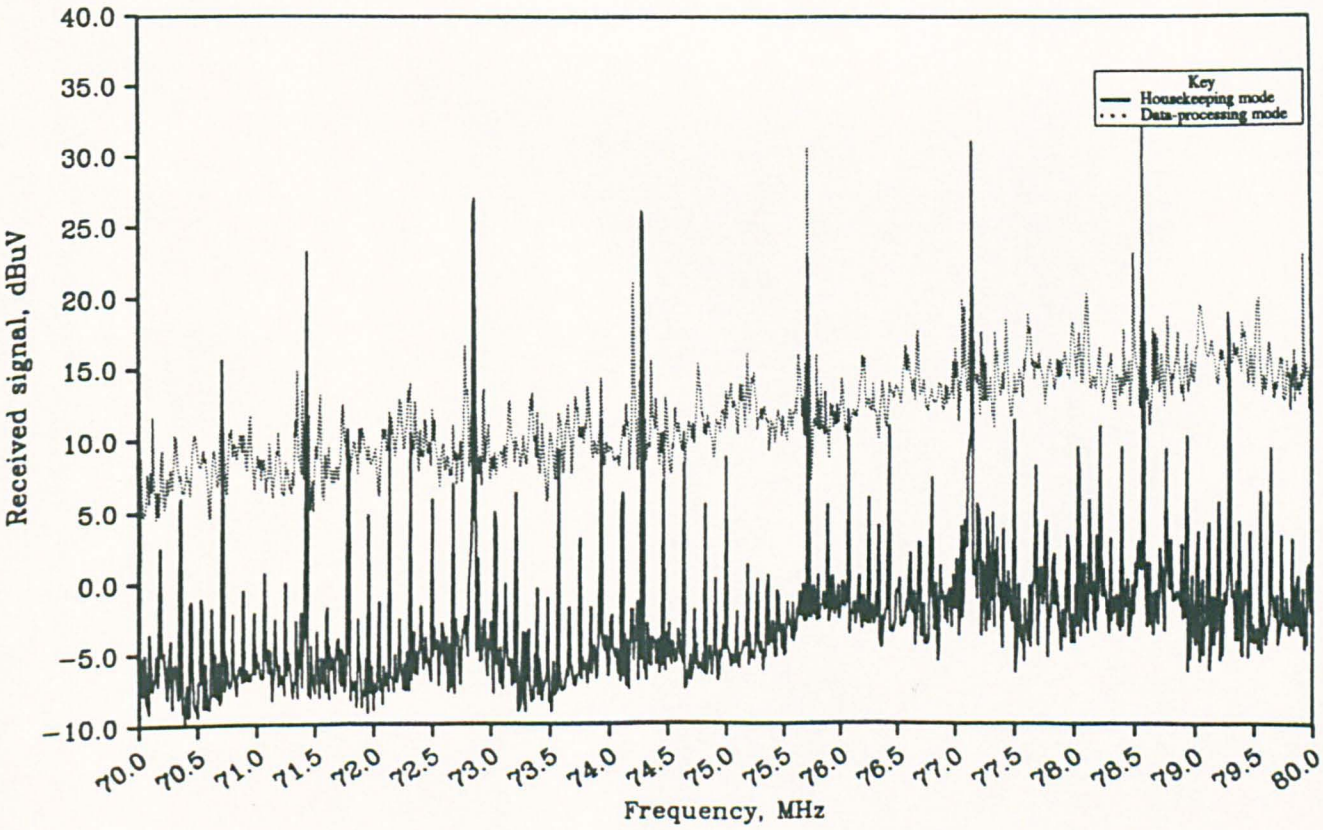


Figure 1: Part of the emission spectrum from a computing audio spectrum-analyser